

Development of Novel Catalysts for the Photocatalytic Hydrogen Formation

Dissertation

zur Erlangung des akademischen Grades
doctor rerum naturalium
(Dr. rer. nat.)

vorgelegt dem Rat der Chemisch-Geowissenschaftlichen Fakultät der
Friedrich-Schiller-Universität Jena

von Diplomchemiker Thomas David Pilz
geboren am 24. Mai 1982 in Rochlitz, Deutschland

Gutachter:

1. Prof. Dr. Sven Rau
2. Prof. Dr. Ulrich S. Schubert
3. Prof. Garry S. Hanan

Tag der öffentlichen Verteidigung: 16. 11. 2011

Diese Arbeit entstand auf Anregung und unter Anleitung von Prof. Dr. Sven Rau und Prof. Dr. Matthias Westerhausen im Zeitraum von Januar 2008 bis Juni 2011 am Institut für Anorganische und Analytische Chemie der Friedrich-Schiller-Universität Jena.

Den Herren Prof. Dr. Sven Rau und Prof. Dr. M. Westerhausen danke ich ganz herzlich für ihre langjährige und großzügige Unterstützung und Förderung, die interessante und zukunftsrelevante Themenstellung und die damit verbundenen, stets aufschlussreichen und inspirierenden Diskussionen.

Der *Carl-Zeiss-Stiftung* danke ich für die Gewährung und Verlängerung eines großzügigen Promotionsstipendiums.

Weiterhin danke ich dem Bayerischen Hochschulzentrum für Mittel-, Ost- und Südosteuropa *BAYHOST* für ein Reiestipendium nach Lviv (Ukraine). Dem DFG Graduiertenkolleg 1626 *Chemical Photocatalysis* danke ich für die finanzielle Unterstützung bei der Teilnahme an der ISPPCC Konferenz in Strasbourg (Frankreich) sowie für die vielen Weiterbildungsangebote.

Außerdem danke ich meinen Kooperationspartnern, der Arbeitsgruppe von Prof. Dr. D. M. Guldi aus Erlangen, speziell K. Peuntinger, und der Arbeitsgruppe Prof. Dr. B. Dick aus Regensburg, speziell R.-J. Kutta, für die photophysikalischen Untersuchungen an den Rutheniumkomplexen. Weiterhin danke ich der Arbeitsgruppe von Herrn Prof. Dr. T. Drewello aus Erlangen, speziell J. Li, für die Durchführung detaillierter massenspektrometrischer Untersuchungen und Prof. Dr. J. G. Vos aus Dublin für das Mitwirken an der Arbeit zu den NHC-Komplexen. Zudem sei meiner gesamten Arbeitsgruppe und den Arbeitsgruppen von Prof. Dr. H. Kisch, Prof. Dr. K. Meyer und von Prof. Dr. M. Westerhausen, speziell Dr. C. Koch, für die angenehme und freundschaftliche Atmosphäre im Laboralltag gedankt.

An dieser Stelle möchte ich mich bei allen Mitarbeitern des IAAC in Jena und des IAC in Erlangen bedanken, die mich bei der Anfertigung dieser Arbeit unterstützt und zu ihrem Gelingen beigetragen haben. Insbesondere bedanke ich mich bei Herrn Dr. M. Friedrich, Frau A. Blayer und Frau B. Rambach für die Aufnahme von NMR-Spektren in Jena sowie bei den Herren Dr. A. Zahl und Dr. M. Moll für Einweisung und Hilfestellungen bei der Bedienung der NMR-Spektrometer in Erlangen. Herrn Dr. W. Poppitz, Frau M. Heineck und Frau S. Schönau aus Jena danke ich für die Durchführung weiterer massenspektrometrischer Untersuchungen. Zudem danke ich Frau R. Suxdorf, Frau H. Schönfeld, Frau B. Lentvogt und Frau C. Wronna für die Anfertigung der Elementaranalysen in Jena und Erlangen. Herrn Dr. H. Görls aus Jena und Dr. F. W. Heinemann aus Erlangen möchte ich für die röntgenstrukturanalytischen Untersuchungen sowie die anregenden Diskussionen danken. Für Mitbenutzung der Glovebox und die Bereitstellung der Geräte zur Cyclovoltammetrie und der Inertlösemittelanlage danke ich dem Erlanger Arbeitskreis von Prof. Dr. K. Meyer und speziell Dr. R. Beranek, Frau C. Vogel und Herrn B. Kosog. Herrn M. Pfeffer und Herrn S. Hansen danke ich für die photokatalytischen Vorversuche und Hilfestellungen bei der Handhabung der GC-Apparatur. Bei Herrn M. Schaub möchte ich mich besonders für die gute Zusammenarbeit bei den DLS-Untersuchungen bedanken. Zudem möchte ich speziell Herrn N. Rockstroh, Frau T. Makarowa sowie K. Peuntinger und K. Tenbrink für das ausführliche Korrekturlesen danken.

Den Arbeitsgruppen von Prof. Dr. U. S. Schubert bzw. PD. Dr. M. Gottschaldt aus Jena und von Prof. Dr. S. Yano aus Kyoto danke ich für die Ermöglichung des zweimonatigen Japanaufenthalts am Katsura Campus der Kyoto University. Zudem danke ich besonders meinen Kollegen Dr. H. Ohi und K. Babiuch für die erlebnisreiche Zeit dort.

Weiterhin gilt mein Dank all meinen Labor- und Teamkollegen, im Einzelnen den Herren Dr. M. Schwalbe, Dr. M. Auth, Dr. M. Karnahl und Dr. S. Losse aus Jena sowie meinen neuen Teamkollegen aus Erlangen, den Damen K. Monczak, E. T. Kastl, S. Zheng, J. Schneider, D. Kramer, E. Kowalska und den Herren Dr. C. Koch, N. Rockstroh, R. Staehle, M. Pfeffer, M. Schaub, C. Pehlken für den stets anregenden fachlichen und nicht-fachlichen Gedankenaustausch.

Besonderer Dank gilt meinen Praktikantinnen R. Messerer, L. Mbogo-Wachira und K. Ritter die unterstützende Versuche zum Bisphenanthrolintheema sowie zum Imidazophenanthrolintheema durchgeführt haben.

Insbesondere danke ich Michael Bessel und Kevin Stippich sowie allen weiteren Freunden und Kommilitonen, die mich über die Jahre so hilfreich unterstützt haben.

Ausdrücklich möchte ich mich bei meinen guten Freunden Kay Neumann, German Klink, Jörg Wiesehügel, Robert Staehle und Raquel Knickenberg bedanken, die mir mit vielen geselligen Stunden und angenehmen Unterhaltungen dabei geholfen haben, den Kopf wieder frei zu bekommen und Probleme von einem anderen Blickpunkt aus betrachten zu können.

Zum Schluss möchte ich mich besonders herzlich bei meinen Eltern und meiner Familie und meiner Freundin Katharina für ihre tatkräftige Unterstützung und speziell für ihren Zuspruch und ihre Ermutigungen bedanken, die mir stets ein großer Ansporn waren.

»And Lord, we are especially thankful for nuclear power,
the cleanest, safest energy source there is.
Except for solar, which is just a pipe dream.«

- HOMER SIMPSON^[1]

Contents

1	Introduction	1
1.1	<i>Fossil Fuels and Nuclear Power</i>	2
1.2	<i>Renewable Fuels</i>	5
1.3	<i>Energy Transformation and Storage</i>	6
1.4	<i>Solar Energy Conversion</i>	8
1.5	<i>Photosynthesis</i>	10
1.6	<i>Photocatalyzed Reactions</i>	13
1.7	<i>Mimicking Photosynthesis</i>	17
1.8	<i>Formalisms of Photocatalytic Systems</i>	19
1.9	<i>Multicomponent Systems from Fundamental Building Blocks</i>	21
1.9.1	<i>Photosensitizers - Light Energy Conversion</i>	23
1.9.2	<i>Redox Systems for Charge Separation</i>	29
1.9.3	<i>Oxidation Catalysts - Solar Fuels</i>	34
1.9.4	<i>Reduction Catalysts - Solar Fuels</i>	37
1.10	<i>Intramolecular Photoredoxcatalysts</i>	40
1.10.1	<i>Oligonuclear Coordination Compounds</i>	42
1.10.2	<i>State of the Art Systems</i>	46
1.10.3	<i>Drawbacks and Starting Points</i>	49
2	Scope of the Thesis	52
3	General Section	54
3.1	<i>Brominated Phenanthrolines - A Gate to new Bridging Ligands</i>	54
3.1.1	<i>Selective Bromination of Phenanthrolines</i>	57
3.1.2	<i>Ruthenium Complexes with Brominated Phenanthrolines</i>	63
3.1.3	<i>Structural Analysis</i>	69
3.1.4	<i>Photophysical Behavior</i>	71
3.1.5	<i>Emission Decay Dynamics</i>	76
3.1.6	<i>Electrochemical Characterization</i>	78

3.1.7	Concluding Remarks to phenBr-Ligands	82
3.2	Bisphenanthroline: A Suitable Molecular Bridge?	83
3.2.1	Preparation of phenphen and Related Complexes	85
3.2.2	Identification and Characterization	87
3.2.3	Structural Analysis	94
3.2.4	Photophysical Behavior	97
3.2.5	Excited State Dynamics	99
3.2.6	Electrochemical Characterization	104
3.2.7	Application in Light Driven Catalysis	106
3.2.8	Concluding Remarks on phenphen -Bridged Complexes	108
3.3	NN-NHC-Ligand bbip : Toward Second Generation Catalysts	110
3.3.1	NHCs and NHC Complexes	111
3.3.2	Imidazophenanthrolines: Toward Redox Stable Bridges	115
3.3.3	Structural Characterization of ip-Type Ligands	118
3.3.4	N,N'-Coordinated ip-Type Complexes	122
3.3.5	NHC-Coordinated ip-Type Complexes	124
3.3.6	Structural Characterization of Ruthenium ip-Type Complexes	130
3.3.7	Preparation of bbip-Bridged Catalysts	134
3.3.8	Spectroscopic Characterization	138
3.3.9	Excited State Dynamics of the bbip-Containing Ruthenium Complexes	145
3.3.10	Electrochemical Characterization	148
3.3.11	Application in Catalysis: Prove of Concept	151
3.4	Outlook, Exploratory Investigations and Perspectives	159
3.4.1	Manipulations, Involving the bbip -System	159
3.4.2	Electron Deficient bbip-Systems	161
3.4.3	NHC-Ligand edip : Further Development of Improved Catalysts	164
3.4.4	Concluding Remarks	173
4	Summary	174
5	Zusammenfassung	183

6 Experimental Section	193
6.1 Synthesis of the Organic Ligands	197
6.1.1 Bromination of Phenanthrolines - method L1	197
6.1.2 1-Substitution of 1H-Imidazoles - method L2	198
6.1.3 3-Substitution of 1-Substituted 1H-Imidazoles - method L3	198
6.1.4 5,6-Dibromo-1,10-phenanthroline - phenBr₂	199
6.1.5 5-Bromo-1,10-phenanthroline - phenBr	200
6.1.6 5,6-Dibromo-2,9-dimethyl-1,10-phenanthroline - phenMe₂Br₂	201
6.1.7 5,5'-Bis-1,10-phenanthroline - phenphen	202
6.1.8 1H-Imidazo[4,5-f][1,10]phenanthroline - ip	203
6.1.9 1-Benzyl-1H-imidazo[4,5-f][1,10]phenanthroline - bip	204
6.1.10 1,3-Dibenzyl-1H-imidazo[4,5-f][1,10]phenanthroline bromide - bbip	205
6.1.11 Attempted Synthesis of the triethylborane adduct of 1,3-dibenzyl-1H-imidazo[4,5-f][1,10]phenanthroline-2-ylidene - bbipBEt₃	207
6.1.12 1-Ethyl-1H-imidazo[4,5-f][1,10]phenanthroline - eip	207
6.1.13 3,3'-(2,3,5,6-tetramethyl-1,4-phenylene)bis(methylene)bis-(1-ethyl-1H-imidazo[4,5-f][1,10]phenanthroline-3-ium) dibromide - edip	208
6.1.14 5,10-Dibromo-1H-imidazo[4,5-f][1,10]phenanthroline - Br₂ip	210
6.1.15 1,3-Dibenzyl-5,10-dibromo-1H-imidazo[4,5-f][1,10]phenanthroline bromide - Br₂bbip	210
6.2 Synthesis of the Metal Complexes	211
6.2.1 Synthesis of $[Ru(\widehat{LL})_2(\widehat{LL}')]^{2+}$ -type complexes - method C1	211
6.2.2 Synthesis of $[Ag(NHC)X]$ -type complexes from azolium salts - method C2	211
6.2.3 Transmetalation of $[Ag(NHC)X]$ -type complexes - method C3	212
6.2.4 $[Ru(tbbpy)_2(\text{phen-5-Br})][PF_6]_2$ - Ru(phenBr)	212
6.2.5 $[Ru(tbbpy)(\text{phen-5,6-Br}_2)][PF_6]_2$ - Ru(phenBr₂)	213
6.2.6 $[Ru(\text{phenBr}_2)_2Cl_2]$ - Ru(phenBr₂)Cl₂	215
6.2.7 $[Ru(\text{phenBr}_2)_2(tbbpy)][PF_6]_2$ - Ru(phenBr₂)₂	215
6.2.8 $[Ru(\text{phenBr}_2)_3][PF_6]_2$ - Ru(phenBr₂)₃	217
6.2.9 $\{[Ru(tbbpy)_2]_2(\mu\text{-phenphen})\}[PF_6]_4$ - Ru(phenphen)Ru	218
6.2.10 $[Ru(tbbpy)_2(\text{phenphen})][PF_6]_2$ - Ru(phenphen)	219

6.2.11	$[\{Ru(tbbpy)_2\}(\mu\text{-phenphen})\{PtCl_2\}][PF_6]_2$ - Ru(phenphen)Pt	221
6.2.12	$[Ru(tbbpy)_2(ip)][PF_6]_2$ - Ru(ip)	222
6.2.13	$[Ru(tbbpy)_2(bip)][PF_6]_2$ - Ru(bip)	224
6.2.14	$[Ru(tbbpy)_2(bbip)][PF_6]_3$ - Ru(bbip)	225
6.2.15	$[Ru(tbbpy)_2(bbip)]Cl_3$	227
6.2.16	Attempted Preparation of $[(bbip)AgBr]_n$ - (bbip)Ag	228
6.2.17	$[\{(tbbpy)_2Ru\}(\mu\text{-bbip})\{AgCl\}]Cl_2$ - Ru(bbip)Ag	228
6.2.18	Attempted Synthesis of $[\{(tbbpy)_2Ru(\mu\text{-bbip})\}_2Ag][PF_6]_5$ - Ru(bbip)Ag(bbip)Ru	230
6.2.19	Attempted Synthesis of $[(tbbpy)_2Ru(bbip)BEt_3][PF_6]_2$ - Ru(bbip)BEt₃	231
6.2.20	$[\{Ru(tbbpy)_2\}(\mu\text{-bbip})\{Rh(cod)Cl\}]Cl_2$ - Ru(bbip)Rh	231
6.2.21	$[\{Ru(tbbpy)_2\}(\mu\text{-bbip})\{PdCl_2\}]Cl_2$ - Ru(bbip)Pd	232
6.2.22	Attempted Synthesis of $[Ru(tbbpy)_2(Br_2bbip)][PF_6]_2$ - Ru(Br₂bbip)	233
6.2.23	$[Ru(tbbpy)_2(eip)][PF_6]_2$ - Ru(eip)	234
6.2.24	$[\{Ru(tbbpy)_2\}_2(\mu\text{-edip})][PF_6]_6$ - Ru₂(edip)	236
6.2.25	$[\{(tbbpy)_2Ru\}_2(\mu\text{-edip})\{AgCl\}_2]Cl_4$ - Ru₂(edip)Ag₂	237

7 Appendix

238

1 Introduction

The exhaustive use of cheap and abundant resources was always the most important stimulus for the industrial revolution, boosting economic growth, scientific development and social prosperity. Considering ethical and environmental aspects secondary, society followed the call for competitiveness, development and growth with mainly social, economical and political interests on the agenda.

But maintaining this course is very energy intensive and becomes noticeable in a huge imbalance of total worldwide energy consumption and regeneration. To give an example, in 2008, about 470 exajoules ($4.7 \cdot 10^{20}$ J) of energy were used (produced from fuels), which is equivalent to an average power production/consumption of 15 terawatts ($1.5 \cdot 10^{13}$ W), but only the fraction of 61 exajoules (regeneration rate = 13%) came from renewable sources, which means that 87% could not be restored (see figure 1).^[2, 3]

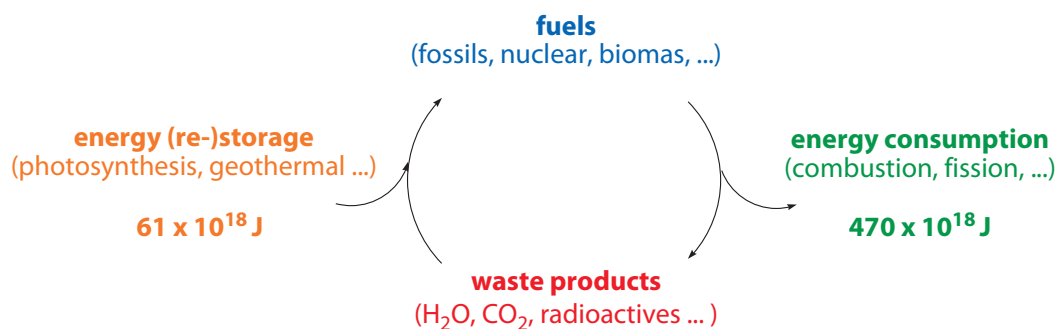


Figure 1: General energy flux diagram for the use of energy by mankind.

As a result of this modern desire for accelerated industrialization and globalization, world population grows and raises its living standard on the expense of infamous handling of nature and dissipative usage of resources. Every day, along with worldwide growing energy consumption, environmental destruction and pollution increases. In the same way fossil energy resources decrease at an ever faster rate. The exponentially growing number of energy consuming processes counters all advances in efficiency and sustainability, with the result that half of all the energy utilized since the beginning of the industrial revolution has been consumed within the last twenty years.^[3] Especially developing countries like India, China or Brazil will accelerate this process in the intermediate future.^[3]

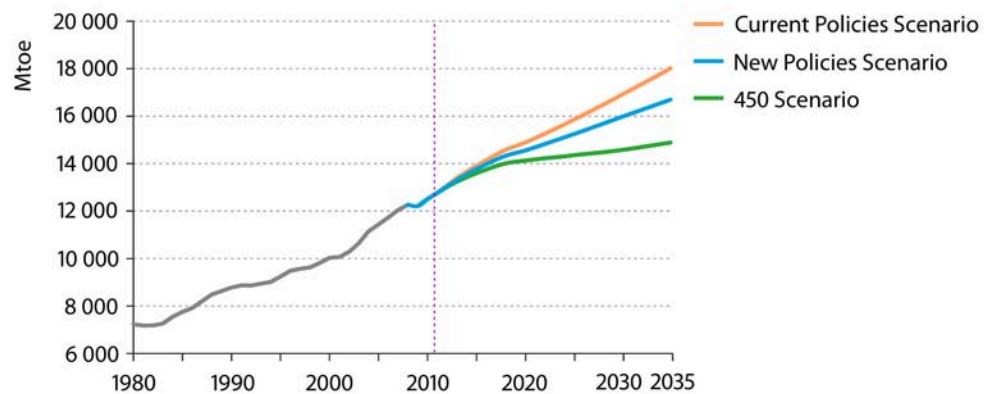


Figure 2: Projection of the world primary energy demand according to the different OECD scenarios. Demand is given in million tonnes of oil equivalent (Mtoe, 1 Mtoe = 11 630 GWh = 41.868 PJ).^[3]

According to the OECD World Energy Outlook (the OECD and IEA represent the interests of the industrial nations), the different scenarios can be imagined for governments all over the world to handle the resulting problems by policy actions that affect technology, the price of energy services as well as the end-user behavior within the next 25 years (see figure 2). The Current Policy Scenario depicts what happens if governments do not change the use of energy. In contrary, the New Policies Scenario assumes that the broad policy commitments and plans that have been announced by countries around the world will be implemented. Finally the 450 scenario depicts the pathway that would be necessary to limit global warming to 2°C by limitation of the atmospheric CO₂ concentration to 450 parts per million.

By this means, it has become an important research aim to compensate negative effects and to overcome the looming energy crisis.^[4] Hence we need to understand the key issues of recent energy production to identify the novel resources and technologies capable of producing energy in a sustainable manner. Otherwise, if not a change in mind, at the latest the depletion of non-renewable resources will force drastic changes of modern technological society and possibly even of human culture.^[5]

1.1 Fossil Fuels and Nuclear Power

Fossil fuels are resources with general abundance and a very high energy density as well as general adaptability. Hence their very low prices on the world market allow for their use in even extremely demanding or inefficient processes, required by modern society (e.g. flying in an airplane instead

of walking or mining and purification of rare elements for electronic devices). These demanding processes drive our economy and represent the basis of our wealth. Therefore, we are tremendously dependent on cheap energy, as can be imagined exemplarily in the way how a doubling of the gasoline price would decelerate economic growth due to increased transportation cost and decreased flexibility.

Nowadays, about 90% of the world's primary energy supply is provided by nuclear fuels or fossil fuels, such as coal, oil and natural gas, which are burned in power plants and engines (see figure 3). Germany represents a typical example, even though it is among the countries which use a higher fraction of sustainable energies and nuclear power:

Compared to 2009, in 2010, the primary energy consumption has increased by 5.0% from 13.3 to 14 exajoules, which were produced from oil (33.7%), gas (21.6%), bituminous coal (12.1%), lignite (10.9%), nuclear fuel (10.8%) and renewable energy sources (9.9%) such as biomass, wind, hydro and solar energy.^[6] By doing so, Germany reached rank six in the top ten of the highest CO₂ emitting countries with an emission of 800 Mt of carbon dioxide, which equals to 2.6% of the world's carbon dioxide emission.^[7]

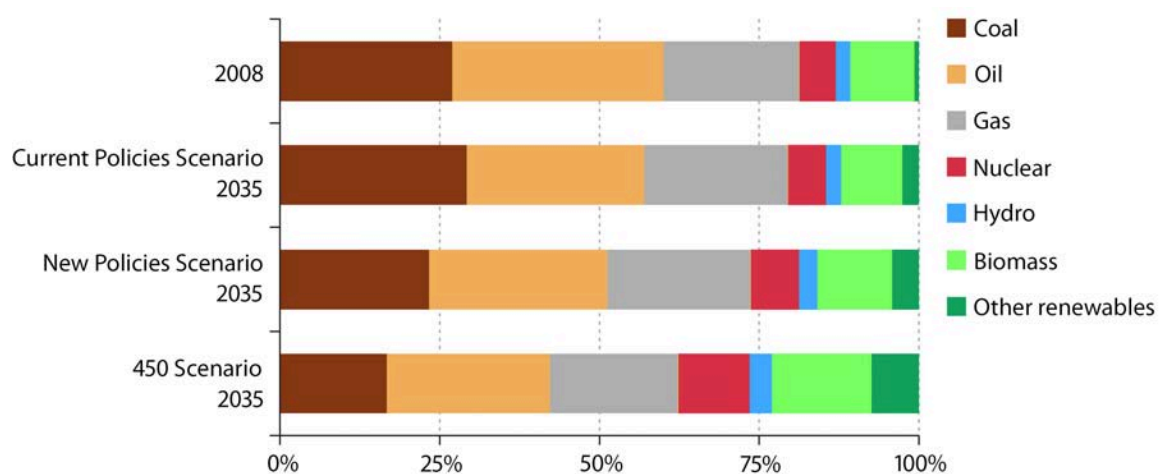


Figure 3: Fractions of energy sources in world primary demand according to the different OECD scenarios.^[3]

The increasing carbon dioxide emission was identified to be one of the major reasons for global warming. Only the limitation of the release of this greenhouse gas into the world's atmosphere to 450 ppm will ensure that global warming does not exceed 2°C (see figure 4). Hence an increased use of nuclear power, which is considered to be a CO₂-neutral energy source, can help to

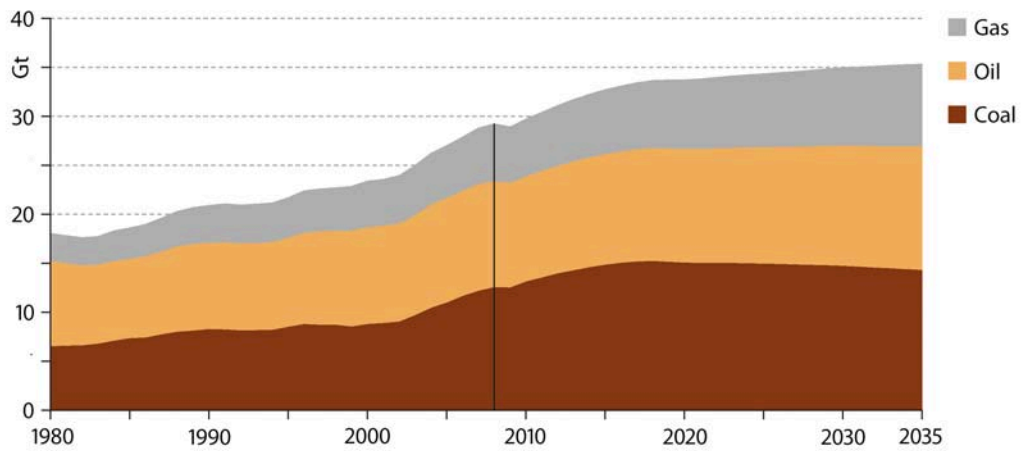


Figure 4: Projection of the world’s energy-related CO₂ emissions by fossil fuels in the OECD-New Policies Scenario where governmental policies will limit CO₂ emission through a significant contribution of carbon-free power to the total energy mix to reduce global warming.^[3]

decrease CO₂-deposition in the atmosphere. Due to its low price on market and stock buildings from nuclear disarmament it is increasingly used in the world (55 nuclear power plants under construction in 2009). Unfortunately, nuclear energy cannot be considered safe because the risk of a disastrous accident. As well the difficult disposal of the nuclear waste remains an unsolved problem. Hence, some governments are forced to think about nuclear phaseout.

In addition, nuclear as well as fossil resources are limited and shrink at an accelerating rate. Seemingly, oil will be the first energy source that runs out (see figure 5). The point of peak oil production is almost reached or was already passed, depending on the respective study.^[3] Supply

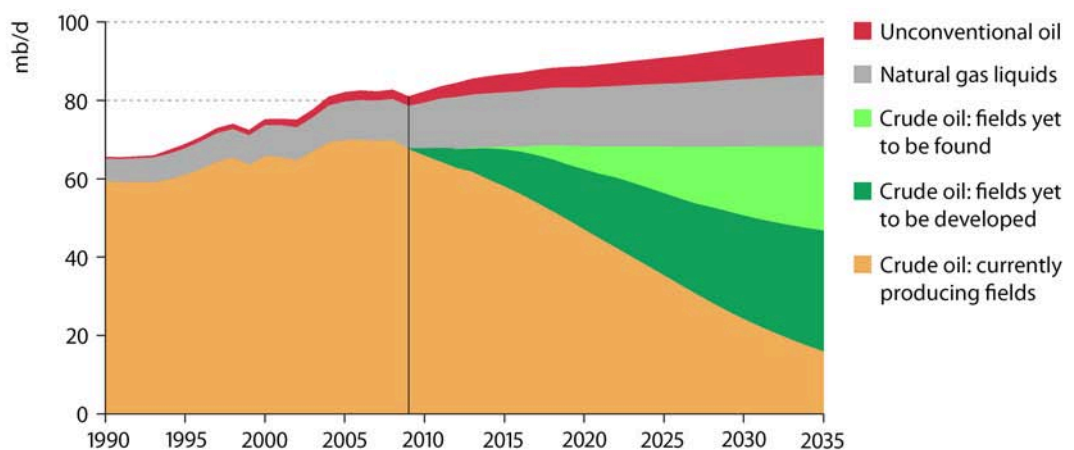


Figure 5: Projection of the world oil production in the OECD-New Policies Scenario.^[3]

of natural gas is less limited and coal is the energy source with the highest geological availability. The final question, when we will run out of these cheap energy sources, is very political and cannot be answered satisfactorily. Depending on different scenarios and the considerations therein, this is believed to happen on an intermediate timescale, within the next 35 to 200 years.^[8]

A fact which shall not to be forgotten is that fossil fuels are very important raw material for the chemical industry. Therefore, they should be preserved for later generations to avoid that eventually agriculture will have concur with food production and chemical industry. Fossil fuels should better be used for a smooth transition toward the development of new energy sources.

1.2 Renewable Fuels

Sustainable energies derive from solar, geothermal or gravitational activity, processes which may be considered unlimited (on the human timescale). Therefore, renewable fuels have become essential contributors to the energy supply portfolio because they contribute to world energy supply security by reducing the dependency on the limited fossil fuel resources.^[9] In addition they provide opportunities for mitigating greenhouse gases such as CO₂.

Nevertheless, they only sum up a tiny fraction to the world's energy mix (compare figure 3), which can be explained by the high costs, compared to the abundant fossil fuels. This makes them especially unattractive to the developing countries with little money and a very high energy demand. An additional effect is that the availability of such energies is strongly dependent on limiting climatic and regional conditions. Delicate counter-arguments can also be found for every one of the renewable energy sources:

For example, in agriculture, food production will concur with bio fuel production to a considerable extent, while about 2 billion people suffer from underfeeding. This is because sustainable vegetable products such as corn, wheat or canola are converted into ethanol, methane or bio diesel because of the high demand in Europe and Northern America as well as governmental subsidies for renewable fuels. For an adequate energy supply by wind energy huge wind parks are necessary, but they influence wildlife by noise emission and shadow casting. Likewise, hydro-electric power plants have challenging environmental demands which cause problems like habitat altering, forests covering, erosion and sedimentation (e.g. Three Gorges Dam in the Yangtze River, China). Finally, solar electricity is more expensive than most of the other alternative energy

sources and therefore it is less affordable. In addition, solar power is only available during daytime and depends on changing irradiation angles. Especially weather and climate dependent intensities results in the production of solar hot water or solar space heat in times when it is not needed (summer). Even geothermal units may cause problems, when drilling holes cause a destabilization of the underground.

Despite these counter arguments, due to the debate on climate change and the arising economic and political problems, resulting from scarce of unsustainable strategical resources, renewable energy technologies have become of increasing interest. Recent years have witnessed a change in the way governments approach energy-related issues. Many governments now give important impulses for their development, granting subsidies for the installation of green energy sources, offering mandating “feed-in tariffs” for green electricity or supporting sustainable energy research. “Green stimulus” efforts by many of the world’s major economies totaled close to \$200 billion in 2009 and almost all renewable energy industries experienced manufacturing growth that year.^[10] According to the recent REN21 Status Report in the United States and Europe more renewable power capacity was added than conventional power capacity (coal, gas, nuclear) in 2009 as well as in 2010.^[10]

As can be concluded from the future projections of the world’s energy demand as well as from the problems referring to recent energy alternatives, mankind is threateningly far away from secure, sustainable, clean and readily available energy supply. Therefore it is important to further increase the ambitions in future energy research.

1.3 Energy Transformation and Storage

Due to the great dependency of the renewable energy power supply on natural phenomena (which are the result of the solar, geothermal or gravitational energy source) some kind of energy storage is necessary to compensate overproduction as well as overconsumption. The resulting fluctuations are undesired and may even damage the power supply system especially in the case of produced electricity. Nevertheless, large-scale electric energy storages such as batteries are still very expensive or ineffective.^[11]

Nowadays, 99% of the used energy comes from energy which is stored in some way. Including biomass, in 2009, about 90% of the world’s primary energy supply was provided by combustibles,

a reduced form of matter that needs to be oxidized to make the stored energy available. In reverse, fuel production (storage in chemical energy) generally represents a reduction reaction (see figure 6).

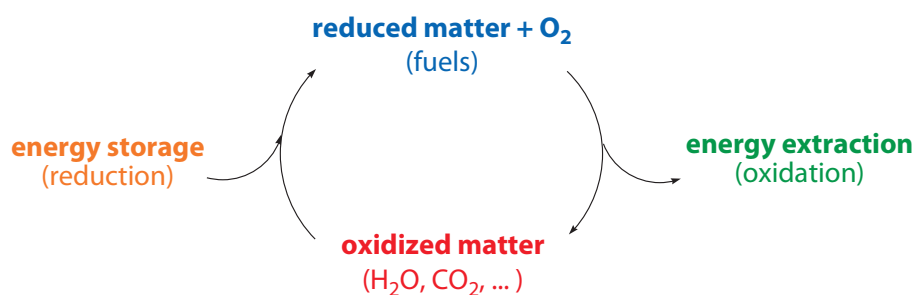


Figure 6: Energy production and consumption considered as redox reaction.

Modeling upon nature, storage is best achieved with reversible chemical energy carriers, e.g. carbohydrates like sugar or cellulose, in general high energy compounds, formed during photosynthesis. Many of these compounds, i.e. alcohols, fats or gases like methane and hydrogen, are potentially useful fuels. To choose an appropriate storage compound, there are three main issues that have to be considered: formation (energy conversion), storage and consumption (back-conversion). All of these have to be evaluated according to economic and ecological considerations such as degree of efficiency, cost, sustainability and possible hazardous side effects. Due to lack of proper techniques, carbon dioxide incorporating cycles are very difficult to handle.

In the scope of sustainability, the direct use of hydrogen gas as a sustainable (carbon and carbon dioxide free) energy source with a high energy storage potential is also very appealing.^[9] The enthalpy of combustion for hydrogen is -286 kJ/mol and the exhaust gas is water vapor. Back-conversion of the stored energy for end uses can be accomplished by direct combustion in engines or its use in fuel cells to obtain thermal or electric energy.

Hydrogen is not only a fuel, but has countless industrial applications as well, e.g. in the upgrading of fossil fuels (35% of total use), and in the production of ammonia likewise (51% of total use).^[9] Because hydrogen is not a natural resource on earth it is especially important to find a sustainable way of its production. The key consumers of H₂ in the petrochemical industry include hydrodealkylation, hydrodesulfurization, and hydrocracking. Although there are some hazards in handling hydrogen, like the low boiling point (20.28 K, -252.87°C) and the high flammability (it will burn in air at a range of concentrations between 4% and 75%), large quantities of hydrogen are

needed in the petroleum and chemical industries. Therefore, its handling is possible on a multi-megaton scale.

Nowadays, industrial hydrogen production is mainly accomplished by steam reforming of natural gas (48%). It is less often produced from more energy-intensive energy conversion methods like the electrolysis of water (high overpotential) which accounts for 4% of the hydrogen production.^[9] In this context the investigation of light-driven water cleavage with formation of oxygen and particular hydrogen provided very promising results.^[4, 12]

1.4 Solar Energy Conversion

The most desirable and seminal but almost untapped energy source appears to be the sun. Solar average energy uptake of the earth surface ($3.9 \cdot 10^{24}$ J) is almost four orders of magnitude higher than the average energy consumption of mankind ($4.7 \cdot 10^{20}$ J).^[4, 11, 13] However, the energy density of the sunlight is very low, compared to fossil fuels. This makes it unattractive because large collector areas are necessary (the average flux density of the sunlight on earth, solar constant, is 1.37 kW/m^2 which would refer to 0.15 l of gasoline production in one hour at an energy conversion efficiency of $\eta = 100\%$ whereat a car uses ~ 7.0 l to drive 100 km in that time). Another fact is, that sunlight, filtered through the earth atmosphere is still very polychromatic (compare figure 7).

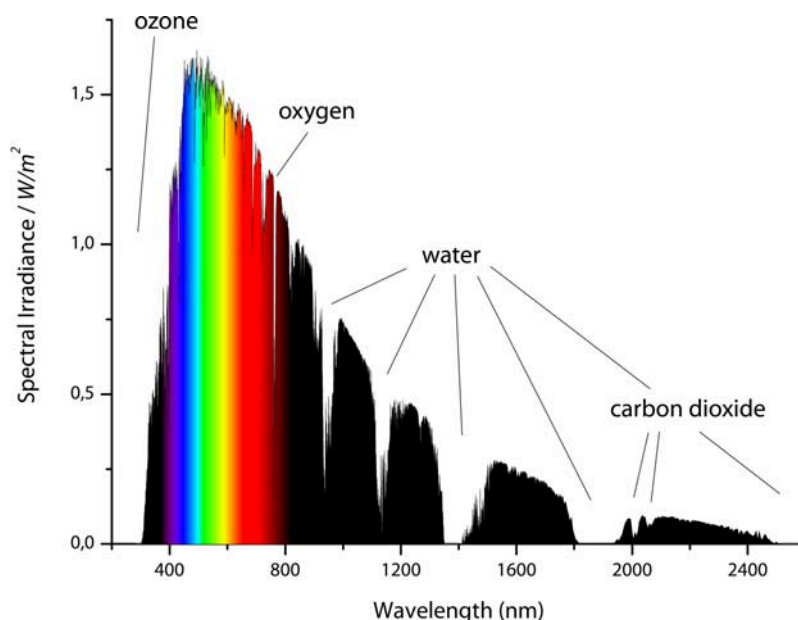


Figure 7: Solar radiation spectrum at sea level with assigned atmospheric absorption bands.^[13]

A fraction of about 53% is infrared (IR) light and about 3% result from ultra violet (UV) light. The spectrum has a maximum in the blue of the visible light region (vis), which contributes about 44% of the solar energy input to earth's surface. For solar energy utilization a main fraction of the light energy must be captured and converted into heat, electricity or chemical energy at an affordable cost. Several concepts are available at present to achieve this conversion:

Solar thermal energy is currently the cheapest method of solar energy capture, conversion, and storage. Devices, using solar heat span from small cloaking devices and domestic heat systems up to large-scale power plants which concentrate visible light via mirror systems to drive a steam turbine with the heated water vapor like the PLANTA SOLAR 10 in Spain (see figure 8).



Figure 8: The 11 MW solar heat power plant *Planta Solar 10*, Seville, Spain.^[14]

One kW-hr can cost as little as \$ 0.10 - 0.15 for electricity production, which is only five times higher than conventional electricity.^[12] Photovoltaics (PV) accomplishes direct light into electric energy conversion, using the photovoltaic effect. In this process photons excite the electrons of a semiconductor into higher states or bands, creating charge separation with formation of an electric potential that can be tapped. Typical light absorbing semiconductor materials are doped monocrystalline silicon in conventional PV or conjugated polymers for organic solar cells. Photo-electrochemical cells and dye-sensitized solar cells (DSSC) also known as GRÄTZEL cells are also of interest.^[15, 16, 17] Here an excited sensitizer molecule (e.g. Chlorophyll or $\text{Ru}(\text{bpy})_3^{2+}$) is capable of donating an electron into the conduction band of a linked semiconductor to generate an electric potential. A redox shuttle system (e.g. I_3^-/I^-) accomplishes contact with the counter electrode and is used for the regeneration of the oxidized chromophore.

To counter the low solar energy flux, materials for energy conversion without foregoing concentration must be long-term stable and cheap to make the process economical. Today, the cost of solar electricity is about ten times higher than conventional energy.

A direct conversion of solar energy into chemical energy (fuels) represents the third alternative for its exploitation. Light-driven reactions can copy principles of nature in which chemical bonds are broken and formed to keep the organism alive and to build up biomass. The basis for such artificial photosynthesis process is the detailed understanding of important principles of photophysics, photochemistry, electrochemistry and catalysis as well as of the natural photosynthesis.

1.5 Photosynthesis

Already about 3.5 billion years ago, nature learned how to utilize sunlight in a primitive way. Starting from bacteria photosynthesis evolutionary processes led to the photosynthesis of higher plants. Until today, bacteria, algae and green plants are capable of transforming vast amounts of solar energy into biomass via different types of photosynthesis. The primary processes from light to chemical energy conversion are very efficient and sustain the organism's life. Besides, only a small fraction (1% of the available light energy) is used by plants for biomass production. By that means, solar energy conversion accounts for the formation of nowadays biomass as well as for the formation of fossil fuels.

These primary steps of the so called light-dependent reactions involve light absorption, charge separation and transfer as well as catalytic oxidation and reduction processes within two photosystems at the thylakoid membrane of chloroplasts.^[18] Figure 10 gives a résumé of these extremely organized processes in the so called Z-scheme of photosynthesis.^[19]

Photosynthesis starts with the simultaneous excitation of special pairs of chlorophyll(a) molecules (**P680**) in photosystem II (**PS II**, see figure 9) and (**P700**) in photosystem I (**PS I**), the only step where light energy is converted into chemical energy stored in excited electrons with high reduction potential. This can be achieved by direct absorption of visible light by the special pairs ($\lambda_{\max}^{\text{PS II}} = 680 \text{ nm}$ and $\lambda_{\max}^{\text{PS I}} = 700 \text{ nm}$). However, more likely is the activation by excitation energy transfer via FÖRSTER or DEXTER mechanisms from nearby arranged chlorophylls and carotenoids. A great number of these antenna pigments is precisely arranged in light harvesting complexes (**LHI** and **LH II**) and increases the absorption area as well as the absorption band of **P680** and

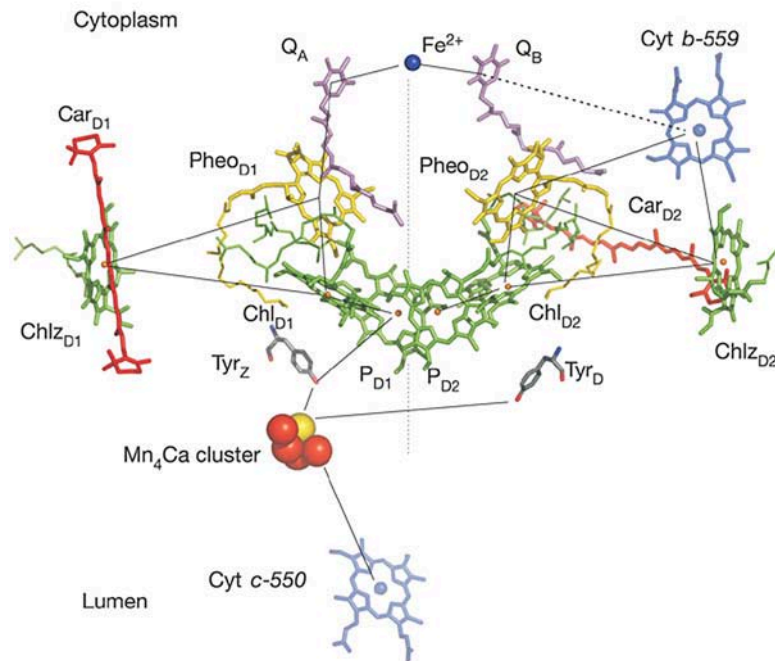


Figure 9: Molecular structure of important redox-active species involved in the initial charge separation of **PS II**. Depicted parts to conform to the present text: **OEC** (Mn_4Ca), **tyr** (Tyr_Z), special pair **P680** (P_{D1}/P_{D2}) and antenna pigments (Car and Chl), **Pheo** ($Pheo_{D1}/Pheo_{D2}$), **PQ** (Q_A/Q_B), and **cyt f** (Cyt b-559). The protein surrounding is omitted for clarity.^[20]

P700. Interestingly, chlorophylls exhibit two major absorption maxima in the blue and red of the visible region. One between 600 and 700 nm, the so called Q_y -band and the Soret Peak between 400 and 500 nm. Therefore, plants can use a major fraction of solar energy, except a part of green and yellow light.

Nevertheless, ultrafast charge separation and electron transfer processes away from the special pairs, finally start the true chemical steps. The key process for life on earth is the electron entering the first redox shuttle. This happens by oxidative quenching of the excited **P680*** by nearby pheophytin (**Pheo**) with formation of the strong oxidant **P680⁺** and reduced **Pheo⁻** in **PS II**. In a similar way excited **P700*** in **PS I** donates its excited electron to a nearby electron acceptor (**A₀**, a chlorophyll-a molecule, not depicted in figure 10), with formation of **P700⁺** and **A₀⁻**.

Regeneration of the photooxidized special pairs **P680** and **P700** happens almost simultaneously. The missing electron in **P680⁺** is recovered from water oxidized by a multiple reducible Mn_4Ca cluster also known as oxygen evolving complex (**OEC**). This complex sequentially extracts four

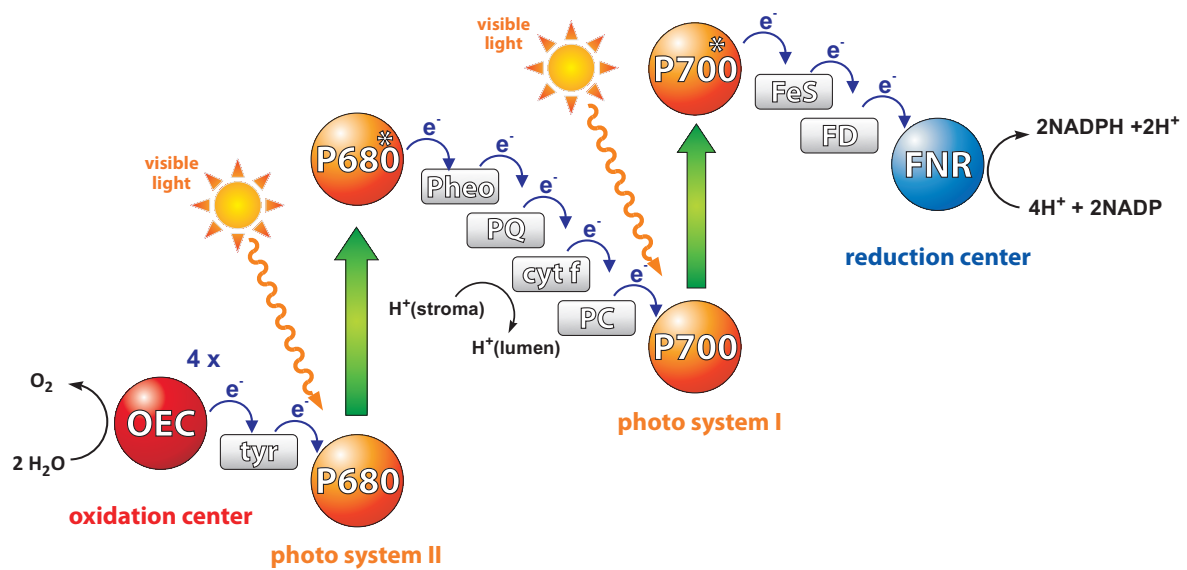
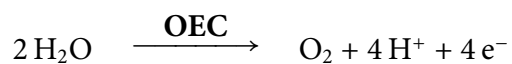


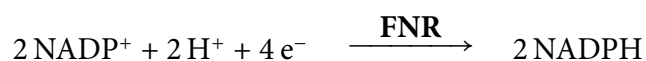
Figure 10: Z-Scheme of photosynthesis, representing important processes of light absorption, charge separation and electron transfer, involved in water splitting (see text for details).^[19]

electrons from two water molecules (serving as sacrificial donor) and liberates molecular oxygen and four protons to the lumen. Four single electron transfer steps via a specific tyrosine moiety (**tyr**) replenish the photooxidized **P680**.



P700⁺ becomes reoxidized to **P700** by the reception of an electron from plastocyanine (**PC**, a mobile copper-protein) which had previously been passed down through the redox gradient originating in **PS II**. The reduced primary electron acceptor **A₀⁻** passed the electron ultimately to nicotinamide adenine dinucleotide phosphate (**NADP**⁺). This happens via several other intermediates, including redox shuttles like phyloquinone (vitamin K), several membrane bound iron sulfur proteins (**FeS**) and ferredoxin (**Fd**), a slightly mobile **FeS**.

Eventually, the enzyme ferredoxin-NADP reductase (**FNR**), an oxido-reductase, gathers two of such electrons and uses one proton for the final transfer step. The reduction of **NADP**⁺ with formation of **NADPH** represents a "fuel production" step in the plant. Importantly, the resulting **NADPH** is a hydride carrier molecule which is one of the most widely used energy storage molecules and reducing agents in cells, e.g. essential for the production of sugars from **CO₂** in the **CALVIN** cycle.



The redox gradient which passes the electrons from **PS II** to **PS I** drives yet another endergonic process to sufficiently exploit the energy of the absorbed light. When a special **PQ** has accepted two electrons from **PS II**, it also takes on two protons from the stroma and it detaches from its binding site. The hydrophobic quinone **PQH₂** may now pass through the hydrophobic core of the thylakoid membrane to a protein complex (**cyt f**) which contains **FeS**, cytochrome *f*, and two cytochrome *b₆* molecules. Having arrived there, it releases the transported protons to the lumen and passes the electrons onward to an incorporated **FeS** protein (also called RIESKE protein) and then to **PC** which is then released and serves as the electron provider for **P700⁺**.

With the help of a proton gradient between lumen and stroma, light reactions in their turn provides the energy of adenosine triphosphate **ATP** in a way that is similar to the ancient forms of photosynthesis in *archae bacteria*. This proton gradient between stroma (pH 8) and lumen (pH 6) derives from the release of protons by the **OEC** as well as from transport of protons against the gradient by **PQ** in the Q-cycle. An osmotic pressure and a difference in potentials between stroma and lumen of approximately 120 mV is the result. **ATP** is produced through ATP synthase (not depicted), using adenosine diphosphate (**ADP**), inorganic phosphate and energy from a proton gradient across the thylakoid membrane. Protons, driven out from the lumen have to pass through the central core of the transmembrane enzyme ATP synthase. This causes rotational conformational changes in the enzyme and catalyzes the phosphorylation of **ADP** along with the release of **ATP** into the stroma.

A total of 8 photons, are required to transfer four electrons and protons from two molecules of water to two molecules of **NADP⁺**. This produces two molecules of **NADPH** and one molecule of **O₂**. Additionally, four protons are passed in the Q-cycle and additional four protons derive from water oxidation to build up the proton gradient, eventually causing the formation of approximately three **ATP** molecules from **ADP**.

1.6 Photocatalyzed Reactions

As nature demonstrates in a very impressive way, it is possible to utilize sunlight for the conversion of carbon dioxide and water into energy-carrying molecules like sugars and oxygen. Capturing

an average power of approximately 100 terawatts of sunlight, natural photosynthesis directly and indirectly provides the basis for nearly all life on earth. G. CIAMICIAN, an important pioneer of photochemistry research, realized the relevance of that fact (see figure 11). Although his understanding was certainly basic, he found out that the use of solar energy would help to:^[21, 22]

- (1) carry out reactions under mild conditions,
- (2) look for activation conditions that allow for more direct reactions and thus improve atom economy,
- (3) increase the use of renewable materials or reagents (using directly light rather than fossil solar energy) and
- (4) minimize the use of energy.

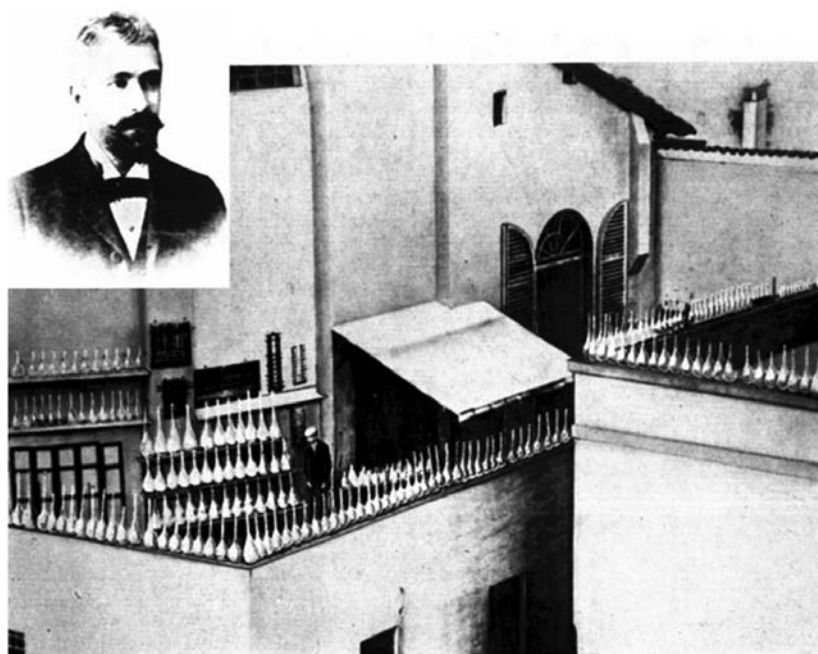


Figure 11: Photochemistry pioneer GIACOMO CIAMICIAN, as he watches his reactions, driven by solar irradiation in flasks on the balcony on top of his laboratory at the University of Bologna, Italy, circa 1910.^[4]

Today, these statements are incorporated into the "12 principles" of green chemistry as formulated by ANASTAS and WARNER.^[23]

According to TURRO, today it is known that photochemical reactions differ from thermal reactions in three important respects:^[24]

- (1) as opposed to reactions that are mainly activated by heat, activation of photoreactions occurs mainly by absorption of light
- (2) hence, electronic structure as well as nuclear configuration of a photoexcited molecule differs substantially from those of the thermally activated one
- (3) due to the high energy excess, far more thermodynamically favorable products are accessible to a photoexcited molecule than those accessible to ground state molecules

Importantly, this excess of absorbed light energy may be used to drive a catalysis in the non spontaneous (thermodynamically uphill) direction, thus allowing the formation of high-energy products from low-energy educts or the conversion of light energy into chemical energy, as seen in nature. IUPAC defines a photocatalytic reaction as a *change in the rate of a chemical reaction or its initiation under the action of ultraviolet, visible, or infrared radiation in the presence of a substance - the photocatalyst - that absorbs light and is involved in the chemical transformation of the reaction partners.*^[25] Also according to IUPAC, this photocatalyst is a *substance able to produce, by absorption of ultraviolet, visible, or infrared radiation, chemical transformations of the reaction partners, repeatedly coming with them into intermediate chemical interactions and regenerating its chemical composition after each cycle of such interactions.*^[25]

For the construction of a system that utilizes light energy in the catalytic cycle, different possibilities are available. According to CHANON, a reaction is considered to be photocatalytic, when catalytic amounts of photons or chemical substances are enough to allow for the photochemical conversion of substrates or to accelerate such reactions. It is possible to subdivide photocatalytic reactions into two groups, according to the catalytic demand of photons or substances respectively (see figure 12).^[26]

While in the first class (photoinduced catalysis) single photon absorption yields the catalytically active species that lasts several cycles even in the dark, stoichiometric amounts of photons need to be added in the second case to drive a potentially more endergonic reaction. All reactions of second class stop right away when light input is blocked. The second class can be further subdivided according to the role of the excited molecule in the reaction. Three important groups are also depicted in figure 12.

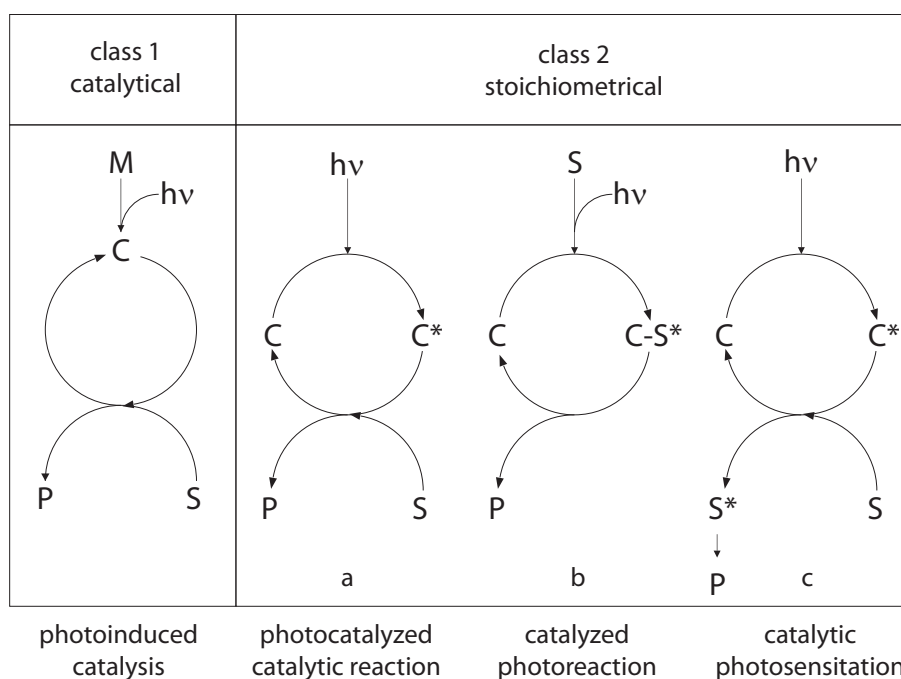


Figure 12: Classification of photocatalytic reactions by the rate of photon consumption. S: substrate, P: product, C: catalyst, M: transition metal complex, *: excited state.^[26]

In the first case, photocatalyzed catalytic reaction, the (pre)catalyst possesses the chromophore and forms the true catalyst upon excitation, which eventually falls back to the ground state after one turnover. Furthermore, in a catalyzed photoreaction, (b) in figure 12, the substrate holds the chromophore, but photoreaction with formation of P needs to be catalyzed. And in the case of catalytic photosensitization, (c) in figure 12, catalytic amounts of sensitizer molecules C hold the chromophore, and excitation is only passed on to a substrate, thus driving the catalysis.

Classifying photosynthesis according to this concept, it is obvious that this is a matter of a light-driven catalytic reaction that runs a thermodynamically uphill reaction under stoichiometric consumption of photons (class 2). It consists of two subprocesses which accomplish on one side the reduction of NADP^+ under use of electrons and protons which are produced on the other side by water oxidation. Considering **PS II**, including substructures like **P680** and **OEC**, to be one supramolecular catalyst, photosynthetic water oxidation has to be put into group (a), the photocatalyzed catalytic reaction. Here water is the substrate that becomes oxidized under release of molecular oxygen.

So the reduction side **PS I**, including substructures like **P700** and **FNR**, assumed to be one catalyst, photosynthetic **NADP⁺** reduction has to be put into group (a). Considering the functionality of light harvesting complexes with energy transfer toward the special pair, we have to deal with group (c) because excitation is only passed on to the special pairs. Reactions of type (b) cannot play a role, because water is no chromophore in the visible light region.

1.7 Mimicking Photosynthesis

Since the efficient conversion of solar energy into fuels has become a topic of general interest, photosynthesis as well as photocatalysis research have a significant upturn. Natural photosynthesis demonstrates how to use solar energy cost-efficiently, stably, nontoxically and renewably. Nevertheless, it uses most of the captured energy to sustain the plants' life instead of providing fuels for man and it is limited to aqueous media and a small temperature range.^[18] Synthetic catalysts are often very efficient, less limited to physiological conditions and bio-available metal centers but in many cases expensive, toxic or not sustainable. A combination of these two spheres of knowledge may potentially result in an artificial system that outflanks natural photosynthesis in efficiency, using most of the captured energy for synthetic fuel production but retains the positive effects such as low cost or sustainability.

Several approaches try to combine synthetic catalysts with natural systems to access new reactivities and products.^[12] Other approaches focus on the development of models, mimicking key processes of natural energy production for their better understanding. In addition, genetic altering of organisms can be used to tune the natural bio reactions.^[27] All of these efforts may help to identify an access to solar fuels and can be summarized in the category of artificial photosynthesis research.

According to IUPAC definition, artificial photosynthesis is the *photocatalytic production of substances from simple compounds (e.g., H₂ and O₂ from water, H₂ from hydrogen sulfide, etc.) using ultraviolet, visible, or infrared radiation absorbed by chromophoric systems, often included in microheterogeneous media, mimicking the action of antennas and reaction centers in natural photosynthetic organisms* (compare figures 13 and 14).^[25]

Especially the development of techniques which allow for the direct formation of fuels from water in a light-driven, non-polluting and sustainable cycle of energy capture, energy storage and energy

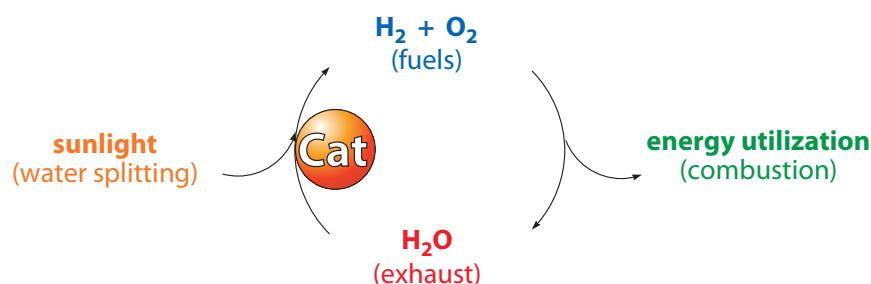
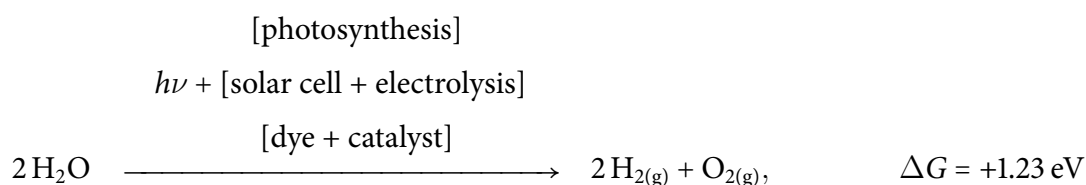


Figure 13: Carbon free cycle for solar energy utilization by photocatalytical hydrogen production from water.

extracting (depicted in figure 13) is a main focus of current research. Ingenious is the fact that the raw material as well as the combustion product is cheap and abundant water, whereat valuable hydrogen gas will be the product as depicted for the one-electron process:



The energy that is required for hydrogen and oxygen formation by water splitting is equivalent to the energy that is released during combustion of hydrogen ($\Delta_f G^\ominus = -272,9 \text{ kJ/mol}$). This is equivalent to an electric potential of -1.23 V in solution or to photons with an energy higher than $h\nu > 1.23 \text{ eV}$, and accordingly to a wavelength shorter than 1008 nm (IR).

However, water is no chromophore and cannot be split by absorption of light. Otherwise an electrode reaction against a high overpotential is necessary to drive the thermodynamically not accessible reaction without direct use of visible light energy. Hence, solar water splitting is accessible by electrolysis, an inefficient (5%) and expensive method when powered by photovoltaic cells.^[28, 29] The process is pH dependent and occurs at standard conditions at the following potentials (vs. NHE):





The use of a catalyst at the electrode can help to improve the efficiency of the process, reducing the overpotential of the redox or electrode reaction.^[28,30] An advanced approach is the formation of oxyhydrogen from water at room temperature with the help of a photoredox catalyst which allows for the direct capture and conversion of light energy into redox energy to drive the above reaction.

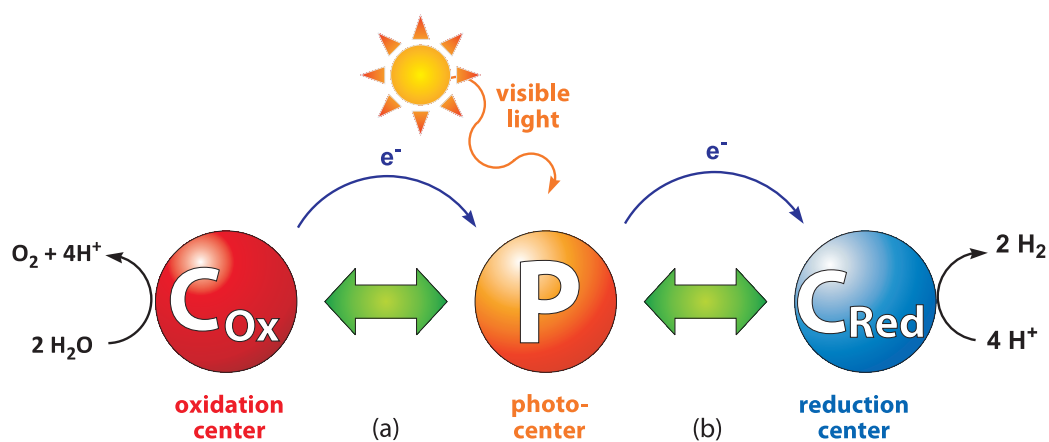


Figure 14: Half reactions of artificial water splitting (a and b); interplay (green arrow) of oxidation catalyst (C_{Ox}), photocenter (P), and reduction catalyst (C_{Red}).

Accordingly, a light reaction inspired multicomponent catalyst with two coupled redox-processes of water oxidation (a) and water reduction (b) can be imagined to accomplish oxyhydrogen formation, as depicted in figure 14.

1.8 Formalisms of Photocatalytic Systems

As described before, a great variety of potentially important processes interacts in natural photocatalytic systems. The identification and categorization of functional components and separate catalysis cycles in natural systems is a general starting point for the development of new artificial systems. Based on that, a subsummarization of similar processes (chains) and a judicious choice of substitutes can be made to manage the complexity of a resulting artificial

multicomponent system and to ease the handling thereof. Table 1 lists a series of important functional units which may be identified in natural photocatalytic systems.

Table 1: Important components of (artificial) photosynthetic systems according to functionality

function	substructure	abbreviation
visible light absorption, directional energy propagation	antenna pigment	AP
visible light absorption, conversion into redox energy	photocenter	P
irreversible charge separation, unidirectional transfer	electron relay	R_{Q/D/A}
center for concerted (multi-electron) redox reaction	catalyst	C_{Ox/Red}
irreversible electron donor/acceptor	(sacrificial) substrate	S_{Q/D/A}
structural support, linking, spacing, embedding	scaffold (bridge)	B_N

Q) quencher, **D)** electron donor, **A)** electron acceptor, **Ox)** for oxidation, **Red)** for reduction, **N)** photochemically not directly involved.

Through appropriate combination of the desired functionalities or functional units respectively it is possible to project a scheme for any artificial photosynthetic system (e.g. for water splitting as depicted in figure 15), similar to the ones, observed in nature.

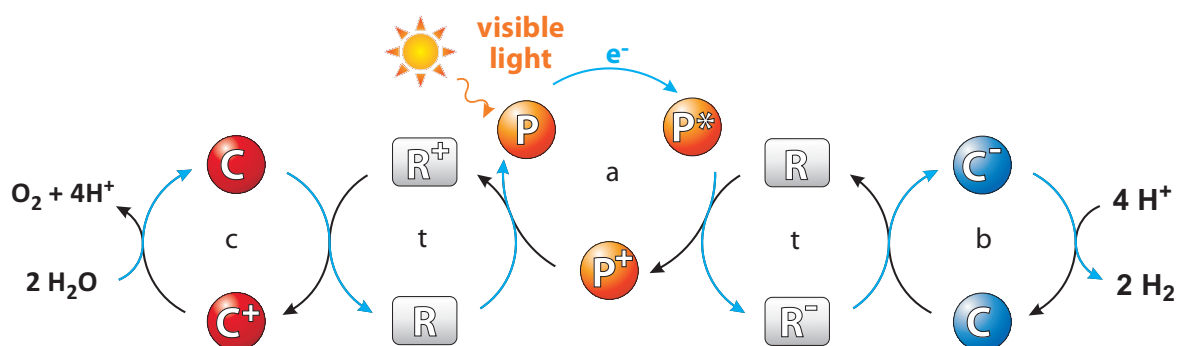


Figure 15: Derived from natural photosynthesis: a simplified catalytic cycle for light induced water splitting capable of visible light absorption and conversion into redox energy (a), unidirectional electron transfer (t) and concerted redox reactions for water reduction (b) and oxidation (c).

Furthermore, it is possible to focus on a particular sub-process (a and b in figure 14) at a time to reduce side reactions and complexity of the resulting artificial photosynthetic systems to characterize, understand and optimize the interplay within the system in detail.

Complete catalytic systems (or complex substructures thereof) as well as interesting processes can also be described in a simplified notation. A catalytic system is expressed in double brackets

“[[]]”, in which contact pairs of independent substructures are separated by a “/” and covalently linked substructures within the same superstructure are separated by a “~”, external substrates are written on the outside of the system. Using the previously described half reactions of the natural photosynthetic system as an example and adapting the notation according to table 1 it is possible to express the arrangement of components as well as relevant processes (e.g. initial vector of quenching and charge separation) in the following formalism:



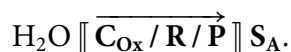
As described before, both half reactions are initiated through the oxidative quenching of the excited photocenter (P^*) by an accepting quencher ($\text{R}_{\text{Q,A}}$) which may also act as redox shuttle. This is followed by multiple redox-steps with an overall electron flow from the donor substrate ($\text{S}_\text{D}/\text{H}_2\text{O}$), being irreversibly oxidized at the oxidation catalyst (C_{Ox}), toward the acceptor substrate ($\text{S}_\text{A}/\text{NADP}^+$, eventually irreversibly reduced at a reduction catalyst (C_{Red}).

1.9 Multicomponent Systems from Fundamental Building Blocks

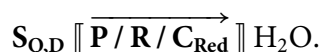
From the above discussions it is clear that a photochemical reaction can supply the required energy ($E = 1.23 \text{ eV}$) to drive an artificial system for water splitting. Therefore a suitable photosensitizer is needed. It is also obvious that a simple system has to exhibit two reaction sites with opposing potentials to allow for oxidation as well as reduction. Furthermore, two different charge separation- and electron transport mechanisms (mediators, chains) between chromophore and reaction centers have to be established to design a simple system. Two different aspects of importance can be attached to the resulting half reactions, so that it is possible to focus on the desired subprocess:

The half reaction of light-driven water oxidation is particularly interesting because in general it deals with the exploration of cheap and sustainable “sacrificial” electron donors S_D (water) and an efficient mechanisms to deprive the electrons thereof as well as to provide them for fuel production. The two essential steps that have to be simulated are water oxidation with the help of a catalyst C_{Ox} and electron transfer of the received electrons to the chromophore. To generate

a catalytic cycle an external electron accepter as well as an electron mediator might need to be added to give the following three component system:



The subprocess of light-driven water reduction has great importance because it generally represents the exploration of suitable acceptor substrates S_A (such as water, but also for H_2S , CO_2 ^[31] or NADP^+) and efficient mechanisms to power the storage of electrons along with the formation of fuels. In this case, the easiest system accomplishes electron transfer away from P and water reduction by C_{Red} . Here as well, an external electron donor and some mediator need to be added to close the cycle:



To translate these basic catalytic cycles into working systems, several parameters have to be considered. The use of a one-pot reaction in homogeneous media is a good starting point. This allows for the easy and fast build-up of multicomponent systems where each function is fulfilled by one molecule (compare figure 15). Concentration dependent statistical collision processes ensure that the corresponding reaction partners will find each other. Therefore, no specific geometry has to be applied because the complete catalytic cycle will “self-assemble” statistically, although solubility problems or undesired side reactions like charge recombination, radical chains, or irreversible redox reactions may appear to some extend.

Particular advantages arise from the fact that this kind of setup allows for easy adjustments or replacements within the system. This way, it is possible to screen libraries of suitable electron donors, chromophores, redox shuttles and catalysts to find suitable candidates for a system with defined geometry. Furthermore, a separation of catalyst and product, often difficult in homogeneous catalytic systems, is not a problem because gas bubbles will evolve, which can be detected in the headspace of the catalysis setup.

Indeed, the first working systems were based on this intermolecular setup as was reported in the 1970s.^[32, 33, 34, 29] Since then many model systems of hydrogen production or oxygen production from water have been proposed. In this scope an enormous amount of data on new dyes, electron relays or catalysts was presented.^[29, 35] A closer analysis of the presented systems reveal the

specific requirements of each component according to its predetermined functionality in the photocatalytic system.

1.9.1 Photosensitizers - Light Energy Conversion

The exploration of suitable photosensitizers (**P**) is the initial step for the modeling of artificial photosynthetic processes.

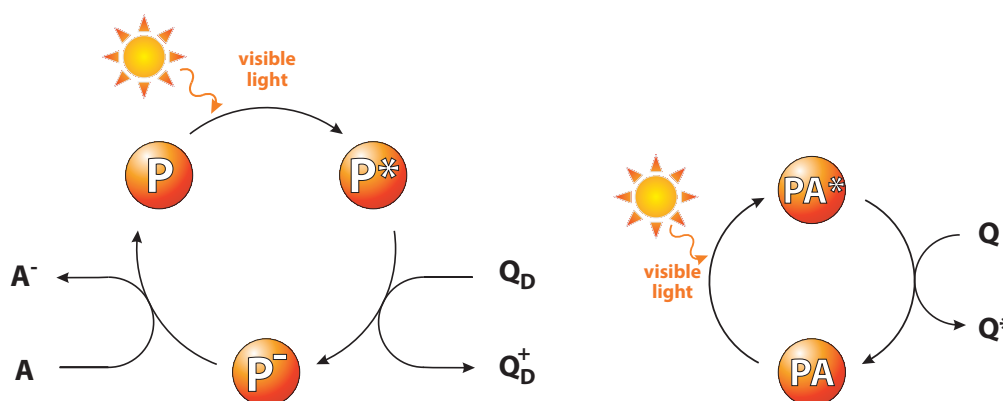


Figure 16: Energy conversion of redoxactive photosensitizers in a three-step excitation – electron transfer – ground state regeneration cycle (left, reductive quenching mechanism is not depicted) and two-step excitation – energy transfer cycle of sensitizers with antenna function (right).

As depicted on the left side in figure 16, photosensitizers have to accomplish three important functionalities: First, light absorption with formation of an excited species (**P***), second, energy conversion and electron transfer by a quenching mechanism and, third, ground state regeneration via redox reaction. Photosensitizers or antenna pigments (**AP**), that accomplish excitation transfer can be used to increase the effective absorption area.

To match the requirements, needed for the use in photocatalytic water reduction according to the basic catalytic cycle, the photosensitizer has to possess several essential properties. These properties are according to BALZANI:^[36]

- (1) reversible redox behavior
- (2) suitable ground and excited state potentials (E_{Ox} , E_{Red} , E_{Ox^*} , E_{Red^*})
- (3) stability toward thermal and photochemical decomposition
- (4) intense absorption in a suitable spectral region (ϵ , λ , **PA**)

- (5) small energy gap between relevant excited states
- (6) high efficiency of population of the reactive excited state (η)
- (7) suitable lifetime of the reactive excited state (τ)
- (8) high energy content of the reactive excited state ($E_{0,0}$)
- (9) good kinetic factors for outer sphere electron transfer reactions (k_{ET}).

In the research of multicomponent systems for photocatalytic water reduction, many chromophores, including acridine dyes, metalloporphyrins, metallophthalocyanines, and transition metal complexes of Os, Cr, Ir or Ru were screened.^[29, 37, 35] Because of their outstanding properties, especially ruthenium complexes with polypyridine ligands, and $[\text{Ru}(\text{bpy})_3]^{2+}$ in particular, may be considered as prototype workhorse-chromophores (see figure 17 for examples).

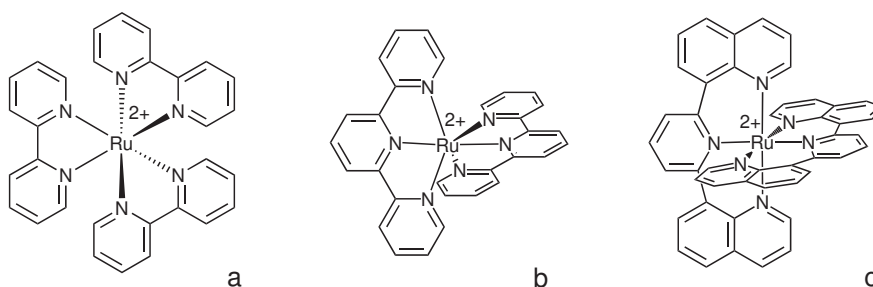


Figure 17: Representative ruthenium polypyridine chromophores: a) $[\text{Ru}(\text{bpy})_3]^{2+}$,^[36] b) $[\text{Ru}(\text{tpy})_2]^{2+}$,^[38] c) $[\text{Ru}(\text{bqp})_2]^{2+}$.^[39]

For a better understanding of the capacity of this type of complex, it is important to understand the ground state, excited state and redox characteristics. Therefore, it is useful to consider its molecular orbitals, instead of being uniformly distributed across the molecule, to be localized on a specific part of it. According to the localized molecular orbital approximation, molecular orbitals of the complex derive from orbitals of its precursor components (metal ion and free ligand). In general, upon complex formation, energies of the existing orbitals will be shifted, but their positions remain predominantly localized on whether metal fragment (M) or ligand (L). As a result of that, although slightly changed, several features of the components will be retained in the resulting complex (e.g. possible electronic transitions).^[40]

Therefore, metal centered (MC, e.g. d-d-transition) as well as a ligand centered transitions (LC, e.g. π - π^* -transition), possible in the precursors, may be observed in the resulting complex as well. In addition, new electronic transitions, involving two localized orbitals on different moieties of the complex will be possible. Importantly, such transitions result in charge transfer (CT) between the involved substructures of the molecule. The resulting electronic structure yields a biradical-type situation with high dipole momentum and comes along with oxidation as well as reduction potential of the excited molecule, hence it allows for further light into redox energy conversion by further charge separation. Metal to ligand charge transfer (MLCT), ligand to metal charge transfer (LMCT) or ligand to ligand charge transfer (LLCT) are typical examples. Intra ligand charge transfer (ILCT) and charge transfer to coordinated solvent molecules (CTTS) may also be observed.

Furthermore, the population of an excited state of a chromophore (\mathbf{P}^*) typically competes with several depopulation pathways. Radiative deactivation processes involve spin allowed fluorescence (F) and spin forbidden phosphorescence (P). Nonradiative deactivation processes (nr) such as internal conversion (IC), intersystem crossing (ISC, e.g. through conical intersections) as well as vibronic relaxation (VR) are also possible. The most important nonradiative deactivation processes in the scope of artificial photosynthesis are quenching processes such as energy transfer (EnT) and photo electron transfer (PET) processes.

The energy positions of the MC, LC, MLCT and other excited states depend on the ligand field strength, the redox properties of metal and ligands, and intrinsic properties of the ligands, respectively. Furthermore, the excited-state energy ordering in the spin-allowed and spin-forbidden manifolds may be different from each other. The occupation probability and lifetime thereof depends on many factors, e.g. differences in energy between relevant states, Franck-Condon factor, spin states or kinetics of the occurring deactivation processes.^[40]

Octahedral ruthenium(II) polypyridine complexes are 18-electron systems with a low spin $\pi_M(t_{2g})^6$ -configuration of the metal center due to the strong σ -donating ligands. The photophysical behavior of these complexes (absorption and emission bands in UV-vis spectra of such complexes, e.g. orbital energy ordering and deactivation kinetics) is very similar and can be explained with the help of a Jablonski diagram.^[36] Figure 18 depicts a typical absorption and emission spectrum and the corresponding Jablonski diagram of octahedral ruthenium(II) polypyridine complexes.

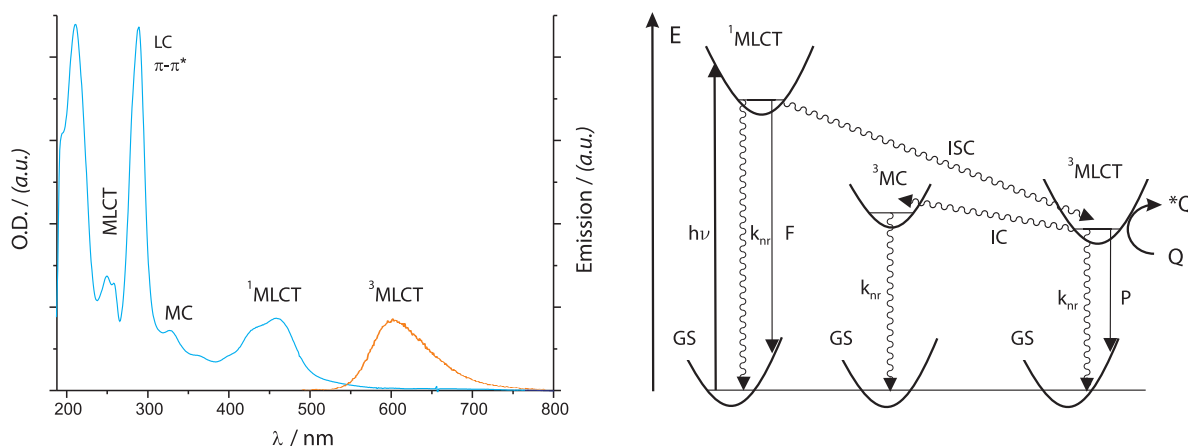


Figure 18: Typical absorption (blue) and emission (orange) spectrum of $[\text{Ru}(\text{bpy})_3]^{2+}$ -type complexes following from the orbital positions, depicted in the related Jablonski diagram (right).

Absorption bands found between 250 and 350 nm in the UV region of the spectrum such as ruthenium centered d-d-transitions as well as bipyridine centered π - π^* -transitions are inherited from the precursors.

However, more interesting is the strong absorption band (requirement 4) between 400 and 500 nm with a maximum at about 450 nm and extinction coefficients as high as $\epsilon = 14\,600 \text{ l}/(\text{mol cm})$. In the case of ruthenium(II) polypyridine complexes this band typically refers to the HOMO-LUMO transition, because the LC π^*_L -orbitals are lower in energy than the MC σ^*_M orbital.^[41]

As depicted in the Jablonski diagram, for most Ru(II) polypyridine complexes, the lowest excited state is a $^3\text{MLCT}$ which is reached from the initial $^1\text{MLCT}$ under spin flip ($\Delta E_{^1\text{MLCT}/^3\text{MLCT}} \approx 0.64 \text{ eV}$, requirement 5). This intersystem crossing is very efficient because of a strong spin-orbit interaction in these complexes and occurs within femtoseconds in quantitative yield (requirement 6, compare example a and c in figure 17). With respect to energy conversion and excited state chemistry, it is important that this CT state undergoes relatively slow radiationless transitions and thus exhibits long lifetime ($\tau \sim 1 \mu\text{s}$, requirement 7). The excited state energy of this triplet is still high ($E_{^3\text{MLCT}} \approx 2 \text{ eV}$, requirement 8) and results in an intense luminescence emission at wavelengths around 600 nm (requirement 8). However, the luminescence quantum yield is rather small with only 2%.

In other cases (b in figure 17), with respect to excited state chemistry, an undesired ^3MC state is the lowest excited state, which is reached via IC from the a very short living $^3\text{MLCT}$ state ($\tau < 1 \text{ ns}$).

Table 2: Selected properties of important ruthenium polypyridine chromophores.

	[Ru(bpy) ₃] ²⁺ [36]	[Ru(tpy) ₂] ²⁺ [36, 39]	[Ru(bqp) ₂] ²⁺ [42]
$\lambda_{\text{max, Abs.}}^{\text{a}}$ [nm]	452	474	490
$\epsilon_{\text{MLCT}}^{\text{a}}$ [l/mol cm]	14 600	14 600	14 000
$\lambda_{\text{max, Em.}}^{\text{a}}$ [nm]	590	628 ^b	700
E_{0-0}^{a} ³ MLCT [eV]	2.12	1.98 ^b	1.77
$\tau_{\text{MLCT}}^{\text{a}}$ [ns]	870	< 0.5 ^b	3000
$\phi_{\text{Em.}}^{\text{a}}$ [%]	8		2
$E_{\text{Ox}}^{\text{a,c}}$ [V]	+0.8	+0.82	+0.71
$E_{\text{Red}}^{\text{a,c}}$ [V]	-1.76	-1.85	-1.70
geometry	octahedral	distorted octahedral	octahedral
symmetry	D_3 (chiral)	D_{2d} (achiral)	D_2 (chiral)

^a measured at room temperature in acetonitrile under inert conditions if not stated otherwise

^b measured in water

^c referenced vs. Fc/Fc⁺

The energy ordering of the various excited states, and, importantly, the orbital nature of the lowest excited state can be controlled by a judicious choice of the ligands. For example, the 2,2',6',2''-terpyridine ligand (tpy) in [Ru(tpy)₂]²⁺ can only achieve a severely distorted octahedral surrounding of the ruthenium center and, thus, changes energy ordering of the d-orbitals. This opens up a nonradiative deactivation pathway of the ³MLCT via the thermal population of the lower lying ³MC state, resulting in a lifetime of this excited state of 0.26 ns and a luminescence quantum yield near 0%. Otherwise, using the 2,6-bis(8'-quinolinyl)pyridine ligand (bqp) fulfills the criteria of octahedral coordination and increases the energy gap between the ³MLCT and ³MC states. Thus [Ru(dqp)₂]²⁺ exhibits a very long lifetime ($\tau \sim 3 \mu\text{s}$), and intense luminescence emission with a quantum yield of about 2% (see table 2).

As can be concluded by comparison of the complexes in table 2, it is possible to design complexes possessing, at least to a certain degree, the desired properties to play the role of energy donor, electron donor, or electron acceptor in the excited state.^[36] In the case of [Ru(bpy)₃]²⁺ and [Ru(bqp)₂]²⁺, the ³MLCT states live long enough (see table 2) to encounter other solute molecules and allow for excited state chemistry.

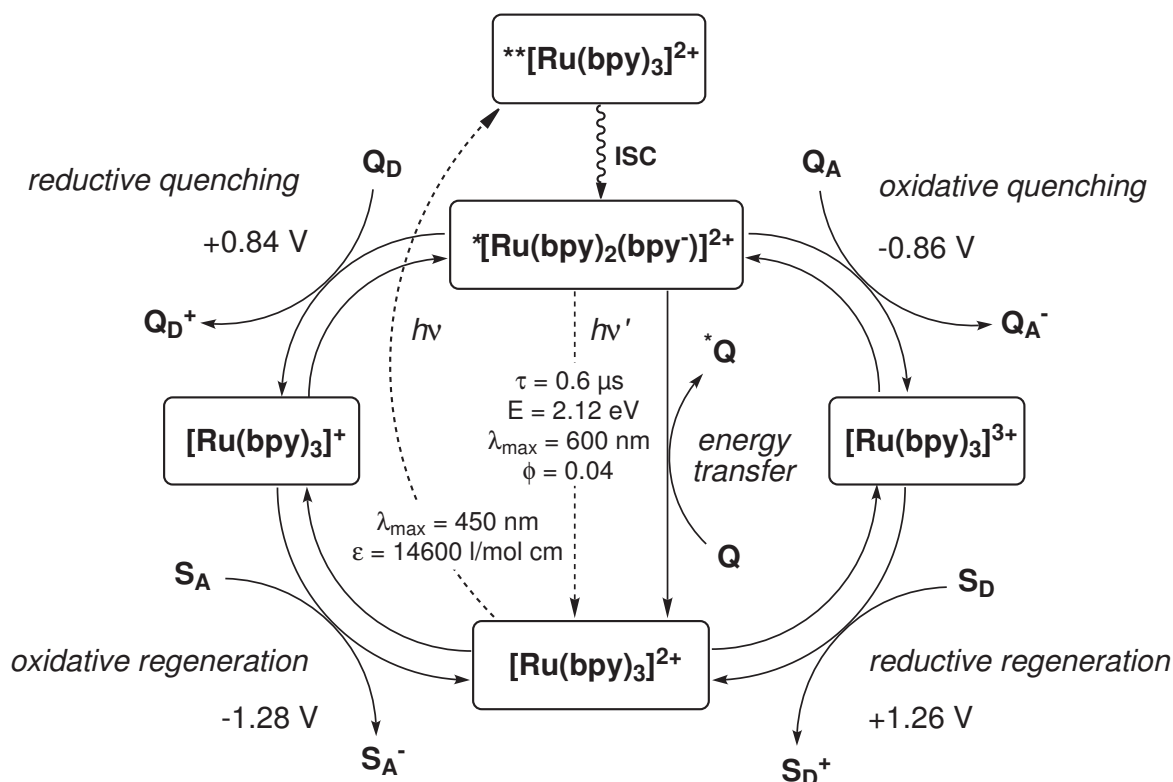


Figure 19: Relevant energy and electron transfer processes of [Ru(bpy)₃]²⁺. After photoexcitation the spin allowed ¹MLCT state ¹[Ru(bpy)₃]²⁺ is reached. ³[Ru(bpy)₂(bpy⁻)]²⁺ represents the long-living spin-forbidden ³MLCT state which is existent after intersystem crossing. During the lifetime of 600 ns different quenching processes may occur by the reaction with a quencher Q, followed by ground state redox chemistry with a substrate S. The redox potentials are given in aqueous solution, referenced vs. SCE.^[36]

The correlation between spectroscopy and electrochemistry is depicted in figure 19. It is known that the energy available to the ³MLCT-excited ³[Ru(bpy)₃]²⁺ ($E_{0-0} = 2.12$ eV) by far exceeds the energy necessary for over all water splitting (1.23 eV per transferred electron). This energy can be tapped during the lifetime of the excited state via different quenching mechanisms and leads to the regeneration of the ground state species of the sensitizer, if the quenching process involves only energy transfer processes (EnT). The biradical nature of the MLCT results at the same time in a fairly high oxidizing and reducing power (+0.84 and -0.86 V in water vs. NHE) of the excited complex. Therefore, it is also possible to tap the excited state energy in an electron transfer

reaction (ET) which leads to the formation of the groundstate sensitizer in an oxidized (oxidative quenching) or reduced form (reductive quenching). These redox reaction involving quenching mechanisms lead to the formation of charge pairs and, hence, represent a particularly important step toward long term charge separation.

In accordance to the HOMO-LUMO $^1\text{MLCT}$ -absorption, also ground state redox chemistry typically involves the metal centered HOMO and the LUMO which is localized on the ligand. Hence, electrochemical GS-oxidation of $[\text{Ru}(\text{bpy})_3]^{2+}$ -type complexes takes place at the metal fragment with simultaneous formation of a complex with $\pi_{\text{M}}(\text{t}_{2\text{g}})^5$ -configuration (compare figure 19). Whereas GS-reduction takes place at a ligand centered orbital with retention of the $\pi_{\text{M}}(\text{t}_{2\text{g}})^6$ -configuration of the metal fragment.^[40] The oxidation and reduction potential of the ground state ions (-1.28 and +1.26 V in water vs. NHE) are stronger than that of the excited biradical species and may also be used to oxidize or reduce water.

It is important that these processes are quasi reversible so that a reductively or oxidatively quenched chromophore can be regenerated without decomposition (requirement 1). This regeneration of the Ru(II) chromophore by a second component **S** may complete the hypothetical light-driven catalytic electron transfer cycle (excitation, quenching, regeneration), e.g. in the photoreduction of water.

It follows that $^*[\text{Ru}(\text{bpy})_3]^{2+}$ is at the same time a fairly good energy donor, electron acceptor, and electron donor.^[36] Whereas the potentials of charged quenching products are very high and are definitely sufficient to oxidize or reduce water respectively. Although its excited state $^*[\text{Ru}(\text{bipy})_3]^{2+}$ is thermodynamically capable of both oxidizing and reducing water at neutral pH, this has not been found to occur.

1.9.2 Redox Systems for Charge Separation

As described before, light excitation increases both the oxidizing and the reducing power of a chromophore. Therefore, light excitation of **P** can often be utilized by subsequent electron transfer (ET) processes. Unfortunately, a direct oxidation or reduction of water by $^*[\text{Ru}(\text{bipy})_3]^{2+}$ -type complexes has not been found to occur. Thus, suitable redox mediators **R** have to account for the fast and irreversible charge separation via quenching mechanisms to gather or deliver electrons from or to the chromophore. Furthermore, such redox ferries have the function to mediate the

unidirectional electron transfer between electron donor **D** and acceptor **A** via ground state redox processes (see figure 20).

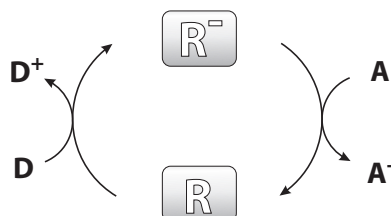


Figure 20: Reversible redox cycle of an electron ferry which can be used in a multicomponent system to allow for long distant charge separation and electron transfer between distant reactants, such as **D** and **A** in fluid media.

According to LEHN et al., a suitable shuttle species in a multicomponent setup for water reduction should have the following characteristics:^[34]

- (1) reversible redox behavior;
- (2) suitable redox potentials;
- (3) ability to accumulate multiple electrons;
- (4) ability to accumulate multiple protons;
- (5) good kinetic factors for outer sphere electron (and proton) transfer reactions;
- (6) stability toward thermal and photochemical decomposition;

Depending on the particular quenching mechanism, it should be reducible by the excited chromophore **P^{*}** or by the photoreduced species **P⁻** in the catalytic system (e.g. ^{*}[Ru(bpy)₃]²⁺ or [Ru(bpy)₃]⁺). And secondly, the shuttle species itself must be able to reduce water or the reduction catalyst (-0.86(-1.28) V < E₀ < -0.41 V, at pH 7 vs. NHE) to takeover transfer functionalities in the reduction half reaction. The converse argumentation applies for the water oxidation half reaction. To be a proper redox shuttle in the reduction chain, it can be helpful if the mediator is able to accumulate two or more electrons at about the same reduction potential to potentially allow for dielectronic reduction. According to natural systems it can also be helpful if reversible combination with protons can be coupled to the reduction reaction (e.g. quinones in photosynthesis or homogeneous hydrogenation catalysts). Proton coupled electron transfer offers a route to compensate charge effects in intercomponent ET reactions. In addition this may

potentially provide a pathway for hydrogen release from an intermediate hydride.^[34] In the case of pure redox shuttles it would also be helpful if docking groups such as -CN, COOH, -pyridyl are present which can be ligated to the involved species (chromophore, catalyst) allow for a directed electron transfer.

Commonly used mediators are bipyridinium ions (methylviologens like diquat and paraquat), phenanthroline ions, metal ions such as Eu^{3+} , V^{3+} or Cr^{3+} , metal complexes of Rh, Co, and proteins like cytochrome c_3 .^[29] The compounds depicted in figure 21, represent commonly used redox shuttles with suitable redox potentials and in some cases also the property to combine reversibly with hydrogen.

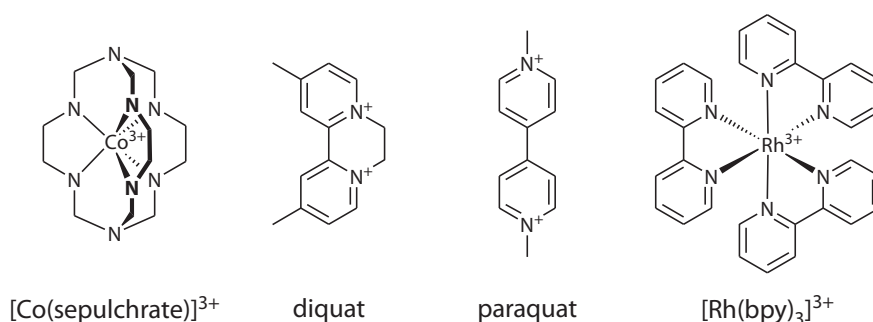


Figure 21: Representative electron mediators.^[29, 34, 37]

Additionally, it may be necessary to use sacrificial electron donors (tertiary amines like EDTA, triethylamine (TEA) or triethanolamine (TEOA), reduced metal complexes like Eu^{2+} -salts or other reducing agents like ascorbate, H_2S or **NADPH**) as well as sacrificial electron acceptors (peroxo species like $\text{K}_2\text{S}_2\text{O}_8$ or oxidizing complexes such as $[\text{Ce}^{\text{IV}}(\text{NH}_3)_2(\text{NO}_4)_6]$ or $[\text{Co}^{\text{III}}(\text{NH}_3)_5\text{Cl}]\text{Cl}_2$) to represent the second half reaction which is not relevant respective. Sacrificial substrates are also used as fast quenchers to increase the efficiency of electron transfer and importantly to make the back-reaction (charge recombination) less likely. In the case of $\text{TEA}/\text{TEA}^-\text{H}^+$ it is speculated that the (tertiary amine) buffer may serve both as electron donor and proton source^[32]

A quantitative theory of ET was developed by RUDOLPH A. MARCUS, who for this achievement was eventually honored with the Nobel Prize in 1992.^[43, 44] This powerful theory describes a number of important processes in chemistry and biology, including ground state electron transfer reactions as well as photoinduced electron transfer processes (PET), chemiluminescence and

charge recombination processes.

Upon reduction or oxidation of a molecule, multiple reorganization processes therein take place (bond lengths and angles as well as position and orientation of surrounding solvent molecules change). Therefore, for an electron exchange reaction to take place, transition state energies and geometries of the involved molecules (redox partners, intervening medium as well as field strength of solvent cage) have to represent a minimum on a multidimensional potential energy surface.

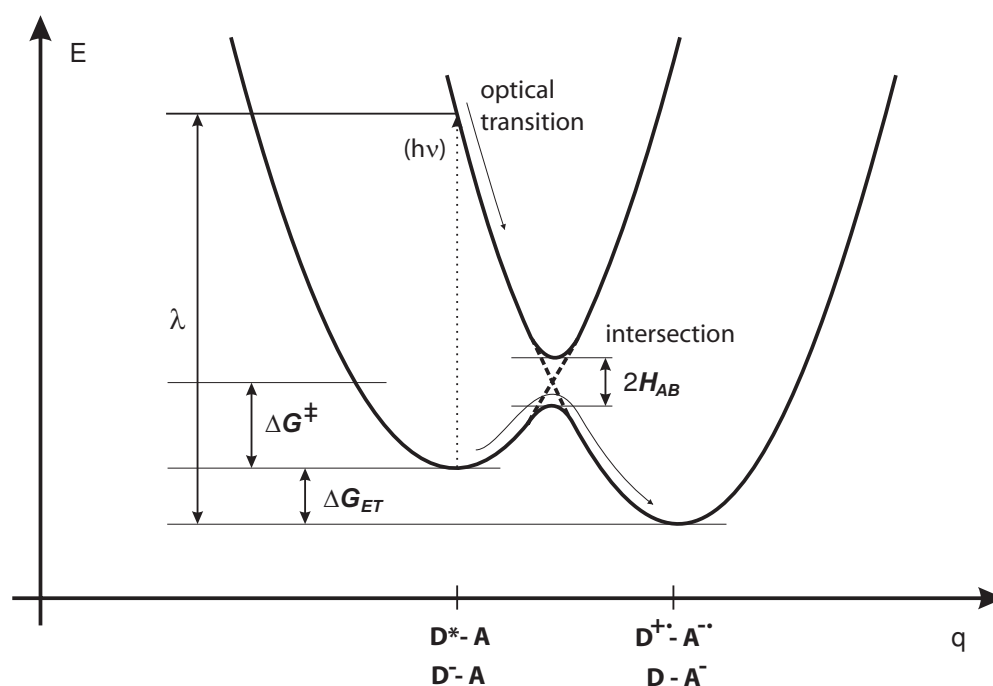


Figure 22: Profiles of the many-dimensional potential surfaces of reactants plus surrounding medium before and after an electron transfer reaction. Dotted lines indicate splitting due to electronic interaction of reactants. The minima denote nuclear coordinates for an equilibrium configuration of reactants and products. The saddle point denotes the nuclear configuration at the intersection of the two potential-energy surfaces.^[43, 44]

MARCUS was able to abstract this to a two-dimensional problem, combining all parameters into a single reaction coordinate q , which represents the motion of all the atomic nuclei. The GIBBS free energy is used to account for the nuclear motion of solvent molecules as well as reaction partners of the system. This way, it is possible to represent the potential energy surface of the reactants in the shape of two simple parabolas (see figure 22). One for the initial state (electron is still on the donor molecule/group), and another one for the final state (after the electron has been transferred

to the acceptor).

Nonradiative electron transfer is only possible at an intersection of the potential energy surfaces, which means that the nuclear coordinates of the involved molecules are the same in the initial state as well as in the resulting state (usually accessible with the help of fast rearranging solvent molecules). Otherwise, ET processes will always be vertical transitions under absorption or emission of photons, following the FRANCK-CONDON-principle.

The position of the parabolas is characterized by three parameters: The first is the free activation energy barrier ΔG^\ddagger (represents the activation enthalpy necessary to stimulate nuclear motion of solvent molecules as well as reaction partners, required to reach the intersection). The second is the free reaction enthalpy ΔG_{ET} released upon electron transfer, and the third is λ , which is a reorganization term called reorganization energy. It represents the energy that would be required to reorganize the nuclear positions of solvent molecules and reaction partners for the product situation (after the electron is transferred) to fit the initial conformation (represented by the potential minimum of the initial situation), without making the charge transfer (vertical transition). Thus it involves the distance between the reaction partners as well as the dielectric constant of the solvent and measures the absolute change in structure of the overall system during the ET process.

The interaction of the parabolas is defined by $|H_{\text{AB}}|$ which represents the electronic coupling between the initial and final states.

According to the ARRHENIUS transition state theory a rate constant k_{ET} can be derived for the depicted ET process (arrow passing through intersection in figure 22).

$$k_{\text{ET}} = A \exp \left\{ -\frac{\Delta G^\ddagger}{k_{\text{B}}T} \right\}$$

The prefactor A is based on the electronic coupling between the initial and final state and depends on the type of electron transfer reaction (e.g. inter- or intramolecular transfer). It also describes the frequency of nuclear movement as well as the transmission coefficient of this reaction or the fraction of back reaction.

$$A = \frac{2\pi}{\hbar} \frac{H_{\text{AB}}^2}{\sqrt{4\pi\lambda k_{\text{B}}T}}$$

Importantly, due to the simplifications and parabola approximation it is also possible to find a

formula for the activation energy ΔG^\ddagger , based on the reorganization energy λ and free reaction enthalpy ΔG_{ET} .

$$\Delta G^\ddagger = \frac{(\Delta G_{\text{ET}} + \lambda)^2}{4\lambda}$$

Interestingly, the quadratic relationship between ΔG^\ddagger and ΔG_{ET} causes a dependency of the rate constant for the ET to pass through a maximum $k_{\text{ET, max}}$ in the case of $-\Delta G_{\text{ET}} = \lambda$ ($\Delta G^\ddagger = 0$). Otherwise, in the case of $-\Delta G_{\text{ET}} > \lambda$ or $-\Delta G_{\text{ET}} < \lambda$ the ET reaction will be slower, even though the reaction will be very exergonic. This consequence of the MARCUS theory is termed MARCUS inverted region.

A combination of the above reaction gives the basic equation of Marcus theory:

$$k_{\text{ET}} = \frac{2\pi}{\hbar} |H_{\text{AB}}|^2 \frac{1}{\sqrt{4\pi\lambda k_{\text{B}}T}} \exp \left\{ -\frac{(\Delta G_{\text{ET}} + \lambda)^2}{4\lambda k_{\text{B}}T} \right\}$$

After having covered photophysical, photochemical and electron transfer aspects the essential influence of the catalytic centers on the over all efficiency shall be discussed.

1.9.3 Oxidation Catalysts - Solar Fuels

From the above discussion it is clear that the cleavage of water into oxygen and hydrogen represents a four-electron redox reaction which can be subdivided into oxidation and reduction half-reactions and which requires an energy of 1.23 eV per transferred electron. The main problem is the large overpotential (activation energy) for the multi-electron processes which has to be applied to the electrodes in an electrochemical setup in addition to the required energy of the thermodynamically uphill process.^[45, 28] A key step for light-induced water splitting will be the discovery of an efficient catalyst which achieves a stepwise one-electron transfer oxidation reaction and, therefore, bears a lower overpotential toward water oxidation (see figure 23).

Such molecules have to be multiply reducible or have to exhibit multiple electron “holes” to gather up to four electrons. Between the binding of H₂O and the release of O₂, three ideal intermediates have to be considered to be involved in the water oxidation reaction at the catalyst: C_{Ox}-OH, C_{Ox}=O and C_{Ox}-OOH. Accordingly, fitting binding sites and fine-tuned redox potentials of the involved processes have to be present in the catalyst.

Plants, algae, and cyanobacteria oxidize water with the help of solar energy and a μ -oxo bridged

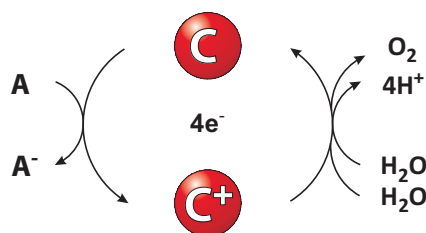


Figure 23: Oxidation catalyst for the multi-electron oxidation of water.

Mn_4Ca cluster which represents the active site in the OEC to bind two water molecules.^[20, 46]

Figure 24 depicts the successive removal of protons and electrons from the Mn_4Ca cluster with coordinated water (S) in ten steps.

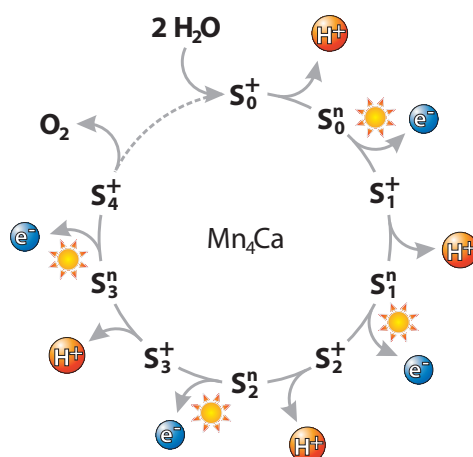


Figure 24: Extended S-state cycle model. Electrons and protons are removed alternately from the Mn_4Ca -cluster. The nine intermediate states of the Mn complex are denoted as $S_i^{+/-n}$ where the subscript denoted the number of accumulated oxidizing equivalents and the superscript indicates the relative charge: positive (+) or neutral (n) relative to the dark-stable S_1 -state.^[28]

This mechanism has not been completely explained until today but it is known that it involves the successive oxidation of separate Mn-centers within the cluster by tyr^{++} upon illumination and concerted release of protons from the manganese coordinated water molecules to the liquid phase (see figure 25-d for the structure of the active site).

In addition to the biocatalytic water oxidation in photosynthesis, different artificial approaches to water oxidation exist. They include heterogeneous electrocatalysis at electrode surfaces (e.g. cobalt phosphates referred to as CoP_1 ^[47]), heterogeneous photocatalysis by oxidic bulk materials in colloidal form or deposited on electrodes (e.g. metal oxides such as TiO_2 , IrO_2 , Co_3O_4 , Mn_3O_4 ^[48])

and homogeneous photocatalysis by transition metal complexes.^[28, 29]

Nevertheless, only a relatively small number of homogeneous molecular water oxidation catalysts is hitherto known and the prediction of suitable molecular structures for water oxidation catalysis at low overpotentials is rather difficult. Based on the multinuclear structure of the OEC and the discovery of the “blue dimer” by MEYER et al. in 1982, it is expected that a multinuclear structure is required (at least in the transition state) to accomplish the mechanistically demanding oxidative coupling of two water molecules to yield oxygen.^[49] As a result several binuclear catalysts that allow for high oxidation states of the metal center have been proven to be active catalysts for water oxidation (compare figure 25).

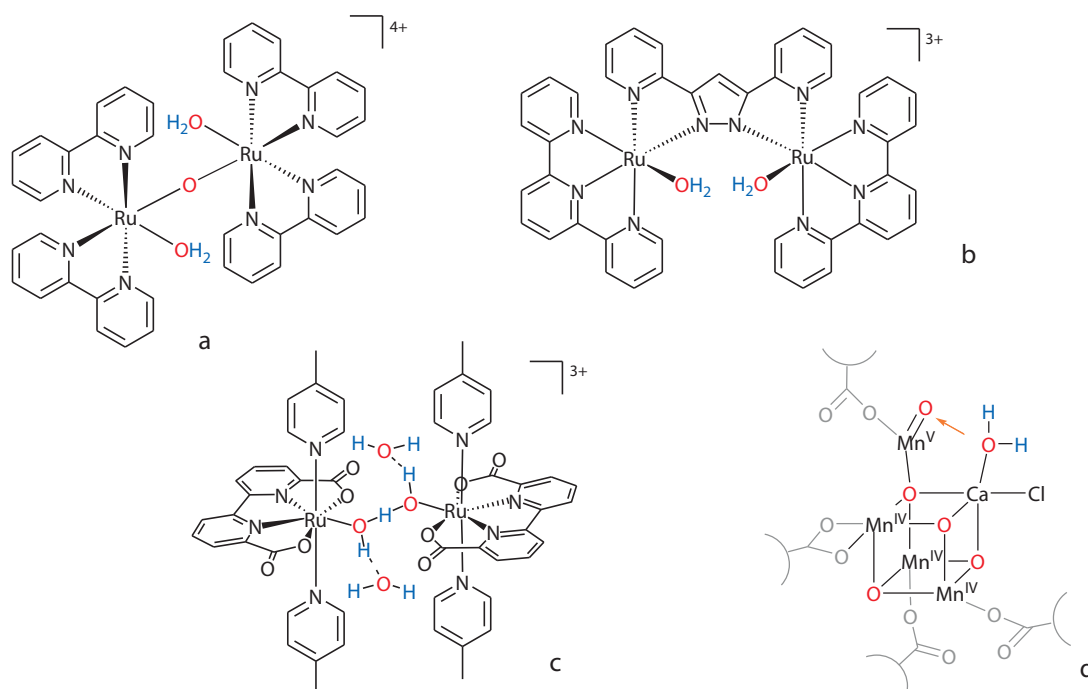


Figure 25: Important molecular oxidation catalysts: (a) “blue dimer” $[(\mu\text{-O})\{\text{Ru}^{\text{III}}(\text{H}_2\text{O})(\text{bpy})_2\}_2]^{4+}$ MEYER et al.^[49], (b) $[(\mu\text{-bpp})\{\text{Ru}^{\text{II/III}}(\text{H}_2\text{O})(\text{tpy})\}_2]^{3+}$ LLOBET et al.^[50] (bpp = bis(2-pyridyl)-3,5-pyrazolate), (c) $[(\mu\text{-HOHOH})\{\text{Ru}^{\text{IV}}(\text{dcbpy})(\text{pic})_2\}_2]^{3+}$ SUN et al.^[51] and (d) active center of the OEC as confirmed by BARBER et al. through X-ray analysis.^[52, 53]

However, water oxidation catalyzed by the blue dimer is nowadays explained by a mechanism that involves only a single ruthenium site. Therefore, water oxidation catalysis must also be possible with mononuclear metal complexes.^[28, 54, 55]

A common motif is $[\text{Ru}(\overline{\text{LLLL}})(\text{L})_2]^{n+}$, which contains a planar tetradentate $\overline{\text{LLLL}}$ -ligand

(e.g. rings systems like porphyrines) to exclude other chelating (tightly binding) ligands from coordinating the metal center and, therefore, allows for the ligation of H₂O during catalysis. Open $\overline{\text{LLLL}}$ -ligands may distort the octahedral coordination geometry around the central ion and ease the access for water in the ligand plane.^[56] In the research on mononuclear catalysts SUN et al. choose carboxy-substituted bipyridine as an $\overline{\text{LLLL}}$. Interestingly, the sterically less demanding ligand opens up a fifth coordination site at the ruthenium center in the bipyridine plane.^[51, 57, 58] In this way they succeeded in crystallizing a possible intermediate structure on the oxidation reaction with a μ -HOHOH-bridge between two of these μ -complexes with a very unusual heptacoordinated ruthenium center (see figure 25 c).

Complex (b) in figure 25, prepared by LLOBET et al. represents another commonly used structural motif: $[\text{Ru}(\overline{\text{LLL}})(\overline{\text{LL}})(\text{H}_2\text{O})]^{n+}$, exhibiting a combination of tightly bound tridentate $\overline{\text{LLL}}$ and bidentate $\overline{\text{LL}}$ ligands. Furthermore, a mobile monodentate ligand is present in the precursor which is predetermined to leave the complex to generate an open reaction site for water oxidation.^[50, 56, 54]

Finally, in addition to the commonly used ruthenium complexes a number of mono and oligonuclear manganese, osmium and iridium complexes with different catalytic sites are known to catalyze the water oxidation reaction.^[28]

Generally, hard ligands with strong σ -donating properties (e.g. μ -O, -COO⁻, halides or N-donor ligands) or strong-field ligands (e.g. cyclopentadienyle or phosphines) are part of the catalytic center to stabilize high oxidation states of the involved metal centers during the redox reaction.

1.9.4 Reduction Catalysts - Solar Fuels

The reduction of two protons under formation of molecular hydrogen is a two-electron reduction reaction. Similar to the water oxidation reaction, here as well an overpotential has to be applied to overcome the barriers in this multi-electron reaction within an electrocatalytical system. Undoubtedly, hydrogen evolution from water (protons) is less complex as compared to the evolution of oxygen which is a four-electron process. Nevertheless, it involves several catalyst adsorbed intermediates at different redox potentials, which may contribute to voltage and efficiency losses and need to be optimized (see figure 26).

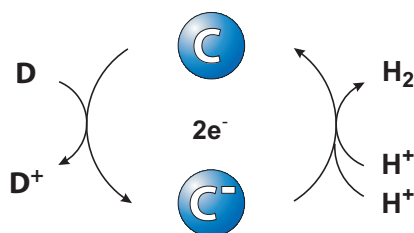


Figure 26: Reduction catalyst for the multi-electron reduction of protons (water).

According to BOLTON, systems for the reduction half reaction can be subdivided into photochemical systems, semiconductor systems^[48, 59], photobiological systems^[60], hybrid systems and thermochemical systems.^[61] The different approaches include heterogeneous electrocatalysis at electrode surfaces (e.g. platinized platinum electrodes). Examples for heterogeneous catalysis by oxidic bulk materials in colloidal form or deposited on electrodes are metal oxides such as RuO₂, IrO₂^[62], PtO₂, PdO₂ or Fe₂O₃ and supported materials like RuO₂ + IrO₂ on zeolite. Furthermore, photocatalysis with colloid metals and metal powders of Ir, Pt, Ni, Au, Ag, Pt, partially in situ generated from suitable salts like K₂PtCl₆ as well as core/shell-structured nanoparticles (noble metal/metal oxide core and Cr₂O₃ shell) is known.^[29, 48]

The biological example catalysts for water reduction can be found in hydrogenases, enzymes found in several microorganisms such as bacteria, protozoa or fungi.^[63, 60, 64] Three types of hydrogenases with different functions are known to date: iron-only-hydrogenases ([FeFe]), nickel-iron-hydrogenases ([NiFe]) and the so called “metal-free”-hydrogenases ([Fe]). Iron-only-hydrogenases which mediate the formation of hydrogen from protons and electrons or in other cases the back reaction with extremely high efficiency as a part of the microorganisms metabolism are of particular importance for the reversible production and consumption of fuels. From X-ray crystallographic and FTIR spectroscopic experiments it is known that the reaction center of the [FeFe]-hydrogenases consists of a [Fe₂S₂]-subcluster with a free coordination site for proton reduction, linked to one or several heterocubane [Fe₄S₄]-subclusters with intermediate electron storage capacity (compare figure 27).^[63] Impressive is the precisely fine-tuned, structurally and electronically flexible ligand environment around the dinuclear reaction site which exhibits mobile and soft carbonyl, cyanide and thiolate ligands, predominantly to stabilize low spin configuration and low oxidation states of the iron centers and to facilitate the binding and formation of hydrogen or protons.^[60]

As a result, a large number of bio-inspired hydrogenase models were prepared. They typically reproduce the $[\text{Fe}_2\text{S}_2]$ -motif, in addition, a variety of carbonyl and other ligands is added to account for open or closed reaction sites (compare figure 27).^[65, 66]

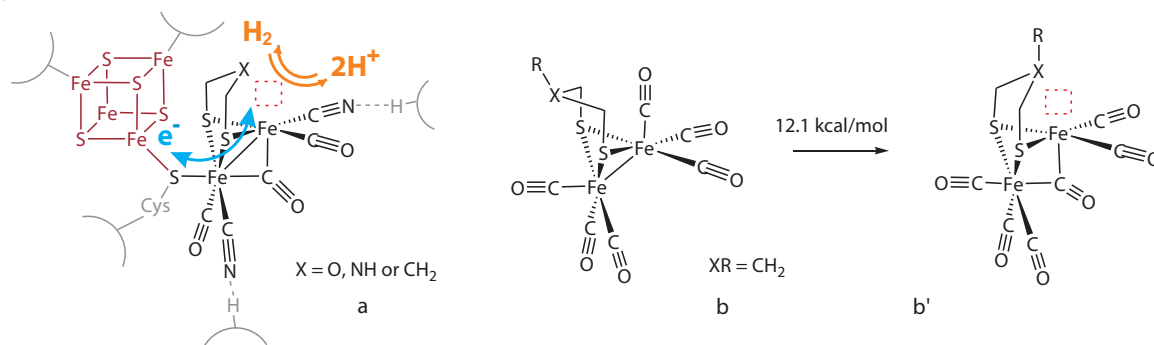


Figure 27: Natural $[\text{FeFe}]$ -hydrogenase from *Clostridium pasteurianum* (a)^[67] and bioinspired mimics with occupied (b) or vacant coordination site (b') at the second iron center.^[64, 68]

In not hydrogenase inspired homogeneous photo and electrocatalysis, commonly transition metal complexes of cobalt(I/III) or rhodium(0/II) are used (figure 28).^[37]

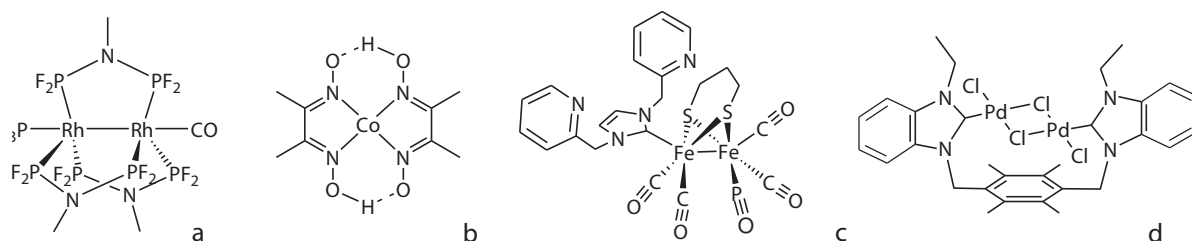


Figure 28: Different reduction catalysts (a) NOCERA^[69], (b) ARTERO^[37], (c) SUN^[70], (d) RAU^[71]

In principle, catalysts for proton reduction should be constituted similar to hydrogenation catalysts or catalysts for organic coupling reactions which exhibit low valent metal centers and vacant coordination sites to intermediately allow for the formation of hydrido-complexes that can be protonated to form hydrogen. Important ligands that stabilize low valent metal centers are phosphines and N-heterocyclic carbenes (NHC) as can be easily concluded from the development of the first and second generation of GRUBBS catalysts for metathesis reactions. Interestingly, not many examples for molecular catalysts are known in which phosphine or NHC-ligands are used to stabilize the metal. In figure 28, two examples for active hydrogen evolving catalysts with NHC-ligands are presented.

1.10 Intramolecular Photoredoxcatalysts

From the discussion about intermolecular catalysis, it is clear that working systems can be easily assembled from the available building blocks with respect to the desired functionality that shall be generated. The main focus of attention for the optimization of an artificial photosynthetic system is the improvement of charge separation and electron transfer processes. However, intermolecular electron transfer processes are naturally dependent on diffusion and collision processes. Therefore, usage of a multicomponent systems in a one-pot setup will increasingly generate problems the more “condiments” are added. Considering a system of independent components such as electron donor, photosensitizer, electron mediator, catalytic center and water in a supporting media, e.g. $S_D \llbracket \overrightarrow{P/R_A/C_{Red}} \rrbracket H_2O$, a variety of aspects has to be taken into account to understand all possible side reactions (e.g. $P^- \llbracket \overrightarrow{P^*/R_A} \rrbracket P^+$ or $P^+ + P^- \rightarrow 2P + h\nu$) and the involved mechanisms, to plan and perform the experiment respectively. Especially undesired electron transfer reactions or radical reactions (e.g. $R^{\bullet+} + R^{\bullet-} \rightarrow R-R$) are difficult to control.

To avoid diffusion generated problems a preorientation or linking of the reaction partners without changing their functionalities is necessary.^[40] According to the constitution of natural systems and based on pioneering work of D. J. CRAM, C. J. PEDERSEN and J.-M. LEHN who were honored with the Nobel Price in 1987 *for the development and use of molecules with structure-specific interactions of high selectivity*, this is best achieved in a supramolecular structure.^[72, 73, 74] The great advantage of such supramolecular systems is the localization of orbitals on specific substructures due to small interaction energies between them (see figure 29). Therefore, although slightly shifted, partial charges, involved redox processes and electronic transitions featured by the molecular components will be maintained in a resulting superstructure. This generates functional subunits which may act more or less independent of the rest of the molecule, whereat communication is improved in comparison to the bimolecular case.

In general, the classification of a compound according to figure 29 is not completely strict but gradual. Communication (delocalization/orbital overlap) between the components A and B changes with the distance and bond type of \sim between them and increases in the following order: electrostatic interaction < hydrogen bonds < host guest interaction < coordinative bonds < covalent bonds. Furthermore, shuttle type building blocks (e.g. molecular bridges/bridging ligands) can be used to establish a connection between distant substructures

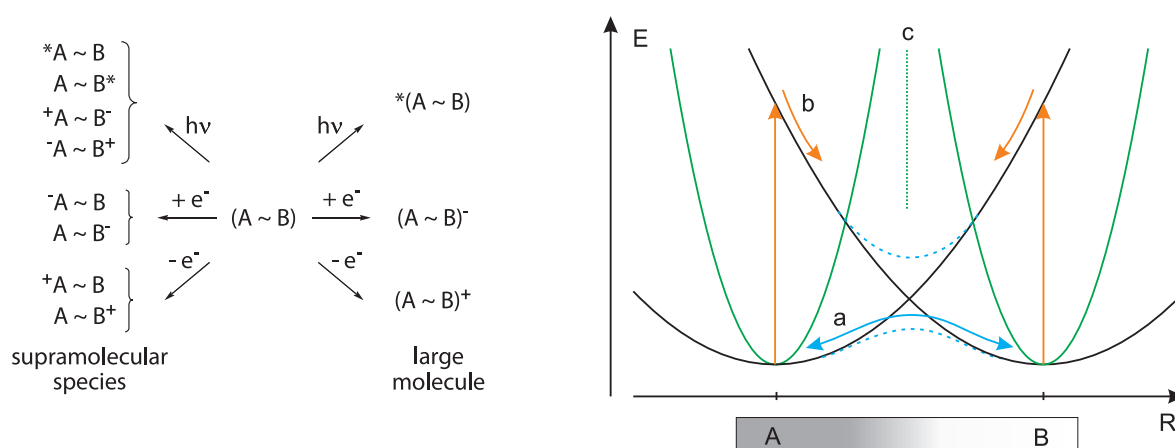


Figure 29: According to BALZANI the photochemical and electrochemical properties featured by supramolecular species and large molecules (left)^[40] and representation of strong (a) intermediate (b) and weak (c) communication between different components of compound $A \sim B$ in dependence of the electronic coupling and resulting energy barrier between them (right).

to allow for inner sphere electron transfer in addition to the outer sphere electron transfer. Thus, fast and directed intramolecular electron transfer processes may take place between the compartments, which dramatically reduces intermolecular side reactions. Importantly, in difference to intermolecular reactions, in the ground state any intercomponent electron transfer is, by definition, energetically uphill and must always be induced externally, e.g. by MLCT-excitation of an incorporated sensitizer.^[75] Starting from intermolecular working systems, the development toward intramolecular systems for the overall water splitting (e.g. $H_2O \llbracket C_{Ox} \sim R_D \xrightarrow{P} R_A \sim C_{Red} \rrbracket H_2O$) proceeded in stages and is not finished yet. First constructions of supramolecular systems focused on energy and electron transfer properties (e.g. orbital energies and positions, ET/EnT-kinetics, distance dependency or quenching processes) in simple supramolecular structures, constituted of photocenter and electron donor or acceptor respectively.^[36]



Later, research focused on long-term charge separation and on donor-acceptor assemblies:^[76]



In addition, antenna like systems and other supramolecular structures for intramolecular electron and particularly energy transfer were investigated:^[77]



Working intramolecular photocatalysts, consisting of photocenter and catalyst to perform a complete half-reaction were developed very late in the case of water reduction or are still unknown as in the case of water oxidation:^[35]



It turned out that in addition to organic systems, especially oligonuclear coordination compounds (dyads, triads, tetrads, ...) possess ideal properties to investigate the desired processes in supramolecular systems and to reproduce concepts of nature.

1.10.1 Oligonuclear Coordination Compounds

The necessary charge separation for redox-catalysis can be generated with organometallic chromophores **P** which represents one component of supramolecular catalyst. In addition, a second metal center will serve as redox-catalyst **C**. The use of fine-tuned bridging ligands **B** will increase the range and thus the lifetime of the charge separation in the first place. Furthermore, it will allow for an unidirectional inner sphere electron transfer toward the second metal to allocate the electrons for consecutive reactions. In general, three different processes exist which transform the absorbed excitation energy into redox-energy that can be tapped by the catalyst metal (see figure 30): (a) energy transfer, (b) photoinduced electron transfer and (c) photoinduced charge separation.

Electronic energy transfer (EnT) is equivalent to electron transfer between different intracomponent-LUMOs and parallel "hole transfer" between different intracomponent-HOMOs via FÖRSTER and DEXTER mechanisms and shifts the localization of excited state energy to an energetically lower lying excited state on a different component. Photoinduced electron transfer (PET) shifts an excited electron from a high intracomponent-LUMO (LUMO+1) toward a lower lying LUMO (KASHA's rule) which is localized on a different component. This can be seen as a intraligand electron transfer process from a high MLCT+1-state which populates a lower MLCT-

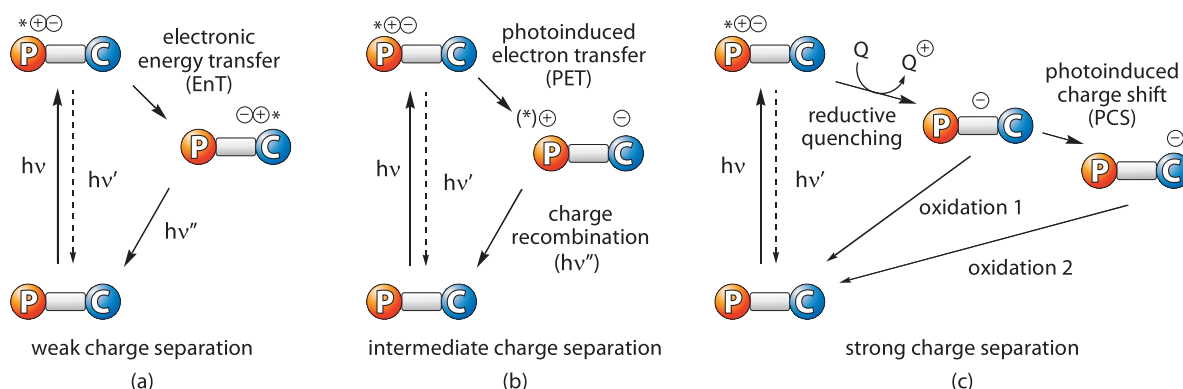


Figure 30: Charge separation by different types of photoinduced electron transfer processes (PET) and energy transfer processes (EnT) within a covalently linked system.

state when a direct HOMO-LUMO transition by MLCT-absorption is not possible due to a weak electronic coupling of the involved orbitals. Photoinduced charge shift occurs after reductive or oxidative quenching and refers to intercomponent redox-processes in the ground state. Especially when compared to figure 19, it becomes obvious that the increased efficiency of charge separation along with increased lifetimes is at the expense of a decreased redox-energy available for the desired process.

Particularly the chemical nature of the bridge which not only acts as passive spacer to provide for structural support, but rather mediates the electronic coupling between the involved substructures at the same time is of great interest. Accordingly, the degree of electronic communication can be fine-tuned by changing the distance between the metal centers, using innocent bridges (B_N) with high rigidity. Another possibility of fine-tuning is to change the role of the bridge by introducing functional groups or complexation of different metal centers. They determine the intracomponent HOMO and LUMO energies and electron withdrawing or releasing capacity as well as intracomponent redox potentials and the resulting function in the superstructure (see figure 31). Thus, a bridge can play the role of quencher (B_Q), donor and depot (B_D), acceptor and storage (B_A) or molecular wire for ET and EnT processes between two components. Aromatic bridges (e.g. tetrapyridophenazine) behave as efficient mediators of energy and electron transfer between metals.

From the above discussion the following list of requirements for the design of an optimal bridging ligand can be derived:

- (1) intrinsic and intercomponent stability toward thermal, photo- and electrochemical decomposition and reaction products or intermediates
- (2) reversible redox behavior
- (3) distance control of the interlinked metal centers
- (4) suitable electronic coupling between the components
- (5) suitable intracomponent HOMO and LUMO energies (redox-, ground state- and excited state potentials)
- (6) unidirectional charge separation or long lifetimes of the charge-separated state
- (7) sufficiently small energy gap between relevant excited/redox states to guarantee for (6), while conserving maximal redox activity
- (8) high energy/potential of the reactive excited/redox state
- (9) good kinetic factors for inner sphere electron transfer reactions for:
- (10) electron storage capacity
- (11) high efficiency of population of the reactive (excited) redox state at the catalyst site

Nevertheless, it is difficult to predict the properties of a single component, the bridging ligand in particular, without considering the other components on the supramolecular structure.

The series of $[\text{Ru}(\text{bpy})_2(\text{tpphz})]$ -type complexes (tpphz = tetrapyrrodo[3,2-a:2',3'-c:3'',2''-h:2''',3'''-j]phenazine) in figure 31 nicely exemplifies the difficult interdependences and interactions in a supramolecule.

Interestingly, the bridging ligand tpphz exhibits two types of empty π^* -orbitals in close energetic proximity, the LUMO_{bpy} , which is mainly localized on the bipyridine like moieties and the LUMO_{pz} which is localized on the pyrazine moiety of the molecule. The orbital energies of these LUMOs will be shifted in dependence of the oxidation state and the type of metal fragments, coordinated to it. As a result of that, differently localized LUMO orbitals will be involved in the charge transfer processes and charge separated states between the attached metals and the bridging ligand which will be indicated by MLCT_{bpy} and MLCT_{pz} in the following passages.

The mononuclear complex $[\text{Ru}(\text{phen})_2(\text{tpphz})]^{2+}$ (**Ru(tpphz)**, phen = 1,10-phenanthroline) shows the typical $^1\text{MLCT}_{\text{bpy}}$ -absorption between 400 and 500 nm and MLCT_{bpy} -emission from its LUMO_{bpy} ($\lambda_{\text{max}} = 625 \text{ nm}$, $\tau = 1.25 \text{ ms}$, $\Phi = 0.07$, depicted in orange). The electron-transfer process after excitation of the molecule, leading to deactivation of MLCT_{bpy} and population of MLCT_{pz}

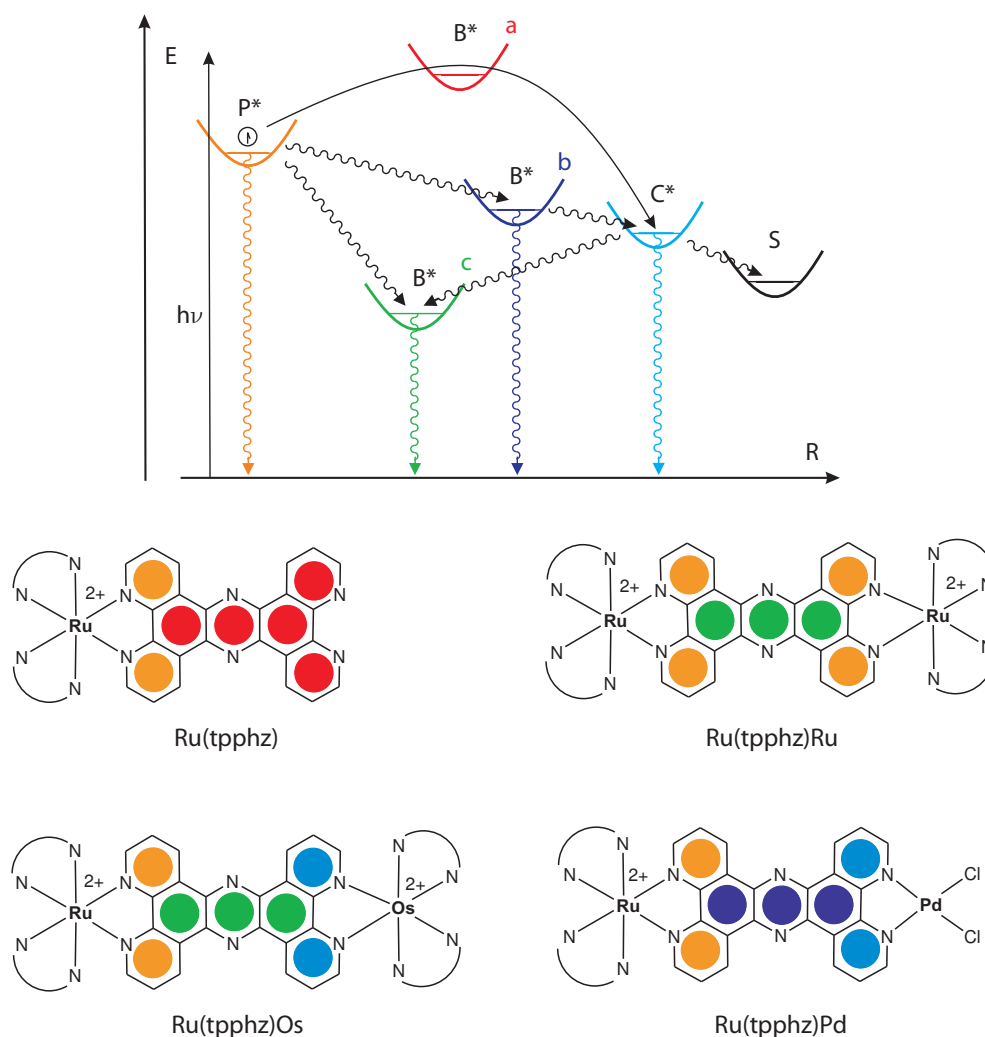


Figure 31: Idealized Jablonski diagram of photoinduced intercomponent energy- and electrontransfer processes, in competition with intracomponent decay in a supramolecular $[\text{P} \sim \text{B} \sim \text{C}]$ dyad (top). The different types of bridges can be subdivided according to their relative intracomponent LUMO-orbital energies (LUMO_{B}) in (a) not involved, (b) mediating and (c) trap ligands. Example complexes with $\text{Ru}(\text{bpy}_3)$ -type chromophores and tpphz bridges (bottom). The color coded π -systems refers to the diagram above.

(depicted in red) is according to CAMPAGNA et al. an endoenergetic process ($\Delta G = +0.2$ eV, case (a) in figure 31).^[78]

In contrary, the dinuclear complex $[(\text{phen})_2\text{Ru}(\mu\text{-tpphz})\text{Ru}(\text{phen})_2]^{4+}$ (**Ru(tpphz)Ru**) exhibits unchanged LUMO_{bpy} (depicted in orange) but a lowered LUMO_{pz} (depicted in green) which results in an intraligand charge transfer to the pyrazine moiety (case (c) figure 31) to populate

a MLCT_{pz} -like state. This process traps the electron on the bridge and gives rise to a weak, red shifted, short living MLCT -emission ($\lambda_{\text{max}} = 710 \text{ nm}$, $\tau = 0.10 \text{ ms}$, $\Phi = 0.005$) when compared to the mononuclear complex **Ru(tpphz)**. It is to note, that a direct singlet MLCT_{pz} excitation into the LUMO_{pz} is inefficient due to the low oscillator strength of the transition.^[78]

In the case of $[(\text{bpy})_2\text{Ru}(\mu\text{-tpphz})\text{Os}(\text{bpy})_2]^{4+}$ (**Ru(tpphz)Os**) two different chromophores are attached to the bridge, therefore two different ${}^3\text{MLCT}_{\text{bpy}}$ and two ${}^3\text{MLCT}_{\text{pz}}$ -like states are available. As experiments show, after excitation of an electron into the LUMO_{bpy} from the ruthenium center the system will eventually equilibrate to the lowest excited state which is the ${}^3\text{MLCT}_{\text{pz}}$ that involved the osmium fragment (type (c) figure 31) and relax to the ground state from there. In between, two possible pathways which lead to this result exist. They differ only in the succession of the following two processes, (a) ruthenium to osmium energy transfer and $(\text{Ru}^{3+}(\text{tpphz})\text{Os}^{2+} \rightarrow \text{Ru}^{2+}(\text{tpphz})\text{Os}^{3+})$ (b) ${}^3\text{MLCT}_{\text{bpy}}$ to ${}^3\text{MLCT}_{\text{pz}}$ relaxation. Which pathway is followed by the system is according to the MARCUS theory solvent-dependent. Whereat process (a) is followed by (b) in dichloromethane, process (b) is followed by (a) in acetonitrile.^[79]

The complex $[(\text{tbbpy})_2\text{Ru}(\mu\text{-tpphz})\text{PdCl}_2]^{2+}$ (**Ru(tpphz)Pd**) exhibits the LUMO_{pz} at an intermediate energy level between the LUMO_{bpy} and the accepting orbital at the palladium center (type (b) figure 31). As a result, a rapid population of MLCT_{pz} and subsequent electron transfer toward the palladium component takes place after initial excitation of the well-known MLCT_{bpy} which completely quenches the emission of the complex.^[80, 81]

1.10.2 State of the Art Systems

Pioneering efforts to develop complete supramolecular catalysts which mimic essential subreactions of water splitting with the help of metal complexes were described in detail by SUN et al. in 2001, particularly for the water oxidation half reaction.^[18] For the water reduction side, the first intramolecular photocatalysts were presented by the work groups of NOCERA, SAKAI and RAU.^[69, 82, 80] Until today a series of intramolecular photocatalytic systems for the energetically unfavorable activation of small molecules (water reduction and oxidation or CO_2 reduction) and other redox reactions are known.^[83, 35]

Figure 32 depicts the general scheme of intramolecular working systems for hydrogen evolution.

As can be seen, an array of sensitizer, molecular bridge and catalyst gives rise to an active $[[P \sim B \sim C]]$ -type superstructure.

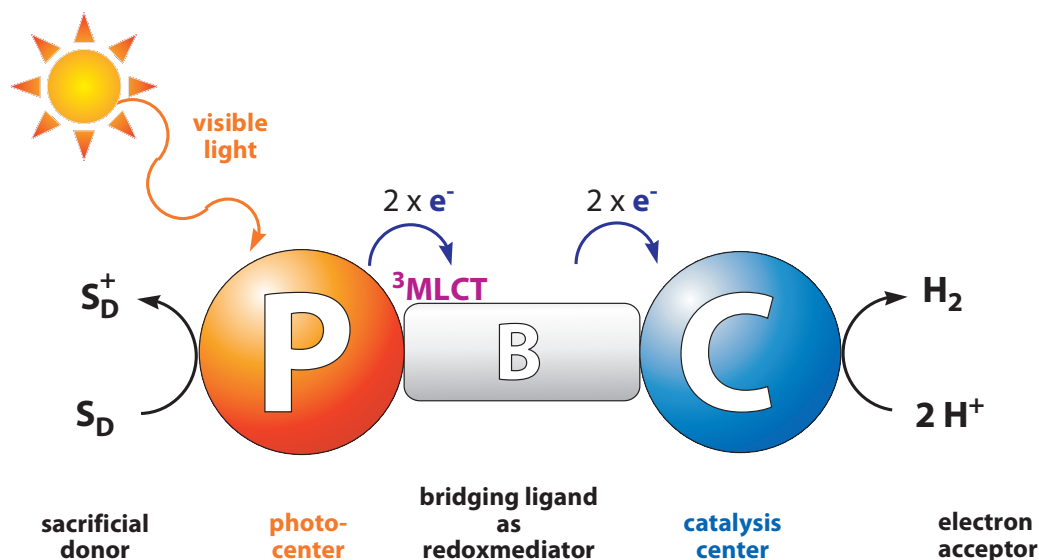


Figure 32: Model of a bimetallic *intramolecular* catalyst for hydrogen generation from water under irradiation with visible light. Important building blocks for this functionality are the organometallic chromophore **P** (charge-transfer complex for charge separation), the second metal complex **C** (redox active catalyst) and the bridging ligand **B** (connection of photo- and reaction center, intramolecular pathway for the directed electron and energy transfer).

Typical state of the art systems include bimetallic and polymetallic assemblies (see figure 33).^[35] The incorporated photosensitizers are chosen according to the results from the intermolecular catalysis to be ruthenium polypyridine complexes with the well behaved photophysics and redox chemistry. Some examples with iridium, rhodium and other sensitizers are known as well.^[69, 85] Going from intermolecular catalysis to intramolecular systems, a paramount substitution of the previously used colloids or other heterogeneous catalysts toward molecular well defined catalysts has to be made. As a result, all catalysts exhibit metal fragments (Pd, Pt, Rh, Co) that are well known from electrocatalysis or organometallic coupling reactions to allow for multiple electron uptake and a low valent catalytic species. Furthermore, all catalysts exhibit metastable terminal ligands at the catalytic center to open up hydrogen binding sites during the catalysis.^[29, 35, 83] Special attention has to be paid to the molecular bridge which has to take over the electron relay functionality. Interestingly, different kinds of bridging ligands were used in terms of rigidity

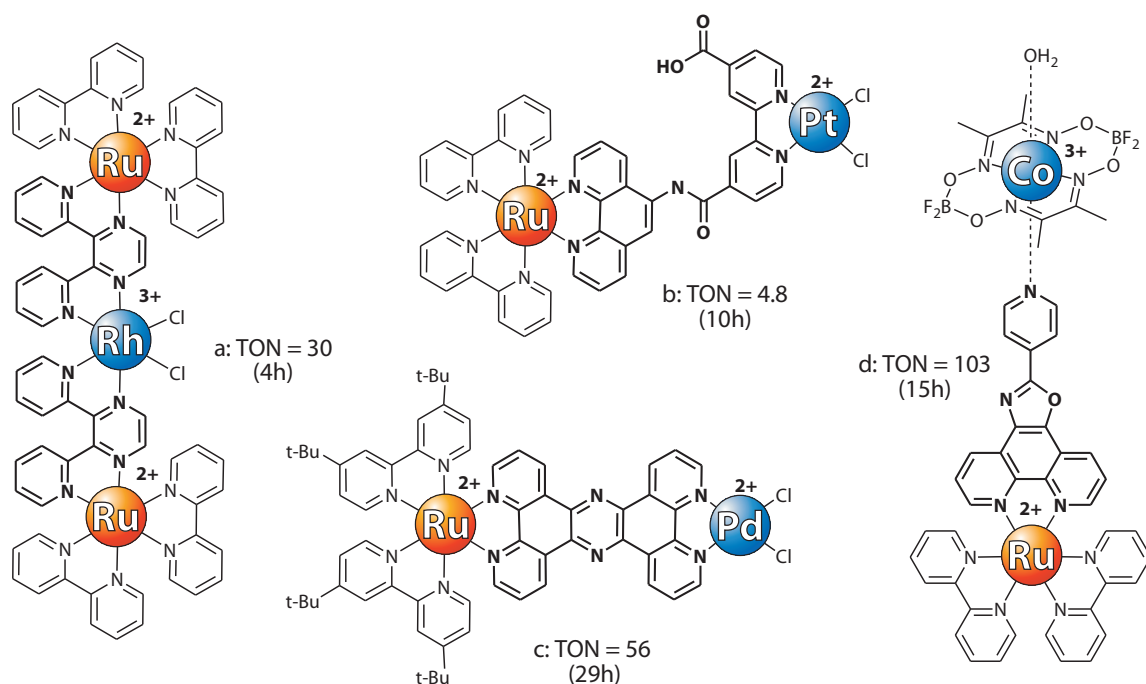


Figure 33: Representative systems for the intramolecular hydrogen evolution, reported by the workgroups of BREWER (a)^[84], SAKAI (b)^[82], RAU (c)^[80] and ARTERO (d)^[85, 86]. The dyads and triads typically contain a $[\text{Ru}(\text{bpy})_3]^{2+}$ -type photocenter (orange). A second NN-chelated metal center (blue) provides redox activity and coordination sites for catalytic hydrogen evolution. Covalent bridges (bold) constitute the framework of the substructures.

(distance control) and activity in ET and EnT processes.^[83] Especially the amide linked bridge in the SAKAI system represents a very flexible bridge which may flip back and forth (allow for outer sphere ET). The RAU system, based on tpphz, exhibits a very rigid π -system with high distance control between the metals (forces inner sphere mechanism).^[82, 80] Very short distances with high electronic communication between the metals are achieved in the BREWER system (metal-metal interaction) whereas the ARTERO system exhibits the largest distance between the metal centers (through-bond versus outer sphere mechanism).^[84, 87] In addition, the type of the coordinative bond will influence the integrity (e.g. reversible redox behavior, photostability) of the supramolecular scaffold during the high energy processes. For historical and photochemical reasons, typically N-donor ligands are used to bind the photocenter metal in the different redox states. Catalysis experiments with the $[\text{P} \sim \text{B} \sim \text{C}_{\text{Red}}]$ systems are very similar to previous experiments with intermolecular systems in set up and analysis. Usually, a sacrificial electron

donor is used to support the half reaction, a suitable solvent is used to achieve a good solvation of the large molecules and adjustment of the pH value, while water is added to serve as the proton source for the hydrogen evolution.^[29] A proper light source (sunlight, filtered white-light, LED sources or LASER) is used for the required excitation of the system. The formation of hydrogen can be detected and quantified by gas chromatography from the headspace of the solution.^[88] Nevertheless, a systematic permutation of C_{Red} or \mathbf{B} in a series of photocatalysts with otherwise unchanged components and conditions to derive structure-activity correlations and possibly something like a “golden rule” for the purposeful construction of a supramolecular catalyst has been performed only incompletely and for few examples.^[89, 90, 91, 92, 93] At least a number of problems found in the few catalytic systems known today can be used to yield a starting point for the development and improvement of intramolecular photocatalysts.

1.10.3 Drawbacks and Starting Points

A main disadvantage which was supposed to be overcome by going from *inter-* to *intramolecularly* working catalysts is the number of unwanted side reactions which decrease the stability and quantum yield of the system.

Especially the hardly predictable behavior of the bridging ligand in a superstructure during a multi-electron redox reaction makes it difficult to choose a proper candidate. Interestingly, often N-donor ligands are used to bind the catalyst metal as well. This is due to a convenient access to these systems with high synthetic flexibility and due to the positive results from the good expertise in dealing with $[\mathbf{P}^1 \sim \mathbf{B} \sim \mathbf{P}^2]$ -type polyads. As a consequence, upon multiple reduction only limited stability of the acceptor metal (e.g. Pd(0)) can be achieved. With the help of TEM and XPS experiments in a very similar photocatalytic system HAMMARSTRÖM et al. could show that photoreduction upon visible light irradiation in the presence of TEA as sacrificial substrate leads to the cleavage of the N-donor-stabilized palladium metal from the supramolecular array. Furthermore, appearance of palladium colloids, for a long time known to be catalytically active themselves, strongly correlates with the formation of hydrogen (see figure 34).^[94]

The proven formation of colloidal palladium emphasizes the major drawback of the, by definition, weak interactions between the components in a supramolecular system in general and the use of N-donor ligands to link low valent catalyst centers in particular. Hence, these findings reopen

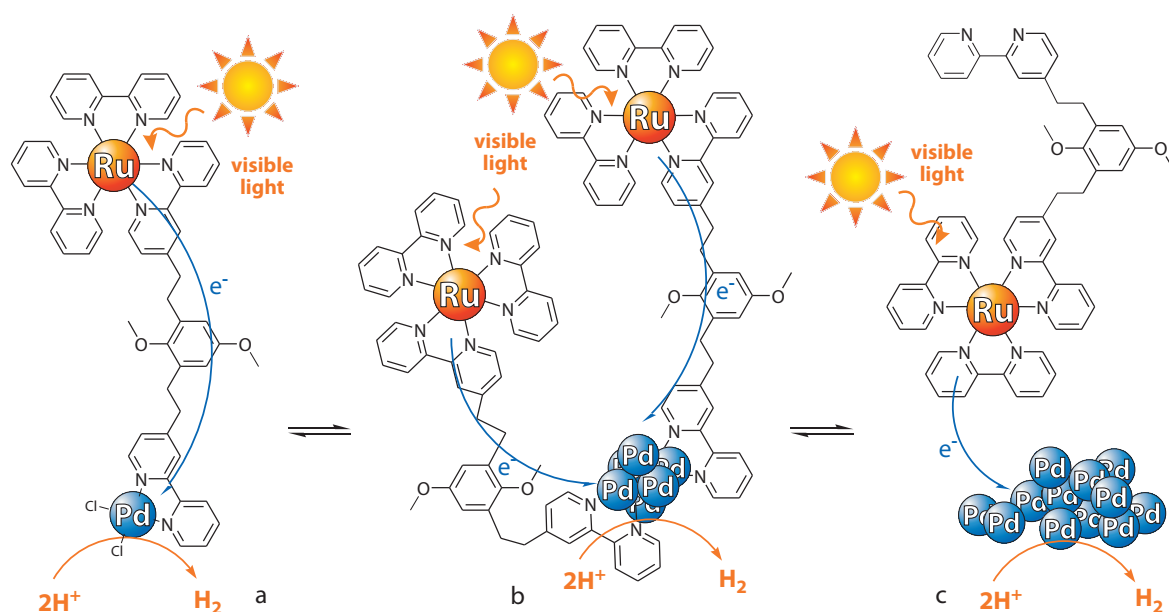


Figure 34: Photoinduced degeneration of the intramolecular homogeneous catalyst (a) to an intramolecular micro-heterogeneous system (b) and finally an intermolecular operating heterogeneous system (c) as observed by HAMMARSTRÖM *et al.* clouds the true nature of the catalyst.^[94]

the compromising question for the true nature of the catalyst in all supramolecular assemblies. To answer this important question it requires the careful consideration of alternative mechanisms and improved techniques of investigation. Accordingly, different coordination motifs need to be tested and applied to assure the stability of the scaffold during the high energy photocatalysis processes. Promising candidates are phosphine or N-heterocyclic carbene ligands (NHC) which can be adapted from low valent metalorganic catalysis (e.g. HECK reaction catalyst) or the chemistry of complex hydrides.

Another problem with the molecular bridge is the difficult determination and adjustment of the properties relevant for interaction between the participating metal centers (compare tpphz complexes). Using the trial-and-error method causes an intensive cost-, work- and time effort to accomplish even little progress toward an improved catalyst.

From the economic and environmental point of view the use of expensive materials especially noble metals for chromophores (Ru, Ir, Os) and catalysts (Pt, Pd, Rh, Au, Ag) is a major drawback as well as low yielding multistep syntheses of molecular bridges. Screening experiments with multimolecular and supramolecular catalysts can help to find cheap active compounds (Fe and

Ni as known from hydrogenases or Co) to substitute the noble metals. The exploration of new pathways toward easily accessible building blocks is essential to have the chance to make the overall process short, cost efficient and sustainable.

The final challenge is coupling of the reduction and the oxidation half reaction into an overall water-splitting device. Until today only a few reduction catalysts are known to tolerate singlet or triplet oxygen or even to operate under aerobic conditions, generated by the water-oxidation site. To avoid this problem, a separation of oxidation and reduction half reaction in different compartments or half cells will be sufficient. This can be realized with surface/electrode bound photocatalysts as well.^[62] Here, molecular anchoring groups (e.g. $-\text{COO}^-$, $-\text{PO}_3^{2-}$ or $-\text{S}^-$) have to attach the photocatalyst to the surface and need to allow for electron transfer to the surface to mediate them between the half reactions.

The artificial photosynthesis research is still in the fledgling stages, as can be seen in the low turnover numbers (TON) and turnover frequencies (TOF) which nowadays can be achieved in the separated half reactions. To make the process interesting for applications an increase by several orders of magnitude is necessary which is accompanied by the elimination of the sacrificial reagents. Exactly for these reasons, fundamental research is important to increase the knowledge in this area to have the chance to contribute to the energy supply of future generations.

2 Scope of the Thesis

The utilization of sustainable energy sources represents one of the major challenges of the future. In the scope of solar to chemical energy conversion and having the natural photosynthesis in mind, simple photocatalytic systems shall be generated.

With respect to the potentials of the field of inorganic chemistry, oligonuclear metal complexes, consisting of a photoredoxactive chromophore **P**, a bridging ligand **B**, and a catalyst center **C**, shall be prepared. At the same time, a purposeful combination of the individual subunit properties shall be accomplished to generate new artificial photosynthetic systems ($[[\mathbf{P} \sim \mathbf{B} \sim \mathbf{C}]]$ -systems, see figure 35). After visible light excitation of the photo center **P** a directed electron transfer across the bridging ligand **B** toward the catalysis center **C** shall occur. In this way, the light energy should be applied to reduce protons from water at the catalyst center to form hydrogen (fuels) during the lifetime of the charge separated state.

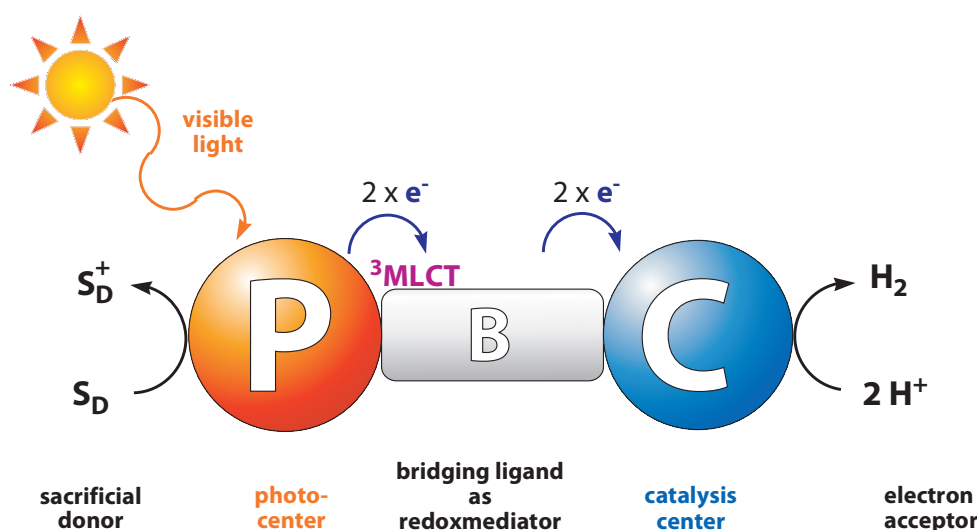


Figure 35: Model of a bimetallic *intramolecular* $[[\mathbf{P} \sim \mathbf{B} \sim \mathbf{C}]]$ -catalyst for hydrogen generation from water under irradiation with visible light.

In the envisaged systems, well known $[\text{Ru}(\text{bpy})_3]$ -type centers shall be incorporated to serve as photosensitizer. Leaving the chromophore unchanged but focusing on bridging ligand and reaction center allows characterizing and understanding the nature of electron transfer and supramolecular catalysis.

Thus, a special interest will be placed on the bridging ligand. Here, particularly new structural

motifs with high synthetic flexibility and tunable electronic properties shall be generated, applied and tested. Important is the good stabilization of **P** and **C** at the bridge, therefore, old bridging concepts shall be advanced and new donor functionalities shall be introduced into the binding sites. This will additionally allow for the application of new catalytically active metals, to overcome the drawbacks of the first generation catalysts. In this respect, especially the easy to functionalize phenanthroline derivatives are of interest, as they can be extended by a second coordination sphere e.g. by a NHC moiety.

Furthermore, the electron storage/mediating capacity of the bridge is important, thus, different bridging concepts (conjugated/isolated systems) shall be developed and applied to optimize the electronic communication across the bridge. The introduction of different groups at the bridge shall be applied to generate an electronic situation that localizes the excited electron predominantly on the bridge.

With respect to the catalytic center, a number of different metals, e.g. the previously used platinum metals such as Rh, Re, Pd or Pt shall be applied, but also new metals with a better availability such as Co, Fe or Ni shall be considered. A comparison within a series of similar catalysts can be used to increase the efficiency of the system.

With a complete $[[\mathbf{P} \sim \mathbf{B} \sim \mathbf{C}]]$ -system in hands, using the established methods from the workgroup of RAU, detailed catalytic (screening)experiments shall be performed to test their activity in the light driven hydrogen production and to advance the systems in the future.

Toward these new $[[\mathbf{P} \sim \mathbf{B} \sim \mathbf{C}]]$ -systems, at first, new methods for the preparation of the new ligands shall be developed and applied. The intermediately obtained ligands shall be analyzed and characterized. Furthermore, a number of new ruthenium complexes with these ligands shall be generated and characterized. Using the prepared ruthenium complexes, particularly those containing bridging ligands, as starting materials, additional catalyst centers shall be attached to obtain suitable $[[\mathbf{P} \sim \mathbf{B} \sim \mathbf{C}]]$ -model systems. In this way different series of ruthenium and ruthenium/catalyst metal complexes, varying in ligand parameters or catalyst parameters shall be prepared. Especially with the help of different spectroscopic and electrochemical experiments, using the mono- and oligo-nuclear complexes, detailed insights into the electronic behavior of the ground and excited state molecules shall be obtained. With respect to the performed changes and in the scope of an application in catalysis, structure-property relationships shall be revealed.

3 General Section

Artificial photosynthetic systems for solar fuel production on a molecular level represent a great challenge for modern chemistry.^[9, 29, 35] In this context, especially coordination chemistry offers a variety of compounds with adequate properties to adopt functionalities similar to biological enzymes in artificial systems. Supramolecular arrays with incorporated photo- and reaction center bear the necessary requirements for light energy uptake and proton reduction or oxygen formation. Especially ruthenium complexes are among the important representatives of a widely used class of charge transfer chromophores that can be used for light into redox energy conversion. As mentioned, it is possible to fine-tune their energy and localization of the electronic ground and excited state by changing the ligand environment around the metal center which influences the absorption, luminescence and redox properties. In addition, multiple functional units may be linked in a predesignated order via bridging ligands, which opens the route toward higher integrated systems capable of processing various interlocking functionalities.^[95] Such ligands have to connect the active sites of the complex to serve as intramolecular pathway for the directed electron and energy transfer, thus turning a supramolecular array into an operational photocatalyst. Of paramount importance are bridging ligands with increased synthetic flexibility and adjustable electronic properties. The following chapters will follow the path, starting from bridging ligand synthesis, toward fully functional artificial photocatalytic systems. Special interest will be placed on the detailed characterization of the intermediates and on hydrogen evolution experiments, using the final catalysts and references.

3.1 Brominated Phenanthrolines - A Gate to new Bridging Ligands

Due to their intense luminescence properties and their ability to interact with DNA in an intercalative fashion, phenanthroline based compounds have found many applications in almost all areas of coordination chemistry and supramolecular chemistry, ranging from sensing application to the use in catalysis.^[96]

The most important parameter to influence the properties of the phenanthroline derivatives are the substitution patterns at the molecular scaffold. Over the years a huge number of manipulations were performed to customize phenanthrolines for the particular application. Figure 36 denotes the

possible positions that can be used to introduce functional groups.

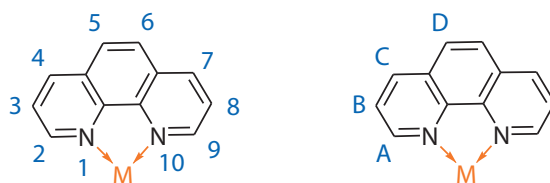


Figure 36: Numbering scheme for the positions of the 1,10-phenanthroline backbone.

The 1,10-positions represent the N,N'-coordination site which is accessible to almost all known metal centers M. Reversible transformation (oxidation, alkylation) in this positions can be used to protect the binding site or to activate the pyridine rings for further manipulations.^[96]

The introduction of substituents in the 2,9-positions is rather simple and, thus, generally used to influence the metal binding properties. Via the introduction of a variety of functional groups (e.g. through transformation of the chloro-compound)^[97] it is possible to introduce aryl-^[98], pyridyl-^[99, 100], amine-^[101, 102], phenole-, and carboxy-groups^[103] to expand the coordination sites and to tailor them for a variety of metal ions. The introduction of bulky groups such as extended aliphatic- or substituted aryl-groups result in a blocking of the coordination site and decrease of the binding capacity especially for metal fragments with square planar or octahedral geometry.^[104] Thus, it is possible to force tetrahedral coordination geometry or to selectively exclude metal ions.^[105]

Introduction of functional groups in the 3,8-positions is particularly interesting because the most intense electronic transition in phenanthrolines is polarized along the 3-8 axis. TZALIS and TOR showed very nicely how to increase or decrease the conjugation along this direction in order to built a new family of highly emissive chromophores with tunable emission wavelength, dictated by the nature of the substituents at the 3,8-positions.^[106, 107, 108]

Substituents in the 4,7 positions have a strong influence on the MLCT-transition in the resulting metal complexes. The introduction of conjugation-extending aryl-substituents in this position is best approached by nucleophilic aromatic substitution of halogen atoms in 4,7-dihalo-1,10-phenanthrolines whose synthesis has been optimized by SCHMITTEL et al.^[109] TOR and coworkers exploited this concept for the development of dual emissive ruthenium complexes.^[110, 111]

Interesting are manipulations of the 5,6-positions because they have only a minor influence on the primary photophysical and photochemical processes of the metal phenanthroline complexes but allow for a linear alignment of two metal centers in a symmetrical molecule. Furthermore,

3.1 Brominated Phenanthrolines - A Gate to new Bridging Ligands

extended 5,6-annulated aromatic systems play an important role in DNA binding and sensing applications.^[112] Important transformations of these positions represent electrophilic substitution reactions such as nitration or oxidation to generate homo- and heteroditopic ligands such as tpphz.^[113, 114, 115]

In order to further explore this interesting ligand class, concepts have to be implemented which allow for the introduction of a multitude of potential connecting groups which can be transformed selectively. But, according to the BENCINI et al., it is more difficult to achieve synthetic

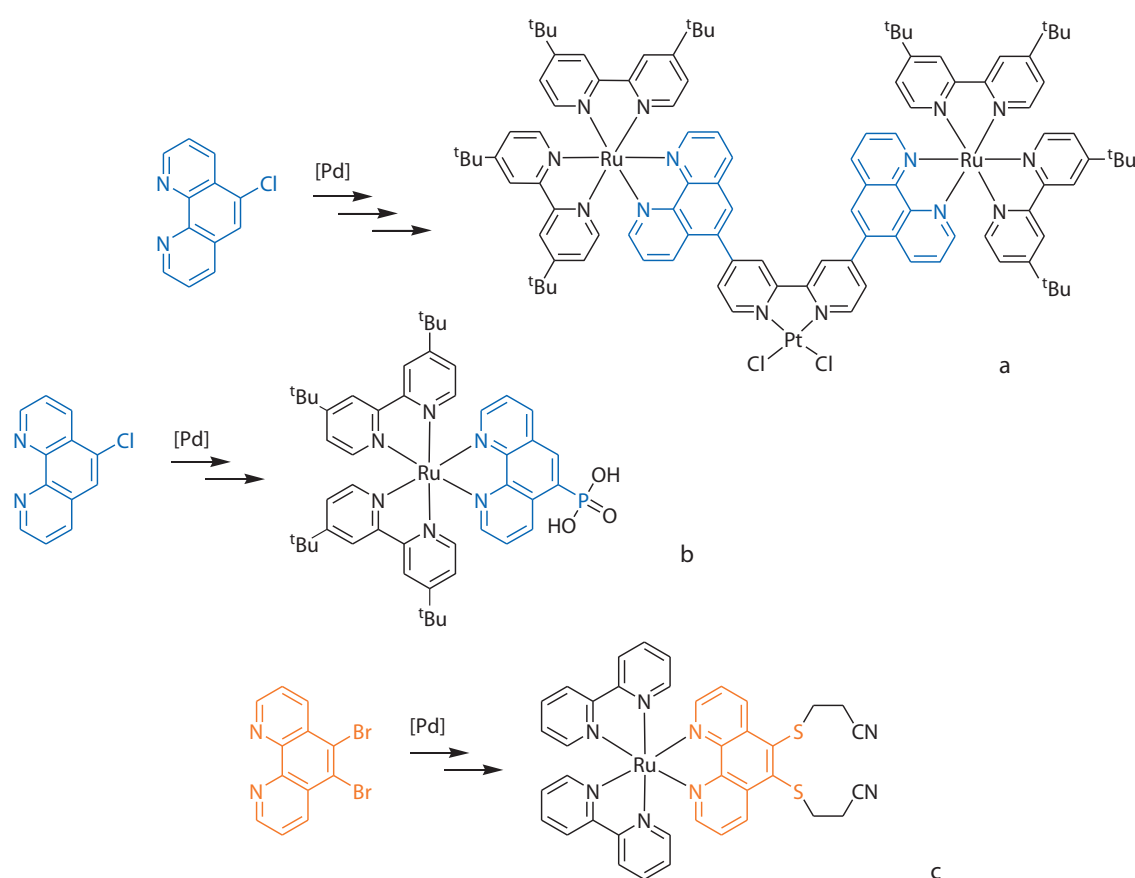


Figure 37: Important examples of the use of 5- and 5,6- halogenated phenanthrolines in the synthesis of bridging ligands for extended arrays with multiple chromophores e.g. for the multi-photon uptake of efficient photocatalysts (a)^[116, 117], preparation of anchor ligands for surface bound (e.g. TiO₂) chromophores for the application in dye-sensitized solar cells or photoelectrochemical cells and heterogeneous catalysis (b), and ligands with thio-functionalities for the application in [FeFe]-hydrogenase models^[118] or for colloid binding (e.g. gold surfaces^[119]) in example (c).

manipulations at the interesting 3,8-, 4,7- and 5,6-positions of the phenanthroline and therefore much fewer synthetic options are available today.^[96]

In this respect, especially bromo-substituted phenanthrolines are especially interesting, as they have been proven to be extremely flexible and useful starting materials for the preparation of mononuclear^[120] and multinuclear complexes.^[40] Thus, predominantly organometallically catalyzed coupling reactions were applied to quickly generate new terminal ligands and heterodentate bridging ligands with N-, P-, or S-donor functionalities from halogenated phenanthrolines (see figure 37 for examples).^[108] This opened the route toward molecular systems with controlled binding of the interlinked metal centers and surfaces, which is crucial for aspects such as tuning of the functional center or long term stability thereof.

The results presented below will summarize the efforts to broaden the available synthetic options for manipulations at the 5- and 6-positions of phenanthroline derivatives. Furthermore, the synthesis and complete characterization of resulting ruthenium complexes will be presented. Through the analysis of spectroscopic and electrochemical data a possible influence of the substituents at the 5,6-positions on the excited state characteristics of the resulting chromophores was investigated.

3.1.1 Selective Bromination of Phenanthrolines

Despite the interest in the resulting compounds, especially the regioselective bromination in the 5- and 5,6-position was obviously not sufficiently explored or optimized. Instead, expensive and less reactive chloro-derivatives had to be used as starting materials in challenging coupling reactions (a and b in figure 37).^[116]

According to MLOCHOWSKI et al. it was believed that the direct bromination of 1,10-phenanthroline would be impossible to be carried out under standard conditions, so that only very drastic conditions (pressurized sealed tube reaction in 60% oleum, at 120°C) are necessary to obtain 6-bromo-1,10-phenanthroline (**phenBr**) in very low yields, or 5,6-dibromo-1,10-phenanthroline (**phenBr₂**) in moderate yields (20%).^[121] DÉNES and CHIRA describe the formation and extraction of **phenBr** and **phenBr₂** in low yields from the resulting product mixture of phenanthroline bromination in thionyl bromide (24 h).^[122] CHAN et al. describe for the first time the nonpressurized formation of **phenBr₂** in yields as low as 30%.^[123] Parallel to this thesis

research, HUDHOMME et al. published the improved preparation of **phenBr₂** (150°C, 60 h, schlenk tube, 62%) in 2009.^[124]

In the methods described above, usually high temperatures (>120°C), long reaction times (24 to 60 h) and in most cases increased pressure (sealed tube) have been applied to perform the bromination of phenanthroline in the 5- and 6-position. The result is a difficult to separate product mixture of up to five different brominated derivatives with a maximum yield of 65% of the desired product.^[121, 122, 123, 124] The use of high reaction temperatures is quite surprising as it is known that bromine as well as sulfur trioxide have low boiling points (58.8°C and 45°C respectively) and will, therefore, leave the reaction mixture at evoked temperatures.

Accordingly, a low-temperature regime (lower than the boiling point of SO₃) as shown in the reaction in figure 38 represented an interesting starting point to achieve a more selective bromination and possibly higher yields.

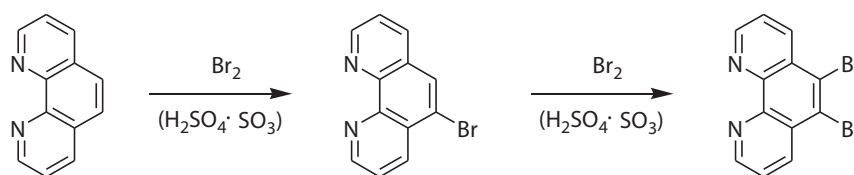


Figure 38: Synthesis of 5-bromo-1,10-phenanthroline and 5,6-dibromo-1,10-phenanthroline.

The conversion of 1,10-phenanthroline with an excess of elemental bromine in 65% oleum at room temperature yielded **phenBr₂** in unexpectedly high yields (>90%) and purity according to the equation in figure 38 within 16 hours. In this reaction a careful addition of the oleum to the phenanthroline charged reaction vessel at 0°C avoided preliminary decomposition of the phenanthroline in the exothermic mixing process. A high concentration of oleum was chosen to compensate the water of crystallization in commercial phenanthroline or water absorbed from the atmosphere and to support the electrophilic aromatic substitution at the deactivated ring.

Following the same procedure (**method L1**) in a second reaction, but using only one half equivalent of bromine it was possible to stop the consecutive reactions at the intermediate stage. Vanishing of the brown undissolved bromine drops in the mixture and bromine vapor in the gas phase after three hours was taken as a sign of the completed reaction. First TLC experiments indicated the expected impurities phenanthroline and **phenBr₂** as well as a main product, eventually identified to be the desired **phenBr**. Further recrystallization from ether

was used to remove the educt and recrystallization from chloroform/dichloromethane gave pure monosubstituted product in 70% yield.

In addition to $^1\text{H-NMR}$ and $^{13}\text{C-NMR}$ spectroscopy as well as mass spectrometry was used for the characterization of the products. Especially the loss of the signals, referring to the protons in 5- and 6-position in $^1\text{H-NMR}$ spectroscopy were good indicators for the completed transformation. Furthermore, it was as well possible to obtain suitable crystals of both compounds by recrystallization from chloroform to perform X-ray diffraction experiments. The obtained molecular structures are depicted in figure 39.

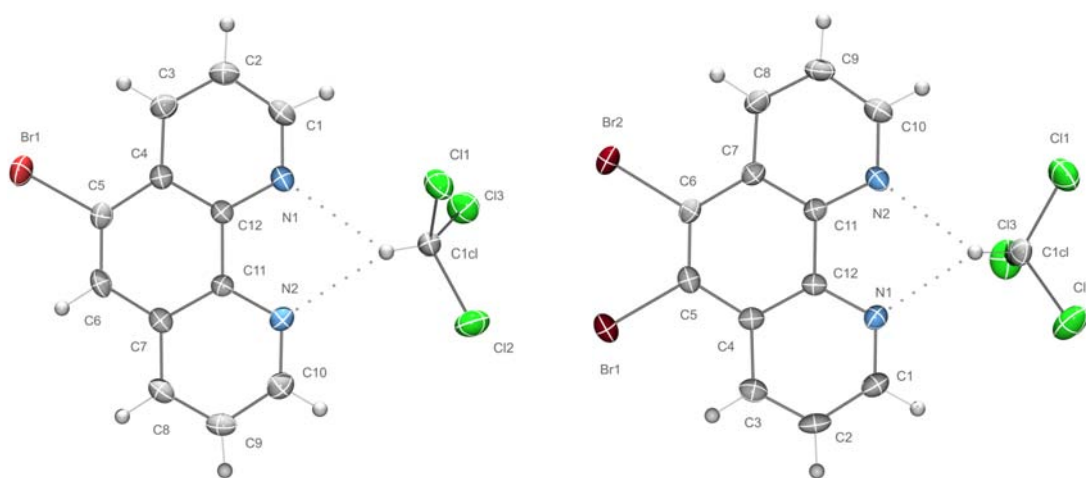


Figure 39: ORTEP representation of the molecular structures of 5-bromo-1,10-phenanthroline and 5,6-dibromo-1,10-phenanthroline coordinated to the solvent chloroform via hydrogen bonds. Ellipsoids were drawn at 50% probability level (see table 3 for selected bond lengths and angles).

Both phenanthroline derivatives crystallize in the monoclinic crystal system with the space group $P2(1)/n$. An alternating orientation of the phenanthrolines and π -stacking effects of the planar aromatic systems were prominent in the crystal lattice (" $\pi - \pi$ " in table 3, example depicted in figure 40). Furthermore, via hydrogen bonds coordinated solvent chloroform was found in the N_1N_2 -coordination site with H-N-distances in the region of $d(\text{H1Cl-N}) = [2.312 - 2.493 \text{ \AA}]$. A significant influence of the bromination on the phenanthroline skeleton was not observed by comparison of the bond lengths and angles (see table 3 on page 62).

After the successful synthesis, it was important to focus on other phenanthroline derivatives such as bathophenanthroline or 2,9-dimethyl-1,10-phenanthroline to explore this type of reaction with a broadened palette of possible substrates for future applications.

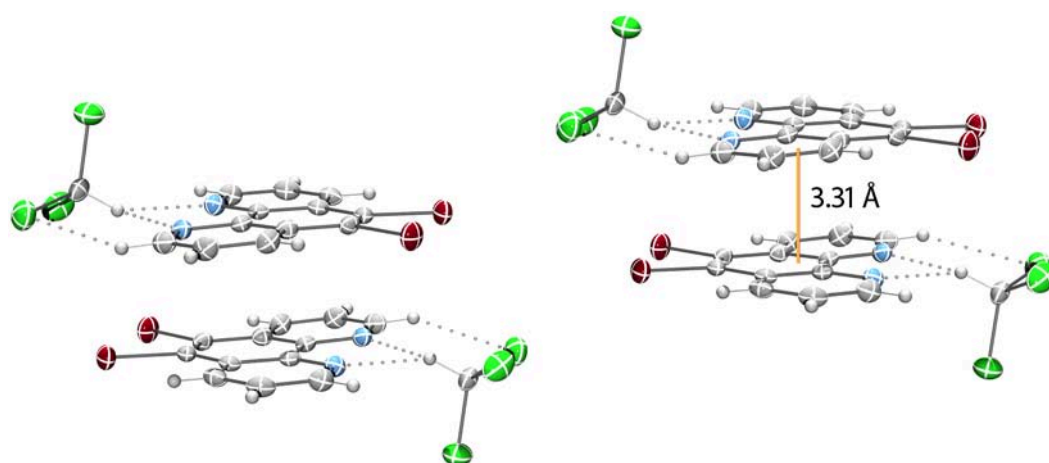


Figure 40: Typical stacking pattern of the planar **phenBr₂** molecules in the crystal lattice due to π - π interaction, as observed in other crystal structures of substituted phenanthrolines.

Because of the high tolerance of the methyl substituents toward the harsh conditions 2,9-dimethyl-1,10-phenanthroline was chosen as a substrate for the next test reaction. The bromination was performed under the identical conditions (**method L1**), using a surplus (1.05 equivalents) of bromine to achieve substitution of both, 5- and 6-position. Interestingly, a complete consumption of bromine was observed according to the lightening of the formerly brown solution (see figure 41).

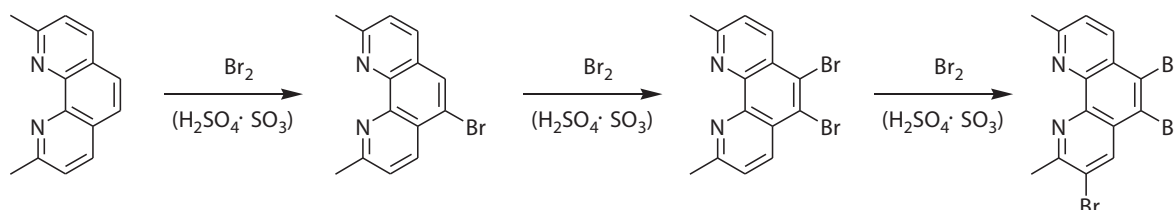


Figure 41: Successive bromination of 2,9-dimethyl-1,10-phenanthroline leading to triple substitution.

The formation of the 5,6-dibromo-2,9-dimethyl-1,10-phenanthroline could be confirmed by NMR- and DEI-MS-experiments. Characteristic was the isotopic pattern of the molecular ion (M^+ , $m/z = 364$) as well as the patterns of the expected fragments where one or two bromine atoms were lost ($[M-Br]^+$, $m/z = 285$ and $[M-2Br]^+$, $m/z = 206$). In addition, a fraction of 10% of triply brominated phenanthroline (3,5,6-position) was found in the product mixture, which equals the surplus of used bromine ($[M+Br]^+$, $m/z = 444$). Due to the high solubility of the methyl substituted

compounds and similar chemical properties, it was not possible to completely separate the brominated products neither by chromatography nor by recrystallization. Nevertheless, suitable crystals for X-ray diffraction experiments could be obtained by recrystallization from chloroform.

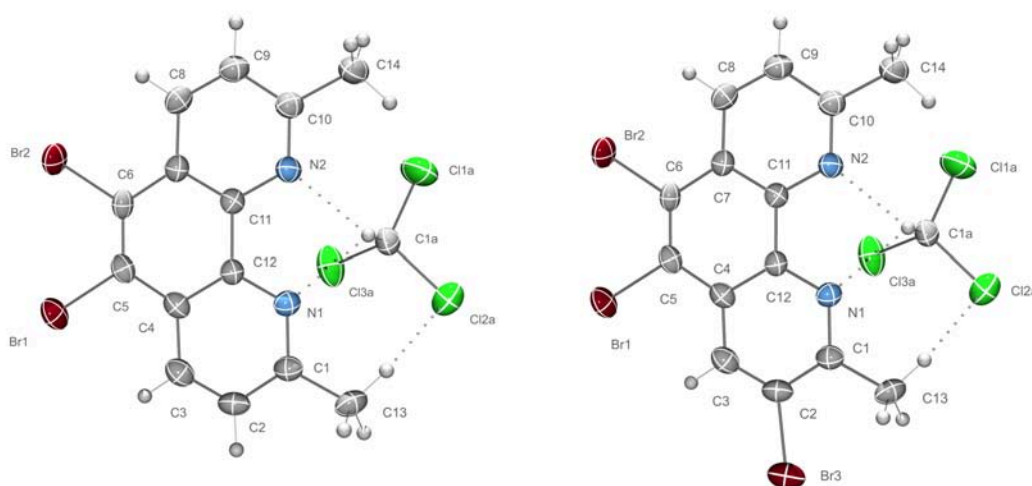


Figure 42: Molecular structures of **Me₂phenBr₂** (left) and **Me₂phenBr₃** (right) with coordinated solvent, obtained via cocrystallization of the 90:10-mixture from chloroform. Ellipsoids were drawn at 50% level in this ORTEP representation (see table 3 for selected bond lengths and angles).

A superposition of both compounds was found in the crystal lattice with **phenMe₂Br₃** occupying 10% and **phenMe₂Br₂** 90% of the phenanthroline positions. Therefore, it was possible to confirm both structures by X-ray diffraction (see figure 42 and table 3). The monoclinic crystal system has the space group P2(1)/c. An alternating orientation of the phenanthrolines and weak π -stacking of the planar aromatic systems is prominent in the crystal lattice (not depicted). Again, coordinated chloroform with hydrogen bond distances of $d_{(\text{HCl}-\text{N1}/\text{N2})} = 2.403/2.483 \text{ \AA}$ was present in the N,N'-coordination site of the phenanthroline derivatives. And again, no significant influence of the bromination upon the phenanthroline backbone was observed by comparison of the bond lengths and angles (see table 3).

The important bond length and angles of the brominated phenanthroline ligands are presented in table 3 (page 62), for comparison with the prepared ruthenium complexes see table 4 (page 70). Comparison of the **phenBr**-type structures to each other revealed strong structural similarities in terms of bond lengths and angles. The phenanthroline systems remain almost unchanged upon bromination in the 5- and 6-position as a result of this. Therefore, N1-C1/N2-C10 bond

lengths (1.311(5) – 1.330(4) Å) as well as the N1-C12/N2-C11 bond lengths (1.352(4) – 1.368(4) Å) differ negligibly. The C5-C6 bond lengths (1.342(5) – 1.357(5) Å) remain completely unchanged and the Br-C bond lengths (1.886(3) – 1.899(3) Å) are in the range of typical values for this bond type. The packing of the ligands in the crystal exhibits π -stacking effects with differing π - π -distances in the range of 3.312(4) to 3.707(4) Å between the planes of the aromatic systems (given as π - π in table 3). Hydrogen bond formation with differing bond lengths between the phenanthroline nitrogen atoms and coordinated chloroform was observed in all crystal structures ($d_{\text{Cl-Cl-N1/N2}}^{\text{phenBr}} = 3.156/3.229$ Å, $d_{\text{Cl-Cl-N1/N2}}^{\text{phenBr}_2} = 3.132/3.191$ Å, and $d_{\text{Cl-N1/N2}}^{\text{Me}_2\text{phenBr}_{3/3}} = 3.225/3.249$ Å).

Table 3: Selected bond lengths [Å] and angles [°] of the brominated phenanthroline derivatives

bond length [Å] / angle [°]	phenBr	phenBr ₂	phenMe ₂ Br ₂	phenMe ₂ Br ₃
Br1 - C5	1.899(3)	1.886(3)	1.890(3)	1.890(3)
Br2 - C6	-	1.891(3)	1.887(3)	1.887(3)
Br3 - C2	-	-	-	1.837(3)
N1 - C1	1.311(5)	1.327(4)	1.330(4)	1.330(4)
N2 - C10	1.317(5)	1.324(4)	1.318(4)	1.318(4)
N1 - C12	1.361(4)	1.358(4)	1.364(4)	1.364(4)
N2 - C11	1.352(4)	1.352(4)	1.368(4)	1.368(4)
C1 - C2	1.389(5)	1.400(5)	1.405(5)	1.405(5)
C2 - C3	1.376(5)	1.364(5)	1.358(5)	1.358(5)
C4 - C5	1.441(5)	1.439(5)	1.437(5)	1.437(5)
C5 - C6	1.342(5)	1.354(5)	1.357(5)	1.357(5)
C6 - C7	1.432(5)	1.441(5)	1.438(4)	1.438(4)
C11 - C12	1.453(4)	1.464(4)	1.447(4)	1.447(4)
π - π	3.408(4)	3.312(4)	3.707(4)	3.707(4)
H1Cl - N1	2.429(5)	2.312(4)	2.483(4)	2.483(4)
H1Cl - N2	2.493(4)	2.376(4)	2.403(4)	2.403(4)
Cl2a - H13a/H1	-	3.236(4)	3.150(4)	3.150(4)
C1 - C2 - C3	118.1(3)	119.1(3)	120.4(3)	120.4(3)
C4 - C5 - C6	122.4(3)	121.0(3)	121.2(3)	121.2(3)
C5 - C6 - C7	120.6(3)	121.3(3)	121.0(3)	121.0(3)
C10 - N2 - C11	117.8(3)	117.4(3)	118.9(3)	118.9(3)
N2 - C11 - C12	119.1(3)	117.3(3)	118.0(3)	118.0(3)
C11 - C12 - N1	117.8(3)	117.5(3)	117.7(3)	117.7(3)
C12 - N1 - C1	118.0(3)	117.6(3)	118.6(3)	118.6(3)

To further expand the series of possible phenanthroline backbones bathophenanthroline was used as substrate in the bromination reaction (see figure 43) according to **method L1**.

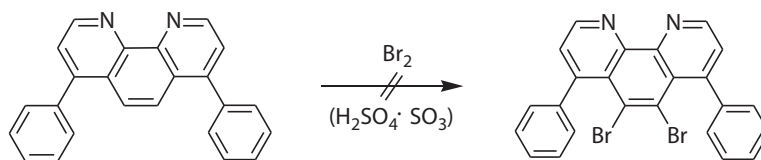


Figure 43: Attempted bromination of 2,9-dimethyl-1,10-phenanthroline.

Unfortunately, all attempts to brominate this compound resulted in the complete decomposition of bathophenanthroline so that no desired product could be isolated after the reaction.

These results render the picture of a very selective and stepwise bromination of phenanthrolines using **method L1** with highest reactivity at the 5- and 6-positions and lower reactivity at the 3,8-positions which need to be activated, e.g. by alkyl groups in the 2,9-positions. Aryl-groups in the 4,7-positions do not tolerate the harsh conditions, so that this type of reactions can only be applied to a limited number of substrates. It can be assumed that 5-chloro-phenanthroline can be brominated to yield 5-bromo-6-chloro-1,10-phenanthroline derivatives which are ideal for the application in selective coupling reactions for consecutive substitution reactions. In summary it was possible to simplify the reaction conditions, to increase the selectivity and to improve the workup for the 5,6-bromination of phenanthrolines.

3.1.2 Ruthenium Complexes with Brominated Phenanthrolines

To explore and understand the influence of the 5,6-bromination at the phenanthrolines on their ligating properties a set of model compounds with permutation of the number of **phenBr₂**-ligands like $[\text{Ru}(\text{tbbpy})_{3-n}(\text{phenBr}_2)_n]^{2+}$ ($n = 1,2,3$) was prepared to compare these complexes to each other and to other complexes.

A second important reason for the preparation of such complexes was the fact that a common route for the derivatization of halogenated phenanthroline ligands uses the complexes as substrates for coupling reactions.^[108] They have a protecting group in the phenanthroline coordination sphere to avoid catalyst metal coordination therein.

Finally, the exploration of the coordination affinity of the 5,6-halogenated phenanthroline derivatives toward the positively charged metal is important since it is known from experiments

with inequivalently halogenated tpphz derivatives that halogenation causes lower coordination affinity at the brominated phenanthroline sphere due to the electron withdrawing effect of these groups. This results in a selective ruthenium coordination into the unsubstituted N,N' pocket of tpphz.^[125, 126]

Furthermore, it is known from experiments by RAU et al. that 3,5,6,8-tetrabromophenanthroline (**phenBr₄**) has a low coordination tendency toward ruthenium.^[127] The attempts to prepare the series $[\text{Ru}(\text{tbbpy})_{3-n}(\text{phenBr}_4)_n]^{2+}$ ($n = 1, 2, 3$) succeeded only for $n = 1$ while the intermediates and products toward the complexes with $n = 2, 3$ could not be prepared (even with longer reaction times) or isolated, so that their characterization remains incomplete.

In the first attempt, simple model complexes were prepared which consist of a number of the well known, solubility providing 4,4'-tert-butyl-2,2'-bipyridine (tbbpy) ligands at the ruthenium center and a brominated ligand for metalorganic coupling reactions (see figure 44).

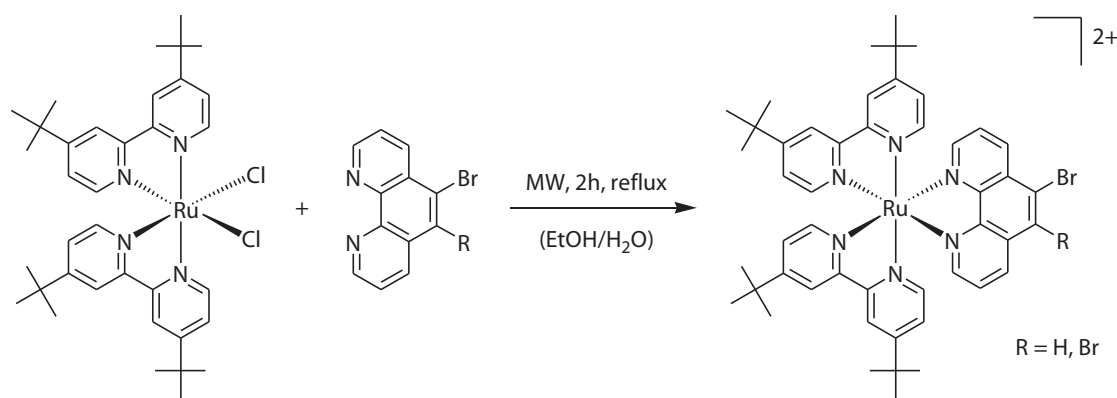


Figure 44: Synthesis of the ruthenium complexes with one **phenBr**-type ligand.

The synthesis of heteroleptic ruthenium polypyridine complexes of the type $[\text{Ru}(\widehat{\text{LL}})_2(\widehat{\text{LL}}')]^{2+}$ is typically achieved from the cisoidal dichloro complex $[\text{Ru}(\widehat{\text{LL}})_2\text{Cl}_2]$ and can be performed according to the procedure of the work group of RAU et al. (**method C1**). Thereby a special microwave reaction was used which allows for high yields and short reaction times.^[120]

First, the starting materials $[\text{Ru}(\text{tbbpy})_2\text{Cl}_2]$ and tbbpy were prepared according to the mentioned procedures. Then, following the protocol of **method C1**, one equivalent of brominated phenanthroline derivative was used in a microwave reaction together with $[\text{Ru}(\text{tbbpy})_2\text{Cl}_2]$ to prepare the desired complexes. The end of the reaction was indicated by a color change from dark purple to bright red after refluxing the mixture for two hours in ethanol/water (4:1). Directly

after removal of the ethanol a solution of NH_4PF_6 was added to exchange the chloride ions and to precipitate the desired product from the reaction mixture. Application of this procedure yielded $[\text{Ru}(\text{tbbpy})_2(\text{phenBr})]^{2+}$ (**Ru(phenBr)**) and $[\text{Ru}(\text{tbbpy})_2(\text{phenBr}_2)]^{2+}$ (**Ru(phenBr₂)**) in high yields (>90%) and high purity.

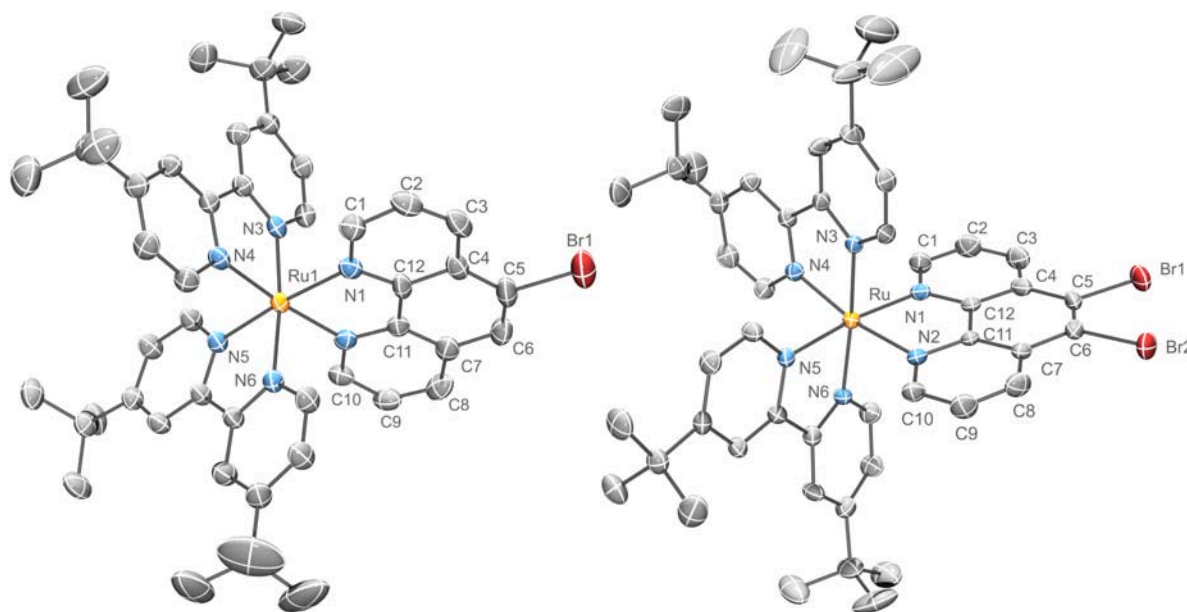


Figure 45: Solid state structures of **Ru(phenBr)** (left) and **Ru(phenBr₂)** (right). Counter ions, coordinated solvents and hydrogen atoms were omitted for clarity. Ellipsoids were drawn at 60% level in this ORTEP representation.

For the characterization of the products ^1H - and ^{13}C -NMR methods were applied. In the case of **Ru(phenBr₂)** nine signals in the aromatic region of the ^1H -NMR spectrum and two signals in the aliphatic region were observed which indicated a dissimilar magnetic environment around the pyridine units of the tbbpy-ligand as expected. In the ^{13}C -NMR spectrum, all carbon atoms could be assigned according to COSY, HMBC and HSQC methods. Electrospray mass spectrometry (ESI MS) exhibited a molecular ion at $m/z = 1121.9$ which corresponds to the fragment $[\text{M}-\text{PF}_6]^+$ and matches the calculated isotopic pattern of $(\text{C}_{48}\text{H}_{54}\text{N}_6\text{Br}_2\text{RuPF}_6)$.

For the compound **Ru(phenBr)** 13 signals in the aromatic region of the ^1H -NMR spectrum and two signals in the aliphatic region were observed. A singlet at $\delta = 8.612$ ppm for the 6-position and six more aromatic signals were assigned to the **phenBr**-ligand which indicated a slightly changed magnetic environment of the two phenanthroline halves due to the bromination in

addition to the previously observed shift in the case of the tbbpy-ligand. All 26 carbon atoms could be assigned in the ^{13}C -NMR spectrum according to a combination of COSY, HMBC and HSQC methods. ESI MS experiments exhibited two prominent peaks at $m/z = 1042.1$ and 897.2 which correspond to the fragments $[\text{M}-\text{PF}_6]^+$ and $[\text{M}-2\text{PF}_6]^+$. Both isotopic patterns matched the calculated patterns for the correct sum formula and thus the desired compounds. The chemical shifts in the NMR spectrum and the observed molecular ions of **Ru(phenBr)** are very similar to the complex $[\text{Ru}(\text{tbbpy})_2(5\text{-chloro-1,10-phenanthroline})]$ (**Ru(phenCl)**), previously prepared by RAU et al.^[116]

In addition, it was possible to obtain suitable crystals for X-ray diffraction of both compounds by recrystallization from acetone/water and acetonitrile/water respectively as depicted in figure 45. These data support the assignment of a conventional distorted octahedral coordination sphere for both complexes. The detailed discussion of the solid state structure can be found in the combined discussion of all other prepared **phenBr**-type complexes at the end of this section (page 69 ff.).

The synthesis of the higher **phenBr**₂-substituted complexes $[\text{Ru}(\text{tbbpy})_{3-n}(\text{phenBr}_2)_n]^{2+}$ ($n = 2, 3$) required the preparation of the $[\text{Ru}(\widehat{\text{LL}})_2\text{Cl}_2]$ -derivative (**Ru(phenBr₂)₂Cl₂**) as depicted in figure 46.

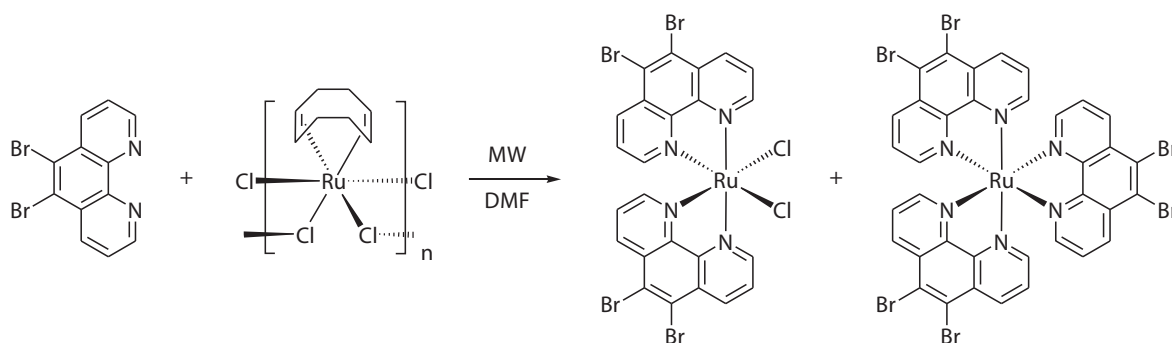


Figure 46: Synthesis of the, relating to **phenBr**-type ligands, homoleptic ruthenium complexes.

When these conditions were applied to the related **phenBr**₄ ligand to prepare the higher substituted complexes $[\text{Ru}(\text{tbbpy})_{3-n}(\text{phenBr}_4)_n]^{2+}$ ($n = 2, 3$), no product could be isolated. It has been speculated that this finding correlated to the electronic structure of **phenBr**₄, i.e. a reduced electron density at the N-donor set of the phenanthroline.^[127]

The required precursor for this synthesis $[\text{Ru}(\text{cod})\text{Cl}_2]_n$ was prepared according to literature

procedures.^[128] Using this starting material and two equivalents of **phenBr₂** in a microwave reaction in dry DMF according to an adapted literature procedure the formation of a blue, almost insoluble compound was observed. After the removal of the solvent and washing with water it was possible to extract the solid with methylene chloride and to precipitate the product with ether. Characterization of the solid by ¹H-NMR spectroscopy in CD₂Cl₂ exhibited two sets of three signals in the aromatic region of the spectrum with partly very far low-field shifted signals which corresponds to the protons in the 2,9-positions at the corresponding phenanthroline halves. Carbon-NMR spectroscopy as well as mass spectroscopy could not be applied due to the poor solubility in the applied solvents. Slow recrystallization from dichloromethane yielded black crystals which were taken for X-ray diffraction experiments (compare figure 47). A detailed discussion follows in section 3.1.3 on page 69 ff.

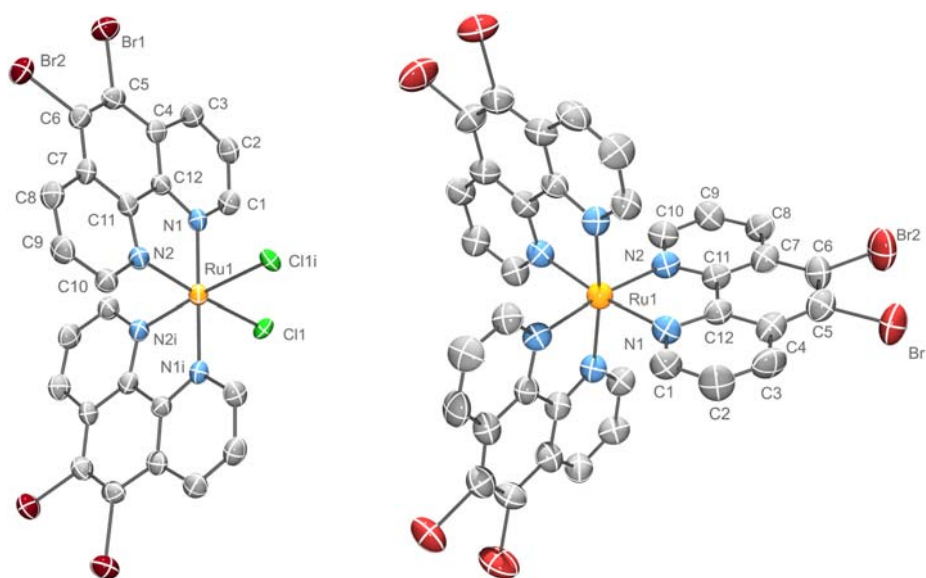


Figure 47: ORTEP representations of the molecular structures of **Ru(phenBr₂)₂Cl₂** (left) and the homoleptic complex **Ru(phenBr₂)₃** (right). Counter ions, coordinated solvent and hydrogen atoms were omitted for clarity. Ellipsoids were drawn at 50% level.

If the same reaction was performed with three equivalents of **phenBr₂** in a mixture of ethanol/water over the period of 16 hours at reflux temperatures, the formation of a red solution was observed. Precipitation of the PF₆⁻-salt yielded the trishomoleptic complex **Ru(phenBr₂)₃** in good yields. Hydrogen NMR spectroscopy revealed a very simple spectrum with three signals in the aromatic region due to the high symmetry of this complex. In the ¹³C-NMR spectrum all six chemically

inequivalent carbon atoms could be assigned by HMBC- and HSQC-methods. Electrospray mass spectroscopy exhibited a prominent peak at $m/z = 1259.2$ which exactly fits the calculated isotopic pattern of the fragment $[M-PF_6]^+$. Recrystallization from acetonitrile yielded orange crystals which could be used for X-ray diffraction experiments (compare figure 47). A detailed discussion follows in section 3.1.3.

The preparation of $[Ru(tbbpy)(phenBr_2)_2]$ (**Ru(phenBr₂)₂**) succeeded by adaptation of the microwave reaction protocol **method C1**, taking tbbpy and **Ru(phenBr₂)₂Cl₂** as starting materials (see figure 48).

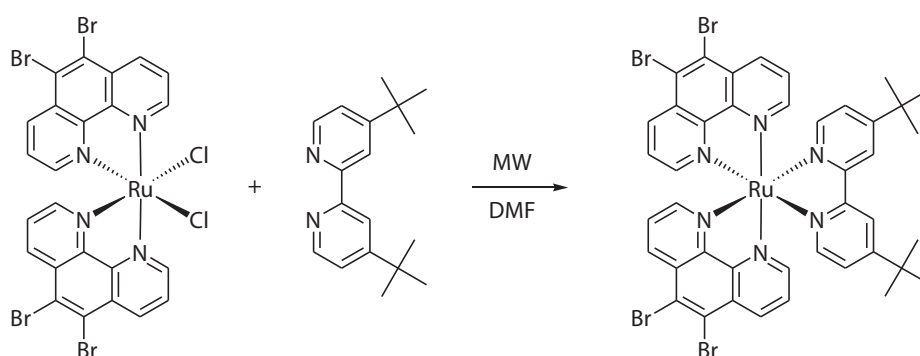


Figure 48: Synthesis of **Ru(phenBr₂)₂**.

¹H-NMR spectroscopy revealed two sets of three **phenBr₂**-signals and one set of three tbbpy-signals in the aromatic region. With the help of two-dimensional methods (COSY, HMBC, HSQC) it was possible to assign all carbon signals in the ¹³C-NMR spectrum. Electrospray mass spectroscopy exhibited two prominent peaks at $m/z = 1190.5$ and 522.8 which exactly fit the calculated isotopic patterns for the fragments $[M-PF_6]^+$ and $[M-2PF_6]^{2+}$ respectively. Recrystallization from acetonitrile/water yielded orange crystals which were used for X-ray diffraction experiments (compare figure 49). The detailed discussion is given in the following section.

It is clearly evident that 5,6-dibromo-1,10-phenanthrolines can be employed as conventional N,N'-chelating ligands for the preparation of all possible $[Ru(tbbpy)_{3-n}(phenBr_2)_n]^{2+}$ ($n = 1, 2, 3$) complexes. This result suggests that for **phenBr₂** a more conventional electronic situation may be expected in contrast to **phenBr₂**.

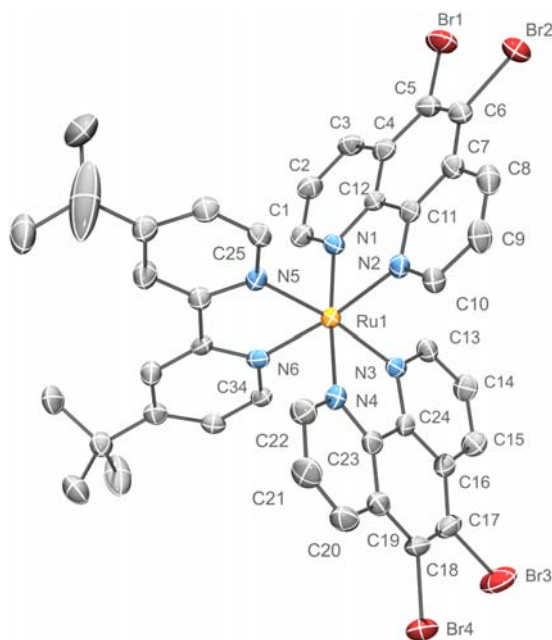


Figure 49: ORTEP representation of the molecular structure of **Ru(phenBr₂)₂**. Counter ions, solvent molecules and hydrogen atoms were omitted for clarity. Ellipsoids were drawn at 50% level.

3.1.3 Structural Analysis

The important distances and angles are given in table 4 for comparison of all prepared ruthenium complexes. Comparison of the **phenBr**-type complexes revealed strong structural similarities in terms of bond lengths and angles.

As well, comparison of the phenanthroline backbones did not show relevant structural changes, when going from the free to the coordinated ligands. As a result of this, typical Ru-N1/N2 bond lengths (phenanthroline ligand) are found to be between 2.062(4) and 2.081(4) Å and typical Ru-N3/N4/N5/N6 bond lengths (bipyridine ligand) are found to be between 2.042(4) and 2.065(4) Å in all examined [Ru(bpy)₃]²⁺-type complexes, which exactly matches the known bond lengths of the mother compounds [Ru(tbbpy)₂(phen)]²⁺ (**Ru(phen)**) and [Ru(tbbpy)₂(phenBr₄)]²⁺ (**Ru(phenBr₄)**), with phenBr₄ = 3,5,6,8-tetrabromophenanthroline) prepared by RAU et al.^[120, 108] Only the cisoidal chloro complex **Ru(phenBr₂)Cl₂** represents an exception with slightly shortened Ru-N3 bond lengths of 2.027(4) Å which can be attributed to the trans effect of the chlorido ligands.

The phenanthroline systems remain almost unchanged upon coordination if compared to

3.1 Brominated Phenanthrolines - A Gate to new Bridging Ligands

the free ligands. Interestingly, complexation of the ligands to the ruthenium fragment did not influence the C-N bond angles at the coordination sites. Therefore, N1-C1/N2-C10 bond

Table 4: Selected bond lengths [Å] and angles [°] of the bromo-phenanthroline complexes.

bond length [Å] angle [°]	Ru(phenBr)	Ru(phenBr) ₂	Ru(phenBr) ₂ ₂	Ru(phenBr) ₂ ₃	Ru(phenBr) ₂ Cl ₂	Ru(Br ₂ phen) ^[123]
Ru - N1	2.068(4)	2.073(3)	2.066(4)	2.069(7)	2.059(4)	2.040(5)
Ru - N2	2.081(4)	2.070(3)	2.062(4)	2.067(7)	2.027(4)	2.058(5)
Ru - N3 (Cl1)	2.055(3)	2.049(3)	2.060(4)	-	2.4405(12)	2.049(4)
Ru - N4	2.042(4)	2.061(3)	2.063(4)	-	-	2.048(5)
Ru - N5	2.045(4)	2.051(3)	2.061(4)	-	-	2.047(5)
Ru - N6	2.062(3)	2.065(3)	2.062(4)	-	-	2.052(4)
Br1 - C5 (C2)	1.906(5)	1.895(4)	1.881(6)	1.888(9)	1.882(6)	1.886(7)
Br2 - C6 (C9)	-	1.885(4)	1.887(3)	1.887(5)	1.893(6)	1.888(7)
C5 - C6	1.346(8)	1.357(6)	1.368(8)	1.365(14)	1.348(8)	1.377(13)
N1 - C1	1.332(6)	1.333(5)	1.338(6)	1.328(10)	1.315(7)	1.355(8)
N2 - C10	1.332(6)	1.333(5)	1.329(6)	1.349(10)	1.341(7)	1.338(8)
N1 - C12	1.370(6)	1.364(5)	1.365(6)	1.369(11)	1.371(7)	1.362(8)
N2 - C11	1.363(6)	1.360(5)	1.370(6)	1.362(11)	1.375(7)	1.368(8)
C11 - C12	1.431(7)	1.433(5)	1.437(7)	1.444(11)	1.427(7)	1.437(10)
N1 - Ru - N2	79.80(15)	79.24(12)	79.60(15)	79.8(3)	79.99(17)	79.7(2)
N3(Cl1) - Ru - N4(Cl1i)	78.18(14)	78.30(12)	79.18(16)	-	92.99(6)	78.49(18)
N5 - Ru - N6	78.13(14)	78.17(11)	78.37(16)	-	-	78.38(18)
Br1 - C5 - C6	119.1(4)	120.8(3)	121.6(4)	120.7(7)	121.5(4)	-
Br2 - C6 - C5	-	120.9(2)	121.0(3)	120.5(4)	121.0(4)	-
C4 - C5 - C6	122.9(5)	122.5(4)	121.0(5)	122.0(9)	121.7(5)	121.3(7)
C5 - C6 - C7	120.3(5)	120.5(4)	121.5(4)	121.1(9)	121.8(5)	121.4(7)
C10 - N2 - C11	118.2(4)	118.3(3)	117.7(4)	118.3(7)	117.1(5)	117.5(5)
C12 - N1 - C1	117.6(4)	117.9(3)	117.8(4)	117.4(7)	118.3(5)	116.6(6)
N2 - C11 - C12	116.6(4)	116.7(3)	116.3(4)	116.4(7)	115.8(5)	115.9(5)
C11 - C12 - N1	116.9(4)	116.9(3)	116.0(4)	116.1(7)	116.0(5)	115.7(5)

lengths ($d_{(N1-C1/N2-C10)}^{\text{complexes}} = [1.328(10) - 1.349(10)] \text{ \AA}$) as well as the N1-C12/N2-C11 bond lengths ($d_{(N1-C12/N2-C11)}^{\text{complexes}} = [1.360(5) - 1.370(6)] \text{ \AA}$) are slightly elongated in the ruthenium complexes, when compared to the ligands ($d_{(N1-C1/N2-C10)}^{\text{lignds}} = [1.311(5) - 1.330(4)] \text{ \AA}$ and $d_{(N1-C12/N2-C11)}^{\text{lignds}} = [1.352(5) - 1.368(4)] \text{ \AA}$). The C5-C6 bond lengths ($d_{(C5-C6)}^{\text{complexes}} = [1.346(8) - 1.368(8)] \text{ \AA}$) and the Br-C bond lengths ($d_{(C-Br)}^{\text{complexes}} = [1.881(6) - 1.906(6)] \text{ \AA}$) remain completely unchanged, fluctuations can be assigned to packing effects.

Independent of the nature of the ligand, typically N-Ru-N' bite angles of 78-80° can be observed within the series of ruthenium complexes. Due to the small bite angle which is considerably less than 90°, it is not possible to achieve perfect octahedral geometry around the ruthenium fragment, so that the ligands are somewhat flexible, which can be seen in a distortion (see figure 50).

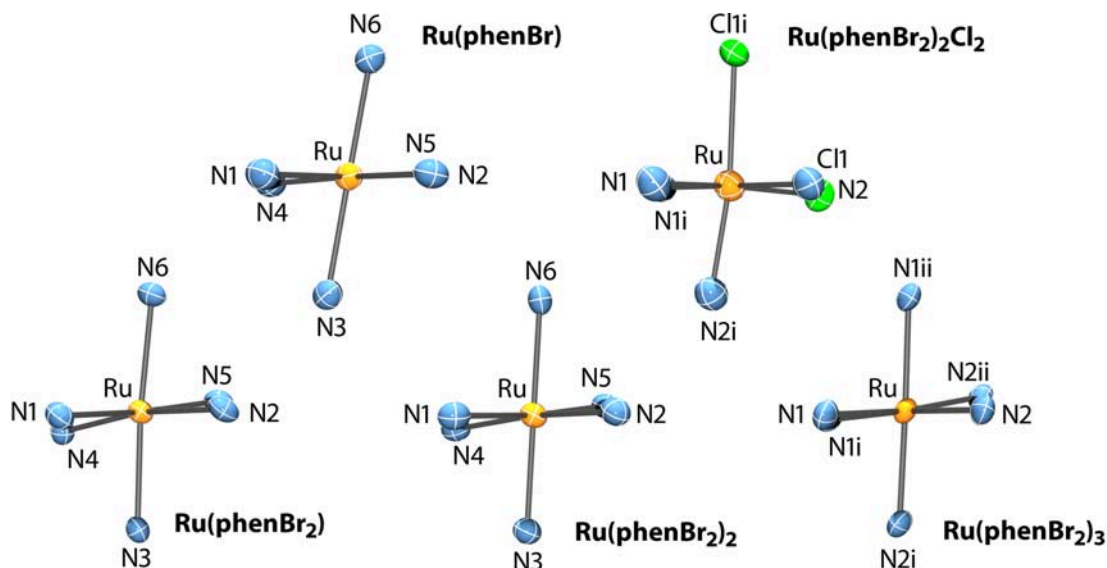


Figure 50: Coordination geometry around the ruthenium centers of the prepared complexes. View along the bisecting line of the N1-Ru-N2 angle.

The two chloride ligands in $\text{Ru}(\text{phenBr}_2)\text{Cl}_2$ are arranged in a 93.0° angle. In difference to the packing in the ligand crystals, generally no special packing effects upon π -stacking or hydrogen bond formation were observed in the ruthenium complexes.

3.1.4 Photophysical Behavior

The following presented data arose from a cooperation project with K. PEUNTINGER of the group of Prof. Dr. D. GULDI (University of Erlangen).

A first analysis of the absorption and emission properties of the new complexes of the two series $[\text{Ru}(\text{tbbpy})_{3-n}(\text{phenBr}_2)_n]^{2+}$ ($n = 0, 1, 2, 3$) and $[\text{Ru}(\text{tbbpy})_2(\text{phenBr}_m)]^{2+}$ ($m = 0, 1, 2, 4$), the precursor **Ru(phenBr₂)₂Cl₂** was excluded, revealed a typical $[\text{Ru}(\text{bpy})_3]^{2+}$ -like behavior (see table 5 for the obtained data and selected references).

Table 5: UV/vis absorption and emission data of selected references and the two series of ruthenium complexes $[\text{Ru}(\text{tbbpy})_{3-n}(\text{phenBr}_2)_n]^{2+}$ ($n = 0, 1, 2, 3$) and $[\text{Ru}(\text{tbbpy})_2(\text{phenBr}_m)]^{2+}$ ($m = 0, 1, 2, 4$).

Complex	Solvent	$\lambda_{\text{max, abs}}$ [nm]	$\epsilon_{\lambda_{\text{max}}}$ [l mol ⁻¹ cm ⁻¹]	$\lambda_{\text{max, em}}$ [nm]	Φ	τ^{a} [ns]	τ^{b} [ns]
$[\text{Ru}(\text{tbbpy})_3]^{2+}$	DCM	464	16 000	607		248 ^[90]	609 ^[90]
	ACN	458	17 900	615		107 ^[90]	730 ^[90]
Ru(phen)^c , ^[120, 125]	DCM	455	19 000	602	0.03	272	
	ACN	454	16 000	610		211	1 423
Ru(phenCl)	DCM	450	16 600	620			
	ACN	446	18 700	633			
Ru(phenBr)	DCM	451	13 500	621		452	
	ACN	449	17 800	630		139	
Ru(Br₂phen)^[125]	DCM	440	18 000	638	0.05	525	
Ru(phenBr₂)	DCM	452	17 500	621		438	
	ACN	449	14 300	631		140	1 347
Ru(phenBr₄)^[108, 125]	DCM	440	19 000	657	0.05	591	
	ACN	441	15 000	672		100	1 336
Ru(phenBr₂)₂	DCM	433	20 500	611		573	
	ACN	434	22 200	621		196	2 190
Ru(phen)₃^[108]	DCM	448	17 000	578		460	
	ACN	450	18 200	593		150	
Ru(phenBr₂)₃	DCM	451	19 000	587		353	
	ACN	450	18 200	600		247	1 380
Ru(Br₂phen)₃^[129]	ACN	424	8 700	599		126	

a) aerated, b) deaerated, c) **Ru(phen)** = $[\text{Ru}(\text{tbbpy})_2(\text{phen})]^{2+}$

All substances exhibit the relevant strong ¹MLCT-absorption band between 400 and 500 nm in acetonitrile and dichloromethane solutions as well as the typical strong emission between 600 and 800 nm in both solvents respectively (compare figures 51 – 53).

In the series $[\text{Ru}(\text{tbbpy})_{3-n}(\text{phenBr}_2)_n]^{2+}$ ($n = 0, 1, 2, 3$) all complexes exhibit a strong absorption

band with the typical “camel hump” shaped structure which is the result of the superposition of several $^1\text{MLCT}$ -absorption bands with slightly differing energies, localized on different ligands.

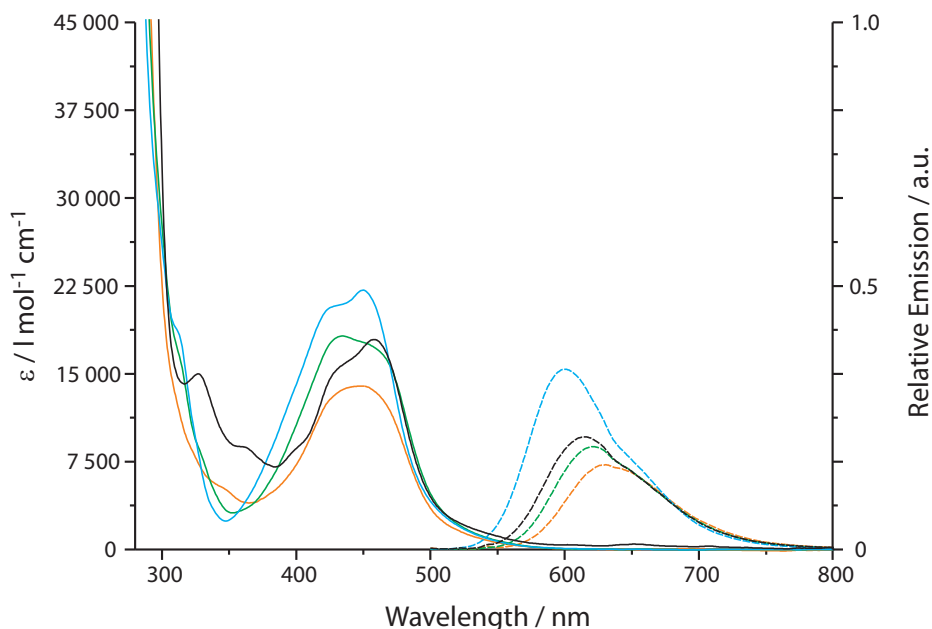


Figure 51: Absorption spectra of the $[\text{Ru}(\text{tbbpy})_{3-n}(\text{phenBr}_2)_n]^{2+}$ -series ($n = 0, 1, 2, 3$) in acetonitrile and corresponding concentration independent relative emission upon excitation at 467 nm. $[\text{Ru}(\text{tbbpy})_3]^{2+}$: Abs. (—), Em. (- -), **Ru(phenBr₂)**: Abs. (—), Em. (- -), **Ru(phenBr₂)₂**: Abs. (—), Em. (- -), **Ru(phenBr₂)₃**: Abs. (—), Em. (- -).

A rough trend in the absorption behavior, being followed in both solvents, can be observed as the molar extinction coefficients increase with the number n of **phenBr₂**-ligands from $\epsilon^{(n=0)} \sim 16\,000 \text{ l mol}^{-1}\text{cm}^{-1}$ in $[\text{Ru}(\text{tbbpy})_3]^{2+}$ to $\epsilon^{(n=3)} \sim 19\,000 \text{ l mol}^{-1}\text{cm}^{-1}$ in $[\text{Ru}(\text{phenBr}_2)_3]^{2+}$ (e.g. in acetonitrile, see figure 51). In acetonitrile, absorption energies increase in the same direction with increasing number of **phenBr₂**-ligands (n) as can be seen best in the blue shift of the center of the absorption bands and particularly in the shift of the hypsochromic flanks of the absorption bands (e.g. $\lambda_{\text{flank, ACN}}^{(n=0,1)} = 420 \text{ nm} > \lambda_{\text{flank, ACN}}^{(n=2)} = 400 \text{ nm} > \lambda_{\text{flank, ACN}}^{(n=3)} = 380 \text{ nm}$) (see figure 51). In dichloromethane, as well, the center of the MLCT-absorption band (full width at half maximum) is successively shifted by about 5 nm toward higher energies when tbbpy ligands are stepwise exchanged by **phenBr₂** ligands ($\lambda_{1/2, \text{DCM}}^{(n=0)} = 449 \text{ nm} > \lambda_{1/2, \text{DCM}}^{(n=1)} = 443 \text{ nm} > \lambda_{1/2, \text{DCM}}^{(n=2)} = 439 \text{ nm} > \lambda_{1/2, \text{DCM}}^{(n=3)} = 432 \text{ nm}$). This can be explained by the increased contribution of phenanthroline-centered MLCT-absorption. The maximum of the $^1\text{MLCT}$ band as well as

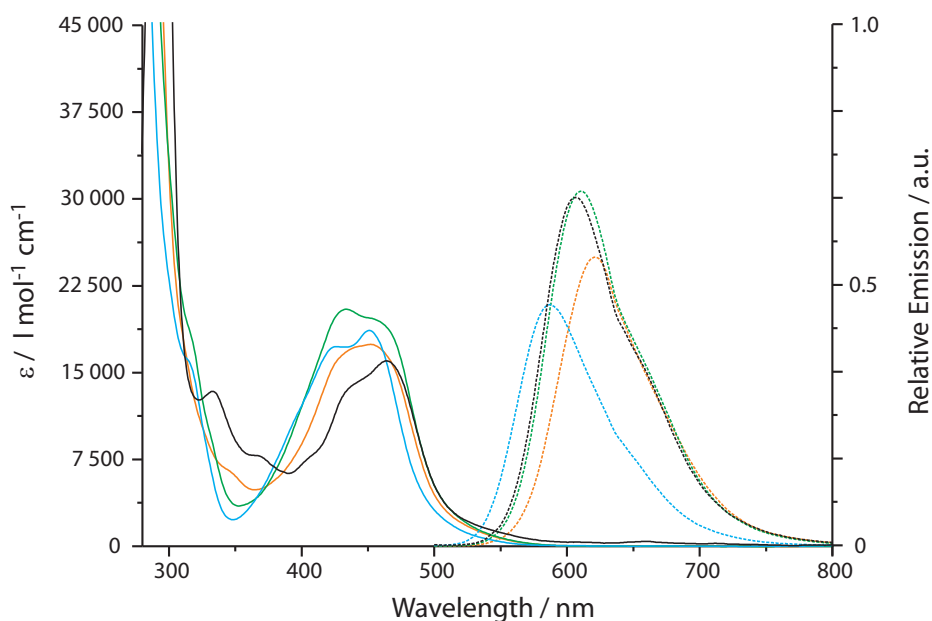


Figure 52: Absorption spectra of the $[\text{Ru}(\text{tbbpy})_{3-n}(\text{phenBr}_2)_n]^{2+}$ -series ($n=0, 1, 2, 3$) in dichloromethane and corresponding concentration independent relative emission upon excitation at 467 nm. $[\text{Ru}(\text{tbbpy})_3]^{2+}$: Abs. (—), Em. (- -), **$\text{Ru}(\text{phenBr}_2)_2$** : Abs. (—), Em. (- -), **$\text{Ru}(\text{phenBr}_2)_2$** : Abs. (—), Em. (- -), **$\text{Ru}(\text{phenBr}_2)_3$** : Abs. (—), Em. (- -).

the bathochromic and hypochromic shoulders are slightly sensitive to the solvent and thus suggests an instantaneous sensing of the formation of the dipolarity of the excited structure $[\text{Ru}^{3+}(\overline{\text{LL}})_2(\overline{\text{LL}}^-)]^{2+}$. The “camel hump” shape of the band can be explained by a combination of effects which result of the distorted octahedral geometry which might influence the energy levels of the MLCT-involved ruthenium centered t_{2g} -orbitals (as seen in the homoleptic complexes) and the different ligand centered $\text{LUMO}_{(\overline{\text{LL}})}$ energies (in the heteroleptic complexes).

The emission behavior of the $[\text{Ru}(\text{tbbpy})_{3-n}(\text{phenBr}_2)_n]^{2+}$ -series in acetonitrile exhibits a similar tendency. A blue shift of the emission band and an increase in the relative emission intensity can be observed with increasing number of the phenanthroline ligands ($\lambda_{\text{max}}^{(n=1)} = 631 \text{ nm} > \lambda_{\text{max}}^{(n=2)} = 621 \text{ nm} > \lambda_{\text{max}}^{(n=3)} = 600 \text{ nm}$). This can be explained by the phenanthroline-centered emission (KASHA’s rule). Interestingly, the homoleptic complex $[\text{Ru}(\text{tbbpy})_3]^{2+}$ exhibits an emission maximum ($\lambda_{\text{max}}^{(n=0)} = 615 \text{ nm}$) and an emission intensity which is between the **phenBr₂**-substituted complexes. Obviously, no lower lying phenanthroline centered $^3\text{MLCT}$ emission is available in this complex, so that emission is only possible from the higher lying tbbpy-centered $^3\text{MLCT}$ state (compare

electrochemistry discussion of these complexes in chapter 3.1.6 on page 78).

The ordering of the emission spectra in dichloromethane solutions follows the same tendency as observed in acetonitrile solutions. A successive blueshift of the emission maximum can be observed by going from $n=1$ to 3. Again, $[\text{Ru}(\text{tbbpy})_3]^{2+}$ with $n=0$ represents an exception. Furthermore, by substitution of acetonitrile by dichloromethane, a two-fold increase in the relative emission intensities and a 10 nm blue shift of the wavelength of the emission maximum can be observed. This was attributed to the lower concentration of dissolved oxygen in dichloromethane solutions (less quenching) and the lower solvent polarity thereof (k_{ET} , MARCUS theory).

For a better comparison of the characteristic absorption and emission behavior in the series $[\text{Ru}(\text{tbbpy})_2(\text{phenBr}_m)]^{2+}$ ($m=1, 2$), a small quantity of the complex $[\text{Ru}(\text{tbbpy})_2(\text{phenCl})]^{2+}$ (**Ru(phenCl)** with phenCl = 5-chloro-1,10-phenanthroline) was prepared according to literature procedures and values for the related ruthenium complexes **Ru(phen)** ($[\text{Ru}(\text{tbbpy})_2(\text{phen})]^{2+}$) and **Ru(phenBr₄)** ($[\text{Ru}(\text{tbbpy})_2(3,5,6,8\text{-tetrabromo-1,10-phenanthroline})]^{2+}$) were taken from the literature (compare figure 53 and table 5 on page 72).^[116, 108, 120]

All complexes in this series exhibit a similar absorption maximum at 450 nm with exception of **Ru(phenBr₄)** which shows a hypsochromically shifted absorption maximum at 441 nm. The molar extinction coefficients at the maxima of the MLCT vary roughly between 14 000 and 18 000 l mol⁻¹cm⁻¹ for the different **phenBr_m**-substituted complexes with two tbbpy ligands, but is found in the same region, as observed in the reference compounds **Ru(phen)** ($\epsilon_{\lambda_{\text{max}}}^{(n=0)} = 16\,000 \text{ l mol}^{-1}\text{cm}^{-1}$), **Ru(phenCl)** ($\epsilon_{\lambda_{\text{max}}} = 18\,700 \text{ l mol}^{-1}\text{cm}^{-1}$) and **Ru(phenBr₄)** ($\epsilon_{\lambda_{\text{max}}}^{(n=4)} = 15\,000 \text{ l mol}^{-1}\text{cm}^{-1}$) in acetonitrile solutions.

The emission behavior of the $[\text{Ru}(\text{bpy})_2(\text{phenBr}_m)]^{2+}$ complexes ($m=1, 2$) is only slightly changed by the increasing number m of bromo- or chloro substituents in the 5,6-positions. These complexes and **Ru(phenCl)** show similar emission properties with a weaker emission in acetonitrile ($\lambda_{\text{Em., ACN}}^{(m=1,2)} \approx 630 \text{ nm}$) and a stronger emission in dichloromethane ($\lambda_{\text{Em., DCM}}^{(m=1,2)} \approx 620 \text{ nm}$) (see figure 53). Emission of these compounds is hypsochromically shifted by 40 nm, when compared to the reference compound **Ru(phenBr₄)** ($\lambda_{\text{Em., ACN}}^{(m=4)} = 672 \text{ nm}$) and bathochromically shifted by 20 nm when compared to **Ru(phen)** ($\lambda_{\text{Em., ACN}}^{(m=0)} = 610 \text{ nm}$). From this result, it can be concluded that substitution of the phenanthroline backbone with halogen substituents has an (-I) effect on the σ -backbone of the ligand and thus on the orbital energy of the metal centered HOMO orbital (making it more difficult to oxidize) and thus on the excited ³MLCT

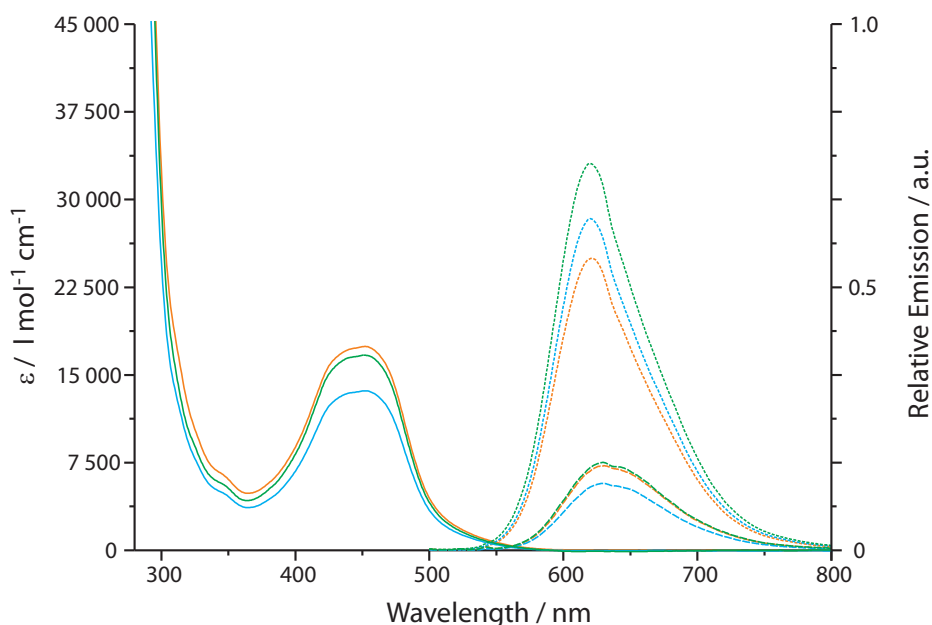


Figure 53: Absorption spectra of **Ru(phenCl)** and the $[\text{Ru}(\text{tbbpy})_2(\text{phenBr}_m)]^{2+}$ -complexes ($m = 1, 2$) in dichloromethane and corresponding concentration independent relative emission in dichloromethane and acetonitrile upon excitation at 467 nm. **Ru(phenBr)**: Abs._(DCM) (—), Em._(DCM) (---), Em._(ACN) (- - -), **Ru(phenBr₂)**: Abs._(DCM) (—), Em._(DCM) (---), Em._(ACN) (- - -) and reference **Ru(phenCl)** (phenCl = 5-chloro-1,10-phenanthroline): Abs._(DCM) (—), Em._(DCM) (---), Em._(ACN) (- - -).

state energy of the resulting ruthenium complex. The (-I/+M) effect of the bromo substituents lowers the energy of the ligand centered π^* -orbitals, making them easier to reduce. According to the emission data, it was figured that substitution in 5,6-position has less influence on the excited state energy than substitution in the 3,8-position.

3.1.5 Emission Decay Dynamics

The determination of the emission decay dynamics of the $^3\text{MLCT}$ states of the complexes with time correlated single photon count experiments (TCSPC) in acetonitrile and dichloromethane reflect the findings of the emission data of increased emission intensity in dichloromethane solutions (see table 5). Generally, the lifetimes in aerated solutions of dichloromethane ($\tau_{\text{DCM}} \approx 450$ ns) are longer than lifetimes in aerated acetonitrile ($\tau_{\text{DCM}} \approx 140$ ns), which can be attributed to the dependency on the quencher (triplet oxygen) concentration in the more polar solvent. A result of this, an increased lifetime in deaerated acetonitrile ($\tau_{\text{deaerated}} \approx 1500$ ns) was observed due to the decrease

of concurring quenching processes (see figure 54 for an example).

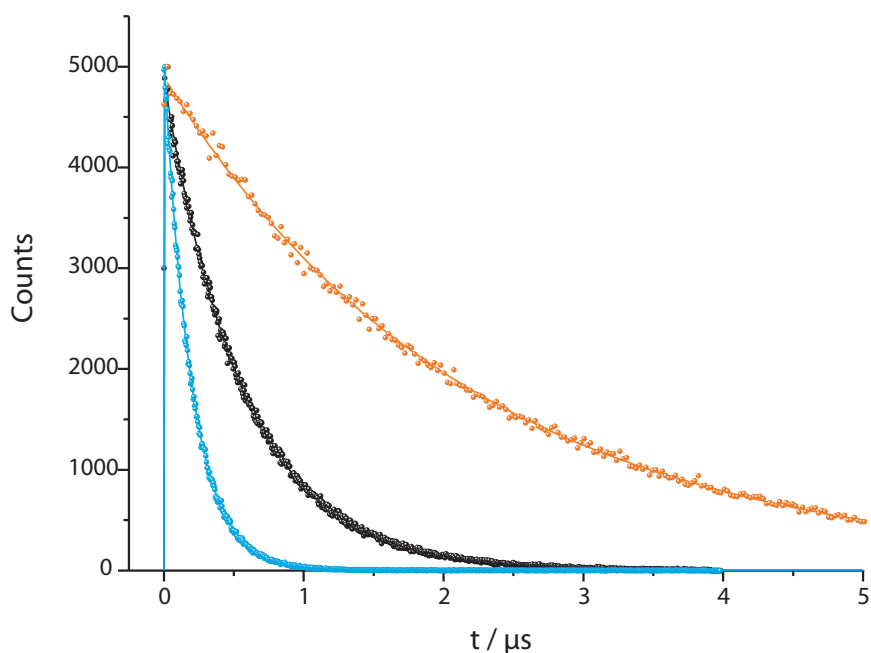


Figure 54: Representative emission decays from the time correlated single photon counting experiment (TCSPC). Depicted are the values for **Ru(phenBr₂)₂** in dichloromethane (—), acetonitrile (—) and inert acetonitrile (—) with 467 nm excitation. The decays are well fitted to a mono-exponential decay.

The emission decay behavior in aerated solvents of the complexes is slightly changed by the increasing number of bromo substituents in the 5,6-positions. The complexes $[\text{Ru}(\text{tbbpy})_2(\text{phenBr}_m)]^{2+}$ ($m = 1, 2$) show about the same deactivation behavior with shorter lifetimes in acetonitrile ($\tau_{\text{ACN}}^{(m=1,2)} \approx 140$ ns) and longer lifetimes in dichloromethane ($\tau_{\text{DCM}}^{(m=1,2)} \approx 450$ ns). These compounds have a 40 ns longer lifetime, when compared to the reference compound **Ru(phenBr₄)** ($\tau_{\text{ACN}}^{(m=4)} = 100$ ns) and a by 50 ns shortened lifetime when compared to **Ru(phen)** ($\tau_{\text{ACN}}^{(m=0)} = 211$ ns). From this result it was concluded that substitution of the phenanthroline backbone with halogen substituents (-I/+M effect) has an effect on the excited ³MLCT state lifetime of the resulting ruthenium complex. According to the emission data in the series $[\text{Ru}(\text{tbbpy})_{3-n}(\text{phenBr}_2)_n]^{2+}$ ($n = 1, 2, 3$), it can be figured that substitution of the 5,6-positions has less influence on the excited state energy than substitution in the 3,8-position. The ordering of the lifetimes within this series of ruthenium complexes is the same as the ordering of the relative steady state emission intensities in dichloromethane ($\tau_{\text{DCM}}^{(n=3)} = 353$ ns < $\tau_{\text{DCM}}^{(n=1)} = 438$ ns

$\tau_{\text{DCM}}^{(n=2)} = 572$ ns) and in acetonitrile ($\tau_{\text{ACN}}^{(n=1)} = 140$ ns $<$ $\tau_{\text{ACN}}^{(n=2)} = 196$ ns $<$ $\tau_{\text{ACN}}^{(n=3)} = 247$ ns). This correlation between short lifetimes and low emission intensities or long lifetimes and high emission intensities can be explained by the tolerance of the complexes versus other deactivating processes such as excited state quenching by oxygen.

Determination of the emission decay dynamics of the $[\text{Ru}(\text{tbbpy})_{3-n}(\text{phenBr}_2)_n]^{2+}$ complexes with $n = 1, 2, 3$ in deaerated acetonitrile revealed significantly longer lifetimes ($\tau_{\text{deaerated}}^{(n=1)} = 1347$ ns, $\tau_{\text{deaerated}}^{(n=2)} = 2190$ ns and $\tau_{\text{deaerated}}^{(n=3)} = 1380$ ns). These lifetimes are in close proximity to the determined values of the available reference compounds **Ru(phen)** ($\tau_{\text{deaerated}}^{(m=0)} = 1423$ ns) and **Ru(phenBr₄)** ($\tau_{\text{deaerated}}^{(m=4)} = 1336$ ns), except of $n = 2$ which is even longer.

3.1.6 Electrochemical Characterization

The electrochemical behavior of the two series of the $[\text{Ru}(\text{tbbpy})_{3-n}(\text{phenBr}_2)_n]^{2+}$ complexes ($n = 0, 1, 2, 3$) and $[\text{Ru}(\text{tbbpy})_2(\text{phenBr}_m)]^{2+}$ ($m = 0, 1, 2, 4$) was determined in 0.1 M solutions of Bu_4NPF_6 in dry acetonitrile under argon atmosphere in a glove box. All values were determined with a glassy carbon working electrode and platinum counter and reference electrodes. The measured values were referenced versus the redox couple Fc/Fc^+ set at $E_{1/2} = 0$ V. Table 6 contains the collected electrochemical data as well as selected references from the literature.^[120, 108]

Table 6: Selected redox potentials $E_{1/2}$ (V) of the two series of ruthenium complexes $[\text{Ru}(\text{tbbpy})_{3-n}(\text{phenBr}_2)_n]^{2+}$ ($n = 0, 1, 2, 3$) and $[\text{Ru}(\text{tbbpy})_2(\text{phenBr}_m)]^{2+}$ ($m = 0, 1, 2, 4$), referenced vs. Fc/Fc^+ in a 0.1 M solution of Bu_4NPF_6 in dry acetonitrile under argon atmosphere.

Complex	$E_{1/2}(\widehat{\text{L}}^3)$ [V]	$E_{1/2}(\widehat{\text{L}}^2)$ [V]	$E_{1/2}(\widehat{\text{L}}^1)$ [V]	$E_{1/2}(\text{Ru}^{2+/3+})$ [V]
$[\text{Ru}(\text{tbbpy})_3]^{2+}$ ^[90]	-2.28	-2.02	-1.82	0.73
Ru(phen) ^[108, 120]	-2.23	-1.99	-1.80	0.78
Ru(phenBr)	-2.23	-1.98	-1.78 (-1.65, ir)	0.83
Ru(phenBr₂)	-2.32	-2.00	-1.79 (-1.68/-1.58, ir)	0.85
Ru(phenBr₂)₂	-2.27	-1.99	-1.89(-1.67 ir)	0.90
Ru(phenBr₂)₃	-2.18 (ir)	-1.79 (ir)	-1.54 (ir)	0.95
Ru(phenBr₄) ^[108]	-	-	-	0.92

For **Ru(Br₂phen)** and for **Ru(Br₂phen)₃** no literature data were available.

Within the series of ruthenium complexes $[\text{Ru}(\text{tbbpy})_{3-n}(\text{phenBr}_2)_n]^{2+}$ ($n = 0, 1, 2, 3$) an interesting

shift of the potentials of the ruthenium centered oxidation ($E_{1/2}(\text{Ru}^{2+/3+})$) toward higher values with increasing number n of **phenBr**₂-ligands was observed ($E_{1/2}^{(n=0)} = 0.73 \text{ V} < E_{1/2}^{(n=1)} = 0.85 \text{ V} < E_{1/2}^{(n=2)} = 0.90 \text{ V} < E_{1/2}^{(n=3)} = 0.95 \text{ V}$). In addition, all complexes in this series (except for $n = 3$) exhibited three quasi reversible reduction potentials at $E_{1/2}(\widehat{\text{LL}}^1) \approx -1.8 \text{ V}$, $E_{1/2}(\widehat{\text{LL}}^2) \approx -2.0 \text{ V}$ and $E_{1/2}(\widehat{\text{LL}}^3) \approx -2.3 \text{ V}$ which were assigned to the three ligand centered reductions. Furthermore, a number of irreversible reductions were observed which increased with the number of bromine atoms in the molecule (see figure 55 for an example). Therefore, it was assumed that these irreversible reductions account for the irreversible reduction of bromine atoms with subsequent dehalogenation of the ligand.

Within the series of ruthenium complexes $[\text{Ru}(\text{tbbpy})_2(\text{phenBr}_m)]^{2+}$ ($m = 0, 1, 2, 4$) a similar shift of the potential of the ruthenium centered oxidation ($E_{1/2}(\text{Ru}^{2+/3+})$) toward higher values was observed with an increasing number n of bromo substituents at the phenanthroline backbone ($E_{1/2}^{(m=0)} = 0.74 \text{ V} < E_{1/2}^{(m=1)} = 0.83 \text{ V} < E_{1/2}^{(m=2)} = 0.85 \text{ V} < E_{1/2}^{(m=4)} = 0.92 \text{ V}$). The complexes of this series exhibited three quasi reversible reduction potentials at $E_{1/2}(\widehat{\text{LL}}^1) \approx -1.8 \text{ V}$, $E_{1/2}(\widehat{\text{LL}}^2) \approx -2.0 \text{ V}$ and

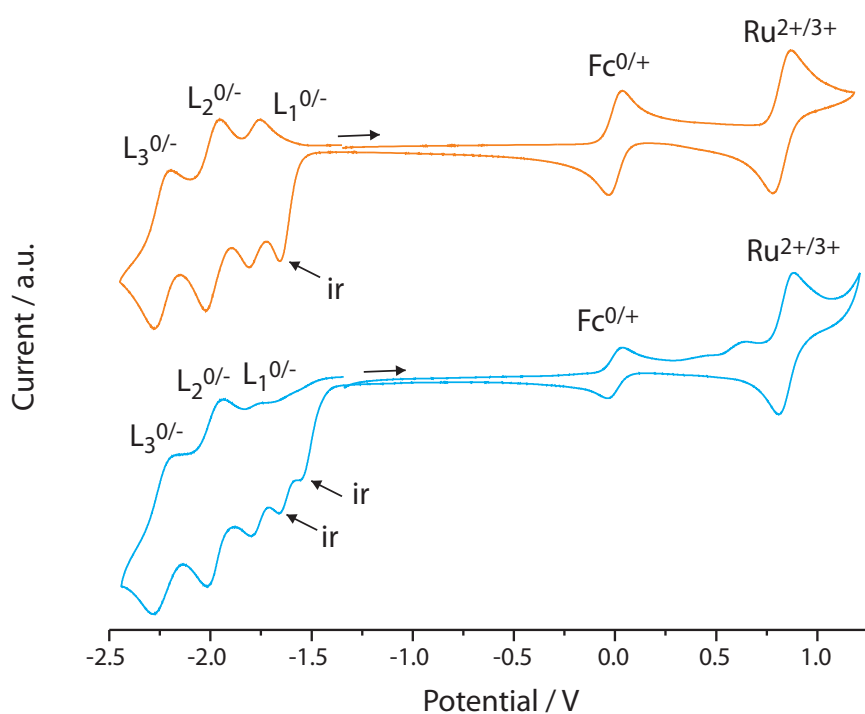


Figure 55: Cyclic voltammograms of **Ru(phenBr)** (—) and **Ru(phenBr₂)** (—) in a 0.1 M solution of Bu₄NPF₆ in dry acetonitrile under argon atmosphere, referenced vs. Fc/Fc⁺, scan rate 20 mV/s.

$E_{1/2}(\widehat{LL}^3) \approx -2.3$ V which were assigned to the three ligand centered reductions.

A correlation of the ground state redox properties of a compound A and the emission properties (one electron potential corresponding to the zero-zero excited state energy) allows a first approximation of the redox potentials of excited state couples according to the following equations:^[130]

$$E(A^+/A^*) \approx E(A^+/A) - E_{0-0}$$

$$E(A^*/A^-) \approx E(A/A^-) + E_{0-0}$$

This correlation for the series of ruthenium complexes $[\text{Ru}(\text{tbbpy})_{3-n}(\text{phenBr}_2)_n]^{2+}$ ($n = 0, 1, 2, 3$) is depicted in figure 56.

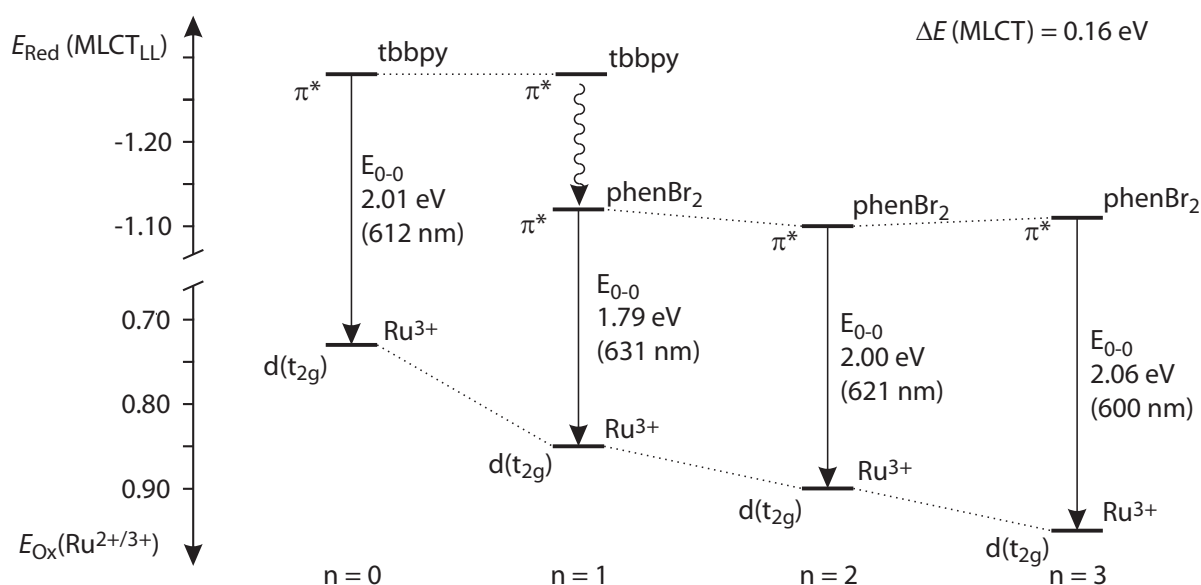


Figure 56: Combination of the redox potentials of the $^3\text{MLCT}$ excited states that can be tapped via oxidative quenching mechanism ($E(A^+/A^*)$), the ground state redox potential for the oxidation of the complexes ($E(A^+/A)$) and the emission energies (E_{0-0}) of the series of ruthenium complexes $[\text{Ru}(\text{tbbpy})_{3-n}(\text{phenBr}_2)_n]^{2+}$ ($n = 0, 1, 2, 3$).

It can be seen that the excited state oxidation potential remains unchanged at a value of about 1.1 V in the case of $n = 1, 2, 3$ although the ground state ruthenium centered oxidation potential is shifted toward higher potentials with increasing number of **phenBr₂**-ligands. Furthermore, the reduction potential of the excited state in the complex with $n = 0$ (**phenBr₂**-free complex) is about -0.16 V higher. This leads to the conclusion that the energy of the **phenBr₂**-centered $^3\text{MLCT}$ -state

is independent of possible influences which result from other ligands around the ruthenium ion. Therefore, the **phenBr₂**-localized ³MLCT-states represent the emitting excited states (KASHA's rule) in all complexes with $n = 1, 2, 3$ because they are about 0.16 eV lower in energy than the tbbpy-centered ³MLCT-states. These findings explain as well the unexpected emission properties in the case of $n = 0$ within this series very well. A statement about the oxidation potentials of the excited states is difficult because reductive quenching mechanism will probably lead to a dehalogenation reaction upon formation of the reduced species as observed in electrochemical measurements. If this interpretation is correct, $[\text{Ru}(\text{tbbpy})_{3-n}(\text{phenBr}_m)_n]^{2+}$ -type complexes would be of limited value as photoredoxactive centers as they would decompose during electron transfer processes. Note: A correlation of the stokes shifts within this series is rather difficult because the number of overlapping ¹MLCT absorption bands gives rise to several hard to separate stokes shifts for each complex which cover the particular phenanthroline centered shift.

The corresponding correlation for the series $[\text{Ru}(\text{tbbpy})_2(\text{phenBr}_m)]^{2+}$ ($m = 0, 1, 2, 4$) is depicted in figure 57 and focuses on the influence of the number bromo substituents at the phenanthroline backbone on photochemical properties of the complex.

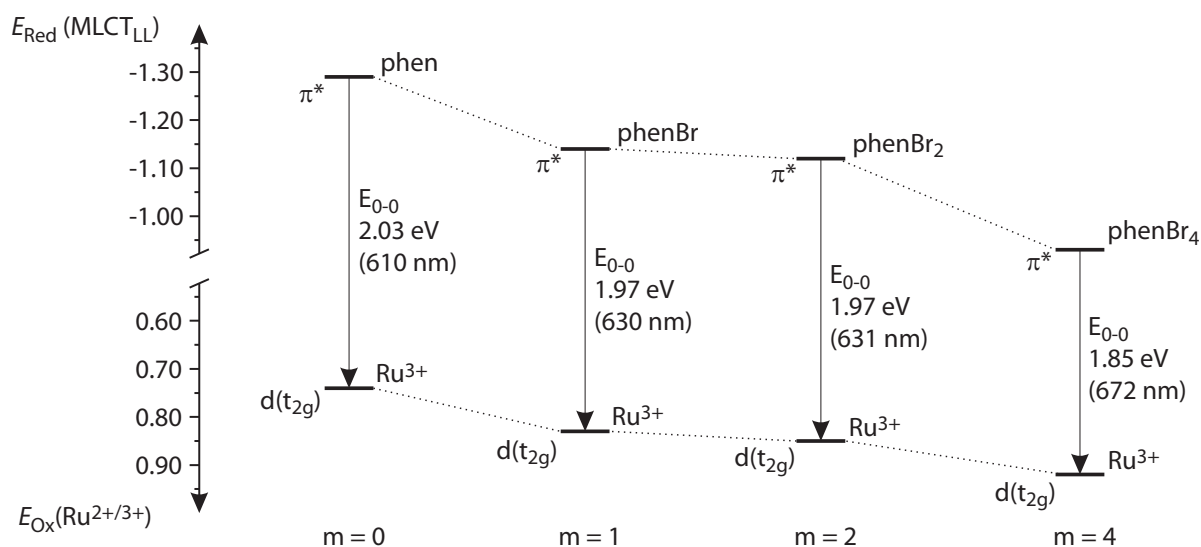


Figure 57: Combination of the redox potentials of the ³MLCT excited states that can be tapped via oxidative quenching mechanism ($E(A^+/A^*)$), the ground state redox potential for the oxidation of the complexes ($E(A^+/A)$) and the emission energies (E_{0-0}) of the series of ruthenium complexes $[\text{Ru}(\text{tbbpy})_2(\text{phenBr}_m)]^{2+}$ ($m = 0, 1, 2, 4$).

Unfortunately, no emission data for **Ru(Br₂phen)** in acetonitrile was available. Nevertheless it

can be seen that the ground state ruthenium centered oxidation potential is shifted toward higher potentials with increasing number m of bromo substituents. The excited state oxidation potentials change with increasing m as well. From this correlation it becomes clear that bromination of the phenanthroline ligand reduces the excited state oxidation potential which is centered thereon. Therefore, a lowering in energy for the **phenBr_m**-centered ³MLCT is the result, eventually causing emission from this state. These findings clearly demonstrate the photochemical importance of the 5,6-position in the phenanthroline system for the redox and emission properties of the resulting ruthenium complexes.

3.1.7 Concluding Remarks to phenBr-Ligands

With respect to the importance of starting materials for the design and adjustment of bridging ligands, a number of interesting ligands and complexes were prepared. The selective bromo-functionalization of phenanthrolines in the 5- and 6-position, thus, enables a high synthetic flexibility for the introduction of new functional groups via catalyzed cross coupling reactions. Especially the synthesis of the series of ruthenium complexes $[\text{Ru}(\text{tbbpy})_{3-n}(\text{phenBr}_2)_n]^{2+}$ ($n = 0, 1, 2, 3$) allowed to picture the potential of the obtained ligands.

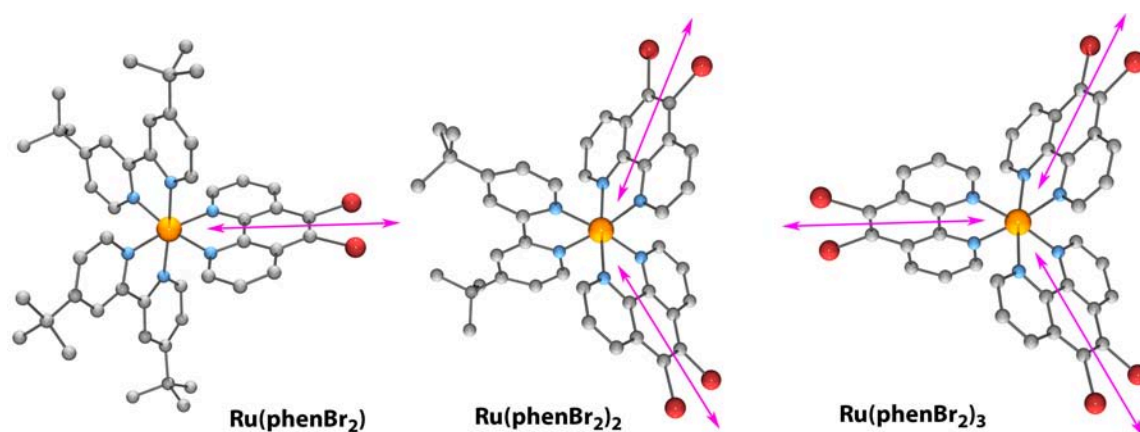


Figure 58: The possible directions for an expansion of the ligand structure.

As depicted in figure 58, it should be possible to apply these complexes to obtain linear or branched three dimensional arrangements and, thus, molecular devices with multiple functionalities and directed intercomponent electron transfer.

3.2 Bisphenanthroline: A Suitable Molecular Bridge?

The investigation of molecular artificial photosynthetic systems for hydrogen evolution from water, in the context of an efficient solar into chemical energy conversion, represents a main goal of this thesis.^[9, 12, 29] The required $[[\mathbf{P} \sim \mathbf{B} \sim \mathbf{C}]]$ -systems (\mathbf{P} = photocenter and \mathbf{C} = catalytic center) typically bear bridging ligands (\mathbf{B}) which do not only connect photo and reaction center but serve as intramolecular pathways for the directed electron and energy transfer.^[35]

An easy access to tunable molecular bridges represents the transformation of halogenated ligands into bridging ligands via catalyzed coupling reactions. With respect to the subsequent transformation into $[\text{Ru}(\text{bpy})_3]^{2+}$ -type chromophores (a massively applied class of “workhorse chromophores”), especially brominated bpy- or phen-type ligands represent viable candidates. In the previous chapter, an optimized synthesis for brominated phenanthrolines was presented. Furthermore, the influence of the substitution pattern, especially at the 5-position of the phenanthroline skeleton, was demonstrated using a variety of **phenBr**-type ligands and complexes. In addition, the introduction of bipyridine type coordination spheres into phenanthroline systems was demonstrated as previously demonstrated by RAU et al. (compare figure 37 on page 56).^[116, 127]

In this context a very interesting bridging ligand motif has been prepared by CAMPAGNA and coworkers.^[131] It was found that the redox potentials of the homobinuclear complexes of Ir, Ru and Os (e.g. in $[(\text{bpy})_2\text{Ru}(\mu\text{-phenphen})\text{Ru}(\text{bpy})_2]^{4+}$) account for simultaneous two-electron reductions of the bridging ligand spheres instead of separate one-electron reductions.

Thus, use of the symmetric 5,5'-bi-1,10-phenanthroline bridge (**phenphen**) is very interesting because it exhibits two diazadiene coordination spheres which are linked by a single bond in the electronically somewhat shielded 5-position. Additionally, atropisomers of this ligand are formed due to the hindered rotation about the single bond. This interesting effect disturbs the extended π -system due to the skew-whiff arranged and electronically weakly coupled coordination spheres in the ground state.

Nevertheless, it is possible that heterobinuclear systems with limited electronic communication in the ground state display a considerable communication in the excited state.^[75] Therefore, it is an aim to obtain a better understanding of the processes in the bridging ligand as a part of a $[\text{Ru}(\text{bpy})_3]^{2+}$ -type chromophore after photo excitation.

Furthermore, **phenphen** has no electron storage moiety which compares to the pyrazine moiety of the tpphz ligand. According to CAMPAGNA et al., this results in more negative reduction potentials for the bridge in $[(\text{bpy})_2\text{M}(\mu\text{-phenphen})\text{M}(\text{bpy})_2]^{4+}$ ($\text{M} = \text{Ru}, \text{Os}, \text{Ir}$), when compared to tpphz complexes.^[131]

These two facts, missing electron storage capacity and negative reduction potentials, hold the potential that a reduction of other metal centers such as Pt(II), Rh(III) or Co(III) would be possible after excitation of the MLCT in a heteronuclear **phenphen**-bridged complex.

Thus, the use of **phenphen** shall be applied in heteronuclear $[[\text{P} \sim \text{B} \sim \text{C}]]$ -type systems. Leaving the chromophore unchanged but focusing on the bridging ligand and reaction center allows characterizing and understanding the nature of charge separation and electron transfer in the supramolecular catalyst. Therefore, one of the two $[\text{Ru}(\text{bpy})_3]$ -type centers at the binuclear **phenphen** bridged ruthenium complex of CAMPAGNA et al. may represent the chromophore which offers high synthetic flexibility, high stability and well understood photophysical and redox properties. The second metal center has to be replaced by a variety of reaction centers such as noble metals Rh, Re, Pd, Pt or other metal centers such as Co or Ni which have been found to be suitable for different kinds of redox catalysis.^[88]

With respect to the resulting $[[\text{P} \sim \text{B} \sim \text{C}]]$ -system, two major drawbacks were identified until today which reduce the quantum yield of the overall reaction:

On the one hand, decomplexation processes of the catalyst-systems with possible colloid formation or chromophore decomposition are side reactions that may occur after photo reduction.^[94, 132] On the other hand, it is difficult but essential to tune the kinetic and thermodynamic properties of the bridging ligand (e.g. electronic communication/insulation or electron storage to a greater or lesser extent as previously discussed for the tpphz ligand) because these factors may potentially limit the type of reducible metal centers and the rate of side reactions or charge recombination.^[80]

In the following section, the synthesis of mononuclear and hetero-dinuclear **phenphen**-bridged complexes will be presented. The characterization of the photo- and electrochemical properties will be discussed toward the application potential within $[[\text{P} \sim \text{phenphen} \sim \text{C}]]$ -type systems in light driven catalysis. Special emphasis will be placed on the characterization of stereoisomers.

3.2.1 Preparation of phenphen and Related Complexes

The synthesis of 5,5'-bi-1,10-phenanthroline (**phenphen**) was performed according to a procedure described by THUMMEL et al. using a Ni-mediated homocoupling reaction. Scale up of this reaction and application of the previously prepared **phenBr** as substrate instead of the otherwise used 5-chloro-1,10-phenanthroline resulted in the formation of **phenphen** in moderate yields (see figure 59).^[131, 133]

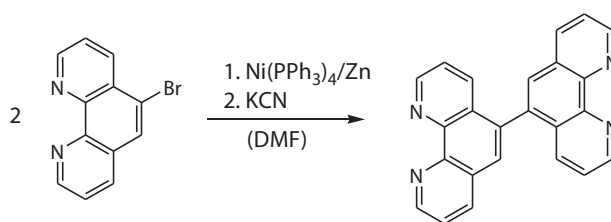


Figure 59: Synthesis of **phenphen** from **phenBr**.

The scheme in figure 60 gives an overview of the applied synthesis steps toward the heterobinuclear photocatalyst and important reference compounds.

In a first attempt it was possible to prepare the homobinuclear **phenphen**-bridged ruthenium complex $[(\text{tbbpy})_2\text{Ru}(\mu\text{-phenphen})\text{Ru}(\text{tbbpy})_2]^{4+}$ (**Ru(phenphen)Ru**) in quantitative yield via reaction of **phenphen** and $[\text{Ru}(\text{tbbpy})_2\text{Cl}_2]$ in 1:2-stoichiometry through the protocol for the preparation of ruthenium complexes from the RAU group (**method C1**).^[120] This complex is very similar to the complex of CAMPAGNA et al. which contains bpy-ligands instead of tbbpy-ligands but in contrary, was not prepared via $[\text{Ni}(\text{PPh}_3)_4]$ -mediated cross-coupling of $[(\text{bpy})_2\text{Ru}(5\text{-chloro-1,10-phenanthroline})]^{2+}$ as described there.^[131]

The same microwave reaction was applied to the 1:1 mixture of **phenphen** and $[\text{Ru}(\text{tbbpy})_2\text{Cl}_2]$ for the mononuclear ruthenium complex **Ru(phenphen)** ($[(\text{tbbpy})_2\text{Ru}(\text{phenphen})]^{2+}$). But counter ion exchange with NH_4PF_6 and work up yielded a mixture of the desired mononuclear complex **Ru(phenphen)** and the binuclear ruthenium byproduct **Ru(phenphen)Ru**, as first indicated by TLC-experiments and later supported by ¹H-NMR-experiments. Using a solvent mixture of $\text{KNO}_3/\text{water}/\text{ACN}$ (very polar), it was possible to separate the two products by column chromatography over silica and to obtain the mononuclear complex in 65% yield.

Platinum was chosen as active metal at the reaction center due to its increased stability under reductive conditions in a NN-coordination sphere and, furthermore, because platinum

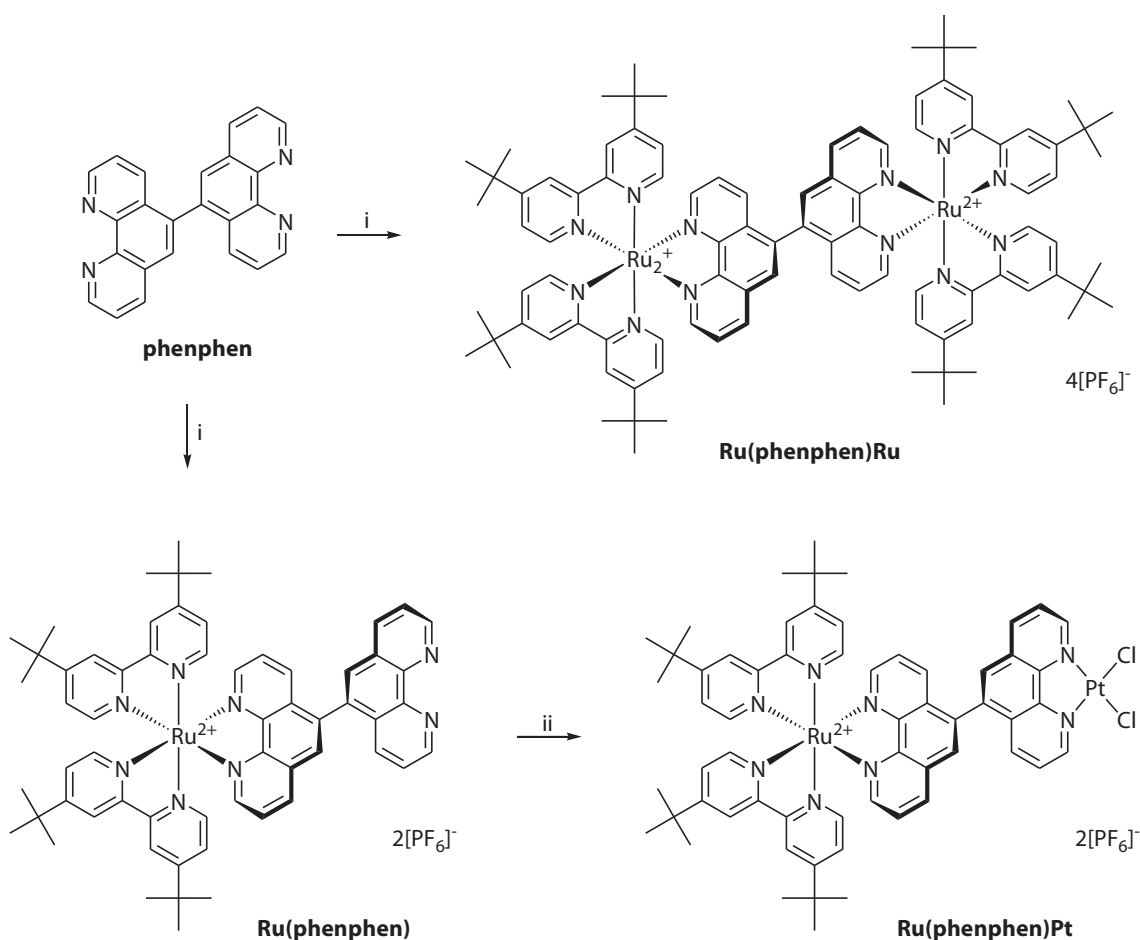


Figure 60: Synthesis of the homo- and binuclear ruthenium and platinum complexes **Ru(phenphen)**, **Ru(phenphen)Ru** and **Ru(phenphen)Pt** from **phenphen**. i) $[\text{Ru}(\text{tbbpy})_2\text{Cl}_2]$, (EtOH/H₂O), 2 h, microwave, reflux. ii) K_2PtCl_4 (DMF), 28 h, reflux, 36%.

compounds display about the same high catalytic activity as their related palladium compounds.^[82, 134, 135] In this way the system would be protected from decomposition by colloid formation after the photoreduction with retention of the catalytic activity of the palladium catalyst. For this synthesis, **Ru(phenphen)** was treated with K_2PtCl_4 for 28 hours in a two-phase system of dichloromethane/water and later DMF to obtain the hetero-binuclear ruthenium-platinum complex $[(\text{tbbpy})_2\text{Ru}(\mu\text{-phenphen})\text{PtCl}_2]^{2+}$ (**Ru(phenphen)Pt**) in 36% yield according to the reaction pathway in figure 60.

3.2.2 Identification and Characterization

To characterize the obtained products, detailed NMR-experiments were performed. For the better understanding of the obtained NMR-data a short excursus will be given to recall some structural features of **phenphen** and its derived complexes.^[136]

An interesting effect is the formation of different atropisomers of **phenphen** due to the hindered rotation about the single bond which connects the two equivalent phenanthroline moieties in the 5,5'-positions (see figure 61).

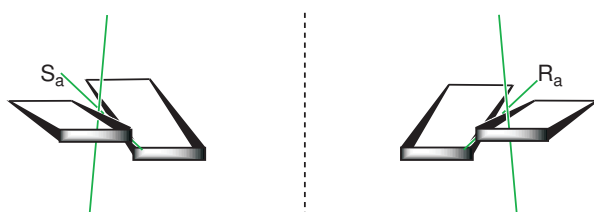


Figure 61: Enantiomeric pair of the atropisomers of **phenphen** with the S_a - and R_a -conformation.

This results in a frozen rotation about this C-C-single bond on the NMR-timescale and causes, in combination with a second stereo-center such as a stereogenic ruthenium fragment in a tris(chelate) environment, the peculiarity of four inisochronic sets of phenanthroline protons in the resulting ^1H -NMR-spectrum of **Ru(phenphen)** and **Ru(phenphen)Pt**, whereas **phenphen** exhibits one set because no additional stereocenters are present, and thus the two phenanthroline moieties experience the same field anisotropy effects (see figures 61 and 62).

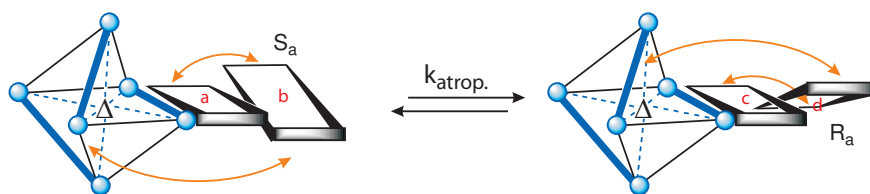


Figure 62: The on the NMR-timescale slow atropisomerization between the S_a - and R_a -conformers of **phenphen** in combination with the second stereo center in Δ/Λ -conformation of the octahedral metal in **Ru(phenphen)** or **Ru(phenphen)Pt** shifts the field anisotropy (symbolized by orange arrows) around the phenanthroline moieties (black rectangles) and results in the occurrence of four inisochronic sets of phenanthroline signals (a, b, c, d) in the resulting ^1H -NMR-spectrum of the racemic mixture.

Note: A related atropisomerism of an axis chiral ligand (4,4'-biquinazoline), bound to an octahedral ruthenium complex has been discussed by CONSTABLE and coworkers.^[137]

The addition of the different Λ -conformers to the mixture of S_a, Δ - and R_a, Δ -conformers (depicted in figure 62) will give the complete racemic product mixture but will not result in additional sets of phenanthroline signals in the NMR-spectra because the Δ -set comprises the isochronic enantiomers of the Λ -set (see figure 63).

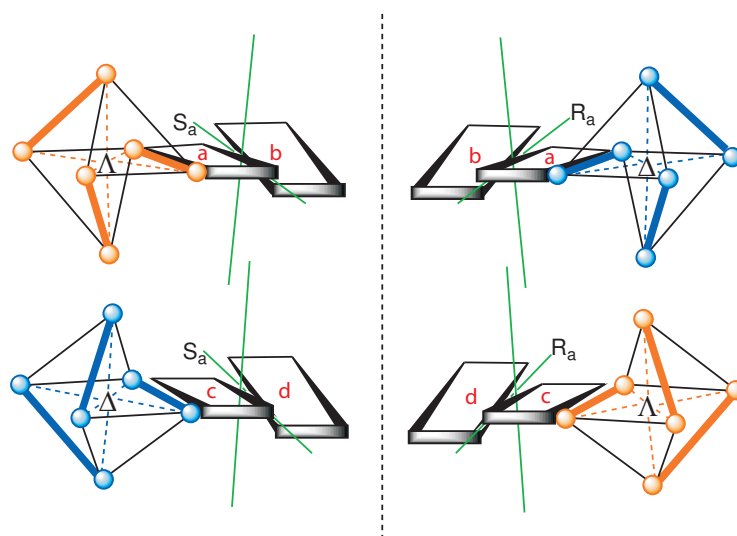


Figure 63: Two pairs of enantiomers with $(\Lambda, S_a)/(\Delta, R_a)$ -conformation and $(\Delta, S_a)/(\Lambda, R_a)$ -conformation respective represent all possible stereoisomers of **Ru(phenphen)** or **Ru(phenphen)Pt**.

For a combination of two stereogenic octahedral metal fragments such as $\{\text{Ru}(\widehat{\text{LL}})_2\}^{2+}$ and the axis chiral bridging ligand **phenphen**, as in the case of **Ru(phenphen)Ru**, in principle eight differently configured stereoisomers can be found in the racemic mixture (see figure 64). If all terminal ligands are equivalent and the bridging ligand exhibits two C_2 -axes along the axes of chirality, this number decreases to six in a 1:2:1-ratio because the molecules with (Λ, S_a, Δ) - and (Δ, S_a, Λ) -conformation become identical for symmetry reasons. This effect decreases as well the number of isochronic sets of phenanthroline signals in the resulting NMR-spectra, as can be derived from figure 64.

For the elucidation of the ^1H -NMR spectra of the **Ru(phenphen)M**-series, especially two-dimensional NMR methods were used as exemplarily depicted in figure 65 for the mononuclear complex **Ru(phenphen)**.

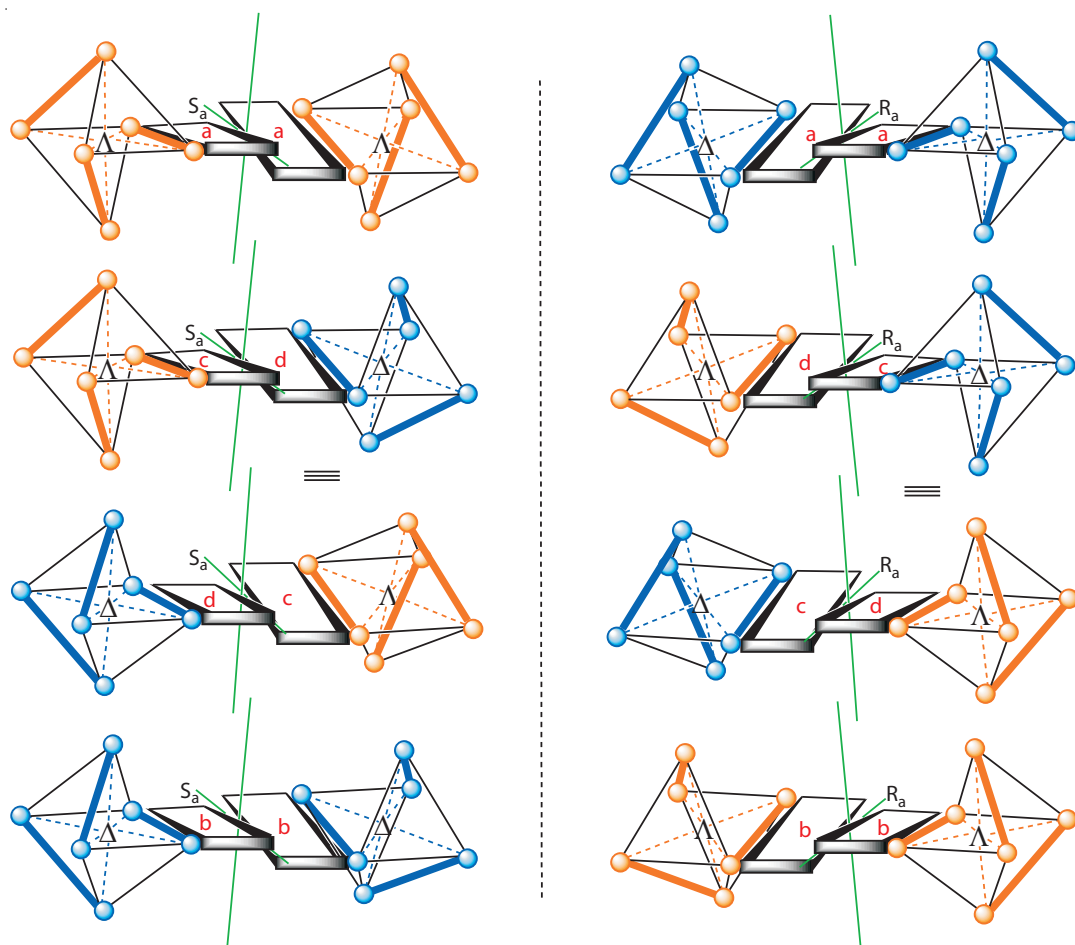


Figure 64: Three pairs of enantiomers with $(\Lambda, S_a, \Lambda)/(\Delta, R_a, \Delta)$ -conformation, $(\Lambda, S_a, \Delta)/(\Delta, R_a, \Lambda)$ -conformation and $(\Delta, S_a, \Delta)/(\Lambda, R_a, \Lambda)$ -conformation respectively represent the six possible stereoisomers of **Ru(phenphen)Ru** and give rise to four homotopic/isochronic sets of seven phenanthroline signals each (a, b, c, d) in a 1:1:1:1-ratio in the $^1\text{H-NMR}$ spectrum of the racemate.

The existence of meso-forms and symmetry equivalent molecule sides prevents a further splitting of the **phenphen** NMR-signals beyond four sets. In the first place, it was possible to identify sets of hydrogen signals with similar chemical shift due to the fact that asymmetric **phenphen** ligand displays very similar signals e.g. for the hydrogen atoms in 2-, 9-, 2'- and 9'-position, slightly shifted by the asymmetric surrounding in each of the stereoisomers.

Nevertheless, according to the coupling constants and by comparison of the different complexes (see figure 64), it was possible to distinguish the **phenphen**-related sets of signals which refer to the 2/9- (A-position, (○), dd, $^3J = 5.4 \text{ Hz}$, $^4J = 1.2 \text{ Hz}$), 3/8- (B-position (●), dd, $^3J =$

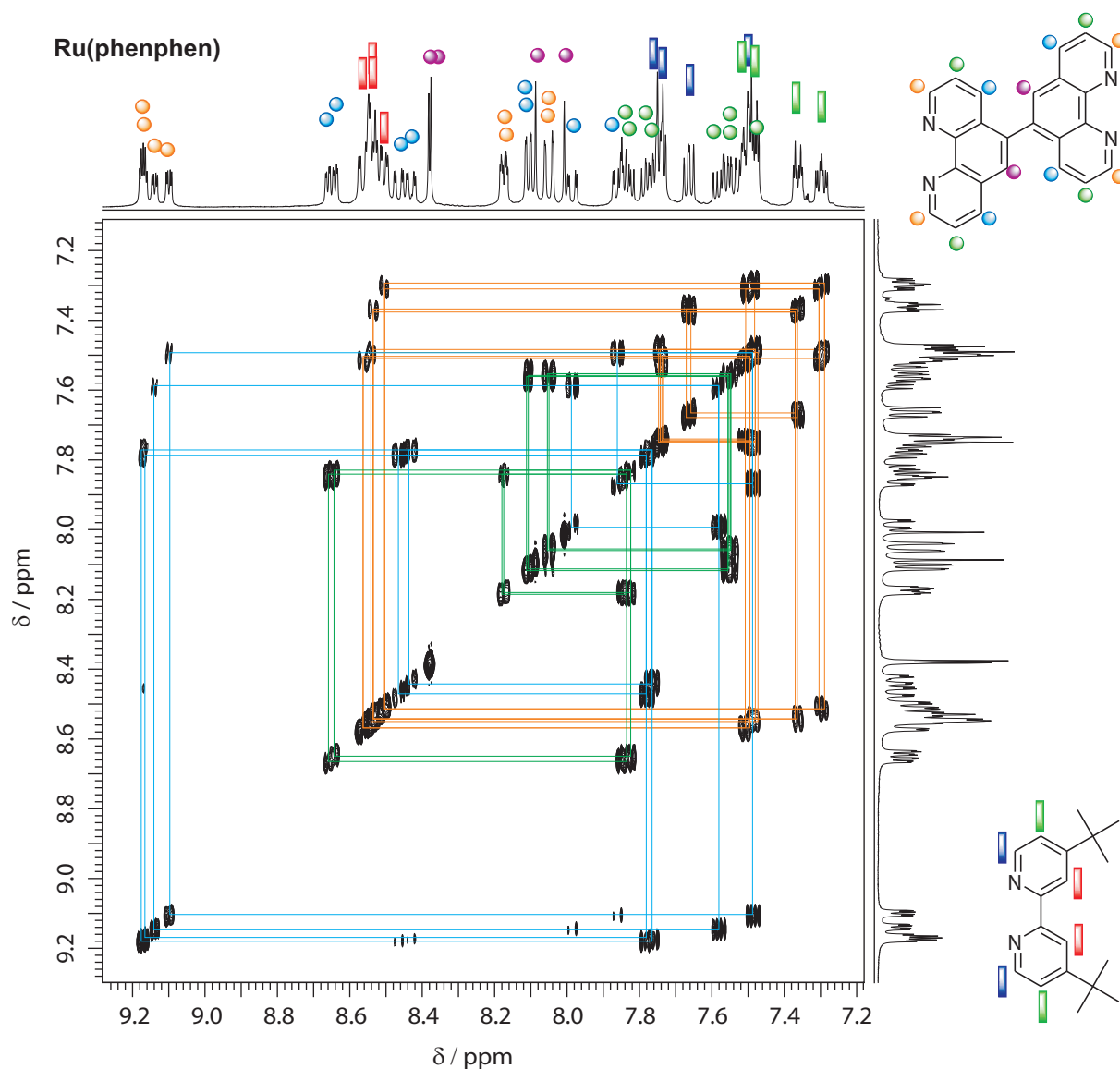


Figure 65: H,H-COSY NMR spectrum (400 MHz) of racemic **Ru(phenphen)** in dichloromethane- d_2 with denoted couplings of the free- (—) and ruthenium coordinated phenanthroline signals (—) plus terminal bipyridine ligand signals (—).

8.2 Hz, $^3J = 5.4$ Hz), and 4/7-position (c-protons (\odot), dd, $^3J = 7.2$ Hz, $^4J = 1.2$ Hz) of the ruthenium bound (Ru), platinum bound (Pt), and free (f) phenanthroline sphere-hydrogen atoms. Two dimensional NMR spectroscopy further supported the assignment of the proton signals. Temperature dependent NMR experiments in acetonitrile- d_3 at 60°C or dimethylformamide- d_7 at 80°C did not result in a change or even simplification of the observed spectra. To clearly decide

about the purity of the particular complexes the dominant singlet signals, resulting from isolated protons in 6-position (D-position, \bullet) were the most useful.

The racemic mixture of the homobinuclear **Ru(phenphen)Ru**-complexes represents the example with high chemical resemblance of the phenanthroline moieties. In this case, all differences in terms of chemical shifts in the NMR-spectra of **Ru(phenphen)Ru** with respect to a specific phenanthroline proton result from a differing field anisotropy in the different stereoisomers. For example, in acetonitrile- d_3 two sets of, in each case, four closely spaced similar proton signals were identified in the ^1H -NMR spectrum for the characteristic phenanthroline c-position with $^3J = 8.0$ Hz and $^4J = 1.6$ Hz ($4 \times \text{dd}$, $\delta_{\text{C}(4)}^{\text{Ru}} = [8.66 - 8.78]$ ppm and $4 \times \text{dd}$, $\delta_{\text{C}(7)}^{\text{Ru}} = [8.10 - 8.30]$ ppm) which refer to the 4- and 7-positions of the four inhomotopic **phenphen**-moieties (a, b, c, d in figure 64). The widest scattering of proton signals ($\Delta\delta_{\text{C}}^{\text{Ru}} = 0.2$ ppm) in **Ru(phenphen)Ru** is found for the eight protons in the phenanthroline-c-positions which experience the strongest field anisotropy due to the chiral environment/conformational differences within this set of stereoisomers.

The monometallic ruthenium complex **Ru(phenphen)** exists according to figure 63 in two inisochronic variants which might interconvert at a low rate. For the ruthenium coordinated side, chemical shifts were observed which were very similar to the **Ru(phenphen)Ru**-shifts. The formal loss of a $\{\text{Ru}(\text{tbbpy})_2\}^{2+}$ -fragment gives rise to a second pair of phenanthroline signals (f) which roughly resemble the chemical shifts of **phenphen**. For example, the far low-field shifted positions of the A-protons were found in the same region as the **phenphen**-signals ($\delta_{\text{A}(2)}^{\text{f}} = [9.20 - 9.26]$ ppm $\approx \delta_{\text{A}(2)}^{\text{phenphen}} = 9.20$ ppm, and $\delta_{\text{A}(9)}^{\text{f}} = [9.14 - 9.22]$ ppm $\approx \delta_{\text{A}(9)}^{\text{phenphen}} = 9.13$ ppm respectively). The same accounts for the slightly low-field shifted B-protons and the high-field shifted C-protons (see table 7).

In **Ru(phenphen)Pt** the achiral, square planar, neutral $\{\text{PtCl}_2\}$ -fragment is present at the formerly free phenanthroline sphere of **Ru(phenphen)**. This results in a retention of the possible stereoisomers as discussed for **Ru(phenphen)**. Furthermore, only slight changes in the chemical shift of the platinum substituted coordination sphere, in comparison to the unsubstituted phenanthroline moiety, are the result. The most significant difference in the ^1H -NMR-spectra between **Ru(phenphen)** and **Ru(phenphen)Pt** is the typical low-field shift of the signals in A-position ($\delta_{\text{A}(2)}^{\text{f}} = [9.20 - 9.26]$ ppm $< \delta_{\text{A}(2)}^{\text{Pt}} = [9.22 - 9.28]$ ppm, and $\delta_{\text{A}(9)}^{\text{f}} = [9.14 - 9.22]$ ppm $< \delta_{\text{A}(9)}^{\text{Pt}} = [9.28 - 9.38]$ ppm) due to platinide coordination.^[138] Furthermore, the chemical shift of

Table 7: Selected ^1H -NMR-shifts of **phenphen**-compounds in acetonitrile- d_3 .

Signal (Position)	Coordinated Fragment	phenphen δ [ppm]	Ru(phenphen)Ru δ [ppm]	Ru(phenphen) δ [ppm]	Ru(phenphen)Pt δ [ppm]
A (2)	f / Pt	9.20		9.20 - 9.26	9.22 - 9.28
	Ru		8.15 - 8.20	8.12 - 8.16	8.06 - 8.10
(9)	f / Pt	9.13		9.14 - 9.22	9.28 - 9.38
	Ru		8.08 - 8.15	8.04 - 8.10	8.00 - 8.04
B (3)	f / Pt	8.43		7.92 - 7.98	7.84 - 7.90
	Ru		7.80 - 7.90	7.80 - 7.86	7.72 - 7.78
(8)	f / Pt	7.84		7.62 - 7.74	7.66 - 7.76
	Ru		7.54 - 7.72	7.52 - 7.56	7.46 - 7.52
C (4)	f / Pt	7.78		8.66 - 8.70	8.76 - 8.84
	Ru		8.66 - 8.78	8.60 - 8.66	8.54 - 8.50
(7)	f / Pt	7.49		8.00 - 8.14	8.18 - 8.30
	Ru		8.10 - 8.30	8.00 - 8.04	8.08 - 8.20

f = free coordination sphere, Pt = {PtCl₂}, Ru = {Ru(tbbpy)₂}²⁺.

the platinum atom of **Ru(phenphen)Pt** was determined by ¹⁹⁵Pt-NMR experiments to be at -2334 ppm which is exactly in the expected region for [Pt(bpy)Cl₂]-type complexes.^[138, 139]

The interpretation of the ¹³C-NMR spectra was difficult because of the closely lying peaks due to stereoisomerization and the extensively broadened signals in the related two dimensional HMBC and HSQC spectra and, thus, did not lead to a further-reaching understanding of the structural properties of the prepared compounds.

For the identification and affirmation of the purity of all prepared compounds, as well as for further characterization of the obtained products, different mass spectrometric experiments were performed. The examination of the three ruthenium complexes with the ESI method revealed very clear mass spectra which allowed for the straight forward assignment of the obtained signals according to the match in shape and intensity between calculated and measured isotopic patterns. Predominant in all spectra are the strong signals for the molecular ions [M-PF₆]⁺, where one or two counter ion were lost ([**Ru(phenphen)**-PF₆]⁺ = 1141.1 m/z, [**Ru(phenphen)Ru**-PF₆]⁺ = 2069.2 m/z and [**Ru(phenphen)Pt**-2 PF₆]⁺ = 1261.1 m/z).

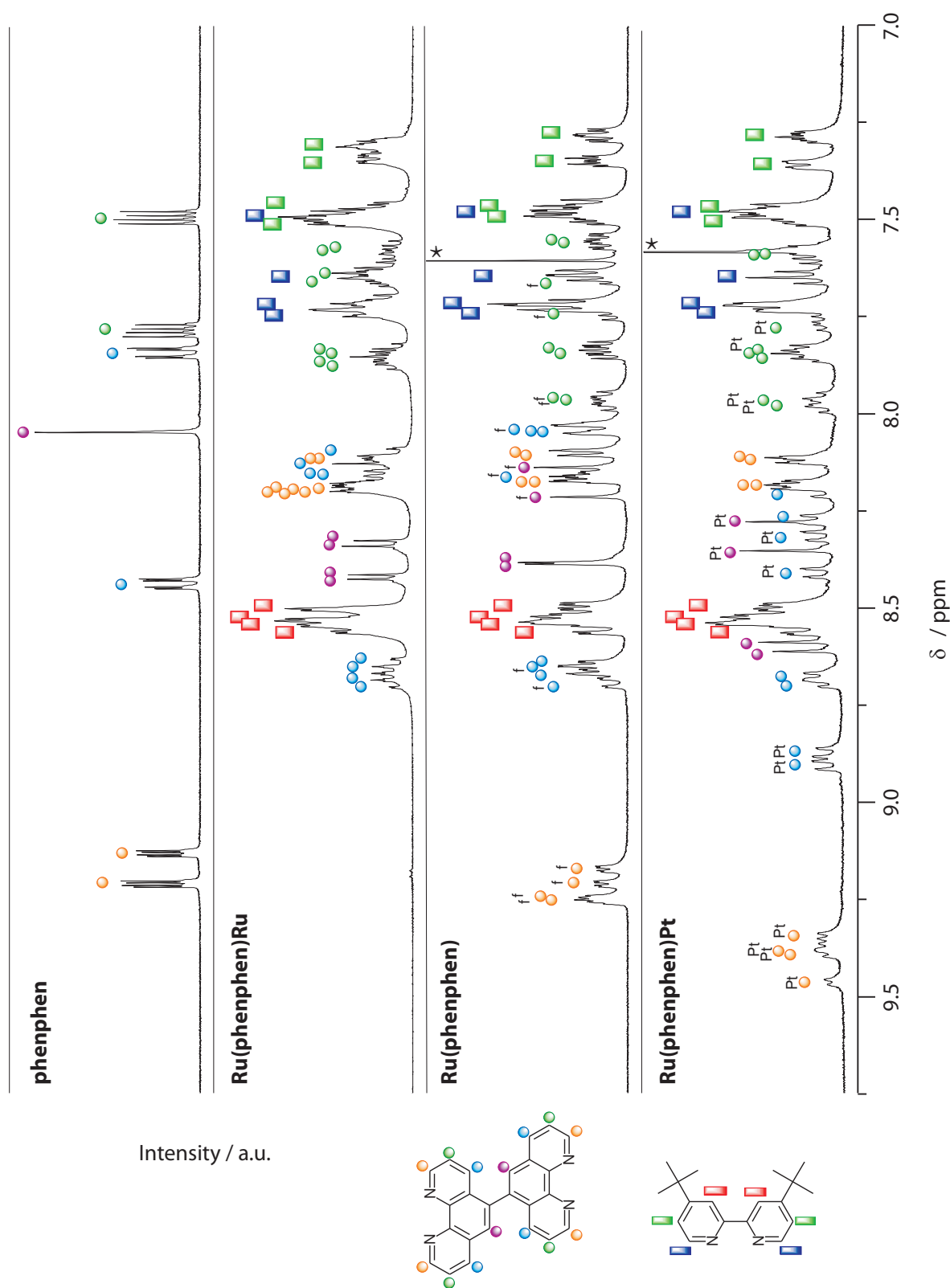


Figure 66: Aromatic region of the $^1\text{H-NMR}$ spectra of **phenphen** and the resulting ruthenium complexes **Ru(phenphen)Ru**, **Ru(phenphen)** and **Ru(phenphen)Pt** in acetonitrile- d_3 .

3.2.3 Structural Analysis

Fortunately, after the synthesis X-ray suitable crystals of **phenphen** and **Ru(phenphen)** were obtained from solvent mixtures of water and ethanol (see figure 68).

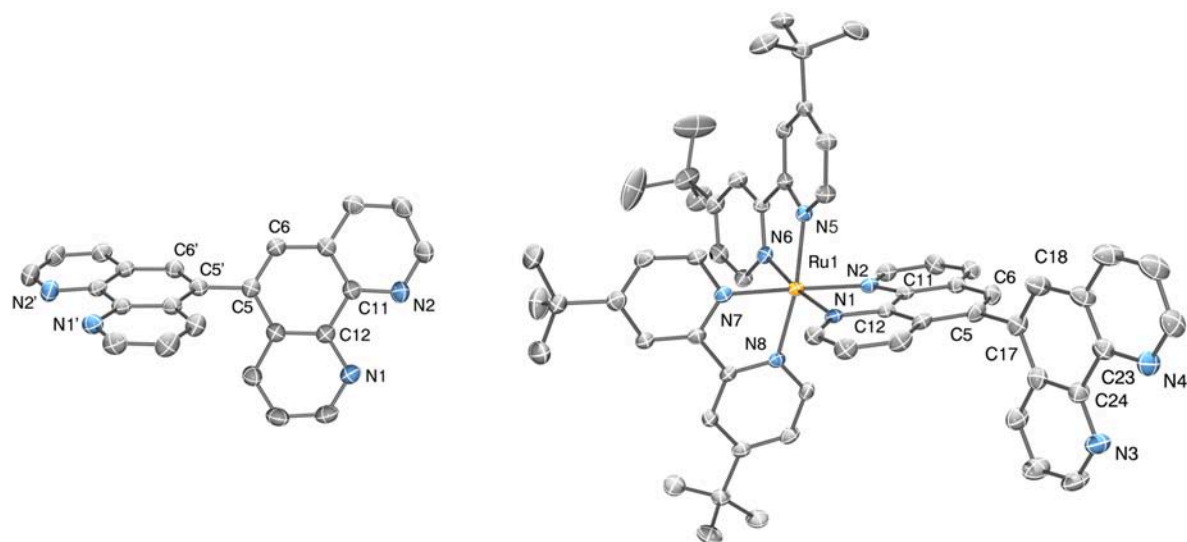


Figure 67: Molecular structure of **phenphen** (left) and **Ru(phenphen)** (right). Hydrogen atoms, solvent molecules and anions were omitted for clarity. The torsion angle between the rotational hindered phenanthroline moieties is $65.7(2)^\circ$ in **phenphen** and $83.9(3)^\circ$ in the ruthenium complex respectively.

Most prominent is the fact that both crystal structures emphasize the twisted nature of the bridging ligand. The determined torsion angles θ about the C-C-single bonds between the two phenanthroline spheres differ from each other ($\theta^{\text{phenphen}} = 65.7(2)^\circ < \theta^{\text{Ru(phenphen)}} = 83.9(3)^\circ$) but this may be attributed to packing effects according to the low energy barrier for the rotation. The bond length of the bridging C-C-single bond remains unchanged upon complexation ($d_{(\text{C}5-\text{C}5')}^{\text{phenphen}} = 1.489(3) \text{ \AA}$ in **phenphen** and $d_{(\text{C}5-\text{C}17)}^{\text{Ru(phenphen)}} = 1.500(4) \text{ \AA}$ in the mononuclear complex) but turns out to be slightly longer than the typical $\text{C}(\text{sp}_2)\text{-C}(\text{sp}_2)$ bond length of 1.47 \AA , possibly due to the torsion. All Ru-N distances in **Ru(phenphen)** differ slightly but remain in the range of $2.053 - 2.070 \text{ \AA}$, which is expected for ruthenium complexes with bipyridine or phenanthroline-type ligands.^[120, 108, 140, 125] Comparison of the different coordination sites exhibits the same values for the bond lengths and angles in **phenphen** and in the free coordination sphere of **Ru(phenphen)**. The ruthenium containing coordination

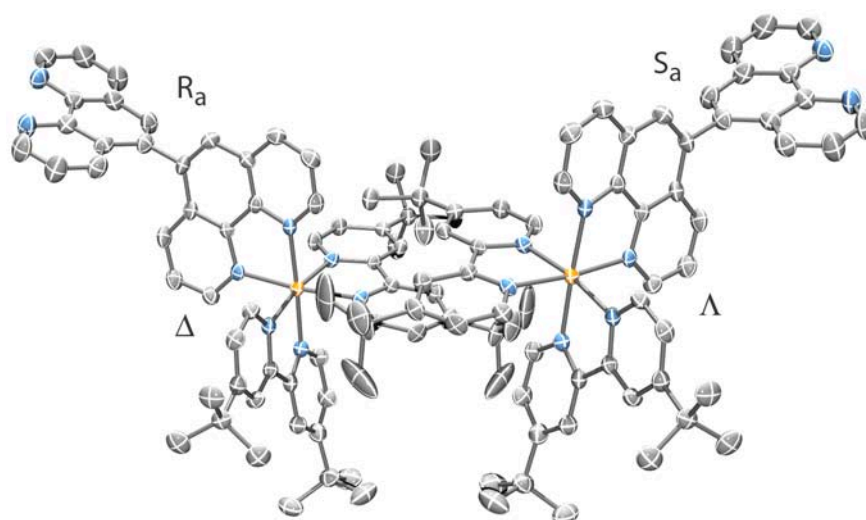


Figure 68: Detail of the crystal structure which contains the enantiomeric pair of **Ru(phenphen)** in close proximity to each other. The complex on the left has (Δ, R_a)-configuration whereas the complex on the right has (Λ, S_a)-configuration.

Table 8: Selected bond lengths [\AA] and angles [$^\circ$] of **phenphen** and **Ru(phenphen)**.

distance [\AA]	phenphen	Ru(phenphen)	angle [$^\circ$]	phenphen	Ru(phenphen)
Ru1 - N1		2.066(3)	N1 - Ru1 - N2		79.60(11)
Ru1 - N2		2.070(3)	N5 - Ru1 - N6		78.41(11)
Ru1 - N5		2.069(3)	N7 - Ru1 - N8		78.53(10)
Ru1 - N6		2.057(3)	θ	65.68(13)	83.9(3)
Ru1 - N7		2.053(3)	N1 - C12 - C11	118.11(16)	116.8(3)
Ru1 - N8		2.065(3)	N2 - C11 - C12	117.91(16)	116.1(3)
C5 - C5'(17)	1.489(3)	1.500(4)	N3 - C24 - C23		118.9(3)
C11 - C12	1.449(3)	1.427(4)	N4 - C23 - C24		116.9(3)
C23 - C24		1.455(4)			
C11 - N2	1.361(2)	1.374(4)			
C12 - N1	1.358(2)	1.368(4)			
C23 - N4		1.379(4)			
C24 - N3		1.356(4)			

sphere differs significantly from the free phenanthroline sphere. Especially a shortening of the C11-C12-bond ($d_{\text{C11-C12}}^{\text{phenphen}} = 1.449 \text{ \AA} > d_{\text{C11-C12}}^{\text{Ru(phenphen)}} = 1.427 \text{ \AA}$) and decrease of the N1-C12-C1-angle ($\angle_{\text{N1,C12,C1}}^{\text{phenphen}} = 118.11^\circ > \angle_{\text{N1,C12,C1}}^{\text{Ru(phenphen)}} = 116.8^\circ$) and of the N2-C11-C12-angle ($\angle_{\text{N2,C11,C12}}^{\text{phenphen}} = 117.9^\circ >$

$\angle_{\text{N}_1, \text{Cl}_2, \text{Cl}}^{\text{Ru}(\text{phenphen})} = 116.1^\circ$) was observed upon complexation. For other interesting values for bond lengths and angles see table 8.

Most impressive is the fact that four complex molecules are present in the unit cell of **Ru(phenphen)** but only one pair of enantiomers (in particular the molecules with $(\Delta, R_a)/(\Lambda, S_a)$ -configuration) can be found in the crystal structure. The second set of possible atropisomers with $(\Delta, S_a)/(\Lambda, R_a)$ -configuration is missing in the crystal structure (compare figure 68).

This lucky strike opened the possibility to determine the rate constant for the interchange of sterically hindered atropisomers. Due to the fact that the obtained crystals contain only one enantiomeric pair of **Ru(phenphen)**, it can be expected that only one set of signals would be found in the resulting $^1\text{H-NMR}$ spectrum.

For this experiment one small single crystal of **Ru(phenphen)** was dissolved in dichloromethane- d_2 (to exclude impurities, in particular the second pair of enantiomers). Subsequent observation of the chemical shifts exhibited a simplified spectrum with only one set of signals after 15 minutes (see figure 69).

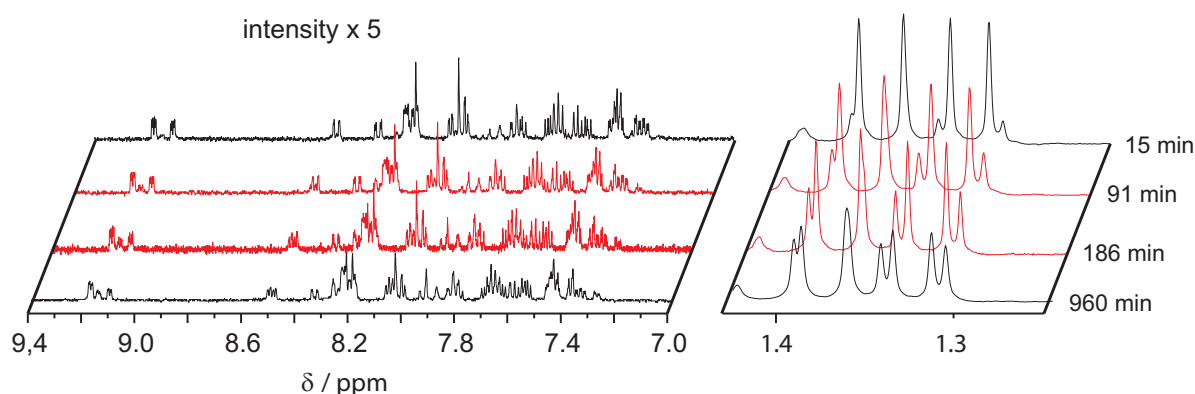


Figure 69: Changes in the aromatic and aliphatic region of the $^1\text{H-NMR}$ spectrum of **Ru(phenphen)** during 16 hours upon formation of the racemic mixture of rotamers from the formerly diastereomeric-pure $(\Delta, R_a)/(\Lambda, S_a)$ -configured compound (single crystal).

Long term tracking of the NMR signals resulted in the slow appearance of the second set of signals, best indicated by the change of the four tert-butyl-signals ($\delta_{\text{tBu}} = [1.3 - 1.4]$ ppm) or by the singlets for the protons at d-position ($\delta_{\text{D}} = 8.05$ ppm/8.20 ppm). As a result of 60 time-correlated $^1\text{H-NMR}$ experiments, peak separation, observation of three different sets of signals, and fitting with first order kinetics, a rate constant of $k_{\text{atrop.}} = 9.68 \times 10^{-5} \text{ s}^{-1}$ and a observed half-life of $t_{1/2, \text{atrop.}} =$

1.99 ± 0.07 h at 25°C in dichloromethane- d_2 could be determined (see figure 69). The determined value is greater than the half-life of 1000 seconds for one rotamer, which is, according to KUHN, required for true atropisomers.^[141] Note: Simple circular dichroism (CD) spectroscopy can be considered rather useless in this case because a set of enantiomers crystallized.

3.2.4 Photophysical Behavior

The detailed characterization of the interactions with light for the **phenphen** based compounds was performed in order to establish their potential as light driven catalysts.

The following presented data arose from a cooperation project with ROGER-JAN KUTTA from the group of Prof. Dr. B. DICK (University of Regensburg). Stationary as well as time resolved spectroscopy data on the **phenphen**-bridged ruthenium and platinum complexes does not only yield insight into electronic states but also into their chemical reactivity. Special focus was placed on a possible formation of reactive species, arise after photo excitation of these compounds.

UV/vis, excitation and emission spectroscopic studies were performed in acetonitrile with and without oxygen in solution. Analysis of the absorption and emission properties of the described complexes revealed the expected $[\text{Ru}(\text{bpy})_3]^{2+}$ -like behavior (see figure 70 for the spectra and table 9 for the complete data).

Table 9: UV/vis absorption and emission data of selected references and **phenphen**-bridged ruthenium complexes.

Complex	$\lambda_{\text{max, abs}}$ [nm]	$\epsilon_{\lambda_{\text{max}}}$ [l mol ⁻¹ cm ⁻¹]	$\lambda_{\text{max, em}}$ [nm]	Φ	τ^{a} [ns]	τ^{b} [ns]
$[\text{Ru}(\text{tbbpy})_3]^{2+}$	458	17 900	615		107 ^[90]	730 ^[90]
Ru(phen)^c,^[120, 125]	454	16 000	610		211	1 423
Ru(phenphen)	455	15 500	630	0.20	127	2 000
Ru(phenphen)Ru	454	34 500	630	0.20	133	1 800
Ru(phenphen)Pt	453	10 000	630	0.21	139	2 000

a) aerated, b) deaerated, c) **Ru(phen)** = $[\text{Ru}(\text{tbbpy})_2(\text{phen})]^{2+}$

In the series $[(\text{tbbpy})_2\text{Ru}(\mu\text{-phenphen})\text{M}]^{2+}$ (f: M = vacant, Ru: M = $\{\text{Ru}(\text{tbbpy})_2\}^{2+}$, and Pt: M = $\{\text{PtCl}_2\}$) all complexes exhibit similar peak shapes and maxima. Relevant is the typical broad ³MLCT-absorption band between 400 and 500 nm ($\lambda_{\text{max}}^{(\text{M}=\text{f})} = 455 \text{ nm} \approx \lambda_{\text{max}}^{(\text{M}=\text{Ru})} = 454 \text{ nm} \approx \lambda_{\text{max}}^{(\text{M}=\text{Pt})}$)

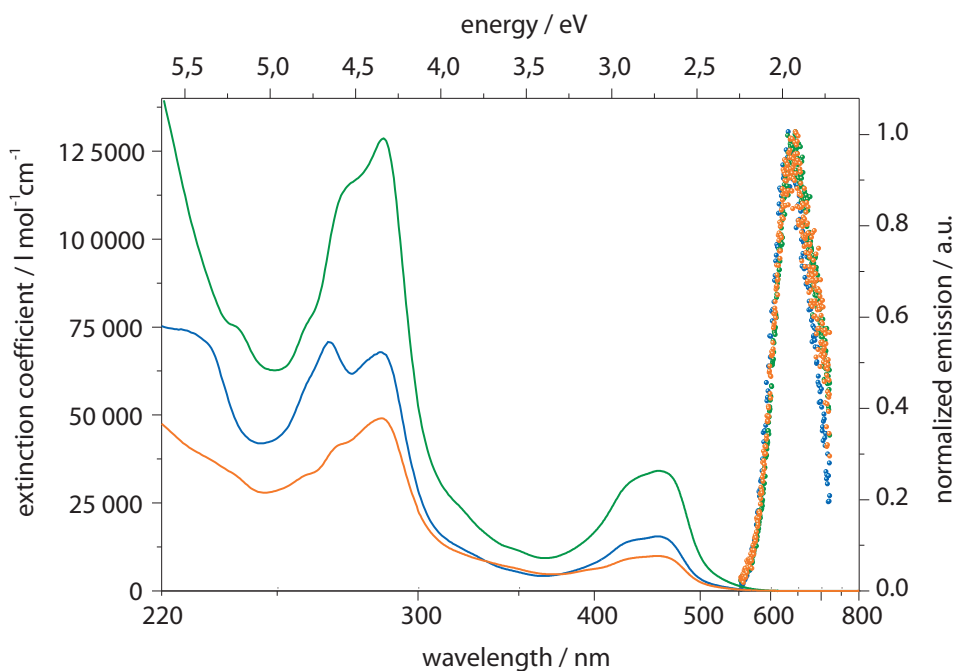


Figure 70: Absorption spectra of the ruthenium **phenphen**-complexes in acetonitrile and corresponding normalized relative emission upon excitation at 450 nm. **Ru(phenphen)**: Abs. (—), Em. (•••), **Ru(phenphen)Ru**: Abs. (—), Em. (•••), **Ru(phenphen)Pt**: Abs. (—), Em. (•••).

= 453 nm) which agrees exactly with the value of the reference **Ru(phen)** ($\lambda_{\max}^{\text{Ru(phen)}} = 454$ nm). In the case of **Ru(phenphen)Ru** a doubling of the absorption coefficients can be detected compared to **Ru(phenphen)** which results from the second chromophore. The absorption of the platinum compound is the least intense ($\epsilon_{\max}^{(\text{M}=\text{Ru})} = 34\,500 \text{ l mol}^{-1}\text{cm}^{-1} > \epsilon_{\max}^{(\text{M}=\text{f})} = 15\,500 \text{ l mol}^{-1}\text{cm}^{-1} > \epsilon_{\max}^{(\text{M}=\text{Pt})} = 10\,000 \text{ l mol}^{-1}\text{cm}^{-1}$). The biggest deviations in shape of these two are in bands at the higher energetic transitions. The additional prominent peaks in the UV-region of the spectra refer to ligand centered π - π^* -transitions ($\lambda_{\pi-\pi^*}^{(\text{M}=\text{f})} = 285$ nm ($\epsilon_{\pi-\pi^*}^{(\text{M}=\text{f})} = 67\,700 \text{ l mol}^{-1}\text{cm}^{-1}$), $\lambda_{\pi-\pi^*}^{(\text{M}=\text{Ru})} = 268$ nm ($\epsilon_{\pi-\pi^*}^{(\text{M}=\text{Ru})} = 128\,600 \text{ l mol}^{-1}\text{cm}^{-1}$), $\lambda_{\pi-\pi^*}^{(\text{M}=\text{Pt})} = 286$ nm ($\epsilon_{\pi-\pi^*}^{(\text{M}=\text{Pt})} = 49\,000 \text{ l mol}^{-1}\text{cm}^{-1}$)).

The excitation spectra of the compounds (not depicted) of **Ru(phenphen)**, **Ru(phenphen)Pt**, rebuild their corresponding absorption spectra. That means that, independent of the excitation wavelength, the system ends up in the emitting MLCT-state for a certain quantum yield. In contrast to that the compound **Ru(phenphen)Pt** does not show 100% independence. Here, the excitation into the higher energetic state does not completely follow to the emitting state in the same amount as excitation into the lower energetic state does, which might be a result of platinum

involving absorption not giving rise to ruthenium centered emission.

Determination of the emission behavior exhibited strong emission bands between 600 and 800 nm with the same maximum at $\lambda_{\text{em}}^{(\text{M}=\text{f,Ru,Pt})} = 630 \text{ nm}$ for all three complexes. Interestingly, emission of the reference **Ru(phen)** is by 20 nm hypsochromically shifted ($\lambda_{\text{em}}^{\text{Ru(phen)}} = 610 \text{ nm}$), which may be attributed to the +M-effect of the substituent at the 5-position. Furthermore, the quantum yields were determined with the integrating sphere method. Moreover, all complexes show similar emission quantum yields of $\Phi_{\text{em}}^{(\text{M}=\text{f,Ru,Pt})} = 0.20$ in oxygen-free acetonitrile which is a very high value.

3.2.5 Excited State Dynamics

For the determination of the emission decay dynamics in a TCSPC-experiment a *Horiba Fluorolog-3* was used. As an excitation light source a N₂-laser ($\lambda_{\text{ex}} = 375 \text{ nm}$, $\Delta t = 4 \text{ ns}$) was used and emitted photons of $\lambda_{\text{obs}} = 630 \text{ nm}$ were observed. UV/Vis, excitation and emission spectroscopic experiments were performed with and without oxygen in solution.

Figure 71 shows the emission decays that were measured in oxygen saturated (exposed to air) acetonitrile for the determination of the lifetimes.

As can be seen, all oxygen saturated samples of the **phenphen**-bridged ruthenium complexes exhibited very similar lifetimes ($\tau_{\text{aerated}}^{(\text{M}=\text{f})} = 127 \text{ ns} \approx \tau_{\text{aerated}}^{(\text{M}=\text{Ru})} = 133 \text{ ns} \approx \tau_{\text{aerated}}^{(\text{M}=\text{Pt})} = 139 \text{ ns}$). The determined values differ from **Ru(phen)**, which exhibits a ~60 ns longer lifetime ($\tau_{\text{aerated}}^{\text{Ru(phen)}} = 211 \text{ ns}$). Subsequent measurements with the oxygen free samples showed the expected strong increase of the excited state lifetimes. This is due to the removal of oxygen, which is known to deactivate the MLCT-state. Again, all complexes show very similar emission decay dynamics with a slightly shorter lifetime in the case of the binuclear compound **Ru(phenphen)Ru** ($\tau_{\text{degassed}}^{(\text{M}=\text{f})} = 2.0 \mu\text{s} \approx \tau_{\text{degassed}}^{(\text{M}=\text{Ru})} = 1.8 \mu\text{s} \approx \tau_{\text{degassed}}^{(\text{M}=\text{Pt})} = 2.0 \mu\text{s}$). The lifetimes are rather long, especially when compared to **Ru(phen)** ($\tau_{\text{degassed}}^{\text{Ru(phen)}} = 1.4 \mu\text{s}$) but remain in the expected range for well degassed samples of $[\text{Ru}(\text{tbbpy})_3]^{2+}$ -type complexes.

For the two-dimensional transient absorption experiments a pulsed Nd:YAG-Laser (third harmonics, $t \approx 10 \text{ ns}$) was used as excitation light source. And for spectra measurement of the transient species a pulsed Xe-lamp was applied as a light source and a combination of spectrograph and streak camera was utilized to transform the temporal profile of a sample-passing light pulse

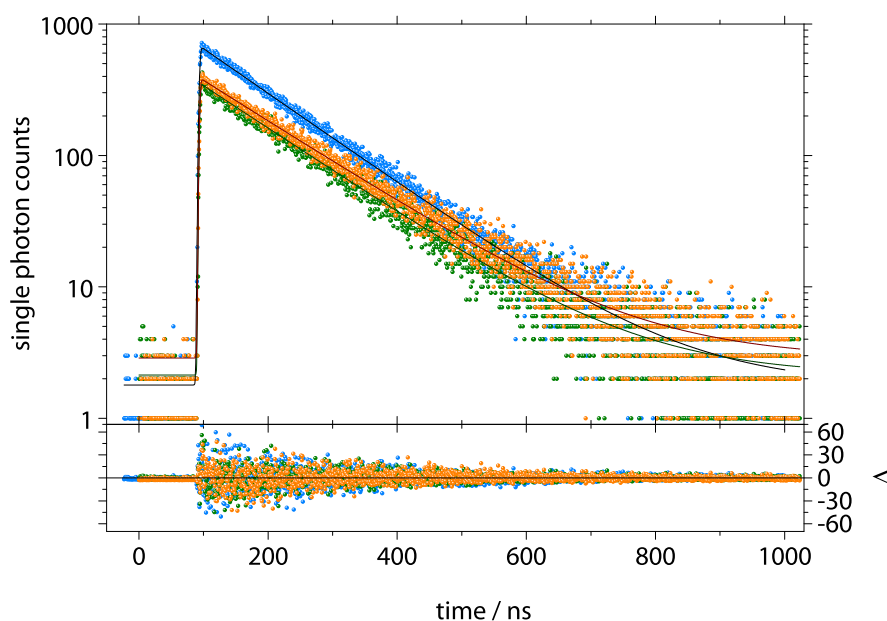


Figure 71: Fitted emission decay plots of **Ru(phenphen)**: (•••), **Ru(phenphen)Ru**: (•••), **Ru(phenphen)Pt**: (•••) in oxygen saturated acetonitrile (top) and residue (bottom).

into a spatial profile on the detector to obtain the two dimensional spectra.

The false color plot in figure 72 shows exemplarily the two-dimensional spectra of the binuclear complex **Ru(phenphen)Ru** in oxygen saturated and oxygen free acetonitrile. Laser excitation at $t=0$ (blue spot at $\lambda = 355$ nm) results in the formation of an $^3\text{MLCT}$ -excited species which possesses a different absorption spectrum. The color code indicates the observed change of the optical density of the sample during the experiment. The ground state bleach in the region between 400 and 500 nm is the result of the decreased concentration of not excited ground state **Ru(phenphen)Ru** upon transition of a fraction of **Ru(phenphen)Ru**-molecules into the excited state (blue and green areas). Furthermore new absorption bands of the excited species between 300 and 400 nm and between 500 and 700 nm become prominent (red and orange areas). After few microseconds the excited molecules relax to the ground state and the initial differential spectrum with no change in optical density (baseline) results.

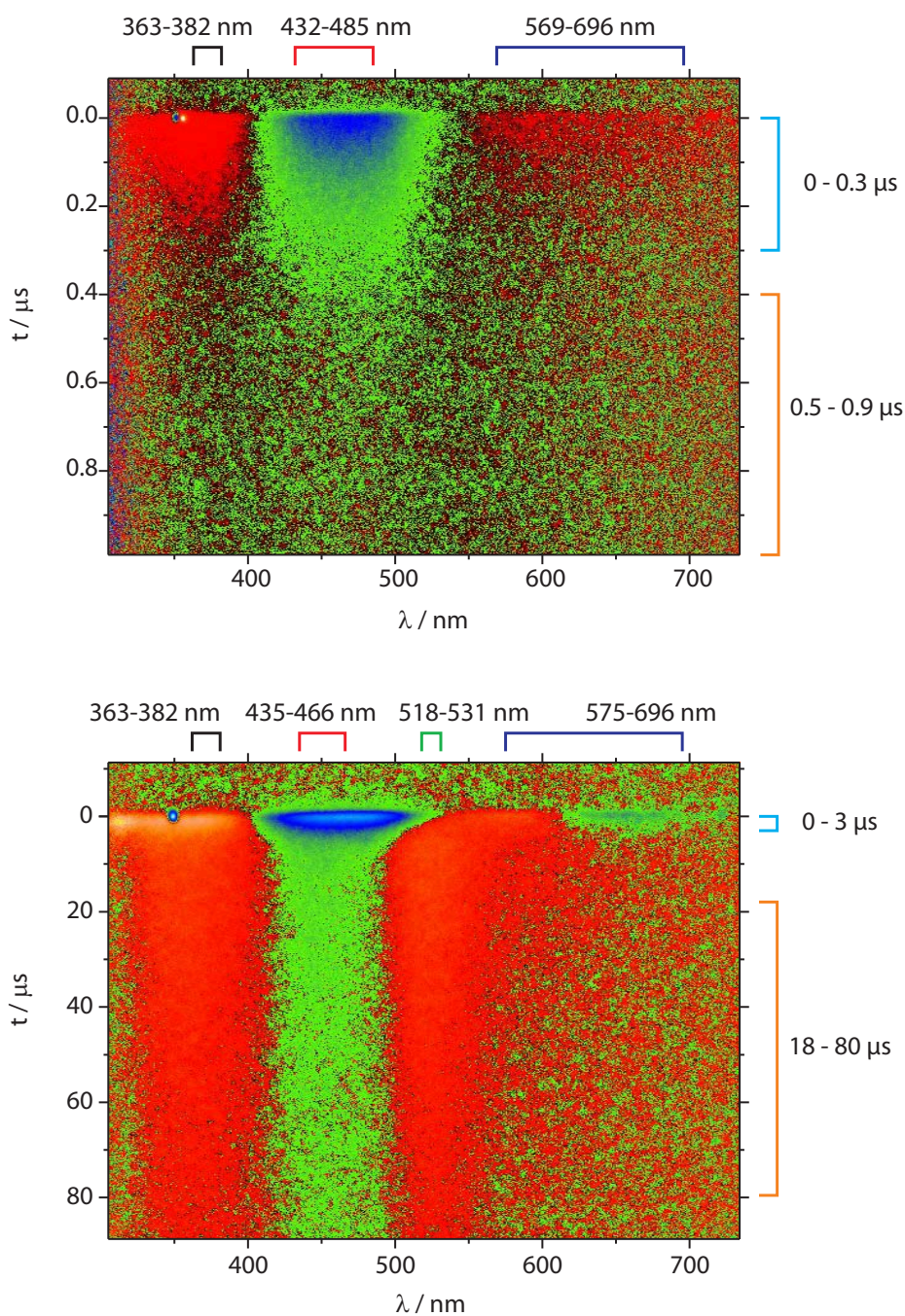


Figure 72: False color plots showing the change in optical density during the decay of the $^3\text{MLCT}$ -excited **Ru(phenphen)Ru** species in oxygen saturated (top) and degassed (bottom) acetonitrile after the laser excitation at 355 nm (~ 3 mJ/pulse, seen as blue spot at $t = 0$, 100 accumulations). Yellow and red areas refer to an increase of the optical density (excited-state absorption), green and blue areas represent a decrease of the optical density (ground state depletion) and black regions show no change compared to the initial solution. The denoted brackets indicate the regions that were used for decay kinetics and differential spectra (compare figure 73 and see text for details).

Repetition of the experiment and averaging over a selected short time range gives rise to the excited state absorption spectra (see figure 73 right). The light blue graph refers to the excited probe and the orange to the probe after relaxation, whereat positive values indicate excited state absorption and negative values indicate ground state bleach or stimulated emission if no absorption band of the ground state molecules is present in this region. Furthermore, averaging over selected wavelength ranges, but the whole time range, affords the time dependent spectra with decay dynamics (see figure 73 left).

The lifetimes of the ruthenium **phenphen**-complexes (streak camera experiment: absorption wavelength region between 435 - 465 nm), determined through the excited state absorption experiment, nicely resemble the values which were determined in the emission decay experiment (TCSPC experiment, emission wavelength 630 nm). Thus, about the same short lifetimes (~150 ns) are found for the aerated samples whereas the degassed probes exhibit longer lifetimes (~2 μ s).

Observation of the differential spectra directly after excitation yielded very similar characteristics for all compounds (M = f, Pt, Ru). Very prominent was the expected ground state bleach of the ³MLCT absorption band in the wavelength region between 400 - 520 nm with a minimum at 465 nm. Furthermore, a new absorption band rises in the high energy region of the spectra between 300 - 400 nm with a maximum at ~360 nm. Also in the low energy region a new broad absorption band was detected in the region between 520 - 630 nm. These characteristic bands were assigned to the absorption of the $^*[\text{Ru}^{\text{III}}(\widehat{\text{LL}})_2(\widehat{\text{LL}}^{-\text{I}})]^{2+}$ -species and vanish after return of the probe into the ground state (compare examples on top in figure 73).^[142]

Surprisingly, in the case of the oxygen-free samples of **Ru(phenphen)Ru** and **Ru(phenphen)** a different behavior was observed. After the relaxation time of the $^*[\text{Ru}^{\text{III}}(\widehat{\text{LL}})_2(\widehat{\text{LL}}^{-\text{I}})]^{2+}$ -species related characteristics the initial absorption spectra (baseline in the differential spectrum) was not retained. Instead, two new absorption bands and a remaining ground state bleach region were present (compare examples on bottom in figure 73) even after very long recording times (80 μ s). The new absorption bands were found in both cases between 315 - 400 nm with a maximum at 355 nm and between 490 - 570 nm with a maximum at 515 nm. Importantly, from the time resolved analysis it becomes clear that this is a very long-living product of a consecutive reaction (compare blue decay, bottom left in figure 73). Unfortunately, nothing is known about this species, but it can be speculated that the reduction of the bridging ligand or effects of a two-photon absorption during the lifetime of the MLCT excited species may be involved in this process. This kind of

process can only be observed in the oxygen free samples which gives rise to the speculation, that possible slow radical reaction or irreversible bridging ligand transformation might occur.

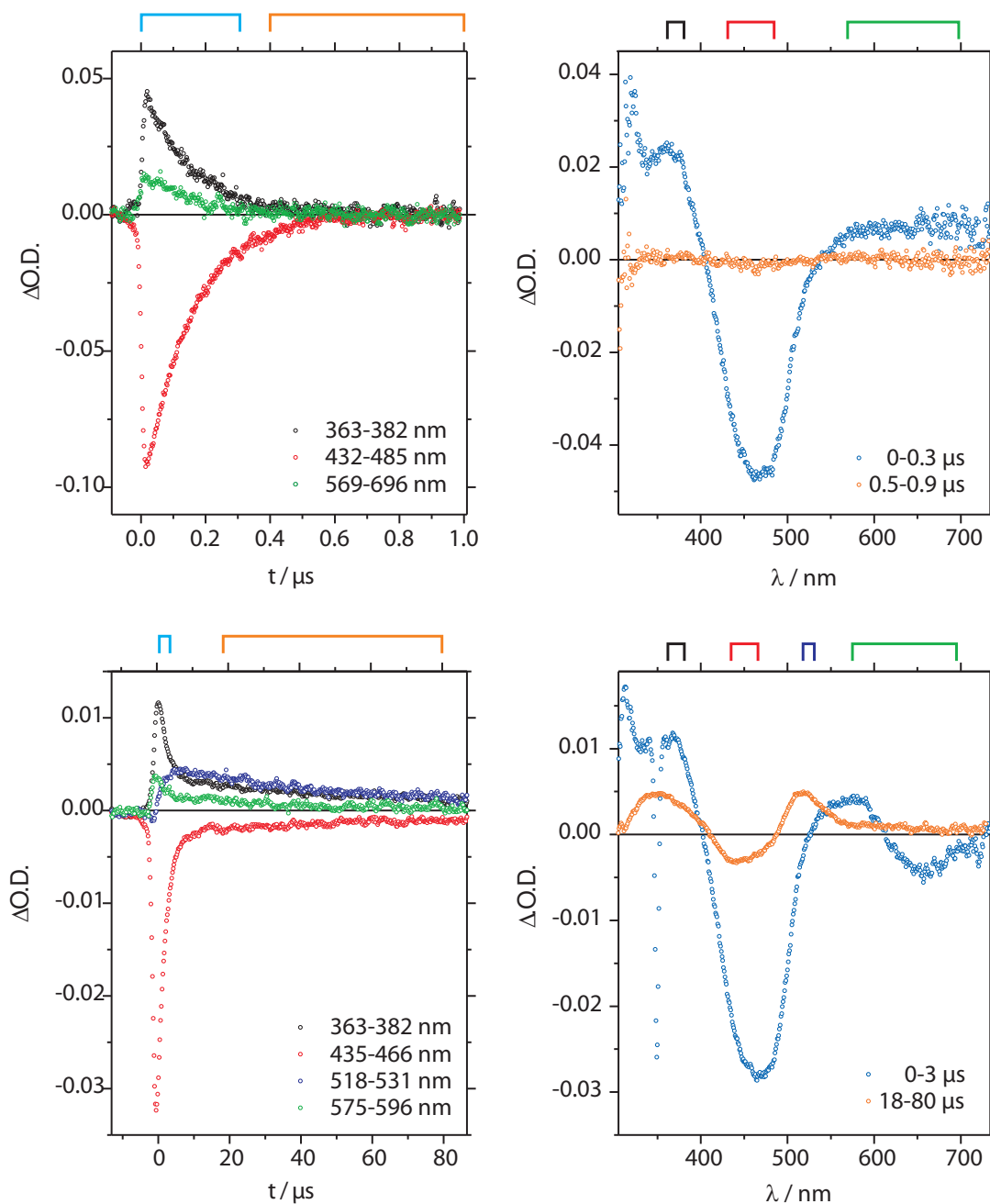


Figure 73: Derived time resolved (left) and wavelength resolved (right) excited state absorption spectra of **Ru(phenphen)Ru** in oxygen saturated (top) and degassed (bottom) acetonitrile, $\lambda_{exc} = 355$ nm (~ 3 mJ/pulse); mean over 100 shots (compare figure 72). The denoted brackets indicate the regions that were used for corresponding decay kinetics and differential spectra.

3.2.6 Electrochemical Characterization

The following presented data of the electrochemical data on the **phenphen**-bridged ruthenium and platinum complexes (see table 10 for the gathered data) does not only give insights into the redox properties of the prepared complexes, but may also help to shine light in the nature of the observed products which arose after photoexcitation in the previous chapter. It will be investigated if, possibly, reduced or oxidized species will arise after ground state oxidation or reduction of these compounds.

Table 10: Selected redox potentials $E_{1/2}$ (V) of the series of ruthenium complexes $[\text{Ru}(\text{tbbpy})_2(\text{phenphen})\text{M}]^{2+}$ ($\text{M} = \text{free}, \{\text{Ru}(\text{tbbpy})_2\}^{2+}, \text{ and } \{\text{PtCl}_2\}$) and selected references, referenced vs. Fc/Fc^+ in a 0.1 M solution of Bu_4NPF_6 in dry and oxygen free acetonitrile under argon.

Complex	$E_{1/2}(\widehat{\text{L}}^3)$ [V]	$E_{1/2}(\widehat{\text{L}}^2)$ [V]	$E_{1/2}(\widehat{\text{L}}^1)$ [V]	$E_{1/2}(\text{Ru}^{2+/3+})$ [V]
$[\text{Ru}(\text{tbbpy})_3]^{2+}$	-2.28	-2.02	-1.83	0.73
Ru(phen) ^[120]	-2.25	-1.98	-1.77	0.74
Ru(phenphen)	-2.26	-1.99	-1.71	0.81
Ru(phenphen)Pt	-2.26	-2.00	-1.77 ir / -1.53	0.81
Ru(phenphen)Ru	-2.26	-1.99	-1.70 ir	0.84
Ru'(phenphen)Ru' ^{b, [131]}	-2.25	-1.94	-1.73	0.84
Os(phenphen)Os ^{c, [131]}	-2.24	-1.93	-1.73	0.39
$[\text{Pt}(\text{phen})\text{Cl}_2]$ ^[143]		-1.83	-1.25	0.30 ^a

^a $E_{1/2}(\text{Pt}^{2+/3+})$, ^b **Ru'(phenphen)Ru'** = $[\{(\text{bpy})_2\text{Ru}\}_2(\mu\text{-phenphen})]$, ^c **Os(phenphen)Os** = $[\{(\text{bpy})_2\text{Os}\}_2(\mu\text{-phenphen})]$

In the series of ruthenium complexes $[\text{Ru}(\text{tbbpy})_2(\text{phenphen})\text{M}]^{2+}$ ($\text{M} = \text{free}, \{\text{Ru}(\text{tbbpy})_2\}^{2+}, \{\text{PtCl}_2\}$) typical similarities in the potentials of the ruthenium centered oxidation ($E_{1/2}(\text{Ru}^{2+/3+})$) were observed ($E_{1/2}^{(\text{M}=\text{f})}(\text{Ru}^{2+/3+}) = 0.81 \text{ V} < E_{1/2}^{(\text{M}=\text{Ru})}(\text{Ru}^{2+/3+}) = 0.84 \text{ V} > E_{1/2}^{(\text{M}=\text{Pt})}(\text{Ru}^{2+/3+}) = 0.81 \text{ V}$). These values are about 0.1 V higher than the determined values for **Ru(phen)** or $[\text{Ru}(\text{tbbpy})_3]^{2+}$. No dependence of the redoxpotentials on the nature of the second metal was observed. Interestingly, in the homobinuclear compound **Ru(phenphen)Ru**, no separated one-electron oxidations were found, which could be expected for binuclear complexes with metal ions that influence one another. Only a slightly broadened and more intense redox wave was present. As in the references **Ru(phen)** and $[\{(\text{bpy})_2\text{Ru}\}_2(\mu\text{-phenphen})]$, all complexes in this series

exhibited three similar reduction potentials at $E_{1/2}(\widehat{\text{LL}}^1) \approx -1.7$ V, $E_{1/2}(\widehat{\text{LL}}^2) \approx -2.0$ V and $E_{1/2}(\widehat{\text{LL}}^3) \approx -2.3$ V which were assigned to the three ligand centered reductions. The two reductions at very negative potentials are quasi reversible and very similar for all three complexes but the $\widehat{\text{LL}}^1$ -reduction waves (assigned to the **phenphen**-ligand based on comparison with data from literature^[131]) differ within this series of complexes (see figure 74).

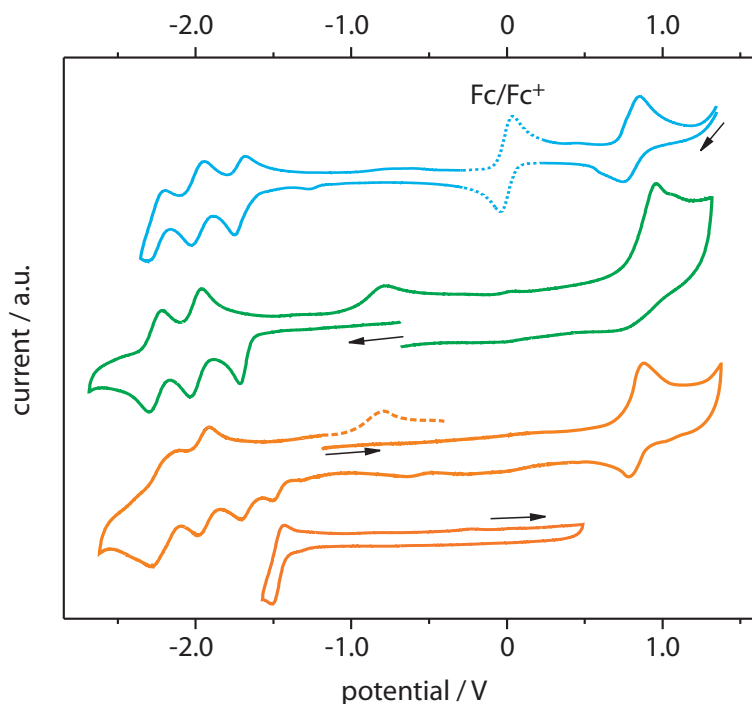


Figure 74: Cyclic voltammograms of the ruthenium complexes with **phenphen** ligands, measured in a 0.1 M solution of Bu_4NPF_6 in dry acetonitrile under argon atmosphere, referenced vs. Fc/Fc^+ , $E_{1/2} = 0.00$ V. **Ru(phenphen)** (—), **Ru(phenphen)Ru** (—), **Ru(phenphen)Pt** (—).

In the case of **Ru(phenphen)** three fully reversible one-electron reduction waves were found but no reduction of the free phenanthroline moiety.

Furthermore, in **Ru(phenphen)Ru** all redox potentials were assigned to two-electron reductions of the equivalent sides of the molecule. Therefore, an irreversible two-electron $\widehat{\text{LL}}^1$ -reduction was found in the CV which may refer to a double bond formation or other side reaction upon reduction. Interestingly, for the related compounds $[\{(\text{bpy})_2\text{Ru}\}_2(\mu\text{-phenphen})]$ and $[\{(\text{bpy})_2\text{Os}\}_2(\mu\text{-phenphen})]$, no irreversible peaks were reported.^[131]

The heteronuclear complex **Ru(phenphen)Pt** exhibits in the same region two (in combination irreversible) one-electron waves at differing potentials which potentially correlate to the

inequivalent sides of the **phenphen**-bridge. Interestingly, a reversible one electron reduction of the bridge is observed for the more positive redox wave (compare detail in figure 74) as observed for single reduction of **Ru(phenphen)**. On contrary, a consecutive double reduction of the bridge is irreversible, as observed for **Ru(phenphen)Ru**. Based on the comparison of the complexes, the more positive, reversible wave was assigned to the platinum coordinated sphere (-1.53 V), the lower wave (-1.77 V) was assigned to the ruthenium coordinated sphere. From this result it can be concluded that a photoreduced bridge at the ruthenium moiety (one-electron reduction during MLCT excitation) has the potential to reduce the platinum sphere at the bridge without irreversible effects. However, a comparison with [Pt(phen)Cl₂] showed only minimal similarities between the two compounds as the first and second reduction potentials differ by more than 0.30 V and 0.05 V, respectively.^[143] However, as the authors state there, the redox chemistry of [Pt(phen)Cl₂] is characterized by highly irreversible processes, complicating correct assignment.

3.2.7 Application in Light Driven Catalysis

Based on the electrochemical and photophysical results **Ru(phenphen)** and **Ru(phenphen)Pt** were tested as $[[\mathbf{P} \sim \mathbf{B} \sim \mathbf{C}]]$ -type photocatalysts (**P**: photocenter, **B**: bridging ligand **C**: catalysis center) for hydrogen formation. Therefore, oxygen free, nitrogen saturated stock solutions ($c_C = 7.0 \times 10^{-5}$ M) were prepared in the dark. Filling of 2 ml samples into GC-vials under inert conditions gave a number of probes for the determination of the catalytic activity. Irradiation of the compounds with visible light (LED-array, $\lambda_{\text{exc}} = 470$ nm, suitable to excite in the MLCT-band) was carried out under identical conditions in a water/triethylamine/acetonitrile (2:6:12/v:v:v) mixture as previously described by the work group of RAU et al. (see figure 75).^[80, 88]

During the course of several hours considerable amounts of hydrogen gas were formed by **Ru(phenphen)Pt**, as quantified in repeat determinations (two different samples for each data point) by GC-TCD. Moderate turn-over-numbers were observed for **Ru(phenphen)Pt** (TON = 7 after 10 hours) at a decreasing frequency of less than one turnover per hour. The increasingly heteroscedasticity after 10 hours represents the end of catalysis due to side and consecutive reactions and may be a result of increasing leakage of the reaction vessels over long periods. On the other hand, the control experiments with the mononuclear **Ru(phenphen)** complex showed no hydrogen production at all. Furthermore, differing concentrations of water (0, 5, 10, 20 and 30%)

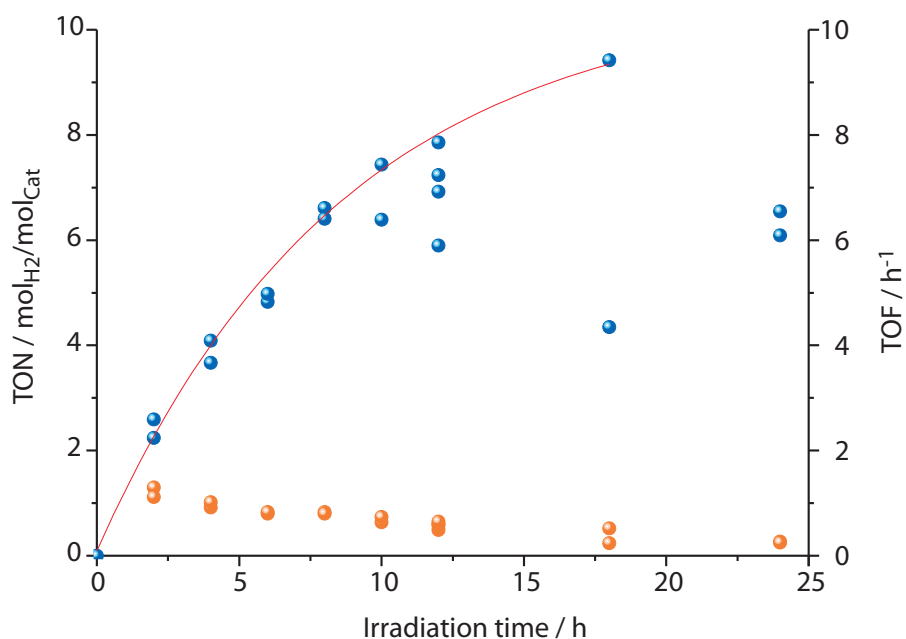


Figure 75: Time dependency of the catalytic activity of **Ru(phenphen)Pt** ($c = 7.0 \times 10^{-5}$ M) in a 2 M solution of triethylamine in acetonitrile with 5% water content. TON (●), TOF (●) and fitted curve (—).

were applied to obtain data on the water-concentration dependency of the catalytic activity as it has been shown for related catalytic systems to be relevant (see figure 76).^[116, 80, 88, 139]

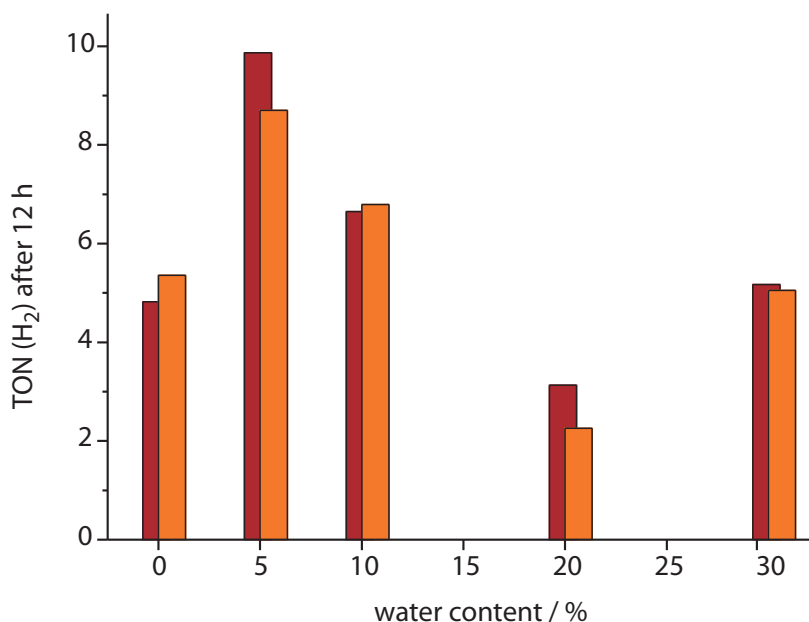


Figure 76: Water concentration dependency of the catalytic activity of **Ru(phenphen)Pt** ($c = 7.0 \times 10^{-5}$ M) in a 2 M solution of triethylamine in acetonitrile after 12 hours in double determinations.

After twelve hours, the most active samples were found to be the ones with a fraction of 5% water added. Interestingly, even without water in the catalyst mixture, hydrogen was formed. Similar results were observed by **Rau** et al.^[80]

Comparison of these results to similar experiments in our group, using the platinum complex $[(tbbpy)_2Ru(\mu\text{-}tpphz)PtCl_2]^{2+}$ under similar conditions showed a very similar catalytic behavior with similar turnover numbers in the same time frame.^[139] In contrast to the extremely similar system $[(bpy)_2Ru(\mu\text{-}phenphen)PtCl_2]$ by **SAKAI** et al., a low but significant catalytic hydrogen evolution could be detected (note: no turnover in the hydrogen formation reaction could be observed in the **SAKAI** system as published in 2011 without any data on preparation, characterization, purity or catalysis details).^[144]

The observed results support the assumption that **phenphen** can be seen as a step toward suitable molecular bridges with sufficient electronic communication for intramolecular photocatalysis. Nevertheless, in these first attempts, only unoptimized catalytic conditions were applied as can be derived from the generally low TONs.

In this scope, it can be expected that a tuning of these conditions will have a positive influence on the activity of the catalyst. The possibilities to increase the formerly moderate turnover numbers by purposeful tuning of the solvent mixture (e.g. change of the pH value by exchange of alkaline electron donor triethylamine by acidic ascorbate) or by synthetic manipulations of the catalyst, as demonstrated by **RAU** et al., give important stimuli for the future development of **phenphen**-derived photocatalysts. Finally, future investigations may help to correlate the photophysical and electrochemical data with a possible in situ formation of a new catalytic species and to clearly decide about the intermolecular reaction mechanism while a bimolecular platinum catalyst is proposed by **SAKAI** and coworkers.^[144]

3.2.8 Concluding Remarks on phenphen-Bridged Complexes

The observed results lead to the conclusion that, in the ground state, the substituent in the second phenanthroline coordination sphere has only a limited influence on the photophysical and electrochemical behavior of the ruthenium chromophore in the first coordination sphere. Importantly, this means that almost very little electronic communication across the C-C-single bond between the different ligand halves is existent in the MLCT-excited state. Instead, the two

metal centers in a binuclear **phenphen**-complex will retain most of their independent properties. Binuclear **phenphen**-complexes, therefore, belong to the Robin-Day class I.^[145]

In the discussion in chapter 1.10.1, a list of requirements for the design of an optimal bridging ligand was formulated (points 1-11 on page 42). As was demonstrated, a number of requirements from this list are fulfilled by the **phenphen** bridge:

The intrinsic and intercomponent stability toward thermal, photo- and electrochemical decomposition and reaction products or intermediates of the bridge (1) is fulfilled to some extent as seen e.g. in reversible one-electron reduction of **phenphen** in **Ru(phenphen)Pt**, in **Ru(phenphen)** or in the binuclear reference, presented by CAMPAGNA et al.^[131] A reversible redox behavior (2) and a possible electron storage capacity (10) of the bridge is arguable based on electrochemical analysis. The irreversibility of the reduction waves upon double reduction of the bridge in might as well be signs of the formation of new compound from pre-catalysts such as **Ru(phenphen)Pt**. Furthermore, time resolved excited state spectroscopy support the active role of the bridge as best seen in **Ru(phenphen)Ru**. A well defined distance control of the interlinked metal centers (3) is present as observed in the crystal structure. Using **phenphen** bridged complexes, only limited electronic coupling between the components (4) across the 5,5'-positions was found in spectroscopic experiments, nevertheless, suitable intracomponent HOMO and LUMO energies (redox-, ground state- and excited state potentials) are present especially for **Ru(phenphen)Pt** (5). This causes long lifetimes ($\sim 2.0 \mu\text{s}$) of the charge-separated states, so that unidirectional charge separation (ruthenium centered bridging ligand reduction is more negative than platinum centered) (6) may be achieved. The small energy gaps between relevant (excited) redox states guarantee for the above mentioned aspects and a conservation of the redox activity (7) in the **phenphen** complexes. This as was proven in the catalysis experiments, using **Ru(phenphen)Pt**. Conclusions about the energies or the potentials of the reactive redox state (8) or about the kinetic factors for inner sphere electron transfer reactions (9) are difficult to draw. Nevertheless, a certain efficiency of the population of the reactive redox state at the catalyst site (11) was found as the complex **Ru(phenphen)Pt** was tested for photocatalytic hydrogen generation from water and the formation of fair amounts of hydrogen was observed.

It can be summarized that the unique structural features of the bridging ligand may (possibly after a foregoing transformation process) lead to new interesting properties such as directed eT in the excited state with a minimum of charge recombination in a **Ru(phenphen)Cat** complex.

3.3 NN-NHC-Ligand bbip: Toward Second Generation Catalysts

To improve the efficiency of photoredox catalysis, it is essential to turn *intermolecular* electron transfer processes between multiple components of a catalytic mixture into *unidirectional intramolecular* electron transfer processes of a stable supramolecular catalyst. Therefore, $[[\mathbf{P} \sim \mathbf{B} \sim \mathbf{C}]]$ -type photocatalysts with integrated photocenter **P** and catalytic active site **C** were developed.

Important is the electronic communication between these two. Therefore, a suitable bridging ligand **B** has to be applied to allow for intramolecular electron transfer between the charge transfer complex and the redox active catalytic moiety during the lifetime of the excited state. In this context, 5,5'-bisphenanthroline bridged $[[\mathbf{P} \sim \mathbf{B} \sim \mathbf{C}]]$ -systems were introduced in the previous chapter. Unfortunately, only low turnover numbers could be achieved with the catalyst **Ru(phenphen)Pt** which was partially assigned to the in situ formation of an active catalytic species and to the limited electronic communication across the bridging single bond.

As expected for **Ru(phenphen)Pt**, RAU et al. could show that a photochemical reduction of the platinum metal center is essential for the production of hydrogen for the similar catalyst $[(\text{tbbpy})_2\text{Ru}(\text{tpphz})\text{PdCl}_2]^{2+}$.^[88] Toward these findings, HAMMARSTRÖM et al. pointed out that the monomolecular nature of the catalyst was still arguable, as it could be demonstrated in a similar $[[\mathbf{P} \sim \mathbf{B} \sim \mathbf{C}]]$ -system that generally used N,N'-donor-stabilized platinum metals may as well be cleaved from the ligand (or supramolecular array) after the photoreduction (see figure 34 on page 50). In addition to the appearance of palladium colloids, which are known to be catalytically active themselves, a strong time correlation with the formation of hydrogen was found.^[94]

For these two reasons, it has become very important to consider new design concepts of the bridge to generate alternative structures with increased stability and electronic communication. Furthermore, it has become of paramount importance to develop new analysis methods and improved catalyst concepts in order to overcome the drawbacks of the first generation (see previous chapter). Therefore, it is necessary to challenge new analysis methods in addition to the TEM and XPS experiments, used by HAMMARSTRÖM et al. to analyze the photocatalytic systems, to answer the compromising question for the true nature of the catalyst in the particular supramolecular assembly.

In addition, a major drawback of the, by definition, weak interactions between the components in

a supramolecular system was pointed out by the formation of colloidal palladium. The particular problem is the general use of N-donor ligands to attach the low valent catalyst centers in the first generation of $[[P \sim B \sim C]]$ -type systems (compare figure 33 on page 48). Accordingly, different coordination motifs such as in phosphines or thioles need to be tested and applied to assure the stability of the scaffold during the high energy redox processes. The very promising candidates for this task are N-heterocyclic carbene ligands (NHCs) which can be adapted from other low valent metalorganic catalysis (e.g. HECK reaction catalyst) or complex hydrides.^[146]

3.3.1 NHCs and NHC Complexes

Carbenes are electron-deficient molecules that contain a divalent neutral carbon atom with an electron sextet. For several decades, great efforts were made to design and examine such species without success, as pioneering works of the scientists prove (compare table 11). Already STAUDINGER and others tried to generate disubstituted carbenes ($:CR_2$) from diazo-compounds by cleavage of nitrogen between 1911 in 1916. As none of the attempts to isolate a carbene was successful over the years, they were finally thought to be too reactive and short living and therefore could not be isolated.

Instead of isolating them, the inorganic chemists FISCHER and WANZLICK succeeded in binding different carbenes to metal centers in the 1960s.^[147, 148] The resulting transition metal carbene complexes were later subdivided into two groups according to their structure, electronic properties and reactivity (see figure 77).^[146, 149]

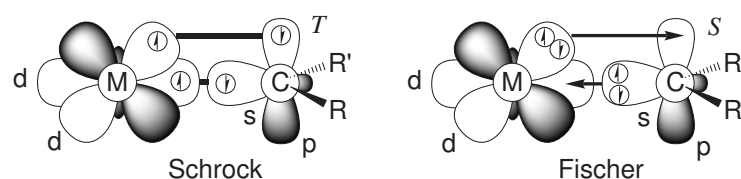


Figure 77: Comparison of FISCHER- and SCHROCK-type carbene-metal complexes.^[149, 150]

The FISCHER-type carbenes have singlet character (S) and feature strong π -acceptor properties at the metal and exhibit electrophilic carbene carbon atoms. SCHROCK-type carbenes on the contrary, have triplet character (T) and may be characterized by more nucleophilic carbene carbon centers. These species typically feature higher valent metals. In 1968, also the first NHC metal

complexes (FISCHER type complex) were prepared by ÖFELE and WANZLICK (see figure 78 a) but only little attention was paid to these results.

In 1991, a breakthrough was achieved. ARDUENGO et al. obtained crystals of a colorless intermediate product during their synthesis. These crystals with a melting point of 240°C turned out to be the first known, isolated, stable, free carbene, a NHC (see figure 78 b).^[151] From then on a great number of chemists started to direct their attention to NHCs.

This “new” class of ligands also reopened an old area in the field of inorganic and organometallic chemistry. And already in 1995, the first NHC metal complex was successfully applied in transition metal catalysis.^[152] Nowadays, N-heterocyclic carbenes and metal complexes thereof are very well understood and research extends into a number of other fields (see figure 78 c).^[153]

Table 11: Historical stages in the field of carbene chemistry.

Year	Workgroup	Development
1835	Dumas	hypothesis: methanol was seen as adduct of methylene and water, attempted removal by strong acids failed ^[154]
1862	Geuther	chloroform was considered as dichlorocarbene adduct of HCl and dichlorocarbene would be involved in the alkaline hydrolysis thereof ^[155]
1912	Staudinger	reactions of methylene by thermolysis of diazomethane ^[156]
1926	Scheibler	proposed synthesis of tetraethoxyethylene and diethoxycarbene thereof ^[157]
1942	Meerwein	decomposition of diazomethane under irradiation yields reactive methylene, directly adding to R-H compounds ^[158]
1954	Doering	addition of dichlorocarbene to olefins, identification by products such as 7,7-dichloronorcarane ^[159]
1956	Woodworth	identification of the structure of methylene, :CH ₂ ^[160]
1962	Wanzlick	theoretical equilibrium of imidazolyl-2-ylidene and tetraaminoethene ^[161]
1964	Fischer	first transition metal (tungsten) complex of a carbene ^[147]
1968	Wanzlick	first NHC mercury complex directly from azolium salt ^[148]
	Öfele	unexpected reaction: synthesis of the chrome NHC complex instead of dihydroimidazole π -complex ^[162]
1991	Arduengo	isolation of a stable, crystalline carbene: NHC with adamantyl groups ^[151]
1995	Herrmann	first NHC metal complex in transition metal catalysis ^[152]
1999	Grubbs	application of NHCs in olefin metathesis (Grubbs II catalyst) ^[153]

From the huge amount of data it was derived that the electronic stabilization, which results from

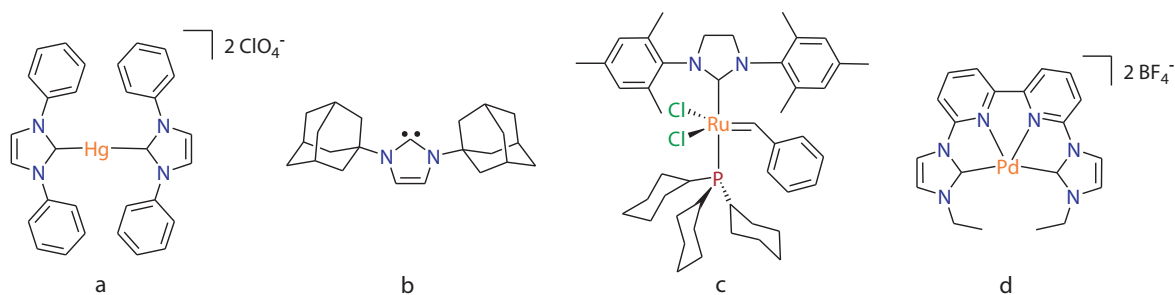


Figure 78: Structures of the first metal NHC complex (a) by WANZLICK et al.^[148], the first isolated carbene (b) by ARDUENGO et al.^[151], the GRUBBS II catalyst (c)^[153], and a palladium complex with a ligand, combining bipyridine and NHC binding sites by KUNZ et al. (d).^[163]

the mesomeric interaction between the non-bonding nitrogen electron pairs and the empty p-orbital of the sp^2 -hybridized carbon atom, is the reason for the exceptional stability of NHCs. This fact furthermore explains the nucleophilic character of NHCs compared to other carbenes which are typically electrophiles.

The resulting NHC metal complexes are far less reactive than the classical representatives of two types of carbene ligands. Due to the strong stabilization by π -donating substituents, NHCs are found to be good σ -donors, but in contrast to the classical carbene ligands, NHCs do not necessarily require π^* -backdonation from the metal into p_π -orbitals in order to form stable compounds. Therefore, NHC complexes of almost all elements are known.^[149] From computational and experimental data it was possible to derive a general idea of the different orbital contributions in metal-NHC complexes (see figure 79).

It was found that group 10 metal centers in d^{10} -configuration (Ni^0 , Pd^0 and Pt^0) as well as their isoelectronic group 11 metal centers (Cu^+ , Ag^+ and Au^+) form stable two-coordinated complexes while d^8 -configured metals such as Pd^{2+} form tetra-coordinated square planar complexes. Furthermore, it could be confirmed that the main bonding occurs through σ -donation from the NHC lone pair into the metal hybrid ($dz^2 + s$) orbital (compare figure 79), which suggests a very low π -contribution to the M-NHC bond.^[149, 150]

According to GLORIUS and NOLAN, NHCs challenge the well-established tertiary phosphine-based ligands in organic synthesis. Like them, NHCs generally serve as spectator ligands that may influence the catalysis, combining a number of advantageous properties such as:^[146, 164]

(1) strong σ -donation of the electron rich ligand resulting in exceptionally stable M-C bonds and

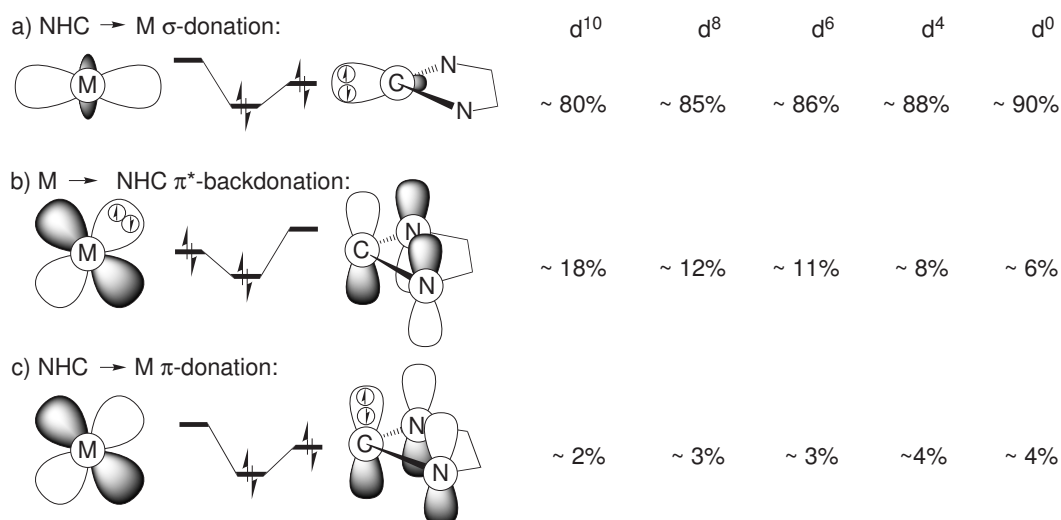


Figure 79: Different orbital contributions to the d-series metal-NHC bond (left) with average percentage of σ - and π -contributions to the orbital interaction energy based on data for 36 M-(NHC) model complexes (right).^[149, 150]

thus high thermal and hydrolytic durability of the complex, (2) easy accessibility of ligand and complex without isolation of the free carbene, (3) no need for an excess of the ligand (excess costly) during the catalysis and strict control of the metal/ligand ratio (optimally 1:1), (4) tunable steric shielding pattern which is higher than in phosphines, allowing for both stabilization of the metal center and enhancement of its catalytic activity, (5) very easy derivatization of NHC ligands for the use in water-soluble catalysts (twophase catalysis), immobilized catalysts, or chiral modifications, and (6) redox stability.

Noticeable examples for metal-NHC catalysis are found in the fields of olefin metathesis (GRUBBS II catalyst, see figure 78 c) or Pd-catalyzed C-C coupling reactions.^[153, 165] Additionally, NHC-ligands lead to unexpected reactivity as in the case of Au-catalyzed reactions.^[164]

The great applicability of NHC complexes in d⁸- and d¹⁰-configuration, even in hydrogenation catalysts, sets the basis for an application in hydrogen evolving catalysts.^[144] For the use in $[[\mathbf{P} \sim \mathbf{B} \sim \mathbf{C}]]$ -type systems it is necessary to create bridging ligands, which combine bipyridine-like structures and NHC-type structures. For such compounds only, very few examples are known (see figure 78 d).^[163, 166] Therefore, a new concept will be presented in the following section.

3.3.2 Imidazophenanthrolines: Toward Redox Stable Bridges

In this section, the first steps toward the synthesis of heteroditopic NHC-NN-bridging ligands and possibly resulting photoredoxactive carbene complexes will be presented. Furthermore, a complete characterization of the prepared intermediates and products will allow further insights into the properties of the bridge and into the interdependence of photocenter and reaction center. Using the NN-NHC-building block, it will be investigated, if it is possible to prepare a number of heterometallic intramolecular photocatalysts of the type $[[\mathbf{P} \sim \mathbf{B} \sim \mathbf{C}]]$ and to determine their activity in photocatalytic hydrogen evolution. Detailed photophysical and electrochemical investigations of the oligonuclear complexes will help to analyze and interpret the results of the catalysis.

Inspired by the π -conjugated nature of the *tpphz* ligand^[80] and by the annulated phenanthroline-systems, used by ARTERO et al.^[85, 86], 1*H*-imidazo[4,5-*f*][1,10]phenanthroline (**ip**, see figure 80) represented an interesting starting point for the development of a new type of bridge. Using **ip** as backbone for a ligand would allow a combination of the well explored phenanthroline-type N,N'-binding site (7,8-position) for $\{\text{Ru}(\widehat{\text{LL}})_2\}^{2+}$ -fragments and a second NHC-type binding site (2-position) for a variety of redox active catalyst metals.

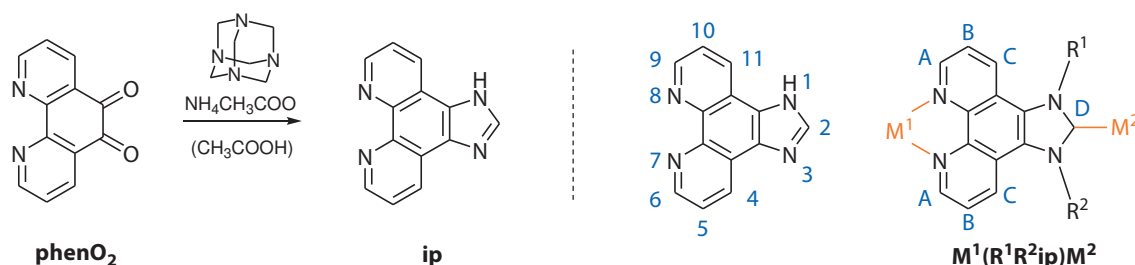


Figure 80: Synthesis of **ip** from 1,10-phenanthroline-5,6-dione (left) and numbering scheme of the imidazophenanthroline-based ligands and complexes (right).

Furthermore, a linear arrangement of two metal centers M^1 and M^2 with a controlled distance and minimized steric and electronic interference between them can be achieved. Nevertheless, high redox activity in terms of electron storing or mediating potential could be expected from the electron deficient, π -conjugated bridge in a binuclear complex.^[167] The steric effect, typically generated by purposeful choice of the R^1 - and R^2 -substituents, is less relevant in proton reduction reactions, but R^1 and R^2 may potentially be used to introduce additional donor functionalities into

the ligand to obtain chelating ligands for a higher stability of the intermediately reduced catalyst metal as demonstrated by LEE and others.^[168, 169, 170, 171, 172, 173]

In the beginning, a simple functionalization of both imidazole nitrogens with aryl- or alkyl groups, to yield an 1,3-substituted 1*H*-imidazo[4,5-*f*][1,10]phenanthroline salt, was taken as the selection criterion for the feasibility of this concept although there was a chance of undesired side reactions in the substitution reaction with organic halogenides which could lead to undesired side reactions at the phenanthroline sphere of **ip**.

The starting material **ip** was prepared in good yields by the adaptation of the available protocol, which is already literature known since 1943 in a condensation reaction of 1,10-phenanthroline-5,6-dione (**phenO₂**), hexamine and ammonium acetate in glacial acetic acid (see figure 81).^[174, 175] The first approach on the bridging ligand synthesis included the introduction of an aliphatic rest into the 1-position of **ip** after the deprotonation of the insoluble compound with NaH in dry DMF and under inert conditions (**method L2**). After dissolution of the sodium imidazolide salt of **ip**, benzyl bromide was added for the substitution reaction. For a related reaction see HERRMANN et al.^[176] This reaction resulted in the formation of 1-benzyl-1*H*-imidazo[4,5-*f*][1,10]phenanthroline (**bip**). Addition of a second equivalent of benzyl bromide to the highly soluble **bip** in DMF yielded the symmetric disubstituted product 1,3-bisbenzyl-1*H*-imidazo[4,5-*f*][1,10]phenanthroline bromide (**bbip**) as a white precipitate which was collected in good yields after 24 hours at 80°C (see figure 81).

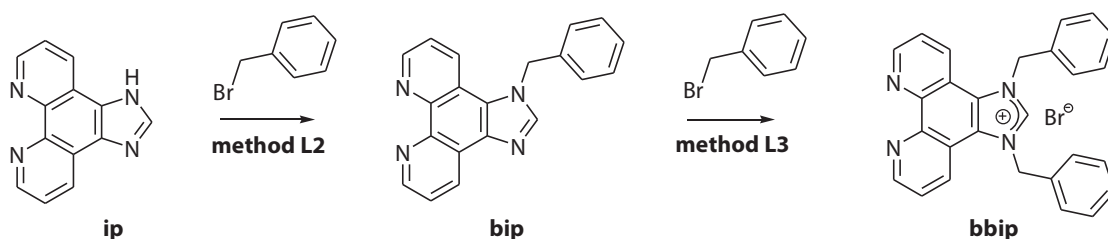


Figure 81: Two step synthesis of **bbip** from **ip**; **method L2:** NaH, (DMF), 80°, 12h; **method L3:** (DMF), 80°, 12h.

The ¹H-NMR and ¹³C-NMR spectroscopic investigation of the different compounds reflects nicely the transformations performed at the imidazole moiety of the **ip**-system. Especially the four signals for the A-, B-, C-, and D-positions in the spectra of **ip** and **bbip** reflect the symmetric nature of the molecules, whereas the intermediate **bip** exhibits an asymmetric NMR-spectrum

due to the substitution pattern. Prominent is the shift of the singlet-signal of the 2-proton e.g. the +I-effect upon the imidazole system in **bip** and the increasing deshielding of the N-CH-N-proton in **bbip** after double-alkylation and accompanying salt formation ($\delta_{(2)}^{\text{ip}} = 8.87$ ppm, $\delta_{(2)}^{\text{bip}} = 8.02$ ppm, and $\delta_{(2)}^{\text{bbip}} = 11.94$ ppm). With the help of H,H-COSY-, HMBC- and HSQC-experiments it was possible to assign all carbon signals of the prepared compounds. The ^{13}C -NMR-experiments of the different imidazophenanthroline derivatives showed no strong influence on the carbon in 2-position by means of the substitution pattern ($\delta_{(2)}^{\text{ip}} = 141.55$ ppm, $\delta_{(2)}^{\text{bip}} = 143.54$ ppm, $\delta_{(2)}^{\text{bbip}} = 143.64$ ppm).

Furthermore, the typical imidazolium salt properties of **bbip** were revealed. In methanol- d_4 **bbip** shows fast H/D-exchange of the active 2-proton which is typical for carbene precursors of this type. By measuring the decrease of the relative peak area of the N-CH-N-proton in the ^1H -NMR-spectra over the period of three days a rate constant for this typical H/D exchange was determined ($k_{\text{H/D}} = 2.36(\pm 0.01) \times 10^{-5} \text{ s}^{-1}$, $t_{1/2} = 490(\pm 2) \text{ min}$, 25°C), fitting the signal decay with a first order kinetics (see figure 82).^[146]

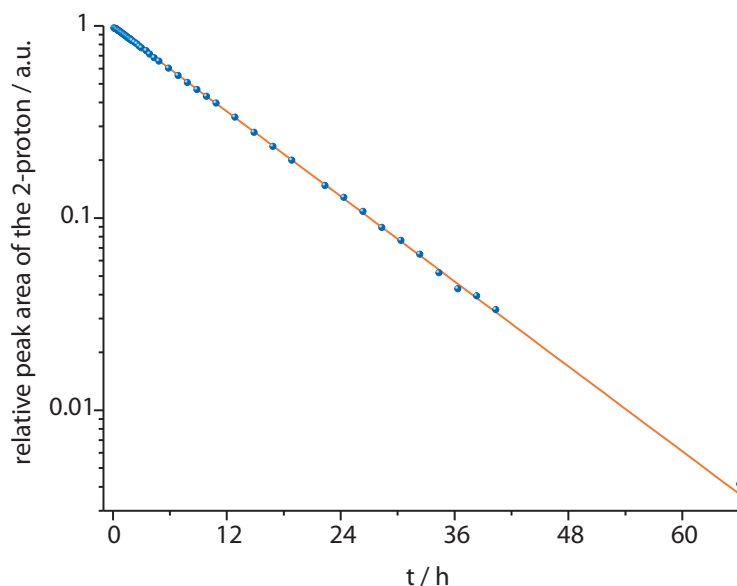


Figure 82: Decay of the ^1H -NMR signal intensity of the **bbip**-2-proton ($\delta_{(2)}^{\text{bbip}} = 11.94$ ppm, 1H, s) in relation to the other proton signals.

EI- and DEI-Mass spectrometry further supported the formation of the organic compounds.

3.3.3 Structural Characterization of *ip*-Type Ligands

Slow recrystallization yielded suitable crystals for X-ray diffraction experiments of all prepared organic compounds in this series of imidazophenanthroline derivatives (see figure 83). The relevant distances and angles are gathered in table 12 on page 119.

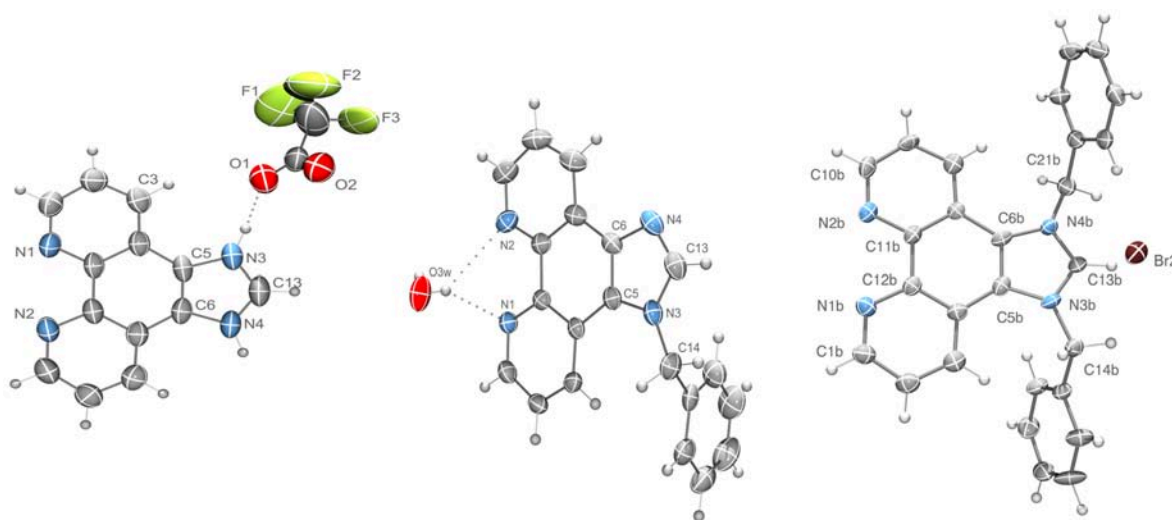


Figure 83: Molecular structures of the prepared imidazophenanthroline derivatives: protonated **ip** (left), **bip** (center) and **bbip** (right). Selected bond lengths and angles can be found in table 12.

The structural features observed for the organic compounds combine both, the general patterns of phenanthrolines and those of the benzimidazole derivatives, respectively. Therefore, it is useful to focus on the two coordination sites for the structural characterization of the new **ip**-type ligands (the same numbering scheme was applied to all **ip**-type ligands in this thesis). With respect to the phenanthroline coordination site, all ligands exhibit a number of typical similarities which can be found in other phenanthroline derivatives as well (see chapter 3.1.1). As expected, the N,N'-coordination environment with respect to the bond lengths and angles remains unaffected by the changes at the imidazole part of the ligands.

Thus, the N1-C12 bond lengths and N2-C11 bond lengths are generally equidistant in this series and vary only in the range between 1.352(2) Å and 1.367(9) Å. The C11-C12 distances vary between 1.454(10) Å and 1.468(4) Å respectively without significant deviations. Furthermore, minor variations in the C1-N1-C12 and the C10-N2-C11 bond angles between 117.2(2)° and 118.38(15)° were found in all **ip** derivatives. Between the N1-C12-C11 and the N2-C11-C12 bond

Table 12: Selected bond lengths [Å] and angles [°] of the imidazole-moiety and the N,N'-coordination sphere of **ip**, **bip** and **bbip**.

bond length [Å] or angle [°]	ip ×CF ₃ COOH	bip ^a	bbip ^b
N3 - C13	1.330 (4)	1.357 (2)	1.330 (9)
N4 - C13	1.331 (4)	1.315 (3)	1.322 (8)
N3 - C5	1.392 (3)	1.391 (2)	1.400 (8)
N4 - C6	1.391 (3)	1.387 (2)	1.391 (9)
C5 - C6	1.365 (4)	1.378 (3)	1.386 (9)
N1 - C12	1.356 (3)	1.352 (2)	1.367 (9)
N2 - C11	1.360 (3)	1.357 (2)	1.358 (8)
C11 - C12	1.468 (4)	1.463 (3)	1.454 (10)
H1N3 - O1	1.722 (4)	-	-
N3 - C13 - N4	110.1 (2)	113.60 (16)	110.9 (6)
C13 - N3 - C5	107.9 (2)	106.09 (16)	108.1 (6)
C13 - N4 - C6	107.8 (2)	104.28 (16)	107.7 (6)
N3 - C5 - C6	106.9 (2)	105.47 (15)	105.8 (6)
C5 - C6 - N4	107.2 (2)	110.56 (16)	107.5 (6)
C1 - N1 - C12	117.6 (2)	118.38 (15)	117.7 (6)
C10 - N2 - C11	117.2 (2)	117.30 (16)	117.8 (6)
N1 - C12 - C11	117.7 (2)	116.59 (15)	116.2 (6)
N2 - C11 - C12	117.0 (2)	117.03 (16)	116.5 (6)

^arefers to the first **bip** molecule in the unit cell, indicated by the letter a.

^brefers to the second **bbip** in the unit cell without packing defects, indicated by the letter b.

angles only minor variations between 116.2(6)° and 117.7(2)° were observed in this series.

Comparison of the changes at the imidazole moieties in this series of ligands reflect the performed changes. In general, it could be expected that a certain degree of asymmetry is present in the imidazole rings of **ip** and **bip** due to the contribution of the resonance structures with a double bond between C13 and N4. Otherwise, the (at the imine nitrogen N3) protonated form of **ip** was found in the crystal structure (which was crystallized from an NMR sample in D₂O with addition of CF₃COOD to dissolve **ip**), so that the resulting imidazolium salt of **ip** was found which is rather similar to **bbip**. Note: the very similar crystal structure of the perchlorate salt of N1-protonated **ip** is literature known.^[177] This structural relationship between the two compounds was supported

by the findings, that all equivalent bond angles and distances in **ip** and **bbip** show insignificant differences. As a result of that they will be discussed together.

The X-ray data indicated that the imidazole rings in **ip/bbip** and **bip** have identical C5-N3 and C6-N4 distances in the range between 1.387(2) Å and 1.400(8) Å as well as C5-C6 in the range between 1.365(4) Å and 1.386(9) Å. A significant asymmetry with shortening of the C13-N4 bond and elongation of the C13-N3 bond is present in **bip** ($d_{(\text{C13-N4})}^{\text{bip}} = 1.315(3)$ Å < $d_{(\text{C13-N3})}^{\text{bip}} = 1.357(2)$ Å) which can be explained by the partial double bond character between C13 and N4 in this 1*H*-imidazole derivative. This effect is even visible when compared to **ip** and **bbip** ($d_{(\text{C13-N4})}^{\text{bip}} = 1.315(3)$ Å < $d_{(\text{C13-N4})}^{\text{ip}} = 1.331(4)$ Å \approx $d_{(\text{C13-N4})}^{\text{bbip}} = 1.322(8)$ Å, and $d_{(\text{C13-N3})}^{\text{bip}} = 1.357(2)$ Å < $d_{(\text{C13-N3})}^{\text{ip}} = 1.330(4)$ Å \approx $d_{(\text{C13-N3})}^{\text{bbip}} = 1.330(9)$ Å), which are symmetric and therefore exhibit equidistant C13-N3 and C13-N4 bond lengths.

The higher symmetry of **ip** and **bbip** is further supported by the similar angles at N3 and N4 which vary between 107.7(6)° and 108.1(6)°, and as well at C5 and C6 atoms which vary between 105.8(6)° and 107.5(6)°. In **bip**, these opposing angles differ in contrary ($\angle_{(\text{C13,N3,C5})}^{\text{bip}} = 106.9(16)$ ° > $\angle_{(\text{C13,N4,C6})}^{\text{bip}} = 104.28(16)$ ° and even more: $\angle_{(\text{N3,C5,C6})}^{\text{bip}} = 105.47(15)$ ° < $\angle_{(\text{N4,C6,C5})}^{\text{bip}} = 110.56(15)$ °) and as a result of that, they significantly differ from the corresponding angles in **ip/bbip**. Prominent is the decrease of the angle at C13 in the imidazolium salts **ip** and **bbip** in comparison to the uncharged **bip** which can be attributed to the mentioned changes in π -character of the C13 and decreased delocalization in the imidazolium salts ($\angle_{(\text{N3,C13,N4})}^{\text{bip}} = 113.60(16)$ ° > $\angle_{(\text{N3,C13,N4})}^{\text{ip}} = 110.1(2)$ ° \approx $\angle_{(\text{N3,C13,N4})}^{\text{bbip}} = 110.9(6)$ °).

The various twist angles of the benzyl groups in **bip** and **bbip** and transoid orientation thereof in the latter indicate that mainly crystal packing forces are responsible for the observed conformations in the structures. In addition to the conformational changes of the benzyl functionalities, a number of packing effects were observed in the crystal lattice of **ip**, **bip** and **bbip** (for an example see figure 84).

In the crystal lattice of **ip**, hydrogen bonds between the protons at the N3 atom and the O1 of the carboxy functionality of trifluoroacetic acid and further between the O2 of the carboxy functionality and the N4-proton of the next **ip** molecule ($d_{(\text{N3-O1})}^{\text{ip}} = 2.671$ Å and $d_{(\text{N4-O2})}^{\text{ip}} = 2.659$ Å) form helical chains with an alternating order of **ipH**⁺ and CF₃COO⁻ molecules, here both molecules act as bridges (see figure 83 (left) on page 118). Furthermore, π - π -interactions ($d_{(\pi-\pi)}^{\text{ip}} = 3.297$ Å) between the opposingly directed planar aromatic phenanthroline systems cause

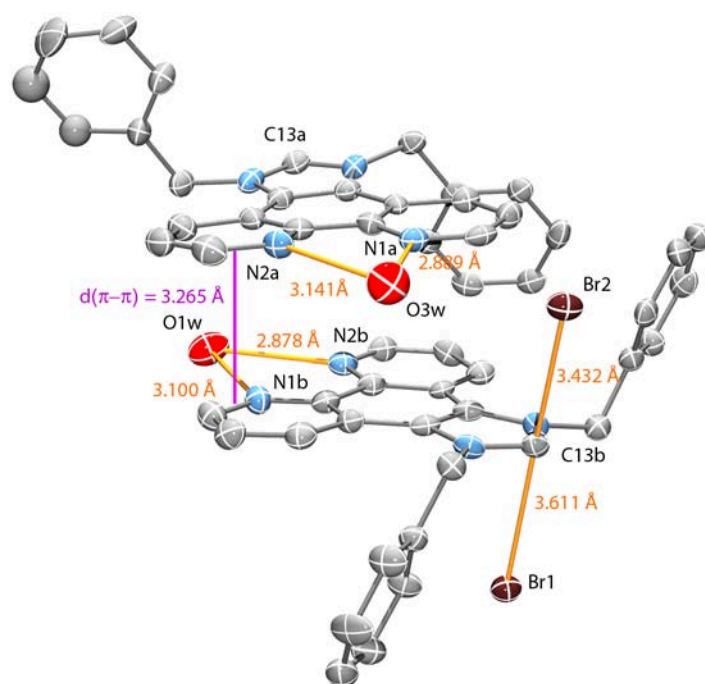


Figure 84: Detail of the crystal structure of **bbip**, showing packing effects of the two inequivalent **bbip**-ions in the crystal matrix (relevant distances are denoted orange/magenta). Bromine counterions can be found in close proximity to the delocalized positive charges of the imidazolium moieties, water molecules coordinate to the phenanthroline spheres via hydrogen bonds, π -stacking effects of the aromatic core are present and arbitrary rotation of the benzyl groups decreases the required space in the cell.

columnar stacking of the **ip** molecules and, furthermore, an interlocking of the different helices to form fence like planes on interlinked helices.

In the crystal of **bip**, three symmetry inequivalent molecules of water and two molecules **bip** were found. Interestingly, parallel, via hydrogen bonds connected, linear chains of water molecules run through the crystal. The distances of the water molecules in the chain vary between 2.656 and 2.774 Å. Attached to this water lattice are the **bip** molecules, which are coordinated via hydrogen bonds either to the N,N'-coordination sites ($d_{(N1A-O3w)}^{bip} = 2.889$ Å and $d_{(N1B-O2w)}^{bip} = 2.936$ Å) or to N4 of the imidazole ring ($d_{(N4A-O1w)}^{bip} = 2.865$ Å), so that the chain is surrounded by **bip** molecules (see figure 83 (center) on page 118). Furthermore, π - π -interactions ($d_{(\pi-\pi)}^{bip} = 3.406$ Å and 3.253 Å) between pairs of **bip** molecules with the same symmetry were found.

The crystal of **bbip** contains four symmetry inequivalent molecules of water and two molecules

bbip (see figure 84). Packing effects due to π - π -interactions between the two inequivalent **bbip**-ions were found ($d_{(\pi-\pi)}^{\text{bbip}} = 3.265 \text{ \AA}$). The negatively charged bromide counter ions were found in close proximity to the delocalized positively charged imidazolium moieties. Furthermore, as in the case of **bip**, water molecules coordinate to the phenanthroline spheres via hydrogen bonds with N-O distances between 2.878 and 3.141 \AA .

3.3.4 N,N'-Coordinated ip-Type Complexes

To investigate whether the N,N-coordinating properties of the potential bridge are similar to the parent phenanthroline, a series of new ruthenium complexes with the obtained ligands was prepared (see figure 85).

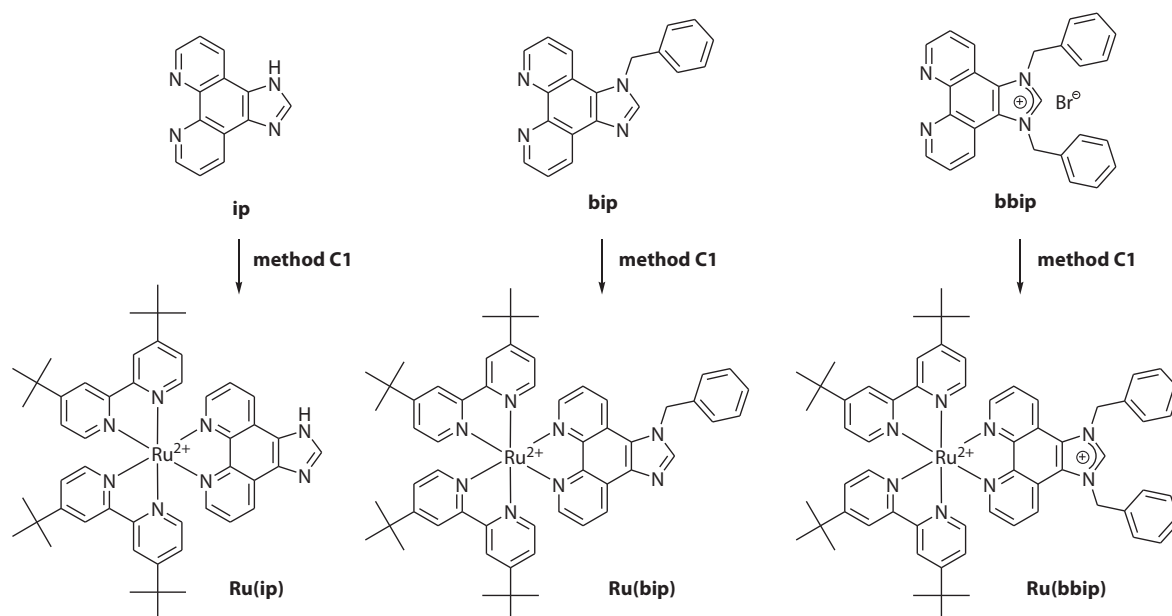


Figure 85: Synthesis of the N,N'-coordinated ruthenium complexes of the prepared ligands through reaction with $[\text{Ru}(\text{tbbpy})_2\text{Cl}_2]$ and subsequent counter ion exchange.

The synthesis of the ruthenium complexes was performed according to the protocol **method C1** through stoichiometric reaction of one equivalent of $[\text{Ru}(\text{tbbpy})_2\text{Cl}_2]$ and one equivalent of $\widehat{\text{LL}}$ -ligand (**ip**, **bip** or **bbip**) in a solvent mixture of ethanol/water in a microwave reaction. After counter ion exchange with NH_4PF_6 , the complexes $[\text{Ru}(\text{tbbpy})_2(\text{ip})][\text{PF}_6]_2$ (**Ru(ip)**), $[\text{Ru}(\text{tbbpy})_2(\text{bip})][\text{PF}_6]_2$ (**Ru(bip)**), and $[\text{Ru}(\text{tbbpy})_2(\text{bbip})][\text{PF}_6]_3$ (**Ru(bbip)**) were obtained in

95%, 95%, and 65% yields, whereat in the case of **Ru(bbip)** a longer reaction time of 5 hours had to be applied to force the reaction between the positively charged ruthenium center and the positively charged ligand. Chromatographic workup with KNO_3 /water/acetonitrile yielded pure **Ru(bbip)**, so that all complexes could be obtained as pure compounds.

The characterization by ^1H -NMR- (see figure 86) and ^{13}C -NMR-spectroscopy and mass spectrometry supported the formation of the expected products.

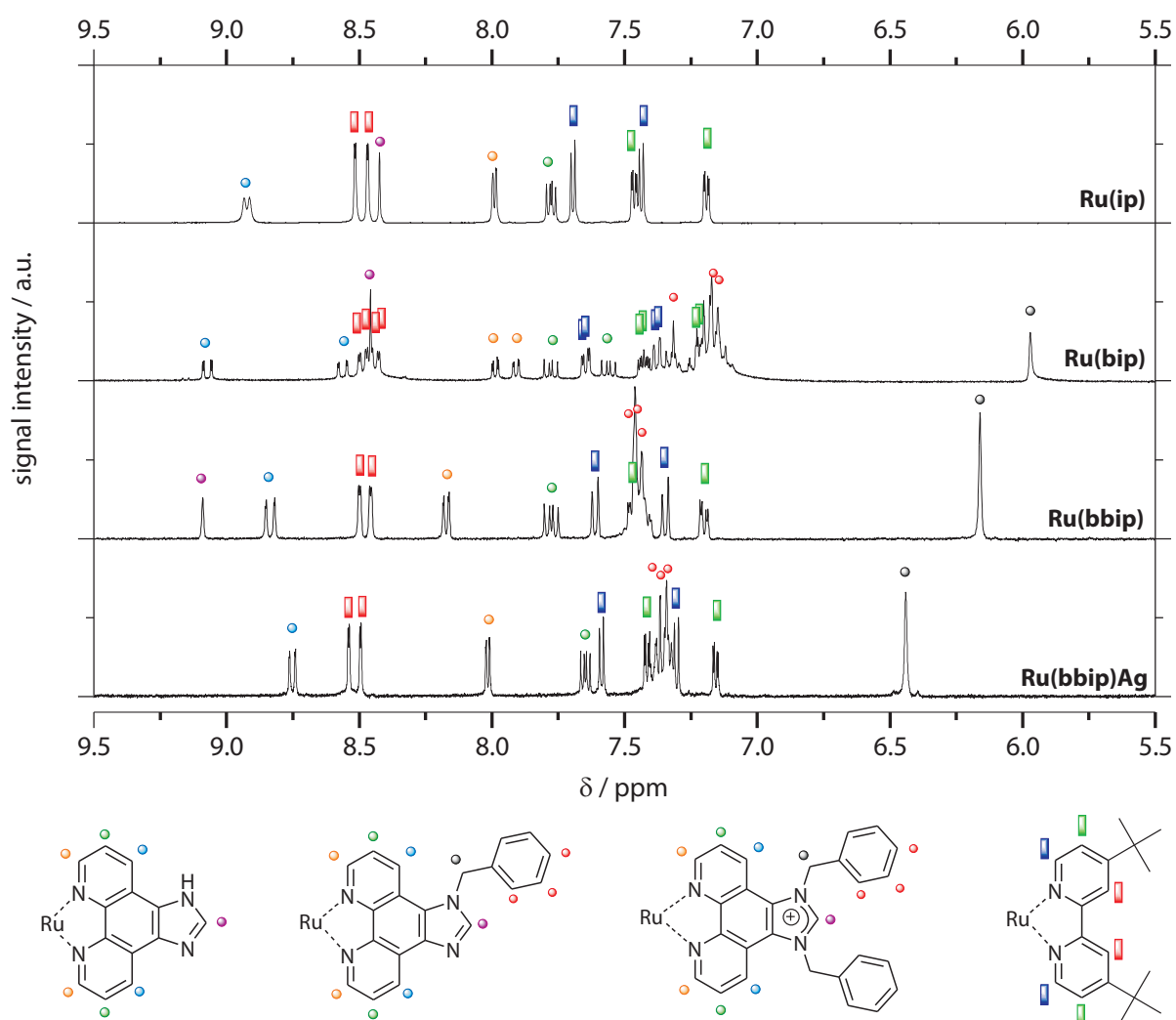


Figure 86: Aromatic region of the ^1H -NMR-spectra of **Ru(ip)**, **Ru(bip)**, **Ru(bbip)**, and **Ru(bbip)Ag** in acetonitrile- d_3 with assigned signals.

Most obvious is the pattern of ligand related A-, B- and C-proton signals which refers to symmetric ligands in the case of **Ru(ip)** and **Ru(bbip)** and to the asymmetry of **Ru(bip)** which exhibits

two sets of A-, B-, C-signals. The CH₂-signals of the benzyl moieties indicate the performed changes just as well ($\delta_{4\text{H}(\text{CH}_2)}^{\text{Ru}(\text{bip})} = 5.97$ ppm and $\delta_{4\text{H}(\text{CH}_2)}^{\text{Ru}(\text{bbip})} = 6.16$ ppm). Comparison of the resonance frequencies of the N-CH-N-protons (D-position) in acetonitrile-*d*₃ exhibited the same tendency in the chemical shifts upon formal addition of one or two benzyl moieties as in the case of the pro-ligands ($\delta_{\text{H}(2)}^{\text{Ru}(\text{ip})} = 8.42$ ppm, $\delta_{\text{H}(2)}^{\text{Ru}(\text{bip})} = 8.45$ ppm, and $\delta_{\text{H}(2)}^{\text{Ru}(\text{bbip})} = 9.07$ ppm). The strongest deshielding effect upon the 2-proton was found in the imidazolium complex **Ru(bbip)** and the weakest in **Ru(ip)**.

Determination of the rate constant for the H/D-exchange of the active 2-proton of **Ru(bbip)** in methanol-*d*₄ was not possible because the exchange was already completed before the first ¹H-NMR experiment could be performed. This observation of a very fast H/D-exchange is very interesting because it reflects the increased acidity of the imidazolium proton and the increased tendency toward carbene formation which was induced by combination of a positively charged ruthenium fragment and a positively charged ligand.

Observation of the ¹³C-NMR-signal of the carbon atom at the 2-position resembles the findings of the ruthenium free compounds and displays the weak influence of the substitution pattern at the 1,3-positions on the chemical shift of the N-CH-N-carbon atom ($\delta_{\text{C}(2)}^{\text{Ru}(\text{ip})} = 143.31$ ppm, $\delta_{\text{C}(2)}^{\text{Ru}(\text{bip})} = 147.48$ ppm, and $\delta_{\text{C}(2)}^{\text{Ru}(\text{bbip})} = 144.49$ ppm).

Mass spectroscopy confirmed the formation of the prepared complexes with prominent peaks and matching isotopic pattern between calculated and observed signal for the [M-PF₆]⁺ species in all complexes (**[Ru(ip)+PF₆]⁺** = 1003.1 m/z (40%), **[Ru(bip)+PF₆]⁺** = 1093.2 m/z (100%), and **[Ru(bbip)+2 PF₆]⁺** = 1329.3 m/z (100%)).

Furthermore, it was possible to isolate suitable crystals for X-ray diffraction experiments of **Ru(ip)** (ethanol/water), **Ru(bip)** (acetonitrile/water), and **Ru(bbip)** (dichloromethane/chloroform). The discussion on distances and angles is found later in this section (see figures 92 and 93 on page 132 for the structures).

3.3.5 NHC-Coordinated ip-Type Complexes

At this stage, transformation of the imidazolium salt into the corresponding carbene derivative became interesting for the subsequent use as precursors for the synthesis of NHC-metal complexes. In this context, a number of different methods for the preparation of metal-

NHC complexes are known from literature.^[178] These strategies include isolation of the free carbene with subsequent complexation to an unsaturated metal fragment, cleavage of the tetraaminoetene-derivatives (from the WANZLICK equilibrium) with suitable metal precursors, preparation of a carbene transfer agent for transmetalation or the synthesis of the NHC-ligand at the metal center.^[179, 180, 181, 182, 183] Several different synthetic routes were studied, attempting the transformation of the imidazolium substructure into the NHC unit.

The deprotonation of the imidazolium salt represented the first attempt to isolate a free carbene species (see figure 87).

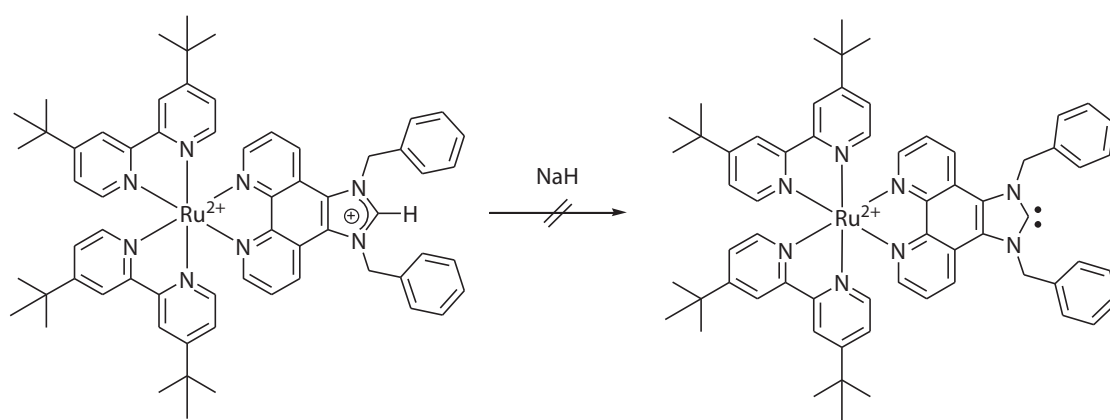


Figure 87: Attempted deprotonation of the imidazolium salt for the preparation of the NHC-species of Ru(*bbip*).

A metal hydride reacts irreversibly with the loss of hydrogen to give the desired carbene, with the inorganic salt by-products and excess hydride being removed by filtration.^[179] Unfortunately, deprotonation in dry THF under inert conditions at -80°C with NaH as base did not lead to a persistent carbene, as experienced by other work groups.^[184] This case, the reaction was possibly too slow in tetrahydrofuran due to the relative insolubility of the metal hydride and the salt. Otherwise, a fast consecutive reaction of the highly reactive carbene with traces of impurities could disguise its intermediate formation. Performance of this reaction in the presence of the previously prepared carbene complex precursor $[\text{Mo}(\text{thf})\text{CO}_5]$ (to trap the carbene intermediate) did not yield the desired carbene complex (see figure 88).

The second attempt aimed at the recently reported preparation of the $\text{NHC}\cdot\text{B}(\text{Et})_3$ adduct. This method was developed by YAMAGUCHI and ITO et al. and yielded in their case a stable adduct in moderate yields (46 - 80%) as could be confirmed through X-ray analysis. Furthermore, the

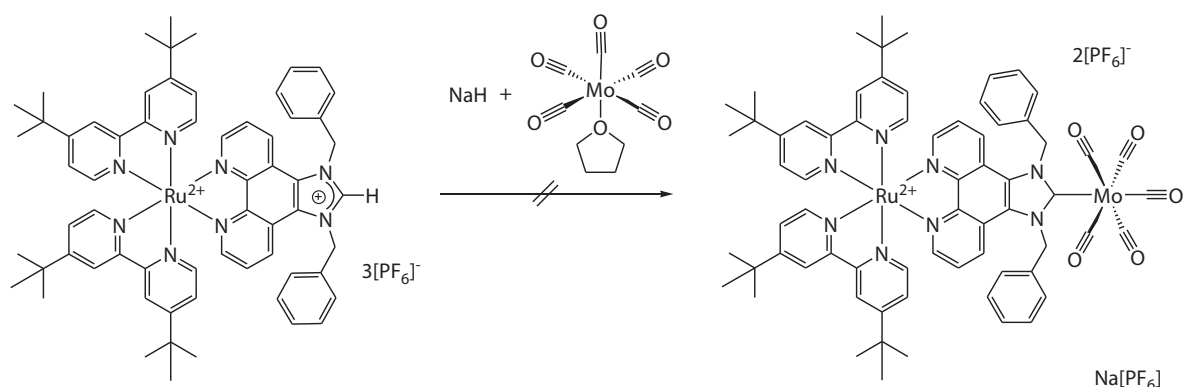


Figure 88: Attempted Mo complexation at the NHC-coordination site at **Ru(bbip)**.

manipulation of B(Et)₃ adducts of NHCs are considered to be very easy due to their stability toward air and moisture.^[181] Nevertheless, application of this method to solutions of **Ru(bbip)** or **bbip** in THF at -78°C resulted in a darkening of the solutions but did not yield the desired product in our hands (see figure 89). On contrary, in both cases the formation of the hydrogenated products was the result of the Li[HB(Et)₃]-addition as could be confirmed by ¹H-NMR-analysis. The strongest indication for the formation of the corresponding 1,3-substituted 2,3-dihydro-1*H*-imidazole derivatives was the shift of the protons in 2-position toward higher field strength and a doubling of the relative peak area which refers to two hydrogen atoms after the reaction ($\delta_{\text{CH}_2(2)}^{\text{Ru}(\text{bbip})+\text{H}^+} = 4.95 \text{ ppm}$ and $\delta_{\text{CH}_2(2)}^{\text{bbip}+\text{H}^+} = 4.76 \text{ ppm}$). Furthermore, in the ¹¹B-NMR spectra, the expected characteristic singlets at $\delta \sim -13 \text{ ppm}$ were not observed. The analogous formation of the NHC·BF₃ adduct was not attempted because such complexes are less reactive in transmetalation reactions.^[181]

Another powerful method for the preparation of carbene transfer agents represents the formation of metastable carbene silver halogenide complexes (e.g. $[(\text{tbbpy})_2\text{Ru}(\mu\text{-bbip})\text{AgX}]^{2+} = \text{Ru}(\text{bbip})\text{Ag}$, $[(\text{tbbpy})_2\text{Ru}(\mu\text{-bbip})]_2\text{Ag}^{5+} = \text{Ru}(\text{bbip})\text{Ag}(\text{bbip})\text{Ru}$, or $[(\text{bbip})\text{AgX}] = (\text{bbip})\text{Ag}$), using Ag₂O as base for the reaction with an imidazolium salt typically in dry and oxygen free dichloromethane solutions. One of the most useful properties of silver carbene complexes is their tendency toward transmetalation reactions (with silver halogenide formation as driving force). Nevertheless, a known from literature, possible sensitivity of the formed silver complexes toward visible light (photographic process) had to be considered, so that all reactions were eventually performed in the dark. Furthermore, addition of molecular sieves to the reaction

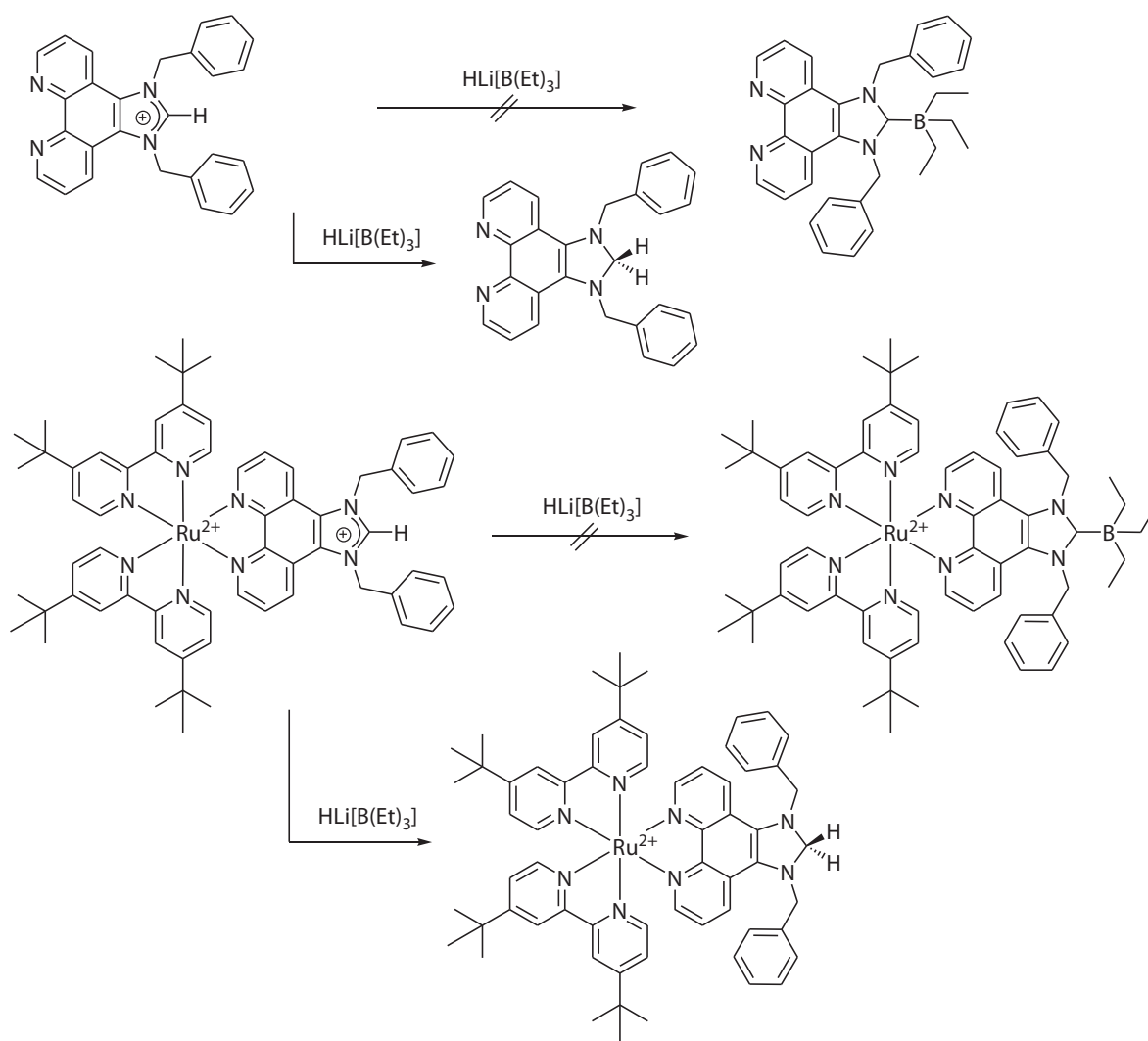


Figure 89: Attempted complexation of B(Et)_3 to the NHC-coordination site of **bbip** (top) and **Ru(bbip)** (bottom).

is necessary due to the high sensitivity of silver carbene complexes toward moisture.

The application of this concept was very promising but did not succeed right away. A direct reaction of **bbip** and Ag_2O under argon atmosphere in dry dichloromethane was not sufficient due to the very low solubility of the reaction partners in the solvent. The second problem represented the existence of the phenanthroline coordination sphere which enables the formation of inhomogeneous products or even very insoluble coordination polymers (see figure 90).^[185]

As a result, a fine gray precipitate in a colorless solution was present at all times during the reaction. Thus, it was impossible to indicate the end of the reaction by visible changes. After the mixture

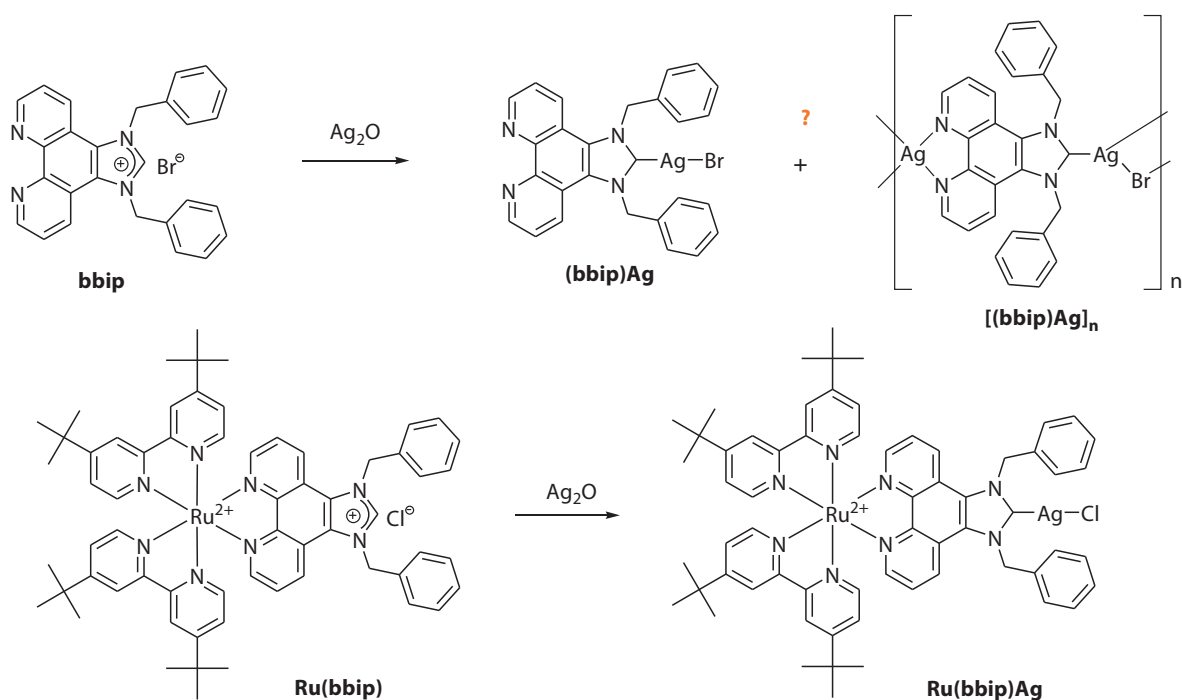


Figure 90: Preparation of the silver NHC-complexes of **bbip** (top) and **Ru(bbip)** (bottom).

was stirred for 7 days, it was filtered through dry celite because of the expected higher solubility of the neutral complex compared to the ionic compounds. Removal of the solvent from the colorless solution gave a thin film of precipitated white solid in very low yields (<1%). From this small quantity of product, it was only possible to obtain a weak ^1H -NMR-spectrum in dry chloroform-*d* under inert conditions. Nevertheless, the loss of the singlet signal for the proton in 2-position (at $\delta_{\text{H}(2)}^{\text{bbip}} = 11.945$ ppm) and retention of the symmetric A-, B-, C-proton pattern with only slight field shifts indicated a possible formation of the corresponding carbene complex $[(\text{bbip})\text{AgBr}]$ **(bbip)Ag**. Furthermore, no signals of the starting material **bbip**, slightly soluble in chloroform, were found in the spectrum. Due to the small amount of the obtained soluble product and the general insolubility of the remaining precipitate, unfortunately, no other analysis method could be successfully applied, so that a clear identification of the product was not possible.

In the next step, the same protocol for the synthesis of the silver carbene complex was applied to **Ru(bbip)**. Due to the good solubility of the different starting material in dichloromethane a positive influence on the course of the reaction was expected. The transformation of the PF_6^- -salt of **Ru(bbip)** with silver oxide in dichloromethane was traced over several days by ^1H -NMR-

experiments without a sign of a successful conversion. Finally, the low driving force of AgOH- or AgPF₆-formation was identified as disadvantage for a successful reaction, yielding [(tbbpy)₂Ru(μ-bbip)AgX][PF₆]₂ (X = OH, PF₆) or [(tbbpy)₂Ru(bbip)Ag(bbip)Ru(tbbpy)₂][PF₆]₅.

The application of higher reaction temperatures (60°C), exchange of the solvent by acetonitrile and longer reaction times (two weeks) gave the first reaction mixture, where ¹H-NMR experiments gave a clear indication at least for a partial formation of the desired product. The prominent sign for the performed complexation is the appearance of a new set of signals in the ¹H-NMR spectrum which can be assigned to a second **Ru(bbip)**-type complex in the reaction mixture, indicated by slightly shifted signals and one missing signal which refers to the N-CH-N-proton in 2-position. Rather unclear is the constitution of the new complex [(tbbpy)₂Ru(μ-bbip)AgX]³⁺ with respect to the second ligand at the silver center (X = OH⁻, {(μ-bbip)Ru(tbbpy)₂}²⁺ or [PF₆]⁻). The formation of the hydroxo complex from silver oxide is the most plausible interpretation of the result, because [PF₆]⁻ is considered to be a noncoordinating anion and the complexation of a second metal fragment is sterically more demanding. Nevertheless, according to the NMR-spectrum no clean product but a 20:80-mixture of starting material and product was obtained after two weeks, therefore, a different technique had to be applied.

To increase the driving force the chloride salt of **Ru(bbip)** was prepared. Counter ion exchange of [PF₆]-salt of **Ru(bbip)** with (Bu)₄NCl in acetone/ethyl acetate gave the corresponding chloride salt [(tbbpy)₂Ru(bbip)]Cl₃ in quantitative yield. The reaction the **Ru(bbip)**-chloride together with silver oxide and a sufficient amount of molecular sieves in dry dichloromethane, finally succeeded. After stirring the mixture for 16 hours in the dark, the chloride salt of [(tbbpy)₂Ru(μ-bbip)AgCl]²⁺ (**Ru(bbip)Ag**) was obtained with full conversion (see figure 90 on page 128) as determined by ¹H-NMR. Separation of the precipitates and the molecular sieve beads and removal of the solvent gave the pure product as indicated by NMR spectroscopy and mass spectrometry.

Disappearance of the characteristic ¹H-NMR-signal of the proton at 2-position (see figure 86 on page 123) and the typical high field shift in the ¹³C-NMR of the N-CH-N-carbon signal (196.50 ppm) supports the proposed carbene complex formation.

The detailed mass spectrometric analysis were performed in cooperation with JING LI from the group of Prof. Dr. T. DREWELLO (Erlangen).

This assumption of the successful carbene complex formation was further confirmed by detailed ESI-MS and MSⁿ studies. An example is shown in figure 91 for the relevant fragment ion

$\{[(\text{tbbpy})_2\text{Ru}(\text{bbip})\text{AgCl}]\text{Cl}\}^+$ ($m/z = 1216.8$).

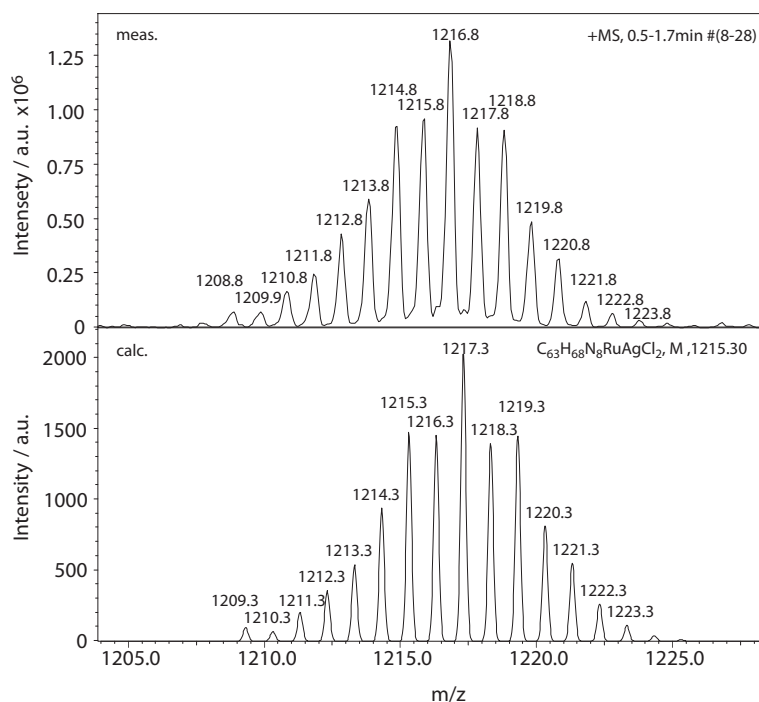


Figure 91: Measured and calculated isotopic pattern of $\{\text{Ru}(\text{bbip})\text{Ag}+\text{Cl}\}^+$ in the ESI-MS experiment.

Finally, it was possible to obtain X-ray suitable crystals of $\text{Ru}(\text{bbip})\text{Ag}$ by crystallization from chloroform/dichloromethane under inert conditions. The detailed discussion is given in the following chapter (see figure 93 on page 132 and table 13 on page 133).

3.3.6 Structural Characterization of Ruthenium *ip*-Type Complexes

Due to the fortunate fact that ruthenium complexes of all stages of the ligand transformation were obtained it was possible to identify trends and tendencies within the series $\text{Ru}(\text{ip})$, $\text{Ru}(\text{bip})$, $\text{Ru}(\text{bbip})$, and $\text{Ru}(\text{bbip})\text{Ag}$ (see figures 92 on page 131 and 93 on page 132 for the solid state structures and table 13 on page 133 for relevant data) and to compare them to the series of pre-ligands *ip*, *bip*, and *bbip* (compare chapter 3.3.3 on page 118).

The structural features observed for the ruthenium complexes combine both, the general patterns of other ruthenium NN-complexes and that of the performed transformations at the imidazole part of the ligands respectively. For the characterization of the new *ip*-type complexes it is useful to focus on the two coordination sites. Therefore, important distances

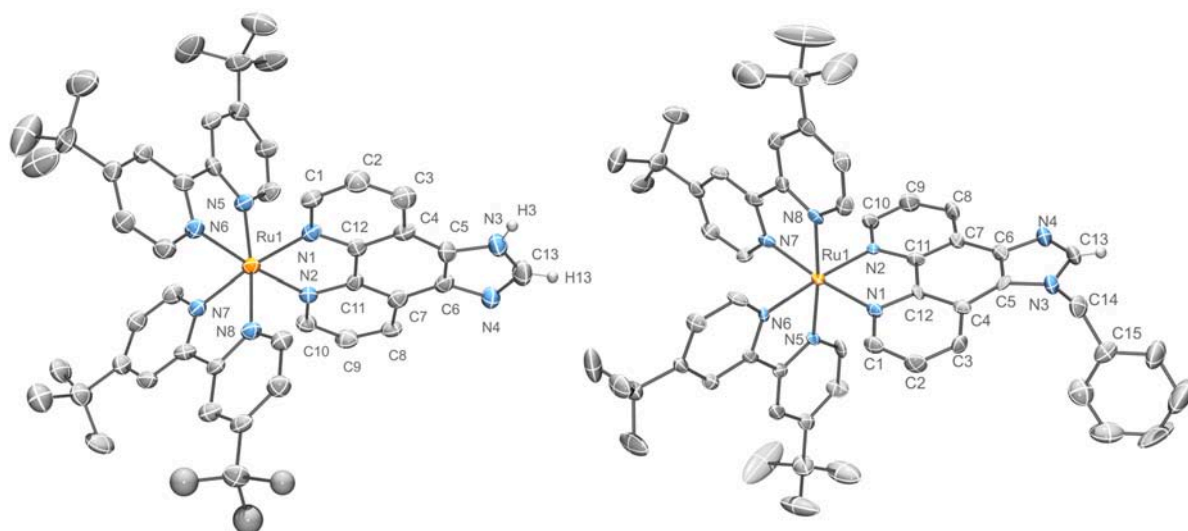


Figure 92: ORTEP drawing of the solid state structures of **Ru(ip)** (left) and **Ru(bbip)** (right). Ellipsoids were drawn at the 70% probability level, counter ions, solvent molecules, and hydrogen atoms except for the imidazole moieties were omitted for clarity.

and angles from the N,N'-chelating site and from the imidazole/carbene site will be discussed. With respect to the phenanthroline coordination site, all complexes exhibit a number of typical similarities which can be found in other ruthenium bipyridine/phenanthroline-type complexes as well. The Ru-N1 and Ru-N2 bond distances vary in a narrow range between 2.055(4) Å and 2.067(5) Å. Even in the complex **Ru(bbip)** no significant influence on the Ru-N distances was found although it bears a positively charged ligand. Furthermore, the resulting N1-Ru-N2 angle varies insignificantly between 79.18(16)° and 80.15(17)° in all complexes of this series. The coordination environment with respect to the nearby bond lengths and angles remains unaffected by the changes at the imidazole part of the ligands. Thus, the N1-C12 bond lengths and N2-C11 bond lengths vary between 1.363(7) Å and 1.385(7) Å and the C11-C12 distances vary between 1.421(8) Å and 1.449(7) Å, respectively. In the N1-C12-C11 and the N2-C11-C12 bond angles only minor variations between 115.1(5)° and 117.4(5)° were observed. Comparison of the N,N'-coordination site in series of ruthenium complexes and in the respective pre-ligands revealed no or only very slight (not in every case significant) changes in the corresponding distances and angles. The tendency goes toward more acute N1-C11-C12 / N2-C12-C11 angles (e.g. $\angle_{(N2,C12,C11)}^{\text{ip}} = 117.0(2)^\circ \geq \angle_{(N2,C12,C11)}^{\text{Ru(ip)}} = 115.8(5)^\circ$), longer C12-N1 / C11-N2 bond lengths (e.g. $d_{(N2-C11)}^{\text{ip}} = 1.360(3) \text{ \AA} < d_{(N2-C11)}^{\text{Ru(ip)}} = 1.385(5) \text{ \AA}$) and shorter C11-C12 distances

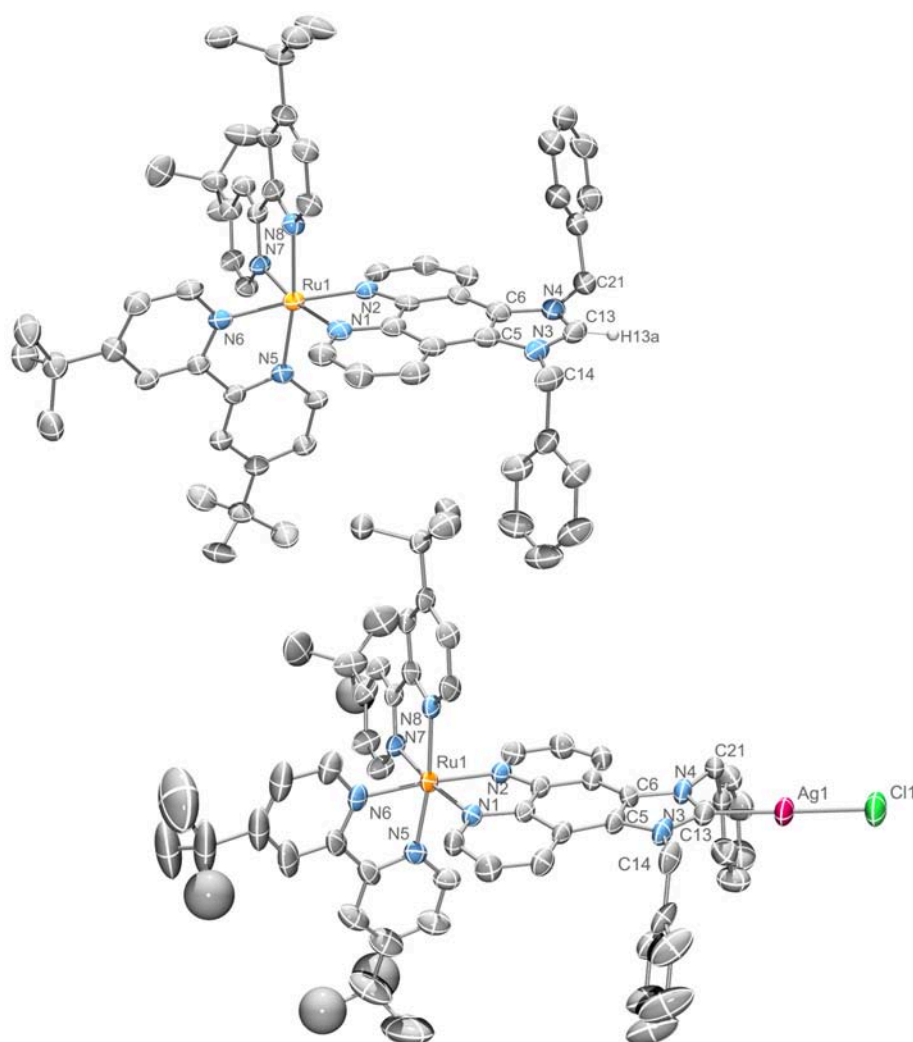


Figure 93: ORTEP representation of the molecular Structure of **Ru(bbip)** (top) and **Ru(bbip)Ag** (bottom). Anions, solvent molecules and protons were omitted from the X-ray structures for clarity.

(e.g. $d_{(\text{C11-C12})}^{\text{bbip}} = 1.463(3) \text{ \AA} > d_{(\text{C11-C12})}^{\text{Ru(bbip)}} = 1.421(8) \text{ \AA}$) in the ruthenium complexes.

Comparison of the changes in the imidazole ring of this series reflect the performed changes. It can be expected that a certain degree of asymmetry is present in the imidazole rings of **Ru(ip)** and **Ru(bbip)** due to the contribution of the resonance structures with a double bond between C13 and N4. Furthermore, a stepwise increase of the π -character of the carbene carbon and a stepwise decrease of the π -delocalization on the imidazole rings can be expected with respect to the starting imidazole **Ru(bbip)** and transformation into the imidazolium salt **Ru(bbip)** and subsequent carbene complex formation.

Table 13: Selected bond lengths [Å] and angles [°] of **Ru(ip)**, **Ru(bip)**, **Ru(bbip)**, and **Ru(bbip)Ag**

bond length [Å] or angle [°]	Ru(ip)	Ru(bip)	Ru(bbip)	Ru(bbip)Ag
Ag1 - C13	-	-	-	2.080 (6)
Ag1 - Cl1	-	-	-	2.3214 (16)
Ru1 - N1	2.060 (4)	2.064 (5)	2.057 (4)	2.055 (5)
Ru1 - N2	2.058 (4)	2.055 (4)	2.056 (4)	2.067 (5)
N4 - C13	1.336 (8)	1.308 (7)	1.318 (7)	1.357 (9)
N3 - C13	1.338 (8)	1.368 (7)	1.323 (7)	1.357 (9)
N3 - C5	1.361 (7)	1.376 (7)	1.395 (7)	1.395 (7)
N4 - C6	1.376 (7)	1.376 (7)	1.395 (7)	1.386 (7)
C5 - C6	1.373 (8)	1.379 (8)	1.380 (8)	1.379 (9)
N1 - C12	1.367 (7)	1.372 (7)	1.363 (7)	1.373 (7)
N2 - C11	1.385 (7)	1.364 (8)	1.375 (7)	1.372 (7)
C11 - C12	1.443 (8)	1.421 (8)	1.449 (7)	1.442 (9)
C13 - Ag1 - Cl1	-	-	-	178.9 (2)
N1 - Ru1 - N2	80.15 (17)	79.43 (17)	79.18 (16)	79.32 (19)
N3 - C13 - N4	112.5 (5)	113.5 (5)	111.0 (5)	105.7 (5)
C13 - N3 - C5	107.5 (5)	105.9 (5)	107.8 (5)	110.6 (5)
C13 - N4 - C6	103.7 (5)	104.1 (5)	107.9 (5)	111.0 (5)
N3 - C5 - C6	105.5 (5)	105.4 (5)	106.6 (5)	106.4 (5)
N4 - C6 - C5	110.7 (5)	111.1 (5)	106.6 (5)	106.4 (5)
N1 - C12 - C11	116.3 (5)	115.1 (5)	115.8 (5)	116.0 (5)
N2 - C11 - C12	115.8 (5)	117.4 (5)	114.9 (5)	115.3 (5)

The X-ray data indicated that the imidazole rings in **Ru(ip)** and **Ru(bip)** have identical C-N and C-C distances and equivalent bond angles at the analogical positions. A significant asymmetry with shortening of the C13-N4 bond with respect to the C13-N3 bond due to the partial double bond character in 1*H*-imidazoles is present in **Ru(bip)** ($d_{\text{C13-N4}}^{\text{Ru(bip)}} = 1.308(7) \text{ \AA} < d_{\text{C13-N3}}^{\text{Ru(bip)}} = 1.368(7) \text{ \AA}$). Furthermore, differences in the opposing C-N-C angles and N-C-C angles of the imidazole rings are present in **Ru(ip)** and **Ru(bip)** as well. Thus, both complexes exhibit by $\sim 5^\circ$ wider N4-C6-C5 angles than N3-C5-C6 angles (e.g. $\angle_{\text{(N4,C6,C5)}}^{\text{Ru(bip)}} = 111.1(5)^\circ > \angle_{\text{(N3,C5,C6)}}^{\text{Ru(bip)}} = 105.4(5)^\circ$). Additionally, **Ru(ip)** exhibits a more acute angle at the N3 atom when compared to the N4 atom ($\angle_{\text{(C13,N3,C5)}}^{\text{Ru(ip)}} = 107.5(5)^\circ > \angle_{\text{(C13,N4,C6)}}^{\text{Ru(ip)}} = 103.7(5)^\circ$). The N3-C13-N4 angles are the widest angles of

the imidazole ring in both complexes ($\angle_{(N3,C13,N4)}^{Ru(ip)} = 112.5(5)^\circ = \angle_{(N3,C13,N4)}^{Ru(bip)} = 113.5(5)^\circ$).

In **Ru(bbip)** and **Ru(bbip)Ag**, only insignificant changes of the bond lengths in the imidazole system were found when compared to **Ru(ip)** and **Ru(bip)**. Surprisingly, the expected elongation of the C-C bond distances in the imidazolium salt and carbene complex were not observed. Nevertheless, a clear evidence of the increasing symmetry with extraordinary small deviations between the bond corresponding lengths (e.g. C13-N4 and C13-N3 or C6-N4 and C5-N3) and angles (e.g. N4-C6-C5 and N3-C5-C6 or C13-N3-C5 and C13-N4-C6) is present in **Ru(bbip)** and **Ru(bbip)Ag**. The N-C-N angles and C-N-C angles represent the mentioned changes in π -character and delocalization. Prominent is the stepwise decrease of the angle at C13 ($\angle_{(N3,C13,N4)}^{Ru(bip)} = 113.5(5)^\circ > \angle_{(N3,C13,N4)}^{Ru(bbip)} = 111.0(5)^\circ > \angle_{(N3,C13,N4)}^{Ru(bbip)Ag} = 105.7(5)^\circ$) and the increasing angle at the N3 and N4 atoms (e.g. $\angle_{(C13,N4,C6)}^{Ru(bip)} = 104.1(5)^\circ < \angle_{(C13,N4,C6)}^{Ru(bbip)} = 107.9(5)^\circ < \angle_{(C13,N4,C6)}^{Ru(bbip)Ag} = 111.0(5)^\circ$). The C13-Ag1 distance ($d_{(C13,Ag1)}^{Ru(bbip)Ag} = 2.080(6) \text{ \AA}$) as well as the Ag1-Cl1 distance ($d_{(Ag1-Cl1)}^{Ru(bbip)Ag} = 2.3214(16) \text{ \AA}$) lie in the expected region for [Ag(NHC)Cl]-type complexes. Furthermore the expected linear coordination geometry is present ($\angle_{(C13,Ag1,Cl1)}^{Ru(bbip)Ag} = 178.9(2)^\circ$) and no indication for a possible dimer formation was found in the crystal structure (For similar X-ray structures of [Ag(NHC)X]-type complexes (X = Br⁻/I⁻) compare ROLAND, ALEXAKIS et al.^[186, 187] and BOUWMAN for dimeric complexes^[188]).

Comparison of all ruthenium complexes with their corresponding ligands with respect to the imidazole ring shows nearly constant values for all distances and angles which is in accordance with a negligible influence of the coordination at the phenanthroline site. Only in the case of **ip** and **Ru(ip)** slight differences can be found which are most likely results of the protonation of **ip** in the crystal structure. As mentioned above, **ip** exhibits distances and angles which are rather consistent with the imidazolium salt **Ru(bbip)**.

In general, the structural features observed for **Ru(ip)**, **Ru(bip)**, **Ru(bbip)** and **Ru(bbip)Ag** combine both, the common patterns of other ruthenium NN-complexes and that of silver-NHC-complexes and the prior imidazole derivatives respectively.

3.3.7 Preparation of *bbip*-Bridged Catalysts

The main advantage of silver carbene complexes is their general applicability as carbene transfer agents which allows to transfer the coordinated NHC ligands to almost any kind of catalyst

metal center in a transmetalation reaction.^[182, 173, 189, 190] Thus, it is possible to apply the previously obtained silver-NHC carrying ruthenium complex **Ru(bbip)Ag** to obtain new heterobinuclear **bbip**-bridged complexes which potentially represent new intramolecular $[[\mathbf{P} \sim \mathbf{B} \sim \mathbf{C}]]$ -type (**P** = photocenter, **B** = bridge, **C** = catalytic center) catalysts (see figure 94).

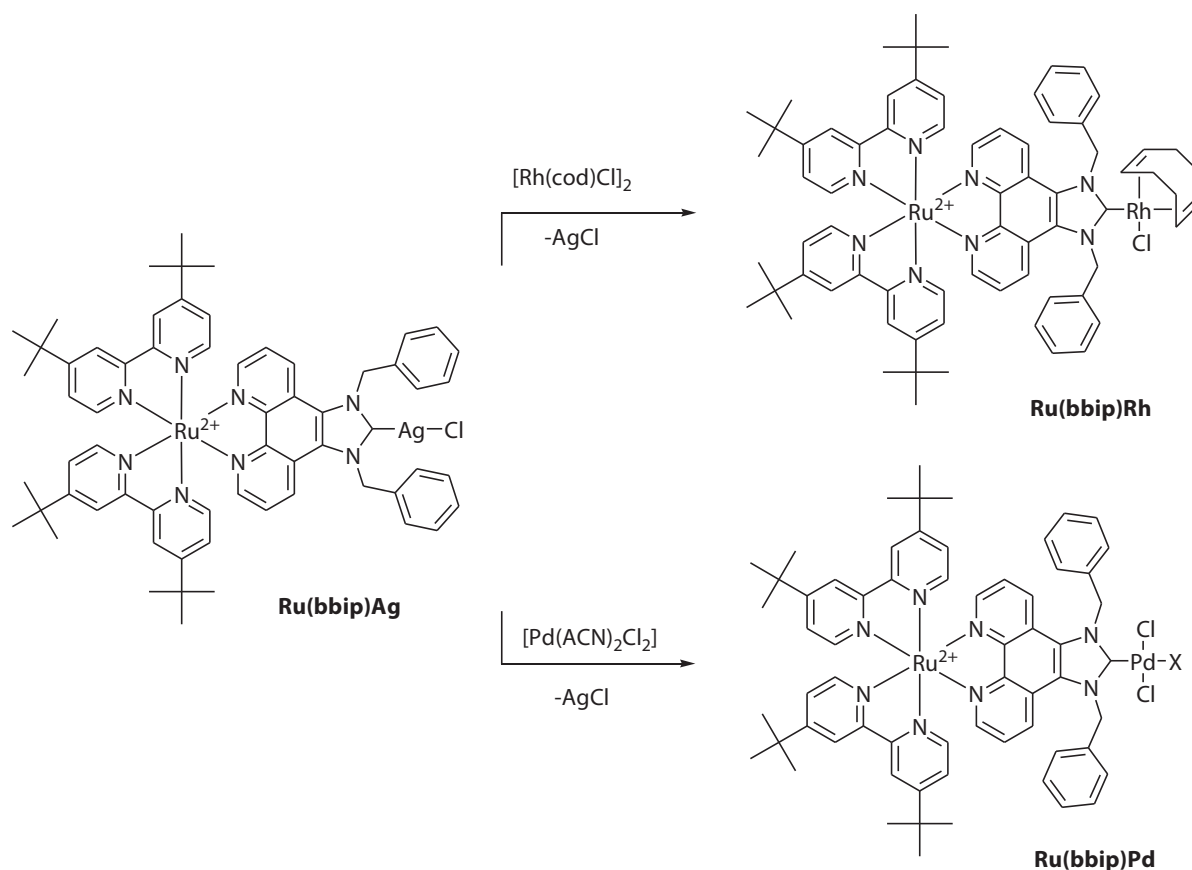


Figure 94: Synthesis of **Ru(bbip)Rh** (top) and **Ru(bbip)Pd** (bottom) from **Ru(bbip)Ag** by treatment with $[\text{PdCl}_2(\text{ACN})_2]$ or $[\text{Rh}(\text{cod})\text{Cl}]_2$, respective (COD = 1,5-cyclooctadiene; X = coordinated solvent or $\{(\mu\text{-bbip})\text{Ru}(\text{tbbpy})_2\}^{2+}$).

By the reaction of **Ru(bbip)Ag** with $\text{Pd}(\text{CH}_3\text{CN})_2\text{Cl}_2$ in dichloromethane, as generally described by **method C3** in the experimental section, an insoluble AgCl -precipitate was formed, indicating the formation of the palladium-NHC complex $[(\text{tbbpy})_2\text{Ru}(\mu\text{-bbip})\text{PdCl}_2\text{X}]^{2+}$ (**Ru(bbip)Pd**, X = coordinated solvent or $\{(\mu\text{-bbip})\text{Ru}(\text{tbbpy})_2\}^{2+}$, see figure 94). Removal of the precipitates and of the remaining solvent yielded the symmetric compound, as indicated by $^1\text{H-NMR}$ experiments. Characterization by $^1\text{H-NMR}$ - and ESI-MS^n -experiments gave evidence for the formation of the

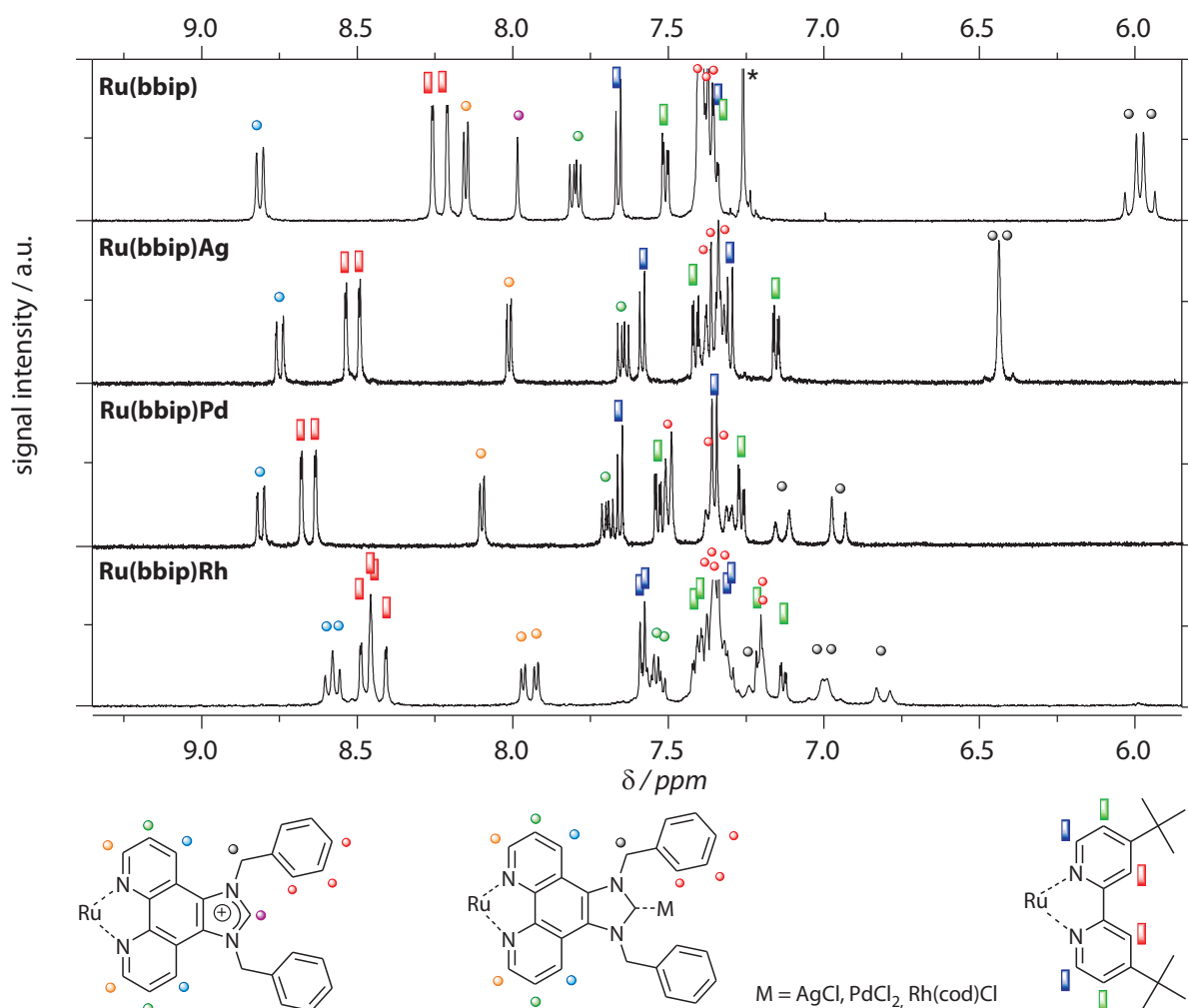


Figure 95: Aromatic region of the ^1H -NMR spectra of **Ru(bbip)** and the series of prepared ruthenium carbene complexes **Ru(bbip)Ag**, **Ru(bbip)Pd**, and **Ru(bbip)Rh** in acetonitrile- d_3

desired complex which is in equilibrium with a dimeric form of the Ru-Pd-complex. Especially the solvent dependent splitting of the ^1H -NMR signals into two sets gives rise to the assumption of an asymmetric complex, possibly similar to ones found in literature.^[165] Interestingly, in nonpolar and weakly coordinating solvents such as dichloromethane, the two CH_2 -groups split into three independent signals with two protons showing diastereotopic splitting ($\delta_{\text{CH}_2}^{\text{Ru(bbip)Pd}} = 7.04$ ppm (d, 1H, $^2J = 20$ Hz), $\delta_{\text{CH}_2'}^{\text{Ru(bbip)Pd}} = 6.83$ ppm (d, 1H, $^2J = 20$ Hz), $\delta_{\text{CH}_2''}^{\text{Ru(bbip)Pd}} = 5.80$ ppm (s, 2H)), whereas in polar acetonitrile no additional splitting of the CH_2 -signals could be observed ($\delta_{\text{CH}_2}^{\text{Ru(bbip)Pd}} = 6.90$ ppm (d, 2H, $^2J = 20$ Hz), $\delta_{\text{CH}_2'}^{\text{Ru(bbip)Pd}} = 7.30$ ppm (d, 2H, $^2J = 20$ Hz), compare figure 95). ESI-mass spectrometry in methanol reveals triply and quadruply charged peaks which refer to

3.3 NN-NHC-Ligand *bbip*: Toward Second Generation Catalysts

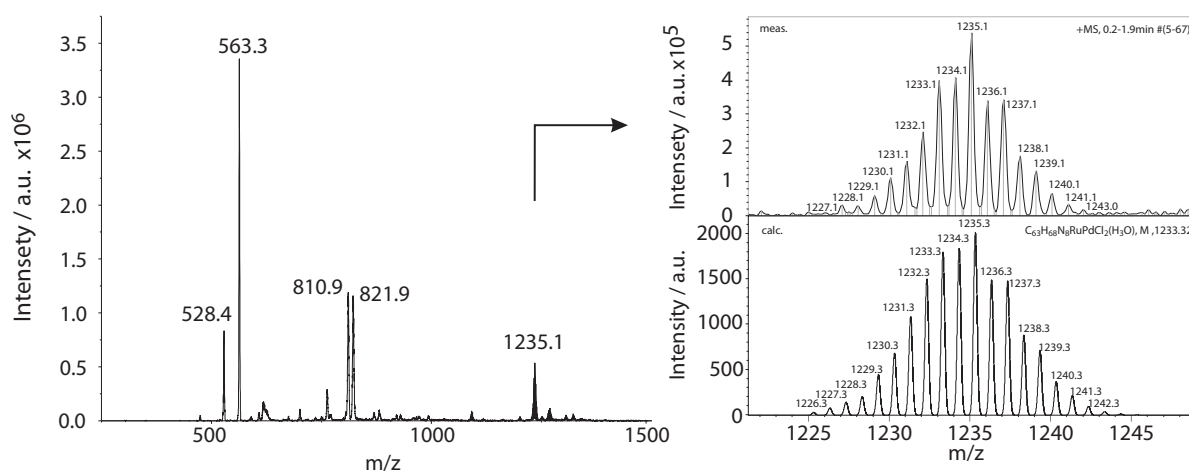


Figure 96: ESI-MS spectrum of **Ru(bbip)Pd** measured in methanol and representative match of the calculated and measured isotopic patterns of the fragment ions. The main peaks belong to the following fragment ions: $m/z = 1235.1$, $\{(\text{tbbpy})_2\text{Ru}(\mu\text{-bbip})\text{Pd}(\text{H}_2\text{O})\text{Cl}_2\}^+$; 821.9 $\{[\{(\text{tbbpy})\text{Ru}(\mu\text{-bbip})\}_2\{\text{Pd}_2\text{Cl}_4\}][\text{Cl}]\}^{3+}$; 810.9 $\{[\{(\text{tbbpy})_2\text{Ru}(\mu\text{-bbip})\}_2\{\text{Pd}_2\text{Cl}_4\}]\}^{3+}$; 563.3 $\{[\{(\text{tbbpy})_2\text{Ru}(\mu\text{-bbip})\}_2\{\text{PdCl}_2\}]\}^{4+}$; and 528.4 $\{[\text{Ru}(\text{tbbpy})_2(\text{bbip})](\text{H}_2\text{O})\}^{2+}$.

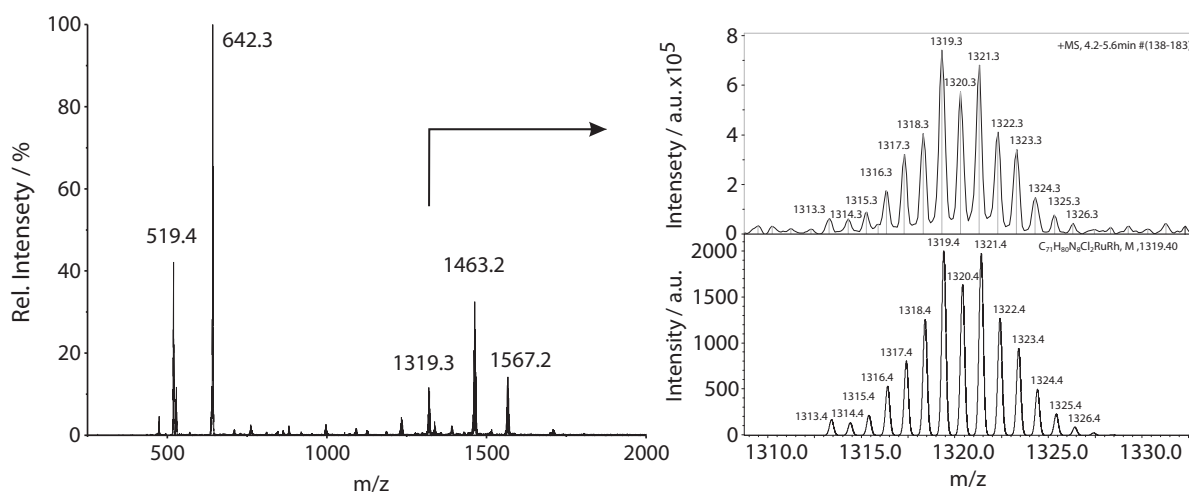


Figure 97: ESI-MS spectrum of **Ru(bbip)Rh** measured in methanol and a representative match of the calculated and measured isotopic patterns of the fragment ions. The denoted peaks belong to the following fragment ions: $m/z = 1567.2$ $\{[\{(\text{tbbpy})_2\text{Ru}\}(\mu\text{-bbip})\{\text{Rh}(\text{cod})\text{Cl}\}_2\text{Cl}]\}^+$, 1463.2 $\{[\{(\text{tbbpy})_2\text{Ru}\}(\mu\text{-bbip})\{\text{Rh}(\text{cod})\text{Cl}\}\{\text{AgCl}\}\text{Cl}]\}^+$, 1319.3 $\{[\{(\text{tbbpy})_2\text{Ru}\}(\mu\text{-bbip})\{\text{Rh}(\text{cod})\text{Cl}\}\text{Cl}]\}^+$, 642.3 $\{[\{(\text{tbbpy})_2\text{Ru}\}(\mu\text{-bbip})\{\text{Rh}(\text{cod})\text{Cl}\}]\}^{2+}$, 519.4 $[\text{Ru}(\text{tbbpy})_2(\text{bbip})]^{2+}$.

a dimeric tetranuclear $\{\text{Pd}_2\text{Cl}_2\}$ -bridged species (**Ru(bbip)Pd-Pd(bbip)Ru**) and a monomeric trinuclear $\{\text{PdCl}_2\}$ -bridged species (**Ru(bbip)Pd(bbip)Ru**) (see figure 96).

In addition to the preparation of the palladium complex, the silver precursor was used to synthesize a rhodium-NHC-complex $[(\text{tbbpy})_2\text{Ru}(\mu\text{-bbip})\text{Rh}(\text{cod})\text{Cl}]^{2+}$ (**Ru(bbip)Rh**) using $[\text{Rh}(\text{cod})\text{Cl}]_2$ (COD = 1,5-cyclooctadiene) for the transmetalation reaction. Similar work-up gave a red solid compound which was characterized by NMR- and MS-methods. In this case all CH_2 -signals of the benzyl group are shifted with respect to the asymmetric NHC-bound $\{\text{Rh}(\text{cod})\text{Cl}\}$ -metal fragment so that all four protons give independent signals with the characteristic 2J -coupling to the respective geminal proton ($\delta_{\text{CH}_2}^{\text{Ru}(\text{bbip})\text{Rh}} = 7.20$ ppm (d, 1H, $^2J = 20$ Hz), $\delta_{\text{CH}_2'}^{\text{Ru}(\text{bbip})\text{Rh}} = 6.75$ ppm (d, 1H, $^2J = 20$ Hz) and $\delta_{\text{CH}_2''}^{\text{Ru}(\text{bbip})\text{Rh}} = 7.05$ ppm (d, 1H, $^2J = 20$ Hz), $\delta_{\text{CH}_2'''}^{\text{Ru}(\text{bbip})\text{Rh}} = 6.95$ ppm (d, 1H, $^2J = 20$ Hz), see figure 95) in contrast to the silver complex ($\delta_{\text{CH}_2}^{\text{Ru}(\text{bbip})\text{Ag}} = 6.50$ ppm, (s, 4H)). Additionally, it was possible to identify the COD-related signals which further supported the formation of the desired compounds.

Mass spectrometric analysis revealed the characteristic pattern (for details see figure 97) which correspond to the calculated isotopic patterns for the expected binuclear complex **Ru(bbip)Rh**. Furthermore, unexpected peaks which refer to AgCl-adducts and Rh(cod)Cl-adducts of **Ru(bbip)Rh** were found. It was concluded that undesired soluble $[\text{AgCl}_2]^-$ or higher AgCl-cluster counter ions which did not precipitate from the solution were still present in the product, which is a common problem in transmetalation reactions with formation of silver halogenides.^[188, 191] Unfortunately, it was not possible to remove the impurities from the mixture by further work up steps such as dissolving the complex in dichloromethane and reprecipitation with diethyl ether. Counter ion exchange with a $[\text{PF}_6]^-$ -salt did not succeed.

3.3.8 Spectroscopic Characterization

For the series of this new ruthenium chromophores photophysical properties were determined. Special interest was placed on the influence of the electronic transformations at the imidazole moiety in the $\text{N,N}'$ -coordinated ruthenium complexes with the new **ip**-type ligands. Preliminary insights were derived from steady-state absorption and emission studies in dichloromethane and acetonitrile (see figures 98 and 99, compare table 14 on page 143).

At first glance, all described complexes show the typical broad $^1\text{MLCT}$ absorption between 400 and 500 nm which give rise to similar $^3\text{MLCT}$ emission in the 550 to 800 nm range (for an example see figure 98).^[36] Upon closer analysis, however, subtle changes become visible as the ligand

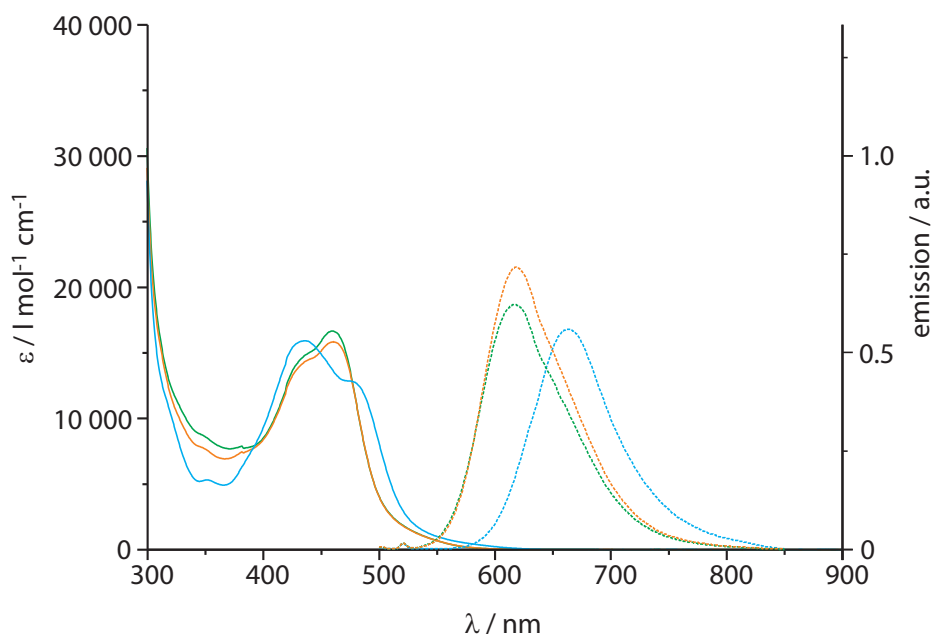


Figure 98: Absorption spectra of the monometallic ruthenium imidazophenanthroline-type complexes in acetonitrile and corresponding relative emission, normalized upon extinction at excitation wavelength ($\lambda = 450$ nm). **Ru(ip)**: Abs. (—), Em. (---), **Ru(bip)**: Abs. (—), Em. (---), **Ru(bbip)**: Abs. (—), Em. (---).

composition is altered. Interestingly, **Ru(ip)** and **Ru(bip)** exhibit slightly bathochromically shifted, but almost similar absorption properties with absorption coefficients of $\epsilon \sim 17\,000 \text{ l mol}^{-1} \text{ cm}^{-1}$ and similar shapes compared to the parent compound without an annulated imidazole moiety $[\text{Ru}(\text{tbbpy})_2(\text{phen})]^{2+}$ (**Ru(phen)**) in acetonitrile and dichloromethane (e.g.: $\lambda_{\text{abs, ACN}}^{\text{Ru(phen)}} = 454 \text{ nm} < \lambda_{\text{abs, ACN}}^{\text{Ru(ip)}} = 460 \text{ nm} = \lambda_{\text{abs, ACN}}^{\text{Ru(bip)}} = 460 \text{ nm}$). The emission properties follow the same tendency with similar maxima as well (e.g.: $\lambda_{\text{em, DCM}}^{\text{Ru(phen)}} = 602 \text{ nm} < \lambda_{\text{em, DCM}}^{\text{Ru(ip)}} = 604 \text{ nm} \approx \lambda_{\text{em, DCM}}^{\text{Ru(bip)}} = 608 \text{ nm}$). It is unclear if the electron rich **ip**-type ligand is involved in the emission properties of **Ru(ip)** or **Ru(bip)** because the absorption and emission properties compare very well to $[\text{Ru}(\text{tbbpy})_3]^{2+}$. Thus, a significant effect of the annealing of the imidazole moiety could not be observed which is in accordance with the findings observed by JING et al. for the complex $[\text{Ru}(\text{ip})(\text{bpy})_2]^{2+}$ and BARTON et al. for $[\text{Ru}(\text{dppz})(\text{bpy})_2]^{2+}$.^[192, 193]

On the contrary, in the case of the positively charged azolium salt **Ru(bbip)**, a dominantly broadened absorption band with a 30 nm hypsochromically shifted absorption maximum and a pronounced shoulder between 470 and 490 nm with a bathochromically shifted flank (especially

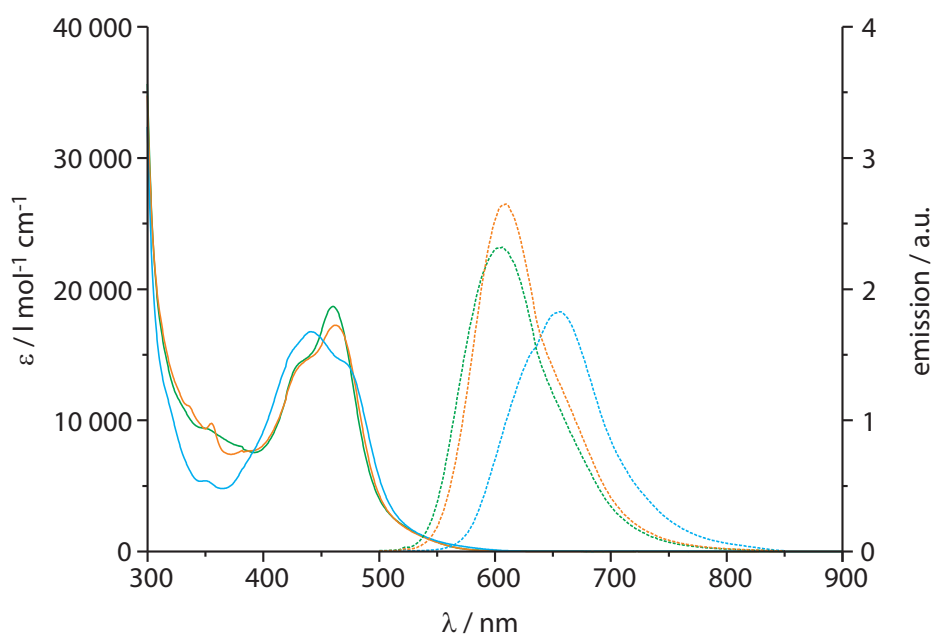


Figure 99: Absorption spectra of the monometallic ruthenium imidazophenanthroline-type complexes in dichloromethane and corresponding relative emission, normalized on extinction at excitation wavelength ($\lambda = 450$ nm). **Ru(ip)**: Abs. (—), Em. (---), **Ru(bip)**: Abs. (—), Em. (---), **Ru(bbip)**: Abs. (—), Em. (---).

in acetonitrile) can be observed when compared to **Ru(phen)**, **Ru(ip)**, or **Ru(bip)** (e.g.: $\lambda_{\text{abs, ACN}}^{\text{Ru(phen)}} = 454$ nm \gg $\lambda_{\text{abs, ACN}}^{\text{Ru(bbip)}} = 435$ nm).

In acetonitrile as well as in dichloromethane, the concentration independent emission intensities (emission intensity divided by the absorbance of the sample at the excitation wavelength of $\lambda = 450$ nm) decrease in the order **Ru(ip)** > **Ru(bip)** > **Ru(bbip)**, whereas emission in dichloromethane is generally stronger as in acetonitrile which is a result of the lower quencher concentration (oxygen) in these solutions. Interestingly, **Ru(bbip)** exhibits a by ~ 50 nm bathochromically shifted emission band when compared to the very alike complexes **Ru(phen)**, **Ru(ip)**, or **Ru(bip)** (e.g.: $\lambda_{\text{em, ACN}}^{\text{Ru(phen)}} = 610$ nm \ll $\lambda_{\text{em, ACN}}^{\text{Ru(bbip)}} = 663$ nm). The best explanation for the observed characteristic of **Ru(bbip)** is the influence of the positive charge at the imidazole moiety of the extended ligand, causing a decreased delocalization in the five membered ring and a lowered π^* -orbital of **ip**. This possibly results in an injection of the excited electron into a different LUMO orbital when compared to the uncharged compounds and, thus, in a **bbip**-centered emission.

Prior to the photophysical characterization of **Ru(bbip)Ag**, experiments were performed to

determine the light sensitivity of this complex, as it is known that some silver-NHC complexes tend to decompose under visible light irradiation (photographic process). For the photostability experiment a sample of the ruthenium complex was dissolved in dry acetonitrile- d_3 under argon atmosphere and an initial $^1\text{H-NMR}$ -spectrum was measured. Then, the Young-tube was placed into the irradiation device and was illuminated with the previously used LED array ($\lambda_{\text{exc}} = 470$ nm). After different irradiation times (1, 2, and 24 h) additional NMR spectra were measured. During the whole experiment no visible changes of the sample or changes in the NMR spectrum were detected.

On the contrary, an exposure of the NMR sample to air led to the decomposition of the complex as indicated by AgCl precipitation and new emerging signals in the NMR spectra.

The impact the nature of the second metal in the bridged $\text{Ru}(\text{bbip})\text{M}$ complexes (M = f: metal free, Ag: silver, Pd: palladium, Rh: rhodium) exerts on absorption and emission properties is illustrated in figure 100 and figure 101 as well as in table 14 on page 143.

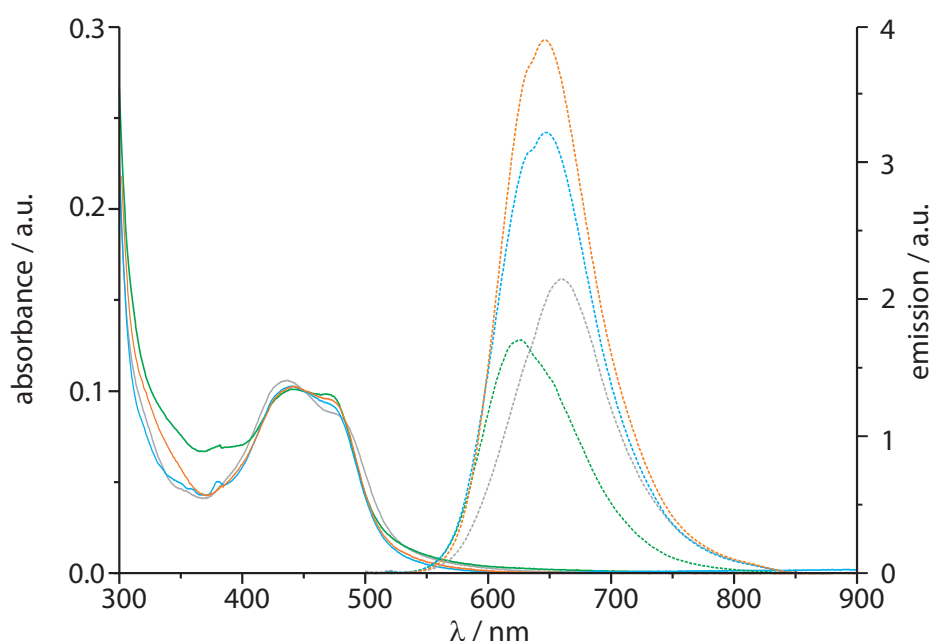


Figure 100: Normalized absorption spectra of the bimetallic **bbip**-bridged complexes in deaerated acetonitrile and corresponding normalized relative emission upon excitation at 450 nm. **Ru(bbip)**: Abs. (—), Em. (---), **Ru(bbip)Ag**: Abs. (—), Em. (---), **Ru(bbip)Pd**: Abs. (—), Em. (---), **Ru(bbip)Rh**: Abs. (—), Em. (---).

For the **bbip** bridged carbene complexes and the azolium salt **Ru(bbip)**, very similar $^1\text{MLCT}$

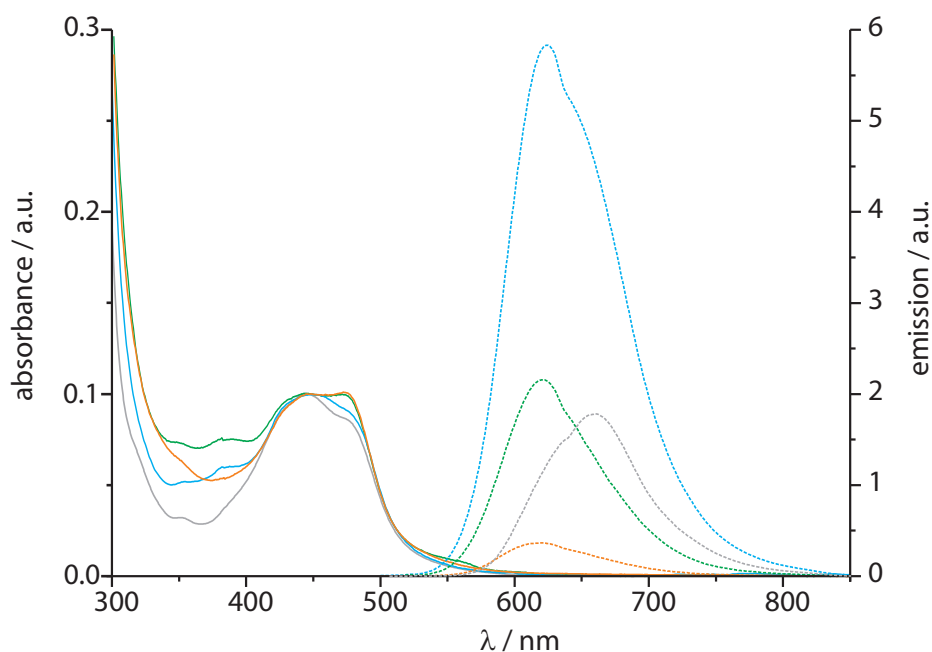


Figure 101: Normalized absorption spectra of the bimetallic **bbip**-bridged complexes in deaerated dichloromethane and corresponding normalized relative emission upon excitation at 450 nm. **Ru(bbip)**: Abs. (—), Em. (---), **Ru(bbip)Ag**: Abs. (—), Em. (---), **Ru(bbip)Pd**: Abs. (—), Em. (---), **Ru(bbip)Rh**: Abs. (—), Em. (---).

absorption spectra, having maxima around $\lambda_{\max} = 440$ nm and only slight differences in the intensity of the bathochromic shoulder around $\lambda_{\text{shoulder}} = 475$ nm were obtained in acetonitrile and dichloromethane. Due to the inert handling of the samples it was not possible to determine exact extinction coefficients. Nevertheless, the palladium and rhodium complexes exhibit the more intense shoulders around $\lambda_{\text{shoulder}} = 475$ nm, whereas the imidazolium salt exhibits the least intense shoulder in both solvents. With respect to the observations between **Ru(bip)** and **Ru(bbip)** it can be assumed that the more bathochromic shoulder refers to the $^1\text{MLCT}$ absorption, involving the carbenoid bridging ligand with a lowered π^* -orbital. Thus, the relative increase of the shoulder in the series of **bbip** containing complexes (in the order $f < \text{Ag} < \text{Rh} < \text{Pd}$ in acetonitrile and $f < \text{Ag} < \text{Rh} \approx \text{Pd}$ in dichloromethane) refers to the increase in carbene character of these complexes.

In the emission properties a clear trend is visible as all carbene complexes have 20-30 nm hypsochromically shifted emission wavelengths ($\lambda_{\text{em, ACN}}^{\text{M} = \text{Ag, Pd}} \approx 640$ nm and $\lambda_{\text{em, DCM}}^{\text{M} = \text{Ag, Pd, Rh}} \approx 620$ nm) when compared to the azolium salt **Ru(bbip)**, but roughly 20-30 nm bathochromically shifted emission wavelengths when compared to **Ru(phen)**, **Ru(ip)**, and **Ru(bip)**. **Ru(bbip)Rh** exhibits

Table 14: UV/vis absorption and emission data of **Ru(bbip)**, **Ru(bbip)Ag**, **Ru(bbip)Pd**, **Ru(bbip)Rh** and $[\text{Ru}(\text{tbbpy})_3]^{2+}$ measured in deaerated acetonitrile at room temperature.

Complex	Solvent	$\lambda_{\text{max, abs}}$ [nm]	$\lambda_{\text{shoulder, abs}}$ [nm]	$\lambda_{\text{max, em}}$ [nm]	Φ^{a}	τ [ns]	$\tau^{\text{a,b}}$ [ns]	$\tau^{\text{a,c}}$ [ns]
$[\text{Ru}(\text{tbbpy})_3]^{2+}$ ^[90]	ACN	458	433	613		107	730	
	DCM	461	437	604		248	610	
Ru(phen) ^[108, 125]	ACN	454	431	610		211	1 400	
	DCM	455		602	0.03	272		
Ru(ip)	ACN	460	431	616				
	DCM	460	431	604				
$[\text{Ru}(\text{ip})(\text{bpy})_2]^{2+}$ ^[192]	ACN	453	425	623	0.14	150	726	
$[\text{Ru}(\text{ip})(\text{phen})_2]^{2+}$ ^[194]	DCM	451		570				
Ru(bip)	ACN	460	429	618				
	DCM	462	429	608				
Ru(bbip)	ACN	435	481	663	0.26	192	920	1 000
	DCM	440	473	654		556	1 300	
Ru(bbip)Ag	ACN	440	474	646	0.34	(183)	1 450	
	DCM	449	473	625		(404)	1 400	
Ru(bbip)Pd	ACN	440	475	646	0.39		1 100	1 000
	DCM	471	441	620			1 400	
Ru(bbip)Rh	ACN	440	473	625	0.17		430	
	DCM	471	441	620			900	

^a oxygen free, ^b emission experiments, ^c transient absorption experiments

a small deviation in acetonitrile ($\lambda_{\text{em, ACN}}^{\text{M=Rh}} \approx 625 \text{ nm}$). These intermediate emission wavelengths represent the influence of the phenanthroline fused NHC moiety on energy of the ³MLCT-emission involving $\text{LUMO}_{(\widehat{\text{L}})}$ s in **bbip**. Seemingly, this differs from the ¹MLCT-absorption involved $\text{LUMO}_{(\widehat{\text{L}})}$ as they are relatively unperturbed by the change of the nature of the second sphere. This observation is very similar to the findings of the *tpphz* and *dppz* containing complexes (see discussion in chapter 1.10.1 on page 42 ff.). Based on this similarity, it can be assumed that a (phenanthroline)/bipyridine centered π^* -orbital ($\text{LUMO}_{(\text{bpy})}$) and a (benz)imidazole centered π^* -orbital ($\text{LUMO}_{(\text{im})}$) exists in such complexes. Furthermore, it can be speculated that the $\text{LUMO}_{(\text{bpy})}$ is mainly involved in the absorption process and that is only little influenced by the imidazole (all

absorption bands, ranging from **Ru(ip)** to **Ru(bbip)Pd**, are rather similar to $[\text{Ru}(\text{bpy})_3]^{2+}$ while the strongly imidazole-influenced $\text{LUMO}_{(\text{im})}$ is mainly involved in the emission of **Ru(bbip)** and the **Ru(bbip)M** complexes, as strong shifts of the emission were observed (see figure 102). In these later two cases a significant degree of carbene character can be assigned to the imidazole moiety.

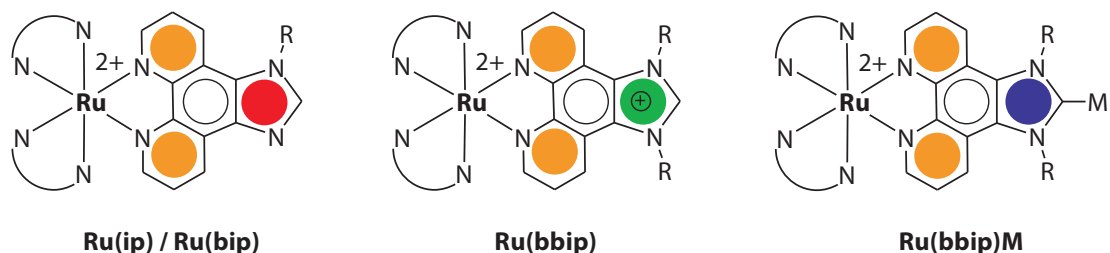


Figure 102: Representation of the proposed $\text{LUMO}_{(\pi\pi^*)}$ -situation in the complexes with **ip**-derived ligands. The $^1\text{MLCT}$ -absorption involved bipyridine centered $\text{LUMO}_{(\text{bpy})}$ is depicted in orange, the higher lying (benz)imidazole $\text{LUMO}_{(\text{im})}$ in **ip** is denoted in red and the lower lying $\text{LUMO}_{(\text{im})}$ in **Ru(bbip)** and **Ru(bbim)M** complexes are denoted in green and blue.

All observations in the **Ru(bbip)M** complexes can be explained by the decreased +M and -I effect in the carbene complexes. In detail, a stepwise increase of the π -character of the carbene carbon and a stepwise decrease of the π -delocalization on the imidazole rings can be expected with respect to the starting imidazole **Ru(bip)** and transformation into the imidazolium salt **Ru(bbip)** and subsequent carbene complex formation.

According to the bathochromically shifted emission in **Ru(bbip)M** complexes with respect to the **Ru(ip)**-type complexes a localization (storage) of the excited electron on the bridge, in particular in the imidazole-centered orbital near the second metal can be expected. Thus, a positive effects on the application of the **Ru(bbip)M**-type complexes in reduction catalysis can be proposed.

Finally, quantum yields were determined in acetonitrile and dichloromethane. The emission quantum yields follow the tendency: $\Phi^{(\text{M}=\text{Pd})} = 0.39 > \Phi^{(\text{M}=\text{Ag})} = 0.34 > \Phi^{(\text{M}=\text{f})} = 0.26 > \Phi^{(\text{M}=\text{Rh})} = 0.17$ in oxygen free acetonitrile. In dichloromethane ordering of the relative emission intensities are different ($\text{Ag} > \text{Rh} > \text{f} > \text{Pd}$), which might be assigned to impurities such as oxygen in the palladium sample or the formation of a dimeric complex, which exhibits an unexpected low emission intensity. Still, even for the weakest emitting new complex a significantly higher quantum yield emerges relative to that reported for the parent complex $[\text{Ru}(\text{bpy})_3]^{2+}$. In short,

ground and excited states for all complexes reveal very similar features in terms of reactivity and stability regardless of the absence or presence of Ag, Rh, or, most importantly, Pd at the NHC-coordination sphere of the **Ru(bbip)M** complexes.

3.3.9 Excited State Dynamics of the bbip-Containing Ruthenium Complexes

In addition to the steady state experiments, time-resolved transient emission and absorption measurements were performed for the series of **Ru(bbip)M** complexes (M = f: metal free, Ag: silver, Pd: palladium, Rh: rhodium). The following photophysical results were obtained in a cooperation with KATRIN PEUNTINGER from the work group of Prof. GULDI (FAU Erlangen-Nürnberg) and might be found in her PhD thesis in a similar form.

With the help of transient emission experiments it was possible to determine the emission lifetimes in oxygen free acetonitrile and dichloromethane (see table 14). In acetonitrile, the **Ru(bbip)**-derived silver and palladium complexes exhibit, with deviations, quantitatively similar lifetimes as observed for **Ru(phen)** ($\tau_{\text{ACN}}^{\text{M}=\text{Pd}} = 1100$ ns, $\tau_{\text{ACN}}^{\text{M}=\text{Ag}} = 1450$ ns, and $\tau_{\text{ACN}}^{\text{Ru(phen)}} = 1400$ ns). The parent compound **Ru(bbip)** and the rhodium complex possess significantly shorter lifetimes ($\tau_{\text{ACN}}^{\text{M}=\text{Rh}} = 430$ ns and $\tau_{\text{ACN}}^{\text{M}=\text{f}} = 920$ ns). In oxygen free dichloromethane, only the rhodium complex exhibits a significantly shortened lifetime ($\tau_{\text{DCM}}^{\text{M}=\text{Rh}} = 900$ ns < $\tau_{\text{ACN}}^{\text{M}=\text{Pd,Ag,f}} \approx 1400$ ns). Data from aerated samples were collected for **Ru(bbip)** and **Ru(bbip)Ag**, but are not necessarily reasonable for the air and moisture sensitive silver complex. Nevertheless, lifetimes of roughly 200 ns were determined in acetonitrile and values of 550 and 400 ns were found in dichloromethane for the mono- and binuclear complex, respectively. These values are in good accordance to the previously determined values of **Ru(phen)**.

The transient absorption experiments were started with a comparative study of ¹MLCT absorption behavior of the monometallic complex **Ru(bbip)** and the potential bimetallic catalyst **Ru(bbip)Pd**. Using femtosecond experiments (see figure 103) shed light exclusively onto the early stages of the MLCT excited state formation (i.e., 480 nm, 150 fs). In line with literature results (cf. [Ru(bpy)₃]²⁺^[41]), it was observed in both complexes how the initial formed ¹MLCT excited states of **Ru(bbip)** and **Ru(bbip)Pd** rapidly underwent intersystem crossings to the corresponding triplet manifold ($\tau_{\text{ISC}}^{\text{Ru(bbip)}} \approx \tau_{\text{ISC}}^{\text{Ru(bbip)Pd}} < 150$ fs, as observed at $\lambda = 560$ nm). Absorption characteristics of the former include the typical minima (ground state bleach) at $\lambda = 443$ nm and maxima (excited

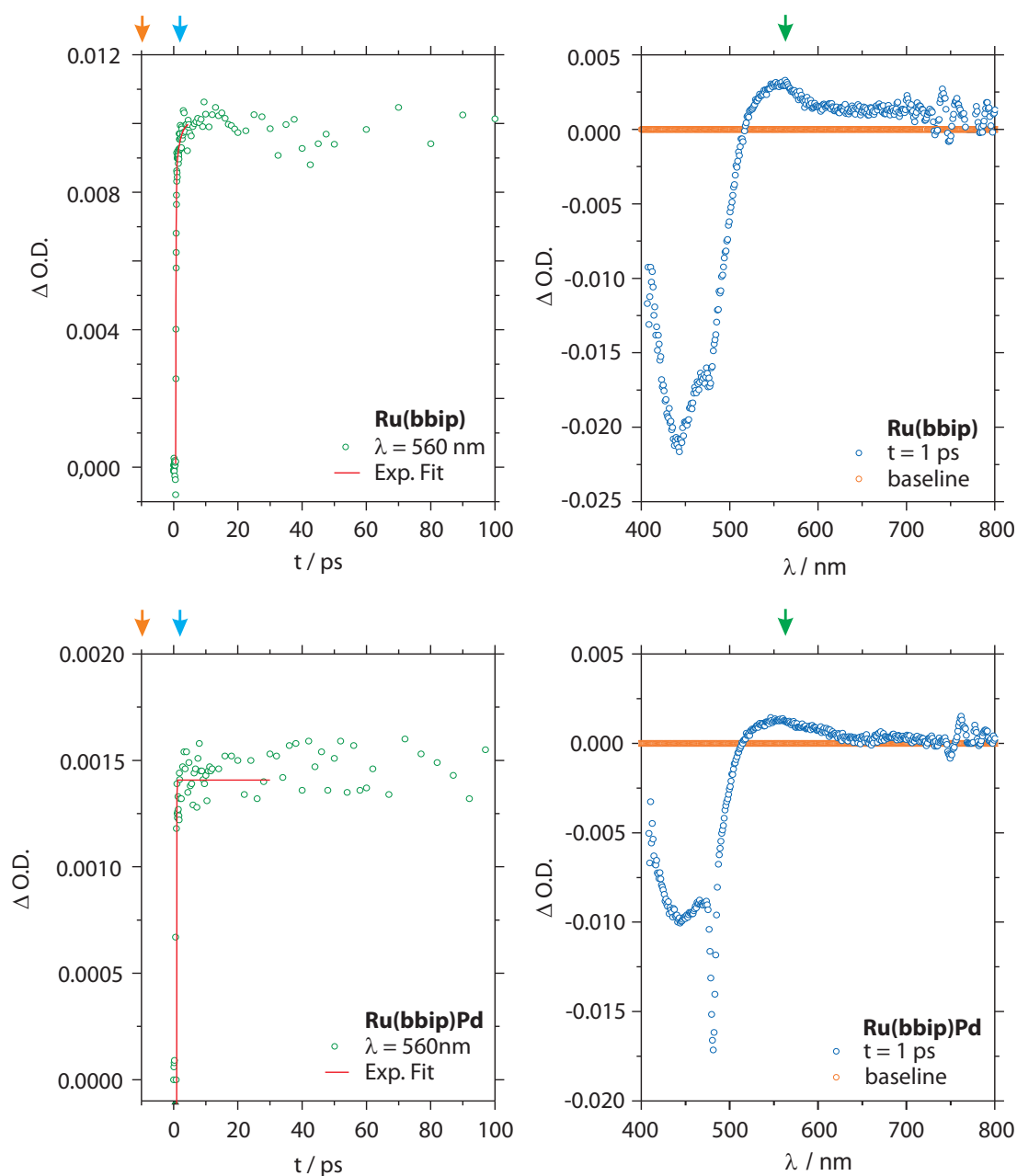


Figure 103: Derived time resolved (left) and wavelength resolved (right) excited state differential absorption spectra of **Ru(bbip)** (top) and **Ru(bbip)Pd** (bottom) in deaerated acetonitrile with femtosecond resolution, $\lambda_{\text{exc}} = 480 \text{ nm}$. The denoted arrows indicate the regions that were used for corresponding decay kinetics and differential spectra.

state absorption) at $\lambda = 560 \text{ nm}$, respectively. As expected, the recorded transient absorption spectra did not give rise to any appreciable decay on the 3 ns scale.

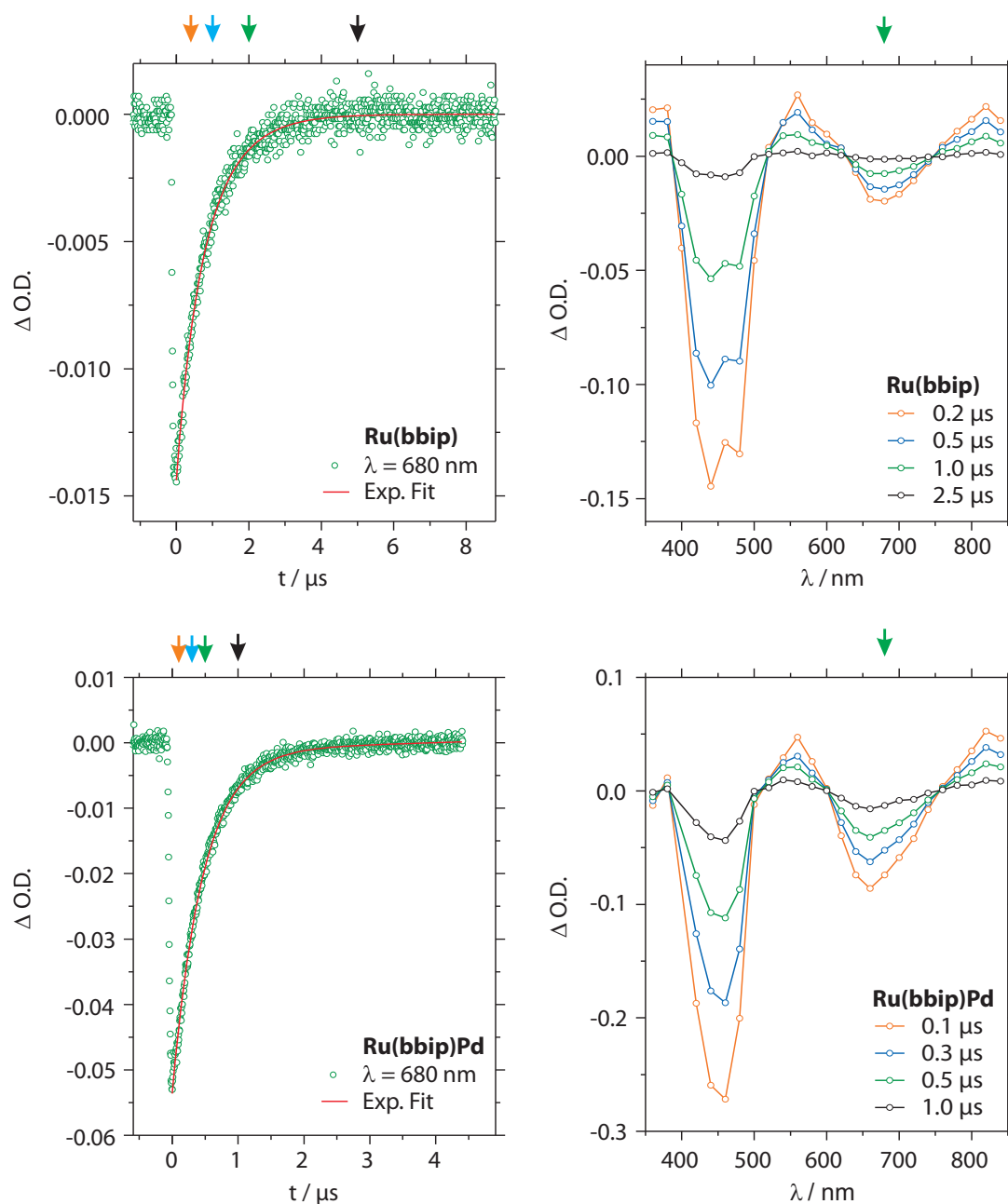


Figure 104: Derived time resolved (left) and wavelength resolved (right) excited state differential absorption spectra of **Ru(bbip)** (top) and **Ru(bbip)Pd** (bottom) in deaerated acetonitrile with nanosecond resolution, $\lambda_{exc} = 480 nm$. The denoted arrows indicate the regions that were used for corresponding decay kinetics and differential spectra.

Extension of the timescale to the microsecond detection window (i.e. $\lambda = 532 nm$, $t_{observed} = 6 ns$) revealed the 3MLCT excited state features with minima and maxima, similar to those seen toward

the end of the femtosecond experiments (see figure 104). However, a significant difference is that the 610 nm to 780 nm range of both transient species is now dominated by $^3\text{MLCT}$ centered emission with emission maxima at $\lambda = 660$ nm. The deviation from the determined emission maxima can be explained by the overlay of the absorption band of the excited species. For **Ru(bbip)Pd**, minima were registered at 460 nm and 665 nm as well as a maximum at 560 nm. The $^3\text{MLCT}$ excited states of both complexes decay back to the ground state with lifetimes of $\tau = 1.0 \mu\text{s}$, which is quantitatively similar to the observations of the time-resolved emission experiments in the absence of molecular oxygen. In these experiments, strict first order kinetics evolve (see figure 104 left). Importantly, no residual transitions, neither bleach nor positive absorption, remain at delay times beyond $20 \mu\text{s}$. In **Ru(bbip)**, and most relevant for catalytic aspects, in **Ru(bbip)Pd** an increased quantum yield of formation and lifetime of the excited state under retention of properties typical for ruthenium complexes were observed.

3.3.10 Electrochemical Characterization

The electrochemical investigations of the series of ruthenium complexes with **ip**, **bip**, **bbip** and **(bbip)Ag** ligands illustrate the rather small influence of the imidazole system on the redox potentials of the phenanthroline-type ligands and coordinated ruthenium centers (see table 15 and figure 105).

Table 15: Selected redox potentials $E_{1/2}$ (V) of the complexes **Ru(ip)**, **Ru(bip)**, **Ru(bbip)**, **Ru(bbip)Ag**, and references $[\text{Ru}(\text{tbbpy})_3]^{2+}$ and **Ru(phen)** (referenced vs. Fc/Fc^+ , $E_{1/2}(\text{Fc}/\text{Fc}^+) = 0.00$ V in a 0.1 M solution of Bu_4NPF_6 in dry acetonitrile under argon atmosphere).

Complex	$E_{1/2}(\widehat{\text{L}}^3)$ [V]	$E_{1/2}(\widehat{\text{L}}^2)$ [V]	$E_{1/2}(\widehat{\text{L}}^1)$ [V]	$E_{1/2}(\text{Ru}^{2+/3+})$ [V]
$[\text{Ru}(\text{tbbpy})_3]^{2+}$ ^[90]	-2.28	-2.02	-1.82	0.73
Ru(phen) ^[108, 120]	-2.23	-1.99	-1.80	0.78
Ru(ip)	-2.43	-2.09	-1.89	0.78
Ru(bip)	-2.23	-1.99	-1.76	0.81
Ru(bbip)	-2.25	-1.96	-1.76	0.86
Ru(bbip)Ag	-2.22	-1.96	-1.64, 1.29 (ir)	0.87

Typically, a fully reversible metal-based oxidation ($E_{1/2}(\text{Ru}^{2+/3+})$) is observed at redox potentials in the region between +0.78 V and +0.87 V with more positive values for the electron deficient

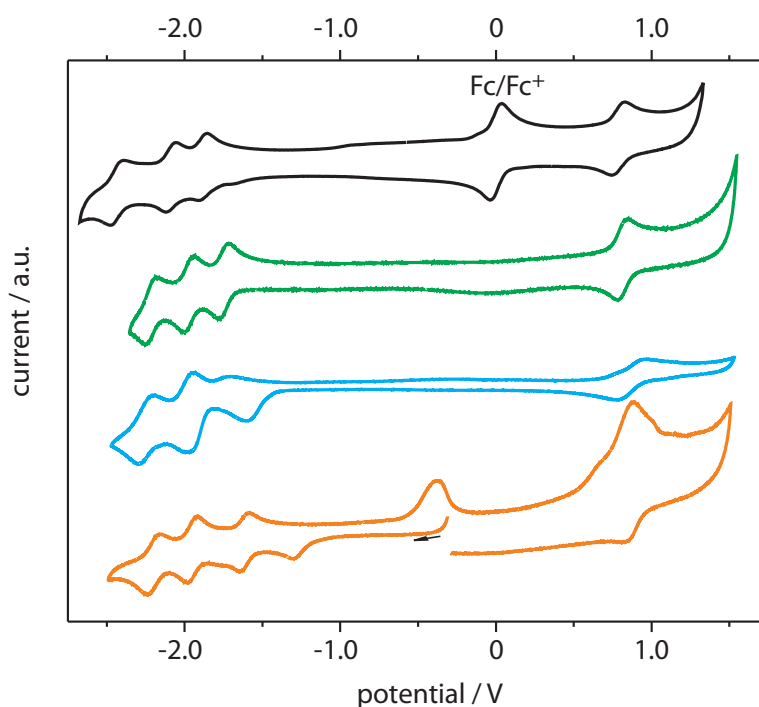


Figure 105: Cyclic voltammograms of ruthenium complexes with imidazophenanthroline derived ligands, measured in a 0.1 M solution of Bu_4NPF_6 in dry acetonitrile under argon atmosphere, referenced vs. Fc/Fc^+ , $E_{1/2} = 0.00$ V. **Ru(ip)** (—), **Ru(bip)** (—), **Ru(bbip)** (—), and **Ru(bbip)Ag** (—).

azolium salt **Ru(bbip)** and the carbene complex **Ru(bbip)Ag**. Furthermore, in all new ruthenium complexes three independent and quasi reversible redox waves were observed for the three reductions of the coordinated ligands ($E_{1/2}(\widehat{\text{LL}}^{1,2,3})$) at roughly -1.8 V, -2.0 V, and -2.2 V respectively. These findings are in accordance with other trislectopic $[\text{Ru}(\text{bpy})_3]^{2+}$ -type complexes such as **Ru(phen)** or $[\text{Ru}(\text{tbbpy})_3]^{2+}$. Among the complexes, the most significant differences exist between the first ligand-based reductions which can be attributed to the imidazophenanthroline systems. While the electron rich complex **Ru(ip)** exhibits a slightly more negative first reduction potential ($E_{1/2}(\widehat{\text{LL}}^1) = -1.89$ V), more positive ligand reductions were observed in **Ru(bip)** ($E_{1/2}(\widehat{\text{LL}}^1) = -1.76$ V) and **Ru(bbip)** ($E_{1/2}(\widehat{\text{LL}}^1) = -1.76$ V), respectively. Interestingly, square wave experiments revealed an unusual behavior of **Ru(ip)** which could be attributed to irreversible reduction of the protonated ligand in the reduction wave with formation of neutral **Ru(ip)** which exhibits a fully reversible electrochemistry (see figure 106).

Furthermore, the first ligand centered reduction in **Ru(bbip)** is not fully reversible which can be explained by reduction and possibly hydrogenation of the imidazolium moiety (see

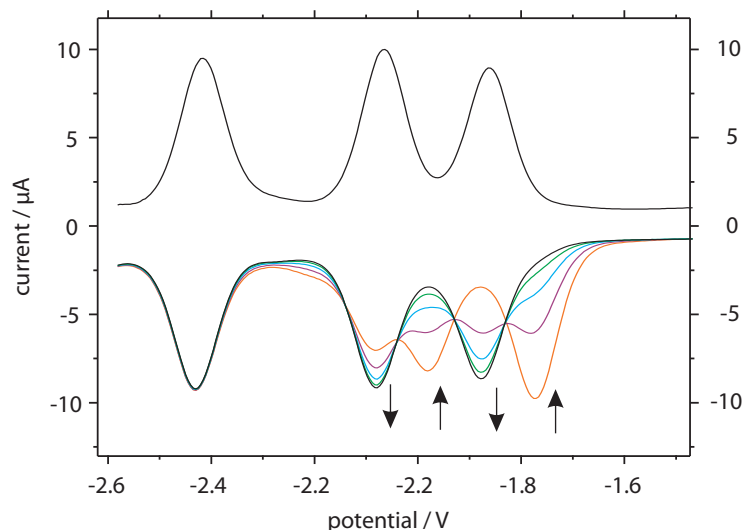


Figure 106: Change in the square wave voltammogram with respect to the three ligand centered reduction waves of **Ru(ip)** due to irreversible reduction of the formerly protonated complex within five cycles (scan rate 25 Hz).

figure 105).^[195] In the case of **Ru(bbip)Ag** additional irreversible reductions ($E_{1/2}(\widehat{\text{ir}}) = -1.29 \text{ V}$) and oxidations ($E_{1/2}(\widehat{\text{ox}}^1) = -0.38 \text{ V}$, and $E_{1/2}(\widehat{\text{ox}}^2) = +0.90 \text{ V}$) were found. A plausible explanation for the irreversible reduction is the decomposition of the NHC-Ag-Cl moiety of the complex, which results in the liberation of Cl^- and Ag^+ ions near the electrode surface. After the complex is altered, first irreversible oxidation peak appear which might be assigned to the Ag/Ag^+ stripping potential at the electrode. The very prominent irreversible oxidation around $+0.90 \text{ V}$ was assigned to the oxidation of the chloride counter ions of the complex.

After one completed cycle, additional irreversible signals are caused by decomposition remains at the electrode. In accordance to the results of the lifetime determinations, none or only little influence of the redox potentials by extension of the phenanthroline system by imidazole derivatives was observed.

The electrochemical characterization of the other binuclear complexes **Ru(bbip)Pd** and **Ru(bbip)Rh** was difficult and is not shown due to the negative effect of the Cl^- counter ions and deposition of reduced silver (from complex counter ions) and other metals on the electrodes.

Using **Ru(bbip)**, in addition, spectroelectrochemical reduction (-1.1 V) and oxidation ($+1.4 \text{ V}$) were performed. The oxidation results in the expected bleach of the MLCT absorption, while the reduction gives rise to the growth of a broad band with two maxima at 525 nm and 600 nm .

3.3.11 Application in Catalysis: Prove of Concept

Based on these results, indicating a retention of the $[\text{Ru}(\text{bpy})_3]^{2+}$ -type chromophore properties and a moderate electronic communication between the metal centers in **bbip**-bridged complexes, all four described **Ru(bbip)M** complexes (M: f = free, Ag = silver, Pd = palladium, Rh = rhodium) were tested as intramolecular $[\text{P} \sim \text{B} \sim \text{C}]$ -type photocatalysts (**P** = photocenter, **B** = bridge, **C** = catalyst) for hydrogen formation. Inspired by the positive results of HANSEN, using $[\text{Ru}(\text{bpy})_3]^{2+}$ and Pd-NHC complexes in intermolecular systems, similar intermolecular catalysis experiments were performed.^[71] In these, **Ru(bbip)** was tested for its capability to serve as chromophore together with $[\text{Pd}(\text{ACN})_2\text{Cl}_2]$ or $[\text{Rh}(\text{cod})\text{Cl}]_2$ as catalysts in $[\text{P} \sim \text{R} / \text{C}]$ -type systems (**R** = redox shuttle). The water concentration dependency, as well as the catalyst concentration dependency was tested. Finally, dynamic light scattering (DLS) experiments were performed to investigate a possible formation of colloids and other particles in the catalytic mixtures.

The photohydrogen production experiments were carried out in a home-built air-cooling apparatus for maintaining room temperature (22°C) and constant irradiation of the sample at a wavelength of $\lambda = 470$ nm (using LED sources suitable to excite the MLCT transition).^[116] 5 ml GC vials with a known headspace/solution ratio (3:2) were used as reaction vessels. Directly before the irradiation experiments, fresh stock solutions of the respective samples with solvent mixtures of acetonitrile, triethylamine and water with the desired concentrations of ruthenium complex were prepared in the dark under nitrogen atmosphere. Gas samples from the headspace were analyzed by GC-TCD after the irradiation to quantify the amounts of hydrogen gas which were formed. All experiments were repeated once for each reaction time and catalyst concentration.

In the beginning, mixtures of acetonitrile (solvent), triethylamine (electron donor) and water (proton source) in a 6:3:1-ratio (v:v:v), containing samples of the series of bimetallic catalyst with a known catalyst concentration of 250 μM , were examined (see figure 107).

The catalysis results for the ruthenium **bbip**-complexes during the course of five hours illustrate the catalytic activity of the palladium and rhodium complex. Surprisingly, even the silver complex exhibits a certain activity for photocatalytic hydrogen formation, whereas the starting material **Ru(bbip)** without a second metal center is inactive.

The highest turnover numbers (TONs) were observed for **Ru(bbip)Pd** with 30 turnovers after five

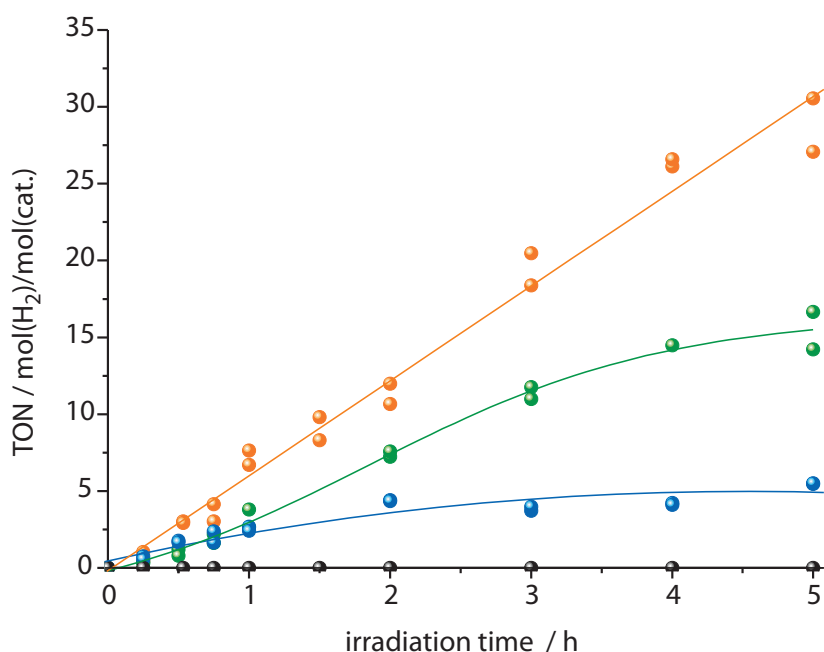


Figure 107: Time dependency of the catalytic activity in a 2 M solution of triethylamine in acetonitrile with 5% water. Determined turnover numbers (TONs) and fitted plots of the hydrogen generation of **Ru(bbip)Pd** (—●—), **Ru(bbip)Rh** (—●—), **Ru(bbip)Ag** (—●—), and reference **Ru(bbip)** (—●—) ($c_{\text{complex}} = 250 \mu\text{M}$).

hours at a constant turnover frequency (TOF) of 6 turnovers per hour. Important is the linearity of the hydrogen production during that time. Furthermore, in contrast to other intramolecular photoredox catalysts like $[(\text{tbbpy})_2\text{Ru}(\mu\text{-tpphz})\text{PdCl}_2]^{2+}$, no induction period was observed since hydrogen could be detected already after a few minutes of irradiation. Between five and ten hours a plateau is slowly reached. This effect is commonly explained by the gas exchange through the septum of the GC-vials (not designed for such catalysis experiments) or by side reactions in the catalytic mixture, e.g. reactions which consume the produced hydrogen or alter the chromophore-bridge-catalyst structure.

Importantly, the catalytic activity of the **Ru(bbip)Pd** catalyst is concentration independent as supported by independent studies with different concentrations ($c = 10 \mu\text{M}$, $25 \mu\text{M}$, $100 \mu\text{M}$ and $250 \mu\text{M}$, see figure 108) while and the intermolecular system **Ru(bbip)** + $[\text{Pd}(\text{ACN})_2\text{Cl}_2]$ loses its activity when low concentrations are applied.

The photocatalyst **Ru(bbip)Rh** ($c = 250 \mu\text{M}$) reaches a lower TON of 16 after 5 hours, whereas the plateau is reached and no further increase in the TON can be detected after longer irradiation

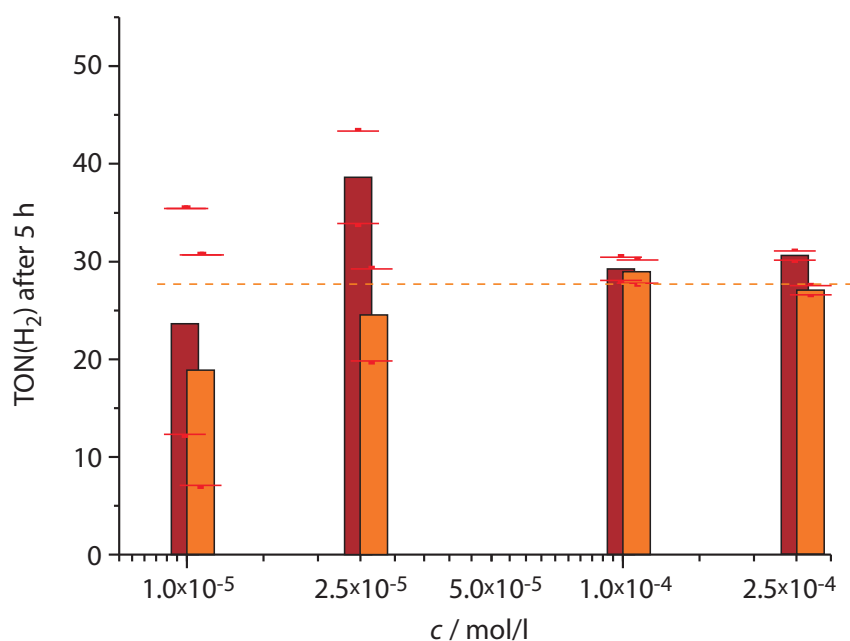


Figure 108: Catalysis concentration dependency of the intramolecularly working system **Ru(bbip)Pd**. Denoted error bars represent the 3σ region of the GC accuracy.

times. The concentration dependency of **Ru(bbip)Rh** was measured, but due to the low activity and the resulting very small concentrations of hydrogen gas in the headspace, the detection limit of the GC method was reached for lower catalyst concentrations (detection limit is 0.05% of H_2 in the GC sample, compare error bars in figure 108). Hence, it was not possible to separate the signal from the noise, so that no clear statement about a possible catalyst concentration dependency of the hydrogen production could be made.

Surprisingly, even the silver complex **Ru(bbip)Ag** showed some catalytic activity with 4 turnovers within five hours (compare figure 107). Again, no concentration dependency could be determined because of technical limitations. Finally, the control experiments, using the mononuclear complex **Ru(bbip)** show, as expected, no hydrogen production.

The observed constant turnover frequency, the missing induction phase and the concentration independency support the proposed *intramolecular* mechanism of the hydrogen formation, using **Ru(bbip)Pd**. To affirm this presumption, further investigations were performed.

Using **Ru(bbip)** as chromophore and $[Pd(ACN)_2Cl_2]$ as pre-catalyst in a $[[P \sim B / C]]$ -system, *intermolecular* control experiments were performed in the next step (see figure 109). All other parameters (light source, solvent mixture, catalyst concentration) were left unchanged.

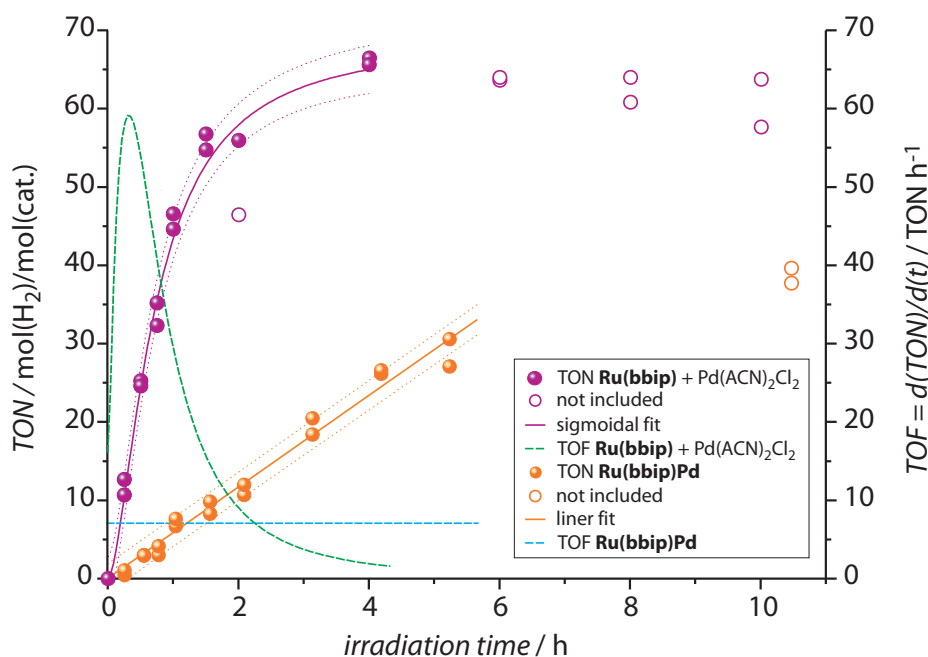


Figure 109: Fitted TONs and TOFs of hydrogen production with a 250 μM solution of **Ru(bbip)Pd** (TON: $\text{---}\bullet\text{---}$ and TOF: ---) and the control experiment (mixture of **Ru(bbip)** and $[\text{Pd}(\text{ACN})_2\text{Cl}_2]$), respectively, (TON: $\text{---}\bullet\text{---}$ and TOF: ---) in acetonitrile/water/triethylamine during the course of four hours. Later data was excluded from the fits.

In this control experiment, considerable amounts of hydrogen gas were found in the head space of the reaction vessels, which proves the photoredoxactivity of the **Ru(bbip)** chromophore. Upon the more detailed investigation, a very different activity could be observed for the intermolecular system in comparison to **Ru(bbip)Pd**, as can be seen in figure 109. A very fast rise in hydrogen production (TOF = 60 h^{-1} after 20 minutes) was detected and, furthermore, higher TONs (55) were detected within the first two hours. After 20 minutes, a beginning collapse of the catalytic activity (TOF = 10 h^{-1} after two hours) was observed in the multi-component system which eventually led to a complete loss of the catalytic activity within four hours (see figure 109, the green function denotes the derivative of the fitted TONs and thus represents the differential TOF). In comparison, a constant TOF of 6 h^{-1} is retained in **Ru(bbip)Pd** over six hours (see figure 109, the blue graph denotes the constant TOF).

In the intermolecular control experiments with **Ru(bbip)** and $[\text{Rh}(\text{cod})\text{Cl}]_2$ ($c = 250 \mu\text{M}$) turnover numbers with a maximum of 6 turnovers were found during the course of four hours. No further raise upon prolonged catalysis times could be observed. These values are low in

comparison to the intramolecular system **Ru(bbip)Rh** which produces 16 moles of hydrogen per mole of catalyst in the same time.

To further investigate the true nature of the catalyst and to obtain insights into the effect of colloid formation on the catalytic activity, dynamic light scattering (DLS) experiments were performed. As depicted in figure 110, catalytic mixtures of **Ru(bbip)Ag**, **Ru(bbip)Pd** and **Ru(bbip) + [Pd(ACN)₂Cl₂]** which were similar (inert cuvette instead of GC-vials) to the previously used hydrogen formation experiments were in situ examined during catalysis.

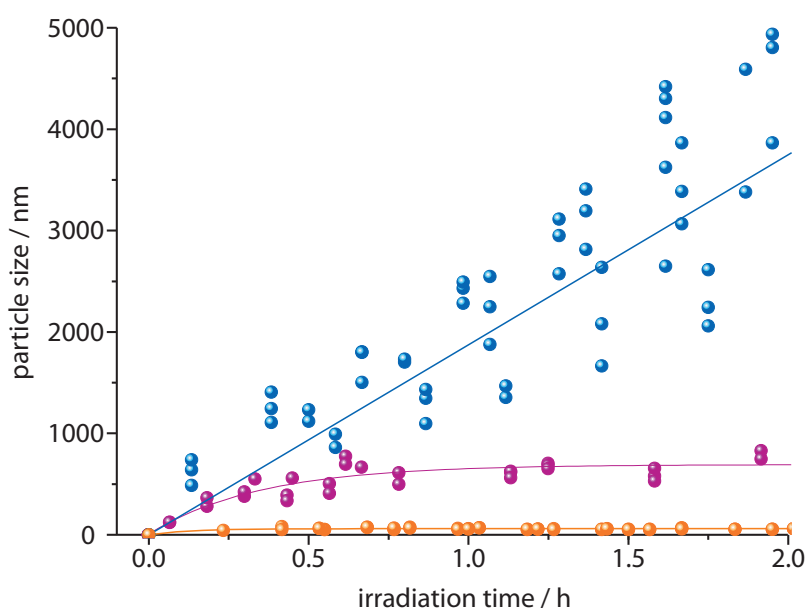


Figure 110: Particle sizes in the catalysis mixtures of **Ru(bbip)Ag** (—●—), **Ru(bbip)Pd** (—●—), and **Ru(bbip) + [Pd(ACN)₂Cl₂]** (—●—) during the first two hours of catalysis as determined by DLS.

The results prove the suitability of this method to detect and trace the formation of particles in the catalysis samples. Very prominent is the fast formation of large colloidal silver particles in the mixture of triethylamine, acetonitrile and water from **Ru(bbip)Ag** during irradiation. It can be expected that processes, similar to the photographic process, with reduction of silver(I) lead to particle formation. This observation corresponds to the electrochemical results of **Ru(bbip)Ag**, where irreversible redox processes were detected. Interestingly, no decomposition of the complex in the catalytic mixture was detected in the dark under otherwise unchanged conditions. Furthermore, light stability experiments in pure acetonitrile-*d*₃ show no signs of decomposition after irradiation of the NMR-sample for several hours (compare chapter 3.3.8

on page 141). From these facts it can be concluded that a combination of MLCT excitation and irreversible reduction by triethylamine have to take place in order to induce the colloid formation from **Ru(bbip)Ag**. Furthermore, it can be assumed that small silver colloids, which are known catalysts for hydrogen production, are responsible for the photocatalytic hydrogen production in corresponding experiments.^[196]

The DLS experiments with the *intermolecular* catalyst **Ru(bbip)** + [Pd(ACN)₂Cl₂] show as well considerable particle formation during the first two hours of the catalysis (see figure 111).

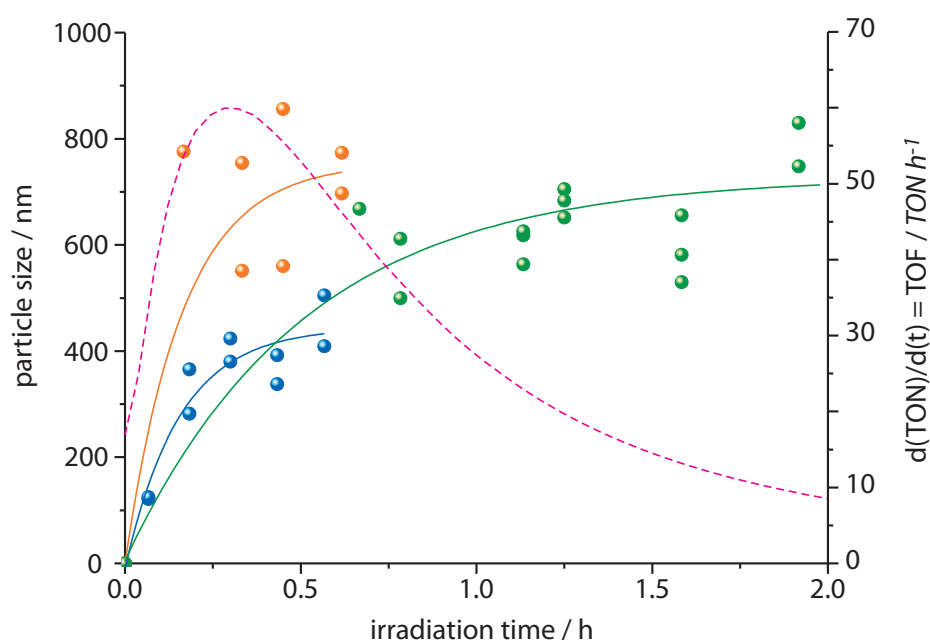


Figure 111: Short term (sample 1 (—●—), sample 2 (—●—)) and long term DLS results (sample 3 (—●—)) of intermolecular catalysis experiments with the mixture of **Ru(bbip)** + Pd(ACN)₂Cl₂ during the course of two hours ($c_{\text{cat.}} = 50 \mu\text{M}$) and TOF of hydrogen production (---) of a similar mixture.

The different samples show slightly differing particle sizes with different growth behavior, but in all cases a plateau is reached after roughly 45 minutes. By that time, particle diameters of several hundred nanometers ($d = 400 - 800 \text{ nm}$) are reached. A correlation of the particle size with the catalytic activity (TOF) of the samples identifies the most active catalytic time span in a region where the particles still grow. Thus, the numerous small colloids in solution present a large surface area during this early phase. The important conclusion that can be drawn here is that obviously small colloids ($<400 \text{ nm}$) which were formed upon photoreduction represent the active catalysts in this mixture and that the catalytic activity breaks down as the colloids grow beyond a value

where the surface/volume ratio becomes disadvantageous.^[32, 34, 94]

Finally, DLS experiments with **Ru(bbip)Pd** were performed. Also in this case a clear formation of particles could be observed (see figure 112).

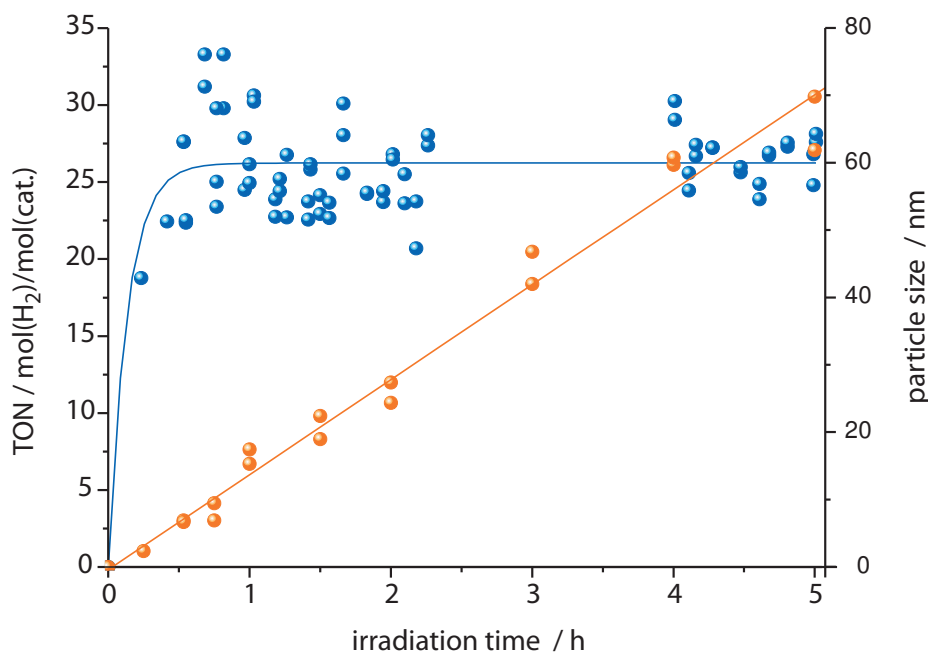


Figure 112: DLS results (—●—) of intramolecular catalysis experiments with **Ru(bbip)Pd** during the course of five hours ($c_{\text{cat.}} = 250 \mu\text{M}$) and TON of hydrogen production (—●—) of a similar mixture.

In contrast to the results obtained for **Ru(bbip) + [Pd(ACN)₂Cl₂]**, first particles form after 15 minutes of irradiation, while no particles were present in the beginning. Furthermore, here diameters reach a plateau at very small average diameters of ~60 nm after roughly one hour and maintain at this value at least for the following five hours. A correlation between the catalytic activity and the particle diameter may be possible because hydrogen is formed while particles were detected. However, DLS does only yield size distributions and an average diameter while numbers of particles cannot be detected, at least two different aspects need to be discussed.

On the one hand, it can be assumed that the particles refer to active catalysts, as the 60 nm colloids are formed after 15 minutes. For the first hour of catalysis small total volumetric amounts of hydrogen are present in the vials, leading to some uncertainties in the assignment of catalytic activity. Furthermore smaller colloids, causing the early catalytic activity (0 - 1 h) could not be detected. As the detection limit of the DLS is 0.6 nm, this is rather unlikely. The late catalytic

activity (1 - 5 h) could be explained by a stabilization of the catalytically active colloids in the mixture, which was found to be active at a constant rate for at least five hours.

On the other hand, it can be assumed that the particles represent an inactive species. Thus, it is possible that remaining complex silver counter ions in solution (found as impurities already in **Ru(bbip)Rh**, see page 137), decompose upon irradiation and leads to the observed particles. Therefore, it is possible to assign the complete catalytic activity (0 - 5 h) to the intramolecular catalyst **Ru(bbip)Pd**. As the catalysis shows very little correlation to the detected particle growth kinetics, they do not seem to be involved in catalytic turnover.

A third explanation for the detected particles could be the formation of hydrogen bubbles with a diameter of roughly 80 nm in the active mixture which would interfere with the detection method and which would be hidden in the other experiments due to the detection of larger particles.

Several relevant conclusions can be drawn from these facts. First, **Ru(bbip)** serves as photocenter in inter- and intramolecular systems with three different catalytic centers.

Second, in the case of **Ru(bbip)Ag**, a correlation between visible light irradiation, catalytic hydrogen formation and colloid formation with steadily growing diameter in the catalytic mixture (in the presence of triethylamine) draws the picture of a photodecomposition reaction of this species, whereas the early formed particles exhibit a limited catalytic activity.

Third, in the case of **Ru(bbip)Rh** and the intermolecular control experiment, only a limited catalytic activity with alike low TONs could be observed.

Fourth, the intermolecular catalyst $\text{Ru}(\text{bbip}) + [\text{Pd}(\text{ACN})_2\text{Cl}_2]$ shows a considerable particle formation which causes, as observed in the case of **Ru(bbip)Ag**, hydrogen formation with a very high activity during the early phase of catalysis.

And fifth, especially for **Ru(bbip)Pd** the lack of an induction phase, the catalyst concentration independence of the activity, the constant turn over frequency and the lack of large particle formation support the assumption of increased chemical stability of the catalyst and importantly a possible intramolecular hydrogen formation mechanism. As no further particle growth was observed, indicating a stabilization in size, an intermolecular mechanism which involves an equilibrium of particle formation and destruction (**Ru(bbip)** is not active itself, palladium particles grow up to 800 nm) could not be ruled out completely.

Finally, with respect to the DLS experiments, it was proven that this new analysis method can be used to quickly and easily obtain on-line insights into important aspects of the catalysis such as

particle formation kinetics and size distributions. Nevertheless, a combination and correlation of DLS and other methods such as TEM and XPS may be necessary to clarify the complete mechanism of the catalysis.

3.4 Outlook, Exploratory Investigations and Perspectives

After the completed work with the binuclear **bbip**-bridged complexes, a number of preliminary results and exploratory work will be presented in this following chapter of the thesis. A number of experiments were performed to fathom future developments of the imidazophenanthroline containing systems. To receive an impression of the potential thereof, it was attempted to increase the already high quantum yields of the ruthenium **bbip**-complexes. Furthermore, it was tried to change the electronic properties of the bridge, particularly of the electron storage capacity of the ³MLCT-involved LUMO, by the introduction of electron withdrawing groups. Finally, an extension of the bridge was attempted to allow for additional chromophores or catalyst centers in the resulting oligonuclear photocatalyst. Note: it is NOT claimed that a complete characterization of the prepared substances or a full evaluation or explanation of observed results was given, therefore, only selected data will be presented.

3.4.1 Manipulations, Involving the **bbip**-System

With **bbip** in hands, it was an interesting starting point to further explore the effect of this ligand on ruthenium type chromophores. From section 3.3.8 (page 138) it was known that **Ru(bbip)** has interesting photophysical properties such as far bathochromically shifted emission wavelength ($\lambda_{\text{em., ACN}}^{\text{Ru(bbip)}} = 663 \text{ nm}$) and very strong emission intensity ($\Phi_{\text{ACN}}^{\text{Ru(bbip)}} = 0.26$).

The usually high quantum yields of **Ru(bbip)** obviously correlate with the presence of one **bbip** ligand. Based on the developed synthetic expertise, it was attempted to prepare the trishomoleptic complex $[\text{Ru}(\text{bbip})_3]^{2+}$ (**Ru(bbip)₃**) which should be even more electron deficient than **Ru(bbip)** and thus should show higher emission quantum yields. Furthermore, a reference compound would be generated to compare the photophysical and electrochemical characteristics (see figure 113). The reaction was performed with an excess of **bbip** to avoid an incomplete formation. $[\text{Ru}(\text{cod})\text{Cl}_2]$ and **bbip** were taken up in DMF and were heated for 2h in the microwave. Already after several minutes a colorchange into blue was observed, which is typically the indication for the

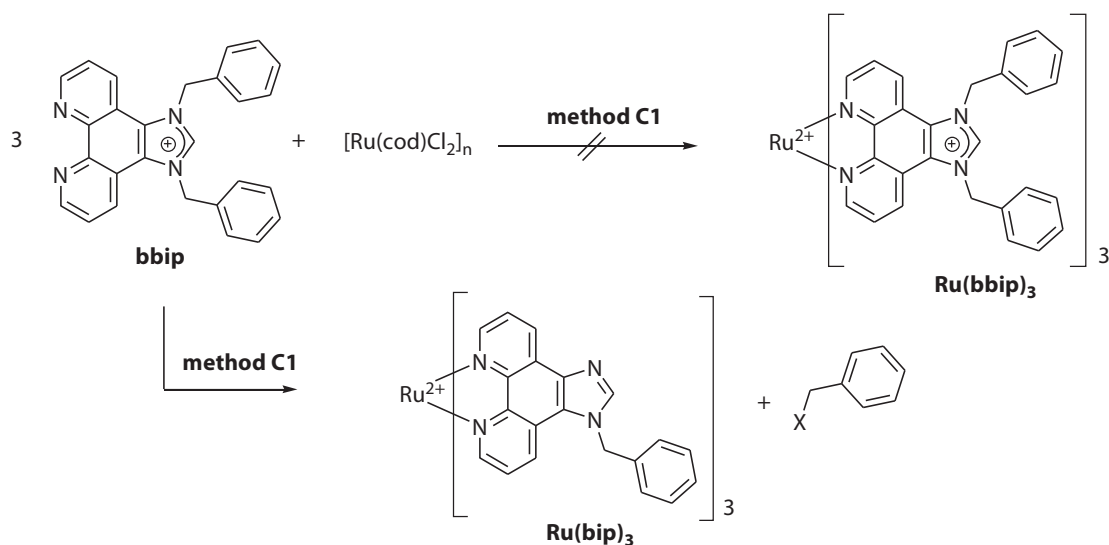


Figure 113: Attempted synthesis of $[\text{Ru}(\text{bbip})_3]^{2+}$.

formation of the $[\text{Ru}(\text{LL})\text{Cl}_2]$ -type complexes. After two hours, DMF was removed and a mixture of ethanol/water was added to the dark residue. Refluxing for two more hours in the microwave according to **method C1** gave a bright red product which was analyzed by ^1H -NMR spectroscopy (see figure 114).

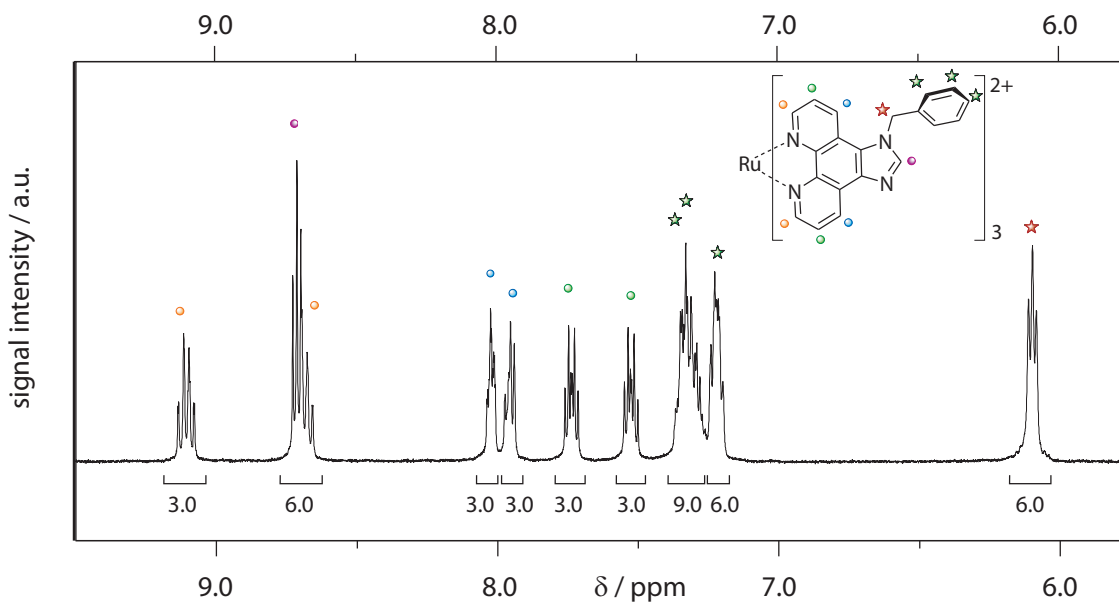


Figure 114: ^1H -NMR spectrum of $\text{Ru}(\text{bip})_3$ in methanol- d_4 .

The analysis of the obtained product gives clear evidence for the decomposition of the

ligand structure since integration of the phenyl ring-related protons does not sum up to 30 but rather 15 protons and, furthermore, a typical spectrum of a complex with asymmetric imidazophenanthroline moiety was found instead of the expected highly symmetric one. Further attempts to obtain ruthenium complexes with multiple NN-NHC bridging ligands were not made because it was concluded, that possibly the high charge of the resulting compound in combination with the applied high temperatures (153°C) might be the reason for the decomposition of the product (**bbip** was prepared from **bip** in DMF at 60-80°C). The alkylation of $[\text{Ru}(\text{bip})_3]^{2+}$ might open the access to such complexes, but was not tried.

3.4.2 Electron Deficient **bbip**-Systems

From the results in chapter 3.1 (page 54 ff.) it was known that bromo substituents at the phenanthroline backbone result in a lowering of the particular ligand LUMO orbital in a $[\text{Ru}(\text{LL})_3]$ -type complex. This may be the reason that the resulting $^3\text{MLCT}$ state in a heteroleptic tris-chelate complex is predominantly localized on that particular ligand as observed in bromo substituted *tpphz* derivatives.^[125, 126] Therefore, it is of great interest to design electron accepting bridging ligands to enforce the unidirectional electron transfer to a second metal center in a monomolecular $[\text{P} \sim \text{B} \sim \text{C}]$ -type photocatalyst. In a targeting study 1,3-dibenzyl-5,10-dibromo-1*H*-imidazo[4,5-*f*][1,10]phenanthroline bromide (**Br₂bbip**) was prepared in a two step synthesis from 3,8-dibromo-1,10-phenanthroline-5,6-dione (**Br₂phenO₂**) according to a combination of **method L2** and **method L3** in a similar manner as the case of the previously prepared ligand **bbip** (see figure 115).

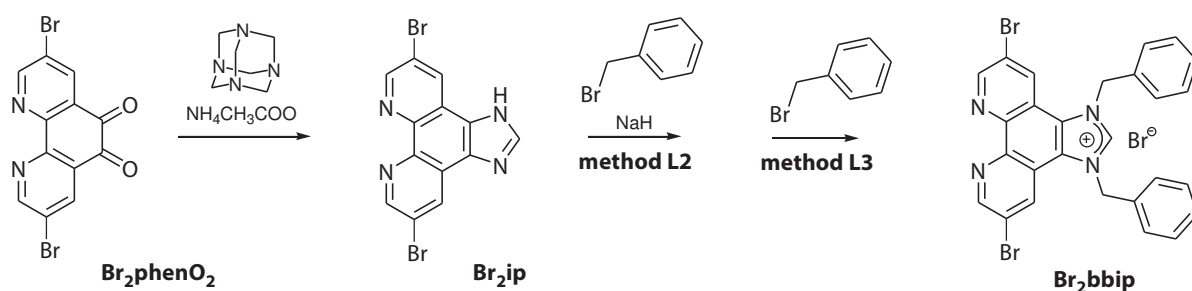


Figure 115: Three step synthesis of **Br₂bbip**.

Detection of the product and determination of the product purity was performed, using ^1H -NMR

techniques. The reaction of **Br₂phenO₂** with hexamine and ammonium acetate in acetic acid gave 5,10-dibromo-1*H*-imidazo[4,5-*f*][1,10]phenanthroline (**Br₂ip**) -very similar to **ip** in color and solubility- in 70% yield. A clear indication for the formation was the singlet signal of the proton in 2-position at $\delta_{(2)}^{\text{Br}_2\text{ip}} = 8.90$ ppm in combination with a symmetric ¹H-NMR-spectrum, similar to that of **ip** but without signals for the 5,10-positions.

Subsequent benzylation if **Br₂ip** was performed according to a combination of **method L2** and **method L3** in a one pot reaction. Workup of the product gave a pure compound in an overall yield of 57% as indicated by ¹H-NMR studies. The NMR-spectrum showed similar peak patterns with the expected symmetry of the **ip**-backbone, the singlet signal of the 2-proton ($\delta_{(2)}^{\text{Br}_2\text{bbip}} = 9.76$ ppm) and the aromatic and aliphatic signals of the benzyl groups with the expected integral values as observed for **bbip**. Furthermore, no signals of the asymmetric intermediate were found. Mass spectrometry or ¹³C-NMR spectroscopy were not available at that time and further characterizations were set aside after the results of the following step emerged.

Finally, the synthesis of $[\text{Ru}(\text{tbbpy})_2(\text{Br}_2\text{bbip})]^{2+}$ (**Ru(Br₂bbip)**) was attempted next. As previously described for the synthesis of **Ru(bbip)**, **Br₂bbip** was reacted with $[\text{Ru}(\text{tbbpy})_2\text{Cl}_2]$ in a mixture of ethanol/water in the microwave according to **method C1** (see figure 116).

For this reaction long irradiation times (5h) had to be applied before the typical color change into red could be observed. Workup and counter ion exchange with NH₄PF₆ yielded a dark red product. Counter ion back-exchange and precipitation with Bu₄NCl in aprotic solvents (ethyl acetate/acetone) was used to remove the dark starting material $[\text{Ru}(\text{tbbpy})_2\text{Cl}_2]$ soluble therein. ¹H-NMR investigation of the obtained chloride salt exhibited an unexpectedly asymmetric set of five **ip**-type signals instead of three. Furthermore, a 50% lower integral value of the aromatic and aliphatic benzyl signals was observed. These findings were once again strong indicators for a decomposition of the ligand during the reaction, as observed in the previous case of the attempted preparation of **Ru(bbip)₃** which lead to **Ru(bip)₃** instead.

Recrystallization of the obtained product from a mixture of diethyl ether/chloroform by slow evaporation gave suitable crystals for X-ray diffraction experiments. The results clearly indicate the formation of $[\text{Ru}(\text{tbbpy})_2(\text{Br}_2\text{bip})\text{Cl}_2]$ which was not attempted (see figure 117 and see table 16 on page 171). Note: KARNAHL et al. have also observed unusual reactions of bromo-substituted phenanthroline derivatives.^[126]

The X-ray data indicated that the imidazole rings in **Ru(Br₂bip)** and the formerly prepared

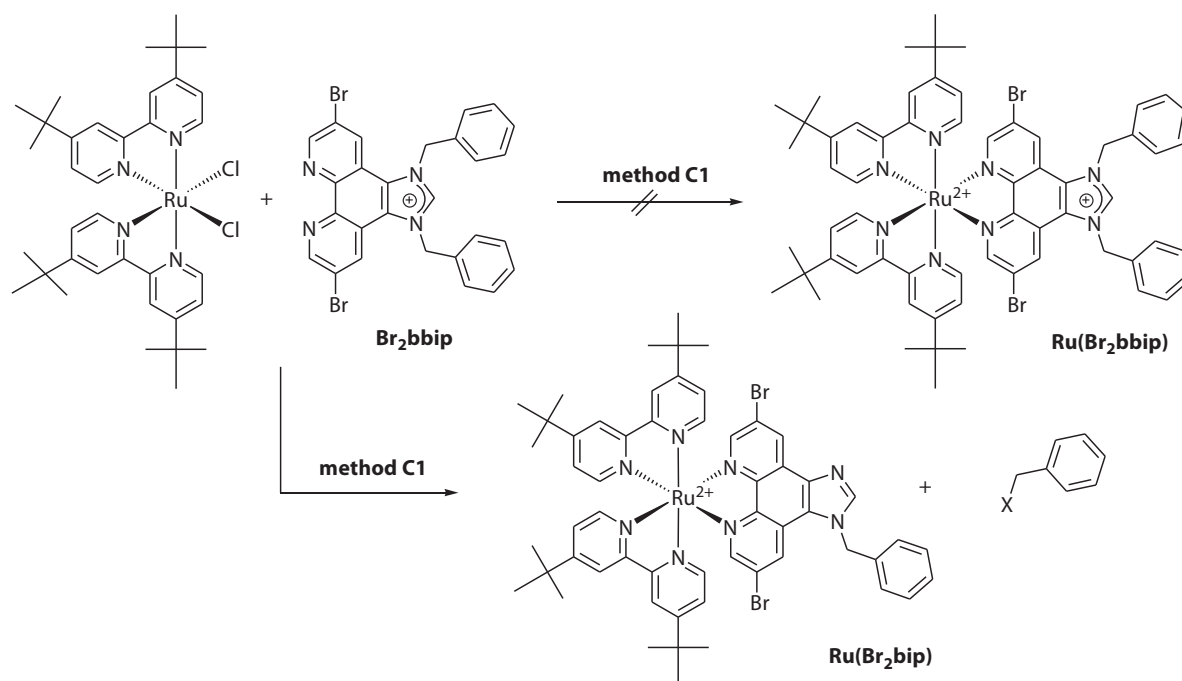


Figure 116: Attempted synthesis of $[Ru(tbbpy)_2(Br_2bbip)]^{2+}$ ($Ru(Br_2bbip)$), yielding $[Ru(tbbpy)_2(Br_2bip)]^{2+}$ ($Ru(Br_2bip)$) as product of the reaction instead.

$Ru(bip)$ (compare chapter 3.3.6 on page 130 ff.) have identical C-N and C-C distances and equivalent bond angles at the analogical positions, except for the C13-N4 distance which is shorter in the brominated compound. In both complexes, differences in the opposing C-N-C angles and N-C-C angles of the imidazole rings are present. Thus, $Ru(Br_2bip)$ exhibits a by $\sim 7^\circ$ wider N4-C6-C5 angle than N3-C5-C6 angle (e.g. $\angle_{(N4,C6,C5)}^{Ru(Br_2bip)} = 111.4(6)^\circ > \angle_{(N3,C5,C6)}^{Ru(Br_2bip)} = 104.7(6)^\circ$). Additionally, $Ru(Br_2bip)$ exhibits a more acute angle at the N4 atom when compared to the N3 atom ($\angle_{(C13,N3,C5)}^{Ru(Br_2bip)} = 106.3(6)^\circ > \angle_{(C13,N4,C6)}^{Ru(Br_2bip)} = 102.9(6)^\circ$). The N3-C13-N4 angles are the widest angles of the imidazole ring in both complexes ($\angle_{(N3,C13,N4)}^{Ru(Br_2bip)} = 114.7(7)^\circ = \angle_{(N3,C13,N4)}^{Ru(bip)} = 113.5(5)^\circ$). The angles of the twisted benzyl functionality differ from the previously observed and are, therefore, arbitrary due to packing effects. In comparison to the imidazole system, a higher symmetry was found in the phenanthroline sphere which exhibits identical bond lengths and angles at opposing positions. A dominant structural influence of the bromo substituents was not observed. The values for the Ru-N distances are consistent with the previously obtained data and with other ruthenium phenanthroline complexes.

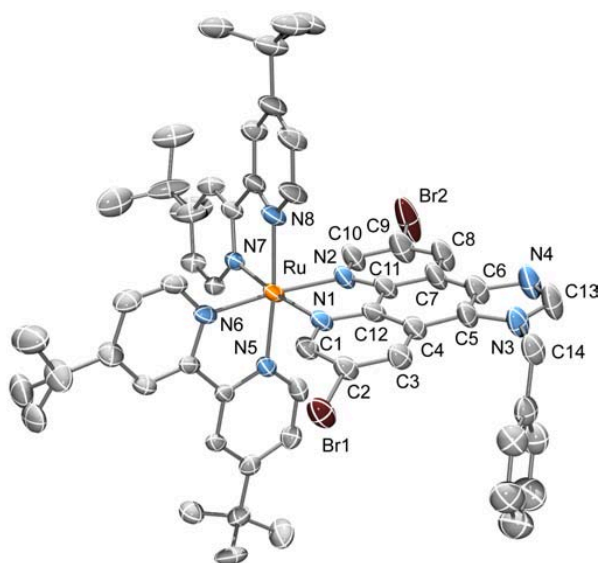


Figure 117: Solid state molecular structure of **Ru(Br₂bbip)**. Counter ions, hydrogen atoms and coordinated solvents were omitted for clarity. Ellipsoids were drawn at the 50% probability level. Compare table 16 on page 171 for selected bond lengths and angles.

3.4.3 NHC-Ligand edip: Further Development of Improved Catalysts

For a further stabilization of the NHC bound metal center and thus to avoid colloid formation during photoreduction, it is important to expand the coordination sphere around the active metal. With respect to the constitution of natural systems, such as the oxygen evolving complex or the iron hydrogenases it may be helpful to construct multimetallic active sites. Furthermore, it was shown by AUTH et al. that an increased number of photocenters, as observed in natural photosynthesis, may have a positive effect on the catalytic activity of the catalyst.^[116, 117, 95, 19] In a wider scope, polydentate ligands may lead to a self-assembly of polynuclear coordination arrays with interesting application potential in catalysis, as shown by SAKAI et al., and other fields such as molecular information storage or molecular magnetism as demonstrated by LEHN et al.^[92, 197, 198] In this context, caliper-like NHC ligands were prepared by LIU et al. to stabilize binuclear silver complexes.^[55] The transmetallation to the resulting palladium complexes was performed in the work group of RAU (compare figure 28 (d) on page 39). Importantly, the latter was proven to be an active catalyst for proton reduction in intermolecular photoredox catalyses in mixtures of acetonitrile/triethylamine/water.^[71]

Inspired by this work, the concept of a new bridging ligand was designed (see figure 118) which

combines the concept of **ip**-bridges with the binuclear palladium catalyst, so that intramolecular photocatalysts can be generated which carry two $\{\text{Ru}(\widehat{\text{LL}})_3\}^{2+}$ -type chromophores. Thus, purposeful functionalization of the imidazole nitrogens with aryl bridge/spacer was attempted to yield a suitable 1-substituted, 3-bridged bis-1*H*-imidazo[4,5-*f*][1,10]phenanthroline salt (see figure 118).

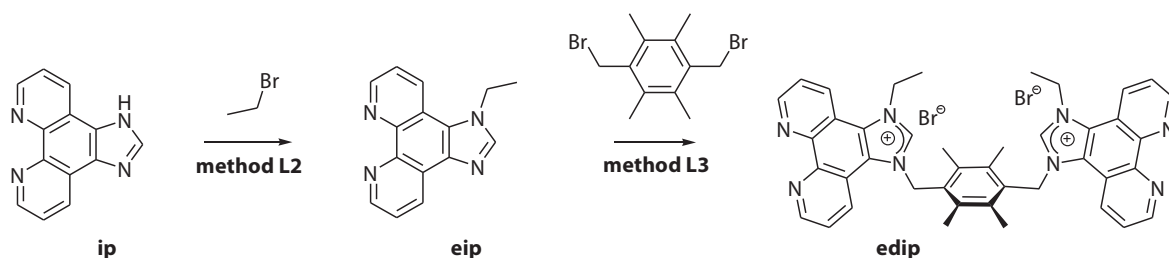


Figure 118: Two-step synthesis of 1,1'-[(2,3,5,6-tetramethylbenzene-1,4-diyl)dimethanediyl]bis(3-ethyl-1*H*-imidazo[4,5-*f*][1,10]phenanthroline) dibromide (**edip**).

The selective introduction of an ethyl moiety into the 1-position of **ip** was achieved according to **method L2** via the substitution reaction with ethyl bromide to yield 1-ethyl-1*H*-imidazo[4,5-*f*][1,10]phenanthroline (**eip**) in good yields.

The ^1H -NMR-spectrum showed similar peak patterns as **ip**, with the expected asymmetry of the **ip**-backbone, the singlet signal of the 2-proton ($\delta_{(2)}^{\text{eip}} = 7.96$ ppm) as well as the aliphatic signals of the ethyl group with the correct integral values and similar chemical shifts, as observed in the case of **bip** ($\delta_{(\text{CH}_2)}^{\text{bip}} = 4.611$ ppm (q, 2H, $^3J = 7.2$ Hz) and $\delta_{(\text{CH}_3)}^{\text{bip}} = 1.655$ ppm (t, 3H, $^3J = 7.2$ Hz)). Assignment of the ^{13}C -NMR-signals reveals chemical shifts, which are consistent with previous data (e.g. $\delta_{(\text{C}2)}^{\text{eip}} = 141.98$ ppm, compare $\delta_{(\text{C}2)}^{\text{bip}} = 143.54$).

After its successful synthesis, **eip** was used as starting material in the reaction with 4,6-dibromomethylidurene according to **method L3**. This transformation gave 1,1'-[(2,3,5,6-tetramethylbenzene-1,4-diyl)dimethanediyl]bis(3-ethyl-1*H*-imidazo[4,5-*f*][1,10]phenanthroline) dibromide (**edip**) as a white precipitate in 50% yield. The formation of the desired compound was confirmed via ^1H - and ^{13}C -NMR spectroscopy and mass spectrometry. In the ^1H -NMR spectrum of the asymmetric compound all eleven (seven aromatic and four aliphatic) signals were found (see figure 119 on page 166). Of interest is the characteristic singlet of the proton in 2-position ($\delta_{(2)}^{\text{edip}} = 9.04$ ppm) and the singlet of the durene methyl groups ($\delta_{(\text{CH}_3\text{-Ar})}^{\text{edip}} = 2.25$ ppm).

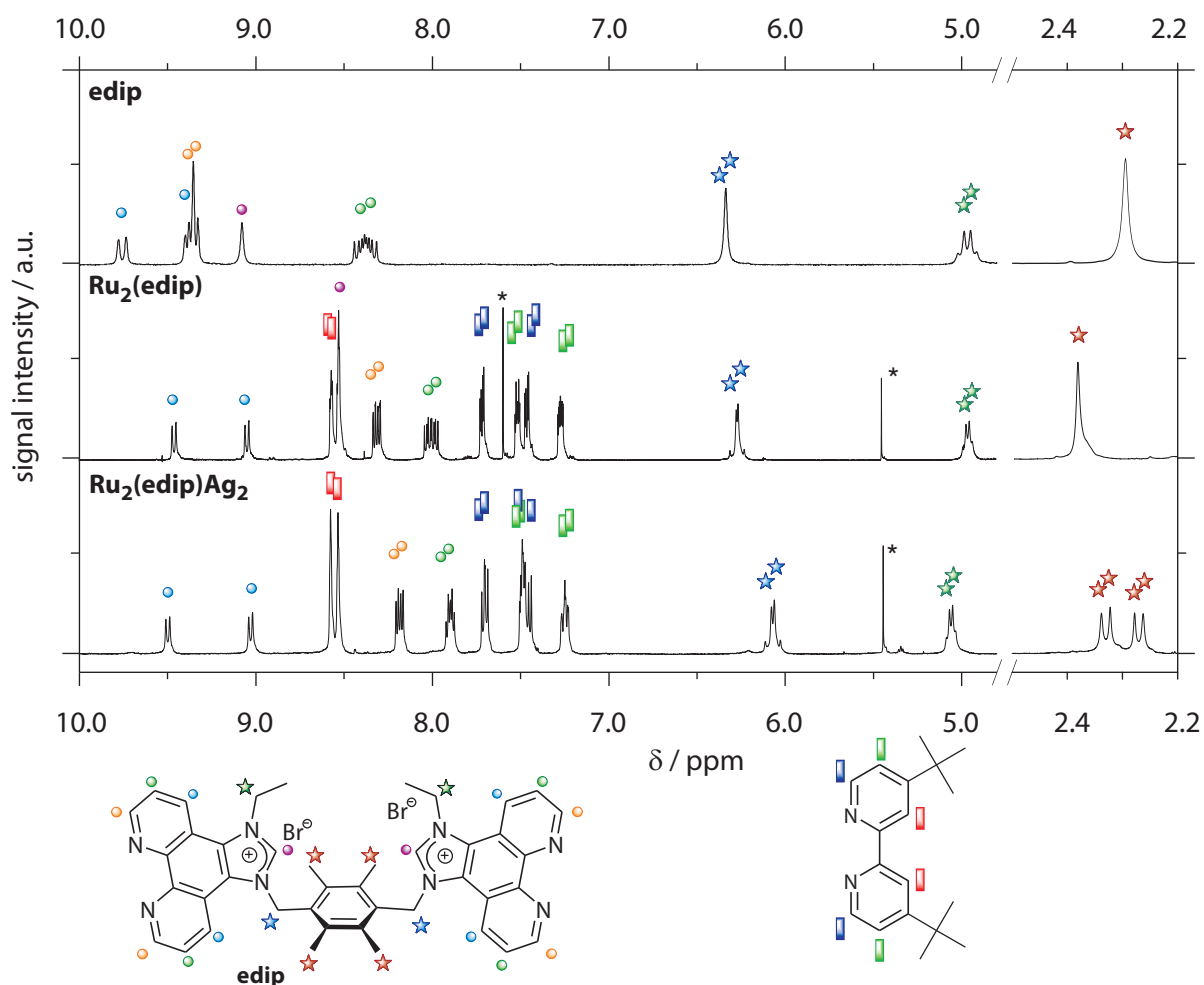


Figure 119: Relevant region of the ^1H -NMR spectra of the series of prepared **edip** carrying complexes **Ru₂(edip)** and **Ru₂(edip)Ag₂** in acetonitrile-*d*₃ and of the parent compound in methanol-*d*₄ with denoted peak assignments (signals with black asterisk are solvent impurities).

Furthermore, all signals were assigned in the carbon NMR-spectrum (e.g. $\delta_{(2)}^{\text{edip}} = 140.07$ ppm and $\delta_{(\text{CH}_3\text{-Ar})}^{\text{edip}} = 15.67$ ppm). FAB-MS showed the molecular ion $[\text{M}+\text{H}+2\text{Br}]^+$ at 812 m/z.

In addition to the MS and NMR characterization of the products, it was possible to obtain suitable crystals of the compounds for X-ray diffraction experiments (see figure 120 and compare table 16 on page 171).

The structural features, observed for the organic compounds combine both, the general patterns of phenanthrolines and that of benzimidazole derivatives, respectively. Therefore, attention was focused on the two coordination sites in the structural characterization of the new **ip**-type ligands.

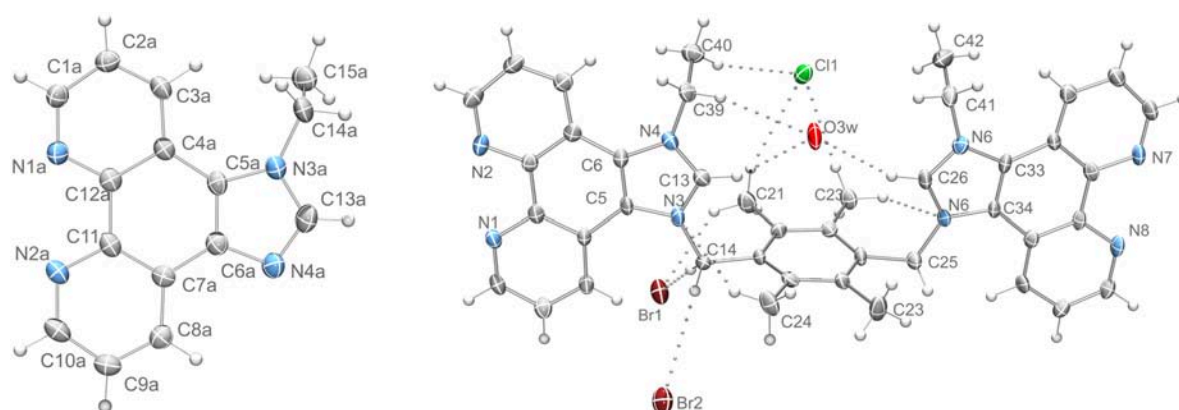


Figure 120: Solid state molecular structures of **eip** (left) and **edip** (right). Ellipsoids were drawn at the 50% and 70% probability level respectively. Compare table 16 on page 171 for selected bond lengths and angles.

Furthermore, similar chemical behaviors and good structural relationships exist between **eip** and **bip**, and between **edip** and **bbip** respectively, therefore, the same numbering scheme was applied to all ligands for convenience reasons (see chapter 3.3.3 on page 118).

With respect to **bip**, no significant changes in distances and angles of the **ip**-skeleton were observed in **eip**. Only the C1-N1-C12 angle of the phenanthroline sphere is slightly increased in **bip**, which might be an effect of the coordinated solvent water in the latter ($\angle_{\text{Cl,N1,C12}}^{\text{bip}} = 118.38(15)^\circ > \angle_{\text{Cl,N1,C12}}^{\text{eip}} = 117.6(2)^\circ$).

Furthermore, **eip** exhibits the same asymmetry of bond lengths and angles in the imidazole ring of the imidazophenanthroline backbone as observed in **bip**, which is a result of the partial double bond character between C13 and N4 and of the asymmetric substitution. Therefore, **eip** exhibits a significantly shortened C13-N4 bond in comparison to the C13-N3 bond ($d_{\text{C13-N3}}^{\text{eip}} = 1.361(3) \text{ \AA} > d_{\text{C13-N4}}^{\text{eip}} = 1.314(4) \text{ \AA}$). An other effect is that the opposing angles of the imidazole moiety at C5/C6 and N3/N4 differ significantly ($\angle_{\text{C13,N3,C5}}^{\text{eip}} = 105.9(2)^\circ > \angle_{\text{C13,N4,C6}}^{\text{eip}} = 103.7(2)^\circ$ and even more: $\angle_{\text{N3,C5,C6}}^{\text{eip}} = 105.3(2)^\circ < \angle_{\text{N4,C6,C5}}^{\text{eip}} = 111.1(2)^\circ$), which was also observed in **bip**. The opposing sides of the phenanthroline sphere show no asymmetry which supports the picture of a phenanthroline sphere which is independent of the variable imidazole moiety.

The imidazolium salt **edip** is best compared to the imidazolium salt **bbip**. Although **edip** exhibits an asymmetric substitution pattern, a highly symmetric **ip**-skeleton with respect to bond distances and angles was found. The only difference exists between the opposing angles around C5 and C6

($\angle_{\text{N3,C5,C6}}^{\text{edip}} = 107.8(5)^\circ > \angle_{\text{N4,C6,C5}}^{\text{edip}} = 105.6(5)^\circ$). These effects are possibly due to the loss of double bond character between C13 and N4 in comparison to **eip** and sterical or packing effects of the alkyl moieties. Importantly, no significant changes at all were found between the equivalent bond lengths and angles, comparing **edip** and **bbip** (e.g. $\angle_{\text{N3,C13,N4}}^{\text{bbip}} = 110.9(6)^\circ = \angle_{\text{N3,C13,N4}}^{\text{edip}} = 110.8(5)^\circ$ or $d_{\text{C13-N4}}^{\text{bbip}} = 1.322(8) \text{ \AA} = d_{\text{C13-N4}}^{\text{edip}} = 1.320(7) \text{ \AA}$).

The packing in **edip** crystal is rather interesting. In the unit cell, four symmetry equivalent **edip** molecules, 32 water molecules and four HCl molecules were found. Very prominent is the cisoidal arrangement of the coplanar ($\angle_{\text{ip,ip}} = 9.4^\circ$) imidazophenanthroline moieties which is forced by hydrogen bond formation between the two N-CH-N protons of the ligand and one bridging water molecule. This preoriented bidentate coordination sphere is very wide ($d_{\text{C13-C26}}^{\text{edip}} = 5.991(8) \text{ \AA}$) and is therefore suitable for multicenter fragments (the corresponding C-C distance in the $\{\text{Pd}_2\text{Cl}_4\}$ -bridged complex by HANSEN et al. was found to be equidistant, $d_{\text{C-C}}^{\text{Pd(NHC)}} = 6.034 \text{ \AA}$). The sterically demanding durene moiety is twisted out of the plane of the two **ip**-moieties ($\angle_{\text{ip,durene}} = 81.8^\circ$) and therefore out of the coordination site. Coordinated water is present in both phenanthroline spheres, which is not uncommon and was observed previously in other cases as well (e.g. **bbip**). The counter ions can be found embedded into a matrix of hydrogen bonded water molecules. Significant π -stacking effect between neighboring aromatic systems are missing. Therefore, the **edip** molecules are arranged in a superstructure of alternating molecules according to steric effects.

For comparison reasons and to characterize the N,N-coordinating properties of the new ligands **eip** and **edip**, the resulting ruthenium complexes were prepared (see figure 121). Furthermore, the binuclear **edip**-bridged ruthenium complex represents the next step toward the target system.

The synthesis of the ruthenium complexes was performed in a similar manner as synthesis of other **ip**-type complexes according to the protocol **method C1** through stoichiometric reaction of one equivalent of $[\text{Ru}(\text{tbbpy})_2\text{Cl}_2]$ and one equivalent of $\widehat{\text{LL}}$ -ligand (**eip**, or **edip**) in a solvent mixture of ethanol/water in a microwave reaction. After counter ion exchange with NH_4PF_6 , the mononuclear complex $[\text{Ru}(\text{tbbpy})_2(\text{eip})][\text{PF}_6]_2$ (**Ru(eip)**) and the binuclear **edip**-bridged complex $[\{\text{Ru}(\text{tbbpy})_2\}_2(\mu\text{-edip})][\text{PF}_6]_6$ (**Ru₂(edip)**) were obtained in high yields, whereat in the case of **Ru₂(edip)** a longer reaction time of 5 hours had to be applied to force the reaction between positively charged ruthenium center and positively charged ligand. Back and forth counter ion exchange and reprecipitation with Bu_4NCl and NH_4PF_6 yielded both complexes, **Ru(eip)** and

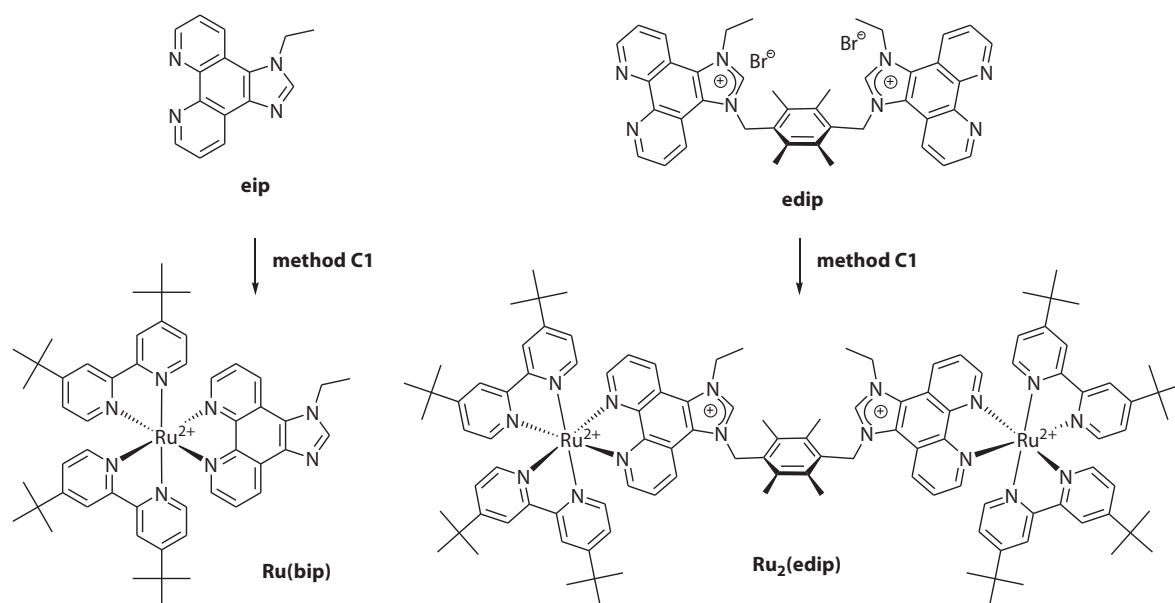


Figure 121:Complexation reaction with the new ligands **eip** and **edip**, yielding the N,N'-coordinated ruthenium complexes **Ru(eip)** (left) and **Ru₂(edip)** (right).

Ru₂(edip), as pure compounds in 90% and 60% yield, respectively.

The characterization by ¹H-NMR-, ¹³C-NMR-spectroscopy and mass spectrometry supported the formation of the expected complexes (for **Ru₂(edip)** see figure 119 on page 166).

Most obvious in the spectra of both compounds are the ligand related double sets of A-, B- and C-proton signals which refer to the asymmetric **ip**-backbones in **Ru(eip)** and **Ru₂(edip)**. In addition, the CH₂-signals of the alkyl moieties (Ar/Al) indicate the performed complexation without ligand decomposition ($\delta_{(\text{CH}_2)}^{\text{Ru(eip)}} = 4.77 \text{ ppm}$ (q, 2H, ³J = 7.2 Hz)) and $\delta_{(\text{CH}_2\text{-Ar})}^{\text{Ru}_2(\text{edip})} = 6.21 \text{ ppm}$ (d, 2H, ²J = 14.4 Hz), $\delta_{(\text{CH}_2\text{-Ar}')}^{\text{Ru}_2(\text{edip})} = 6.25 \text{ ppm}$, (d, 2H, ²J = 14.4 Hz) and $\delta_{(\text{CH}_2\text{-Al})}^{\text{Ru}_2(\text{edip})} = 5.00 \text{ ppm}$ (q, 4H, ³J = 7.0 Hz)). Comparison of the resonance frequencies of the N-CH-N-protons (D-position) in acetonitrile-*d*₃ exhibited the same tendency in the chemical shifts upon formal addition of one or two benzyl moieties as in the case of the **bip** and **bbip** ligands ($\delta_{\text{H}(2)}^{\text{Ru(eip)}} = 8.34 \text{ ppm}$ and $\delta_{\text{H}(2)}^{\text{Ru}_2(\text{edip})} = 8.55 \text{ ppm}$) with the stronger deshielding effect in the imidazolium complex **Ru₂(edip)**. Furthermore, all signals of the carbon NMR-spectra could be assigned (e.g. $\delta_{(2)}^{\text{eip}} = 146.03 \text{ ppm}$ and $\delta_{(2)}^{\text{Ru}_2(\text{edip})} = 140.80 \text{ ppm}$). In addition, FAB-MS showed the molecular ions *m/z* = 1031.1 (100%, [**Ru(eip)**-PF₆]⁺) and *m/z* = 1110.1 (10%, [**Ru₂(edip)**-2 PF₆]²⁺) respectively. Finally, it was possible to obtain suitable crystals of the mononuclear complex **Ru(eip)** by slow evaporation from

water/acetone to perform X-ray diffraction experiments (see figure 122 and table 16 on page 171).

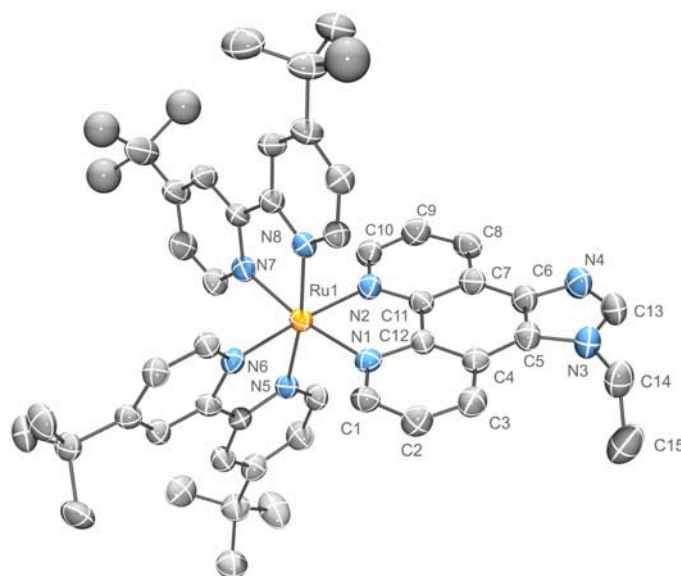


Figure 122: Solid state structures of **Ru(eip)**. Hydrogen atoms, counter ions and coordinated solvent molecules were omitted for clarity. Ellipsoids were drawn at 50 percent level. Compare table 16 an page 171 for selected bond lengths and angles.

Because of the general structural and chemical similarities, it is useful to compare **Ru(eip)** to the pre-ligand **eip** and to the formerly prepared **Ru(bip)** with respect to the different coordination sites. A first glance indicated that the imidazole rings in **Ru(eip)** and the similar complex **Ru(bip)** (compare chapter 3.3.6 on page 130) have identical bond lengths and equivalent bond angles at the analogical positions of the **ip**-backbone. The obtained data supported furthermore the significant asymmetry in the imidazole ring system with shortened C13-N4 bonds with respect to the C13-N3 bond ($d_{(C13-N4)}^{Ru(eip)} = 1.269(10) \text{ \AA} < d_{(C13-N3)}^{Ru(eip)} = 1.361(9) \text{ \AA}$). In **Ru(eip)**, furthermore, differences in the opposing C-N-C angles and N-C-C angles of the imidazole rings are present, which are similar to **Ru(bip)**. Thus, it exhibits a by $\sim 5^\circ$ wider N4-C6-C5 angle in comparison to the N3-C5-C6 angle ($\angle_{(N4,C6,C5)}^{Ru(eip)} = 110.9(6)^\circ > \angle_{(N3,C5,C6)}^{Ru(eip)} = 104.8(5)^\circ$). The N3-C13-N4 angle the widest angle of the imidazole ring, as it is in the case of **Ru(bip)**. ($\angle_{(N3,C13,N4)}^{Ru(eip)} = 114.5(6)^\circ$). In comparison to the imidazole system, a higher symmetry was found in the phenanthroline sphere which exhibits identical bond lengths and angles at opposing positions. The values for the Ru-N distances and the surrounding phenanthroline sphere are consistent with the previously obtained data and with other ruthenium phenanthroline complexes.

Table 16: Selected bond lengths [Å] and angles [°] of new ligands and complexes with imidazophenanthroline backbone.

bond length [Å] or angle [°]	eip	Ru(eip)	edip	Ru(Br ₂ bip)
Ru1 - N1		2.060 (5)		2.054 (5)
Ru1 - N2		2.062 (5)		2.064 (6)
N4 - C13	1.314 (4)	1.269 (10)	1.323 (8)	1.319 (10)
N3 - C13	1.361 (3)	1.361 (9)	1.320 (7)	1.345 (10)
N3 - C5	1.384 (3)	1.390 (8)	1.389 (7)	1.380 (9)
N4 - C6	1.385 (3)	1.385 (8)	1.402 (7)	1.379 (10)
C5 - C6	1.379 (4)	1.385 (8)	1.374 (8)	1.390 (10)
N1 - C12	1.353 (3)	1.386 (7)	1.366 (7)	1.362 (9)
N2 - C11	1.360 (3)	1.361 (8)	1.359 (7)	1.370 (9)
N1 - C1	1.315 (3)	1.332 (8)	1.319 (8)	1.324 (9)
N2 - C10	1.327 (3)	1.321 (8)	1.314 (8)	1.328 (10)
C11 - C12	1.477 (4)	1.447 (8)	1.451 (9)	1.443 (10)
N1 - Ru1 - N2		80.0 (2)		79.5 (2)
N3 - C13 - N4	113.9 (3)	114.5 (6)	110.8 (5)	114.7 (7)
C13 - N3 - C5	105.9 (2)	105.7 (6)	107.6 (5)	106.3 (6)
C13 - N4 - C6	103.7 (2)	104.0 (6)	108.2 (5)	102.9 (6)
N3 - C5 - C6	105.3 (2)	104.8 (5)	107.8 (5)	104.7 (6)
N4 - C6 - C5	111.1 (2)	110.9 (6)	105.6 (5)	111.4 (6)
N1 - C12 - C11	117.2 (2)	115.1 (5)	117.1 (5)	115.6 (6)
N2 - C11 - C12	117.4 (2)	117.4 (5)	116.4 (5)	116.0 (6)
C1 - N1 - C12	117.6 (2)	118.0 (5)	119.4 (5)	118.2 (6)
C10 - N2 - C11	117.2 (2)	117.2 (5)	117.9 (5)	118.5 (6)

Comparison of the N,N'-donor site in the ruthenium complex and in the respective pre-ligand **eip** revealed only very slight (not in every case significant) changes in the corresponding distances and angles, which are mainly located at the phenanthroline site. The tendency goes toward more acute N1-C11-C12 / N2-C12-C11 angles (e.g. $\angle_{(N2,C12,C11)}^{eip} = 117.2(2)^\circ \geq \angle_{(N2,C12,C11)}^{Ru(eip)} = 115.1(0)^\circ$), shorter C12-N1 / C11-N2 bond lengths (e.g. $d_{(N1-C12)}^{eip} = 1.353(3) \text{ \AA} < d_{(N1-C12)}^{Ru(eip)} = 1.386(7) \text{ \AA}$) and longer C11-C12 distances (e.g. $d_{(C11-C12)}^{eip} = 1.477(4) \text{ \AA} > d_{(C11-C12)}^{Ru(eip)} = 1.447(8) \text{ \AA}$) in the ruthenium complexes, which is consistent with the changes that generally occur in such systems upon ruthenium coordination.

As described for **Ru(bbip)**, a transformation of the imidazolium salt into the corresponding carbene derivatives of different metal centers is very important. For the subsequent use as starting material in the transmetalation reactions, formation of the NHC-silver complex of **Ru₂(edip)** became interesting at this stage. In this context **method C2** was applied, using Ag₂O as base for the transformation of the imidazolium salt into the corresponding metal-NHC complex (see figure 123) as described for **Ru(bbip)**.

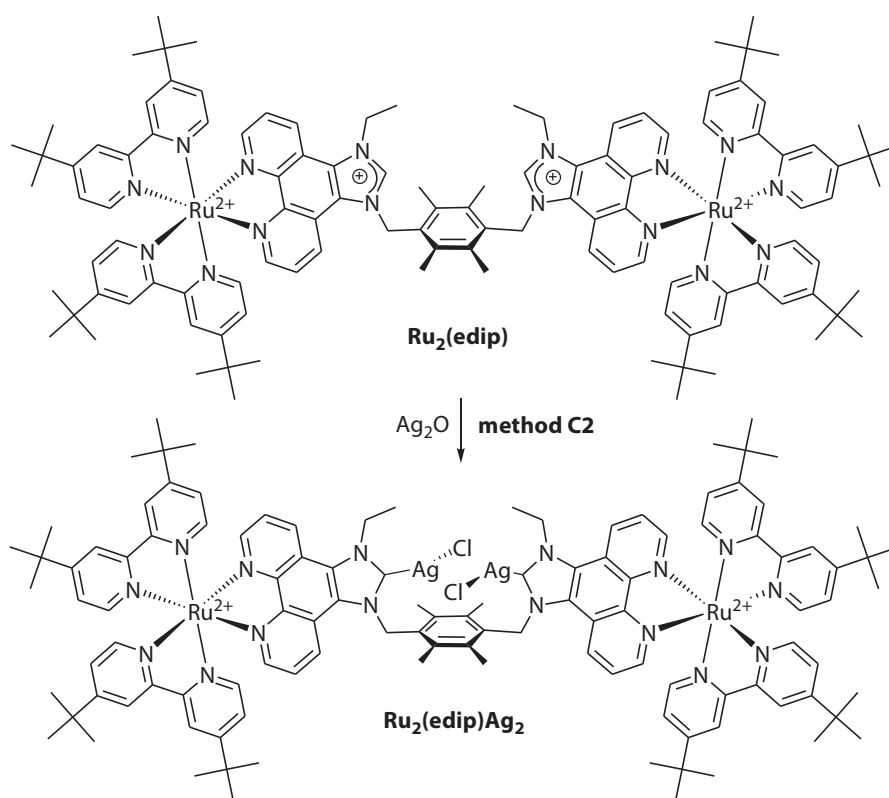


Figure 123: Preparation of the tetranuclear heterobimetallic silver NHC-complex of **Ru₂(edip)**.

To increase the driving force the chloride salt of **Ru₂(edip)** was prepared. Counter ion exchange of the [PF₆]-salt of **Ru₂(edip)** with (Bu)₄NCl in acetone/ethyl acetate gave the corresponding chloride salt in quantitative yield. The complexation reaction was carried out in dichloromethane. After stirring **Ru₂(edip)** and Ag₂O in the presence of molecular sieves in dichloromethane for 16 hours, the solids were filtered off and the volatiles were removed from the remaining solution. Analysis of the remaining solid gave clear evidence for a complete conversion into the pure product [**{(tbbpy)₂Ru₂(μ-edip){AgCl₂}₂Cl₄** (**Ru₂(edip)Ag₂**). The disappearance of the

characteristic ^1H -NMR-signal of the proton at the 2-position (see figure 119 on page 166) support the proposed carbene complex formation.

An interesting observation is the splitting of the durene CH_3 -protons, which might be an indication of the formation of chlorido bridges between the two silver ions which decreases the degree of freedom in the durene moiety. Note: a similar effect was not observed in the related compound by HANSEN et al. ^{13}C -NMR spectroscopy was not available at that time, so that the shift of N-CH-N-carbon signal could not be used as indication for the NHC complexation. Nevertheless, the transformation was further confirmed by detailed ESI-MS and MS^n studies. Four relevant fragment ions with fitting isotopic patterns were identified for $\text{Ru}_2(\text{edip})\text{Ag}_2$ ($m/z = 1143.8$ (25%, $[\text{M} - 2 \text{Cl}]^{2+}$), 751.1 (50%, $[\text{M} - 3 \text{Cl}]^{3+}$), 715.1 (50%, $[\text{M} - 3 \text{Cl} - \text{Ag}]^{3+}$), and 554.7 (100%, $[\text{M} - 3 \text{Cl}]^{4+}$)).

Finally, with the formation of the tetranuclear complex $\text{Ru}_2(\text{edip})\text{Ag}_2$, an ideal starting material was obtained. This compound contains already two ruthenium chromophores and can be used to introduce a variety of catalyst centers by transmetalation reactions to obtain new oligonuclear photocatalysts, as exemplary demonstrated by HANSEN et al.^[71]

3.4.4 Concluding Remarks

In conclusion it can be stated that a number of experiments were performed which may lead to the future development of new imidazophenanthroline containing catalyst systems. The attempts to increase the already high quantum yields of the ruthenium **bbip**-complexes led to an unexpected reactivities which resulted in the decomposition of the ligand system. Furthermore, it was tried to change the electronic properties of the bridge, particularly of the electron storage capacity of the $^3\text{MLCT}$ -involved LUMO. By the introduction of electron withdrawing bromine groups into the **ip**-backbone, three new ligands were obtained. Finally, an extension of the bridge was performed which allows for multiple chromophores and extended catalyst centers. With this ligand a the resulting tetranuclear ruthenium/silver complex $\text{Ru}_2(\text{edip})\text{Ag}_2$ was prepared which can be easily transformed into different photocatalysts according to previous results.

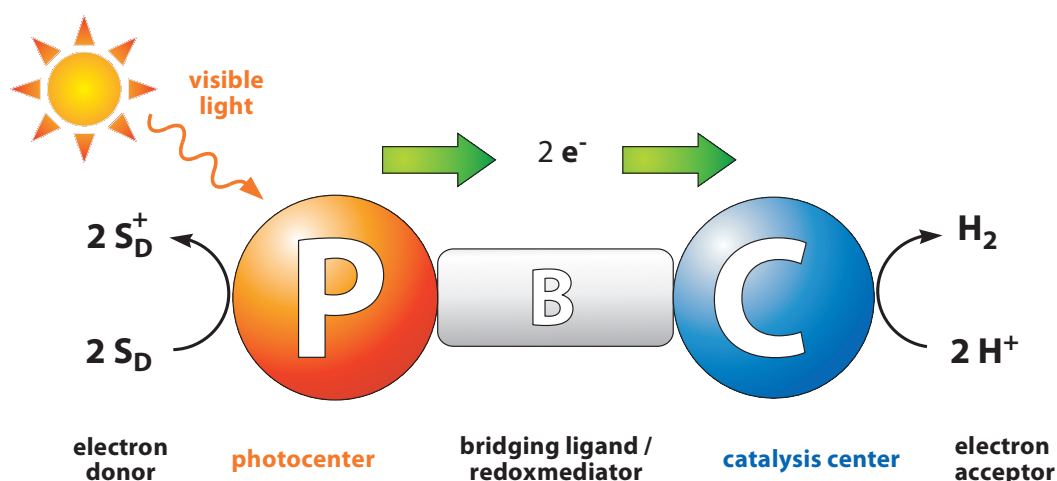
Hopefully, some of these findings will be useful to develop the next generation of *intramolecular* photocatalysts on the way toward a sustainable method of the solar into chemical energy conversion.

4 Summary

Against the background of a worldwide increase of energy demand and simultaneous scarcity of the fossil fuel resources, an increased utilization of solar energy is indispensable. In this scope, the development of light driven catalysis might enable a direct conversion of solar energy into storable chemical bond energy. Intramolecular photocatalysis represent a potential route toward this aim. Therefore, a number of new ligands and metal complexes was prepared with the aim to obtain heteronuclear $[[\mathbf{P} \sim \mathbf{B} \sim \mathbf{C}]]$ -type diads or polyads which comprise covalently linked subunits with the following functionalities:

- P:** a $\{\text{Ru}(\text{tbbpy})_2\}^{2+}$ -type photocenter with well established photophysical and electrochemical properties, serving as workhorse chromophore,
- B:** a variable bridging ligand such as **phenphen**, **bbip** or **edip**, which has to assure the stability of the assembly and the electronic communication between the attached metals, and
- C:** a catalytically active metal complex such as $\{\text{PdCl}_2\}$, $\{\text{PtCl}_2\}$, $\{\text{Rh}(\text{cod})\text{Cl}\}$, or even $\{\text{AgCl}\}$ for the catalytic redox processes.

These subunits may interact in a purposeful way to operate as supramolecular photocatalysts.

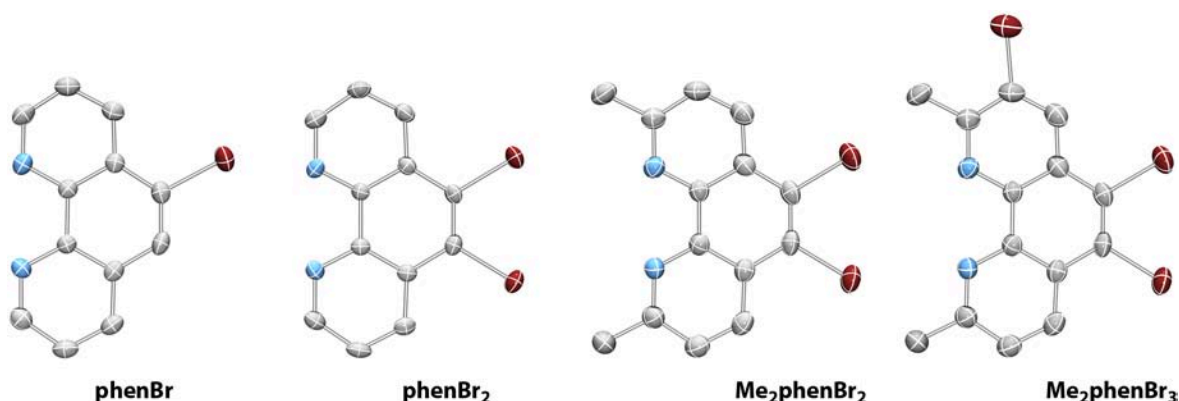


The preparation, characterization, including structural, photophysical and electrochemical analysis, of these complexes, their precursors and reference compounds was achieved. Based on the comparison of the generated $[[\mathbf{P} \sim \mathbf{B} \sim \mathbf{C}]]$ -catalysts and reference compounds interpretations

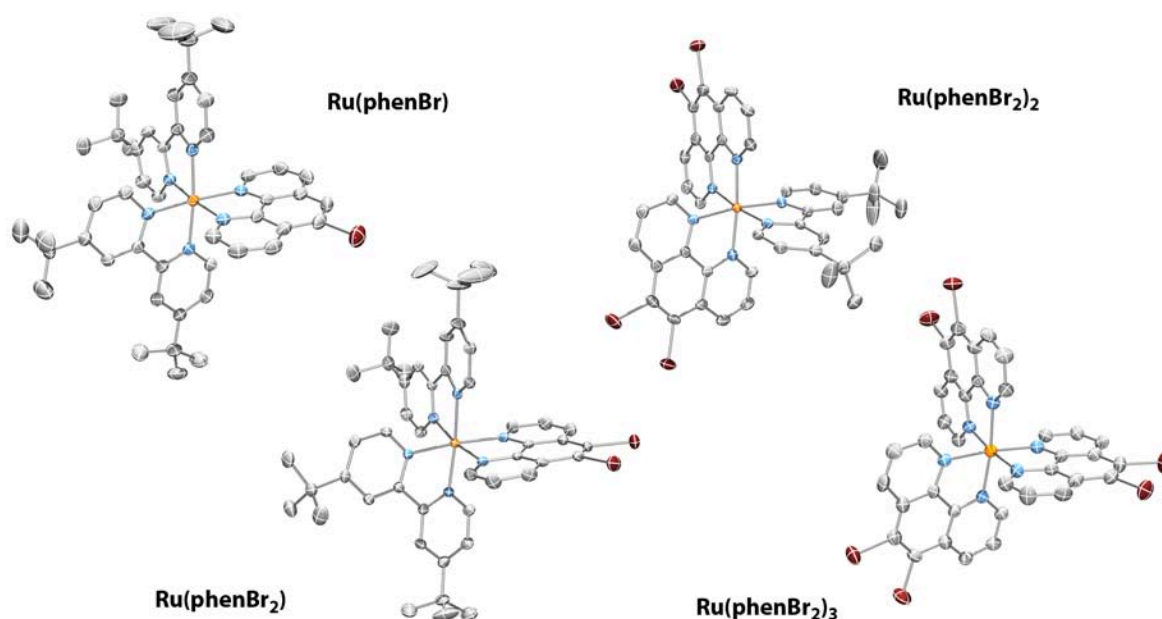
toward a structure-activity correlation were possible. In addition, photocatalysis experiments with respect to hydrogen evolution from water were performed with the complexes. Representative control experiments and in-depth analysis were performed as well.

In detail, the following results were achieved:

1. A low temperature regime synthesis for the selective and efficient bromination of phenanthrolines in the 5-, and 5,6-positions was developed (**method L1**) and applied to 1,10-phenanthroline and 2,9-dimethyl-1,10-phenanthroline. The resulting phenanthroline derivatives **phenBr**, **phenBr₂**, **Me₂phenBr₂**, and **Me₂phenBr₃** were prepared and fully characterized, including X-ray analysis of all four potential ligands. Exploration of other starting materials such as 4,7-diphenyl-1,10-phenanthroline was not successful but gave important insights into the limitations of this new method for the preparation of precursors for metalorganic coupling reactions.

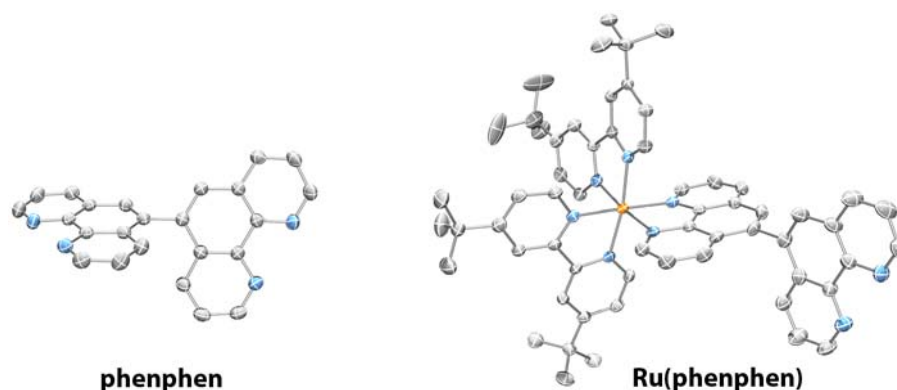


2. Off the ligands **phenBr** and **phenBr₂**, new complexes with a ruthenium core and additional bipyridine-type ligands (**Ru(phenBr)**, **Ru(phenBr₂)**, **Ru(phenBr₂)₂**, **Ru(phenBr₂)₂Cl₂**, and **Ru(phenBr₂)₃**) were prepared according to a modified literature procedure, so that the two series of ruthenium complexes, $[\text{Ru}(\text{tbbpy})_2(\text{phenBr}_m)]^{2+}$ ($m = 0, 1, 2, 4$) and $[\text{Ru}(\text{tbbpy})_{3-n}(\text{phenBr}_2)_n]^{2+}$ ($n = 0, 1, 2, 3$), could be completed.



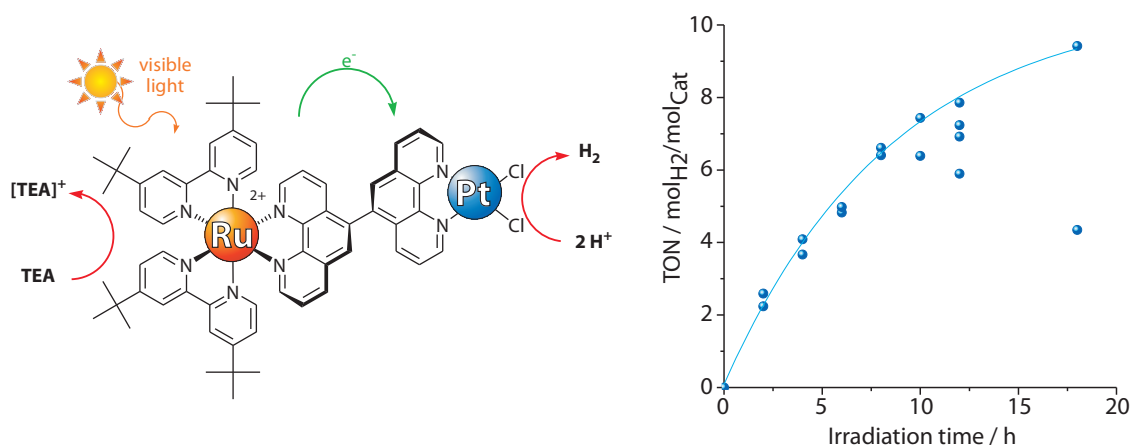
The resulting complexes were characterized, especially with respect to the absorption and emission behavior, electrochemical behavior and structural properties of the $[\text{Ru}(\overline{\text{LL}})_3]$ -type compounds. Categorization and comparison with complexes known from literature gave insights into the way in which the substitution pattern of the bromo substituents influences the ground and excited state properties of the ruthenium complex. It was concluded that the phenanthroline π^* -LUMO is lowered in energy and that the metal centered oxidation potential is shifted toward more positive values with increasing number of bromine atoms, so that triplet MLCT emission involves predominantly that particular ligand centered orbital.

3. In a nickel mediated coupling reaction, the axial chiral, bidentate ligand **phenphen** was prepared from **phenBr**. Thereof, the new mono- and bridged binuclear ruthenium complexes **Ru(phenphen)**, **Ru(phenphen)Ru** and furthermore, the heterobinuclear $[\text{P} \sim \text{B} \sim \text{C}]$ -type platinum complex **Ru(phenphen)Pt** were prepared and characterized. The solid state structures of **phenphen** and **Ru(phenphen)** were obtained and used to further support the spectroscopic results.

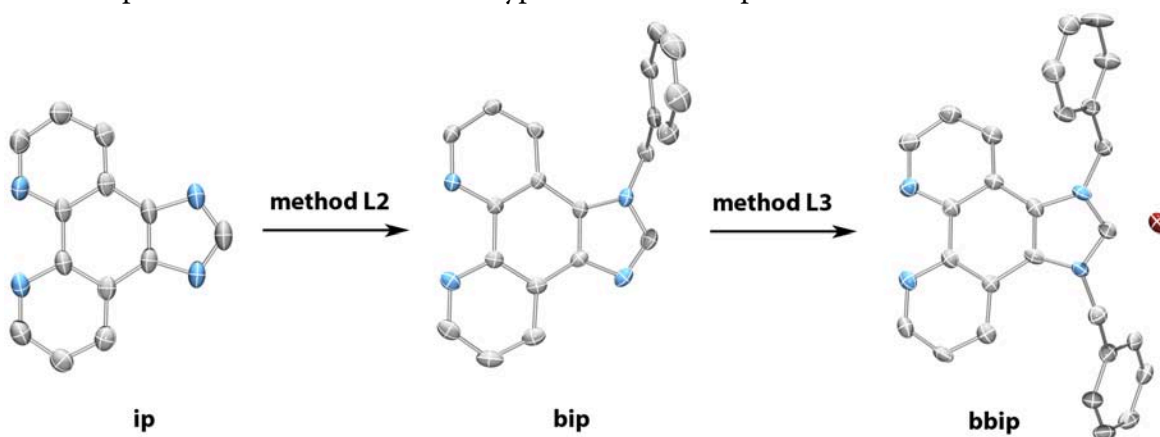


In particular, a detailed isomer analysis with NMR investigations was used to characterize the inisochronal atropisomers of the ruthenium complexes which are caused by the sterical hindrance of the rotation about the connecting single bond. In a time-dependent NMR-investigation, using the obtained single crystals of $\Delta R_a/\Lambda S_a$ -**Ru(bbip)**, a half-life of $t_{1/2} = 1.99$ h for the interconversion into the $\Delta S_a/\Lambda R_a$ -configured rotamers could be calculated. The absorption and emission behavior indicated the formation of the typical $[\text{Ru}^{3+}(\overline{\text{LL}})(\overline{\text{LL}})_2]$ -type transient species and additional new photoproducts in the platinum free complexes upon MLCT excitation.

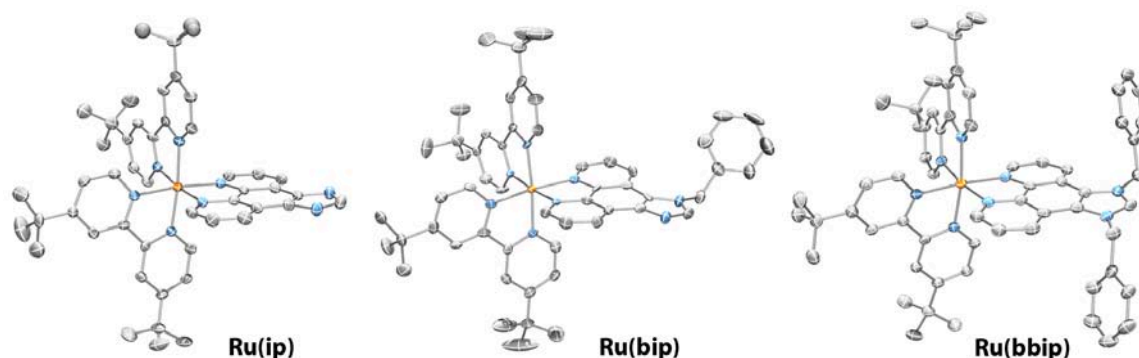
4. The performed photophysical and electrochemical investigation indicated suitable redox potentials and a fair electronic communication between the two phenanthroline moieties. Thus, catalysis experiments with **Ru(phenphen)Pt** were performed under standard conditions (in TEA:ACN:H₂O / 6:3:1) and moderate amounts of hydrogen were detected. The observed TONs are still low but lie in the same order of magnitude as observed for the catalyst $[(\text{tbbpy})_2\text{Ru}(\mu\text{-tpphz})\text{PtCl}_2]^{2+}$. Furthermore, a water concentration dependency of the activity with a maximum at 5% water content was observed.



5. The development of new procedures was used to create the new ligands **bip** and the imidazolium salt **bbip** in a stepwise synthesis (**method L2 and L3**) from **ip**. Elemental analysis, mass spectrometry, different NMR techniques and, importantly, X-ray diffraction were used for the characterization of the new bridging ligand and its precursors. NMR studies were used to trace and fit the H/D-exchange kinetics of the active N-CH-N-proton at the imidazolium salt in methanol- d_4 , whereat a rate constant of $k = 2.36 \times 10^{-5} \text{ s}^{-1}$ and a half life of $t_{1/2} = 490 \text{ min}$ were determined. The results indicate that **bbip** successfully combines two important ligand motifs, a phenanthroline- and a NHC-type coordination sphere.

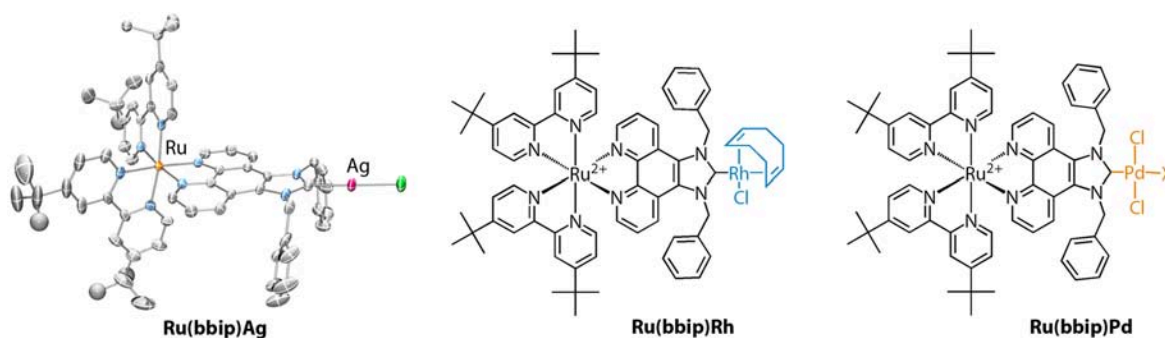


6. Off the **ip**-ligands, the series of mononuclear ruthenium complexes **Ru(ip)**, **Ru(bip)**, and **Ru(bbip)**, carrying the $\{\text{Ru}(\text{tbbpy})_2\}^{2+}$ -fragment, was prepared. The resulting complexes were fully characterized, but particular attention was paid to solid state structural analysis, absorption and emission behavior, and electrochemical behavior.



According to X-ray analysis of the compounds, no significant influence of the imidazolium sphere on the phenanthroline binding properties was found. However, the imidazole unit displays similar changes as observed in **ip**, **bip** and **bbip**. Electrochemistry shows the typical reversible behavior of ruthenium complexes but absorption and emission studies exhibit a strong influence of the imidazolium system which possesses very high emission quantum yields and far red-shifted emission wavelengths.

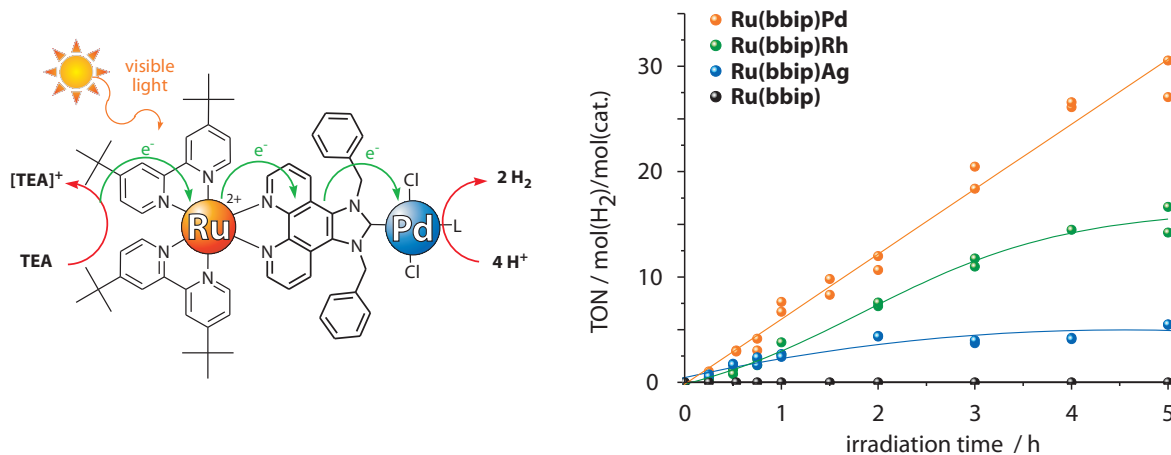
- Different attempts to access the NHC-coordination sphere of **bbip** or **Ru(bbip)**, including deprotonation, complexation with $[\text{Mo}(\text{thf})(\text{CO})_5]$ or formation of the NHC·BET₃ adduct, were made. Finally, the preparation of the bridged complex **Ru(bbip)Ag** succeeded according to a modified literature procedure.



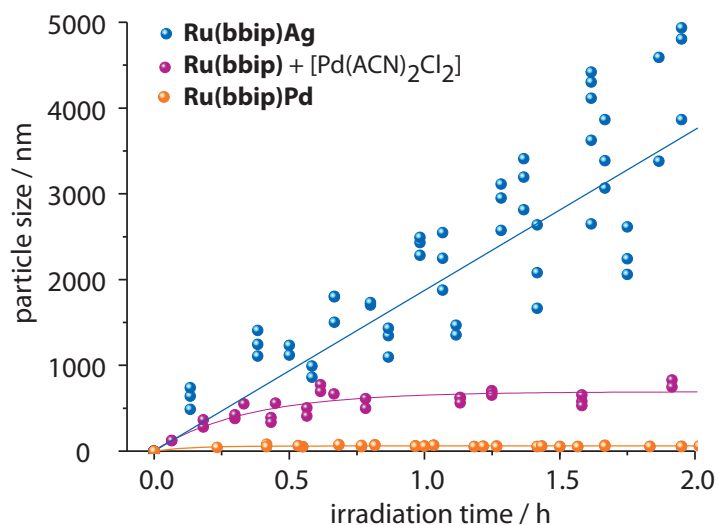
Using this precursor, the $[\text{P} \sim \text{B} \sim \text{C}]$ -type dyads **Ru(bbip)Rh** and **Ru(bbip)Pd** were exemplarily prepared to demonstrate the potential of the carbene transfer agent. The characterization, including X-ray analysis of **Ru(bbip)Ag**, detailed MS and MSⁿ studies as well as spectroscopic characterization of the **bbip**-bridged complexes was achieved. All **Ru(bbip)**-complexes display properties of the well known $\text{Ru}(\text{bpy})_3$ -moiety, like ¹MLCT-

absorption between 430 nm and 500 nm, but surprisingly with very strong $^3\text{MLCT}$ -emission between 600 nm and 700 nm and corresponding redox properties. The comparison of the complexes with the **ip**-motif allowed conclusions about the orbital nature of the ligand.

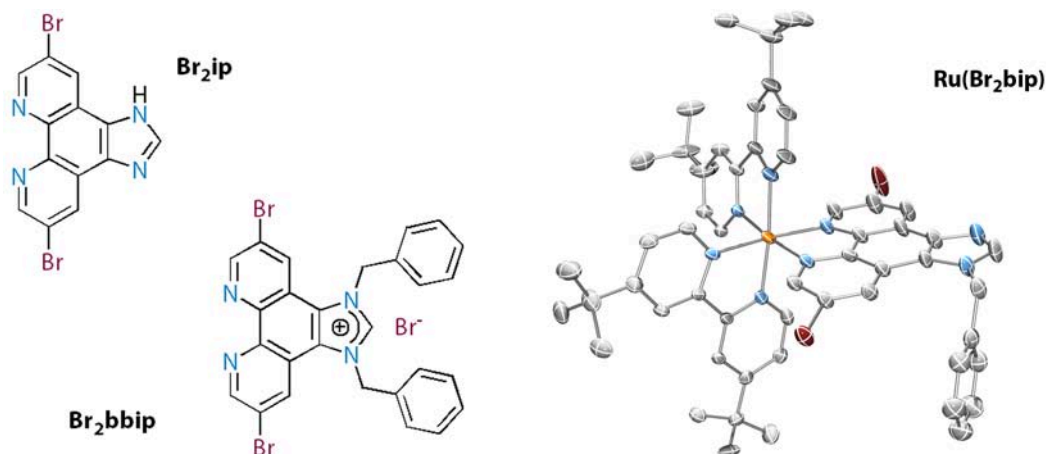
8. Using with **Ru(bbip)Pd**, **Ru(bbip)Rh** and the reference compounds **Ru(bbip)Ag** and **Ru(bbip)** a number of intramolecular catalysis experiments were performed. The determined irradiation time and catalyst concentration dependencies of the hydrogen evolution prove the activity of the palladium and rhodium complexes. Both dinuclear complexes may be reviewed as tunable molecular photoredoxcatalysts. Interestingly, even the silver complex showed some activity, whereas the reference **Ru(bbip)** was inactive. Control experiments with intermolecular $[\text{P} \sim \text{B} / \text{C}]$ -type systems of **Ru(bbip)** and $[\text{Pd}(\text{ACN})_2\text{Cl}_2]$ or $[\text{Rh}(\text{cod})_2\text{Cl}]_2$ also showed light-driven hydrogen formation, but gave very different catalysis kinetics, when compared to the intramolecular systems.



9. A number of dynamic light scattering measurements was performed with the intramolecular catalysts and the intermolecular control systems to evaluate the influence of the molecular structure on colloid formation and catalysis. It was demonstrated that **Ru(bbip)Pd** complexes act as model compounds for supramolecular photocatalysts, whilst in the case of **Ru(bbip)Ag** (photographic process) and **Ru(bbip)** + $[\text{Pd}(\text{ACN})_2\text{Cl}_2]$ (Pd-black) formation and growth of particles was detected and a clear correlation between particle ripening and catalytic activity was demonstrated.



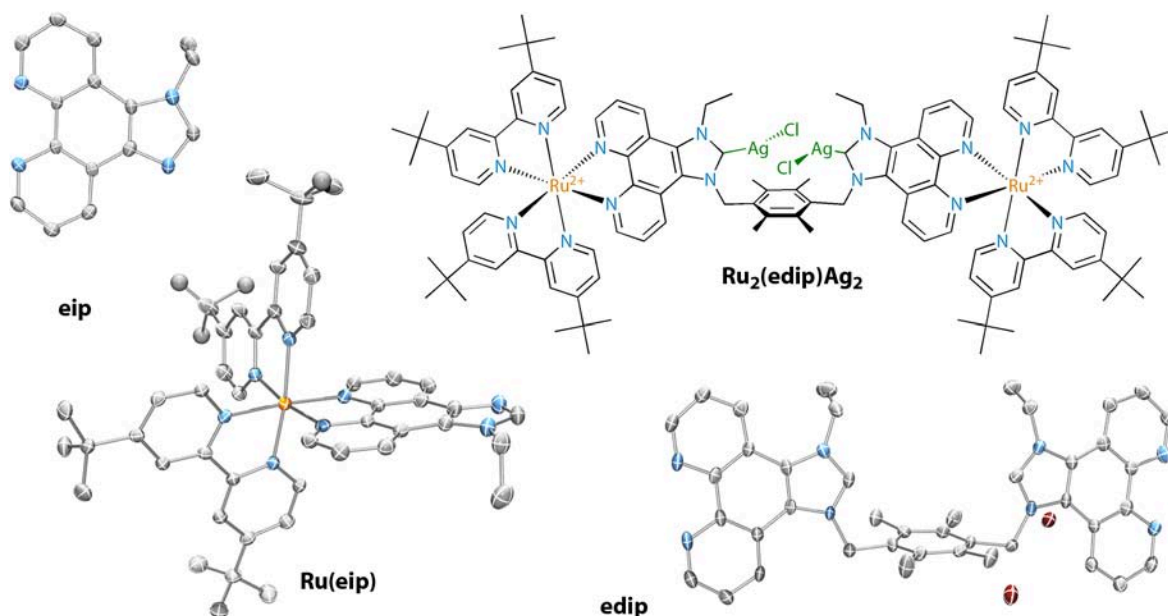
10. In an explorative investigation on the development of electron deficient compounds such as $\text{Ru}(\text{bbip})_3$ or $\text{Ru}(\text{Br}_2\text{bbip})$, the new ligands Br_2ip , Br_2bip , and Br_2bbip were prepared. However, application of standard procedures for the complexation resulted in both cases in an unexpected reactivity of the ligand structure and, interestingly, yielded the compounds $\text{Ru}(\text{bip})_3$ and $\text{Ru}(\text{Br}_2\text{bip})_3$, as first indicated by NMR-analysis.



The X-ray analysis of the latter exhibited similar properties to the related $\text{Ru}(\text{bip})_3$. From these results, an impression of the limitations of the ligand stability and the scope of the synthesis of electron deficient complexes was received.

11. Starting from ip , the new ligands eip and edip were prepared, using methods developed for the bbip synthesis, and fully characterized. With this development a bridging ligand with

additional NN- and NHC-coordination sphere was obtained, opening up the access toward multimetallic catalyst centers and extended light harvesting systems.



The x-structural analysis of **edip** exhibits a pre-organized NHC-NHC chelating sphere which is suitable for multimetallic metal fragments with a diameter of roughly 0.6 nm. From the ligands, the N,N'-coordinated $\{\text{Ru}(\text{tbbpy})_2\}^{2+}$ -type complexes **Ru(eip)**, and **Ru₂(edip)** could be prepared and characterized, including X-ray analysis of **Ru(eip)**. In a final exploratory study the tetranuclear compound **Ru₂(edip)Ag₂**, containing the silver NHC moiety was prepared and characterized by different NMR and MS analysis.

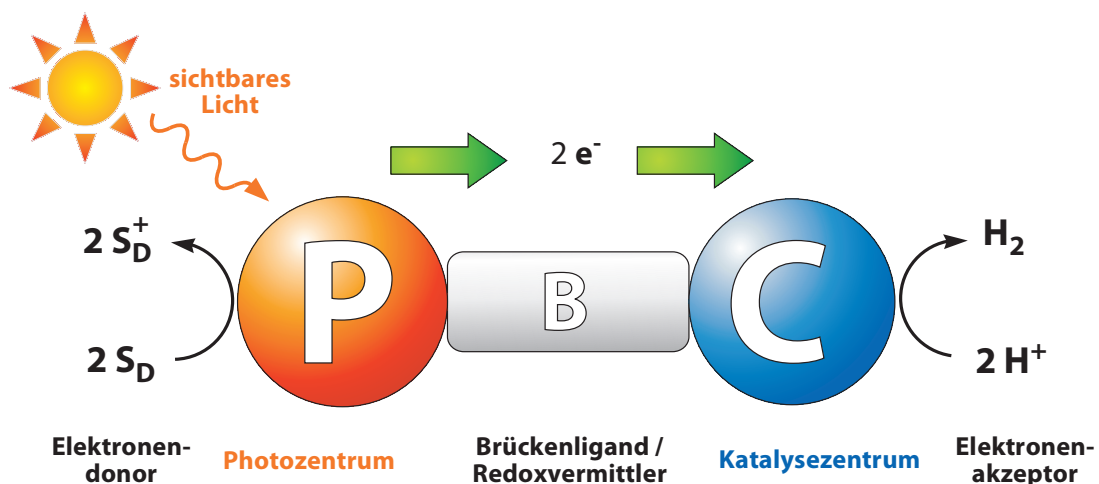
In general, the prepared phenanthroline and imidazophenanthroline ligands such as **phenphen**, **bbip** or **edip** were found to be suitable starting materials for the further incorporation into intramolecular photocatalytic systems. Especially the combination of azadiene and NHC coordination spheres was found to be ideal for the design of stable molecular $[\text{P} \sim \text{B} \sim \text{C}]$ -type devices in which the catalytic center as well as the photocenter may be widely varied in terms of metal fragment and co-ligand environment to even allow a change in the nature of the catalytic reaction, which is driven by light.

There is to hope that these achieved results will pave the way for further research and development and thus that possibly a contribution was made to the answer the energy problem of the future.

5 Zusammenfassung

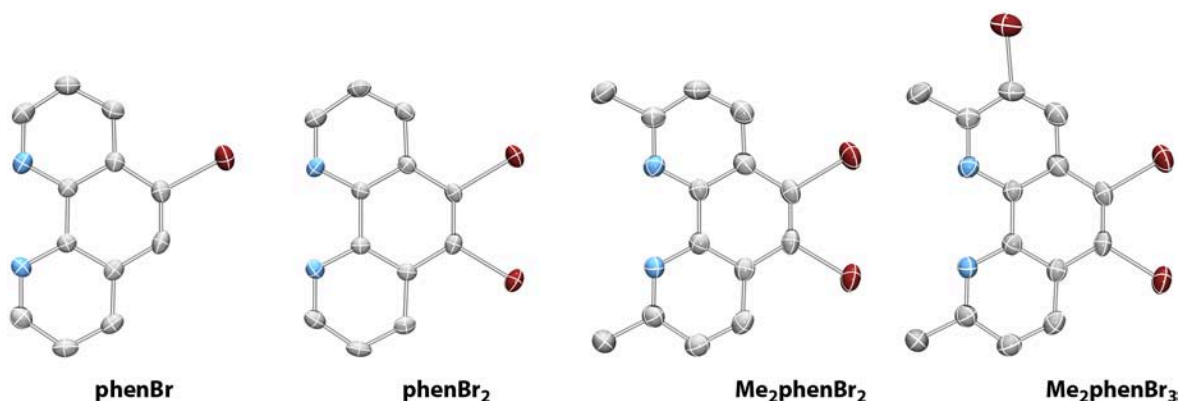
Mit dem Hintergrund eines weltweit ansteigenden Energiebedarfs bei gleichzeitiger Verknappung der fossilen Energiereserven wird eine gesteigerte Nutzung der Solarenergie in Zukunft unausweichlich werden. In diesem Zusammenhang könnte die lichtgetriebene Katalyse einen Zugang für die direkte Umwandlung von Sonnenlicht in chemische Energie eröffnen. Die intramolekulare Photokatalyse stellt dabei einen interessanten Weg in diese Richtung dar. Aus diesem Grund wurde eine Anzahl von neuen Liganden und den resultierenden Metallkomplexen hergestellt, mit dem Ziel zu heteronuklearen $[[P \sim B \sim C]]$ -artigen Diaden oder Polyaden zu gelangen, welche aus kovalent verbundenen Funktionseinheiten bestehen sollen. Dabei sollen die folgenden drei Komponenten gezielt so zusammengestellt werden, dass ihre Einzelfunktionen im Zusammenspiel als supramolekularer Photokatalysator fungieren:

- P:** ein $\{Ru(tbbpy)_2\}^{2+}$ -artiges Photozentrum mit den bereits gut untersuchten und bekannten photophysikalischen und elektrochemischen Eigenschaften, das als Arbeitschromophor dient,
- B:** ein variabler Brückenligand wie zum Beispiel **phenphen**, **bbip** oder **edip**, welcher die Stabilität der Überstruktur und die elektronische Kommunikation zwischen den gebundenen Metallzentren gewährleisten soll, sowie
- C:** ein katalyseaktives Metallkomplexfragment wie beispielsweise $\{PdCl_2\}$, $\{PtCl_2\}$, $\{Rh(cod)Cl\}$ oder auch $\{AgCl\}$ an dem der katalytische Redoxprozess abläuft.



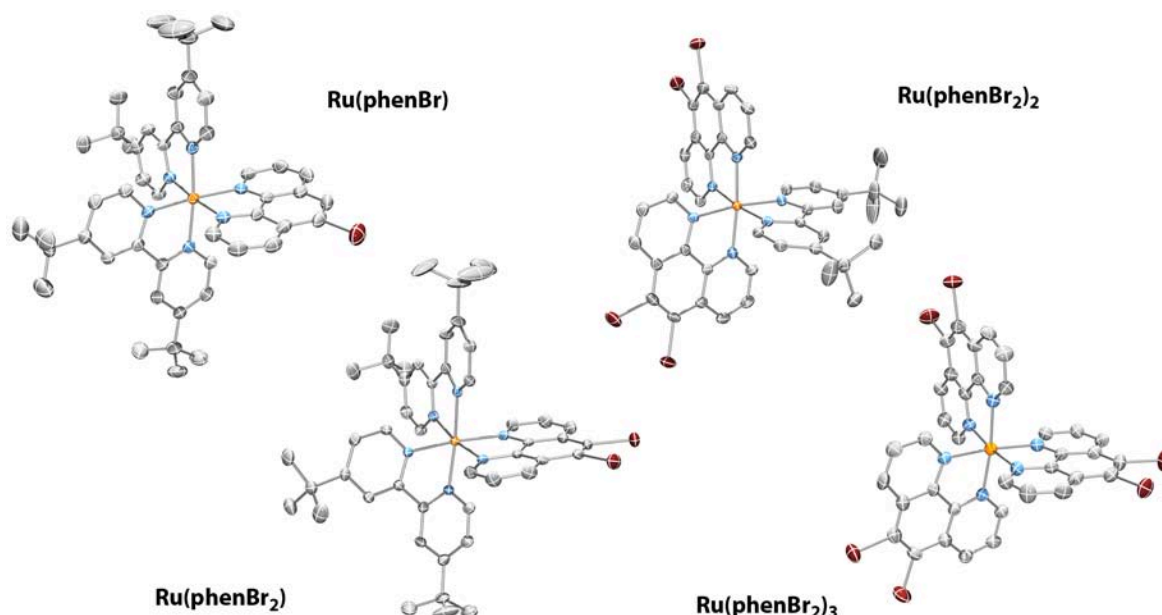
Die Herstellung, Charakterisierung und der Vergleich, inklusive struktureller, photophysikalischer und elektrochemischer Analyse, einer Anzahl von Komplexen, ihrer Ausgangsverbindungen sowie geeigneter Referenzverbindungen wurde erreicht. Zusätzlich wurden Experimente zur photokatalytischen Wasserstoffentwicklung aus Wasser mit den erzeugten Komplexen durchgeführt. Ebenso wurden repräsentative Kontrollexperimente und zusätzliche Analysen für ein tiefergehendes Verständnis durchgeführt. Auf dem Vergleich der hergestellten Katalysatoren mit ausgewählten Referenzverbindungen beruhend, konnten dann einige Interpretationen über die Struktur-Eigenschaftsbeziehungen abgeleitet werden. Im Einzelnen wurden folgende Ergebnisse erreicht:

1. Eine bei niedrigen Temperaturen geführte Synthese für die selektive und effiziente Bromierung von Phenanthrolinderivaten in der 5- und 5,6-Position wurde entwickelt und an 1,10-Phenanthrolin sowie 2,9-Dimethyl-1,10-phenanthrolin angewendet. Die resultierenden Phenanthrolinderivate **phenBr**, **phenBr₂**, **Me₂phenBr₂**, und **Me₂phenBr₃** wurden hergestellt und vollständig, inklusive der Röntgenstruktur- aufklärung aller vier potentiellen Liganden, charakterisiert. Die Ausweitung dieser Methode auf andere Ausgangs- verbindungen wie beispielsweise 4,7-Diphenyl-1,10-phenanthrolin gelang nicht, erbrachte allerdings wichtige Einblicke in die Grenzen der neuen Methode zur Herstellung von Liganden, die später als Ausgangsstoffe für metallorganisch katalysierte Kopplungs- reaktionen verwendet werden können.



2. Von den genannten Liganden **phenBr** und **phenBr₂** wurden die folgenden neuen Rutheniumkomplexe **Ru(phenBr)**, **Ru(phenBr₂)**, **Ru(phenBr₂)₂**, **Ru(phenBr₂)₂Cl₂** und **Ru(phenBr₂)₃** mit Rutheniumkern

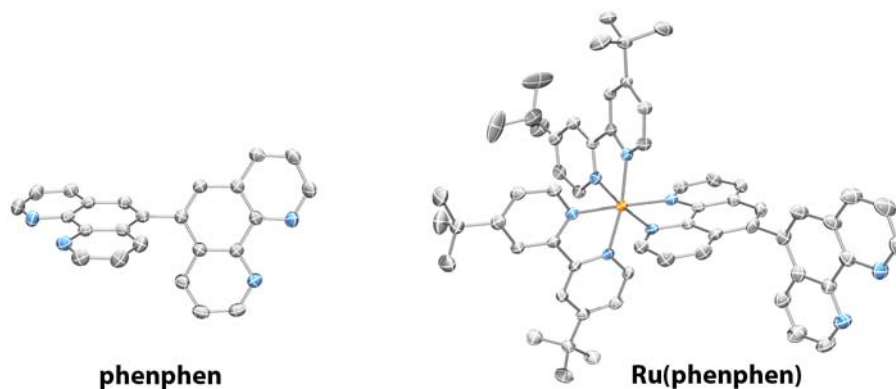
und bipyridinartigen Coliganden anhand einer modifizierten Literaturvorschrift hergestellt, sodass die zwei Serien von Komplexen, $[\text{Ru}(\text{tbbpy})_2(\text{phenBr}_m)]^{2+}$ ($m = 0, 1, 2, 4$) und $[\text{Ru}(\text{tbbpy})_{3-n}(\text{phenBr}_2)_n]^{2+}$ ($n = 0, 1, 2, 3$), vervollständigt werden konnten.



Die resultierenden Komplexe wurden eingehend charakterisiert. Dabei wurde besonderes Augenmerk auf das Absorptions- und Emissionsverhalten, das elektrochemische Verhalten sowie auf die strukturellen Eigenschaften der $[\text{Ru}(\widehat{\text{LL}})_3]$ -artigen Verbindungen gelegt. Die Charakterisierung und der Vergleich mit literaturbekannten Komplexen erbrachte wichtige Einblicke in die Art und Weise, in der das Substitutionsmuster der Bromosubstituenten den Grund- bzw. den angeregten Zustand der Rutheniumkomplexe beeinflusst. Es konnte gefolgert werden, dass mit zunehmender Anzahl an Bromsubstituenten das Phenanthrolin-lokalisierte π^* -LUMO in seiner Energie erniedrigt wird und dass das metallzentrierte Oxidationspotential zu positiveren Werten hin verschoben wird, sodass an der $^3\text{MLCT}$ -Emission hauptsächlich das jeweilige ligandzentrierte Orbital beteiligt ist.

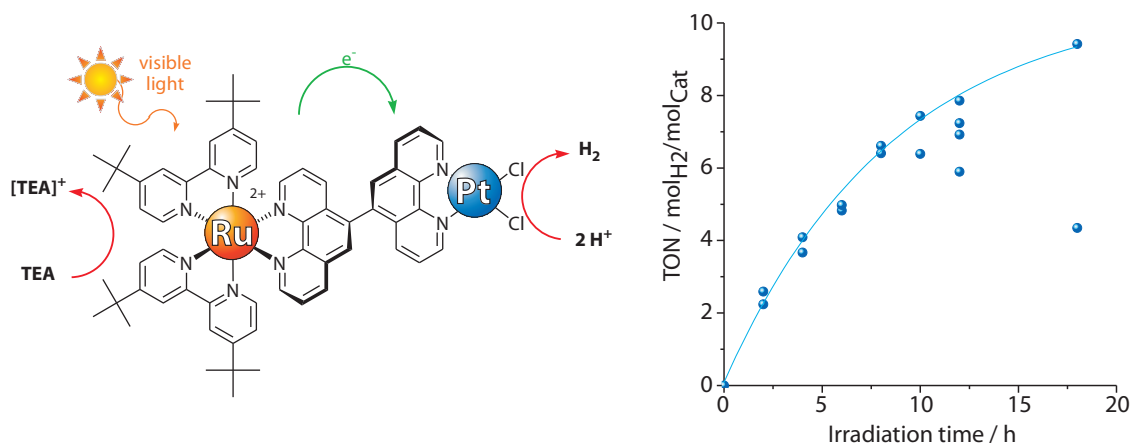
3. In einer Nickel-vermittelten Reaktion wurde der achsenchirale, bidentate Ligand **phenphen** aus dem zuvor genannten **phenBr** hergestellt. Weiterhin wurden damit die neuen mono- und dinuklearen unverbrückten und verbrückten Rutheniumkomplexe **Ru(phenphen)**, **Ru(phenphen)Ru**, sowie der heterodinukleare $[\text{P} \sim \text{B} \sim \text{C}]$ -artige Platinkomplex **Ru(phenphen)Pt** hergestellt und anschließend charakterisiert, wobei Kristallstrukturen von

phenphen und **Ru(phenphen)** gewonnen werden konnten, die die spektroskopischen Daten weiter unterstützen.

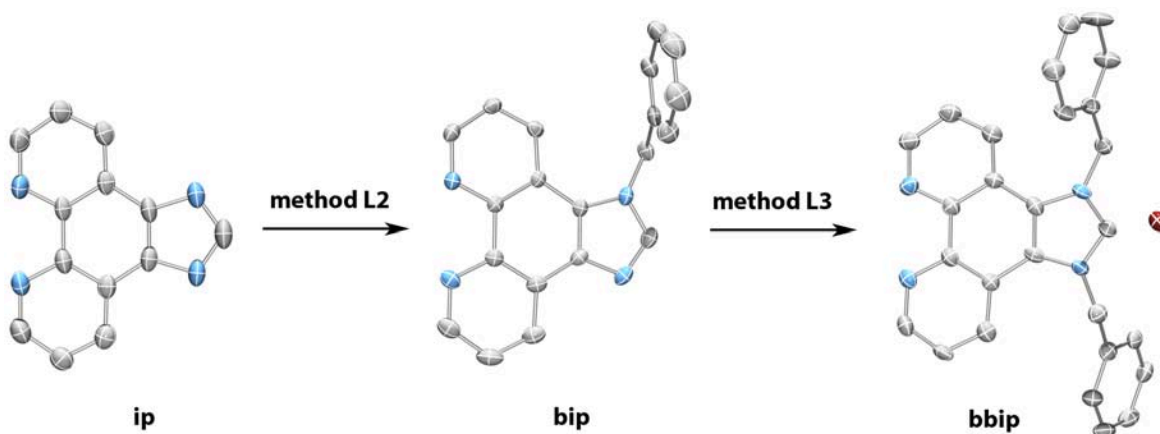


Insbesondere wurde eine detaillierte Isomerenanalyse mittels NMR-Untersuchungen angewendet, um die inisochronen Atropisomere der Rutheniumkomplexe zu untersuchen, die aufgrund der sterischen Hinderung der Rotation um die verbrückend wirkende Einfachbindung hervorgerufen werden. Anhand eines zeitabhängigen NMR-Experiments von erhaltenen Einkristallen der $\Delta R_a/\Lambda S_a$ -**Ru(phenphen)**-Isomere konnte eine Halbwertszeit von $t_{1/2} = 1.99$ h für die Umwandlung in die $\Delta S_a/\Lambda R_a$ -konfigurierten Rotamere errechnet werden. Weiterhin konnte aus dem Absorptions- und Emissionsverhalten die Ausbildung einer typischen $[\text{Ru}^{3+}(\overline{\text{LL}})(\overline{\text{LL}})_2]$ -artigen transienten Spezies, sowie neuer Photoprodukte aus den platinfreien Komplexen beobachtet werden.

4. Da aus den photophysikalischen und elektrochemischen Untersuchungen eine begrenzte elektronische Kommunikation zwischen den beiden Phenanthrolinsphären, sowie eine günstige Lage der Redoxpotentiale der enthaltenen Metallzentren abgeleitet werden konnte, wurden Katalyseexperimente mit **Ru(phenphen)Pt** und **Ru(phenphen)** unter geeigneten Bedingungen (in TEA:ACN:H₂O / 6:3:1) durchgeführt. Bei Katalysen mit dem Platinkomplex wurden beträchtliche Mengen an Wasserstoff detektiert, die zwar gering erscheinen, jedoch in der gleichen Größenordnung wie mit dem Katalysator $[(\text{tbbpy})_2\text{Ru}(\mu\text{-tpphz})\text{PtCl}_2]^{2+}$ liegen. Zusätzlich konnte aus den entsprechenden Messungen eine auf Wasser bezogene Konzentrations- abhängigkeit der Katalyse beobachtet werden, wobei die optimale Katalyseaktivität mit 5% Wasserzusatz erreicht wurde.

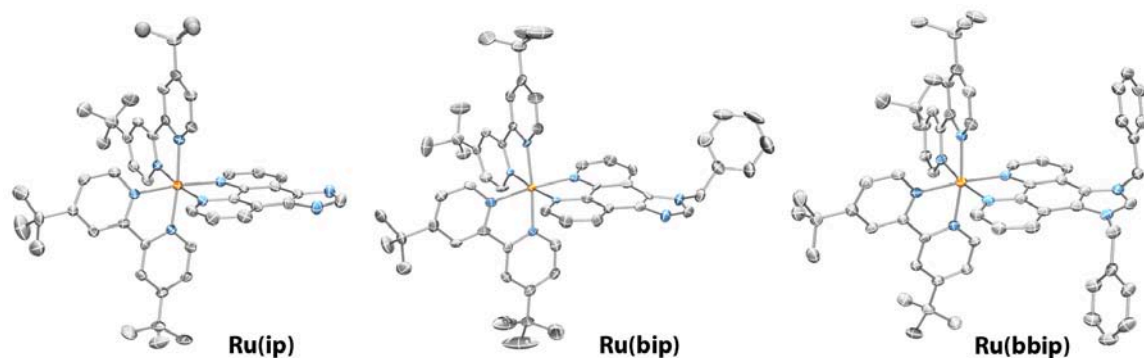


5. Durch die Entwicklung einer neuen Vorschrift wurden **bip** und das Imidazoliumsalz **bbip** in einer stufenweise verlaufenden Synthese (**method L2** und **L3**) aus **ip** hergestellt. Elementaranalyse, Massenspektrometrie, verschiedene NMR-Techniken und, am wichtigsten, Röntgendiffraktometrie wurden angewendet, um den neuen Brückenliganden sowie dessen Vorgängermoleküle zu untersuchen. Anhand von NMR-Kinetikstudien konnte der H/D-Austausch des aktiven N-CH-N-Protons des Imidazoliumsalzes in Methanol-*d*₄ verfolgt und gefittet werden, dabei ergab sich eine Geschwindigkeitskonstante von $k = 2.36 \times 10^{-5} \text{ s}^{-1}$ und eine Halbwertszeit für den Austausch von $t_{1/2} = 490 \text{ min}$. Die erhaltenen Resultate untermauern die Folgerung, dass es sich bei **bbip** um die erfolgreiche Kombination der beiden wichtigen Ligandmotive, einer Phenanthrolin- und einer NHC-Koordinations-sphäre, handelt.



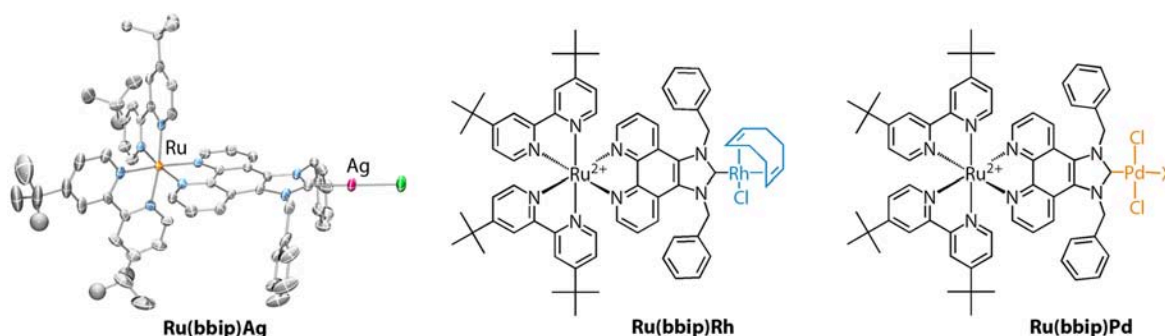
6. Aus der Serie von **ip**-artigen Liganden wurde die Serie von mononuklearen Ruthenium-komplexen **Ru(ip)**, **Ru(bip)**, und **Ru(bbip)** hergestellt, die alle das bekannte $\{\text{Ru}(\text{tbbpy})_2\}^{2+}$ -

Fragment tragen. Die resultierenden Komplexe wurden vollständig charakterisiert, wobei das besondere Augenmerk auf der Festkörper- strukturanalyse, dem Absorptions- und Emissionsverhalten, sowie dem elektrochemischen Verhalten lag.



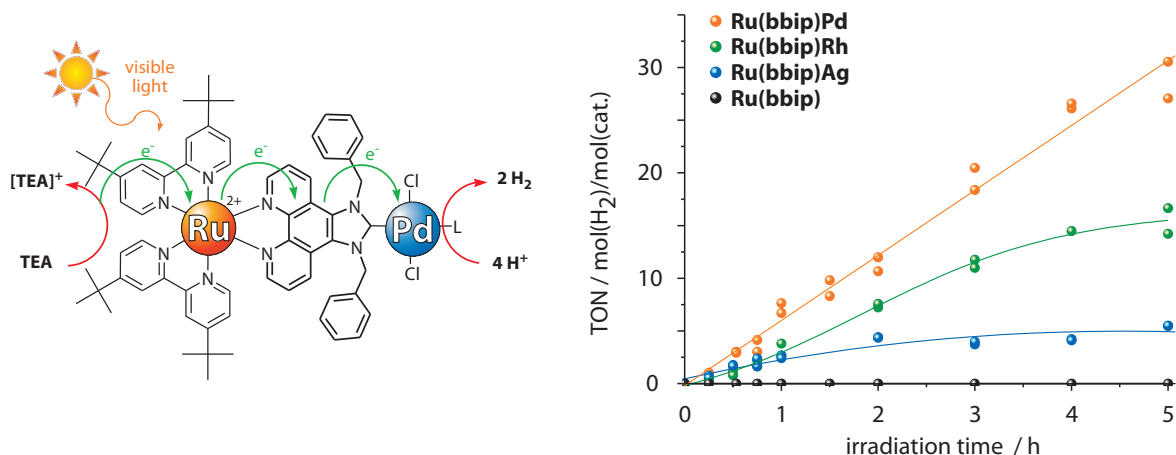
Aus der Strukturanalyse dieser Verbindungen wurde geschlossen, dass durch den Einfluss der Imidazolsphäre keine signifikanten Unterschiede an der Chelatsphäre der Phenanthrolinseite auftreten, wohingegen die Imidazoleinheit selbst ähnliche Veränderungen durchläuft, wie die zuvor untersuchten Liganden **ip**, **bip** und **bbip**. Elektrochemische Untersuchungen belegten das Ruthenium-typische reversible Verhalten, wohingegen Absorption- und Emissionsstudien einen starken Einfluss des Imidazoliumsystems aufzeigen, wobei sehr hohe Emissionsquanten- ausbeuten und stark rotverschobene Emissionswellenlängen gefunden wurden.

7. Eine Anzahl von Versuchen wurde unternommen, um zu einer Koordination der NHC-Seite von **bbip** oder **Ru(bbip)** zu gelangen, wobei weder Deprotonierung, noch Komplexierung mit $[\text{Mo}(\text{thf})(\text{CO})_5]$ oder Bildung des $\text{NHC}\cdot\text{BEt}_3$ Addukts erfolgreich waren. Durch die gezielte Modifikation einer Literaturvorschrift (**method C2**) gelang schließlich die Herstellung des verbrückten Komplexes **Ru(bbip)Ag**. Durch die Verwendung dieses Precursors als Carben-transferagens wurden die $[\text{P} \sim \text{B} \sim \text{C}]$ -artigen Diaden **Ru(bbip)Rh** und **Ru(bbip)Pd** hergestellt, um das Anwendungspotential der Silberverbindung in Transmetallierungsreaktionen exemplarisch zu zeigen.

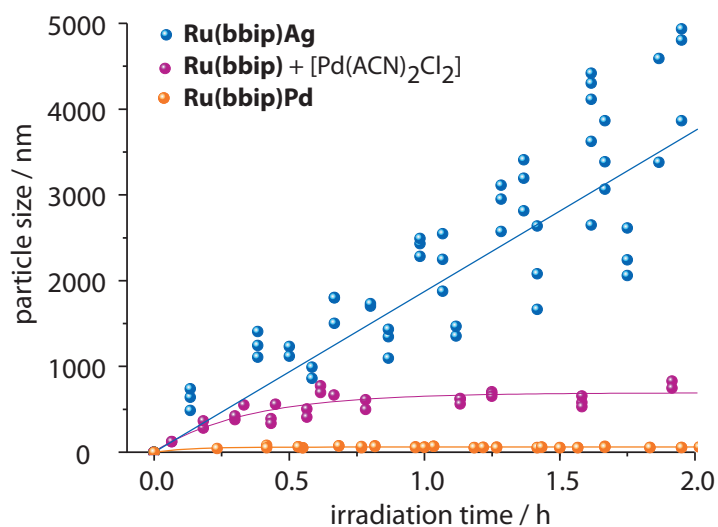


Die Charakterisierung, inklusive detaillierter MS und MSⁿ-Untersuchungen, spektroskopischer Messungen der **bbip**-verbrückten Komplexe, sowie der Röntgenstrukturanalyse von **Ru(bbip)Ag** wurde erzielt. In allen **Ru(bbip)**-Komplexen wurden die Eigenschaften der gut bekannten Ru(bpy)₃-Untereinheit, wie beispielsweise ¹MLCT-Absorption zwischen 430 und 500 nm wiedergefunden, allerdings mit sehr starken ³MLCT-Emissionsbanden zwischen 600 und 700 nm, sowie den korrespondierenden Redox Eigenschaften. Dabei erreichen die Quantenausbeuten Werte bis zu 39%.

8. Eine Anzahl von intramolekularen Katalyseexperimenten wurde mit **Ru(bbip)Pd** und **Ru(bbip)Rh**, sowie den Referenzverbindungen **Ru(bbip)Ag** und **Ru(bbip)** durchgeführt. Aus den ermittelten, auf die Bestrahlungszeit bezogenen sowie auf die Katalysatorkonzentration bezogenen Abhängigkeiten der Wasserstoffentwicklung konnten Belege für die Aktivität der Palladium- und der Rhodiumkomplexe erhalten werden, mit denen weiterhin das Konzept einer molekularen Photoredoxkatalyse gestützt wird. Interessanterweise wurde sogar beim Silberkomplex eine gewisse Katalyseaktivität festgestellt, wohingegen die Referenz **Ru(bbip)** inaktiv blieb. Anhand der durchgeführten Kontrollexperimente mit intermolekularen $[[\mathbf{P} \sim \mathbf{B} / \mathbf{C}]]$ -artigen Systemen, das heißt mit **Ru(bbip)** als Chromophor und [Pd(ACN)₂Cl₂] oder [Rh(cod)₂Cl]₂ als Katalysator konnte ebenfalls lichtgetriebene Wasserstoffbildung demonstriert werden, wobei deutlich verschiedene Katalysekinetiken im Vergleich zu den intramolekularen Systemen gefunden wurden.

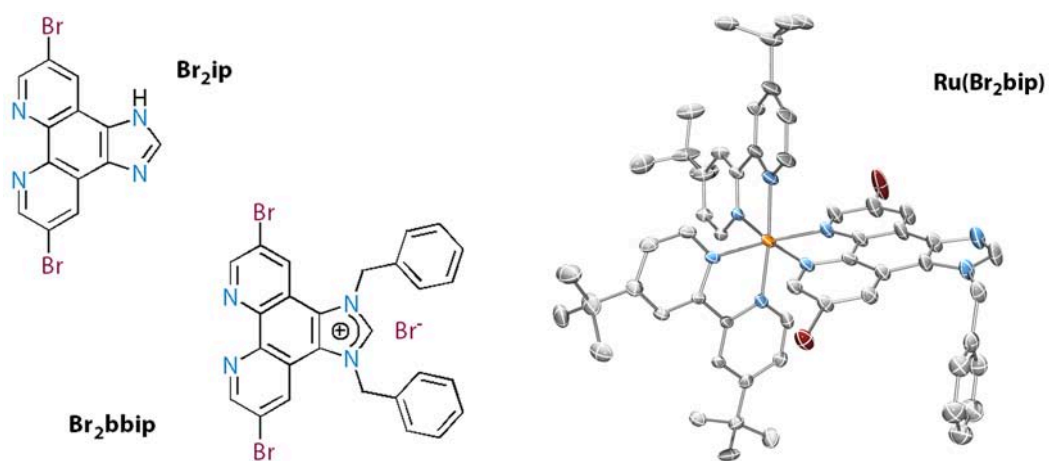


9. Mit Hilfe eine Reihe von dynamischen Lichtstreuungsmessungen an den intramolekularen Katalysatoren sowie den intermolekularen Katalyselösungen konnte der Einfluss der Molekülstruktur auf die Kolloidbildung und auf die Katalyse genau untersucht werden. Es wurde gezeigt, dass der Komplex **Ru(bbp)Pd** als Modellverbindung für supramolekulare Photokatalysatoren angesehen werden kann, während im Fall von **Ru(bbp)Ag** (photographischer Prozess) und von **Ru(bbp) + [Pd(ACN)₂Cl₂]** (Pd-Kolloid) deutliche Mengen an wachsenden Partikeln gebildet werden, wobei eine klare Korrelation zwischen Partikelwachstum und intermolekularer Katalyseaktivität demonstriert wurde.



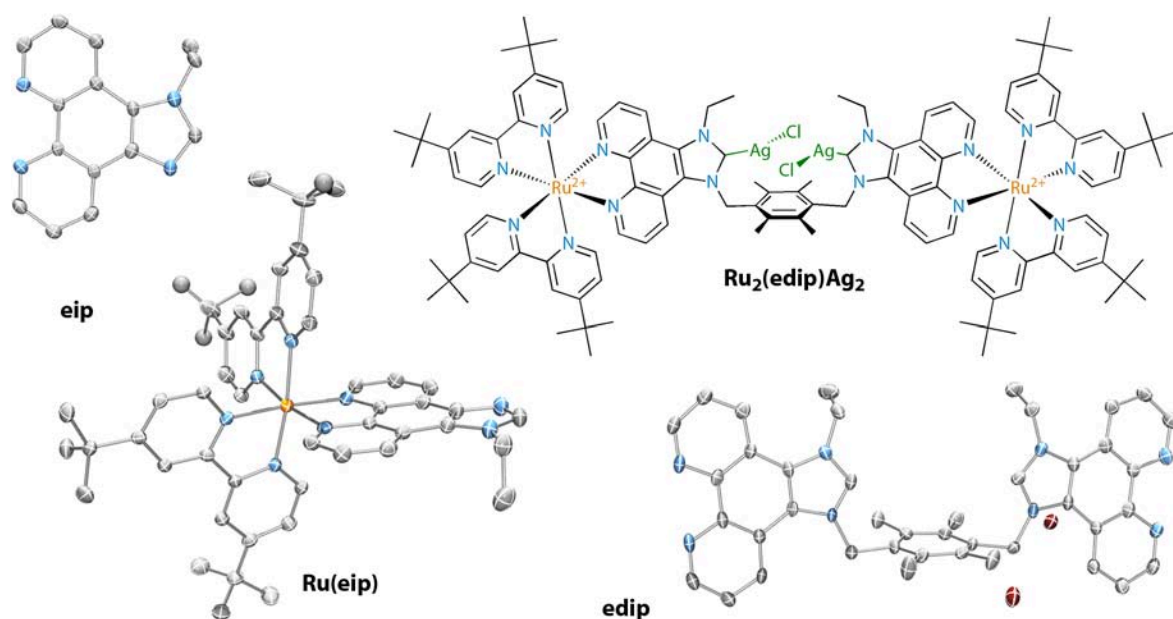
10. Im Rahmen von Vorversuchen zur Entwicklung von besonders elektronenarmen Verbindungen wie **Ru(bbp)₃** oder **Ru(Br₂bbp)** wurden die Liganden **Br₂ip**, **Br₂bbp**, und **Br₂bbip** hergestellt. Die Anwendung der Standardvorschrift zur Komplexierung führte in beiden

Fällen zur Zersetzung der Ligandsysteme und führte somit zu den Verbindungen $\text{Ru}(\text{bip})_3$ und $\text{Ru}(\text{Br}_2\text{bip})_3$, wie anhand von NMR-Untersuchungen gezeigt wurde.



Anhand der Röntgenstrukturanalyse von $\text{Ru}(\text{Br}_2\text{bip})_3$ konnte gezeigt werden, dass diese Verbindung ähnliche Eigenschaften zum verwandten $\text{Ru}(\text{bip})_3$ aufweist. Diese Resultate konnten genutzt werden, um einen Eindruck der Grenzen dieser Synthesemethode und der Ligandstabilität im elektronenarmen Komplex zu gewinnen.

- II.** Um Zugang zu multimetallischen Katalysezentren und erweiterten Lichtsammelinheiten zu schaffen wurde ein Ligand mit einer, um die **ip**-Einheit erweiterten Koordinationssphäre entwickelt. Ausgehend von **ip** wurden die neuen Liganden **eip** und **edip** unter Verwendung der zuvor entwickelten Vorschriften hergestellt und anschließend vollständig charakterisiert. Wie die Röntgenstrukturanalyse von **edip** zeigt, enthält dies eine vorgebildete NHC-NHC Koordinationstasche, die für größere mehrkernige Metallzentren mit einem Durchmesser von etwa 6,0 Å geeignet ist. Weiterhin wurden aus den Liganden die N,N'-koordinierten $\{\text{Ru}(\text{tbbpy})_2\}^{2+}$ -enthaltenden Komplexe $\text{Ru}(\text{eip})$ und $\text{Ru}_2(\text{edip})$ hergestellt und anschließend charakterisiert, wobei eine Kristallstruktur von $\text{Ru}(\text{eip})$ erhalten wurde.



In einer abschließenden Machbarkeitsstudie wurde der Vierkernkomplex $\text{Ru}_2(\text{edip})\text{Ag}_2$ hergestellt, welcher die Ag-NHC-Carben-Transfereinheit aufweist. Die Charakterisierung erfolgte mittels verschiedener NMR- und MS-Methoden.

Im Allgemeinen konnten die neuen Imidazophenanthrolinliganden, wie beispielsweise **bbip** oder **edip**, als geeignete Ausgangsstoffe für die weitere Entwicklung von intramolekularen Mehrkernsystemen identifiziert werden. Besonders die Kombination einer Azadien- mit einer Carbenkoordinationssphäre ist ideal für das Design von stabilen molekularen $[\text{P} \sim \text{B} \sim \text{C}]$ -artigen Katalysatoren, in denen sowohl Katalysezentrum als auch Photozentrum in weiten Grenzen variiert werden können. Der besonders einfache Austausch von Metallfragmenten, sowie der Coligandumgebung am NHC-System, erlaubt in Zukunft möglicherweise sogar die Veränderung der Natur der jeweiligen katalytischen Reaktion, welche durch Licht angetrieben wird.

Es bleibt zu Hoffen, dass die hier erzielten Resultate den Weg für zukünftige Forschungen ebnen, und so möglicherweise ein Beitrag zur Lösung des zukünftigen Energieproblems geliefert werden konnte.

6 Experimental Section

General

Steady state UV/vis absorption spectroscopy:

Steady state absorption spectra were obtained using a *Perkin Elmer Lambda2* UV/vis two-beam spectrophotometer using a slit width of 2 nm and a scan rate of 480 nm/min. All spectra were recorded using a quartz glass cuvette of 10·10 mm.

Steady state emission spectroscopy:

Steady state emission spectra were recorded using a *Jasco FP-6200* spectrofluorometer and a *Horiba Jobin Yvon FluoroMax-3* spectrometer using a slit width of 2 nm for excitation and emission and an integration time of 0.5 s. The studies were performed in a 10·10 mm quartz glass cuvette.

Time resolved emission studies:

Emission lifetimes were determined via time correlated single photon counting (TCSPC) on a *Horiba Jobin Yvon FluoroLog-3* emission spectrometer with a *Hamamatsu MCP* photomultiplier (R3809U-58). For excitation a laser diode (*NanoLED-405L*, 403 nm, pulse width = 200 ps, maximum of repetition rate 100 kHz) was used. All measurements were performed in a 10·10 mm quartz glass cuvette.

Electrochemistry:

Electrochemical data were obtained by cyclic voltammetry using a conventional single-compartment three-electrode cell arrangement in combination with a potentiostat "AUTOLAB", eco chemie". As auxiliary and reference electrode two Pt wires were used; working electrode: glassy carbon. The measurements were carried out in anhydrous and argon saturated acetonitrile. Tetrabutylammonium hexafluorophosphate ($c_{(TBAPF_6)} = 0.1\text{M}$) was used as supporting electrolyte at ambient temperature (20 (± 5)°C). All potentials are referenced to ferrocene/ferrocenium ($E_{(Fc/Fc^+)} = 0.00\text{V}$).

Spectroelectrochemistry:

Spectroelectrochemical experiments were carried out using a *HEKA Elektronik Potentiostat/Galvanostat PG284* and a *SPECORD S600 Analytic Jena* spectrophotometer. The measurements were performed in a homemade three neck cell ($d = 0.3$ cm) with a platinum gauze (working electrode), a platinum wire (counter electrode) versus a silver wire (pseudo reference electrode) under argon atmosphere. Tetrabutylammonium hexafluorophosphate ($c_{(TBAPF_6)} = 0.2$ M) was used as supporting electrolyte.

Femtosecond transient absorption spectroscopy:

Femtosecond transient absorption studies were performed with an amplified Ti/sapphire laser system (Model *CPA 2101*, *Clark-MXR Inc.* - output: 775 nm, 1 kHz and 150 fs pulse width) in the TAPPS - Transient Absorption Pump / Probe System - *Helios* from *Ultrafast Systems*. That is referred to as a two-beam setup where the pump pulse of 480 nm and 200 nJ, generated out of a NOPA - noncollinear optical parametrical amplifier, *Clark MRX Inc.* - is used as excitation source for transient species and the delay of the probe pulse is exactly controlled by an optical delay rail of 3.3 ns. As probe beam (white light continuum), a small fraction of 775 nm pulses stemming from the CPA laser system was focused by a 50 mm lens into a 3 mm thick sapphire disc. Finally, the changes in optical density (ΔA) are measured against the wavelength in both visible and near-infrared regions. The transient spectra were recorded in a 2 mm quartz glass cuvette.

Nanosecond transient absorption spectroscopy:

For nanosecond transient absorption experiments the samples were excited with the output of the second harmonic (532 nm) coming from a Nd:YAG laser. Moreover, pulse widths of less than 5 ns with energies of up to 7 mJ were selected. The optical detection was based on a pulsed Xenon lamp, a monochromator, a photomultiplier tube or a fast silicon photodiode with a 1 GHz amplification and a 500 MHz digital oscilloscope. The laser power of every laser pulse was registered using a bypath with a fast silicon photodiode. The experiments were performed in a 5-10 mm quartz glass cuvette.

Elemental Analysis

Elemental analysis was performed on a Euro Vector Euro EA.

Mass spectrometry:

The mass spectra were recorded with a *SSQ 710* spectrometer (*Finnigan MAT*). Electrospray ionization spectra were recorded with a *MAT 95 XL* (*Thermoquest-Finnigan MAT*).

NMR-Experiments:

The NMR spectra were recorded on a *Bruker 400 MHz* spectrometer and on a *Jeol EX-270 DELTA* and no a *Jeol EX-400 DELTA* spectrometer (270/400 MHz), respectively.

Crystal-structure Analysis:

The intensity data for the compounds (**Ru(bbip)**) and (**Ru(bbip)Ag**) were collected on a *Nonius Kappa-CCD* diffractometer, using graphite-monochromated Mo-K α radiation ($\lambda = 0.71069 \text{ \AA}$, graphite monochromator) at $-140(2)^\circ\text{C}$. Data were corrected for Lorentz and polarization effects, but not for absorption effects.^[199, 200] The structures were solved by direct methods (*SHELXS* [10.1107/S0108767390000277]) and refined by full-matrix least squares techniques against Fo_2 (*SHELXL-97*).^[201, 202, 203] The hydrogen atoms were included at calculated positions with fixed thermal parameters. All nonhydrogen atoms were refined anisotropically.^[201, 202, 203] *XP* (*SIEMENS Analytical X-ray Instruments, Inc.*) was used for structure representations. The data is freely available on the internet: www.ccdc.cam.ac.uk/data_request/cif (or can be required under the following address in Great Britain: Cambridge Crystallographic Data Centre, 12 Union Road, GBCambridge CB21EZ; Fax:(+44)1223-336-033; or deposit@ccdc.cam.ac.uk): **Ru(bbip)** (CCDC-765499), **Ru(bbip)Ag** (CCDC-796734),

Dynamic Light Scattering Experiments

DLS data were obtained, using a *Delsa Nano C* particle analyzer from *Beckman Coulter*. As light source dual 30 mW laser diodes with a wavelength of 658 nm were used. All measurements were performed at 25°C . For the viscosity a value of 0.58 mPas and for the refractive index a value of

1.3648 was determined for the catalytic mixture. All size calculations were done with standard calculation methods. All measurements were performed applying 10×10 mm quartz SUPRASIL inert cuvettes from Hellma. All experiments were repeated with three identical solutions to ensure the reproducibility of the data. Before measuring, the cuvettes were cleaned with aqua regia, concentrated ammonia, distilled water and filtrated acetonitrile (syringe filter pore size 0.2 μm). After this procedure every cuvette was filled with filtrated acetonitrile and investigated by DLS to exclude any remaining particles. All solvents were degassed with nitrogen before use. The catalytic mixtures consisted of 1.2 ml acetonitrile (with the photo catalyst), 0.6 ml Et₃N and 0.2 ml water. The final concentration of the photo catalyst in the catalytic solution was 50 μM. This mixture was filled into the cuvettes through a syringe filter (pore size 0.2 μm) under inert conditions. All solutions were measured immediately. In the beginning every solution was investigated without irradiation. Each experiment was repeated several times. Between the measurements the solutions were irradiated with the previously used led-arrays ($\lambda = 470$ nm).

Catalysis Experiments

The photohydrogen production experiments were carried out using a home-built air-cooling apparatus for maintaining room temperature (22°C) and constant irradiation of the sample. 5 ml GC vials (diameter = 13 mm, VWR) with a known headspace of 3 ml and a headspace/solution ratio of 3/2 were used as reaction vessels. Directly before the irradiation experiments, fresh stock solutions of the respective samples with solvent mixtures of acetonitrile, triethylamine and water in a 6:3:1 ratio (v:v:v) and with the desired concentrations of ruthenium complex (10 μM, 50 μM, 100 μM and 250 μM) were prepared in the dark. Then, the required number of GC vials was charged in the dark and under nitrogen atmosphere. For the dynamic light scattering experiments inert cuvetts (10×10 mm, quartz glass) were used instead of GC vials. Subsequently, the samples were irradiated with a LED-array (54 LEDs, exit angle 15°, luminous intensity 14.0 cd each, from Innotas Elektronik GmbH, Zittau, Germany) at a wavelength of ($\lambda = 470$ nm, suitable to excite in the MLCT-band). After the irradiation, 100 μl gas samples were drawn from the headspace and injected immediately into the GC apparatus. The concentration of evolved hydrogen was quantified by headspace GC on a GCMS-QP2010S chromatograph from Shimadzu, with a thermal conductivity detector and a Rtx®-5MS (fused silica) column (length 30 m, 0.25 mm inner diameter,

layer thickness 0.25 μm) with nitrogen as carrier gas (purity 99.999%) an oven temperature of 70°C, a flow rate of 22.5 ml/min, a detector temp. of 220°C, and a pressure of 102.1 kPa were used. The GC was calibrated by mixing different volumes of pure hydrogen (0-100%) together with nitrogen into a Schlenk vessel. The obtained signal (retention time for H₂, t_R = 1.95 min) was plotted against the calibration curve and multiplied accordingly to receive the total produced hydrogen content in the headspace. Irradiation experiments and hydrogen measurements were repeated several times for each reaction time (between 2 and 12 h) and catalyst concentration.

Used Chemicals:

All chemicals were reagent grade and were used without any further purification. Where necessary all manipulations were carried out by using Schlenk techniques under argon atmosphere. Prior to use dichloromethane was distilled over CaH₂. Acetonitrile was dried and distilled over mole sieves A 4, methanol was dried and distilled over magnesium. THF and toluene and triethylamine were dried over KOH and distilled over Na/benzophenone.

Prepared Chemicals

The following chemicals were prepared according to literature procedures: [Ru(tbbpy)₂Cl₂]^[120], [Ru(tbbpy)₃][PF₆]₂^[120], [Ru(tbbpy)₂(5-chloro-1,10-phenanthroline)][PF₆]₂^[116], 4,4'-ditertbutyl-2,2'-bipyridine^[204, 205], 1,10-Phenanthroline-5,6-dione^[206], [Ru(COD)Cl₂]^[128], 3,8-dibromo-1,10-phenanthroline-5,6-dione^[126], bisbromomethyldurene^[207], NiCl₂(PPh₃)₂^[208], [Pd(Cl)₂(ACN)₂]^[208], [Mo(CO)₅(thf)]^[183],

6.1 Synthesis of the Organic Ligands

6.1.1 Bromination of Phenanthrolines - method L1

To a round bottom flask, charged with 4.0 g of the phenanthroline derivate, 30 ml of fuming sulfuric acid (65%) were added with cooling (0°C). Then a big stir bar was carefully added to the mixture and the neck of the flask was closed with a watch glass. After stirring complete dissolution (~2 hours stirring at 10°C) of the phenanthroline an the desired amount of bromine was added to the solution in one portion and the mixture was stirred until the brown color of the bromine

disappeared. Heating of the mixture (60°C) may accelerate the reaction. After the reaction time the mixture was poured onto 200 ml of ice and was neutralized (pH 7) with ammonia. The formed precipitate was extracted with chloroform. Subsequently, the combined organic layers were dried over Na₂SO₄ and the solvent was removed under vacuum. Then, the crude was dissolved in hot toluene and insoluble impurities were filtered off. After removal of the solvent purification was achieved by recrystallization from (ethanol, chloroform or ether/methylene chloride). Drying in high-vacuum yielded the desired brominated product.

6.1.2 1-Substitution of 1H-Imidazoles - method L2

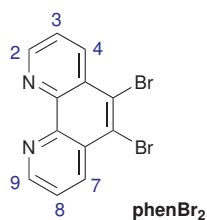
Under argon atmosphere the desired amount of the desired 1H-imidazole (~1.5 g) and 1.1 equivalent of sodium hydride (60% in paraffin) were suspended in 50 ml of dry DMF. After stirring and/or sonicating for several minutes the solids were completely reacted and no further gas evolution or solid material was observed. Then one equivalent of halogenated compound was added and the solution. Stirring for several hours at room temperature yielded a tinted solution. After the reaction time, the solvent was removed completely under vacuum and the residue was redissolved in chloroform and washed with water. The combined organic phases were dried over Na₂SO₄. After removal of the organic solvent the crude product was purified by column chromatography using chloroform and silica gel 60 as phase system.

6.1.3 3-Substitution of 1-Substituted 1H-Imidazoles - method L3

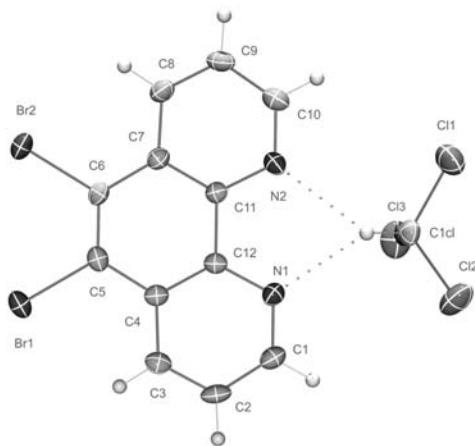
One equivalent (~2.0 g) of the desired 1-substituted 1H-imidazole was dissolved in a mixture of DMF and an excess of the halogenated compound. The solution was heated to 60-120°C for one to sixteen hours to form a viscous yellow precipitate, which was collected after cooling and was washed with toluene or petrol ether and diethyl ether. The crude product was purified by recrystallization from hot toluene with a small amount of methanol to yield the 1,3-substituted 1H-imidazolium halide as cream colored solid. A combination of **method L2** and **method L3** is possible for the preparation of 1,3-homosubstituted 1H-imidazolium halides without intermediate workup.

6.1.4 5,6-Dibromo-1,10-phenanthroline - phenBr₂

Following **method L1**, 30 ml of fuming sulfuric acid (65%) were added with cooling to 4.0 g (20.2 mmol) of 1,10-phenanthroline hydrate. After the phenanthroline was completely dissolved (2 hours) an excess of bromine 1.7 ml (33.3 mmol) was added to the solution. This mixture was heated to 60°C for two hours. This mixture was poured onto 200 ml of ice after the reaction time. Upon neutralization (pH 7) precipitate formed, which was extracted with chloroform. The combined organic layers were dried over Na₂SO₄ and the solvent was removed under vacuum. Then the crude was dissolved in hot toluene, the insoluble dark impurities were filtered off and the solvent was removed under vacuum. Purification was achieved by recrystallization from chloroform. After drying at high-vacuum the pure compound was obtained as white powder. Yield: 90% (6.7 g, 18.2 mmol).



¹H-NMR (CDCl₃, 400 MHz): δ = 9.232 (dd, 2H_(2/9), ³J = 4.4 Hz, ⁴J = 1.6 Hz), 8.778 (dd, 1H_(4/7), ³J = 8.6 Hz, ⁴J = 1.6 Hz), 7.739 (dd, 1H_(3/8), ³J = 8.6 Hz, ³J = 4.4 Hz) ppm. ¹³C-NMR (CDCl₃, 100 MHz): δ = 150.92 (2C_(2/9)), 145.09 (2C_(10a/10b)), 137.56 (2C_(4a/6a/9)), 128.74 (2C_(4/7)), 125.27 (2C_(5/6)), 124.60 (2C_(3/8)) ppm. MS: 338 m/z (100%, M⁺). elementary analysis: calc.: C: 42.64%, H: 1.79%, N: 8.29%, Br: 47.28% found: C: 37.95%, H: 2.71%, N: 8.22%, Br: 46.17%.

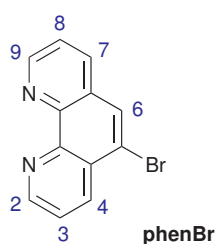


Crystals suitable for X-ray diffraction were obtained from chloroform. Crystal data for **phenBr₂**: C₁₂H₆N₂ × CHCl₃, M_r = 2071.08 g/mol, colorless cuboid, size 0.05 × 0.05 × 0.04 mm³, monoclinic, space group P2₁/n (No. 14), a = 11.7492(4), b = 11.7577(4), c = 12.3256(4) Å, α = 90.000, β = 118.106(2), γ = 90.000°, V = 1501.92 Å³, T = -90(2)°C, Z = 4, $\rho_{\text{calcd.}}$ = 2.023 g/cm³, $\mu_{(\text{Mo-K}\alpha)}$ = 5.920 cm⁻¹, F(000) = 880, 10426 reflections in h(-15/15), k(-14/15), l(-16/15) measured in the range 2.55° ≤ Θ ≤ 27.505°, completeness

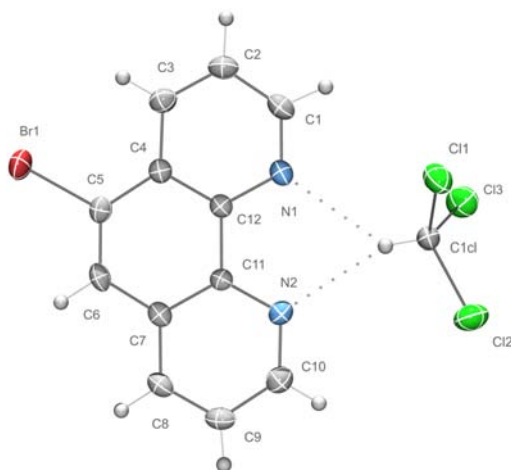
Φ_{max} = 99.6%, 3429 independent reflections, R_{int} = 0.0311, 3429 reflections with F_o > 4σ(F_o), 181 parameters, 0 restraints, R_{obs.} = 0.0311, wR_{obs.}² = 0.0702, R_{all} = 0.0532, wR_{all}² = 0.0786, GOOF = 0.959, largest difference peak and hole: 0.572 / -0.487 e/Å³. The data file TT3789 includes the full crystallographic data and can be obtained from DR. HELMAR GÖRLS (IAAC, FSU-Jena).

6.1.5 5-Bromo-1,10-phenanthroline - phenBr

As described in **method L1**, 30 ml of fuming sulfuric acid (65%) were added with cooling to 4.0 g (20.2 mmol) of 1,10-phenanthroline hydrate. After the phenanthroline was dissolved a slight excess of bromine (0.6 ml, 11.75 mmol) was added to the solution in one portion. Upon stirring for 3 hours at room temperature the reaction mixture turned colorless due to the complete consumption of bromine. The reaction was not stopped until 16 hours later by pouring the solution on 250 ml on ice and neutralization (pH 5) with ammonia. Extraction with small amounts of chloroform drying of combined organic phases over Na_2SO_4 yielded a crude after removal of the solvent. Redissolving in boiling toluene and hot filtration was used to remove impurities. A crude mixture of **phenBr** and **phenBr**₂ with small traces of the starting material phenanthroline was obtained. Purification by column chromatography did not succeed. Starting material phenanthroline was removed by stirring in ether over night and subsequent collection of the solids. Slow recrystallization from chloroform yielded the pure compound (**phenBr** × CHCl_3) as colorless crystals in good yields (70%, 4.0 g, 14.1 mmol). In this way as well suitable crystals for X-ray diffraction were obtained.



¹H-NMR (CDCl_3 , 400 MHz): δ = 9.1 (m, 2H_(2/9)), 8.526 (dd, 1H₍₄₎), ³J = 8.4 Hz, ⁴J = 1.6 Hz), 8.034 (dd, 1H₍₇₎), ³J = 8.1 Hz, ⁴J = 1.6 Hz), 7.979 (s, 1H₍₆₎), 7.624 (dd, 1H₍₃₎), ³J = 8.3 Hz, ³J = 4.4 Hz), 7.520 (dd, 1H₍₈₎), ³J = 8.1 Hz, ³J = 4.3 Hz) ppm.
¹³C-NMR (CDCl_3 , 100 MHz): δ = 150.89, 150.68, 146.65, 145.67, 135.89, 135.06, 145.09, 129.64, 128.80, 124.00, 123.64, 120.78 ppm.



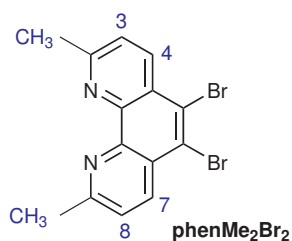
Crystals suitable for X-ray diffraction were obtained from chloroform. Crystal data for **phenBr**: $\text{C}_{12}\text{H}_7\text{N}_2 \times \text{CHCl}_3$, $M_r = 378.47 \text{ g/mol}$, colorless crystal, size $0.065 \times 0.065 \times 0.05 \text{ mm}^3$, monoclinic, space group $\text{P}2_1/\text{n}$ (No. 14), $a = 6.9802(2)$, $b = 20.3654(6)$, $c = 9.8052(3) \text{ \AA}$, $\alpha = 90.000$, $\beta = 92.768(2)$, $\gamma = 90.000^\circ$, $V = 1392.23(7) \text{ \AA}^3$, $T = -90(2)^\circ\text{C}$, $Z = 4$, $\rho_{\text{calcd.}} = 1.806 \text{ g/cm}^3$, $\mu_{(\text{Mo-K}\alpha)} = 35.13 \text{ cm}^{-1}$, $F(000) = 744$, 9838 reflections in $h(-9/9)$, $k(-25/26)$, $l(-12/10)$ measured in the range

$2.00^\circ \leq \Theta \leq 27.48^\circ$, completeness $\Phi_{\text{max}} = 99.8\%$, 3182 independent reflections, $R_{\text{int}} = 0.0449$, 2576 reflections with $F_o > 4\sigma(F_o)$, 204 parameters, 0 restraints, $R_{\text{obs.}} = 0.0433$, $wR_{\text{obs.}}^2 = 0.1016$, $R_{\text{all}} =$

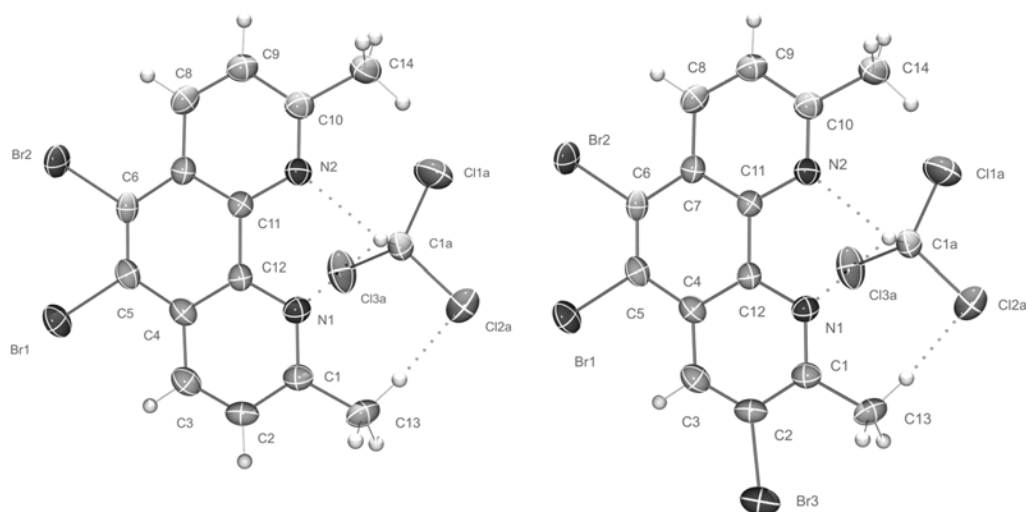
0.0583, $wR_{\text{all}}^2 = 0.1080$, GOOF = 1.052, largest difference peak and hole: 0.914/-0.486 e/Å³. The data file TT3588 includes the full crystallographic data and can be obtained from DR. HELMAR GÖRLS (IAAC, FSU-Jena).

6.1.6 5,6-Dibromo-2,9-dimethyl-1,10-phenanthroline - phenMe₂Br₂

The title compound was prepared by the application of **method LI**. After dissolving 1.0 g (4.9 mmol) of 2,9-dimethyl-1,10-phenanthroline in 30 ml of fuming sulfuric acid (65%) under cooling 0.38 ml (7.3 mmol) bromine were added. The emulsion was stirred over night at room temperature and was poured on 45 ml of ice after the reaction time. The mixture was neutralized with ammonia (pH 7) and the formed precipitate was extracted with chloroform. Removal of the solvent yielded the crude product. For the purification, recrystallization of the crude product from ethanol, ether, methylenchlorid and other solvents did not succeed. In all cases a mixture of the 5,6-dibromo- (**phenMe₂Br₂**) and the 3,5,6-tribromocompound (**phenMe₂Br₃**) was obtained.



¹H-NMR (CDCl₃, 400 MHz): $\delta = 8.43$ (d, 2H_(4/7), ³J = 8.6 Hz), 7.41 (d, 2H_(3/8), ³J = 8.6 Hz), 2.83 (s, 6H_(CH₃)) ppm. ¹³C-NMR (CDCl₃, 100 MHz): $\delta = 150.92$ (2C_(2/9)), 145.09 (2C_(10'/10'')), 137.56 (2C_(4'/6'/9)), 128.74 (2C_(4/7)), 125.27 (2C_(5/6)), 124.60 (2C_(3/8)) 25.60 (2C_(CH₃)) ppm.
MS (DEI): $m/z = 338$ (100%, M⁺)

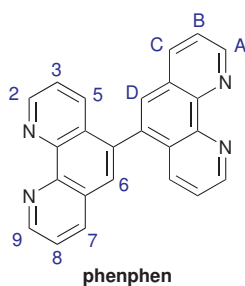


Crystals suitable for X-ray diffraction were obtained from chloroform. Crystal data for **phenMe₂Br₂/phenMe₂Br₃**: C₁₄H₁₀N₂Br₂ × 2 CHCl₃ and C₁₃H₁₀N₂Br₃ × 2 CHCl₃, M_r = 610.32 g/mol, colorless cuboid, size 0.05 × 0.05 × 0.05 mm³, monoclinic, space group P2₁/c (No. 14), a =

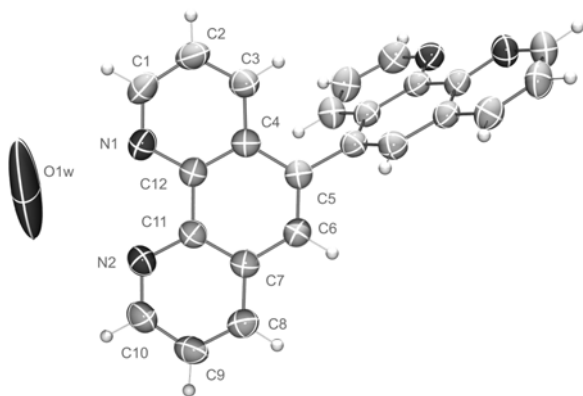
9.2640(2), $b = 16.4066(5)$, $c = 14.7540(4)$ Å, $\alpha = 90.000$, $\beta = 107.931(2)$, $\gamma = 90.000^\circ$, $V = 2133.55(10)$ Å³, $T = -90^\circ\text{C}$, $Z = 4$, $\rho_{\text{calcd.}} = 1.900$ g/cm³, $\mu_{(\text{Mo-K}\alpha)} = 46.87$ cm⁻¹, $F(000) = 1186$, 14976 reflections in $h(-11/12)$, $k(-21/20)$, $l(-19/18)$ measured in the range $2.48^\circ \leq \Theta \leq 27.48^\circ$, completeness $\Phi_{\text{max}} = 99.9\%$, 4882 independent reflections, $R_{\text{int}} = 0.0629$, 3740 reflections with $F_o > 4\sigma(F_o)$, 247 parameters, 0 restraints, $R_{\text{obs.}} = 0.0388$, $wR_{\text{obs.}}^2 = 0.0954$, $R_{\text{all}} = 0.0571$, $wR_{\text{all}}^2 = 0.1031$, GOOF = 1.041, largest difference peak and hole: 0.689 / -0.795 e/Å³. The data file TT3606 includes the full crystallographic data and can be obtained from DR. HELMAR GÖRLS (IAAC, FSU-Jena).

6.1.7 5,5'-Bis-1,10-phenanthroline - phenphen

To a well degassed solution of 2.86 g NiCl₂·6H₂O and 10.5 g PPh₃ in 80 ml DMF 787 mg of zinc powder were added in one portion. The resulting mixture was stirred for one hour under argon at 60°C forming a bright red precipitate. After the catalyst has formed 2.60 g of **phenBr**, dissolved in 20 ml of well degassed DMF was added. This mixture was stirred for 14 h at 60°C. After the reaction time this mixture was poured into 180 ml of aqueous ammonia (10%) with 8.0 g KCN dissolved in it and was stirred for one hour at room temperature. The solids were filtered off and redissolved in chloroform. After washing of the organic layers with water and drying with Na₂SO₄ heptane was added to this solution. By the removal of chloroform from this mixture under vacuum a precipitate formed. The crude material was filtered off and purified by chromatography using deactivated (III) alumina and chloroform/hexane 1:3 as eluent. Yield: 650 mg (1.81 mmol, 18%) of pale yellow powder. Recrystallization from ethanol yielded crystals suitable for X-ray diffraction.



¹H-NMR (CDCl₃, 400 MHz): $\delta = 9.260$ (dd, 2H₍₂₎, ³J = 4.4 Hz, ⁴J = 1.6 Hz), 9.190 (dd, 1H₍₉₎, ³J = 4.4 Hz, ⁴J = 1.6 Hz), 8.274 (dd, 1H₍₄₎, ³J = 8.0 Hz, ⁴J = 1.6 Hz), 7.907 (s, 1H₍₆₎), 7.731 (dd, 2H₍₇₎, ³J = 8.0 Hz, ⁴J = 1.6 Hz), 7.694 (dd, 2H₍₃₎, ³J = 8.0 Hz, ³J = 4.4 Hz), 7.431 (dd, 1H₍₈₎, ³J = 8.0 Hz, ³J = 4.4 Hz) ppm. ¹³C-NMR (CDCl₃, 100 MHz): $\delta = 150.89, 150.54, 146.25, 146.15, 136.05, 135.30, 134.49, 128.57, 128.09, 127.99, 123.58, 123.14$ ppm.



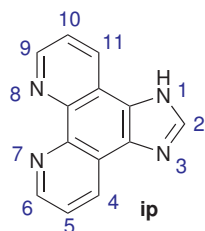
Crystals

suitable for X-ray diffraction were obtained from ethanol/water. Crystal data for **phenphen**: $C_{24}H_{14}N_4Ru \times 2 H_2O$, $M_r = 394.42 \text{ g/mol}$, colorless crystal, size $0.06 \times 0.06 \times 0.05 \text{ mm}^3$, monoclinic, space group $C2/c$ (No. 15), $a = 16.979(3)$, $b = 11.113(2)$, $c = 11.884(2) \text{ \AA}$, $\alpha = 90.000$, $\beta = 121.35(3)$, $\gamma = 90.000^\circ$, $V = 1914.8(7) \text{ \AA}^3$, $T = -$

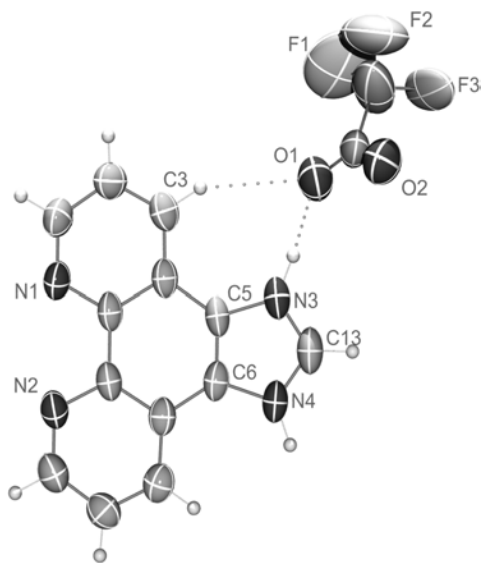
90°C , $Z = 4$, $\rho_{\text{calcd.}} = 1.368 \text{ g/cm}^3$, $\mu_{(\text{Mo-K}\alpha)} = 0.9 \text{ cm}^{-1}$, $F(000) = 824$, 6270 reflections in $h(-21/20)$, $k(-14/14)$, $l(-15/15)$ measured in the range $3.51^\circ \leq \Theta \leq 27.47^\circ$, completeness $\Phi_{\text{max}} = 98.6\%$, 2167 independent reflections, $R_{\text{int}} = 0.0336$, 1604 reflections with $F_o > 4\sigma(F_o)$, 146 parameters, 0 restraints, $R_{\text{obs.}} = 0.0628$, $wR_{\text{obs.}}^2 = 0.1834$, $R_{\text{all}} = 0.0851$, $wR_{\text{all}}^2 = 0.0851$, GOOF = 0.970, largest difference peak and hole: $0.710/-0.202 \text{ e/\AA}^3$. The data file TT3698 includes the full crystallographic data and can be obtained from DR. HELMAR GÖRLS (IAAC, FSU-Jena).

6.1.8 1H-Imidazo[4,5-f][1,10]phenanthroline - ip

In a round bottom flask 5.0 g (23.8 mmol) of 1,10-phenanthroline, 6.7 g (47.6 mmol) of hexamine and 9.2 g (0.12 mol) of ammonium acetate were suspended in 70 ml of glacial acetic acid. After refluxing the resulting mixture for two hours, the volatiles were removed under reduced pressure. The resulting solid was dissolved in water and neutralized with ammonia. Stirring this mixture over night yielded an off-white precipitate. The solid was filtered off, and washed twice with water and dried under vacuum. Further purification was achieved by recrystallization from water. Yield: 4.45 g (20.2 mmol, 85%) of a white powder.



$^1\text{H-NMR}$ (200 MHz, $\text{CDCl}_3/\text{CF}_3\text{COOD}/\text{CD}_3\text{OD}$): 9.28 (dd, $2\text{H}_{(4,11)}$, $^4J = 1.3 \text{ Hz}$, $^3J = 8.4 \text{ Hz}$), 9.12 (dd, $2\text{H}_{(6,9)}$, $^4J = 1.3 \text{ Hz}$, $^3J = 5.0 \text{ Hz}$), 8.87 (s, $1\text{H}_{(2)}$), 8.12 (dd, $2\text{H}_{(5,10)}$, $^3J = 5.0 \text{ Hz}$, $^3J = 8.4 \text{ Hz}$) ppm. $^{13}\text{C-NMR}$ (400 MHz, $\text{D}_2\text{O}/\text{CF}_3\text{COOD}/\text{KNO}_3$) 145.27 ($2\text{C}_{(6,9)}$), 141.55 ($1\text{C}_{(2)}$), 133.33 ($2\text{C}_{(5,10)}$), 132.84 ($2\text{C}_{(7,7'')}$), 126.56 ($2\text{C}_{(3,1'')}$), 125.59 ($2\text{C}_{(4,11)}$), 119.67 ($2\text{C}_{(3,11'')}$) ppm. MS (DEI): $m/z = 220$ (100%, M^+), 193 (25%, $[\text{M-HCN}]^+$). Elementary analysis ($\text{C}_{13}\text{H}_8\text{N}_4 \cdot 2\text{H}_2\text{O}$): calc.: C: 60.93%, H: 4.72%, N: 21.86%, meas.: C: 61.18%, H: 4.41%, N: 21.97%.

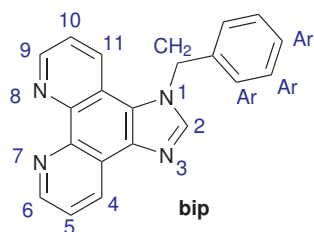


Crystals suitable for X-ray diffraction were obtained from diluted trifluoroacetic acid. Crystal data for **ip**: $[\text{C}_{13}\text{H}_8\text{N}_4]^+ \times [\text{CF}_3\text{COO}]^-$, $M_r = 334.26 \text{ g/mol}$, colorless cuboid, size $0.05 \times 0.05 \times 0.04 \text{ mm}^3$, monoclinic, space group $\text{P}1_1/\text{n}$ (No. 14), $a = 13.6042(8)$, $b = 6.9560(6)$, $c = 16.6210(12) \text{ \AA}$, $\alpha = 90.000$, $\beta = 111.634(4)$, $\gamma = 90.000^\circ$, $V = 1462.06(19) \text{ \AA}^3$, $T = -90(2)^\circ\text{C}$, $Z = 2$, $\rho_{\text{calcd.}} = 1.519 \text{ g/cm}^3$, $\mu_{(\text{Mo-K}\alpha)} = 1.3 \text{ cm}^{-1}$, $F(000) = 680$, 9652 reflections in $h(-17/17)$, $k(-7/9)$, $l(-21/21)$ measured in the range $2.64^\circ \leq \Theta \leq 27.45^\circ$, completeness $\Phi_{\text{max}} = 99.3\%$, 3308 independent reflections, $R_{\text{int}} = 0.0508$, 2023 reflections with $F_o >$

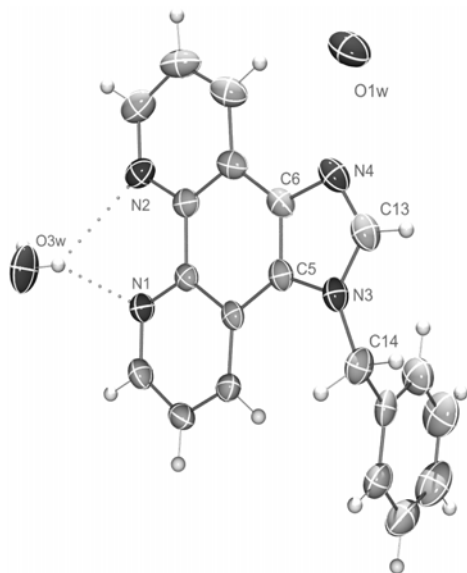
$4\sigma(F_o)$, 248 parameters, 0 restraints, $R_{\text{obs.}} = 0.0669$, $wR_{\text{obs.}}^2 = 0.1695$, $R_{\text{all}} = 0.1152$, $wR_{\text{all}}^2 = 0.1971$, $\text{GOOF} = 1.017$, largest difference peak and hole: $0.403/-0.341 \text{ e/\AA}^3$. The data file TT3762 includes the full crystallographic data and can be obtained from DR. HELMAR GÖRLS (IAAC, FSU-Jena). In the molecular structure of **ip** false-ordered fluorine atoms are omitted for clarity. Ellipsoids are drawn at 70% probability. Selected bond length (\AA) and angles ($^\circ$):

6.1.9 1-Benzyl-1H-imidazo[4,5-f][1,10]phenanthroline - bip

Following the general procedure according to **method L2**, 2.0 g (9.1 mmol) of **ip** were deprotonated with 523 mg (13.1 mmol) of sodium hydride (60% in paraffin) under argon atmosphere in 10 ml of dry DMF. Then 1.30 ml (10.9 mmol) of benzyl bromide were added to the stirred sodium imidazolide solution. After the reaction time of three hours at room temperature the solvent was removed completely under vacuum and the residue was redissolved in chloroform and washed with water. The combined organic phases were dried over Na_2SO_4 . Purification was achieved by column chromatography using chloroform and silica gel 60 as phase system. Yield: 1.9 g (6.1 mmol, 74%) of a colorless solid.



$^1\text{H-NMR}$ (CDCl_3 , 400 MHz): $\delta = 9.168$ (dd, $2\text{H}_{(6,9)}$, $^3J = 4.6$ Hz, $^4J = 1.6$ Hz), 9.039 (dd, $2\text{H}_{(9,6)}$, $^3J = 4.6$ Hz, $^4J = 1.6$ Hz), 8.999 (dd, $2\text{H}_{(4,11)}$, $^3J = 8.2$ Hz, $^4J = 1.6$ Hz), 8.191 (dd, $2\text{H}_{(11,4)}$, $^3J = 8.2$ Hz, $^4J = 1.6$ Hz), 8.020 (s, $1\text{H}_{(2)}$), 7.729 (dd, $2\text{H}_{(5,10)}$, $^3J = 8.2$ Hz, $^3J = 4.4$ Hz), 7.413 (dd, $2\text{H}_{(5,10)}$, $^3J = 8.2$ Hz, $^3J = 4.4$ Hz), 7.3 (m, $3\text{H}_{(\text{Ar})}$), 7.1 (m, $2\text{H}_{(\text{Ar})}$), 7.3 (m, $3\text{H}_{(\text{Ar})}$), 5.794 (s, $2\text{H}_{(-\text{CH}_2)}$) ppm. $^{13}\text{C-NMR}$ (CDCl_3 , 400 MHz): $\delta = 149.00$ ($1\text{C}_{(6,9)}$), 148.06 ($1\text{C}_{(9,6)}$), 144.68 ($1\text{C}_{(3;11'')}$), 144.15 ($1\text{C}_{(11;3'')}$), 143.54 ($1\text{C}_{(2)}$), 137.67 ($1\text{C}_{(3;11'')}$), 134.99 ($1\text{C}_{(\text{Cl-Ar})}$), 130.48 ($1\text{C}_{(4,11)}$), 129.41 ($2\text{C}_{(\text{Ar})}$), 128.74 ($1\text{C}_{(\text{C4-Ar})}$), 128.58 ($1\text{C}_{(11,4)}$), 126.00 ($2\text{C}_{(\text{Ar})}$), 124.38 ($1\text{C}_{(11';3'')}$), 124.35 ($1\text{C}_{(7;7'')}$), 123.68 ($1\text{C}_{(5,10)}$), 122.59 ($1\text{C}_{(10,5)}$), 119.58 ($1\text{C}_{(7'';7'')}$), 51.29 ($1\text{C}_{(\text{CH}_2)}$) ppm.

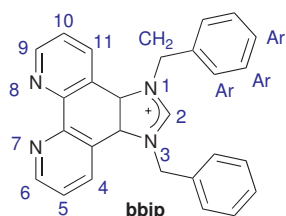


Crystals suitable for X-ray diffraction were obtained from methanol/water. Crystal data for **bip**: $\text{C}_{20}\text{H}_{14}\text{N}_4 \times 1.5 \text{H}_2\text{O}$, $M_r = 337.38 \text{ g mol}^{-1}$, colorless cuboid, size $0.06 \times 0.04 \times 0.04 \text{ mm}^3$, triclinic, space group $\text{P}\bar{1}$ (No. 2), $a = 11.2481(3)$, $b = 12.1858(5)$, $c = 12.4532(6) \text{ \AA}$, $\alpha = 79.993(2)$, $\beta = 86.406(2)$, $\gamma = 85.159(2)^\circ$, $V = 1672.95(11) \text{ \AA}^3$, $T = -90(2)^\circ\text{C}$, $Z = 4$, $\rho_{\text{calcd.}} = 1.339 \text{ g cm}^{-3}$, μ ($\text{Mo-K}\alpha$) = 0.88 cm^{-1} , $F(000) = 708$, 11572 reflections in $h(-14/14)$, $k(-15/14)$, $l(-16/15)$ measured in the range $3.18^\circ \leq \Theta \leq 27.48^\circ$, completeness $\Phi_{\text{max}} = 99.2\%$, 7621 independent reflections, $R_{\text{int}} = 0.0322$, 5013 reflections with $F_o > 4\sigma(F_o)$, 460 parameters, 0 restraints, $R_{\text{obs.}} = 0.0558$, $wR_{\text{obs.}}^2 = 0.1143$, $R_{\text{all}} = 0.1012$, $wR_{\text{all}}^2 = .01331$, GOOF = 1.006, largest difference peak and hole: $0.256 / -0.326 \text{ e\AA}^{-3}$. The data file TT3947 includes the full crystallographic data and can be obtained from DR. HELMAR GÖRLS (IAAC, FSU-Jena). In the ORTEP representation of the molecular structure of **bip** solvent molecules were omitted for clarity. Ellipsoids were drawn at 70% probability level.

6.1.10 1,3-Dibenzyl-1H-imidazo[4,5-f][1,10]phenanthroline bromide - bbip

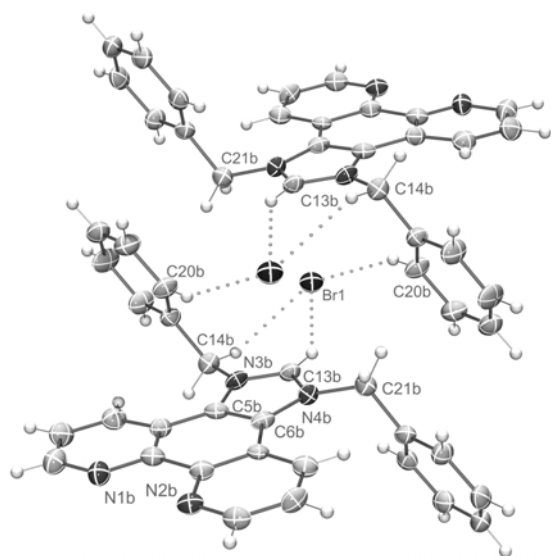
As described in **method L3**, 2.00 g (6.44 mmol) of **bip** were dissolved in 10 ml of benzyl bromide. The solution was stirred at 120°C for one hour, forming a viscous yellow precipitate. Then 5 ml of DMF were added to the stirred solution. After two more hours at 120°C a light yellow precipitate

was formed. The crude was allowed to cool down, the precipitate was filtered off and was washed twice with diethyl ether. The crude product was purified by recrystallization from toluene with a small amount of methanol. Yield: 2.44 g (4.96 mmol, 77%) of a white solid. (The crude product of **bip** is also a suitable educt for this reaction.)



$^1\text{H-NMR}$ (CD_3OD , 270 MHz): $\delta = 9.61$ (s, $1\text{H}_{(2)}$), 9.21 (dd, $2\text{H}_{(6/9)}$, $^3J = 4.6$ Hz, $^4J = 1.4$ Hz), 9.06 (dd, $2\text{H}_{(4/11)}$, $^3J = 8.6$ Hz, $^4J = 1.5$ Hz), 7.97 (dd, $2\text{H}_{(5/10)}$, $^3J = 4.6$ Hz, $^3J = 8.6$ Hz), 7.46 (m, $10\text{H}_{(\text{ph})}$), 6.37 (s, $2\text{H}_{(\text{CH}_2)}$) ppm;

$^1\text{H-NMR}$ (CDCl_3 , 400 MHz): $\delta = 11.945$ (s, $1\text{H}_{(2)}$), 9.283 (dd, $2\text{H}_{(6/9)}$, $^3J = 4.4$ Hz, $^4J = 1.6$ Hz), 8.555 (dd, $2\text{H}_{(4/11)}$, $^3J = 8.5$ Hz, $^4J = 1.6$ Hz), 7.685 (dd, $2\text{H}_{(5/10)}$, $^3J = 8.5$ Hz, $^3J = 4.4$ Hz), 7.40 (m, $10\text{H}_{(\text{ph})}$), 6.456 (s, $2\text{H}_{(\text{CH}_2)}$) ppm; $^{13}\text{C-NMR}$ (CDCl_3 , 100 MHz): $\delta = 150.64$ ($2\text{C}_{(6/9)}$), 143.64 ($3\text{C}_{(2/11/7'11'')}$), 134.54 ($2\text{C}_{(4/11)}$), 133.55 ($2\text{C}_{(\text{tc-ph})}$), 130.83 ($4\text{C}_{(2/6-\text{ph})}$), 130.49 ($2\text{C}_{(4-\text{ph})}$), 128.76 ($4\text{C}_{(3/5-\text{ph})}$), 127.64 ($2\text{C}_{(3'/11'')}$), 126.28 ($2\text{C}_{(5/10)}$), 120.10 ($2\text{C}_{(3''/11'')}$), 55.21 ($2\text{C}_{(\text{CH}_2)}$) ppm;



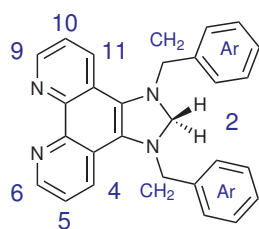
Crystals suitable for X-ray diffraction were obtained from hot toluene/water after cooling. Crystal data for **bbip**: $[\text{C}_{27}\text{H}_{21}\text{N}_4]^+[\text{Br}]^- \times 2\text{H}_2\text{O}$, $M_r = 517.42$ g mol^{-1} , colorless crystal, size $0.05 \times 0.04 \times 0.04$ mm^3 , triclinic, space group P-1 (No. 2), $a = 13.9804(8)$, $b = 14.0396(6)$, $c = 14.3866(9)$ \AA , $\alpha = 65.191(2)$, $\beta = 74.784(3)$, $\gamma = 72.977(3)^\circ$, $V = 2419.0(2)$ \AA^3 , $T = -140^\circ\text{C}$, $Z = 4$, $\rho_{\text{calcd.}} = 1.421$ g cm^{-3} , μ (Mo-K α) = 17.31 cm^{-1} , $F(000) = 1064$, 16704 reflections in $h(-15/18)$, $k(-18/15)$, $l(-16/18)$ measured in the range $2.47^\circ \leq \Theta \leq 27.45^\circ$,

completeness $\Phi_{\text{max}} = 98.2\%$, 10849 independent reflections, $R_{\text{int}} = 0.0682$, 6120 reflections with $F_o > 4\sigma(F_o)$, 612 parameters, 0 restraints, $R_{\text{obs.}} = 0.0919$, $wR_{\text{obs.}}^2 = 0.2339$, $R2_{\text{all}} = 0.1632$, $wR_{\text{all}}^2 = 0.2788$, GOOF = 1.036, largest difference peak and hole: $2.448 / -1.054$ $\text{e}\text{\AA}^{-3}$. The data file TT3958 includes the full crystallographic data and can be obtained from DR. HELMAR GÖRLS (IAAC, FSU-Jena). In the ORTEP representation of the molecular structure of **bbip** solvent molecules were omitted for clarity. Ellipsoids were drawn at 50% probability level.

6.1.11 Attempted Synthesis of the triethylborane adduct of

1,3-dibenzyl-1*H*-imidazo[4,5-*f*][1,10]phenanthroline-2-ylidene - **bbip**BEt₃

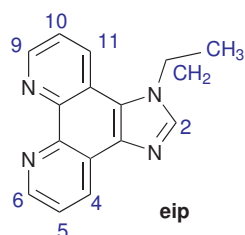
For the synthesis, 0.41 ml of a 1 M solution of HLiB(Et)₃ were added to a stirred solution of 100 mg **bbip** in 20 ml of dry tetrahydrofuran under argon atmosphere at -80°C. Upon addition a darkening of the solution toward yellow was observed. The temperature was raised to room temperature within 12 hours after the reaction time of 20 minutes at -80°C. After removal of the solvent and drying under high vacuum ¹H-NMR spectra were recorded in dry chloroform-*d* and dry acetonitrile-*d*₃. It was observed that the formed product is not sensitive to air. According to the obtained NMR-spectra it could be concluded that the hydrogenated product was formed. Indicators are signals for the A-, B-, C-protons which refer to the symmetric ligand, a signal which refers to the D-position with an peak area of two protons at 4.7 ppm and the missing characteristic triplet and quartet signals for the ethyl groups at ~1 ppm.



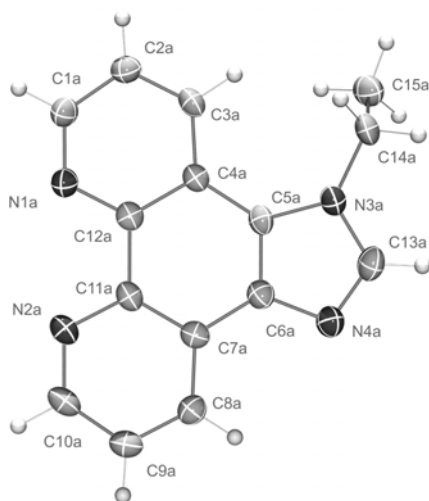
¹H-NMR (CDCl₃, 400 MHz): δ = 8.97 (d, 2H_(6/9), ³J = 3.6Hz), 8.35 (dd, 2H_(4/11), ³J = 8.3 Hz, ⁴J = 1.0 Hz), 7.62 (dd, 2H_(5/10), ³J = 4.5 Hz, ³J = 8.3 Hz), 7.31 (m, 10H_(Ar)), 4.76 (s, 2H₍₂₎), 4.25 (d, 2H_(CH₂), ²J = 23.7 Hz), 4.19 (d, 2H_(CH₂), ²J = 26.0 Hz) ppm. ¹H-NMR (CD₃OD, 400 MHz): δ = 8.91 (dd, 1H_(6/9), ³J = 4.4Hz, ⁴J = 1.6 Hz), 8.36 (dd, 2H_(4/11), ³J = 8.3 Hz, ⁴J = 1.6 Hz), 7.64 (dd, 2H_(5/10), ³J = 8.3 Hz, ³J = 4.3 Hz), 7.29 (m, 6H_(Ar)), 7.20 (m, 4H_(Ar)), 4.69 (s, 2H₍₂₎), 4.13 (s, 4H_(CH₂)) ppm.

6.1.12 1-Ethyl-1*H*-imidazo[4,5-*f*][1,10]phenanthroline - **eip**

Under argon atmosphere 1.3 g (5.9 mmol) of **ip** and 260 mg (6.49 mmol) of sodium hydride (60% in paraffin) were suspended in 50 ml of dry DMF as described in **method L2**. After stirring and sonicating for 30 min the imidazolide anion was completely dissolved and no further gas evolution was observed. Then 440 μ l (5.9 mmol) of bromoethane were added and the solution was stirred for three more hours at room temperature. After the reaction time the solvent was removed completely under vacuum and the residue was redissolved in chloroform and washed with water. The combined organic phases were dried over Na₂SO₄. After removal of the solvent the crude product was purified by column chromatography using chloroform and silica gel 60 as phase system. Yield: 1.43 g (5.8 mmol, 98%) of a colorless solid.



$^1\text{H-NMR}$ (400 MHz, CDCl_3/DMF): 9.116 (dd, $2\text{H}_{(6/9)}$, $^3J = 4.2$ Hz, $^4J = 1.4$ Hz), 8.929 (dd, $1\text{H}_{(4)}$, $^3J = 8.0$ Hz, $^4J = 1.6$ Hz), 8.488 (dd, $1\text{H}_{(11)}$, $^3J = 8.2$ Hz, $^4J = 1.4$ Hz), 7.959 (s, $1\text{H}_{(2)}$), 7.675 (dd, $1\text{H}_{(5)}$, $^3J = 8.0$ Hz, $^4J = 4.4$ Hz), 7.649 (dd, $1\text{H}_{(10)}$, $^3J = 8.0$ Hz, $^3J = 4.4$ Hz), 4.611 (q, $2\text{H}_{(\text{CH}_2)}$, $^3J = 7.2$ Hz), 1.655 (t, $3\text{H}_{(\text{CH}_3)}$, $^3J = 7.2$ Hz) ppm. $^{13}\text{C-NMR}$ (100 MHz, CDCl_3/DMF): 148.82 ($1\text{C}_{(6)}$), 147.85 ($1\text{C}_{(9)}$), 144.76 ($1\text{C}_{(7'')}$), 144.10 ($1\text{C}_{(7')}$), 141.98 ($1\text{C}_{(2)}$), 137.55 ($1\text{C}_{(3')}$), 130.09 ($1\text{C}_{(4)}$), 128.15 ($1\text{C}_{(11)}$), 124.29 ($1\text{C}_{(1')}$), 123.70 ($1\text{C}_{(11'')}$), 123.48 ($1\text{C}_{(5)}$), 122.54 ($1\text{C}_{(10)}$), 119.75 ($1\text{C}_{(3'')}$), 42.79 ($1\text{C}_{(\text{CH}_3)}$) ppm.

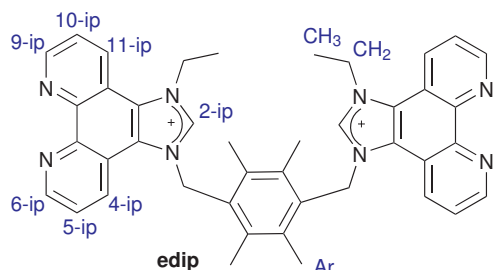


Crystals suitable for X-ray diffraction were obtained from hot toluene. Crystal data for **eip**: $\text{C}_6\text{H}_{12}\text{N}_4$, $M_r = 1.419$ g/mol, colorless crystal, size $0.05 \times 0.05 \times 0.05$ mm³, triclinic, space group $\text{P}\bar{1}$ (No. 2), $a = 7.9463(5)$, $b = 9.0538(.)$, $c = 17.1468(16)$ Å, $\alpha = 103.419(4)$, $\beta = 97.861(5)$, $\gamma = 99.828(5)^\circ$, $V = 1162.13(17)$ Å³, $T = -90(2)^\circ\text{C}$, $Z = 4$, $\rho_{\text{calcd.}} = 1.419$ g/cm³, $\mu_{(\text{Mo-K}\alpha)} = 0.89$ cm⁻¹, $F(000) = 520$, 7840 reflections in $h(-10/9)$, $k(-11/1)$, $l(-22/20)$ measured in the range $1.24^\circ \leq \Theta \leq 27.45^\circ$, completeness $\Phi_{\text{max}} = 96.2\%$, 5114 independent reflections, $R_{\text{int}} = 0.0476$, 2556 reflections with $F_o > 4\sigma(F_o)$, 345 parameters, 0 restraints, $R_{\text{obs.}} = 0.0653$, $wR_{\text{obs.}}^2 = 0.1379$, $R_{\text{all}} = 0.1634$, $wR_{\text{all}}^2 = 0.1718$, GOOF = 0.982, largest difference peak and hole: 0.418/-0.278 e/Å³. The data file TT3766 includes the complete crystallographic data and can be obtained from DR. HELMAR GÖRLS (IAAC, FSU-Jena). Ellipsoids are drawn at 70% probability in the molecular structure of **eip**. Selected bond length (Å) and angles ($^\circ$):

6.1.13 3,3'-(2,3,5,6-tetramethyl-1,4-phenylene)bis(methylene)bis-(1-ethyl-1H-imidazo[4,5-f][1,10]phenanthroline-3-ium) dibromide - edip

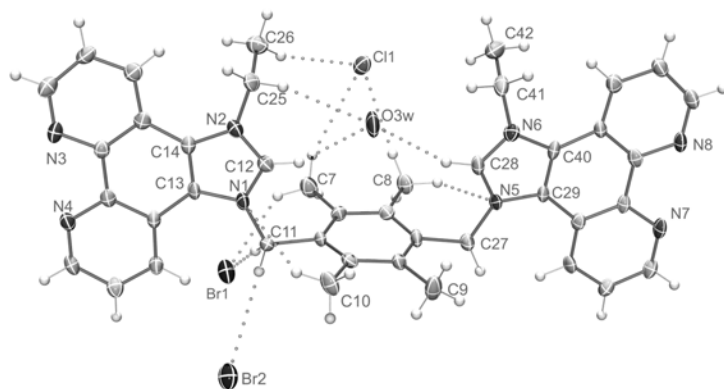
According to the general procedure, described in **method L3**, 200 mg (8005 μmol) of **eip** and 130 mg (405 μmol) of bisbromethyldurene were dissolved in 50 ml of DMF. The reaction mixture was stirred for 60 h at 80°C . Already after 24 h a bulky was precipitate formed. This precipitate

was collected after cooling and washed with ether to give 163 mg (200 μ mol, 50%) of the desired product as white off-white solid. Recrystallization from D₂O yielded suitable crystals for X-ray diffraction.



¹H-NMR (D₂O, 400 MHz): δ = 9.71 (d, 2H_(6/9-ip), ³J = 8.7 Hz), 9.31 (m, 6H_(4-ip,6/9-ip,11-ip)), 9.04 (s, 2H_(2-ip)), 8.36 (dd, 2H_(5/10-ip), ³J = 5.0 Hz, ³J = 8.4 Hz), 8.30 (dd, 2H_(5/10-ip), ³J = 5.1 Hz, ³J = 8.4 Hz), 6.29 (s, 4H_(CH₂-Ar)), 4.92 (q, 4H_(CH₂), ³J = 7.0 Hz), 2.25 (s, 12H_(CH₃-Ar)), 1.57 (t, 6H_(CH₂), ³J = 7.2 Hz) ppm. ¹³C-NMR (D₂O,

100 MHz): δ = 147.05 (2C_(4/11-ip)), 140.07 (2C_(2-ip)), 137.20 (2C_(6/9-ip)), 136.73 (4C_(2,3,5,6-Ar)), 136.63 (2C_(4/11-ip)), 136.07 (2C_(6/9-ip)), 128.97 (2C_(1,4-Ar)), 126.72 (2C_(5/10-ip)), 126.40 (2C_(5/10-ip)), 126.03 (2C_(7'/7''-ip)), 125.63 (2C_(7'/7''-ip)), 120.01 (2C_(3''/11''-ip)), 119.46 (2C_(3''/11''-ip)), 118.80 (2C_(3'/11'-ip)), 113.00 (2C_(3'/11'-ip)), 50.64 (2C_(CH₂-Ar)), 45.97 (2C_(CH₂)), 15.67 (2C_(CH₃-Ar)), 14.03 (2C_(CH₃)) ppm. MS: (FAB) m/z = 812 (5%, [M+2Br]⁺), 737 (80%, [M+Br]⁺), 655 (30%, [M]⁺), 407 (60%, [M-eip]⁺), 249 (100%, [eip]⁺).

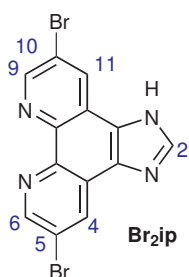


Crystals suitable for X-ray diffraction were obtained from D₂O. Crystal data for **edip**: [C₄₂H₄₀N₈]²⁺[Br⁻]₂ × 9 H₂O, M_r = 1014.23 g/mol, colorless crystals, size 0.05 × 0.05 × 0.04 mm³, monoclinic, space group P2₁/n (No. 14), a = 14.988(3), b = 20.766(4), c = 16.172(3) Å, α = 90.00, β = 116.51(3),

γ = 90.00°, V = 4504.2(16) Å³, T = 20°C, Z = 4, $\rho_{\text{calcd.}}$ = 1.496 g/cm³, $\mu_{(\text{Mo-K}\alpha)}$ = 19.22 cm⁻¹, F(000) = 2100, 30434 reflections in h(-19/17), k(-25/26), l(-16/20) measured in the range 2.51° ≤ Θ ≤ 27.52°, completeness Φ_{max} = 98.6%, 10221 independent reflections, R_{int} = 0.1049, 5526 reflections with F_o > 4 σ_{F_o} , 565 parameters, 0 restraints, R_{obs.} = 0.0829, wR_{obs.}² = 0.2074, R_{2all} = 0.1598, wR_{all}² = 0.2421, GOOF = 1.028, largest difference peak and hole: 3.239/-1.511 e/Å³. The data file TT3999 includes the full crystallographic data and can be obtained from DR. HELMAR GÖRLS (IAAC, FSU-Jena). In the molecular structure of **edip**. Hydrogen atoms (except H12a and H28a), solvent molecules and anions are omitted for clarity. Ellipsoids are drawn at 70% probability.

6.1.14 5,10-Dibromo-1H-imidazo[4,5-f][1,10]phenanthroline - Br₂ip

In a round bottom flask 368 mg (1.0 mmol) of 3,8-dibromo-1,10-phenanthrolindione, 280 mg (2.0 mmol) of hexamine and 385 mg (5.0 mol) of ammonium acetate were suspended in 10 ml of glacial acetic acid. After refluxing the resulting mixture for two hours, the volatiles were removed under reduced pressure. The resulting solid was dissolved in a small amount of water and neutralized with ammonia. Stirring this mixture over night yielded an off-white precipitate. The solid was filtered off, and washed twice with ethanol and ether and was dried under vacuum. Yield: 265 mg (700 μ mol, 70%) of a light yellow powder.



¹H-NMR (400 MHz CDCl₃/CF₃COOD): δ = 12.78 (s, 1H_(NH)), 9.36 (d, 1H_(A), ⁴J = 2.0 Hz), 9.34 (d, 1H_(A), ⁴J = 2.0 Hz), 9.11 (d, 1H_(C), ⁴J = 2.1 Hz), 8.90 (s, 1H_(D)), 8.37 (d, 1H_(C), ⁴J = 2.1 Hz) ppm. ¹H-NMR (400 MHz, DMSO-*d*) δ = 9.06 (d, 2H_(A), ⁴J = 2.3 Hz), 9.00 (d, 2H_(C), ⁴J = 2.3 Hz), 8.51 (s, 1H_(D)) ppm.

6.1.15 1,3-Dibenzyl-5,10-dibromo-1H-imidazo[4,5-f][1,10]phenanthroline bromide - Br₂bbip

According to **method L2**, 250 mg of **Br₂ip** and 55 mg of sodium hydride (60% in paraffin) were suspended in 15 ml of dry DMF and were reacted for 30 minutes in the ultrasonic sound bath until the imidazolide was dissolved. Then, 200 μ l of benzylbromide were added and the reaction mixture was stirred for two hours. After the reaction the typical color change from dark brown into a light brown was observed and 300 μ l of benzylbromide were added according to **method L3**. One NMR-sample was taken inbetween and analyzed. Without isolation of the intermediately formed monoalkylated product, the mixture was stirred over night at 80°C. The formed yellow precipitate (product) was collected and washed with ether. Complete removal of the volatiles of the organic phase in high vacuum gave additional fraction. The residue was dissolved in chloroform, filtrated and washed with water in an extraction funnel. And the combined organic layers were dried with Na₂SO₄. Removal of the solvent gave a yellow powder. Overall yield 57% (mg, μ mol) with respect to **Br₂ip**.

¹H-NMR (400 MHz DMSO-*d*₆, intermediately formed **Br₂bbip**) δ = 9.11 (d, 1H_(A), ⁴J = 2.4 Hz), 9.06

(d, $1H_{(A)}$, ${}^4J = 2.4$ Hz), 9.02 (d, $1H_{(C)}$, ${}^4J = 2.1$ Hz), 8.63 (d, $1H_{(C)}$, ${}^4J = 2.2$ Hz), 7.95 (s, $1H_{(D)}$), 7.32 (m, $3H_{(Ar)}$), 7.15 (d, $2H_{(Ar)}$, $J = 7.2$ Hz), 6.10 (s, $1H_{(CH_2)}$) ppm. 1H -NMR (400 MHz methanol- d_4 , **Br₂bbip**) $\delta = 9.76$ (s, 1H), 9.15 (d, $2H_{(A)}$, ${}^4J = 2.0$ Hz), 8.94 (d, $2H_{(C)}$, ${}^4J = 2.0$ Hz), 7.46 (m, $10H_{(Ar)}$), 6.32 (s, $4H_{(CH_2)}$) ppm.

6.2 Synthesis of the Metal Complexes

6.2.1 Synthesis of $[Ru(\widehat{LL})_2(\widehat{LL}')]^{2+}$ -type complexes - method C1

One equivalent (~ 50 - 300 mg) of the cis- $[Ru(\widehat{LL})_2Cl_2]$ compound and one equivalent of the desired ligand \widehat{LL}' were dissolved in 100 ml of a mixture of ethanol/water (4:1 / v:v). This mixture was refluxed in the microwave for 60-300 minutes with a power of 150 W. Ethanol was removed after cooling to precipitate impurities from the remaining aqueous solution. After filtration, 9 equivalents of NH_4PF_6 were added. The formed precipitate was collected after stirring for 30 minutes and was washed with water several times. Purification was either achieved by recrystallization from mixtures of acetone, acetonitrile or water, or by column chromatography with mixtures of acetonitrile/sat. solution of KNO_3 /water. To remove water from the product, it was dissolved in dichloromethane, dried with Na_2SO_4 and filtered. After removal of the solvent under vacuum pure product compound $[Ru(\widehat{LL})_2(\widehat{LL}')][PF_6]_2$ was obtained. Yield: (70-95%)

6.2.2 Synthesis of $[Ag(NHC)X]$ -type complexes from imidazolium salts - method C2

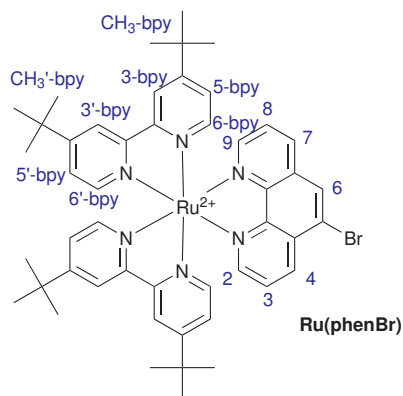
Under argon atmosphere one equivalent (200 μ mol) of the imidazolium halogenide, (110 μ mol) of silver(I) oxide, and 2 g of dry molecular sieves were suspended in 25 ml of dry dichloromethane (acetonitrile for insoluble compounds). This mixture was stirred in the dark for 16 hours at room temperature. After the reaction time, the remaining solids were removed by filtration through oven dried celite. The celite was washed with dry dichloromethane or acetonitrile. A pure product $[Ag(NHC)X]$ was obtained after removal of the solvent under reduced pressure. Yield: ($\sim 90\%$) of a powder, sensitive to air, moisture and possibly light.

6.2.3 Transmetalation of [Ag(NHC)X]-type complexes - method C3

Under argon atmosphere one equivalent (e.g. 100 μmol) of $[\text{Ru}(\text{tbbpy})_2(\mu\text{-bbip})\text{AgCl}]\text{Cl}_2$ and one equivalent of the starting complex for the transmetalation reaction were dissolved in 20 ml of dry dichloromethane. After stirring for 2-16 hours at room temperature a colorless precipitate was formed. The solid was removed by filtration through oven dried celite after the reaction time. The celite was washed with dry dichloromethane or acetonitrile to obtain remaining product. Finally the solvent was removed completely under vacuum. The product was obtained as a red powder which decomposes under air. Yield: (~95%).

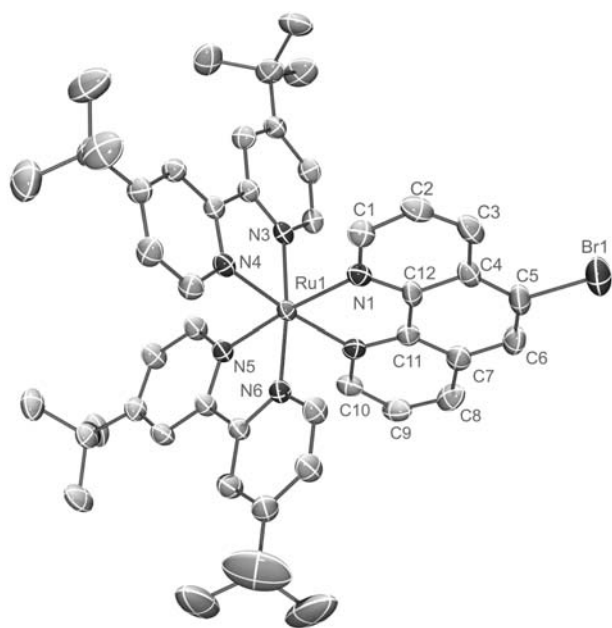
6.2.4 $[\text{Ru}(\text{tbbpy})_2(\text{phen-5-Br})][\text{PF}_6]_2$ - Ru(phenBr)

According to **method C1**, 664 mg (936 μmol) of $[\text{Ru}(\text{tbbpy})_2\text{Cl}_2]$ and 355 mg (936 μmol) of **phenBr** were reacted in the microwave for 90 minutes in 125 ml of ethanol/water. After cooling, ethanol was removed and precipitated impurities were filtered off. Then 916 mg (5.62 mmol) NH_4PF_6 were added and the formed precipitate was filtered collected and was washed with water. Purification was achieved by recrystallization from acetone/water by slow evaporation. This yielded also crystals suitable for X-ray diffraction. After removal of water the pure **Ru(phenBr)** was obtained as red powder. The yield is 1.07 g (898 μmol , 96%).



$^1\text{H-NMR}$ (CD_3CN , 400 MHz): $\delta = 8.79$ (dd, $1\text{H}_{(4)}$, $^3J = 8.2$ Hz, $^4J = 1.2$ Hz), 8.61 (s, $1\text{H}_{(6)}$), 8.51 (dd, $1\text{H}_{(7)}$, $^3J = 8.2$ Hz, $^4J = 1.2$ Hz), 8.50 (m, $2\text{H}_{(3\text{-bpy})}$), 8.46 (m, $2\text{H}_{(3'\text{-bpy})}$), 8.11 (dd, $1\text{H}_{(2)}$, $^3J = 4.8$ Hz, $^4J = 0.8$ Hz), 8.07 (dd, $1\text{H}_{(9)}$, $^3J = 4.6$ Hz, $^4J = 1.2$ Hz), 7.83 (dd, $1\text{H}_{(3)}$, $^3J = 8.4$ Hz, $^3J = 5.2$ Hz), 7.67 (dd, $2\text{H}_{(6\text{-bpy})}$, $^3J = 6.0$ Hz, $J = 3.0$ Hz), 7.45 (ddd, $2\text{H}_{(5\text{-bpy})}$, $^4J = 1.6$ Hz, $^4J = 1.8$ Hz, $^3J = 5.8$ Hz), 7.38 (dd, $2\text{H}_{(6'\text{-bpy})}$, $^3J = 5.8$ Hz, $^3J = 4.2$ Hz), 7.21 (m, $2\text{H}_{(5'\text{-bpy})}$), 1.43 (d, $18\text{H}_{(\text{t-Bu}^*)}$, $J = 1.0$ Hz), 1.35

(s, $18\text{H}_{(\text{t-Bu}^*)}$) ppm. $^{13}\text{C-NMR}$ (CD_3CN , 100 MHz): $\delta = 163.73$ ($2\text{C}_{(4\text{-bpy})}$), 163.59 ($2\text{C}_{(4'\text{-bpy})}$), 158.05 ($2\text{C}_{(2\text{-bpy})}$), 157.76 ($2\text{C}_{(2'\text{-bpy})}$), 154.00 ($1\text{C}_{(2)}$), 153.67 ($1\text{C}_{(9)}$), 152.28 ($2\text{C}_{(6'\text{-bpy})}$), 152.06 ($2\text{C}_{(6\text{-bpy})}$), 149.73 ($1\text{C}_{(10'')}$), 148.45 ($1\text{C}_{(10')}$), 137.05 ($1\text{C}_{(4)}$), 136.52 ($1\text{C}_{(7)}$), 132.08 ($1\text{C}_{(6)}$), 131.89 ($1\text{C}_{(6')}$), 131.44 ($1\text{C}_{(4')}$), 127.67 ($1\text{C}_{(3)}$), 127.61 ($1\text{C}_{(8)}$), 125.64 ($2\text{C}_{(5\text{-bpy})}$), 125.45 ($2\text{C}_{(5'\text{-bpy})}$), 122.72 ($1\text{C}_{(5)}$), 122.53 ($2\text{C}_{(3\text{-bpy})}$), 122.44 ($\text{C}_{(3'\text{-bpy})}$), 36.36 ($2\text{C}_{(7'\text{-bpy})}$), 36.27 ($2\text{C}_{(7\text{-bpy})}$), 30.52 ($3\text{C}_{(8'\text{-bpy})}$), 30.44 ($3\text{C}_{(8\text{-bpy})}$) ppm.

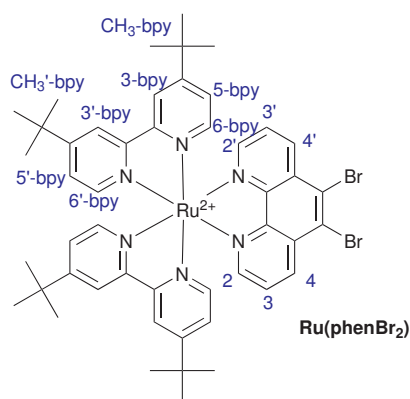


Crystals suitable for X-ray diffraction were obtained from acetonitrile/water. Crystal data for **Ru(phenBr)**: $[\text{C}_{48}\text{H}_{55}\text{N}_6\text{BrRu}]^{2+}[\text{PF}_6]_2^- \times 2 \text{CH}_3\text{CN}$, $M_r = 1269.01 \text{ g/mol}$, red-brown cuboid, size $0.06 \times 0.06 \times 0.05 \text{ mm}^3$, triclinic, space group $P\bar{1}$ (No. 2), $a = 12.5680(3)$, $b = 13.9694(4)$, $c = 16.9912(4) \text{ \AA}$, $\alpha = 70.946(1)$, $\beta = 75.702(1)$, $\gamma = 89.332(2)^\circ$, $V = 2724.56(12) \text{ \AA}^3$, $T = -90^\circ\text{C}$, $Z = 2$, $\rho_{\text{calcd.}} = 1.547 \text{ g/cm}^3$, $\mu_{(\text{Mo-K}\alpha)} = 11.65 \text{ cm}^{-1}$, $F(000) = 1292$, 19983 reflections in $h(-16/15)$, $k(-18/16)$, $l(-22/21)$ measured in the range $2.37^\circ \leq \Theta \leq 27.49^\circ$, completeness Φ_{max}

$= 99.1\%$, 12387 independent reflections, $R_{\text{int}} = 0.0376$, 8826 reflections with $F_o > 4\sigma(F_o)$, 699 parameters, 0 restraints, $R_{\text{obs.}} = 0.0605$, $wR_{\text{obs.}}^2 = 0.1585$, $R_{\text{all}} = 0.0951$, $wR_{\text{all}}^2 = 0.1786$, GOOF = 1.024, largest difference peak and hole: 2.767/-1.715 $\text{e}/\text{\AA}^3$. The data file TT3690 includes the full crystallographic data and can be obtained from DR. HELMAR GÖRLS (IAAC, FSU-Jena).

6.2.5 $[\text{Ru}(\text{tbbpy})(\text{phen-5,6-Br}_2)][\text{PF}_6]_2 - \text{Ru}(\text{phenBr}_2)$

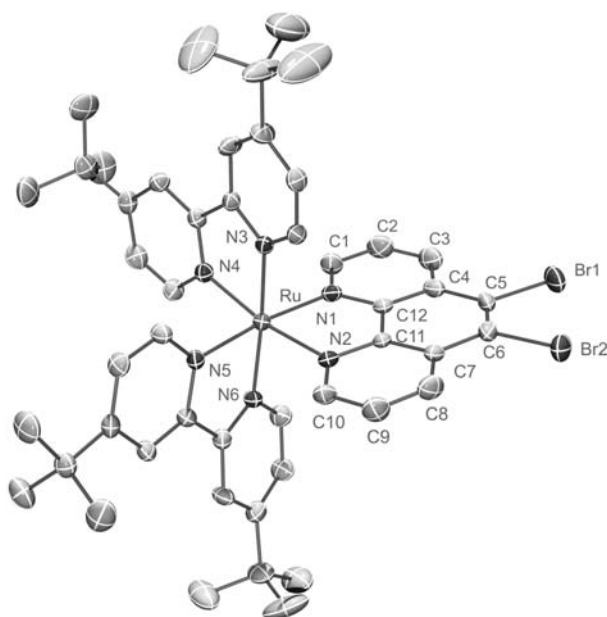
300 mg (423 μmol) of $[\text{Ru}(\text{tbbpy})_2\text{Cl}_2]$ and 143 mg (423 μmol) **phenBr**₂ were reacted in the microwave according to **method C1** in 60 ml of ethanol/water for 90 minutes. After cooling and removal of ethanol impurities were filtered off. Then 415 mg (2.54 mmol) NH_4PF_6 were added to precipitate the desired product. Purification was achieved by recrystallization from acetone/water by slow evaporation. This yielded also crystals suitable for X-ray diffraction. Water was removed by dissolving the crude product in dichloromethane and drying with Na_2SO_4 and removal of the precipitate and solvent. The yield was 466 mg (398 μmol , 90%) of pure **Ru(phenBr**₂) as red powder.



$^1\text{H-NMR}$ (CD_3CN , 400 MHz): $\delta = 8.87$ (dd, $2\text{H}_{(4/4')}$, $^3J = 8.6$ Hz, $^4J = 1.2$ Hz), 8.50 (d, $2\text{H}_{(3\text{-bpy})}$, $^4J = 1.8$ Hz), 8.45 (d, $2\text{H}_{(3'\text{-bpy})}$, $^4J = 1.8$ Hz), 8.12 (dd, $2\text{H}_{(2/2')}$, $^3J = 5.3$ Hz, $^4J = 1.2$ Hz), 7.81 (dd, $2\text{H}_{(3/3')}$, $^3J = 8.6$ Hz, $^3J = 5.2$ Hz), 7.67 (d, $2\text{H}_{(6\text{-bpy})}$, $^3J = 6.2$ Hz), 7.45 (dd, $2\text{H}_{(5\text{-bpy})}$, $^3J = 6.1$ Hz, $^4J = 2.0$ Hz), 7.42 (d, $2\text{H}_{(6'\text{-bpy})}$, $^3J = 6.0$ Hz), 7.50 (dd, $2\text{H}_{(5'\text{-bpy})}$, $^3J = 6.1$ Hz, $^4J = 2.0$ Hz), 1.43 (s, $18\text{H}_{(t\text{-Bu})}$), 1.35 (s, $18\text{H}_{(t\text{-Bu})}$) ppm.

$^{13}\text{C-NMR}$ (CD_3CN , 100 MHz): $\delta = 163.82$ ($2\text{C}_{(4\text{-bpy})}$), 163.67

($2\text{C}_{(4'\text{-bpy})}$), 157.95 ($2\text{C}_{(2\text{-bpy})}$), 157.69 ($2\text{C}_{(2'\text{-bpy})}$), 154.14 ($2\text{C}_{(2/9)}$), 152.36 ($2\text{C}_{(6'\text{-bpy})}$), 152.02 ($2\text{C}_{(6\text{-bpy})}$), 148.68 ($2\text{C}_{(10'/10'')}$), 138.08 ($2\text{C}_{(4/7)}$), 131.96 ($2\text{C}_{(4'/6')}$), 128.31 ($2\text{C}_{(3/8)}$), 127.22 ($2\text{C}_{(5,6)}$), 125.67 ($2\text{C}_{(5\text{-bpy})}$), 125.44 ($2\text{C}_{(5'\text{-bpy})}$), 122.57 ($2\text{C}_{(3\text{-bpy})}$), 122.47 ($\text{C}_{(3'\text{-bpy})}$), 36.36 ($2\text{C}_{(7'\text{-bpy})}$), 36.27 ($2\text{C}_{(7\text{-bpy})}$), 30.50 ($3\text{C}_{(8'\text{-bpy})}$), 30.43 ($3\text{C}_{(8\text{-bpy})}$) ppm. MS: 1120.9 m/z (100%, $\{\text{M-PF}_6\}^+$), 1120.9 m/z (10%, $\{\text{M-PF}_6\text{-Br}\}^+$).

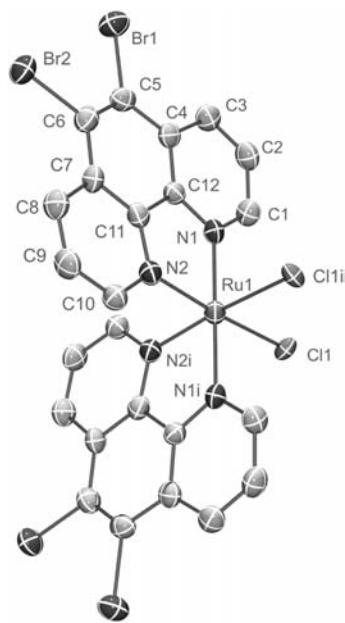


Crystals suitable for X-ray diffraction were obtained from acetone/water. Crystal data for **Ru(phenBr₂)**: $[\text{C}_{48}\text{H}_{54}\text{N}_6\text{Br}_2\text{Ru}]^{2+}[\text{PF}_6]_2^- \times 2 \text{CH}_3\text{COCH}_3$, $M_r = 1381.96$ g/mol, red-orange crystal, size $0.04 \times 0.04 \times 0.04$ mm³, triclinic, space group $\text{P}\bar{1}$ (No. 2), $a = 10.5859(2)$, $b = 11.7274(3)$, $c = 24.0080(7)$ Å, $\alpha = 90.444(1)$, $\beta = 94.113(2)$, $\gamma = 92.976(2)^\circ$, $V = 2968.59(13)$ Å³, $T = -90^\circ\text{C}$, $Z = 2$, $\rho_{\text{calcd.}} = 1.546$ g/cm³, $\mu_{(\text{Mo-K}\alpha)} = 17.46$ cm⁻¹, $F(000) = 1400$, 20454 reflections in $h(-13/13)$, $k(-15/14)$, $l(-31/28)$ measured in the range $2.05^\circ \leq \Theta \leq 27.47^\circ$, completeness Φ_{max}

$= 98.1\%$, 13329 independent reflections, $R_{\text{int}} = 0.0362$, 10002 reflections with $F_o > 4\sigma(F_o)$, 728 parameters, 0 restraints, $R_{\text{obs.}} = 0.0507$, $wR_{\text{obs.}}^2 = 0.1164$, $R_{\text{all}} = 0.0797$, $wR_{\text{all}}^2 = 0.1317$, GOOF = 1.011, largest difference peak and hole: $1.029/-0.718$ e/Å³. The data file TT3422 includes the full crystallographic data and can be obtained from DR. HELMAR GÖRLS (IAAC, FSU-Jena).

6.2.6 $[Ru(\text{phenBr}_2)_2\text{Cl}_2] - Ru(\text{phenBr}_2)\text{Cl}_2$

For this reaction, 280 mg (1.00 mmol) of $[Ru(\text{COD})\text{Cl}_2]_n$ and 676 mg (2.00 mmol) of **phenBr₂** were suspended in 50 ml of dry DMF and heated for two hours at 150 W in the microwave. After cooling, the solvent was removed. The remaining solid was dissolved in a small amount of chloroform heated to reflux very short. Addition of ethanol and recrystallization in the cold yielded a black precipitate. Removal of the sideproduct **Ru(phenBr₂)₃** was achieved via extraction of the methylene chloride solution with water and by column chromatography with acetone/DMF. After removal of the solvent 400 mg (470 μmol) of a black and almost insoluble powder were obtained (Yield = 47%). ¹H-NMR (CD_2Cl_2 , 400 MHz): δ = 10.550 (d, 2H_(2/9), ³J = 4.2 Hz), 9.696 (d, 2H_(2/9), ³J = 5.2 Hz), 8.837 (d, 4H_(4/7), ³J = 8.4 Hz), 8.124 (dd, 2H_(2/9), ³J = 4.2 Hz, ³J = 8.4 Hz), 7.887 (dd, 2H_(2/9), ³J = 5.2 Hz, ³J = 8.4 Hz) ppm.



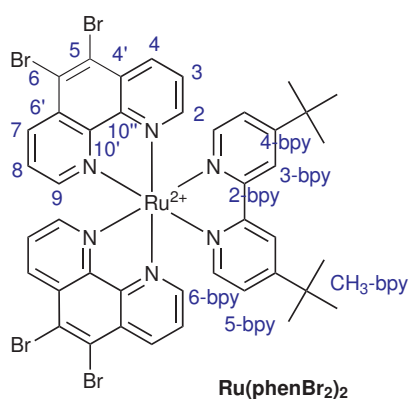
Crystals suitable for X-ray diffraction were obtained from dichloromethane. Crystal data for **Ru(phenBr₂)Cl₂**: $[\text{C}_{24}\text{H}_{12}\text{N}_4\text{Cl}_2\text{Br}_4\text{Ru}] \times 3 \text{CH}_2\text{Cl}_2$, $M_r = 1101.76 \text{ g/mol}$, black crystal, size $0.06 \times 0.06 \times 0.03 \text{ mm}^3$, monoclinic, space group $C2/c$ (No. 15), $a = 18.1042(8)$, $b = 16.7210(13)$, $c = 14.0302(9) \text{ \AA}$, $\alpha = 90.000$, $\beta = 125.740(3)$, $\gamma = 90.000^\circ$, $V = 3447.4(4) \text{ \AA}^3$, $T = -90^\circ\text{C}$, $Z = 4$, $\rho_{\text{calcd.}} = 2.123 \text{ g/cm}^3$, $\mu_{(\text{Mo-K}\alpha)} = 57.39 \text{ cm}^{-1}$, $F(000) = 2108$, 11467 reflections in $h(-23/22)$, $k(-21/21)$, $l(-14/18)$ measured in the range $1.93^\circ \leq \Theta \leq 27.46^\circ$, completeness $\Phi_{\text{max}} = 99.5\%$, 3929 independent reflections, $R_{\text{int}} = 0.0634$, 2688 reflections with $F_o > 4\sigma(F_o)$, 200 parameters, 0 restraints, $R_{\text{obs.}} = 0.0468$, $wR_{\text{obs.}}^2 = 0.1075$, $R_{\text{all}} = 0.0834$, $wR_{\text{all}}^2 = 0.1232$, GOOF = 1.040, largest difference peak and hole: $0.981/-0.738 \text{ e/\AA}^3$.

The data file TT3609 includes the full crystallographic data and can be obtained from DR. HELMAR GÖRLS (IAAC, FSU-Jena).

6.2.7 $[Ru(\text{phenBr}_2)_2(\text{tbbpy})][\text{PF}_6]_2 - Ru(\text{phenBr}_2)_2$

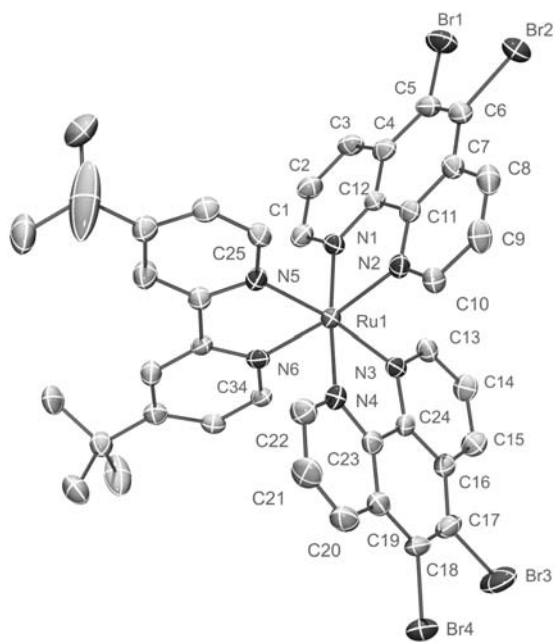
Following **method C1**, 105 mg (124 μmol) of **Ru(phenBr₂)₂Cl₂** and 33,2 mg (124 μmol) of tbbpy were reacted in the microwave for 180 minutes in 100 ml of ethanol/water. After cooling, ethanol was removed and dark precipitated impurities were filtered off. Then, 121 mg (720 μmol)

of NH_4PF_6 were added and the formed precipitate was collected and washed with water. Purification was achieved by column chromatography using acetonitrile/water and subsequent recrystallization from acetonitrile/water. Careful washing of the obtained crystals with very small amounts of methylene chloride yielded pure product. This yielded as well crystals suitable for X-ray diffraction. After removal of water, the pure $\text{Ru}(\text{phenBr}_2)_2$ was obtained as red powder. The yield was 17 mg (12.5 μmol , 10%).



$^1\text{H-NMR}$ (CD_3CN , 400 MHz): $\delta = 8.93$ (dd, $2\text{H}_{(4/4')}$, $^3J = 8.8$ Hz, $^4J = 0.8$ Hz), 8.83 (dd, $2\text{H}_{(4/4')}$, $^3J = 7.6$ Hz, $^4J = 0.8$ Hz), 8.49 (d, $2\text{H}_{(3-\text{bpy})}$, $^4J = 1.8$ Hz), 8.21 (dd, $2\text{H}_{(2/2')}$, $^3J = 5.3$ Hz, $^4J = 0.8$ Hz), 7.93 (dd, $2\text{H}_{(2/2')}$, $^3J = 5.2$ Hz, $^4J = 0.8$ Hz), 7.87 (dd, $2\text{H}_{(3/3')}$, $^3J = 8.8$ Hz, $^3J = 5.3$ Hz), 7.62 (dd, $2\text{H}_{(3/3')}$, $^3J = 7.6$ Hz, $^3J = 5.2$ Hz), 7.48 (d, $2\text{H}_{(6-\text{bpy})}$, $^3J = 6.0$ Hz), 7.23 (dd, $2\text{H}_{(5-\text{bpy})}$, $^3J = 6.1$ Hz, $^4J = 2.0$ Hz), 1.37 (s, $18\text{H}_{(\text{t-Bu})}$) ppm. $^{13}\text{C-NMR}$ (CD_3CN , 100 MHz): $\delta = 164.14$ ($2\text{C}_{(4-\text{bpy})}$), 157.82 ($2\text{C}_{(2-\text{bpy})}$),

154.81 ($2\text{C}_{(2/9)}$), 154.53 ($2\text{C}_{(2/9)}$), 152.68 ($2\text{C}_{(6'-\text{bpy})}$), 148.72 ($2\text{C}_{(10'/10'')}$), 148.49 ($2\text{C}_{(10'/10'')}$), 138.58 ($2\text{C}_{(4/7)}$), 138.45 ($2\text{C}_{(4/7)}$), 132.05 ($2\text{C}_{(4'/6')}$), 132.00 ($2\text{C}_{(4'/6')}$), 128.36 ($2\text{C}_{(3/8)}$), 128.18 ($2\text{C}_{(3/8)}$), 127.30 ($2\text{C}_{(5,6)}$), 127.21 ($2\text{C}_{(5,6)}$), 125.51 ($2\text{C}_{(5-\text{bpy})}$), 122.65 ($2\text{C}_{(3-\text{bpy})}$), 36.35 ($2\text{C}_{(7-\text{bpy})}$), 30.47 ($3\text{C}_{(8-\text{bpy})}$) ppm. MS (ESI): 1190.5 m/z (100%, $\{\text{M-PF}_6\}^+$), 522.8 m/z (60%, $\{\text{M-2PF}_6\}^{2+}$).

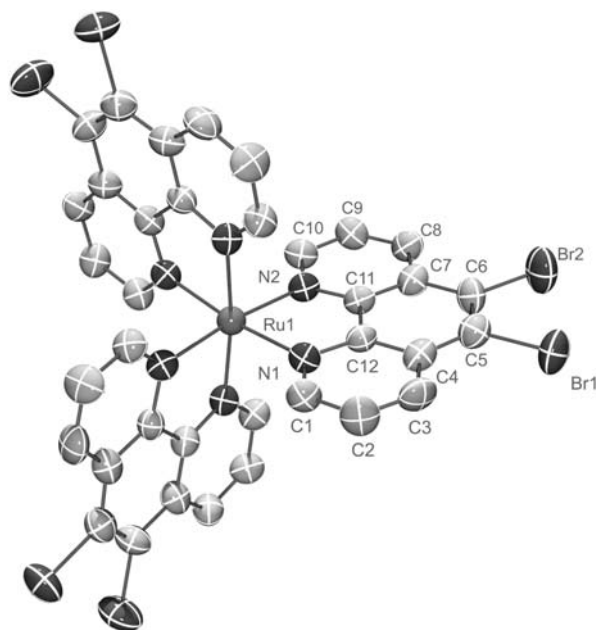


Crystals suitable for X-ray diffraction were obtained from acetonitrile/water. Crystal data for $\text{Ru}(\text{phenBr}_2)_2$: $[\text{C}_{42}\text{H}_{36}\text{N}_6\text{Ru}]^{2+}[\text{PF}_6]_2^- \times \text{CH}_3\text{CN}$, $M_r = 1376.47$ g/mol, red-brown crystal, size $0.05 \times 0.05 \times 0.04$ mm³, triclinic, space group $\text{P}\bar{1}$ (No. 2), $a = 12.0674(4)$, $b = 13.6818(4)$, $c = 16.1755(4)$ Å, $\alpha = 97.260(2)$, $\beta = 93.727(2)$, $\gamma = 98.202(2)^\circ$, $V = 2612.73(13)$ Å³, $T = -90(2)^\circ\text{C}$, $Z = 2$, $\rho_{\text{calcd.}} = 1.750$ g/cm³, $\mu_{(\text{Mo-K}\alpha)} = 35.02$ cm⁻¹, $F(000) = 1348$, 19732 reflections in $h(-15/15)$, $k(-17/17)$, $l(-20/20)$ measured in the range $2.60^\circ \leq \Theta \leq 27.45^\circ$, completeness $\Phi_{\text{max}} = 99.3\%$, 11863 independent

reflections, $R_{\text{int}} = 0.0364$, 8038 reflections with $F_o > 4\sigma(F_o)$, 659 parameters, 0 restraints, $R_{\text{obs.}} = 0.0545$, $wR_{\text{obs.}}^2 = 0.1422$, $R_{\text{all}} = 0.0935$, $wR_{\text{all}}^2 = 0.1618$, GOOF = 1.032, largest difference peak and hole: 1.730 / -0.919 \AA^{-3} . The data file TT3727 includes the full crystallographic data and can be obtained from DR. HELMAR GÖRLS (IAAC, FSU-Jena).

6.2.8 $[\text{Ru}(\text{phenBr}_2)_3][\text{PF}_6]_2 - \text{Ru}(\text{phenBr}_2)_3$

For this reaction 131 mg (468 μmol) of $[\text{Ru}(\text{COD})\text{Cl}_2]_n$ and 474 mg (1.40 mmol) of **phenBr₂** were heated in a mixture of ethanol/water over night at reflux and afterwards for two hours in the microwave (150 W). After removal of the solvent and the in water insoluble side products, NH_4PF_6 was added. Purification was achieved using column chromatography in acetonitrile/water. Recrystallization from acetonitrile gave the desired product in high purity. Yield: 17%, 109 mg, 31.2 μmol . $^1\text{H-NMR}$ (CDCl_3 , 400 MHz): $\delta = 8.876$ (dd, 6H_(4/7), $^3J = 8.2$ Hz, $^4J = 1.2$ Hz), 8.526 (dd, 1H_(2/9), $^3J = 5.6$ Hz, $^4J = 1.2$ Hz), 8.034 (dd, 1H_(3/8), $^3J = 8.8$ Hz, $^3J = 5.2$ Hz) ppm. $^{13}\text{C-NMR}$ (CDCl_3 , 100 MHz): $\delta = 155.14$ ($6\text{C}_{(4/7)}$), 148.49 ($6\text{C}_{(10'/10'')}$), 138.80 ($6\text{C}_{(2/9)}$), 131.99 ($6\text{C}_{(4'/6')}$), 128.21 ($6\text{C}_{(3/7)}$), 127.21 ($6\text{C}_{(5/6)}$) ppm. MS: (ESI) $m/z = 1206.2$ (100%, $[\text{M-PF}_6]^+$).



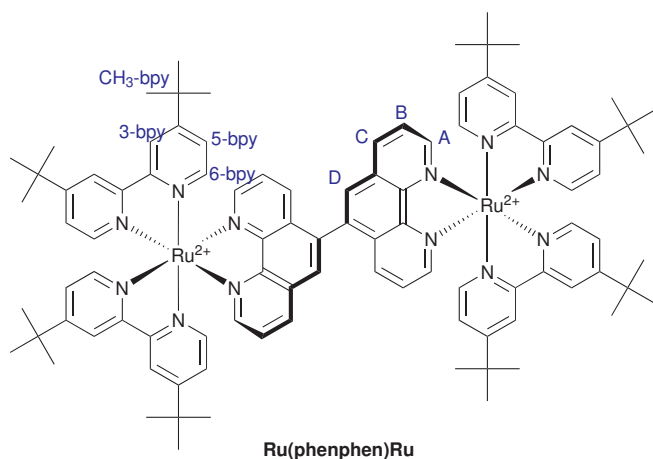
Crystals suitable for X-ray diffraction were obtained from acetonitrile/water. Crystal data for **Ru(phenBr₂)₃**: $[\text{C}_{36}\text{H}_{18}\text{N}_6\text{Br}_6\text{Ru}]^{2+}[\text{PF}_6]_2^- \times 1.5 \text{ CH}_3\text{CN}$, $M_r = 1394.13 \text{ g/mol}$, red-brown cuboid, size $0.06 \times 0.05 \times 0.05 \text{ mm}^3$, hexagonal, space group $\text{P}\bar{3}1\text{c}$ (No.163), $a = 18.4621(4)$, $b = 18.4621(4)$, $c = 21.0210(5) \text{ \AA}$, $\alpha = 90.000$, $\beta = 90.000$, $\gamma = 120.000^\circ$, $V = 6205.1(2) \text{ \AA}^3$, $T = -90^\circ\text{C}$, $Z = 4$, $\rho_{\text{calcd.}} = 1.492 \text{ g/cm}^3$, $\mu_{(\text{Mo-K}\alpha)} = 42.11 \text{ cm}^{-1}$, $F(000) = 2666$, 41120 reflections in $h(-21/23)$, $k(-23/21)$, $l(-27/26)$ measured in the range $3.20^\circ \leq \Theta \leq 27.50^\circ$, completeness Φ_{max}

$= 99.7\%$, 4761 independent reflections, $R_{\text{int}} = 0.0757$, 3113 reflections with $F_o > 4\sigma(F_o)$, 181 parameters, 0 restraints, $R_{\text{obs.}} = 0.0929$, $wR_{\text{obs.}}^2 = 0.2732$, $R_{\text{all}} = 0.1334$, $wR_{\text{all}}^2 = 0.3151$, GOOF = 1.052, largest difference peak and hole: 2.812/-1.127 \AA^{-3} . The data file TT3691 includes the full

crystallographic data and can be obtained from DR. HELMAR GÖRLS (IAAC, FSU-Jena).

6.2.9 $\{[Ru(tbbpy)_2]_2(\mu\text{-phenphen})\}[PF_6]_4$ - Ru(phenphen)Ru

The title compound was obtained, following **method C1**. 250 mg (352 μmol) of $[Ru(tbbpy)_2Cl_2]$ and 126 mg (352 μmol) of **phenphen** were reacted in the microwave for 120 minutes in 125 ml of ethanol/water. After cooling, ethanol was removed and dark precipitated impurities were filtered off. Then 300 mg of NH_4PF_6 were added and the formed precipitate was collected and washed with water several times. Purification was achieved by recrystallization from acetonitrile/water by slow evaporation. After removal of water the pure **Ru(phenphen)Ru** was obtained as red powder. The yield was 700 mg (317 μmol , 90%).



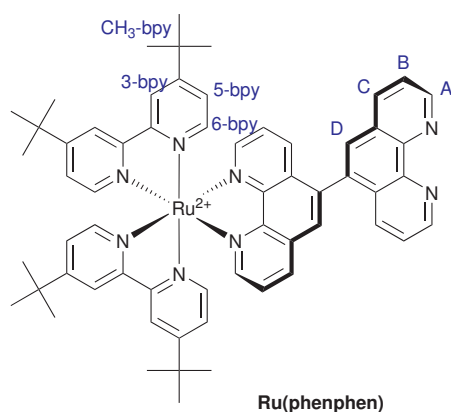
$^1\text{H-NMR}$ (CD_3CN , 400 MHz): δ = 8.693 (dd, 0.5H_(C), 3J = 8.3 Hz, 4J = 1.2 Hz), 8.675 (dd, 0.5H_(C), 3J = 8.2 Hz, 4J = 1.2 Hz), 8.655 (dd, 0.5H_(C), 3J = 8.2 Hz, 4J = 1.7 Hz), 8.638 (dd, 0.5H_(C), 3J = 8.2 Hz, 4J = 1.7 Hz), 8.560 (d, 1H₍₃₎, 4J = 1.9 Hz), 8.542 (d, 2H₍₃₎, 4J = 1.9 Hz), 8.527 (d, 2H₍₃₎, 4J = 1.9 Hz), 8.522 (d, 1H₍₃₎, 4J = 1.9 Hz), 8.502 (d, 2H₍₃₎, 4J = 1.9 Hz), 8.423

(s, 0.5H_(D)), 8.441 (s, 0.5H_(D)), 8.338 (s, 0.5H_(D)), 8.324 (s, 0.5H_(D)), 8.19 (m, 1H_(C)), 8.18 (m, 2H_(A)), 8.150 (dd, 1H_(A), 3J = 4.3 Hz, 4J = 2.0 Hz), 8.120 (dd, 0.5H_(C), 3J = 8.3 Hz, 4J = 1.7 Hz), 8.113 (dd, 0.5H_(C), 3J = 8.2 Hz, 4J = 1.5 Hz), 8.096 (dd, 1H_(A), 3J = 5.3 Hz, 4J = 1.9 Hz), 7.867 (dd, 0.5H_(B), 3J = 8.3 Hz, 3J = 5.2 Hz), 7.861 (dd, 0.5H_(B), 3J = 8.3 Hz, 3J = 5.0 Hz), 7.846 (dd, 0.5H_(B), 3J = 8.1 Hz, 3J = 5.1 Hz), 7.835 (dd, 0.5H_(B), 3J = 8.1 Hz, 3J = 5.1 Hz), 7.739 (d, 0.5H₍₆₎, 3J = 6.0 Hz), 7.721 (d, 0.5H₍₆₎, 3J = 5.8 Hz), 7.711 (d, 0.5H₍₆₎, 3J = 6.0 Hz), 7.703 (d, 0.5H₍₆₎, 3J = 5.8 Hz), 7.654 (dd, 0.5H_(B), 3J = 8.3 Hz, 3J = 4.2 Hz), 7.645 (dd, 0.5H_(B), 3J = 8.4 Hz, 3J = 5.2 Hz), 7.643 (d, 2H₍₆₎, 3J = 6.0 Hz), 7.585 (dd, 0.5H_(B), 3J = 8.4 Hz, 3J = 5.2 Hz), 7.574 (dd, 0.5H_(B), 3J = 8.3 Hz, 4J = 4.1 Hz), 7.669 (d, 1H₍₆₎, 3J = 6.0 Hz), 7.658 (d, 1H₍₆₎, 3J = 5.8 Hz), 7.50 (m, 4H₍₅₎), 7.46 (d, 2H₍₆₎, 3J = 5.8 Hz), 7.434 (dd, 1H₍₅₎, 3J = 6.0 Hz, 4J = 1.9 Hz), 7.432 (dd, 1H₍₅₎, 3J = 6.0 Hz, 4J = 1.8 Hz), 7.306 (dd, 1H₍₅₎, 3J = 4.6 Hz, 4J = 1.9 Hz), 7.300 (dd, 1H₍₅₎, 3J = 4.6 Hz, 4J = 1.9 Hz), 1.466

(s, 4.5H_(CH₃)), 1.462 (s, 4.5H_(CH₃)), 1.448 (s, 4.5H_(CH₃)), 1.438 (s, 4.5H_(CH₃)) 1.399 (s, 4.5H_(CH₃)), 1.396 (s, 4.5H_(CH₃)), 1.389 (s, 4.5H_(CH₃)), 1.387 (s, 4.5H_(CH₃)) ppm. ¹³C-NMR (CD₃CN, 400 MHz): δ = 162.751, 162.626, 162.573, 157.299, 157.208, 156.988, 156.941, 156.908, 156.863, 152.924, 152.825, 152.659, 152.580, 152.513, 152.033, 151.925, 151.412, 151.353, 151.145, 148.418, 148.220, 148.172, 136.801, 136.753, 135.763, 135.509, 135.442, 134.972, 131.154, 130.944, 130.486, 130.331, 130.224, 126.593, 126.419, 126.343, 126.163, 126.101, 124.851, 124.705, 124.649, 124.594, 121.635, 121.567, 35.439, 35.365, 29.603 ppm. **Elemental Analysis** (C₆₀H₆₂N₈RuP₂F₁₂ × CHCl₃): calc.: C: 49.93%, H: 4.79%, N: 7.20%, found: C: 49.57%, H: 4.83%, N: 7.37%. **MS**: (ESI) m/z = 962.1 (100%, [M-2PF₆]²⁺), 2069.2 (25%, [M-PF₆]⁺).

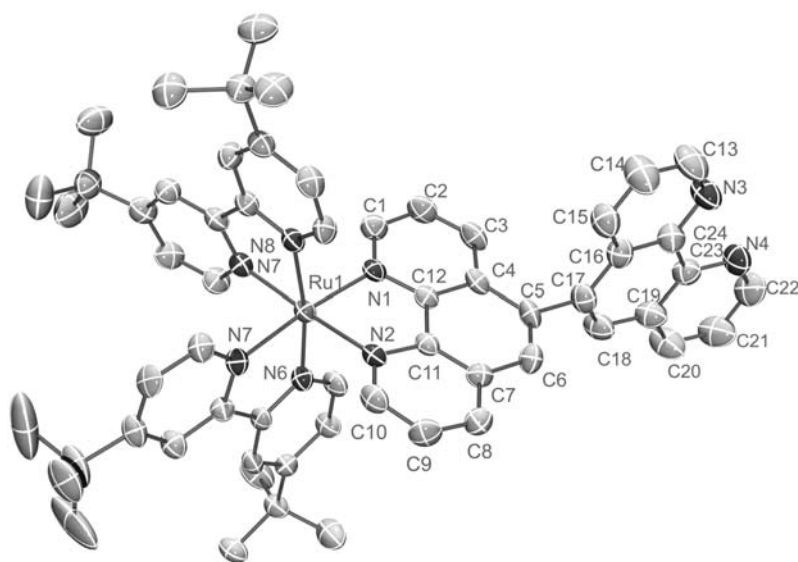
6.2.10 [Ru(tbbpy)₂(phenphen)][PF₆]₂ - Ru(phenphen)

Title compound was obtained according to **method C1**, following exactly the preparation of **Ru(phenphen)Ru** but using 0.5 equivalents of [Ru(tbbpy)₂Cl₂] instead of one equivalent. After removal of ethanol and unreacted [Ru(tbbpy)₂Cl₂] from the aqueous solution, NH₄PF₆ was added. Work up of the crude product mixture (**Ru(phenphen)Ru** and **Ru(phenphen)**) was achieved by column chromatography (sat. KNO₃ : water : acetonitril/5:40:250) and yielded the desired compound in the second fraction. Yield: 294 mg (229 μmol, 65%). Crystals suitable for X-ray diffraction were obtained from ethanol/water. The ¹H-NMR spectrum is complicated due to the two stereo isomers that exist at room temperature due to the hindered rotation of the linked phenanthroline moieties.



¹H-NMR (CD₃CN, 400 MHz): δ = 9.176 (dd, 0.5H_(A), ³J = 4.3 Hz, ⁴J = 2.0 Hz), 9.171 (dd, 0.5H_(A), ³J = 4.3 Hz, ⁴J = 2.0 Hz), 9.142 (dd, 0.5H_(A), ³J = 4.3 Hz, ⁴J = 1.7 Hz), 9.102 (dd, 0.5H_(A), ³J = 4.3 Hz, ⁴J = 1.7 Hz), 8.658 (dd, 0.5H_(C''), ³J = 8.3 Hz, ⁴J = 1.2 Hz), 8.649 (dd, 0.5H_(C''), ³J = 8.2 Hz, ⁴J = 1.2 Hz), 8.576 (d, 1H₍₃₎, ⁴J = 1.9 Hz), 8.555 (d, 1H₍₃₎, ⁴J = 1.9 Hz), 8.548 (d, 2H₍₃₎, ⁴J = 1.9 Hz), 8.536 (d, 1H₍₃₎, ⁴J = 1.9 Hz), 8.530 (d, 1H₍₃₎, ⁴J = 1.9 Hz), 8.515 (d, 1H₍₃₎, ⁴J = 1.9 Hz), 8.501 (d, 1H₍₃₎, ⁴J = 1.9 Hz), 8.468 (dd, 0.5H_(C), ³J = 8.2 Hz, ⁴J = 1.7 Hz), 8.434 (dd, 0.5H_(C), ³J = 8.2 Hz, ⁴J = 1.7 Hz), 8.385 (s, 0.5H_(D)), 8.379 (s, 0.5H_(D)), 8.179 (dd, 0.5H_(A''), ³J = 5.3 Hz, ⁴J =

1.9 Hz), 8.176 (dd, 0.5H_(A''), ³J = 5.3 Hz, ⁴J = 1.9 Hz), 8.110 (dd, 1H_(A''), ³J = 5.2 Hz, ⁴J = 1.0 Hz), 8.090 (s, 0.5H_(D)), 8.053 (dd, 1H_(C''), ³J = 8.5 Hz, ⁴J = 1.0 Hz), 8.011 (s, 0.5H_(D)), 7.988 (dd, 0.5H_(C), ³J = 8.3 Hz, ⁴J = 1.7 Hz), 7.864 (dd, 0.5H_(C), ³J = 8.2 Hz, ⁴J = 1.5 Hz), 7.844 (dd, 0.5H_(B''), ³J = 8.3 Hz, ³J = 5.2 Hz), 7.836 (dd, 0.5H_(B''), ³J = 8.3 Hz, ³J = 5.0 Hz), 7.781 (dd, 0.5H_(B'), ³J = 8.1 Hz, ³J = 5.1 Hz), 7.770 (dd, 0.5H_(B'), ³J = 8.1 Hz, ³J = 5.1 Hz), 4.06 (m, 2H₍₆₎), 7.669 (d, 0.5H₍₆₎, ³J = 6.0 Hz), 7.658 (d, 0.5H₍₆₎, ³J = 5.8 Hz), 7.580 (dd, 0.5H_(B), ³J = 8.3 Hz, ³J = 4.2 Hz), 7.552 (dd, 0.5H_(B''), ³J = 8.4 Hz, ³J = 5.2 Hz), 7.549 (dd, 0.5H_(B''), ³J = 8.4 Hz, ³J = 5.2 Hz), 7.49 (m, 3H_(6,5)), 7.485 (dd, 0.5H_(B), ³J = 8.3 Hz, ⁴J = 4.1 Hz), 7.364 (dd, 0.5H₍₅₎, ³J = 6.0 Hz, ⁴J = 1.9 Hz), 7.360 (dd, 0.5H₍₅₎, ³J = 6.0 Hz, ⁴J = 1.8 Hz), 7.305 (dd, 0.5H₍₅₎, ³J = 4.6 Hz, ⁴J = 1.9 Hz), 7.303 (dd, 1H_(A), ³J = 6.1 Hz, ⁴J = 1.9 Hz), 7.291 (dd, 1H_(A), ³J = 6.1 Hz, ⁴J = 1.9 Hz), 1.469 (s, 4.5H_(CH₃)), 1.465 (s, 4.5H_(CH₃)), 1.440 (s, 9H_(CH₃)), 1.419 (s, 9H_(CH₃)), 1.392 (s, 4.5H_(CH₃)), 1.386 (s, 4.5H_(CH₃)) ppm. ¹³C-NMR (CD₃CN, 100 MHz): δ = 162.78, 162.66, 157.28, 157.24, 157.01, 152.61, 152.58, 152.43, 152.39, 151.70, 151.64, 151.29, 151.22, 151.18, 151.13, 150.90, 150.38, 150.32, 148.29, 148.20, 147.99, 146.39, 146.32, 137.56, 136.59, 136.54, 135.24, 135.22, 134.48, 134.21, 133.54, 133.51, 131.32, 131.24, 130.62, 130.59, 129.74, 129.66, 129.22, 128.53, 128.23, 128.21, 126.55, 126.52, 126.03, 125.99, 124.76, 124.71, 124.67, 124.63, 123.91, 123.87, 123.34, 123.24, 121.57, 121.51, 54.35, 35.46, 35.43, 35.40, 35.37, 29.61, 29.57 ppm. **Elemental Analysis** (C₆₀H₆₂N₈RuP₂F₁₂ × CHCl₃): calc.: C: 52.13%, H: 4.52%, N: 7.97%, found: C: 52.07%, H: 4.66%, N: 7.47%. **MS**: (ESI) m/z = 1141.4 (100%, [M-PF₆]⁺).



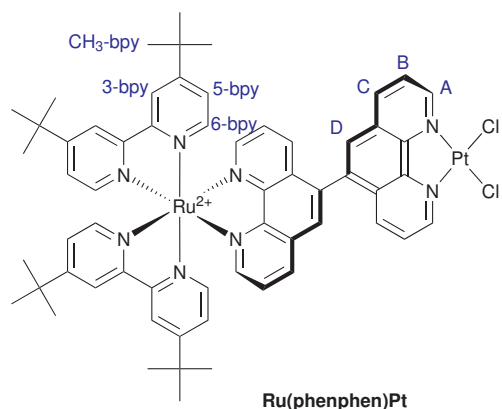
Crystals suitable for X-ray diffraction were obtained from methanol/water. Crystal data for **Ru(phenphen)**: [C₆₀H₆₂N₈Ru]²⁺[PF₆]₂⁻ × 2 CH₃OH, M_r = 1350.27 g/mol, red-brown cuboid, size 0.23 × 0.16 × 0.05 mm³, monoclinic, space group Cc (No. 9), a = 28.7888(14), b = 12.5327(9), c = 18.8750(18) Å, α

= 90.000, β = 114.089(5), γ = 90.000°, V = 6217.05 Å³, T = -123°C, Z = 4, ρ_{calcd.} = 1.443 g/cm³,

$\mu_{(\text{Mo-K}\alpha)} = 0.390 \text{ cm}^{-1}$, $F(000) = 2784$, 89373 reflections in $h(-36/36)$, $k(-16/16)$, $l(-24/24)$ measured in the range $3.10^\circ \leq \Theta \leq 27.10^\circ$, completeness $\Phi_{\text{max}} = 99.8\%$, 13613 independent reflections, $R_{\text{int}} = 0.0717$, 13613 reflections with $F_o > 4\sigma(F_o)$, 855 parameters, 216 restraints, $R_{\text{obs.}} = 0.0363$, $wR_{\text{obs.}}^2 = 0.0789$, $R_{\text{all}} = 0.0491$, $wR_{\text{all}}^2 = 0.0841$, GOOF = 1.020, largest difference peak and hole: 0.574 / -0.429 $\text{e}/\text{\AA}^3$. The data file DP0901 includes the full crystallographic data and can be obtained from DR. FRANK HEINEMANN (IAC, FAU-Erlangen-Nürnberg). In the molecular structure of **Ru(phenphen)** hydrogen atoms, solvent molecules and anions are omitted for clarity. Ellipsoids are drawn at 70% probability level.

6.2.11 $[\{\text{Ru}(\text{tbbpy})_2\}(\mu\text{-phenphen})\{\text{PtCl}_2\}][\text{PF}_6]_2$ - **Ru(phenphen)Pt**

To a stirred solution of 161 mg (0.388 mmol) of K_2PtCl_4 dissolved in 50 ml of DMF 414 mg (0.322 mmol) of **Ru(phenphen)** dissolved in 15 ml in DMF were added. This solution was stirred at 100°C for 28 hours. After the reaction time the solvent was removed under vacuum and water was added to the remaining brown solid. Extraction with dichloromethane yielded the crude product after drying of the organic layers with Na_2SO_4 , filtration over celite and removal of the solvent. The crude product was purified by column chromatography using silica gel 60 and a solvent mixture of acetonitrile/water/saturated KNO_3 -solution (250:30:5/v:v:v). After removal of the KNO_3 and counter ion exchange with NH_4PF_6 **Ru(phenphen)Pt** was obtained as red powder. Yield: 167 mg (0.108 mmol, 34%).

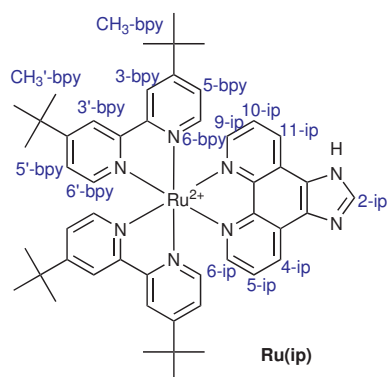


$^1\text{H-NMR}$ (CD_3CN , 400 MHz): $\delta = 9.460$ (d, $0.5\text{H}_{(\text{A})}$, $^3J = 5.2 \text{ Hz}$), 9.387 (d, $0.5\text{H}_{(\text{A})}$, $^3J = 5.2 \text{ Hz}$), 9.367 (d, $0.5\text{H}_{(\text{A})}$, $^3J = 5.4 \text{ Hz}$), 9.341 (d, $0.5\text{H}_{(\text{A})}$, $^3J = 5.4 \text{ Hz}$), 8.902 (dd, $0.5\text{H}_{(\text{C})}$, $^3J = 8.3 \text{ Hz}$, $^4J = 1.0 \text{ Hz}$), 8.869 (dd, $0.5\text{H}_{(\text{C})}$, $^3J = 8.3 \text{ Hz}$, $^4J = 1.0 \text{ Hz}$), 8.690 (dd, $0.5\text{H}_{(\text{C}^{\prime\prime})}$, $^3J = 8.2 \text{ Hz}$, $^4J = 1.0 \text{ Hz}$), 8.675 (dd, $0.5\text{H}_{(\text{C}^{\prime\prime})}$, $^3J = 8.0 \text{ Hz}$, $^4J = 1.0 \text{ Hz}$), 8.609 (s, $0.5\text{H}_{(\text{D})}$), 8.585 (s, $0.5\text{H}_{(\text{D})}$), 8.563 (d, $0.5\text{H}_{(\text{B})}$, $^4J = 1.8 \text{ Hz}$), $8.85\text{-}8.51$ (m, $2.5\text{H}_{(\text{B})}$), 8.502 (d, $0.5\text{H}_{(\text{B})}$, $^4J = 1.9 \text{ Hz}$), 8.488 (d, $0.5\text{H}_{(\text{B})}$, $^4J = 1.9 \text{ Hz}$), 8.407 (dd, $0.5\text{H}_{(\text{C})}$, $^3J = 8.4 \text{ Hz}$, $^4J = 1.0 \text{ Hz}$), 8.350 (s, $0.5\text{H}_{(\text{D})}$), 8.313 (dd, $0.5\text{H}_{(\text{C})}$, $^3J = 8.5 \text{ Hz}$, $^4J = 1.0 \text{ Hz}$), 8.275 (s, $0.5\text{H}_{(\text{D})}$), 8.270 (dd, $0.5\text{H}_{(\text{C}^{\prime\prime\prime})}$, $^3J = 8.3 \text{ Hz}$, $^4J = 1.0 \text{ Hz}$), 8.200 (dd, $0.5\text{H}_{(\text{C}^{\prime\prime\prime})}$, $^3J = 8.4 \text{ Hz}$, $^4J = 1.0 \text{ Hz}$), $8.183\text{-}8.165$ (m, $1\text{H}_{(\text{A}^{\prime\prime})}$), 8.119

(dd, 0.5H_(A^m), ³J = 5.2 Hz, ⁴J = 1.3 Hz), 8.115 (dd, 0.5H_(A^m), ³J = 5.2 Hz, ⁴J = 1.2 Hz), 7.976 (dd, 0.5H_(B^r), ³J = 8.2 Hz, ³J = 6.0 Hz), 7.961 (dd, 0.5H_(B^r), ³J = 8.1 Hz, ³J = 6.0 Hz), 7.847 (dd, 0.5H_(B^r), ³J = 8.2 Hz, ³J = 5.0 Hz), 7.839 (dd, 1H_(B^r;B), ³J = 8.3 Hz, ³J = 5.3 Hz), 7.765 (dd, 0.5H_(B^r), ³J = 8.4 Hz, ³J = 5.5 Hz), 7.74-7.70 (m, 2H₍₆₎), 7.655 (d, 0.5H₍₆₎, ³J = 6.0 Hz), 7.640 (d, 0.5H₍₆₎, ³J = 6.0 Hz), 7.594 (dd, 0.5H_(B^m), ³J = 8.0 Hz, ³J = 5.0 Hz), 7.581 (dd, 0.5H_(B^m), ³J = 8.0 Hz, ³J = 5.0 Hz), 7.52-7.45 (m, 3H_(5,6)), 7.360 (dd, 1H₍₅₎, ³J = 5.9 Hz, ⁴J = 2.0 Hz), 7.355 (dd, 1H₍₅₎, ³J = 5.9 Hz, ⁴J = 2.0 Hz), 7.290 (dd, 1H₍₅₎, ³J = 5.9 Hz, ⁴J = 2.0 Hz), 7.281 (dd, 1H₍₅₎, ³J = 5.9 Hz, ⁴J = 2.0 Hz), 1.469 (s, 4.5H_(CH₃)), 1.466 (s, 4.5H_(CH₃)), 1.440 (s, 9H_(CH₃)), 1.417 (s, 9H_(CH₃)), 1.391 (s, 4.5H_(CH₃)), 1.386 (s, 4.5H_(CH₃)) ppm. ¹³C-NMR (CD₃CN, 100 MHz): δ = 162.81, 162.67, 157.24, 157.19, 156.97, 152.97, 152.61, 152.56, 151.71, 151.31, 151.17, 151.12, 149.18, 148.95, 148.69, 148.21, 139.56, 137.89, 137.68, 136.74, 135.44, 135.35, 135.26, 134.95, 133.41, 131.00, 130.90, 130.82, 130.71, 130.63, 130.58, 130.43, 130.38, 130.02, 126.3, 126.36, 126.15, 126.11, 124.72, 124.61, 121.60, 121.54, 35.44, 29.60 ppm. ¹⁹⁵Pt-NMR (CD₃CN, 129 MHz): δ = -2334 ppm. **Elemental Analysis** (C₆₀H₆₂N₈RuPtCl₂P₂F₁₂ × CHCl₃): calc.: C: 43.83%, H: 3.80%, N: 6.70%, found: C: 43.45%, H: 3.78%, N: 6.95%. **MS** (ESI): m/z = 1407.0 (100%, [M-PF₆]⁺), 1261.1 (24%M [M-2PF₆]⁺), 1141.1 (6% [M-PtCl₂-PF₆]⁺).

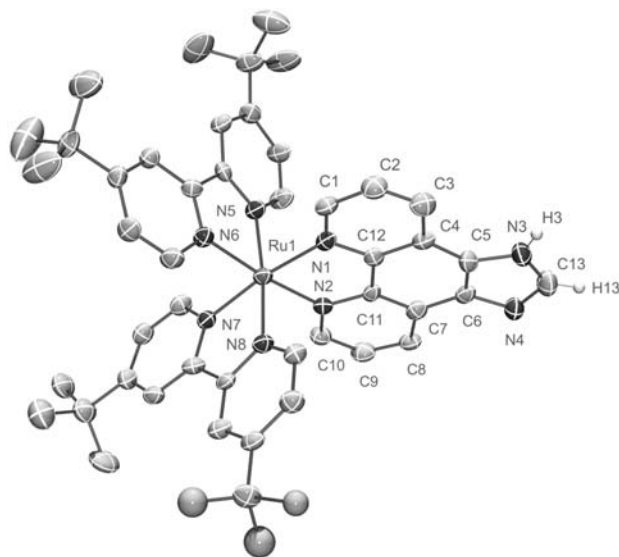
6.2.12 [Ru(tbbpy)₂(ip)][PF₆]₂ - Ru(ip)

The title compound was obtained, following **method C1**. 100 mg (141 μmol) of [Ru(tbbpy)₂Cl₂] and 33.6 mg (141 μmol) of **ip** were reacted in the microwave for 90 minutes in 100 ml of ethanol/water. After cooling and removal of ethanol and a dark precipitate six equivalents of NH₄PF₆ were added. The formed precipitate was collected and washed with water several times. Purification was achieved by recrystallization from acetone/ethanol/water by slow evaporation. After removal of water the pure **Ru(ip)** was obtained as red powder. The yield was 154 mg (134 μmol, 95%) of a red powder.



¹H-NMR (CD₃CN, 400 MHz): δ = 8.92 (d, 2H_(ip 4/11), ³J = 8.1 Hz), 8.52 (d, 2H_(bpy 3/3'), ⁴J = 1.9 Hz), 8.47 (d, 2H_(bpy 3'/3), ⁴J = 1.9 Hz), 8.42 (s, 1H_(ip2)), 7.99 (dd, 2H_(ip6/9), ⁴J = 0.9 Hz, ³J = 5.2 Hz), 7.78 (dd, 2H_(ip 5/10), ³J = 5.3 Hz, ³J = 8.3 Hz), 7.69 (d, 2H_(bpy 6/6'), ³J = 6.0 Hz), 7.46 (dd, 2H_(bpy 5/5'), ⁴J = 2.0 Hz, ³J = 6.0 Hz), 7.44 (d, 2H_(bpy 6'/6), ³J = 6.1 Hz), 7.19 (dd, 2H_(bpy 5'/5), ⁴J = 2.0 Hz, ³J = 6.1 Hz), 1.45 (s, 18H_(tBu)), 1.35 (s, 18H_(tBu')) ppm. **¹³C-NMR** (CD₃CN, 100 MHz): δ = 163.51

(2C_(4/4'-bpy)), 163.33 (2C_(4'/4-bpy)), 157.99 (2C_(2/2'-bpy)), 157.75 (2C_(2'/2-bpy)), 152.07 (2C_(6/6'-bpy)), 151.93 (2C_(6'/6-bpy)), 150.90 (2C_(6/9-ip)), 146.97 (2C_(7'/7''-ip)), 143.32 (1C_(2-ip)), 131.15 (2C_(4/11-ip)), 126.86 (2C_(5/10-ip)), 125.53 (2C_(5/5'-bpy)), 125.37 (2C_(5'/5-bpy)), 122.40 (2C_(3/3'-bpy)), 122.31 (2C_(3'/3-bpy)), 36.29 (2C_(tc-bpy)), 36.18 (2C_(tc'-bpy)), 30.47 (6C_(-CH3-bpy)), 30.37 (6C_(-CH3'-bpy)) ppm. C_(3'/11'') and C_(3''/11') were not found. **MS:** (ESI) *m/z* = 429.1 (100%, [M-2PF₆]²⁺), 856.2 (65%, [M-2PF₆-H]⁺), 1003.1 (40%, [M-PF₆]⁺).

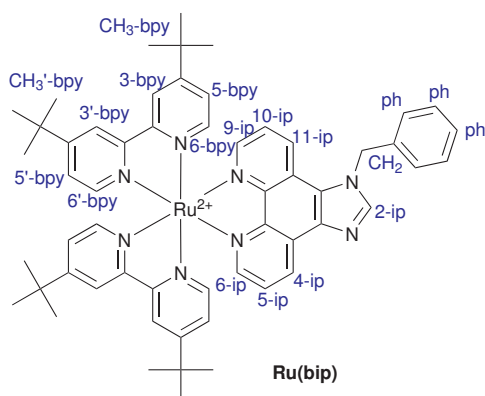


Crystals suitable for X-ray diffraction were obtained from acetone/ethanol/water. Crystal data for **Ru(ip)**: [C₄₉H₅₆N₈Ru]²⁺[PF₆]₂ × 2.5 C₂H₅OH, M_r = 1256.18 g/mol, red crystal, size 0.05 × 0.05 × 0.04 mm³, orthorhombic, space group P2₁/n (No. 29), a = 40.0363(6), b = 12.1313(3), c = 12.4471(3) Å, α = 90.00, β = 90.00, γ = 90.00°, V = 6045.5(2) Å³, T = 183(2) K, Z = 4, $\rho_{\text{calcd.}}$ = 1.380 g/cm³, $\mu_{\text{(Mo-K}\alpha\text{)}}$ = 0.395 cm⁻¹, F(000) = 2596, 32336 reflections in h(-51/50), k(-12/15), l(-16/16) measured in the

range 2.64° ≤ Θ ≤ 27.48°, completeness Φ_{max} = 99.7%, 13558 independent reflections, R_{int} = 0.0512, 13558 reflections with F_o > 4 σ (F_o), 716 parameters, 1 restraint, R_{obs.} = 0.0633, wR_{obs.}² = 0.1658, R_{all} = 0.0934, wR_{all}² = 0.1837, GOOF = 1.025, absolute structure parameter: 0.02(4); largest difference peak and hole: 1.229/-0.554 e⁻/Å³. The data file FO3797 includes the full crystallographic data and can be obtained from DR. HELMAR GÖRLS (IAAC, FSU-Jena).

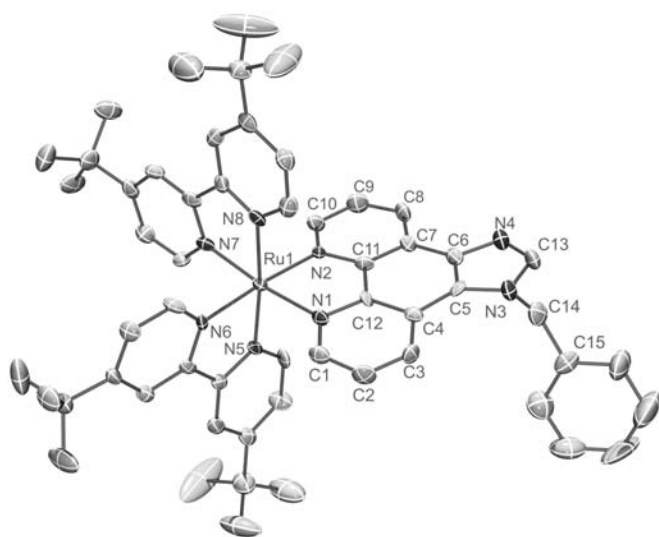
6.2.13 [Ru(tbbpy)₂(bip)]/[PF₆]₂ - Ru(bip)

Following **method C1**, 190 mg (268 μ mol) of [Ru(tbbpy)₂Cl₂] and 83.2 mg (268 μ mol) of **bip** were brought to reaction for 90 minutes to yield 154 mg (134 μ mol, 95%) of the desired complex as red powder. The product was recrystallized from an toluene/dichloromethane mixture and could be purified by column chromatography using dichloromethane/acetone (5:1) as solvent and silicagel 60 as stationary phase. Crystals for suitable for X-ray crystallography were obtained from an acetonitrile/water/methanol mixture (20:2:1).



¹H-NMR (CD₃CN, 400 MHz): δ = 9.080 (dd, 1H_(4/11-bip), ³J = 8.2 Hz, ⁴J = 1.2 Hz), 8.580 (dd, 1H_(11/4-bip), ³J = 8.6 Hz, ⁴J = 1.2 Hz), 8.508 (d, 1H_(3/3'-bpy), ⁴J = 2 Hz), 8.482 (d, 1H_(3/3'-bpy), ⁴J = 2 Hz), 8.463 (d, 1H_(3/3'-bpy), ⁴J = 2 Hz), 8.463 (s, 1H_(2-bip)), 8.436 (d, 1H_(3/3'-bpy), ⁴J = 2 Hz), 8.001 (dd, 1H_(6/9), ³J = 5.3 Hz, ⁴J = 1.3 Hz), 7.923 (dd, 1H_(9/6), ³J = 5.3 Hz, ⁴J = 1.1 Hz), 7.790 (dd, 1H_(5/10), ³J = 8.3 Hz, ³J = 5.3 Hz), 7.66 (dd, 2H_(5/5'-bpy), ³J = 5.9 Hz, ⁴J = 7.1 Hz),

7.58 (dd, 1H_(10/5), ³J = 8.5 Hz, ³J = 5.3 Hz), 7.452 (dd, 1H_(5/5-bpy), ³J = 5.4 Hz, ⁴J = 2.0 Hz), 7.438 (dd, 1H_(5/5-bpy), ³J = 5.4 Hz, ⁴J = 2.0 Hz), 7.394 (d, 1H_(6/6'-bpy), ³J = 6.2 Hz), 7.389 (d, 1H_(6/6'-bpy), ³J = 6.2 Hz), 7.33 (m, 3H_(Ar)), 7.21 (m, 2H_(Ar)), 7.184 (d, 1H_(6/6'-bpy), ³J = 6.2 Hz), 7.178 (d, 1H_(6/6'-bpy), ³J = 6.2 Hz), 5.984 (s, 2H_(CH₂)), 1.44 (s, 9H_(CH₃)), 1.43 (s, 9H_(CH₃)), 1.35 (s, 9H_(CH₃)), 1.34 (s, 9H_(CH₃)) ppm; ¹³C-NMR (CD₃CN, 400 MHz): δ = 163.55 (2C_(4/4'-bpy)), 163.42 (2C_(4/4'-bpy)), 157.97 (2C_(2/2'-bpy)), 157.78 (2C_(2/2'-bpy)), 152.11 (2C_(5/5'-bpy)), 151.92 (2C_(2/2'-bpy)), 151.29 (1C_(6/9-bip)), 150.75 (1C_(9/6-bip)), 147.48 (1C_(2-bip)), 147.22 (1C_(8'/8''-bip)), 147.04 (1C_(8'/8''-bip)), 139.01 (1C_(3'/11''-bip)), 136.47 (1C_(tC-ph)), 131.27 (1C_(4/11-bip)), 130.60 (1C_(11/4-bip)), 130.20 (2C_(ph)), 129.27 (1C_(ph)), 127.58 (1C_(11''/3'-bip)), 127.37 (2C_(ph)), 127.26 (1C_(5/10-bip)), 126.29 (1C_(10/5-bip)), 125.59 (2C_(6/6'-bpy)), 125.40 (2C_(6/6'-bpy)), 122.80 (1C_(3''/11'-bip)), 122.46 (2C_(3/3'-bpy)), 122.40 (1C_(3'/3-bpy)), 122.12 (1C_(11'/3''-bip)), 51.71 (1C_(CH₂-bip)), 36.33 (2C_(tC'/tC'-bpy)), 36.26 (2C_(tC'/tC'-bpy)), 30.49 (6C_(CH₃/CH₃'-bpy)), 30.41 (6C_(CH₃'/CH₃-bpy)) ppm; MS (ESI) m/z = 474.2 (40%, [M-2PF₆]²⁺), 848.2 (5%, [M-2PF₆]⁺), 1093.2 (100%, [M-PF₆]⁺);

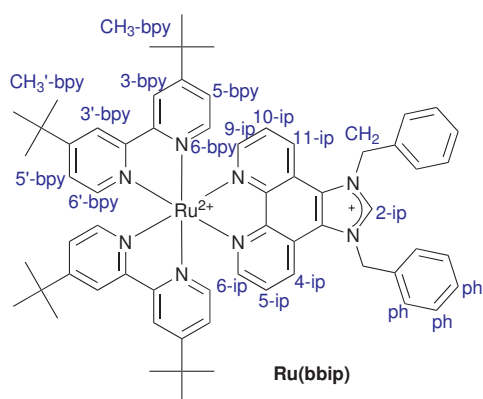


Crystals suitable for X-ray diffraction were obtained from acetonitrile/water. Crystal data for **Ru(bip)**: $[C_{56}H_{62}N_8Ru]^{2+}[PF_6]_2^- \times CH_3CN$, $M_r = 1279.20$ g/mol, red-brown rhombus, size $0.04 \times 0.04 \times 0.04$ mm³, orthorhombic, space group $Pca2_1$ (No. 29), $a = 38.6452(8)$, $b = 11.8866(2)$, $c = 12.7938(3)$ Å, $\alpha = 90.000$, $\beta = 90.000$, $\gamma = 90.000^\circ$, $V = 5877.0(2)$ Å³, $T = -140^\circ\text{C}$, $Z = 4$, $\rho_{\text{calcd.}} =$

1.446 g/cm³, $\mu_{(\text{Mo-K}\alpha)} = 4.06$ cm⁻¹, $F(000) = 2632$, 26981 reflections in $h(-48/50)$, $k(-15/15)$, $l(-16/15)$ measured in the range $2.33^\circ \leq \Theta \leq 27.49^\circ$, completeness $\Phi_{\text{max}} = 92.6\%$, 9804 independent reflections, $R_{\text{int}} = 0.1153$, 8354 reflections with $F_o > 4\sigma(F_o)$, 752 parameters, 1 restraint, $R_{\text{obs.}} = 0.0570$, $wR_{\text{obs.}}^2 = 0.1331$, $R_{\text{all}} = 0.0719$, $wR_{\text{all}}^2 = 0.1411$, GOOF = 1.045, largest difference peak and hole: $0.717/-1.069$ e/Å³. The data file TT3949 includes the full crystallographic data and can be obtained from DR. HELMAR GÖRLS (IAAC, FSU-Jena).

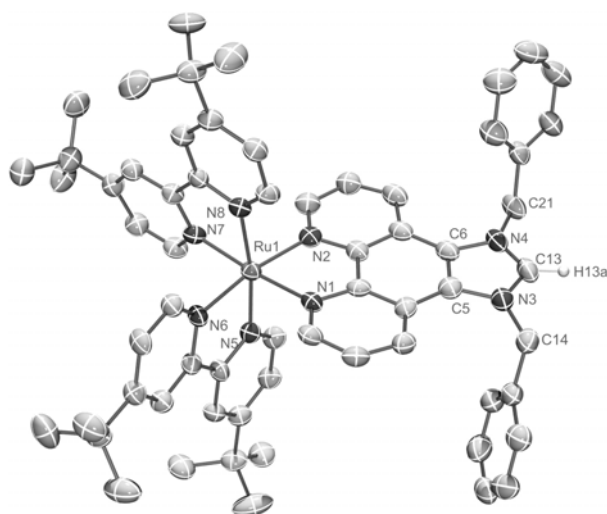
6.2.14 $[Ru(\text{tbbpy})_2(\text{bbip})][PF_6]_3$ - **Ru(bbip)**

As described in **method C1**, 367 mg (518 μmol) of $[Ru(\text{tbbpy})_2Cl_2]$ and 250 mg (518 μmol) of **bbip** were dissolved in 200 ml of ethanol/water (4:1/v:v). This mixture was refluxed for 5 hours in a microwave. After cooling, the solvent was removed under vacuum and the product was taken up in 50 ml of water. The undesired solids were filtered off and 760 mg NH_4PF_6 dissolved in 5 ml of water were added to obtain a red precipitate. The crude was filtered off and washed with water several times. After redissolution in dichloromethane removal of water a red solid was obtained. Purification was achieved via column chromatography (silica gel 60 with gradient elution). Using acetonitrile/water (95:5/v:v) ($R_f [Ru(\text{tbbpy})_2Cl_2] = 0.5$) and later acetonitrile/water/sat. KNO_3 -solution (50:6:1/v:v:v) ($R_{f\text{bbip}} = 0.2$) the pure product ($R_{f\text{Ru}(\text{bbip})} = 0.8$) was obtained after counter ion exchange and drying. Purification could be achieved as well via back and forth counter ion exchange with Bu_4NCl and NH_4PF_6 as described in the case of **Ru₂(edip)**. Yield: 496 mg (337 μmol, 65%) of the desired pure complex.



$^1\text{H-NMR}$ (CDCl_3 , 400 MHz): $\delta = 8.81$ (d, $2\text{H}_{(4,11\text{-ip})}$, $^3J = 8.6$ Hz), 8.26 (d, $2\text{H}_{(3\text{-bpy})}$, $^4J = 1.7$ Hz), 8.21 (d, $2\text{H}_{(3'\text{-bpy})}$, $^4J = 1.3$ Hz), 8.15 (d, $2\text{H}_{(6,9\text{-ip})}$, $^3J = 5.2$ Hz), 7.98 (s, $1\text{H}_{(2\text{-ip})}$), 7.80 (dd, $2\text{H}_{(5,10\text{-ip})}$, $^3J = 5.4$ Hz, $^3J = 8.5$ Hz), 7.66 (d, $2\text{H}_{(6\text{-bpy})}$, $^3J = 6.0$ Hz), 7.51 (dd, $2\text{H}_{(5\text{-bpy})}$, $^3J = 6.0$ Hz, $^4J = 1.8$ Hz), 7.35 (dd, $2\text{H}_{(5'\text{-bpy})}$, $^3J = 6.1$ Hz, $^4J = 1.7$ Hz), 7.38 (m, $12\text{H}_{(\text{ph},6'\text{-bpy})}$), 6.01 (d, $1\text{H}_{(\text{CH}_2)}$, $^2J = 14.7$ Hz), 5.95 (d, $1\text{H}_{(\text{CH}_2)}$, $^2J = 14.6$ Hz), 1.43 (s,

$18\text{H}_{(\text{tBu-bpy})}$), 1.34 (s, $18\text{H}_{(\text{tBu}'\text{-bpy})}$) ppm; $^1\text{H-NMR}$ (CD_3CN , 400 MHz): $\delta = 9.071$ (s, $1\text{H}_{(2\text{-ip})}$), 8.831 (d, $2\text{H}_{(4,11\text{-ip})}$, $^3J = 8.4$ Hz), 8.489 (d, $2\text{H}_{(3\text{-bpy})}$, $^3J = 2.0$ Hz), 8.448 (d, $2\text{H}_{(3'\text{-bpy})}$, $^4J = 2.0$ Hz), 8.167 (d, $2\text{H}_{(6,9\text{-ip})}$, $^3J = 5.2$ Hz), 7.770 (dd, $2\text{H}_{(5,10\text{-ip})}$, $^3J = 5.4$ Hz, $^3J = 8.4$ Hz), 7.604 (d, $2\text{H}_{(6\text{-bpy})}$, $^3J = 6.0$ Hz), 7.44 (m, $12\text{H}_{(\text{ph},5\text{-bpy})}$), 7.74 (dd, $2\text{H}_{(6'\text{-bpy})}$, $^3J = 6.0$ Hz), 7.195 (dd, $2\text{H}_{(5'\text{-bpy})}$, $^3J = 6.6$ Hz, $^4J = 2.0$ Hz), 6.152 (2, $2\text{H}_{(\text{CH}_2)}$), 1.417 (s, $18\text{H}_{(\text{CH}_3\text{-bpy})}$), 1.341 (s, $18\text{H}_{(\text{CH}_3'\text{-bpy})}$) ppm; $^{13}\text{C-NMR}$ (CD_3CN , 100 MHz): $\delta = 163.96$ ($4\text{C}_{(4,4'\text{-bpy})}$), 163.58 ($4\text{C}_{(4',4\text{-bpy})}$), 157.80 ($4\text{C}_{(2,2'\text{-bpy})}$), 157.71 ($4\text{C}_{(2',2\text{-bpy})}$), 154.03 ($2\text{C}_{(6,9\text{-ip})}$), 152.27 ($4\text{C}_{(6,6'\text{-bpy})}$), 151.92 ($4\text{C}_{(6',6\text{-bpy})}$), 148.82 ($2\text{C}_{(7',7''\text{-ip})}$), 144.49 ($1\text{C}_{(2\text{-ip})}$), 132.53 ($2\text{C}_{(1\text{-ph})}$), 131.66 ($2\text{C}_{(4,11\text{-ip})}$), 130.66 ($4\text{C}_{(2,6\text{-ph})}$), 130.51 ($2\text{C}_{(4\text{-ph})}$), 128.79 ($4\text{C}_{(3,5\text{-ph})}$), 128.16 ($2\text{C}_{(3',11''\text{-ip})}$), 127.69 ($2\text{C}_{(5,10\text{-ip})}$), 125.73 ($4\text{C}_{(5,5'\text{-bpy})}$), 125.46 ($4\text{C}_{(5',5\text{-bpy})}$), 122.66 ($4\text{C}_{(3,3'\text{-bpy})}$), 122.60 ($4\text{C}_{(3',3\text{-bpy})}$), 121.81 ($2\text{C}_{(3'',11'\text{-ip})}$), 55.10 ($2\text{C}_{(\text{CH}_2)}$), 36.38 ($2\text{C}_{(\text{C-bpy})}$), 36.30 ($2\text{C}_{(\text{C}'\text{-bpy})}$), 30.50 ($6\text{C}_{(\text{CH}_3\text{-bpy})}$), 30.43 ($6\text{C}_{(\text{CH}_3'\text{-bpy})}$) ppm; **MS** (ESI) $m/z = 1329.3$ (100%, $[\text{M-PF}_6]^+$), 1183.3 (80%, $[\text{M-2PF}_6\text{-H}]$); **Elementary analysis** ($\text{Ru}(\text{bbp})[\text{PF}_6]^3 \cdot 0.5 \text{H}_2\text{O}$): calc.: C: 51.01%, H: 4.76%, N: 7.55%; meas.: C: 50.99%, H: 4.76%, N: 7.48%.



Crystals suitable for X-ray diffraction were obtained from dichloromethane/chloroform. Crystal data for **Ru(bbip)**: $[\text{C}_{63}\text{H}_{69}\text{N}_8\text{Ru}]^{3+}$, $3[\text{PF}_6]^- \times 5 \text{CHCl}_3$, $M_r = 2071.08 \text{ g/mol}$, red-brown cuboid, size $0.05 \times 0.05 \times 0.04 \text{ mm}^3$, triclinic, space group $\text{P}\bar{1}$ (No. 2), $a = 13.0496(5)$, $b = 17.8884(6)$, $c = 20.1331(7) \text{ \AA}$, $\alpha = 105.144(2)$, $\beta = 101.312(2)$, $\gamma = 101.134(2)^\circ$, $V = 4297.7(3) \text{ \AA}^3$, $T = -140^\circ\text{C}$, $Z = 2$, $\rho_{\text{calcd.}} = 1.600 \text{ g cm}^{-3}$, $\mu (\text{Mo-K}\alpha) = 7.89 \text{ cm}^{-1}$, $F(000) = 2088$, 29924

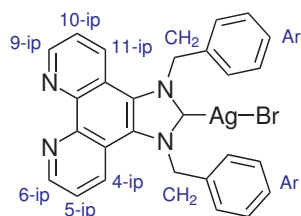
reflections in $h(-16/15)$, $k(-23/22)$, $l(-26/26)$ measured in the range $2.86^\circ \leq \Theta \leq 27.45^\circ$, completeness $\Theta_{\text{max}} = 98\%$, 19232 independent reflections, $R_{\text{int}} = 0.0486$, 12542 reflections with $F_o > 4\sigma(F_o)$, 1029 parameters, 0 restraints, $R_{\text{obs.}} = 0.0766$, $wR^2_{\text{obs.}} = 0.1813$, $R_{\text{all}} = 0.1262$, $wR^2_{\text{all}} = 0.2124$, GOOF = 1.026, largest difference peak and hole: $2.712 / -1.715 \text{ e \AA}^{-3}$. The Cambridge Crystallographic Data Centre file CCDC-765499 includes the full crystallographic data. In the molecular structure of **Ru(bbip)**. Hydrogen atoms (except H13a), solvent molecules and anions are omitted for clarity. Ellipsoids are drawn at 70% probability.

6.2.15 $[\text{Ru}(\text{tbbpy})_2(\text{bbip})]\text{Cl}_3$

For the counter ion exchange 425 mg (1.53 mmol) of NBu_4Cl were dissolved in 20 ml of acetone/ethyl acetate (1:1/v:v). After this a solution of 250 mg (170 μmol) of $[\text{Ru}(\text{tbbpy})_2(\text{bbip})][\text{PF}_6]_3$ dissolved in 10 ml of acetone/ethyl acetate (1:1/v:v) was slowly added to the stirred chloride salt solution. The resulting suspension was stirred for 30 min. Thereafter, the precipitate was filtered off and washed with 10 ml of acetone/ethyl acetate (1:1/v:v) and twice with 20 ml of ethyl acetate. After drying under vacuum, 192 mg (99%) of the desired product were obtained. No changes in the NMR spectra were detected with respect to the hexafluorophosphate salt of **Ru(bbip)**.

6.2.16 Attempted Preparation of $[(\text{bbip})\text{AgBr}]_n - (\text{bbip})\text{Ag}$

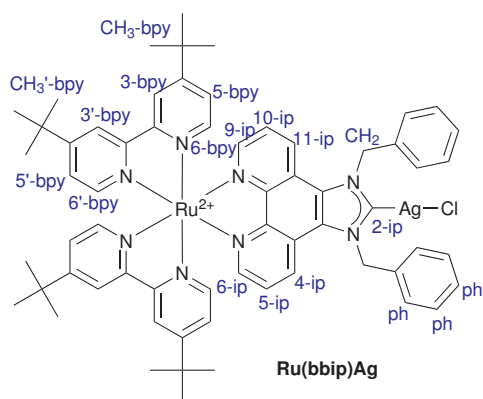
For the complexation reaction 100 mg of imidazolium bromide **bbip** and one equivalent of Ag_2O were suspended under inert conditions in dry dichloromethane according to **method C2**. Then the mixture was stirred for 7 days. Due to the general insolubility of both compounds a no visible change of the reaction mixture during this time. After this time, the reaction mixture was filtered through celite under inert conditions because of the expected higher solubility of the neutral complex compared to the ionic compounds. Removal of the solvent from the colorless solution gave only a thin film of precipitated white solid in very low yields (<1%). By dissolution of the precipitate in dry chloroform-*d* under inert conditions it was possible to obtain a weak $^1\text{H-NMR}$ -spectrum.



$^1\text{H-NMR}$ (CDCl_3 , 400 MHz): $\delta = 9.07$ (dd, $2\text{H}_{(6/9)}$, $^3J = 4.3$ Hz, $^4J = 1.3$ Hz), 8.40 (dd, $2\text{H}_{(4/11)}$, $^3J = 8.5$ Hz, $^4J = 1.3$ Hz), 7.48 (dd, $2\text{H}_{(5/10)}$, $^3J = 8.5$ Hz, $^3J = 4.3$ Hz), 7.22 (m, $6\text{H}_{(\text{Ar})}$), 7.05 (m, $4\text{H}_{(\text{Ar})}$), 6.21 (s, $4\text{H}_{(\text{CH}_2)}$) ppm. Due to the small amount of the obtained product, no other analysis method could be used.

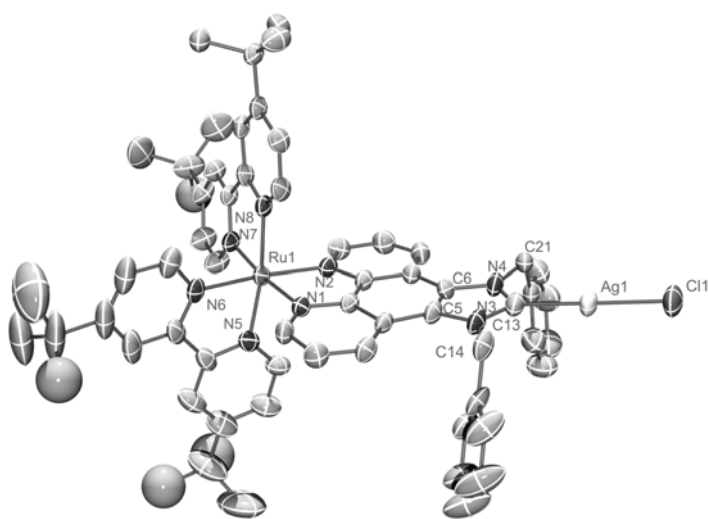
6.2.17 $[\{(\text{tbbpy})_2\text{Ru}\}(\mu\text{-bbip})\{\text{AgCl}\}]_2\text{Cl}_2 - \text{Ru}(\text{bbip})\text{Ag}$

According to **method C2**, 200 mg ($175 \mu\text{mol}$) of $[\text{Ru}(\text{tbbpy})_2(\text{bbip})]\text{Cl}_3$, 40.0 mg ($175 \mu\text{mol}$) of silver(I) oxide and 2 g of dry molecular sieves were suspended in 20 ml of dry dichloromethane under argon atmosphere. This solution was stirred for 16 hours at room temperature. After the reaction time, the remaining solids were removed by filtration through oven dried celite. Remaining product was washed from the celite with dichloromethane or acetonitrile. The pure product is obtained after removal of the solvent under reduced pressure. Yield: 197 mg ($157.5 \mu\text{mol}$, 90%) of a red powder sensitive to air and moisture.



$^1\text{H-NMR}$ (400 MHz, CD_3CN): $\delta = 8.81$ (dd, $2\text{H}_{(4/11\text{-ip})}$, $^3J = 8.7$ Hz, $^4J = 1.1$ Hz), 8.62 (d, $2\text{H}_{(3\text{-bpy})}$, $^4J = 1.9$ Hz), 8.57 (d, $2\text{H}_{(3'\text{-bpy})}$, $^4J = 1.8$ Hz), 8.02 (dd, $2\text{H}_{(6,9\text{-ip})}$, $^3J = 5.3$ Hz, $^4J = 1.0$ Hz), 7.66 (dd, $2\text{H}_{(5,10\text{-ip})}$, $^3J = 8.7$ Hz, $^3J = 5.4$ Hz), 7.60 (d, $2\text{H}_{(6\text{-bpy})}$, $^3J = 6.0$ Hz), 7.42 (dd, $2\text{H}_{(5\text{-bpy})}$, $^3J = 6.1$ Hz, $^4J = 2.0$ Hz), 7.33 (d, $2\text{H}_{(6'\text{-bpy})}$, $^3J = 6.0$ Hz), 7.32 (m, $10\text{H}_{(\text{ph})}$), 7.17 (dd, $2\text{H}_{(5'\text{-bpy})}$, $^3J = 6.0$ Hz, $^4J = 1.9$ Hz), 6.51 (s, $4\text{H}_{(\text{CH}_2)}$), 1.42 (s, $18\text{H}_{(\text{CH}_3)}$),

1.33 (s, $18\text{H}_{(\text{CH}_3)}$) ppm. $^1\text{H-NMR}$ (400 MHz, CDCl_3): $\delta = 8.83$ (d, $2\text{H}_{(4/11\text{-ip})}$, $^3J = 8.7$ Hz), 8.36 (d, $2\text{H}_{(3\text{-bpy})}$, $^4J = 1.8$ Hz), 8.30 (d, $2\text{H}_{(3'\text{-bpy})}$, $^4J = 1.8$ Hz), 8.22 (d, $2\text{H}_{(6,9\text{-ip})}$, $^3J = 5.2$ Hz), 7.99 (dd, $2\text{H}_{(5,10\text{-ip})}$, $^3J = 5.3$ Hz, $^3J = 8.6$ Hz), 7.72 (d, $2\text{H}_{(6\text{-bpy})}$, $^3J = 6.0$ Hz), 7.60 (d, $2\text{H}_{(6'\text{-bpy})}$, $^3J = 6.0$ Hz), 7.54 (dd, $2\text{H}_{(5\text{-bpy})}$, $^3J = 6.1$ Hz, $^4J = 1.9$ Hz), 7.36 (dd, $2\text{H}_{(6'\text{-bpy})}$, $^3J = 6.1$ Hz, $^4J = 1.9$ Hz), 7.28 (m, $10\text{H}_{(\text{ph})}$), 6.47 (d, $2\text{H}_{(\text{CH}_2)}$, $^2J = 17.2$ Hz), 6.40 (d, $2\text{H}_{(\text{CH}_2)}$, $^2J = 17.0$ Hz), 1.44 (s, $18\text{H}_{(\text{CH}_3)}$), 1.35 (s, $18\text{H}_{(\text{CH}_3)}$) ppm; $^{13}\text{C-NMR}$ (CDCl_3 , 100 MHz): $\delta = 196.5$ ($1\text{C}_{(2\text{-ip})}$), 162.89 ($2\text{C}_{(4,4'\text{-bpy})}$), 162.73 ($2\text{C}_{(4',4\text{-bpy})}$), 156.47 ($2\text{C}_{(2,2'\text{-bpy})}$), 152.26 ($2\text{C}_{(2',2\text{-bpy})}$), 152.10 ($2\text{C}_{(6,6'\text{-bpy})}$), 151.85 ($2\text{C}_{(6',6\text{-bpy})}$), 151.22 ($2\text{C}_{(6,9\text{-ip})}$), 146.06 ($2\text{C}_{(7,7'\text{-ip})}$), 134.23 ($2\text{C}_{(1\text{-ph})}$), 131.08 ($2\text{C}_{(4,11\text{-ip})}$), 129.69 ($4\text{C}_{(2,6\text{-ph})}$), 128.77 ($2\text{C}_{(3,11'\text{-ip})}$), 128.33 ($2\text{C}_{(4\text{-ph})}$), 127.84 ($2\text{C}_{(5,10\text{-ip})}$), 126.19 ($4\text{C}_{(3,5\text{-ph})}$), 125.96 ($4\text{C}_{(5,5'\text{-bpy})}$), 120.91 ($2\text{C}_{(3,3'\text{-bpy})}$), 120.75 ($2\text{C}_{(3',3\text{-bpy})}$), 120.53 ($2\text{C}_{(3',11'\text{-ip})}$), 56.17 ($2\text{C}_{(\text{CH}_2)}$), 35.80 ($2\text{C}_{(\text{C-bpy})}$), 35.70 ($2\text{C}_{(\text{C'-bpy})}$), 30.54 ($6\text{C}_{(\text{CH}_3\text{-bpy})}$), 30.43 ($6\text{C}_{(\text{CH}_3'\text{-bpy})}$) ppm; **MS**: (ESI) $m/z = 1216.9$ (100%, $[\text{M}-\text{Cl}]^+$), 1180.7 (80%, $[\text{M}-2\text{Cl}-\text{H}]^+$), 1073 (30%, $[\text{M}-\text{Ag}-2\text{Cl}]^+$), 519 (80%, $[\text{M}-\text{Ag}-3\text{Cl}]^{2+}$).

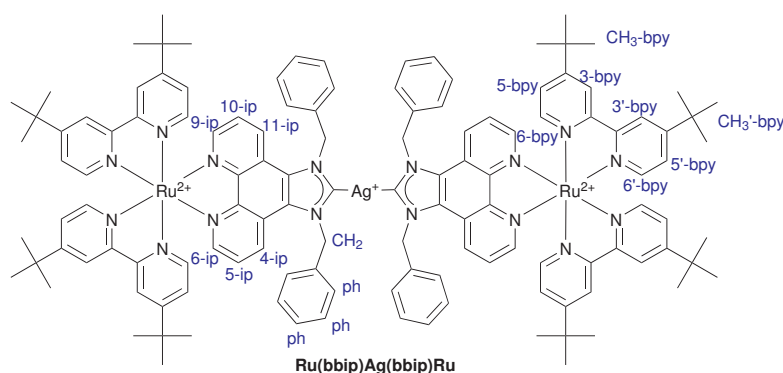


Crystals suitable for X-ray diffraction were obtained under inert conditions from a mixture of dichloromethane and chloroform with the slow evaporation method. Crystal data for **Ru(bbip)Ag**: $2[\text{C}_{63}\text{H}_{68}\text{AgClN}_8\text{Ru}]^{2+}$, $3.5 \text{ CH}_2\text{Cl}_2 \times 9.8 \text{ CHCl}_3 \times 3 \text{ Cl}^- \times \text{OH}^-$, $M_r = 1976.85$ g/mol, red plate, size $0.12 \times 0.12 \times 0.12 \text{ mm}^3$, monoclinic, space group $\text{C}2/c$, $a = 50.774(6)$, $b =$

14.4053(16), $c = 32.847(2)$ Å, $\alpha = 90^\circ$, $\beta = 127.021(6)^\circ$, $\gamma = 90^\circ$, $V = 19182(3)$ Å³, $T = 183(2)$ K, $Z = 8$, $\rho_{\text{calcd.}} = 1.369$ g/cm³, μ (Mo-K α) = 9.78 cm⁻¹, $F(000) = 7982$, 153628 reflections in $h(-64/64)$, $k(-18/18)$, $l(-41/41)$ measured in the range $2.83^\circ \leq \Theta \leq 27.00^\circ$, completeness $\Theta_{\text{max}} = 99.7\%$, 20872 independent reflections, $R_{\text{int}} = 0.0762$, 20872 reflections with $F_o > 4\sigma(F_o)$, 926 parameters, 0 restraints, $R_{\text{obs.}} = 0.0854$, $wR2_{\text{obs.}} = 0.2415$, $R_{\text{all}} = 0.1197$, $wR2_{\text{all}} = 0.2771$, GOOF = 1.039, largest difference peak and hole: 2.233 / -1.816 e Å⁻³. The Cambridge Crystallographic Data Centre file CCDC-796734 includes the full crystallographic data.

6.2.18 Attempted Synthesis of $\{[(\text{tbbpy})_2\text{Ru}(\mu\text{-bbip})]_2\text{Ag}\}[\text{PF}_6]_5$ - Ru(bbip)Ag(bbip)Ru

For the attempted reaction, 147.4 mg (0.1 mmol) of $[(\text{tbbpy})_2\text{Ru}(\text{bbip})][\text{PF}_6]_2$ and 23.2 mg (0.1 mmol) of Ag₂O were dissolved in 20 ml of dry and oxygen free acetonitrile (**method C2**). Then the mixture was stirred for two weeks at room temperature with exclusion of light. After one day and after two weeks small portions of the reaction mixture were separated (syringe with filter). Removal of the solvent and addition of inert acetonitrile-*d*₃ gave suitable NMR-samples. Chloroform was not a good solvent for NMR-experiments due to the low solubility. It is not clear which product was formed since hexafluoro phosphate ions coordinate only very weak, possible also the formation of $[(\text{tbbpy})_2\text{Ru}(\mu\text{-bbip})\text{AgOH}][\text{PF}_6]_2$ instead of the title compound. According to the NMR-spectrum no clean product but a 20:80-mixture of starting material and product was obtained.

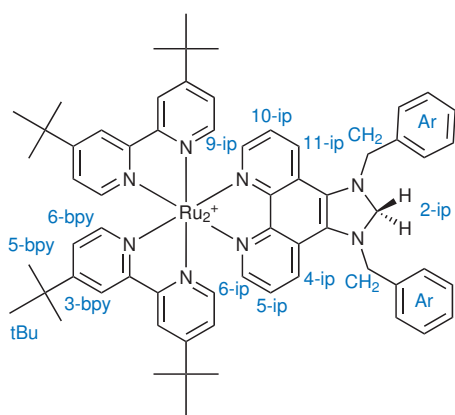


¹H-NMR (CD₃CN, 400 MHz):
 $\delta = 8.70$ (dd, 2H_(4/11-ip), ³J = 8.7 Hz, ⁴J = 1.1 Hz), 8.47 (d, 2H_(3-bpy), ⁴J = 1.7 Hz), 8.43 (d, 2H_(3'-bpy), ⁴J = 1.6 Hz), 8.03 (dd, 2H_(6/9-ip), ³J = 5.3 Hz, ⁴J = 1.0 Hz), 7.65 (dd, 2H_(5/10-ip), ³J = 8.7 Hz, ³J = 5.4 Hz), 7.59 (d,

2H_(6-bpy), ³J = 6.1 Hz), 7.42 (dd, 2H_(5-bpy), ³J = 6.1 Hz, ⁴J = 2.0 Hz), 7.29 (d, 2H_(6'-bpy), ³J = 6.0 Hz), 7.3 (m, 10H_(ph)), 7.16 (dd, 2H_(5'-bpy), ³J = 6.1 Hz, ⁴J = 2.0 Hz), 6.21 (s, 4H_(CH₂)), 1.41 (s, 18H_(CH₃-bpy)), 1.33 (s, 18H_(CH₃'-bpy)) ppm.

6.2.19 Attempted Synthesis of $[(tbbpy)_2Ru(bbipBEt_3)][PF_6]_2 - Ru(bbipBEt_3)$

For the synthesis, 0.03 ml of a 1 M solution of $HLiB(Et)_3$ were added to a stirred solution of 37 mg $Ru(bbip)$ in 20 ml of dry tetrahydrofuran under argon atmosphere at $-80^\circ C$. Upon addition a darkening of the solution toward red-brown was observed. The temperature was slowly raised to room temperature after the reaction time of 20 minutes at $-80^\circ C$. After removal of the solvent and drying under high vacuum 1H -NMR spectra were recorded in dry chloroform- d and dry acetonitrile- d_3 . It was observed that the formed product is not sensitive to air. According to the obtained NMR-spectra it could be concluded that the hydrogenated product was formed. Indicators are signals for the A-, B-, C-protons which refer to the symmetric ligand, a signal which refers to the D-position with an peak area of two protons at 4.5 ppm in chloroform- d and the missing signals for the ethyl groups at ~ 1 ppm.



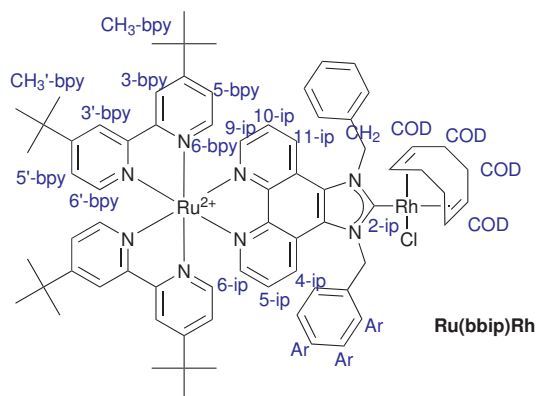
1H -NMR (CD_3CN , 400 MHz): $\delta = 8.50$ (d, $2H_{(3-bpy)}$, $^4J = 1.6$ Hz), 8.47 (d, $2H_{(3'-bpy)}$, $^4J = 1.8$ Hz), 8.42 (dd, $2H_{(4/11-ip)}$, $^3J = 8.6$ Hz, $^4J = 1.2$ Hz), 7.82 (dd, $2H_{(6/9-ip)}$, $^3J = 5.2$ Hz, $^4J = 1.2$ Hz), 7.67 (d, $2H_{(6-bpy)}$, $^3J = 6.0$ Hz), 7.52 (dd, $2H_{(5/10-ip)}$, $^3J = 5.2$ Hz, $^3J = 8.6$ Hz), 7.45 (d, $2H_{(6'-bpy)}$, $^3J = 6.0$ Hz), 7.44 (dd, $2H_{(5-bpy)}$, $^3J = 6.0$ Hz, $^4J = 2.1$ Hz), 7.31 (m, $12H_{(5'-bpy/Ar)}$), 4.95 (s, $2H_{(2-ip)}$), 4.45 (d, $2H_{(CH_2)}$, $^2J = 15.6$ Hz), 4.39 (d, $2H_{(CH_2)}$, $^2J = 15.7$ Hz), 1.43 (s, $18H_{(tBu-bpy)}$),

1.38 (s, $18H_{(tBu'-bpy)}$) ppm. 1H -NMR ($CDCl_3$, 270 MHz): $\delta = 8.27$ (dd, $2H_{(4/11-ip)}$, $^3J = 8.5$ Hz, $^4J = 1.0$ Hz), 8.19 (d, $2H_{(3-bpy)}$, $^4J = 1.7$ Hz), 8.16 (d, $2H_{(3'-bpy)}$, $^4J = 1.5$ Hz), 7.86 (dd, $2H_{(6/9-ip)}$, $^3J = 5.2$ Hz, $^4J = 0.9$ Hz), 7.72 (d, $2H_{(6-bpy)}$, $^3J = 6.0$ Hz), 7.58 (dd, $2H_{(5,10-ip)}$, $^3J = 8.6$ Hz, $^3J = 5.2$ Hz), 7.53 (dd, $2H_{(5-bpy)}$, $^3J = 6.0$ Hz, $^4J = 1.9$ Hz), 7.49 (d, $2H_{(6-bpy)}$, $^3J = 6.0$ Hz), 7.37 (dd, $2H_{(5'-bpy)}$, $^3J = 6.1$ Hz, $^4J = 1.7$ Hz), 7.31 (m, $10H_{(Ar)}$), 4.95 (s, $2H_{(2-ip)}$), 4.60 (d, $2H_{(CH_2)}$, $^2J = 16.0$ Hz), 4.42 (d, $2H_{(CH_2)}$, $^2J = 16.0$ Hz), 1.41 (s, $18H_{(tBu)}$), 1.37 (s, $18H_{(tBu)}$) ppm.

6.2.20 $\{[Ru(tbbpy)_2](\mu-bbip)\{Rh(cod)Cl\}Cl_2 - Ru(bbip)Rh$

Under argon atmosphere 100 mg ($87.3 \mu mol$) of $Ru(bbip)Ag$ and 21.6 mg ($43.6 \mu mol$) of $[Rh(cod)Cl]_2$ were dissolved in 20 ml of dry dichloromethane and stirred for 16 hours at room temperature (**method C3**). A colorless precipitate formed after 30 min. After the reaction time the

solid were removed by filtration through oven dried celite. Remaining product was washed from the celite with dichloromethane and acetonitrile. Finally the solvent was removed under vacuum and the crude was redissolved in THF. The pure product was precipitated by slow addition of diethyl ether. The solid was filtered off and was dried under vacuum. Yield: 103 mg (74.2 μ mol, 85%) of a red powder, sensitive to air and moisture.



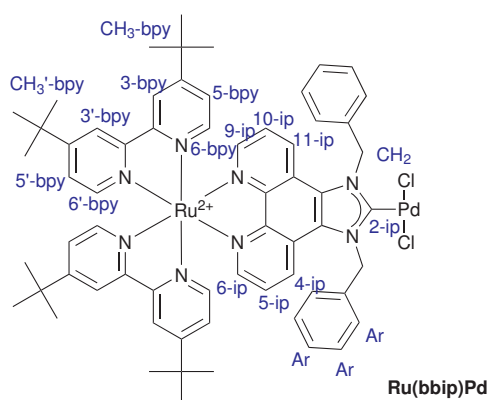
$^1\text{H-NMR}$ (400 MHz, CDCl_3): δ = 8.62 (dd, $1\text{H}_{(4\text{ip})}$, 4J = 1.0 Hz, 3J = 8.6 Hz), 8.59 (dd, $1\text{H}_{(11\text{ip})}$, 4J = 1.0 Hz, 3J = 8.6 Hz), 8.53 (d, $1\text{H}_{(3\text{bpy})}$, 4J = 1.8 Hz), 8.50 (d, $2\text{H}_{(3'\text{bpy}, 3''\text{bpy})}$, 4J = 1.8 Hz), 8.45 (d, $1\text{H}_{(3'''\text{bpy})}$, 4J = 1.8 Hz), 7.98 (dd, $1\text{H}_{(6\text{ip})}$, 4J = 1.0 Hz, 3J = 5.3 Hz), 7.95 (dd, $1\text{H}_{(9\text{ip})}$, 4J = 1.0 Hz, 3J = 5.3 Hz), 7.60 (d, $2\text{H}_{(6,6'\text{bpy})}$, 3J = 5.9 Hz), 7.55 (dd, $1\text{H}_{(5\text{ip})}$, 3J = 5.3 Hz, 3J = 8.7 Hz), 7.57 (dd, $1\text{H}_{(10\text{ip})}$, 3J =

5.1 Hz, 3J = 8.5 Hz), 7.43 (dd, $1\text{H}_{(5\text{bpy})}$, 4J = 2.1 Hz, 3J = 6.0 Hz), 7.41 (dd, $1\text{H}_{(5'\text{bpy})}$, 4J = 2.1 Hz, 3J = 6.0 Hz), 7.35 (m, $11\text{H}_{(\text{Ar}+6''\text{bpy})}$), 7.232 (d, $1\text{H}_{(6''\text{bpy})}$, 3J = 6.0 Hz), 7.23 (dd, $1\text{H}_{(5''\text{bpy})}$, 4J = 1.9 Hz, 3J = 6.0 Hz), 7.14 (dd, $1\text{H}_{(5'''\text{bpy})}$, 4J = 2.0 Hz, 3J = 6.1 Hz), 7.05 (d, $1\text{H}_{(\text{CH}_2)}$, 2J = 17.4 Hz), 7.01 (s, $2\text{H}_{(\text{CH}_2)}$), 7.00 (d, $1\text{H}_{(\text{CH}_2)}$, 2J = 17.4 Hz), 4.99 (s, $2\text{H}_{(\text{COD})}$), 4.03 (s, $2\text{H}_{(\text{COD})}$), 3.41 (m, $2\text{H}_{(\text{COD})}$), 2.31 (m, $4\text{H}_{(\text{COD})}$), 1.79 (m, $2\text{H}_{(\text{COD})}$), 1.41 (s, $9\text{H}_{(\text{CH}_3)}$), 1.41 (s, $9\text{H}_{(\text{CH}_3')}$), 1.36 (s, $9\text{H}_{(\text{CH}_3'')}$) ppm. **MS** (ESI): m/z = 1567.2 (15%, $[\{(\text{tbbpy})_2\text{Ru}\}(\text{bbip})\{\text{Rh}(\text{COD})\text{Cl}\}_2]^{2+}[\text{Cl}]^-$), 1463.2 (35%, $[\{(\text{tbbpy})_2\text{Ru}\}(\text{bbip})\{\text{Rh}(\text{COD})\text{Cl}\}\cdot\{\text{AgCl}\}]^{2+}[\text{Cl}]^-$), 1319.3 (12%, $[\{(\text{tbbpy})_2\text{Ru}\}(\text{bbip})\{\text{Rh}(\text{COD})\text{Cl}\}]^{2+}[\text{Cl}]^-$), 642.3 (100%, $[\{(\text{tbbpy})_2\text{Ru}\}(\text{bbip})\{\text{Rh}(\text{COD})\text{Cl}\}]^{2+}$), 519.4 (45%, $[(\text{tbbpy})_2\text{Ru}(\text{bbip})]^{2+}$), all with well matching isotopic pattern.

6.2.21 $[\{(\text{Ru}(\text{tbbpy})_2)(\mu\text{-bbip})\}\{\text{PdCl}_2\}]\text{Cl}_2$ - $\text{Ru}(\text{bbip})\text{Pd}$

Under argon atmosphere 100 mg (87.3 μ mol) of $[\text{Ru}(\text{tbbpy})_2(\mu\text{-bbip})\text{AgCl}]\text{Cl}_2$ and 26.7 mg (87.3 μ mol) of $[\text{Pd}(\text{acetonitrile})_2\text{Cl}_2]$ were dissolved in 20 ml of dry dichloromethane and were stirred for 16 hours at room temperature (**method C3**). A colorless precipitate formed after 30 min. After the reaction time the solid was removed by filtration through oven dried celite. Remaining product was washed from the celite with dichloromethane and acetonitrile. Finally the solvent was removed completely under vacuum. The product was obtained as a red powder which decomposes

under air. Yield: 106 mg (82.9 μmol , 95%).



$^1\text{H-NMR}$ (400 MHz, CD_3CN): δ = 8.81 (dd, $2\text{H}_{(4\text{-ip},11\text{-ip})}$, 3J = 8.8 Hz, 4J = 0.8 Hz), 8.68 (d, $2\text{H}_{(3\text{bpy})}$, 4J = 1.9 Hz), 8.64 (d, $2\text{H}_{(3\text{bpy}'')}$, 4J = 1.8 Hz), 8.10 (dd, $2\text{H}_{(6\text{-ip},9\text{-ip})}$, 3J = 5.3 Hz, 4J = 0.8 Hz), 7.70 (dd, $2\text{H}_{(5\text{-ip},10\text{-ip})}$, 3J = 5.3 Hz, 3J = 8.9 Hz), 7.66 (d, $2\text{H}_{(6\text{-bpy})}$, 3J = 6.1 Hz), 7.54 (dd, $2\text{H}_{(5\text{-bpy})}$, 3J = 6.1 Hz, 4J = 2.0 Hz), 7.50 (d, $4\text{H}_{(\text{Ar})}$, 3J = 7.4 Hz), 7.34 (m, $8\text{H}_{(\text{Ar}+6\text{-bpy}'')}$), 7.27 (dd, $2\text{H}_{(5\text{-bpy}'')}$, 3J = 6.1 Hz, 4J = 2.0 Hz), 7.14 (d, $2\text{H}_{(\text{CH}_2)}$, 2J = 17.7 Hz), 6.96

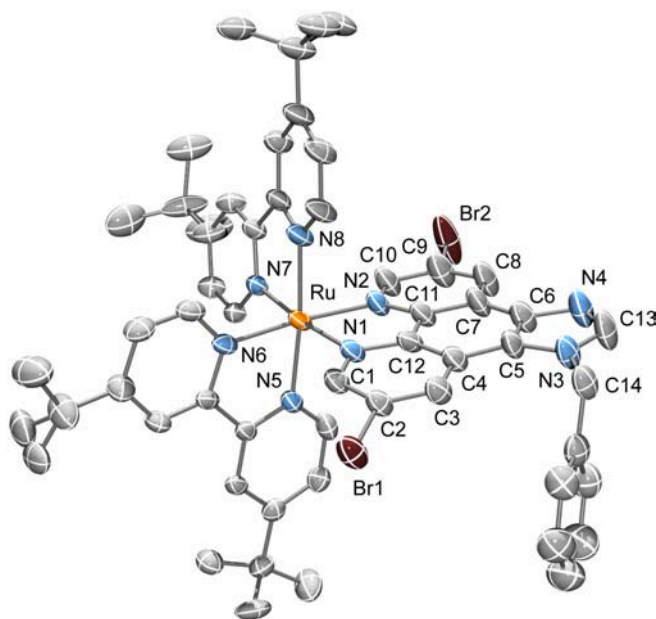
(d, $2\text{H}_{(\text{CH}_2)}$, 2J = 17.6 Hz), 1.43 (s, $18\text{H}_{(\text{CH}_3)}$), 1.35 (s, $18\text{H}_{(\text{CH}_3)}$) ppm. **MS** (ESI): m/z = 1235.1 (20%, $[\{(\text{tbbpy})_2\text{Ru}\}(\text{bbip})\{\text{Pd}(\text{H}_2\text{O})\text{Cl}_2\}]^+$), 821.9 (35%, $[\{(\text{tbbpy})\text{Ru}(\text{bbip})\}_2\{\text{Pd}_2\text{Cl}_4\}]^{4+}[\text{Cl}]^-$), 810.9 (35%, $[\{(\text{tbbpy})_2\text{Ru}(\text{bbip})\}_2\{\text{Pd}_2\text{Cl}_4\}]^{3+}$), 563.3 (100%, $[\{(\text{tbbpy})_2\text{Ru}(\text{bbip})\}_2\{\text{PdCl}_2\}]^{4+}$), 528.4 (25%, $[\{(\text{tbbpy})_2\text{Ru}(\text{bbip})\}(\text{H}_2\text{O})]^{2+}$), all with well fitting isotopic pattern.

6.2.22 Attempted Synthesis of $[\text{Ru}(\text{tbbpy})_2(\text{Br}_2\text{bbip})][\text{PF}_6]_2$ - $\text{Ru}(\text{Br}_2\text{bbip})$

As described in **method C1**, 147.3 mg (208 μmol) of $[\text{Ru}(\text{tbbpy})_2\text{Cl}_2]$ and 100 mg (208 μmol) of **Br₂bbip** were dissolved in 200 ml of DMF/water (4:1/v:v). This mixture was refluxed for 5 hours in a microwave. After cooling, the solvent was removed under vacuum and the product was taken up in 50 ml of water. The undesired solids were filtered off and 760 mg NH_4PF_6 dissolved in 5 ml of water were added to obtain a red precipitate. The crude was filtered off and washed with water several times. After redissolution in dichloromethane removal of water a red solid was obtained. Purification was achieved via back and forth counter ion exchange with Bu_4NCl and NH_4PF_6 as described in the case of **Ru₂(edip)**. Yield: 158 mg (135 μmol , 65%) of the wrong product. The pure complex turned out to be **Ru(Br₂bbip)**.

$^1\text{H-NMR}$ (acetonitrile- d_3 , 400 MHz): δ = 9.22 (d, $1\text{H}_{(4/11\text{-ip})}$, 4J = 1.9 Hz), 8.70 (d, $1\text{H}_{(11/4\text{-ip})}$, 4J = 1.8 Hz), 8.60 (d, $1\text{H}_{(3\text{-bpy})}$, 4J = 1.9 Hz), 8.57 (d, $1\text{H}_{(3'\text{-bpy})}$, 4J = 1.9 Hz), 8.57 (d, $1\text{H}_{(3''\text{-bpy})}$, 4J = 1.9 Hz), 8.56 (s, $1\text{H}_{(2\text{-ip})}$), 8.54 (d, $1\text{H}_{(3'''\text{-bpy})}$, 4J = 1.9 Hz), 7.94 (d, $1\text{H}_{(6/9\text{-ip})}$, 4J = 1.9 Hz), 7.85 (d, $1\text{H}_{(9/6\text{-ip})}$, 4J = 1.7 Hz), 7.60 (d, $2\text{H}_{(5,5'\text{-bpy})}$, 3J = 6.0 Hz), 7.44 (m, $4\text{H}_{(6,6'\text{-bpy},\text{Ar}\text{-ip})}$), 7.36 (m, $3\text{H}_{(\text{Ar}\text{-ip})}$), 7.24 (d, $2\text{H}_{(5''/5'''\text{-bpy})}$, 3J = 6.6 Hz), 7.21 (dd, $1\text{H}_{(6''\text{-bpy})}$, 4J = 2.1 Hz, 3J = 4.0 Hz), 7.19 (dd, $1\text{H}_{(6'''\text{-bpy})}$, 4J = 2.0 Hz, 3J = 4.0 Hz), 6.04 (s, $1\text{H}_{(\text{CH}_2\text{-ip})}$), 1.43 (s, $1\text{H}_{(\text{CH}_3\text{-bpy})}$), 1.42 (s, $1\text{H}_{(\text{CH}_3'\text{-bpy})}$), 1.37 (s,

$1\text{H}_{(\text{CH}_3\text{-bpy})}$, 1.36 (s, $1\text{H}_{(\text{CH}_3\text{-bpy})}$) ppm.



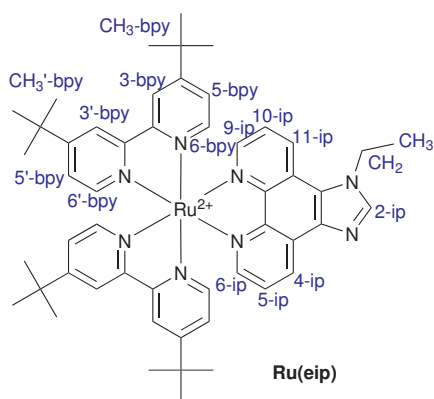
Crystals suitable for X-ray diffraction were obtained from diethyl ether/chloroform. Crystal

data for **Ru(Br₂bip)**: [C₅₆H₆₀N₈Br₂Ru]Cl₂ × 3.5 CHCl₃ × C₂H₅OC₂H₅, M_r = 1668.82 g/mol, red-brown cuboid, size 0.46 × 0.30 × 0.24 mm³, monoclinic, space group C2/c (No. 15), a = 28.494(2), b = 16.7022(14), c = 30.867(3) Å, α = 90.000, β = 96.8970(10), γ = 90.000°, V = 14583(2) Å³, T = 100K, Z = 8, ρ_{calcd.} = 1.520 g/cm³, μ_(Mo-Kα) = 1.815 cm⁻¹, F(000) =

6760, 65649 reflections in h(-34/32), k(-20/19), l(-37/37) measured in the range 2.07° ≤ Θ ≤ 25.35°, completeness Φ_{max} = 99.4%, 13274 independent reflections, R_{int} = 0.0420, 13274 reflections with F_o > 4σ(F_o), 1014 parameters, 393 restraints, R_{obs.} = 0.0711, wR_{obs.}² = 0.1853, R_{all} = 0.1019, wR_{all}² = 0.2087, GOOF = 1.087, largest difference peak and hole: 2.106 / -1.586 e/Å³. The data file dp1004 includes the full crystallographic data and can be obtained from DR. FRANK HEINEMANN (IAC, FAU-Erlangen-Nürnberg).

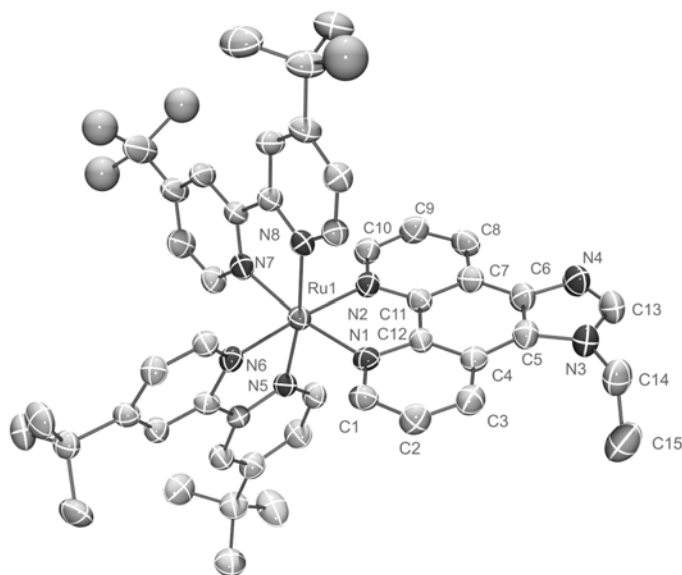
6.2.23 [Ru(tbbpy)₂(eip)][PF₆]₂ - Ru(eip)

The title compound was obtained, following **method C1**. 104 mg (146 μmol) of [Ru(tbbpy)₂Cl₂] and 36.4 mg (146 μmol) of **eip** were reacted in the microwave for 90 minutes in 50 ml of ethanol/water. After cooling and removal of ethanol and a dark precipitate 142 mg (870 μmol) of NH₄PF₆ were added. The formed precipitate was collected and washed with water several times. Purification was achieved by recrystallization from acetone/ethanol/water by slow evaporation. After removal of water the pure **Ru(eip)** was obtained as red powder. The yield was 155 mg (132 μmol, 90%).



$^1\text{H-NMR}$ (CD_3CN , 400 MHz): $\delta = 9.04$ (dd, $1\text{H}_{(4/11\text{-ip})}$, $^3J = 8.2$ Hz, $^4J = 1.1$ Hz), 8.88 (dd, $1\text{H}_{(4/11\text{-ip})}$, $^3J = 8.6$ Hz, $^4J = 1.1$ Hz), 8.50 (dd, $1\text{H}_{(3\text{-bpy})}$, $^4J = 2.0$ Hz, $^4J = 2.0$ Hz), 8.46 (dd, $1\text{H}_{(3'\text{-bpy})}$, $^4J = 1.8$ Hz, $^4J = 1.8$ Hz), 8.34 (s, $1\text{H}_{(2\text{-ip})}$), 7.99 (dd, $1\text{H}_{(6/9\text{-ip})}$, $^3J = 5.4$ Hz, $^4J = 1.2$ Hz), 7.98 (dd, $1\text{H}_{(6/9\text{-ip})}$, $^3J = 5.3$ Hz, $^4J = 1.2$ Hz), 7.80 (dd, $1\text{H}_{(5/10\text{-ip})}$, $^3J = 5.4$ Hz, $^3J = 8.2$ Hz), 7.78 (dd, $1\text{H}_{(5/10\text{-ip})}$, $^3J = 5.3$ Hz, $^3J = 8.4$ Hz), 7.69 (d, $1\text{H}_{(6\text{-bpy})}$, $^3J = 6.1$ Hz), 7.67 (d, $1\text{H}_{(6\text{-bpy})}$, $^3J = 6.1$ Hz), 7.47 (dd,

$1\text{H}_{(5\text{-bpy})}$, $^3J = 5.7$ Hz, $^4J = 2.7$ Hz), 7.46 (dd, $1\text{H}_{(5\text{-bpy})}$, $^3J = 5.5$ Hz, $^4J = 2.4$ Hz), 7.42 (dd, $1\text{H}_{(6'\text{-bpy})}$, $^3J = 6.0$ Hz), 7.41 (dd, $1\text{H}_{(6'\text{-bpy})}$, $^3J = 6.0$ Hz), 7.19 (d, $2\text{H}_{(5'\text{-bpy})}$, $^3J = 6.0$ Hz), 4.77 (q, $2\text{H}_{(\text{CH}_2)}$, $^3J = 7.2$ Hz), 1.65 (t, $3\text{H}_{(\text{CH}_3)}$, $^3J = 7.2$ Hz), 1.44 (s, $18\text{H}_{(\text{CH}_3\text{-bpy})}$), 1.35 (s, $18\text{H}_{(\text{CH}_3'\text{-bpy})}$) ppm. $^{13}\text{C-NMR}$ (CD_3CN , 100 MHz): $\delta = 163.48$ ($2\text{C}_{(4\text{-bpy})}$), 163.31 ($2\text{C}_{(4'\text{-bpy})}$), 157.89 ($2\text{C}_{(2\text{-bpy})}$), 157.70 ($2\text{C}_{(2'\text{-bpy})}$), 151.90 ($2\text{C}_{(6\text{-bpy})}$), 151.83 ($2\text{C}_{(6'\text{-bpy})}$), 150.95 ($1\text{C}_{(6/9\text{-ip})}$), 150.41 ($1\text{C}_{(6/9\text{-ip})}$), 146.99 ($1\text{C}_{(7/17''\text{-ip})}$), 146.73 ($1\text{C}_{(7/17''\text{-ip})}$), 146.03 ($1\text{C}_{(2\text{-ip})}$), 131.20 ($1\text{C}_{(4/11\text{-ip})}$), 130.59 ($1\text{C}_{(4/11\text{-ip})}$), 127.52 ($1\text{C}_{(3''/11'\text{-ip})}$), 127.11 ($1\text{C}_{(5/10\text{-ip})}$), 126.06 ($1\text{C}_{(5/10\text{-ip})}$), 125.97 ($1\text{C}_{(3''/11'\text{-ip})}$), 125.62 ($2\text{C}_{(5\text{-bpy})}$), 125.42 ($2\text{C}_{(5'\text{-bpy})}$), 123.05 ($2\text{C}_{(3'/11''\text{-ip})}$), 122.40 ($2\text{C}_{(3\text{-bpy})}$), 122.29 ($2\text{C}_{(3'\text{-bpy})}$), 43.77 ($1\text{C}_{(\text{CH}_2)}$), 36.30 ($2\text{C}_{(\text{C-bpy})}$), 36.19 ($2\text{C}_{(\text{C'-bpy})}$), 30.54 ($6\text{C}_{(\text{CH}_3\text{-bpy})}$), 30.44 ($6\text{C}_{(\text{CH}_3'\text{-bpy})}$), 15.99 ($1\text{C}_{(\text{CH}_3)}$) ppm. **MS** (ESI): $m/z = 1031.1$ (100%, $[\text{M-PF}_6]^+$).



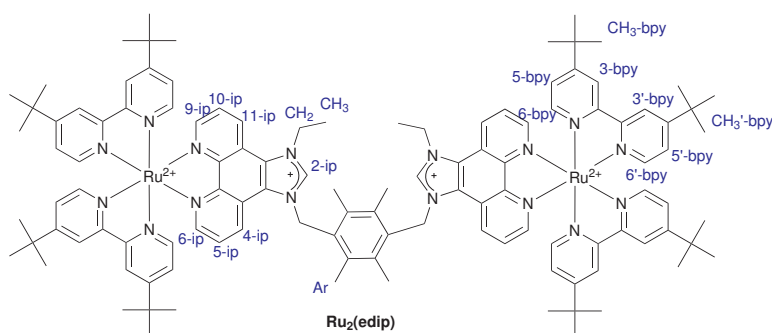
Crystals suitable for X-ray diffraction were obtained from water/acetone. Crystal data for **Ru(eip)**: $[\text{C}_{51}\text{H}_{60}\text{N}_8\text{Ru}]^{2+}[\text{PF}_6]_2 \times 3 \text{CH}_3\text{COCH}_3$, $M_r = 1350.31$ g/mol, red-brown plate, size $0.05 \times 0.05 \times 0.03$ mm³, triclinic, space group $\text{P}\bar{1}$ (No. 2), $a = 13.429(3)$, $b = 14.934(3)$, $c = 19.146(4)$ Å, $\alpha = 107.11(3)$, $\beta = 96.87(3)$, $\gamma = 96.58(3)^\circ$, $V = 3407.7(12)$ Å³, $T = -90(2)^\circ\text{C}$, $Z = 2$, $\rho_{\text{calcd.}} = 1.315$ g/cm³, $\mu_{(\text{Mo-K}\alpha)} = 3.56$ cm⁻¹, $F(000)$

$= 1400$, 20389 reflections in $h(-17/17)$, $k(-18/19)$, $l(-23/21)$ measured in the range $3.96^\circ \leq \Theta \leq 27.49^\circ$, completeness $\Phi_{\text{max}} = 92.4\%$, 14481 independent reflections, $R_{\text{int}} = 0.0396$, 9212 reflections with $F_o >$

$4\sigma(F_o)$, 760 parameters, 0 restraints, $R_{\text{obs.}} = 0.0894$, $wR_{\text{obs.}}^2 = 0.2298$, $R2_{\text{all}} = 0.1440$, $wR_{\text{all}}^2 = 0.2703$, $\text{GOOF} = 1.029$, largest difference peak and hole: $1.311 / -0.740 \text{ e}/\text{\AA}^3$. The data file TT3757 includes the full crystallographic data and can be obtained from DR. HELMAR GÖRLS (IAAC, FSU-Jena).

6.2.24 $[\{\text{Ru}(\text{tbbpy})_2\}_2(\mu\text{-edip})][\text{PF}_6]_6 - \text{Ru}_2(\text{edip})$

The title compound was obtained, following **method C1**. 104 mg (141 μmol) of $[\text{Ru}(\text{tbbpy})_2\text{Cl}_2]$ and 58 mg (70 μmol) of **edip** were reacted in the microwave for 300 minutes in 75 ml of ethanol/water. After cooling and removal of ethanol and a dark precipitate 12 equivalents of NH_4PF_6 were added. The formed precipitate was collected and washed with water and dissolved in methylene chloride. After drying with Na_2SO_4 and removal of the solvent a crude product was obtained. Purification was achieved ion exchange. The crude was dissolved in 10 ml of acetone/ethyl acetate (1:1) and was slowly added to a stirred solution of Bu_4NCl in 40 ml of acetone/ethyl acetate (1:1). The formed precipitate was collected and washed with small amounts of acetone/ethyl acetate to yield pure $[\{\text{Ru}(\text{tbbpy})_2\}_2(\mu\text{-edip})]\text{Cl}_6$. After ion-back-exchange with NH_4PF_6 and removal of water pure **Ru₂(edip)** was obtained as red powder. The yield was 243 mg (85 μmol , 60%).



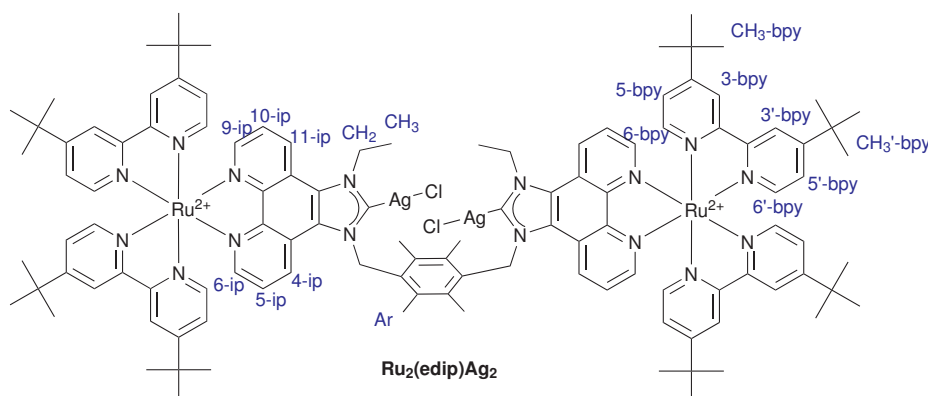
¹H-NMR (CD_3CN , 400 MHz): δ = 9.404 (dd, $2\text{H}_{(4\text{-ip})}$, $^3J = 8.2 \text{ Hz}$, $^4J = 0.9 \text{ Hz}$), 8.994 (dd, $2\text{H}_{(11\text{-ip})}$, $^3J = 8.2 \text{ Hz}$, $^4J = 0.9 \text{ Hz}$), 8.552 (s, $2\text{H}_{(2\text{-ip})}$), 8.525 (m, $4\text{H}_{(3/3'\text{-bpy})}$), 8.485 (m, $4\text{H}_{(3'/3\text{-bpy})}$), 7.976 (dd, $2\text{H}_{(5\text{-ip})}$, $^3J = 8.2 \text{ Hz}$, $^3J = 5.5 \text{ Hz}$),

7.934 (dd, $2\text{H}_{(9\text{-ip})}$, $^3J = 8.2 \text{ Hz}$, $^3J = 5.5 \text{ Hz}$), 7.668 (d, $2\text{H}_{(6/6'\text{-bpy})}$, $^3J = 7.7 \text{ Hz}$), 7.660 (d, $2\text{H}_{(6'/6\text{-bpy})}$, $^3J = 7.7 \text{ Hz}$), 7.467 (m, $4\text{H}_{(5/5'\text{-bpy})}$), 7.415 (d, $2\text{H}_{(6'/6\text{-bpy})}$, $^3J = 6.0 \text{ Hz}$), 7.408 (d, $2\text{H}_{(6/6'\text{-bpy})}$, $^3J = 6.0 \text{ Hz}$), 7.219 (m, $4\text{H}_{(5'/5\text{-bpy})}$), 6.245 (d, $2\text{H}_{(\text{CH}_2\text{-Ar})}$, $^2J = 14.4 \text{ Hz}$), 6.210 (d, $2\text{H}_{(\text{CH}_2\text{-Ar})}$, $^2J = 14.4 \text{ Hz}$), 5.00 (q, $4\text{H}_{(\text{CH}_2\text{-Al})}$, $^3J = 7.0 \text{ Hz}$), 2.353 (s, $12\text{H}_{(\text{CH}_3\text{-Ar})}$), 1.652 (t, $6\text{H}_{(\text{CH}_3\text{-Al})}$, $^3J = 7.3 \text{ Hz}$), 1.436 (s, $18\text{H}_{(\text{tBu})}$), 1.431 (s, $18\text{H}_{(\text{tBu})}$), 1.344 (s, $18\text{H}_{(\text{tBu})}$), 1.342 (s, $18\text{H}_{(\text{tBu})}$) ppm; **¹³C-NMR** (CD_3CN , 100 MHz): δ = 163.05 ($4\text{C}_{(4\text{-bpy})}$), 162.91 ($4\text{C}_{(4'\text{-bpy})}$), 156.90 ($4\text{C}_{(2\text{-bpy})}$), 156.82 ($4\text{C}_{(2'\text{-bpy})}$), 152.98 ($2\text{C}_{(6/9\text{-ip})}$), 151.28 ($4\text{C}_{(3\text{-bpy})}$), 151.05 ($4\text{C}_{(3'\text{-bpy})}$), 147.79 ($2\text{C}_{(6''\text{-ip})}$), 147.70 ($2\text{C}_{(6'''\text{-ip})}$), 140.80 ($2\text{C}_{(2\text{-ip})}$),

137.34 ($2C_{(2,3,5,6\text{-Duro})}$), 131.49 ($2C_{(4\text{-ip})}$), 130.74 ($2C_{(11\text{-ip})}$), 129.38 ($2C_{(1,4\text{-Duro})}$), 127.50 ($2C_{(3'')}$), 127.14 ($2C_{(5)}$), 126.96 ($2C_{(11'')}$), 126.74 ($2C_{(10)}$), 124.82 ($4C_{(5\text{-bpy})}$), 124.58 ($4C_{(5'\text{-bpy})}$), 121.75 ($8C_{(6/6'\text{-bpy})}$), 121.66 ($2C_{(3''\text{-ip})}$), 121.03 ($2C_{(11'\text{-ip})}$), 51.00 ($2C_{(\text{CH}_2\text{-Ar})}$), 46.42 ($2C_{(\text{CH}_2\text{-Al})}$), 35.48 ($2C_{(\text{C-tBu})}$), 35.37 ($2C_{(\text{C-tBu})}$), 29.58 ($12C_{(\text{CH}_3\text{-tBu})}$), 29.49 ($12C_{(\text{CH}_3\text{-tBu})}$), 16.19 ($4C_{(\text{CH}_3\text{-Ar})}$), 14.33 ($2C_{(\text{CH}_3\text{-Al})}$) ppm. **MS** (ESI): $m/z = 1110.2$ (10%, $[\text{M} - 2 \text{PF}_6]^{2+}$) 1031.1 (100%, $[\text{Ru}(\text{eip}) + \text{PF}_6]^+$).

6.2.25 $[\{(\text{tbbpy})_2\text{Ru}\}_2(\mu\text{-edip})\{\text{AgCl}\}_2]\text{Cl}_4 \cdot \text{Ru}_2(\text{edip})\text{Ag}_2$

According to **method C2**, 200 mg (93 μmol) of the chloride salt of $\text{Ru}_2(\text{edip})$, 25.0 mg (220 μmol) of silver(I) oxide and 2 g of dry molecular sieves were suspended in 20 ml of dry dichloromethane under argon atmosphere. This solution was stirred for 16 hours at room temperature. After the reaction time, the remaining solids were removed by filtration through oven dried celite. Remaining product was washed from the celite with dichloromethane and acetonitrile. The pure product is obtained after removal of the solvent under reduced pressure. Yield: 190 mg (80 μmol , 86%) of a red powder which is sensitive to air and moisture.



$^1\text{H-NMR}$ (CD_3CN , 400 MHz): $\delta = 9.50$ (d, $2\text{H}_{(\text{C})}$, $^3J = 8.4\text{Hz}$), 9.03 (d, $2\text{H}_{(\text{C})}$, $^3J = 8.6\text{Hz}$), 8.58 (d, $2\text{H}_{(3\text{-bpy})}$, $^4J = 1.8\text{Hz}$), 8.58 (d, $2\text{H}_{(3'\text{-bpy})}$, 4J

$= 1.8\text{Hz}$), 8.54 (d, $2\text{H}_{(3''\text{-bpy})}$, $^4J = 2.0\text{Hz}$), 8.54 (d, $2\text{H}_{(3'''\text{-bpy})}$, $^4J = 1.8\text{Hz}$), 8.20 (dd, $2\text{H}_{(\text{A})}$, $^3J = 5.3\text{Hz}$, $^4J = 0.7\text{Hz}$), 8.18 (dd, $2\text{H}_{(\text{A})}$, $^3J = 5.4\text{Hz}$, $^4J = 0.8\text{Hz}$), 7.91 (dd, $2\text{H}_{(\text{B})}$, $^3J = 8.8\text{Hz}$, $^3J = 4.8\text{Hz}$), 7.90 (dd, $2\text{H}_{(\text{B})}$, $^3J = 8.7\text{Hz}$, $^3J = 5.1\text{Hz}$), 7.72 (d, $2\text{H}_{(6\text{-bpy})}$, $^3J = 6.1\text{Hz}$), 7.70 (d, $2\text{H}_{(6'\text{-bpy})}$, $^3J = 6.1\text{Hz}$), 7.49 (m, $2\text{H}_{(5,5',6''\text{-bpy})}$), 7.45 (d, $6\text{H}_{(6''\text{-bpy})}$, $^3J = 6.1\text{Hz}$), 7.26 (m, $4\text{H}_{(5,5''\text{-bpy})}$), 6.10 (d, $2\text{H}_{(\text{CH}_2\text{-Ar})}$, $^2J = 13.1\text{Hz}$), 6.05 (d, $2\text{H}_{(\text{CH}_2\text{-Ar})}$, $^2J = 14.3\text{Hz}$), 5.06 (q, $4\text{H}_{(\text{CH}_2\text{-Al})}$, $^3J = 6.8\text{Hz}$), 2.30 (dd, $12\text{H}_{(\text{CH}_3\text{-Ar})}$, $J = 23.9\text{Hz}$, $J = 6.2\text{Hz}$), 1.70 (t, $6\text{H}_{(\text{CH}_3\text{-Al})}$, $^3J = 7.1\text{Hz}$), 1.46 (s, $36\text{H}_{(\text{tBu})}$), 1.38 (s, $36\text{H}_{(\text{tBu})}$) ppm. **MS** (ESI): $m/z = 1143.8$ (25%, $[\text{M} - 2 \text{Cl}]^{2+}$), 751.1 (50%, $[\text{M} - 3 \text{Cl}]^{3+}$), 715.1 (50%, $[\text{M} - 3 \text{Cl} - \text{Ag}]^{3+}$), 554.7 (100%, $[\text{M} - 3 \text{Cl}]^{4+}$).

7 Appendix

*	excited state	<i>dd</i>	dublett of dubletts
~	covalently linked	<i>ddd</i>	dublett of dubletts of dubletts
[]	photocatalytic system	<i>DEI</i>	desorption electron ionization
A	acceptor	<i>DMF</i>	N,N-dimethylformamide
<i>abs.</i>	absorption, absolute	<i>DMSO</i>	dimethylsulfoxide
<i>ACN</i>	acetonitrile	<i>DNA</i>	deoxyribonucleic acid
AP	antenna pigment	<i>dppz</i>	dipyrido[3,2-a:2,3-c]phenazine
<i>a.u.</i>	arbitrary units	<i>dqp</i>	2,6-bis(8'-quinolinyl)pyridine
<i>b</i>	broad	<i>EI</i>	electronic ionization
B	bridge	<i>edip</i>	3,3'-(2,3,5,6-tetramethyl-1,4-phenylene)bis(methylene)bis-(1-ethyl-1 <i>H</i> -imidazo[4,5- <i>f</i>][1,10]phenanthroline) dibromide
<i>bbip</i>	1,3-dibenzyl-1 <i>H</i> -imidazo[4,5- <i>f</i>][1,10]phenanthroline bromide	<i>eip</i>	1-ethyl-1 <i>H</i> -imidazo[4,5- <i>f</i>][1,10]phenanthroline
<i>(bbip)Ag</i>	[Ag(<i>bbip</i>)Br]	<i>em.</i>	emission
<i>bbipBEt₃</i>	triethylborane adduct of 1,3-dibenzyl-1 <i>H</i> -imidazo[4,5- <i>f</i>][1,10]phenanthroline-2-ylidene	<i>ESI</i>	electro-spray ionization
<i>bip</i>	1-benzyl-1 <i>H</i> -imidazo[4,5- <i>f</i>][1,10]phenanthroline	<i>eT</i>	electron transfer
<i>bpy</i>	2,2'-bipyridine	<i>ET</i>	energy transfer
<i>Br₂bip</i>	1-benzyl-5,10-dibromo-1 <i>H</i> -imidazo[4,5- <i>f</i>][1,10]phenanthroline	<i>et al.</i>	et alii
<i>Br₂phen</i>	3,8-dibromo-1,10-phenanthroline	<i>EtOH</i>	ethanol
C	catalyst	<i>F</i>	fluorescence
<i>COD</i>	cyclooctadiene	<i>FAB</i>	fast atom bombardment
<i>COSY</i>	correlation spectroscopy	<i>Fc</i>	ferrocene
<i>conc.</i>	concentrated	<i>Fd</i>	ferredoxin
<i>CT</i>	charge transfer	<i>FeS</i>	membrane bound iron sulfur protein
<i>cyt f</i>	cytochrome <i>f</i>	<i>ff.</i>	and the following
<i>d</i>	dublett	<i>FNR</i>	ferredoxin-NADP reductase
D	donor	<i>FTIR</i>	fourier transform infrared
<i>DCM</i>	dichloromethane	<i>GC</i>	gas chromatography
		<i>GS</i>	ground state

<i>HPLC</i>	high pressure liquid chromatography	<i>Nd:YAG</i>	neodymium-doped yttrium aluminum garnet (Nd:Y ₃ Al ₅ O ₁₂)
<i>HMBC</i>	heteronuclear multiple bond coherence	<i>nr</i>	nonradiative
<i>HSQC</i>	heteronuclear single quantum coherence	OEC	oxygen evolving complex
<i>IC</i>	internal conversion	<i>OECD</i>	Organisation for Economic Co-operation and Development
<i>IEA</i>	International Energy Agency	Os(phenphen)Os	[{Os(bpy) ₂ } ₂ (μ-phenphen)] ⁴⁺
<i>ISC</i>	inter system crossing	Ox	oxidation
ip	1 <i>H</i> -imidazo[4,5- <i>f</i>][1,10]phenanthroline	<i>p.</i>	pages
<i>IR</i>	infrared	<i>P</i>	phosphorescence
<i>L</i>	(monodentate) ligand	P	photosensitizer
<i>LC</i>	ligand centred	P 680/700	special pairs with λ = 680/700 nm
LHI/II	light harvesting complex I and II	PC	plastocyanine
\widehat{LL}	bidentate ligand	<i>PET</i>	photoinduced electron transfer
\widehat{LLL}	tridentate ligand	phen	1,10-phenanthroline
\widehat{LLLL}	tetradentate ligand	phenBr	5-bromo-1,10-phenanthroline
<i>LMCT</i>	ligand to metal charge transfer	phenBr₂	5,6-dibromo-1,10-phenanthroline
<i>m</i>	multiplett	phenBr₄	3,5,6,8-tetrabromo-1,10-phenanthroline
<i>M</i>	mol/l	phenCl	5-chloro-1,10-phenanthroline
<i>MC</i>	metal centered	phenphen	5,5'-Bis-1,10-phenanthroline
<i>MeOH</i>	methanol	Pheo	pheophytin
<i>MLCT</i>	metal to ligand charge transfer	<i>ppm</i>	parts per million
<i>MS</i>	mass spectrometry	PQ	plastoquinone
<i>MV</i>	methylviologene	PSI/II	photosystem I/II
<i>N</i>	noninvolved	Q	quencher, quenching
<i>NHE</i>	normal hydrogen electrode	Red	reduction
Me₂phenBr₂	5,6-dibromo-2,9-dimethyl-1,10-phenanthroline	<i>RT</i>	room temperature
Me₂phenBr₃	3,5,6-tribromo-2,9-dimethyl-1,10-phenanthroline	Ru(eip)	[Ru(tbbpy) ₂ (eip)] ²⁺
<i>NMR</i>	nuclear magnetic resonance	Ru₂(edip)	[{Ru(tbbpy) ₂ } ₂ (μ-edip)] ⁶⁺
<i>m/z</i>	mass-charge ratio	Ru₂(edip)Ag₂	[{Ru(tbbpy) ₂ } ₂ (μ-edip){AgCl} ₂] ⁴⁺
NADP	nicotinamide adenine dinucleotide phosphate	Ru(ip)	[Ru(tbbpy) ₂ (ip)] ²⁺
		Ru(bbip)	[Ru(tbbpy) ₂ (bbip)] ³⁺
		Ru(bbipBEt₃)	[Ru(tbbpy) ₂ (bbipBEt ₃)] ³⁺

<i>Ru(bbip)Ag</i> [Ru(tbbpy) ₂ (μ-bbip)AgCl] ²⁺	<i>Ru(tpphz)Os</i> [Ru(bpy) ₂ (μ-tpphz)Os(bpy) ₂] ⁴⁺
<i>Ru(bbip)Pd</i> [Ru(tbbpy) ₂ (μ-bbip)PdCl ₂] ²⁺	<i>Ru(tpphz)Pd</i> [Ru(tbbpy) ₂ (μ-tpphz)PdCl ₂] ²⁺
<i>Ru(bbip)Rh</i> [Ru(tbbpy) ₂ (μ-bbip)Rh(cod)Cl] ²⁺	<i>Ru(tpphz)Pt</i> [Ru(tbbpy) ₂ (μ-tpphz)PtCl ₂] ²⁺
<i>Ru(bip)</i> [Ru(tbbpy) ₂ (bip)] ²⁺	<i>Ru(tpphz)Ru</i> [{Ru(phen) ₂ } ₂ (μ-tpphz)] ⁴⁺
<i>Ru(Br₂bip)</i> [Ru(tbbpy) ₂ (Br ₂ bip)] ²⁺	S, s singulett
<i>Ru(Br₂bbip)</i> [Ru(tbbpy) ₂ (Br ₂ bbip)] ²⁺	S (sacrificial) substrate
<i>Ru(Br₂phen)</i> [Ru(tbbpy) ₂ (Br ₂ phen)] ²⁺	SCE saturated calomel electrode
<i>Ru(phen)</i> [Ru(tbbpy) ₂ (phen)] ²⁺	sh shoulder
<i>Ru(phenCl)</i> [Ru(tbbpy) ₂ (5-chloro-1,10-phenanthroline)] ²⁺	T, t triplett
<i>Ru(phenBr)</i> [Ru(tbbpy) ₂ (phenBr)] ²⁺	tbbpy 4,4'-di-tertbutyl-2,2'-bipyridine
<i>Ru(phenBr₂)</i> [Ru(tbbpy) ₂ (phenBr ₂)] ²⁺	TCD thermal conductivity detector
<i>Ru(phenBr₄)</i> [Ru(tbbpy) ₂ (phenBr ₄)] ²⁺	THF tetrahydrofuran
<i>Ru(phenBr₂)₂</i> [Ru(tbbpy)(phenBr ₂) ₂] ²⁺	TLC thin layer chromatography
<i>Ru(phenBr₂)₂Cl₂</i> [Ru(phenBr ₂) ₂ Cl ₂]	TOF turnover frequency
<i>Ru(phenBr₂)₃</i> [Ru(phenBr ₂) ₃]	TON turnover number
<i>Ru(phenphen)</i> [Ru(tbbpy) ₂ (phenphen)] ²⁺	tpphz tetrapyrido[3,2-a:2',3'-c:3''-h:2'''-3'''-j]phenazine
<i>Ru(phenphen)Pt</i> [Ru(tbbpy) ₂ (μ-phenphen)PtCl ₂] ²⁺	tpy the 2,2';6';2''-terpyridine
<i>Ru(phenphen)Ru</i> [Ru(tbbpy) ₂] ₂ (μ-phenphen)] ⁴⁺	UV ultraviolet
<i>Ru'(phenphen)Ru'</i> [{Ru(bpy) ₂] ₂ (μ-phenphen)] ⁴⁺	v volume
<i>Ru(tpphz)</i> [Ru(phen) ₂ (tpphz)] ²⁺	Vis, VIS visible
	vs. versus

References

- [1] A. Jean, *Nature*, (2007), 448(7152), 404–405.
- [2] http://www.bp.com/liveassets/bp_internet/globalbp/globalbp_uk_english/reports_and_publications/statistical_energy_review_2008/STAGING/local_assets/2009_downloads/statistical_review_of_world_energy_full_report_2009.xls, accessed on March 10th 2011.
- [3] OECD, *World Energy Outlook 2010*, (2010), OECD Publishing, p. 738.
- [4] N. Armaroli, V. Balzani, *Angew. Chem. Int. Ed.*, (2007), 46(1-2), 52–66.
- [5] *Erste Teilstudie Peak Oil - Sicherheitspolitische Implikationen knapper Ressourcen*, (2010), Zentrum für Transformation der Bundeswehr, Dezernat Zukunftsanalyse, Strausberg, p. 99.
- [6] *Pressemitteilung Nr. 7/2010*, (2010), Arbeitsgemeinschaft Energiebilanzen e.V., Berlin, p. 5.
- [7] OECD/IEA, *CO2 emissions from fuel combustion*, N. Tanaka, (Ed.), (2010), International Energy Agency (IEA), p. 130.
- [8] H. G. Babies, A. Bahr, U. Benitz, J. Bremer, D. Franke, J. Meßner, S. Rehder, H. Rempel, M. Schauer, S. Schmidt, U. Schwarz-Schampera, *Reserven, Ressourcen und Verfügbarkeit von Energierohstoffen 2010*, B. Cramer, H., ruleit, (Eds.), (2010), Bundesanstalt für Geowissenschaften und Rohstoffe, Hannover, Hannover, p. 86.
- [9] N. Armaroli, V. Balzani, *ChemSusChem*, (2011), 4, 21–36.
- [10] J. Sawin, E. Martinot, *REN21 Renewables 2010 Global Status Report*, (2010), Renewable Energy Policy Network for the 21st Century (REN21), Washington, DC, 2010 edition, p. 7.
- [11] T. R. Cook, D. K. Dogutan, S. Y. Reece, Y. Surendranath, T. S. Teets, D. G. Nocera, *Chem. Rev.*, (2010), 110(11), 6474–6502.
- [12] N. S. Lewis, D. G. Nocera, *Proc. Natl. Acad. Sci. U. S. A.*, (2006), 103(43), 15729–15735.
- [13] C. Gueymard, D. Myers, K. Emery, *Sol. Energy*, (2002), 73(6), 443–467.
- [14] http://en.wikipedia.org/wiki/File:PS10_solar_power_tower.jpg, accessed on March 9th 2011.
- [15] N. Serpone, A. V. Emeline, S. Horikoshi, *Photochemistry*, (2009), 37, 300–361.
- [16] B. O'Regan, M. Grätzel, *Nature*, (1991), 353(6346), 737–740.
- [17] M. Grätzel, P. Liska, *US 5084365*, (1990), (28. 01. 1998).
- [18] L. Sun, L. Hammarström, B. Åkermark, S. Styring, *Chem. Soc. Rev.*, (2001), 30(1), 36–49.
- [19] G. Renger, *Curr. Sci.*, (2010), 98(10), 1305–1319.
- [20] B. Loll, J. Kern, W. Saenger, A. Zouni, J. Biesadka, *Nature*, (2005), 438(7070), 1040–1044.
- [21] A. Albin, M. Fagnoni, *ChemSusChem*, (2008), 1(1-2), 63–66.
- [22] G. Ciamician, *Science*, (1912), 36(926), 385–394.
- [23] P. T. Anastas, J. C. Warner, *Green Chemistry: Theory, Practice*, (1998), Oxford University Press, New York, p. 30.
- [24] N. J. Turro, *Modern Molecular Photochemistry*, N. J. Turro, (Ed.), (1991), University Science Books, Sausalito, CA, p. 628.
- [25] S. E. Braslavsky, *Pure Appl. Chem.*, (2007), 79(3), 293–465.

- [26] M. Chanon, M. Schiavello, J. C. Mialocq, L. G. Arnaut, S. J. Formosinho, J. Santamaria, C. Ferroud, C. Kutal, J. Belloni, M. Julliard, E. Amouyal, I. Rico-Lattes, A. Lattes, P. Mathis, *Homogeneous Photocatalysis (Wiley Series in Photoscience, Photoengineering)*, Vol. 2, M. Chanon, (Ed.), (1997), John Wiley & Sons, Chichester, New York, Weinheim, Brisbane, Singapore, Toronto, p. 426.
- [27] G. Kars, U. Gündüz, *Int. J. Hydrogen Energ.*, (2010), 35(13), 6646–6656.
- [28] H. Dau, C. Limberg, T. Reier, M. Risch, S. Roggan, P. Strasser, *ChemCatChem*, (2010), 2(7), 724–761.
- [29] E. Amouyal, *Sol. Energy Mater. Sol. Cells*, (1995), 38(1-4), 249–276.
- [30] A. J. Bard, *J. Am. Chem. Soc.*, (2010), 132(22), 7559–7567.
- [31] S. C. Roy, O. K. Varghese, M. Paulose, C. A. Grimes, *ACS Nano*, (2010), 4(3), 1259–78.
- [32] J.-M. Lehn, J.-P. Sauvage, *Nouv. J. Chim.*, (1977), 1(6), 449–451.
- [33] K. Kalyanasundaram, J. Kiwi, M. Grätzel, *Helv. Chim. Acta*, (1978), 61(7), 2720–2730.
- [34] M. Kirch, J.-M. Lehn, J.-P. Sauvage, *Helv. Chim. Acta*, (1979), 62(4), 1345–1384.
- [35] A. Inagaki, M. Akita, *Coord. Chem. Rev.*, (2010), 254(11-12), 1220–1239.
- [36] A. Juris, V. Balzani, F. Barigelletti, S. Campagna, P. Zelewsky, A. Von Belser, *Coord. Chem. Rev.*, (1988), 84(1), 85–277.
- [37] S. Losse, J. G. Vos, S. Rau, *Coord. Chem. Rev.*, (2010), 254(21-22), 2492–2504.
- [38] U. Schubert, H. Hofmeier, G. R. Newkome, *Modern Terpyridine Chemistry*, (2006), Wiley-VCH, p. 229.
- [39] M. Abrahamsson, M. Jäger, T. Osterman, L. Eriksson, P. Persson, H.-C. Becker, O. Johansson, L. Hammarström, *J. Am. Chem. Soc.*, (2006), 128(39), 12616–12617.
- [40] V. Balzani, A. Juris, M. Venturi, S. Campagna, S. Serroni, *Chem. Rev.*, (1996), 96(2), 759–834.
- [41] N. H. Damrauer, G. Cerullo, A. Yeh, T. R. Boussie, C. V. Shank, J. K. McCusker, *Science*, (1997), 275(5296), 54–57.
- [42] S. Sharma, F. Lombeck, L. Eriksson, O. Johansson, *Chem. Eur. J.*, (2010), 16(24), 7078–7081.
- [43] R. A. Marcus, *Angew. Chem. Int. Ed.*, (1993), 32(8), 1111–1121.
- [44] R. Marcus, N. Sutin, *Biochim. Biophys. Acta*, (1985), 811, 265–322.
- [45] I. Romero, M. Rodríguez, C. Sens, J. Mola, M. Rao Kollipara, L. Francàs, E. Mas-Marza, L. Escriche, A. Llobet, *Inorg. Chem.*, (2008), 47(6), 1824–1834.
- [46] A. Guskov, J. Kern, A. Gabdulkhakov, M. Broser, A. Zouni, W. Saenger, *Nat. Struct. Mol. Biol.*, (2009), 16(3), 334–342.
- [47] M. W. Kanan, D. G. Nocera, *Science*, (2008), 321(5892), 1072–1075.
- [48] K. Maeda, K. Domen, *J. Phys. Chem. Lett.*, (2010), 1, 2655–2661.
- [49] S. W. Gersten, G. J. Samuels, T. J. Meyer, *J. Am. Chem. Soc.*, (1982), 104(14), 4029–4030.
- [50] S. Romain, F. Bozoglian, X. Sala, A. Llobet, *J. Am. Chem. Soc.*, (2009), 131(8), 2768–2769.
- [51] L. Duan, A. Fischer, Y. Xu, L. Sun, *J. Am. Chem. Soc.*, (2009), 131(30), 10397–10399.
- [52] K. N. Ferreira, T. M. Iverson, K. Maghlaoui, J. Barber, S. Iwata, *Science*, (2004), 303(5665), 1831–1838.

- [53] J. Barber, *Phil. Trans. R. Soc. A*, (2007), 365(1853), 1007–1023.
- [54] J. T. Muckerman, D. E. Polyansky, T. Wada, K. Tanaka, E. Fujita, *Inorg. Chem.*, (2008), 47(6), 1787–1802.
- [55] F. Liu, J. J. Concepcion, J. W. Jurss, T. Carolaccia, J. L. Templeton, T. J. Meyer, *Inorg. Chem.*, (2008), 47(6), 1727–1752.
- [56] G. Zhang, R. Zong, H.-W. Tseng, R. P. Thummel, *Inorg. Chem.*, (2008), 47(3), 990–998.
- [57] L. Li, L. Duan, Y. Xu, M. Gorlov, A. Hagfeldt, L. Sun, *Chem. Commun.*, (2010), 46(39), 7307–7309.
- [58] L. Duan, Y. Xu, P. Zhang, M. Wang, L. Sun, *Inorg. Chem.*, (2010), 49(1), 209–215.
- [59] X. Chen, S. Shen, L. Guo, S. S. Mao, *Chem. Rev.*, (2010), 110(11), 6503–6570.
- [60] J. C. Gordon, G. J. Kubas, *Organometallics*, (2010), 29(21), 4682–4701.
- [61] J. R. Bolton, *Solar Energy*, (1996), 57(1), 37–50.
- [62] W. J. Youngblood, S.-H. A. Lee, K. Maeda, T. E. Mallouk, *Acc. Chem. Res.*, (2009), 42(12), 1966–1973.
- [63] L.-C. Song, X. Luo, Y.-Z. Wang, B. Gai, Q.-M. Hu, *Journal of Organometallic Chemistry*, (2009), 694(1), 103–112.
- [64] R. K. Thauer, A.-K. Kaster, M. Goenrich, M. Schick, T. Hiromoto, S. Shima, *Annu. Rev. Biochem.*, (2010), 79, 507–536.
- [65] C. M. Thomas, T. Liu, M. B. Hall, M. Y. Darensbourg, *Inorg. Chem.*, (2008), 47(15), 7009–7024.
- [66] P. Zhang, M. Wang, Y. Na, X. Li, Y. Jiang, L. Sun, *Dalton Trans.*, (2010), 39(5), 1204–1206.
- [67] J. W. Peters, *Science*, (1998), 282(5395), 1853–1858.
- [68] C.-Y. Liu, P. Knochel, *The Journal of organic chemistry*, (2007), 72(19), 7106–15.
- [69] A. F. Heyduk, D. G. Nocera, *Science*, (2001), 293(5535), 1639–1641.
- [70] L. Duan, M. Wang, P. Li, Y. Na, N. Wang, L. Sun, *Dalton Trans.*, (2007), (13), 1277–1283.
- [71] S. Hansen, (2009). Ph.D. thesis.
- [72] J.-m. Lehn, *Angew. Chem. Int. Ed.*, (1988), 27(1), 89–112.
- [73] D. J. Cram, *Angew. Chem. Int. Ed.*, (1988), 27(8), 1009–1020.
- [74] C. J. Pedersen, *Angew. Chem. Int. Ed.*, (1988), 27(8), 1021–1027.
- [75] G. Accorsi, N. Armaroli, V. Balzani, G. Bergamini, S. Campagna, F. Cardinali, C. Chiorboli, M. Indelli, N. A. P. Kane-Maguire, A. Listorti, F. Nastasi, F. Puntoriero, F. Scandola, *Topics in Current Chemistry: Photochemistry, Photophysics of Coordination Compounds I*, Vol. 280 of *Topics in Current Chemistry*, V. Balzani, S. Campagna, (Eds.), (2007), Springer Berlin Heidelberg, Berlin, Heidelberg, p. 265.
- [76] M. R. Wasielewski, *Chemical Reviews*, (1992), 92(3), 435–461.
- [77] J. P. Sauvage, J. P. Collin, J. C. Chambron, S. Guillerez, C. Coudret, V. Balzani, F. Barigelletti, L. De Cola, L. Flamigni, *Chem. Rev.*, (1994), 94(4), 993–1019.
- [78] S. Campagna, S. Serroni, S. Bodge, F. M. MacDonnell, *Inorg. Chem.*, (1999), 38(4), 692–701.
- [79] C. Chiorboli, M. a. J. Rodgers, F. Scandola, *Journal of the American Chemical Society*, (2003), 125(2), 483–91.
- [80] S. Rau, B. Schäfer, D. Gleich, E. ers, M. Rudolph, M. Friedrich, H. Görls, W. Henry, J. G. Vos, *Angew. Chem. Int. Ed.*, (2006), 45(37), 6215–6218.

- [81] S. Tschierlei, M. Presselt, C. Kuhnt, A. Yartsev, T. Pascher, V. Sundström, M. Karnahl, M. Schwalbe, B. Schäfer, S. Rau, M. Schmitt, B. Dietzek, J. Popp, *Chem. Eur. J.*, (2009), 15(31), 7678–7688.
- [82] H. Ozawa, M.-a. Haga, K. Sakai, *J. Am. Chem. Soc.*, (2006), 128(15), 4926–4927.
- [83] S. Rau, D. Walther, J. G. Vos, *Dalton Trans.*, (2007), (9), 915–919.
- [84] M. Elvington, J. Brown, S. M. Arachchige, K. J. Brewer, *J. Am. Chem. Soc.*, (2007), 129(35), 10644–10645.
- [85] A. Fihri, V. Artero, A. Pereira, M. Fontecave, *Dalton Trans.*, (2008), (41), 5567–5569.
- [86] A. Fihri, V. Artero, M. Razavet, C. Baffert, W. Leibl, M. Fontecave, *Angew. Chem. Int. Ed.*, (2008), 47(3), 564–567.
- [87] C. Li, M. Wang, J. Pan, P. Zhang, R. Zhang, L. Sun, *J. Organomet. Chem.*, (2009), 694(17), 2814–2819.
- [88] S. Tschierlei, M. Karnahl, M. Presselt, B. Dietzek, J. Guthmuller, L. González, M. Schmitt, S. Rau, J. Popp, *Angew. Chem.*, (2010), 122(23), 4073–4076.
- [89] B. Schäfer, *Dissertation*, (2006), Friedrich-Schiller-Universität Jena, p. 218.
- [90] M. Schwalbe, *Dissertation*, (2007), Friedrich-Schiller-Universität Jena, p. 194.
- [91] S. M. Arachchige, J. R. Brown, E. Chang, A. Jain, D. F. Zigler, K. Rangan, K. J. Brewer, *Inorg. Chem.*, (2009), 48(5), 1989–2000.
- [92] S. Jasimuddin, T. Yamada, K. Fukuju, J. Otsuki, K. Sakai, *Chem. Commun.*, (2010).
- [93] H. Ozawa, Y. Yokoyama, M.-a. Haga, K. Sakai, *Dalton Trans.*, (2007), (12), 1197–206.
- [94] P. Lei, M. Hedlund, R. Lomoth, H. Rensmo, O. Johansson, L. Hammarström, *J. Am. Chem. Soc.*, (2008), 130(1), 26–27.
- [95] T. D. Pilz, N. Rockstroh, S. Rau, *J. Coord. Chem.*, (2010), 63(14), 2727–2742.
- [96] A. Bencini, V. Lippolis, *Coord. Chem. Rev.*, (2010), 254(17-18), 2096–2180.
- [97] M. Yamada, Y. Nakamura, S. Kuroda, I. Shimao, *Bull. Chem. Soc. Jpn.*, (1990), 63(9), 2710–2712.
- [98] M. Schmittel, A. Ganz, D. Fenske, *Org. Lett.*, (2002), 4(14), 2289–2292.
- [99] R. Zong, R. P. Thummel, *J. Am. Chem. Soc.*, (2004), 126(35), 10800–10801.
- [100] R. Zong, R. P. Thummel, *Inorg. Chem.*, (2005), 44(17), 5984–5986.
- [101] G. Ambrosi, M. Formica, V. Fusi, L. Giorgi, A. Guerri, M. Micheloni, P. Paoli, R. Pontellini, P. Rossi, *Inorg. Chem.*, (2007), 46(11), 4737–4748.
- [102] C. Bazzicalupi, A. Bencini, S. Ciattini, C. Giorgi, A. Masotti, P. Paoletti, B. Valtancoli, N. Navon, D. Meyerstein, *Dalton Trans.*, (2000), (14), 2383–2391.
- [103] D. L. Melton, D. G. Vanderveer, R. D. Hancock, *Inorg. Chem.*, (2006), 45(23), 9306–9314.
- [104] M. Schmittel, A. Ganz, D. Fenske, M. Herderich, *Dalton Trans.*, (2000), (3), 353–359.
- [105] J.-p. Sauvage, *Acc. Chem. Res.*, (1998), 31(10), 611–619.
- [106] D. Tzalis, Y. Tor, S. Failla, J. S. Siegel, *Tetrahedron Lett.*, (1995), 36(20), 3489–3490.
- [107] D. Tzalis, Y. Tor, *Chem. Commun.*, (1996), (9), 1043–1044.
- [108] B. Schäfer, H. Görls, S. Meyer, W. Henry, J. G. Vos, S. Rau, *Eur. J. Inorg. Chem.*, (2007), 2007(25), 4056–4063.
- [109] M. Schmittel, A. Ganz, *Synlett*, (1997), 1997(6), 710–712.

- [110] E. C. Glazer, D. Magde, Y. Tor, *J. Am. Chem. Soc.*, (2005), 127(12), 4190–4192.
- [111] E. C. Glazer, D. Magde, Y. Tor, *J. Am. Chem. Soc.*, (2007), 129(27), 8544–51.
- [112] A. E. Friedman, J. C. Chambron, J. P. Sauvage, N. J. Turro, J. K. Barton, *J. Am. Chem. Soc.*, (1990), 112(12), 4960–4962.
- [113] J. Bolger, A. Gourdon, E. Ishow, J.-P. Launay, *Inorganic Chemistry*, (1996), 35(10), 2937–2944.
- [114] W. Paw, R. Eisenberg, *Inorganic Chemistry*, (1997), 36(11), 2287–2293.
- [115] Y. Pellegrin, A. Quaranta, P. Dorlet, M. F. Charlot, W. Leibl, A. Aukauloo, *Chem. Eur. J.*, (2005), 11(12), 3698–3710.
- [116] M. Auth, *Dissertation*, (2008), Friedrich-Schiller-Universität Jena, p. 311.
- [117] S. Rau, M. Auth, *DE 102007025424*, (2008), (13.08.2009).
- [118] F. Gloaguen, T. B. Rauchfuss, *Chem. Soc. Rev.*, (2009), 38(1), 100–108.
- [119] S. Zhang, G. Leem, L.-O. Srisombat, T. R. Lee, *J. Am. Chem. Soc.*, (2008), 130(1), 113–120.
- [120] S. Rau, R. Fischer, M. Jäger, B. Schäfer, S. Meyer, G. Kreisel, H. Görls, M. Rudolf, W. Henry, J. G. Vos, *European Journal of Inorganic Chemistry*, (2004), 2004(10), 2001–2003.
- [121] J. Mlochowski, *Rocz. Chem.*, (1974), 48(12), 2145–2155.
- [122] V. Dénes, R. Chira, *J. Prakt. Chem.*, (1978), 320(1), 172–175.
- [123] M. Feng, K. S. Chan, *Organometallics*, (2002), 21(13), 2743–2750.
- [124] B. Chesneau, A. Passelände, P. Hudhomme, *Org. Lett.*, (2009), 11(3), 649–652.
- [125] M. Karnahl, S. Krieck, H. Görls, S. Tschierlei, M. Schmitt, J. Popp, D. Chartrand, G. S. Hanan, R. Groarke, J. G. Vos, S. Rau, *Eur. J. Inorg. Chem.*, (2009), 2009(33), 4962–4971.
- [126] M. Karnahl, S. Tschierlei, C. Kuhnt, B. Dietzek, M. Schmitt, J. Popp, M. Schwalbe, S. Krieck, H. Görls, F. W. Heinemann, S. Rau, *Dalton Trans.*, (2010), 39(9), 2359–2370.
- [127] J. Schöffel, *Diploma Thesis*, (2004), Friedrich-Schiller-Universität Jena, p. 79.
- [128] M. Bennett, G. Wilkinson, *Chem. Ind.*, (1959), 48, 1516–1516.
- [129] C. Sotiriou-Leventisa, J. Yanga, P. Duana, N. Leventis, *Synt. Commun.*, (2004), 34(19), 3491–3496.
- [130] V. Balzani, F. Bolletta, M. T. Gandolfi, M. Maestri, *Topics in Current Chemistry: Bimolecular electron transfer reactions of the excited states of transition metal complexes*, (1978), p. Vol. 75, 1–64.
- [131] P. M. Griffiths, F. Loiseau, F. Puntoriero, S. Serroni, S. Campagna, *Chem. Commun.*, (2000), (23), 2297–2298.
- [132] B. Durham, J. V. Caspar, J. K. Nagle, T. J. Meyer, *J. Am. Chem. Soc.*, (1982), 104(18), 4803–4810.
- [133] Y.-Z. Hu, Q. Xiang, R. P. Thummel, *Inorg. Chem.*, (2002), 41(13), 3423–3428.
- [134] K. Yamauchi, S. Masaoka, K. Sakai, *J. Am. Chem. Soc.*, (2009), 131(24), 8404–8406.
- [135] M. Ogawa, G. Ajayakumar, S. Masaoka, H.-B. Kraatz, K. Sakai, *Chemistry (Weinheim an der Bergstrasse, Germany)*, (2011), 17(4), 1148–62.
- [136] C. Wolf, *Dynamic Stereochemistry of Chiral Compounds: Principles, Applications*, (2008), RCS Publishing, Cambridge, p. 512.
- [137] L. Ademi, E. C. Constable, C. E. Housecroft, M. Neuburger, S. Schaffner, *Dalton Trans.*, (2003), (24), 4565–4567.

- [138] L. Pazderski, J. Tousek, J. Sitkowski, L. Kozerski, E. Szlyk, *Magn. Reson. Chem.*, (2007), 45(12), 1045–1058.
- [139] M. Pfeffer, *Personal Communication / Dissertation*, (2011), Friedrich-Alexander-Universität Erlangen-Nürnberg, p. –.
- [140] M. Schwalbe, B. Schäfer, H. Görls, S. Rau, S. Tschierlei, M. Schmitt, J. Popp, G. Vaughan, W. Henry, J. G. Vos, *European Journal of Inorganic Chemistry*, (2008), 2008(21), 3310–3319.
- [141] M. Oki, *Topics in Stereochemistry: Recent Advances in Atropisomerism.*, N. Allinger, N. Eliel, S. Wilen, (Eds.), (1983), John Wiley & Sons, New York, p. 81.
- [142] A. Hauser, E. Krausz, *Chem. Phys. Lett.*, (1987), 138(4), 355–360.
- [143] S. Kamath, V. Uma, T. S. Srivastava, *Inorg. Chim. Acta*, (1989), 161(1), 49–56.
- [144] H. Ozawa, K. Sakai, *Chem. Commun.*, (2011), 47(8), 2227–42.
- [145] M. B. Robin, P. Day, *Adv. Inorg. Chem.*, (1968), 10, 247–422.
- [146] F. Glorius, S. Bellemin-Laponnaz, E. Despagnet-Ayoub, S. Díez-González, L. Gade, J. Louie, S. Nolan, E. Peris, T. Ritter, M. Rogers, S. S. Stahl, T. Tekavec, *Topics in Organometallic Chemistry: N-Heterocyclic Carbenes in Transition Metal Catalysis*, J. M. Brown, P. H. Dixneuf, A. Fürstner, L. S. Hegedus, P. Hofmann, P. Knochel, G. van Koten, S. Murai, M. Reetz, (Eds.), (2007), Springer, p. 240.
- [147] E. O. Fischer, A. Maasböl, *Angew. Chem. Int. Ed.*, (1964), 3(8), 580–581.
- [148] H.-W. Wanzlick, H.-J. Schönherr, *Angew. Chem. Int. Ed.*, (1968), 7(2), 141–142.
- [149] H. Jacobsen, A. Correa, A. Poater, C. Costabile, L. Cavallo, *Coordination Chemistry Reviews*, (2009), 253(5–6), 687–703.
- [150] H. Jacobsen, A. Correa, C. Costabile, L. Cavallo, *J. Organomet. Chem.*, (2006), 691(21), 4350–4358.
- [151] A. J. Arduengo, R. L. Harlow, M. Kline, *J. Am. Chem. Soc.*, (1991), 113(1), 361–363.
- [152] W. A. Herrmann, M. Ellison, J. Fischer, C. Köcher, G. R. J. Artus, *Angew. Chem. Int. Ed.*, (1995), 34(21), 2371–2374.
- [153] M. Scholl, S. Ding, C. W. Lee, R. H. Grubbs, *Org. Lett.*, (1999), 1(6), 953–956.
- [154] J. B. Dumas, E. Peligot, *Ann. Chim. Phys.*, (1835), 58, 5.
- [155] A. Geuther, *Ann. Chem. Pharm.*, (1862), 123, 121.
- [156] H. Staudinger, O. Kupfer, *Berichte der deutschen chemischen Gesellschaft*, (1912), 45(1), 501–509.
- [157] H. Scheibler, *Chem. Ber.*, (1926), 59, 1022–1032.
- [158] H. Meerwein, H. Rathjen, H. Werner, *Berichte der deutschen chemischen Gesellschaft (A, B Series)*, (1942), 75(12), 1610–1622.
- [159] W. V. E. Doering, A. K. Hoffmann, *J. Am. Chem. Soc.*, (1954), 76(23), 6162–6165.
- [160] P. S. Skell, R. C. Woodworth, *J. Am. Chem. Soc.*, (1956), 78(17), 4496–4497.
- [161] H. W. Wanzlick, *Angew. Chem. Int. Ed.*, (1962), 1(2), 75–80.
- [162] K. Öfele, *J. Organomet. Chem.*, (1968), 12(3), P42–P43.
- [163] C. Deissler, F. Rominger, D. Kunz, *Dalton Trans.*, (2009), (35), 7152–7167.
- [164] S. P. Nolan, *Acc. Chem. Res.*, (2011), 44(2), 91–100.
- [165] N. Marion, S. P. Nolan, *Acc. Chem. Res.*, (2008), 41(11), 1440–1449.

- [166] M. Nonnenmacher, D. Kunz, F. Rominger, *Organometallics*, (2008), 27(7), 1561–1568.
- [167] E. L. Rosen, C. D. Varnado, A. G. Tennyson, D. M. Khramov, J. W. Kamplain, D. H. Sung, P. T. Cresswell, V. M. Lynch, C. W. Bielawski, *Organometallics*, (2009), 28(23), 6695–6706.
- [168] H. M. Lee, P. L. Chiu, J. Y. Zeng, *Inorg. Chim. Acta*, (2004), 357(14), 4313–4321.
- [169] H. M. Lee, J. Y. Zeng, C.-H. Hu, M.-T. Lee, *Inorg. Chem.*, (2004), 43(21), 6822–6829.
- [170] F. E. Hahn, M. C. Jahnke, T. Pape, *Organometallics*, (2006), 25(25), 5927–5936.
- [171] A. M. Magill, D. S. McGuinness, K. J. Cavell, G. J. Britovsek, V. C. Gibson, A. J. White, D. J. Williams, A. H. White, B. W. Skelton, *J. Organomet. Chem.*, (2001), 617–618, 546–560.
- [172] H. V. Huynh, D. Yuan, Y. Han, *Dalton Trans.*, (2009), (35), 7262–7268.
- [173] D. Tapu, D. a. Dixon, C. Roe, *Chemical reviews*, (2009), 109(8), 3385–407.
- [174] E. A. Steck, A. R. Day, *J. Am. Chem. Soc.*, (1943), 65(3), 452–456.
- [175] J.-z. Wu, B.-h. Ye, L. Wang, L.-n. Ji, J.-y. Zhou, R.-h. Li, Z.-Y. Zhou, *Dalton Trans.*, (1997), (8), 1395–1402.
- [176] A. Bittermann, P. Härter, E. Herdtweck, S. D. Hoffmann, W. A. Herrmann, *J. Organomet. Chem.*, (2008), 693(12), 2079–2090.
- [177] S.-M. Shen, *Acta Cryst.*, (2009), 65(10), o2332–o2332.
- [178] L. Benhamou, E. Chardon, G. Lavigne, S. Bellemin-Laponnaz, V. Cesar, *Chem. Rev.*, (2011), 111(4), 2705–2733.
- [179] A. J. Arduengo, J. R. Goerlich, W. J. Marshall, *J. Am. Chem. Soc.*, (1995), 117(44), 11027–11028.
- [180] V. Böhm, W. Herrmann, *Angew. Chem. Int. Ed.*, (2000), 39(22), 4036–4038.
- [181] Y. Yamaguchi, T. Kashiwabara, K. Ogata, Y. Miura, Y. Nakamura, K. Kobayashi, T. Ito, *Chem. Commun.*, (2004), (19), 2160–2161.
- [182] H. M. J. Wang, I. J. B. Lin, *Organometallics*, (1998), 17(5), 972–975.
- [183] D. Rieger, *Inorg. Chim. Acta*, (1994), 222(1-2), 275–290.
- [184] B. Bildstein, M. Malaun, H. Kopacka, K. Wurst, M. Mitterböck, K.-h. Ongania, G. Opromolla, P. Zanello, *Organometallics*, (1999), 18(21), 4325–4336.
- [185] P.-G. Li, Q.-L. Wang, D.-S. Li, F. Fu, G.-C. Qi, *Z. Kristallogr.*, (2006), 221(3), 391–392.
- [186] C. Winn, F. Guillen, J. Pytkowicz, S. Roland, P. Mangeney, A. Alexakis, *J. Organomet. Chem.*, (2005), 690(24-25), 5672–5695.
- [187] J. Pytkowicz, S. Roland, P. Mangeney, *J. Organomet. Chem.*, (2001), 631(1-2), 157–163.
- [188] J. Berding, H. Kooijman, A. L. Spek, E. Bouwman, *J. Organomet. Chem.*, (2009), 694(14), 2217–2221.
- [189] F. Ullah, M. K. Kindermann, P. G. Jones, J. Heinicke, *Organometallics*, (2009), 28(8), 2441–2449.
- [190] A. R. Chianese, X. Li, M. C. Janzen, J. W. Faller, R. H. Crabtree, *Organometallics*, (2003), 22(8), 1663–1667.
- [191] X. Hu, Y. Tang, P. Gantzel, K. Meyer, *Organometallics*, (2003), 22(4), 612–614.
- [192] B. Jing, M. Zhang, T. Shen, *Spectrochim. Acta. A, Mol. Biomol. Spec.*, (2004), 60(11), 2635–2641.
- [193] R. M. Hartshorn, J. K. Barton, *J. Am. Chem. Soc.*, (1992), 114(15), 5919–5925.

- [194] C. Liu, J. Li, B. Li, Z. Hong, F. Zhao, S. Liu, W. Li, *Chemical Physics Letters*, (2007), 435(1-3), 54–58.
- [195] T. Ramnial, S. A. Taylor, M. L. Bender, B. Gorodetsky, P. T. K. Lee, D. A. Dickie, B. M. McCollum, C. C. Pye, C. J. Walsby, J. A. C. Clyburne, *J. Org. Chem.*, (2008), 73(3), 801–812.
- [196] C.-K. Tan, V. Newberry, T. R. Webb, C. A. McAuliffe, *Dalton Trans.*, (1987), (6), 1299–1303.
- [197] G. S. Hanan, D. Volkmer, U. S. Schubert, J.-M. Lehn, G. Baum, D. Fenske, *Angew. Chem. Int. Ed.*, (1997), 36(17), 1842–1844.
- [198] G. S. Hanan, U. S. Schubert, D. Volkmer, E. Rivière, J.-M. Lehn, N. Kyritsakas, J. Fischer, *Can. J. Chem.*, (1997), 75(2), 169–182.
- [199] COLLECT, *Data Collection Software*, (1998), Nonius B.V., Netherlands.
- [200] SADABS, (*version 2.06*) 2002., (2002), Bruker Analytical X-Ray Instruments Inc., Madison, Wisconsin (USA).
- [201] G. M. Sheldrick, *Acta Cryst A*, (2008), 64(Pt 1), 112–122.
- [202] G. M. Sheldrick, *Acta Crystallogr., Sect. A: Found. Crystallogr.*, (1990), 46(6), 467–473.
- [203] G. M. Sheldrick, *SHELXTL NT (version 6.12)*, (2002), Bruker Analytical X-Ray Instruments Inc., Madison, Wisconsin (USA).
- [204] T. Hadda, H. L. Bozec, *Polyhedron*, (1988), 7(7), 575–577.
- [205] P. Belser, A. V. Zelewsky, *Helv. Chim. Acta*, (1980), 63(6), 1675–1702.
- [206] S. Itoh, J. Maruta, S. Fukuzumi, *J. Chem. Soc. Perkin Trans 2*, (1996), (7), 1429–1433.
- [207] A. Kleineweischede, J. Mattay, *Eur. J. Org. Chem.*, (2006), 2006(4), 947–957.
- [208] B. Heyn, B. Hippler, G. Kreisel, H. Schreer, D. Walther, *Anorganische Synthesechemie - Ein integriertes Praktikum*, (1990), Springer Verlag, Heidelberg, p. 235.

Tabellarischer Lebenslauf

Name :	Thomas David Pilz
Geburtsdatum :	24. 05. 1982
Geburtsort:	Rochlitz
Staatsangehörigkeit :	deutsch
Familienstand :	ledig
Schullaufbahn:	1988 - 1992 Juri Gagarin Schule Geithain 1992 - 2001 Conrad Felixmüller Gymnasium Geithain 1998 - 1999 Austauschschuljahr in den USA, Tri Point High School, Culom, IL 2001 Erlangung der allgemeinen Hochschulreife (Abitur)
Dienst:	2001 - 2002 Zivildienst beim Deutschen Roten Kreuz in Geithain
Studium:	2002 - 2007 Chemiestudium an der FSU-Jena Diplomarbeit zu <i>“Synthese und Charakterisierung von heterooligo- nuklearen photoredoxaktiven Metallkomplexen”</i> Abschluss Diplom Chemie
Berufliche Tätigkeiten:	2007 Wissenschaftliche Hilfskraft in der Arbeitsgruppe Prof. Dr. Ulrich S. Schubert am IOCMC der FSU-Jena
Promotion:	2008 - 2011 Promotion an der FSU-Jena Thema: <i>Development of Novel Catalysts for the Photocatalytic Hydrogen Formation</i> Betreuer: Prof. Dr. Sven Rau sowie Prof. Dr. Matthias Westerhausen am IAAC der FSU-Jena
Förderung:	2008 - 2011 Gewährung eines dreijährigen Promotionsstipendiums durch die Carl-Zeiss Stiftung
Aufenthalte:	10-11/2008 Auslandsaufenthalt in der Arbeitsgruppe von Prof. Dr. Shigenobu Yano am Innovative Collaboration Center der Kyoto-Universität, Kyoto (Japan) 2009 - 2011 Regelmäßige Forschungsaufenthalte am Department Chemie und Pharmazie der FAU Erlangen-Nürnberg
Sonstiges:	2010 - 2011 Assoziiertes Mitglied im DFG Graduiertenkolleg 1626 <i>Chemical Photocatalysis</i> 09/2010 BAYHOST Reisestipendium zur 3 rd International Summer School <i>Supramolecular Systems in Chemistry and Biology</i> in Lviv (Ukraine)

Selbstständigkeitserklärung:

Ich erkläre, dass ich die vorliegende Arbeit selbständig und nur unter Verwendung der angegebenen Hilfsmittel und Literatur angefertigt habe.

Jena, den 28. 06. 2011

.....

Thomas David Pilz